Developing Implants for Ophthalmic Drug Delivery and Flow Modulation

Shivam Madaan

A thesis submitted for the degree of

Doctor of Philosophy (PhD)

University College London

School of Pharmacy

UCL

2020

Declaration

I, Shivam Madaan, confirm that the work presented in this thesis is my own. Where information has been derived from other sources, I confirm that this has been indicated in the thesis.

Shivam Madaan

Acknowledgements

A great number of individuals have been pivotal in the progress of my PhD, for which I am hugely grateful. First and foremost, I would like to extend my sincerest gratitude to Professors Steve Brocchini and Sir Peng T Khaw for giving me the opportunity to work under their supervision. Their attention to critical details while continually reminding me of the 'big picture' pushed me to re-evaluate commonly accepted paradigms. I further thank them for giving me the freedom that allowed me to make my own mistakes. Thank you for providing and protecting a positive research environment and the academic independence we enjoy as a research group. I would also like to extend my gratitude to Professor Ian Eames, whose guidance broadened my research horizons and whose discussions always brightened my day. I would also like to thank Lady Peggy Khaw for her support.

I would like to thank all my fellow labmates Christina, Raphael, Lesley, Saja and Lok at UCL School of Pharmacy and Christin at UCL Institute of Ophthalmology for the stimulating discussions, and for all the fun we have had throughout the PhD journey. In particular, I am grateful to Yann Bouremel for not only being one of the most meticulous engineers I got the opportunity to work with, but for being a true friend. I thank Richard Lee, Tamara Alhilfi, Clare Heaysman and Sahar Awwad for their help and advice on experiments. I would also like to thank Alastair Lockwood, Abeer Mohammed Ahmed and Athmar Al-Shohani, whose hard work laid the foundations of part of this thesis.

I would like to express my relentless gratitude to Alyssa and our families for their unconditional love and support that kept me going through my PhD journey with a smile on my face.

Finally, I gratefully acknowledge the funding received towards my PhD from The National Institute for Health Research (NIHR) Biomedical Research Centre at Moorfields Eye Hospital NHS Foundation Trust and UCL Institute of Ophthalmology.

List of publications and presentations arising from this thesis

Madaan, S., Bouremel, Y., Eames, I., Khaw, P., Brocchini, S. Using elastic pockets for ophthalmic drug delivery (Manuscript under preparation)

Madaan, S., Bouremel, Y., Khaw, P., Brocchini, S. Mathematical modelling of drug release kinetics from surfactant-laden hydrogels (Manuscript under preparation)

Bouremel, Y., Eames, I., **Madaan, S**., Brocchini, S. and Khaw, P. T. (2018) 'Compression of pressurised elastic pockets', *International Journal of Non-Linear Mechanics*. Elsevier Ltd, 107(October), pp. 10–15.

Madaan, S., Khaw, P. & Brocchini, S., 2018. Fighting Glaucoma with Hydrogels. 2018 *UCL School of Pharmacy*

Bouremel, Y., **Madaan, S.,** Lee, R. Khaw, P., Eames, I. 2017. Pursing of planar elastic pockets. *Journal of Fluids and Structures*, 70(January), pp.261–275.

Madaan, S., Khaw, P. & Brocchini, S., 2017. # T1006 Sub-conjunctival Hydrogel-Drug Implants (poster). In *AAPS Annual Meeting & Exposition*. San Diego, p. 1006.

Madaan, S., Lee, R., Heaysman, C., Alhilfi, T., Khaw, P., Brocchini, S. 2016. In-vitro characterisation of hydrogels for ocular drug delivery (poster). In *UCL School of Pharmacy*. p. 2003.

Abstract

Glaucoma is the leading cause of irreversible blindness worldwide. Surgical interventions are frequently necessary to lower the intraocular pressure (IOP) and do so by creating a new channel for aqueous humour to drain into the subconjunctival space. This channel can be formed by performing a glaucoma filtration surgery (GFS) or by implanting a glaucoma drainage device (GDD). However, excessive scarring at the surgical site blocks aqueous outflow, elevates IOP, and results in treatment failure. Drugs injected locally to control scarring rapidly clear from the subconjunctiva, and current implants are susceptible to a foreign body response. This work investigated strategies that could improve the outcomes of these current glaucoma interventions.

First, drug-eluting spacers were formulated using established biocompatible materials to prolong drug release in conditions representing the subconjunctival space post-GFS or GDD implantation. Of these formulations, the spacer containing non-ionic surfactant, Brij 98, at a concentration of 1.25% w/v was able to prolong the release of dexamethasone from poly(2-hydroxyethyl methacrylate) pHEMA hydrogels significantly longer (>30 days) than hydrogels containing no surfactant (<7 days) at therapeutically relevant drug concentrations *in vitro*.

Next, engineering principles were applied to inflated elastomeric membranes, which provided novel insights into considerations needed to design a novel ophthalmic drug delivery pump. Pocket geometry and material properties had a significant impact on internal pressure and subsequent pump function. Modelling data supports the feasibility of elastomeric pumps for prolonged subconjunctival drug delivery.

Finally, an alternative mechanism of IOP control was investigated. Novel and established hydrogel formulations were evaluated for aqueous permeability and mechanical integrity. Despite evidence to suggest the feasibility of hydrogels to modulate aqueous flow, the *in vitro* permeability of hydrogel candidates was determined to be too low to maintain optimal IOP. Furthermore, hydrogel permeability tended to negate its mechanical integrity, making them unsuitable candidate materials for GDD development.

Impact Statement

In an ever-ageing population, the chronic burden of glaucoma is increasing, and the World Health Organization estimates that 70 million people are affected by this disease worldwide. Pharmacological treatments in the form of eye-drops are the first line of treatment to lower intraocular pressure (IOP) to prevent irreversible vision loss, but poor-efficacy and low patient compliance necessitate surgical intervention. Glaucoma surgery halts disease progression by creating an artificial opening for aqueous humour drainage and lower IOP, but post-operative scar formation increases the failure rate of this therapy. This work investigated strategies that could improve the outcomes of these current glaucoma interventions.

Strategies were explored to formulate drug-eluting implants to prolong drug delivery of commonly used anti-inflammatory drugs in the subconjunctival space. Such an approach could prove beneficial in modulating post-surgical wound healing in glaucoma patients and improve surgical outcomes. Further research in this area could be aimed at characterising this drug-spacer system with different drug-polymer combinations, depending on the intended indication. The use of such an implant might further be extrapolated to different indications requiring localised drug delivery in different parts of the body, minimising the potential for systemic side effects.

Next, crucial relationships governing fluid-release from elastomeric pockets were elucidated that could be directly applied for the development of an elastomeric pump device. Currently, no such pump has been approved for human use, and the findings from this thesis could be used to advance the research in mini-pump design that is implantable in the subconjunctival space. The experimental results were based on the analysis of larger pockets, but through scaling analysis and data modelling, recommendations were provided for designing implantable elastomeric pumps. However, a scaled-down examination of elastomeric pockets is warranted to confirm the relationship coefficients that have been reported in this thesis and further work in this direction is underway.

Finally, biocompatible materials were explored for glaucoma drainage device (GDD) development. Novel and established hydrogels were assessed for their potential to modulate the aqueous flow in the eye. Contrary to previous studies that have reported significant effects of chemical modification on the hydrogel permeability, in

most cases, statistically significant improvements in permeability were not observed. The permeability results were somewhat counterintuitive and raised intriguing questions regarding the nature and extent of water flow through hydrogels and the distinct separation of two phenomena; water flow and water absorption. Even though some hydrogels modulated water flow that was close to the flow of aqueous humour in the eye, these candidate materials failed to meet the criteria for clinical-handling. Further research to disseminate the differences in the underlying mechanisms involved in water transport and water absorption in hydrogels would be of merit. This would help to achieve a better understanding of the molecular interactions involved between water and biomaterials, which could aid in the more precise regulation of water permeability by using these biomaterials, making them even more useful to ongoing GDD development.

The original research described in this thesis has been presented at international conferences and published in peer-reviewed journals.

Table of contents

List of Figures

List of Tables

List of Abbreviations

5-FU	5- Fluorouracil
Ac-HA	Acrylated hyaluronic acid
AC	Anterior chamber
ACG	Angle-closure glaucoma
AIBN	2,2-azobis(2-methylpropionitrile)
AGD	Ahmed glaucoma device
AMD	Acute macular degeneration
APS	Ammonium persulfate
ALT	Argon laser trabeculoplasty
CMC	Critical micelle concentration
Da	Dalton
DDS	Drug delivery system
DEX	Dexamethasone
DI water	De-ionised water
DLS	Dynamic scanning calorimetry
DMF	Dimethylformamide
DOX	Doxycycline
DSC	Differential scanning calorimetry
ECM	Extracellular matrix
EGDMA	Ethylene glycol dimethacrylate
ESEM	Environmental Scanning Electron Microscopy
EWC	Equilibrium water content
FDA	Food and Drug Administration
GDD	Glaucoma drainage device
GFS	Glaucoma filtration surgery
GMA	Glycidyl methacrylate
GP	Glycerophosphate
HA	Hyaluronic acid
HAZ	Heat affected zone
HEMA	2-hydroxyethyl methacrylate
HPMA	2-hydroxypropyl methacrylate
HPLC	High performance liquid chromatography
ID	Inner diameter
IOL	Intraocular lenses
IOP	Intraocular pressure
IPN	Interpenetrating network
IVT	Intravitreal
JCT	Juxtacanalicular tissue
kDa	kiloDalton
kPa	Kilopascal
MAA	Methacrylic acid
MBAM	Methylene bisacrylamide
MMA	Methyl methacrylate
MMC	Mitomycin C
mmHg	Millimetres mercury
MMP	Matrix metalloproteinases
MMPi	Matrix metalloproteinases inhibitor

MPa	Megapascal
MPC	2-methacryloyloxyethyl phosphorylcholine
mV	Millivolt
MW	Molecular weight
NaOH	Sodium hydroxide
NIPAAm	N-isopropyl acrylamide
OAG	Open-angle glaucoma
OD	Outer diameter
Pa	Pascal
PAA	Polyacrylic acid
PAMPS	Poly (2-acrylamide-2-methyl-1-propanesulfonic acid)
PBS	Phosphate buffered saline
PC	Phosphorylcholine
PCL	Poly(ε-caprolactone)
PDI	Poly-dispersity index
PEG	Polyethylene glycol
PEGDA	Poly(ethylene glycol) diacrylate
PEO	Poly(ethyleneoxide)
pHEMA	Poly(2-hydroxyethyl methacrylate)
PLGA	Poly(lactic-glycolic acid)
pMEMA	Poly(2-Methoxyethyl methacrylate)
pMEEMA	Poly(methoxy ethoxy ethyl methacrylate)
PMMA	Poly(methyl methacrylate)
PTFE	Polytetrafluoroethylene
PVA	Poly (vinyl) alcohol
PVP	Poly (N-vinyl pyrrolidone)
RGC	Retinal ganglion cells
SEM	Scanning Electron Microscopy
SIBS	Poly(styrene-b-isobutylene-b-styrene)
SR	Swelling ratio
THF	Tetrahydrofuran
TNF	Tumour necrosis factor
TM	Trabecular meshwork
UV	Ultraviolet
VEGF	Vascular endothelial growth factor
VP	N-Vinyl pyrrolidinone
W_b	Bound water
W_f	Free water

List of Symbols

a	Side length, radius (specified in the text)
$\mathbf{A}$	Area
$\boldsymbol{\beta}$	Coefficient of compression
$\boldsymbol{\rho}$	Density
$\boldsymbol{\gamma}$	Coefficient of stretching
δ	Engineering stress
σ	Poisson's ratio
$\boldsymbol{\varepsilon}$	Engineering strain
D,d	Diameter (specified in the text)
E	Young's modulus
F_{c}	Compressive force
$\boldsymbol{\mu}$	Dynamic viscosity
H,h	Height
L	Hydraulic conductivity
L,l	Length (specified in the text)
K	Permeability
P	Pressure
Q	Flow rate
R	Resistance
T	Thickness
V	Volume

Chapter 1 Introduction

1.1. Glaucoma and its impact

Glaucoma is defined as a group of optic neuropathies that are characterised by the progressive degeneration of retinal ganglion cells, causing structural changes to the optic nerve head and resulting in a gradual loss of the visual field in at least one eye (1). If not diagnosed and treated early, glaucoma will result in blindness as damage to the optic nerve is irreversible. Glaucoma is the leading cause of irreversible blindness worldwide (2–4).

It has been estimated that over 70 million people are currently affected globally by glaucoma and that approximately seven million of these are bilaterally blind (5). The global prevalence of glaucoma and irreversible blindness due to glaucoma has been projected to rise to 80 million and 11 million, respectively, by 2020 (2,6,7), while more recent estimates by the World Health Organization suggest that the number of people affected by glaucoma worldwide will increase to 95 million between 2020 and 2030 alone (4). A meta-analysis of 50 population-based studies predicted that the prevalence of glaucoma would increase even further to 111.8 million by 2040 (8). Increased prevalence of glaucoma will disproportionally affect people residing in Asia and Africa, with 40% of global cases occurring in China and India (8–10).

The economic impact of glaucoma is far-reaching. Glaucoma costs the United States (US) economy $2.9 billion every year in direct costs and productivity losses (11). Total direct cost estimates for glaucoma patients in Australia is approximately AUD 144.2 million (12). In the United Kingdom (UK), the total cumulative costs of glaucoma were projected at £5.5 billion from 2010 to 2020, assuming a 90% diagnosis rate within the patient population (13). In Scotland, the mean cost of glaucoma treatment in one clinic over the patients' lifetime was £3,001, with an annual mean cost per patient of £475 (14). Across Europe, the annual total costs of glaucoma per patient were determined to be between €11,758 and €19,111 (15).

The financial burden of glaucoma on health care systems, payors, and individuals increases as the disease severity increases. A US study found a four-fold increase in direct ophthalmology-related costs from early-stage glaucoma to end-stage glaucoma and blindness, with average direct costs per patient per year increasing from $623 to

$2511 for early-stage and end-stage glaucoma, respectively (16). Another analysis of resource utilisation and direct medical costs of glaucoma in Europe discovered a rise in costs with worsening disease severity, finding annual mean costs per patient increasing from €445 in early-stage glaucoma to €969 in end-stage glaucoma (17).

Glaucoma also impacts patients' individual health-related quality of life (HRQoL) in multiple ways, including by reducing outdoor mobility, the ability to carry out personal or household tasks, and by intensifying the risk for injuries and accidents (18). HRQoL is a metric that reflects a patient's perception of their well-being, focussing on dimensions of physical and social functioning and mental health (19). In a large US study with more than 3,000 participants, glaucoma patients with severe visual field loss had consistently lower self-reported HRQoL scores, independent of whether the patients had prior knowledge of their glaucoma (20). Psychological burdens also escalate as vision deteriorates, and some contributors to this burden include fear of blindness, social withdrawal, and depression (21).

The main risk factors associated with disease progression include ageing, increased intraocular pressure (IOP), ethnicity, myopia, and diabetes; although these risk factors have not yet been fully characterised and the biological basis of glaucoma is not completely understood (see **Section 1.2**) (5,22,23). As optic nerve damage from glaucoma is irreversible, the primary treatment strategy involves slowing this degeneration. The only major risk factor that is clinically modifiable is the level of IOP (24,25). The higher the IOP, the greater the risk is for optic nerve damage; therefore, reducing the IOP is the most effective clinical approach to halt the progression of the disease (26).

Glaucoma can be relatively asymptomatic, especially in the early stages of the disease, and people with glaucoma do not usually have an awareness of any ocular or systemic symptoms, which makes early detection more difficult (27). Glaucomatous vision loss is commonly misrepresented in images developed for patient information in glaucoma awareness programmes. These informational materials depict vision loss as a black periphery that slowly develops into a distinctive "tunnel" vision. Rather, the glaucomatous visual field is characterised by the development of blurred patches and blurred edges (28). Consequently, low public awareness of glaucoma and its risk factors coupled with a lack of symptoms early on have resulted in a large proportion of individuals with glaucoma who remain undiagnosed or receive a delayed diagnosis (29).

In developed countries, as many as 50% of glaucoma cases are undiagnosed, whereas it has been predicted that this number could be as high as 90% in developing countries (30,31). Therefore, by the time the disease is diagnosed, the optic nerve may already have advanced damage, and significant interventions are required to maintain reasonable visual function (32).

1.2. Pathophysiology of glaucoma

Although the pathogenesis of glaucoma is not fully understood, elevated IOP >22 mmHg has been related to retinal ganglion cell death (33). Retinal ganglion cells are a population of neurons of the central nervous system with their soma in the inner retina and axons in the optic nerve (34). Retinal ganglion cell axons exit the posterior of the eye through the lamina cribrosa, which is a collagenous structure with mesh-like perforations in the sclera (35). Because the lamina cribrosa is thinner and more compliant than the scleral tissue, it is more sensitive to changes in pressure. Elevated IOP restricts blood flow in the posterior eye (36) and causes mechanical stress and strain to the lamina cribrosa, which may result in compression, deformation, or remodelling of the tissue (37,38). Deformation of the laminar tissue results in cupping of the optic nerve head that strains the retinal ganglion cell axons and compromises their function (38). These structural changes also disrupt axonal transport and impair the delivery of adenosine triphosphate (ATP) and essential neurotrophic factors to the retinal ganglion cells (33,39–42). Damaged axonal transport of essential factors leads to mitochondrial dysfunction, oxidative stress, and the activation of apoptotic signalling by surrounding glial cells, culminating in retinal ganglion cell death and a loss of synaptic connectivity at the optic nerve head (33,40,43).

Vision loss usually begins with blurred patches in the peripheral vision, followed by deterioration in the central vision (32,35). In healthy individuals, the optic nerve degenerates at a rate of 0.5% per year, and since the brain accepts this rate of degeneration as normal, a patient with glaucoma may only appreciate vision loss when the disease advances (44).

1.2.1 Aqueous humour and IOP

The level of IOP is determined by the balance between the secretion and drainage of aqueous humour. Normal levels of IOP (10–21 mmHg) can vary at different

times of the day, but the average IOP has been determined as 15.5 mmHg in the general population, derived from studies inspecting both eyes of 10,000 individuals (45,46). Aqueous humour, also known as intraocular fluid, is continuously produced inside the eye by non-pigmented ciliary epithelial cells (47). It is composed of 98% water with dissolved amino acids, glucose, electrolytes, ascorbic acid, immunoglobulins, oxygen, and carbon dioxide. The aqueous humour maintains the structure of the eye, transports nutrients, assists in immunity, and provides the means for refractive indexing, which is essential for vision (48). The production, flow, and drainage of the aqueous humour is an active, continuous process required to maintain optimal ocular health, and overproduction or insufficient drainage are the two causes of increased IOP (49,50). Aqueous humour is produced by ciliary body epithelium in the posterior chamber through an active secretion that relies on ATP hydrolysis from ATP sodium-potassium pumps and carbonic anhydrase (51). The production rate has been reported to follow a circadian rhythm, ranging from 1.5 µL minute^{-1} at night to 3.0 µL minute^{-1} in the morning (52–54). An average rate of aqueous humour production at 2.0 ±0.4 µL minute^{-1} is generally accepted (52,55).

After production, the aqueous humour flows from the posterior chamber via passive diffusion through the pupil to the limbal region of the anterior chamber, where it drains through a sponge-like tissue called the trabecular meshwork (TM). Aqueous humour contains cellular debris from upstream tissues that is removed by cells in the outer layer of TM, which are phagocytic (56). From the TM, the aqueous humour drains into Schlemm's canal and then into the episcleral vein and venous circulation in the conventional drainage pathway (51,57). Alternatively, the aqueous humour can drain through the uveal meshwork into the ciliary muscles and other downstream tissues in the unconventional drainage pathway, see **Figure 1-1** (57).

The TM acts as the resistance barrier for the flow of aqueous humour. In order for aqueous humour drainage to occur, a positive pressure gradient must be built inside the eye. Once the IOP reaches 15 mmHg, the aqueous humour will flow through the TM (52,53). For this reason, drainage through the TM is considered the major mechanism for aqueous humour drainage (58,59). The main site of resistance in this pathway has not yet been determined, but it is thought to be at the juxtacanalicular tissue (JCT) portion of the TM, adjacent to Schlemm's canal (60). Approximately 2–20 µm thick (61), the surface area of the JCT has been reported as 1656 ±502 µm^2 (62). The alternative

method of aqueous humour drainage is through the uveal meshwork, which is comprised of connective tissue with irregular openings 25–75 µm in diameter (63). Drainage through the uveal meshwork using the unconventional pathway accounts for only about 10% of the total aqueous drainage (64).

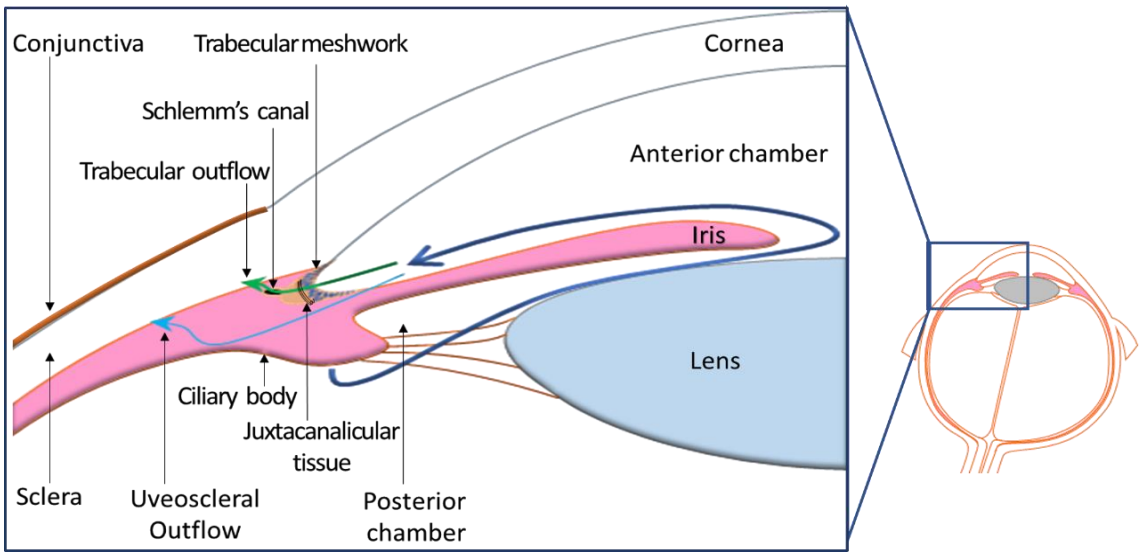

Figure 1-1. A diagram illustrating the flow of aqueous humour and corresponding location in the eye. The dark blue arrow indicates the direction of the movement of the aqueous humour from the ciliary body (pink) around the lens in the anterior chamber towards the trabecular meshwork through the trabecular outflow pathway (green arrow) or towards the uveal meshwork through the uveoscleral outflow pathway (light blue arrow).

Primary open-angle glaucoma (OAG), or chronic glaucoma, is the most common type of glaucoma, accounting for more than 70% of cases (22,65). In OAG, there is increased resistance to aqueous outflow through the TM, which causes the IOP to increase slowly (66). Increased resistance in the TM is thought to be due to excess cells, debris, fibrin or proteins carried by the aqueous humour (67). Mutations in genes encoding myocilin and caveolin proteins have been linked with increased IOP in patients with glaucoma. Mutated myocilin results in intracellular accumulation of misfolded proteins, and mutant caveolins result in disrupted cell signalling involved in endocytosis, but their putative mechanisms in glaucoma have not been established (5).

The other type of glaucoma is angle-closure glaucoma (ACG), or acute glaucoma. In ACG, elevated IOP is due to obstructed access of the aqueous humour to the drainage pathways, typically caused by a narrowing of the angle between the iris and the cornea (68). Some genetic structural variations predispose individuals to ACG (69), and ACG is more prevalent in Chinese, Indians, and Eskimos populations (8,70). Acute glaucoma is a medical emergency and has symptoms such as severe pain, nausea, and blurred vision

(71). Because of these symptoms, this type of glaucoma is easily identified and can be controlled before any irreversible damage occurs if appropriate action is taken.

1.3. Current treatment strategies for glaucoma

The primary goal of glaucoma treatment is to prevent or delay vision loss, and so the treatment strategy centres around decreasing the IOP to a level where sight loss and thus disease progression are reduced to a minimum (72). Irrespective of whether the IOP is within a normal range, in patients with established OAG (defined as having optic nerve damage), lowering the IOP 20–40% was shown to slow the disease progression by decreasing the rate of peripheral vision loss by 50% (1,73,74). Lowering the IOP has been shown to slow disease progression in higher risks patients (75), in those with early stages of the disease (76,77), and at advanced stages of glaucoma (78). The mechanism of action of virtually all current glaucoma therapies is to reduce IOP by either enhancing TM and uveoscleral outflow of aqueous humour or by suppressing aqueous humour production (79,80).

The choice of the treatment takes into account several factors, including the clinical situation of the patient (*i.e.* the stage and severity of the disease) and the invasiveness, effectiveness and safety profile of the treatment (32). Furthermore, the treatment that has the lowest rate of adverse events or postoperative complications is another factor in choosing a glaucoma treatment. Therefore, glaucoma is not managed the same way for all patients (32).

1.3.1 Pharmacological treatments

The first line of treatment to lower the IOP is by topically administering pharmacological therapy in the form of eye drops (81–83). These medications consist of β-blockers, prostaglandin analogues, α2-adrenergic receptor agonists, parasympathomimetics and topical or systemic carbonic anhydrase inhibitors (**Table 1-1**)(84). These treatments aim to lower the IOP either by reducing the rate of aqueous humour production in the ciliary body or by improving the humour outflow in the eye via the trabecular meshwork and uveoscleral tissues.

β-receptors play an important role in the regulation and production of aqueous humour; thus, blocking these receptors reduces the production of aqueous humour. Selective β-blockers, *e.g.* betaxolol, which block β 1-adrenoceptors, and non-selective

β-blockers, *e.g.* timolol, which block both β 1- and β 2-adrenoceptors, reduce the production of aqueous humour by the ciliary body (85,86). Carbonic anhydrase inhibitors, such as dorzolamide, exhibit the same effect on the ciliary body as β-blockers, but through a different mechanism. Carbonic anhydrase is an enzyme important in the production of aqueous humour by converting CO_2 and H_2O to HCO_3, which helps regulate chloride secretion. By inhibiting carbonic anhydrase, the rate of fluid production reduces (87,88). Adrenergic agonists, such as epinephrine, act by stimulating both α- and β-receptors, which restricts blood flow and reduces the rate of aqueous humour production and also increases the rate of flow through the trabecular meshwork (86).

Table 1-1. Current pharmacological treatment strategies for glaucoma (ClinicalTrials.gov identifier NCT03310580, NCT02087085)(83,89–93)

Pharmacological treatment	Examples	Mechanism of action
Topical β-adrenergic blockers	Timolol, carteolol, betaxolol	Reduce aqueous humour production in the ciliary body
Topical α2-adrenergic receptor agonists	Brimonidine, apraclonidine	
Systemic carbonic anhydrase inhibitors	Acetazolamide	
Topical carbonic anhydrase inhibitors	Dorzolamide, brinzolamide	
Parasympathetic muscarinic receptor agonists	Pilocarpine	Increase aqueous humour outflow through the trabecular meshwork
Rho-kinase inhibitors	Netarsudil	
Topical prostaglandin analogues	Latanoprost, bimatoprost, travoprost	Increase aqueous humour outflow through the uveoscleral pathway

Prostaglandin analogues, such as latanoprost, increase the flow of the aqueous humour through the uveoscleral pathway by binding to endogenous prostaglandin receptors, relaxing the interior eye muscles (94). Miotics, such as pilocarpine, and rho kinase inhibitors (*e.g.* netarsudil), which more recently approved, are a class of drugs that act on improving the drainage efficiency of the aqueous humour through the trabecular meshwork. They stimulate ciliary muscle contractions, which leads to relaxation of the trabecular meshwork (91,92,95).

Eye drops exhibit a poor ability to penetrate the corneal barriers of the eye, and it has been determined that fewer than 5% of the drug delivered in eye drop formulations is absorbed, with the remaining entering the bloodstream via transnasal and conjunctival absorption (96). Poor drug delivery has the potential to lead to serious, unwanted side effects in off-target organs. For instance, topical β-blockers are

associated with decreases in blood pressure, reduced pulse rate, fatigue, shortness of breath and even depression (91). β-blockers also cause relaxation of the bronchial, urinary, and vascular smooth muscles, resulting in other adverse reactions (79,97). The prolonged use of eye drops increases the sensitivity of the eye tissues due to chronic exposure to the preservatives commonly added to these formulations, such as benzalkonium chloride (86,98). Due to a fairly acidic pH, many eye drops also cause ocular irritations, such as stinging and redness (99).

Since glaucoma is a chronic disease, low patient adherence and cost play an important role in evaluating the benefit-risk ratio of eye drops as a treatment. An economic analysis of resource utilisation and direct medical costs of glaucoma in Europe discovered that eye drop medications comprised 42–56% of total direct costs for all stages of glaucoma (17). Eye drops need to be used several times a day, which is inconvenient for patients and results in low patient compliance (79). Overall patient compliance is estimated at approximately 50% for the regular administration of eye drops (100). In an observational cohort study using an electronic monitoring device, nearly 45% of glaucoma patients used their prescribed eye drops less than 75% of the recommended time (101). Another study using an eye drop medication monitor determined that over 50% of patients missed at least 20% of doses prescribed for glaucoma treatment (102,103). Finally, using routinely collected data, one clinical practice in the UK found that 51.6% of patients demonstrated poor adherence to prescribed eye drops for glaucoma (104). Patients that are non-compliant with eye drop prescriptions report having difficultly remembering to take them and report other issues like stinging and redness (105,106).

Fixed-dose combinations (FDCs) of eye drops represent another option for patients. For example, the US FDA recently approved a combination of a carbonic anhydrase inhibitor and an α2-adrenergic agonist (90), while a brinzolamide-brimonidine FDC eye drop formulation received European marketing authorisation in 2014 (107). Combining two medications in one formulation has been shown to improve compliance slightly by reducing the time required to administer drops and the frequency of use (88); however, challenges with patient adherence still remain. Patient adherence to FDC eye drops still declined over time, although at a lower rate than was observed in a single-dose formulation control (108). Poor ocular uptake and potential systemic side

effects paired with low patient compliance and high costs all illuminate significant disadvantages for eye drop formulations in treating glaucoma (105,109).

1.3.2 Laser treatments

When eye drops prove insufficient at prolonged management of IOP, laser treatment is sought to correct the blocked trabecular meshwork. There are three types of laser surgeries; Argon Laser Trabeculoplasty (ALT), Selective Laser Trabeculoplasty (SLT), and transscleral diode laser cyclophotocoagulation (TSC). In ALT, the laser ablates the trabecular meshwork by burning small holes into the tissue to increase fluid drainage and open the blocked channels (110). Early clinical studies suggested that ALT might be superior to pharmacological therapy as a first-line treatment for primary OAG (111). However, ALT can cause IOP spikes and inflammation, and because a high-powered laser is employed, its use is limited to two-three times per patient (80,112). SLT targets the pigmented cells of the trabecular meshwork, preserving the overall trabecular meshwork structure, which allows for repeated treatments (113).

Although SLT and ALT both effectively lower IOP, SLT causes less coagulative and structural damage than ALT; however, SLT has a 50% failure rate after two years (114). In TSC, the laser ablates the ciliary body and reduces the formation of aqueous humour, but TSC has been associated with adverse events like suprachoroidal haemorrhaging (115–117). The effects of these laser-based interventions are relatively short-term and the outcomes vary between patients (32,79). The blockage of some of the newly formed channels causes elevated IOP due to fibrin deposition, and patients may require medication even after laser treatment to combat elevated IOP (118).

1.3.3 Surgical treatments

If the progression of glaucoma is not halted by pharmacological or laser treatment, then a surgical procedure known as trabeculectomy, or glaucoma filtration surgery (GFS), may be necessary to preserve visual function in patients (119). GFS involves creating a new drainage channel called a fistula through the sclera between the anterior chamber and the subconjunctival space, as illustrated in **Figure 1-2**. The new fistula is designed to bypass the compromised conventional drainage pathway. The IOP lowers as the aqueous humour drains to the subconjunctival space through a small cavity under the conjunctiva, called a filtering bleb, and is absorbed into the systemic

circulation via the conjunctival and episcleral veins (120). GFS was devised in the late 1960s and is still considered the 'gold standard' surgical procedure for glaucoma because it has been proven as the most effective treatment for lowering IOP (80,121–123).

The GFS technique involves creating a new surgical channel for controlled aqueous draining (**Figure 1-2**). An incision is made in the conjunctiva, followed by elevating a partial-thickness flap of scleral tissue. A portion of scleral tissue is removed as well as part of the iris, directly below the sclera. The conjunctiva is then sutured back in place to allow for the circulation of aqueous humour around the scleral flap, forming a filtering bleb (1). This surgical technique requires considerable skill and technical expertise to achieve the optimal thickness and takes approximately 30−60 minutes per patient to perform (124).

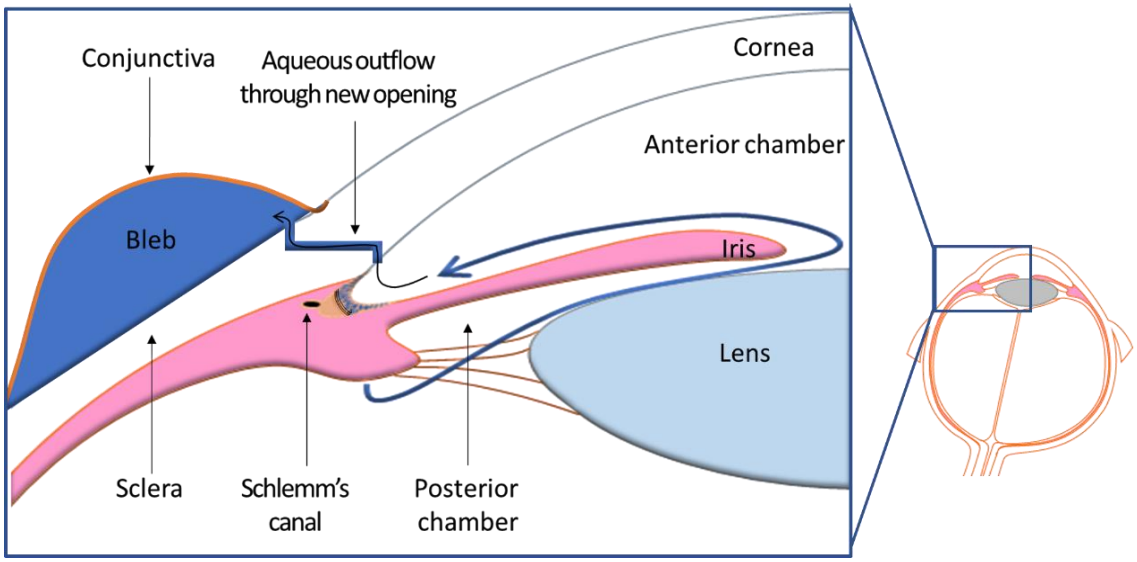

Figure 1-2. A schematic diagram illustrating glaucoma filtration surgery. The black arrow represents the alternative aqueous outflow pathway created during glaucoma filtration surgery where the fluid is directed to the subconjunctival space through a filtering bleb.

Many early postoperative complications of GFS relate to poor initial control over aqueous outflow (125). Hypotony, which is IOP ≤5 mmHg, a flattened anterior chamber, bleb leakage, blebitis (inflammation of the bleb), and failure of filtration due to bleb encapsulation make post-GFS effective management essential (126,127). The postoperative care determines the outcomes of GFS and its long-term success, which means it is not the first choice of treatment for glaucoma management by ophthalmologists (128). GFS outcomes could be considerably enhanced if the flow resistance through the drainage bleb were more effectively regulated (125). Post-

surgical inflammation and scarring make improper wound healing a major problem in GFS. After any surgical procedure of tissue trauma, there is an intrinsic wound healing response that results in the deposition of scar tissue. This scarring process after GFS can effectively close the 'trap door', which results in surgical failure (129,130). If wound healing following a GFS can be controlled, then there would be a greater chance for bleb survival (131).

1.3.4 Glaucoma drainage devices

Glaucoma drainage devices (GDDs) were introduced as an alternative to GFS for patients at a high risk of GFS failure due to the increased risk of fibroblast proliferation and episcleral scarring (128). GDDs create an artificial drainage channel with minimal incisions and a shorter implantation period than GFS (132). Since GFS is a highly technical surgery, GDDs were developed as a means to deskill the procedure and obtain a more uniform IOP reduction. The basic design of GDDs includes a tube that is connected to a flexible end plate or spacer plate. One end of the tube is inserted into the anterior chamber of the eye, and the other end is attached to the plate, which is placed into the subconjunctiva. This artificial tube is employed as a new drainage channel for the aqueous flow into the subconjunctival space. The end plate is designed as a physical placeholder during subconjunctival fibrosis after implantation and relies on the body to undergo foreign body encapsulation. Within four to six weeks after device implantation, a fibrovascular capsule, composed of collagen and vascularised tissue, develops around the spacer and acts as the primary resistance mechanism for aqueous humour flow. (133). Because this capsule is the first resistance to aqueous flow in the postoperative period, it is important for adequate IOP control. Aqueous humour accumulates in the capsule and is later reabsorbed by capillaries and lymphatic vessels, resulting in IOP reduction (134,135). After this 4–6-week period, a filtering bleb forms around the end plate, providing drainage of the aqueous humour (136).

From a clinical standpoint, the bleb progresses through 3 stages (127): the first phase is the hypotensive phase, which lasts approximately 1–4 weeks, during which the IOP is typically low, and the bleb is ill-defined and diffuse, exhibiting congested blood vessels around the bleb. The second phase is a hypertensive phase, which lasts between 1–6 months and is associated with increased IOP. The bleb becomes localised and well-defined with the formation of a dense fibrous capsule separating the aqueous humour

from the conjunctival blood vessels. The incidence of the hypertensive phase has been reported to be between 10% and 50% and varies with the various GDDs. During this phase, the IOP can potentially increase to 30–50 mmHg. Finally, a stable phase is achieved at the end of six months and is characterised by the presence of a bleb with no or little inflammation and well-maintained IOP (15–17 mmHg)(127).

Molteno® developed the first GDD in 1969 (137), which was composed of a polypropylene plate and a silicone tube, see **Figure 1-3**. This was a non-valved tube device that offered little to no resistance to aqueous humour outflow. Due to the lack of control over the outflow, significant fluctuations in the IOP were observed, which led to postoperative hypotony, flattened anterior chambers, and choroidal effusions (138). With a non-valved GDD, the IOP is controlled by the fibrous capsule that eventually forms around the end plate as a part of healing after implantation. Because the implantation relies on the patients' ability to develop a fibrovascular capsule, patients respond differently, which causes inconsistencies in the outcome of the surgery (139).

The first valved GDD was introduced in 1976 by Krupin and contained a silicone tube and end plate (140). The principle used by the Molteno device is the same in the Krupin device, but a unidirectional valve was introduced to provide resistance to the aqueous flow and prevent hypotony after the implantation of the device. When the IOP reaches ~14 mmHg, the valve opens due to the pressure exerted by the IOP. Later in 1993, the Ahmed® glaucoma device (AGD) was introduced, with the valve optimised to open when the IOP would reach 8–12 mmHg. Several devices have been developed since the AGD, which are shown in **Table 1-2**.

Complications that may occur in the early postoperative period while the fibrous capsule forms include hypotony, flattening of the anterior chamber, corneal oedema, uncontrolled high pressure, ptosis, and diplopia (141). Hypotony is crucial to prevent in the first few weeks as it disrupts visual function. Certain surgical techniques are used to try and minimise hypotony, such as external absorbable ligatures or internal removable suture stents to control the aqueous flow temporarily (142,143). Modifications in the design of the device, such as increasing the surface area of the end plate and designing a subsidiary pressure ridge to reduce postoperative hypotony have also been introduced (144).

Complications that occur several weeks post-implantation are harder to predict and include corneal oedema, erosion, chronic iritis, tube obstruction, and GDD failure

(141). The origin of these complications can be traced to either poor aqueous flow control or suboptimal material biocompatibility (134). The most common complication that occurs during this period is increased IOP, which is due to obstruction of the tube caused by excessive capsule formation and fibrosis around the tube and the end plate. (145). A study reported that for AGD and Molteno®, between 40–80% and 20–30% of patients, respectively, experienced increased IOP three to six weeks after GDD implantation (146). The most common causes for a GDD failure are either bleb encapsulation or bleb fibrosis (134,147). The foreign body response to GDDs is characterised by inflammation, collagen deposition and finally, scar tissue formation, which causes the newly formed channel to close and the operation to fail (130). It has been found that most GDD failures occur within the first year, with an estimated failure rate of 10% per year due to excessive fibrosis around the end plate (147). The only option available to the patient after GDD failure is to have an ophthalmologist perform a follow-up operation to either segment the capsule to allow aqueous humour to flow or implant a new GDD. This strategy is not ideal because the non-functioning device will be left in the eye, while the second device is placed in a suboptimal place in the eye (148).

An additional valve-specific complication in valved GDDs is the variability in valve performance between devices that occurs due to manufacturing inconsistencies (149). Modifications in the devices to overcome these problems, such as increasing the plate surface area and modifying the valve in AGD have been introduced, but no significant advantages of IOP control have resulted from these modifications (150). In general, GDDs available in the clinic lack the consistency in controlling IOP among patients for more extended periods (151).

Table 1-2. GDDs currently used or in clinical development, including the materials used for each device, the mechanism of aqueous humour drainage, and the size of each device.

Device	Aqueous humour drainage	Material	Valved? (Y/N)	Size	References
Molteno®	Subconjunctiva	Silicone tube; polypropylene end plate	N	134 mm^2 single end plate, 268 mm^2 double end plate; 340 µm inner tube diameter	(137,139,152)
Baerveldt®	Subconjunctiva	Silicone tube; barium-impregnated silicone end plate	N	250 mm^2, 350 mm^2, and 500 mm^2 end plates available; 300 µm inner tube diameter	(153,154)
ExPress R50	Subconjunctiva	Stainless steel tube; stainless steel disc-like flange	N	3 mm length; 50 µm and 200 µm inner tube diameters available	(155–157)
Ahmed®	Subconjunctiva	Silicone tube; polypropylene end plate	Y	End plate is 185 mm^2; 300 µm inner tube diameter	(158,159)
Krupin	Subconjunctiva	Silicone tube; silicone end plate	Y	End plate is 180 mm^2; 300 µm inner tube diameter	(140)
MIDI-Arrow	Subconjunctiva	SIBS tube	N	8.5 mm length; 70 µm inner diameter, 350 µm outer diameter	(NCT01563237)(160,161)
SOLX®	Suprachoroidal space	24-carat gold	N	5.2 x 3.2 mm flat implant	(162)
CyPass®	Suprachoroidal space	Polyamide	N	6.35 mm length; 0.3 mm lumen	(80,163)
Hydrus™	Schelmm's canal	Nitinol	N	15 mm length	(NCT03065036)(164)
iStent®	Schelmm's canal	Titanium	N	1 mm length (body); 250 µm (snorkel) [GTS100], 360 µm length [GTS400]	(NCT02024464)(165,166)
Xen implant	Subconjunctiva	Porcine-gelatine cross-linked with glutaraldehyde	N	6 mm long; 45, 63 and 140 µm inner diameters available	(167,168)
Optimed	Subconjunctiva	PMMA	N	14 mm length; 10 mm width; 1.3 mm thickness	(134)
Aquaflow™	Subconjunctiva	Lyophilised porcine scleral collagen	N	2.5 mm length; 1 mm dry width; 1 mm thickness	(169)
STARflo™	Suprachoroidal	Porous silicone	N	8 mm length; 27µm diameter	(170)
Aquashunt™	Suprachoroidal	Polypropylene	N	10 mm length; 4 mm width; 250 µm lumen diameter	(171)

Abbreviations: PMMA, polymethylmethacrylate; SIBS, poly(styrene-b-isobutylene-b-styrene).

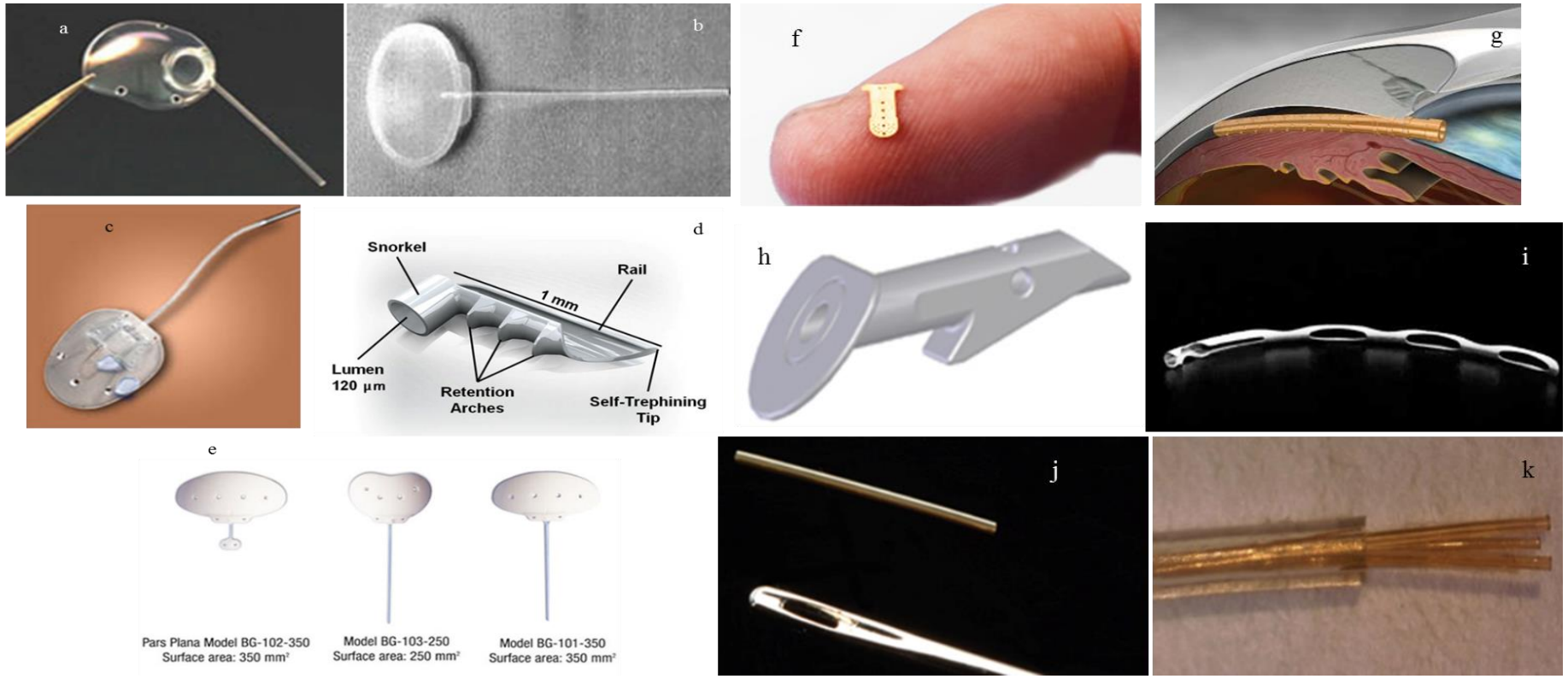

Figure 1-3. Current glaucoma drainage devices (GDD) in the clinic. **(A)** Molteno's single plate GDD; **(B)** Krupin's unilaterally valved GDD; **(C)** Ahmed® GDD with pressure sensitive valve; **(D)** iStent® minimally invasive GDD; **(E)** Baerveldt® GDD; **(F)** SOLX® Gold-shunt 24 carat gold supraciliary device to increase uveoscleral outflow; **(G)** CyPass® supraciliary Micro-stent to improve uveoscleral outflow; **(H)** ExPress R50 translimbal GDD made of a stainless steel tube; **(I)** Ivantis Hydrus™ Microstent, an intracanalicular scaffold that dilates Schlemm's canal; **(J, K)** Xen Collagen implants for glaucoma drainage (168,833–835).

More recent GDDs include the ExPress R50, SOLX® Gold, and iStent®. The ExPress R50 is a stainless steel non-valved tube with a disc-like flange instead of an end plate at one end and a spur-like projection at the other end (**Figure 1-3H**). These modifications were introduced to prevent tube migration. Initially, it was placed underneath the conjunctiva, but issues with hypotony and conjunctival erosion were common, so it is now placed under a partial thickness scleral flap similar to GFS (172). While the ExPress R50 has been demonstrated to improve IOP postoperatively (173), there is minimal evidence from clinical trials to suggest superior efficacy compared with GFS (174). The SOLX® Gold (**Figure 1-3F**) is another newer GDD that was developed to direct the aqueous humour to the suprachoroidal space to drain out of the uveoscleral outflow pathway, but has been associated with a high failure rate (162). The Istent® is a 1 mm long, L-shaped titanium tube (**Figure 1-3D**) that is inserted surgically into the eye through the trabecular meshwork into Schlemm's canal. This creates a permanent opening in the trabecular meshwork to direct the aqueous humour into Schlemm's canal. A systematic literature review of clinical studies reported that iStent® implantation lowers IOP and reduces dependency on glaucoma medications, but that it is unknown whether these effects last beyond 18 months (175).

The materials used for manufacturing a GDD must be biocompatible to minimise the initial inflammatory foreign body response and avoid the common complications mentioned previously (176). Polypropylene and silicone are the most commonly used materials in GDD development; however, blood plasma and proteins can bind to both of these materials, which can lead to cellular adhesion, inflammation and fibrosis (128). Polypropylene, used in Molteno® and some AGD implants, has been associated with higher rates of inflammation compared with silicone in animal studies (177). This has been attributed to the polypropylene's rigidity, flexibility and shape. In a clinical study where patients underwent AGD implantation, those with silicone AGDs experienced fewer complications than those with polypropylene AGDs (178). Silicone is used as a material in Baerveldt®, Krupin and some AGD devices (147).

Most GDDs are made of silicone and polypropylene, but stainless steel (ExPress R50) and gold (SOLX®) are also used due to their inert qualities (**Figure 1-3**)(176,179,180). Cross-linked gelatine (Xen Implant; **Figure 1-3D**) and poly(styrene-b-isobutylene-b-styrene)(SIBS)(MIDI-Arrow) have been introduced as biocompatible

materials in GDD development. Although these materials demonstrate improved biocompatibility to silicone and polypropylene, inflammation and scarring are still observed requiring significant postoperative manipulation (181). Biomaterials such as Vivathane and polymethylmethacrylate (PMMA)(Optimed) have been tested in GDD development, but they were not found to be less inflammatory than the materials currently in use (182,183).

Regarding GDD design, a systematic literature review of 54 articles comparing different GDDs, including 29 with Molteno® (single- and double-end plates) with some form of intraoperative modifications performed to prevent hypotony, 6 with single-end plated Molteno® without any surgical modifications, 9 with Baerveldt®, 8 with AGD, and 2 with Krupin valves, found similar IOP control and success rates with no statistical differences across devices (184). A sub-analysis comparing GDDs with the smallest (Molteno®, 130 mm^2) and largest (Baerveldt® 350 mm^2) surface area also found no statistical difference in end IOP (184). Another long-term study compared polypropylene AGD implants (185 mm^2) with double plate Molteno® valves (270 mm^2) also found no difference in end IOP (184). In contrast, there is evidence that GDDs with smaller surfaces (e.g. single-plate Molteno®) areas have lower IOP reduction than those GDDs with larger surface areas (e.g. double-plate Molteno®)(185). However, the IOP reduction was not proportional to the increase in surface area of the GDD (184). This seems to suggest that end-plate size does not affect IOP control. There might be a minimum end-plate area to achieve IOP lowering, after which additional surface area does not decrease IOP, but no definitive data on the ideal size is currently available (146,147).

The general success rate of GDDs has been estimated at approximately 70% after the first year and 40% after five years, with as many as 30% of GDD-implanted eyes developing excessive scar tissue (184). Given that most GDD failure is due to fibrosis around the end-plate, research has been conducted on making the end plate a drug-delivery system for slow, sustained release of an antifibrotic drug. However, large fluctuations in IOP and the considerable postoperative manipulation that is required are the major limitations of GDDs.

1.3.5 Antimetabolites

A successful GFS or GDD implantation is dependent upon the wound healing process. After surgical trauma to the conjunctiva or any epithelial surface, a sequence of overlapping events occurs that results in either tissue reconstruction or scarring. This process can be divided into four major phases; the coagulative phase, the inflammatory phase, the proliferation phase, and the tissue remodelling phase (186). Although these phases are distinct, their timelines overlap, see **Figure 1-4**.

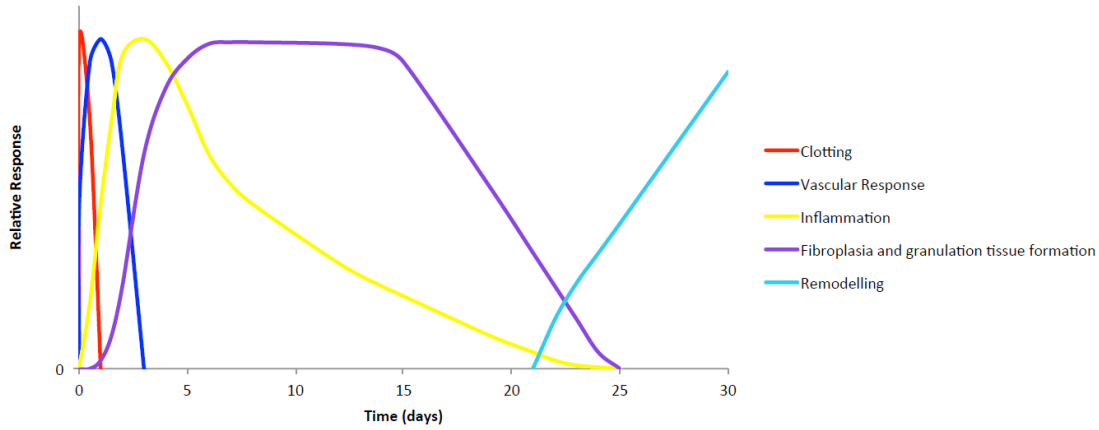

Figure 1-4. The wound healing process consists of a series of overlapping events; the coagulation phase, the inflammatory phase, the proliferation phase, and the tissue remodelling phase. The first one month is regarded as the critical period of maximum postoperative fibrosis. Figure reproduced from (353).

During the coagulation phase, platelets and plasma proteins are released from disrupted vessels. These activated platelets aggregate and release factors that attract inflammatory cells, such as macrophages and neutrophils (131). Macrophages release various growth factors that contribute to wound healing regulation. The proliferation phase begins in parallel with the inflammatory phase and includes the proliferation of epithelial cells, fibroblasts, and endothelial cells to seal the wound, form a temporary extracellular matrix, and carry out angiogenesis (with the help of matrix metalloproteinases), respectively (187). The final phase of wound maturation is the process of tissue remodelling, which may continue for months. Fibroblasts are the main cells involved in remodelling, and they, degrade, deposit and arrange collagen fibres. Persistent inflammation and fibroblast formation can intensify scarring (188). While scarring in certain situations, *e.g.* of the skin, is usually innocuous, scarring of the eye

tissues can result in blindness (189). Targeting these phases of wound healing could modulate wound healing and could potentially mediate scar formation.

Since the 1980s, surgeons have attempted to delay or prevent GFS failure due to excessive scarring through the use of antimetabolites (80,190). Mitomycin-C (MMC) and 5-fluorouracil (5-FU) are the most widely used off-label antimetabolites to modulate wound healing in the clinic (127,191). MMC is a naturally occurring antibiotic and antineoplastic compound that acts as an alkylating agent, after activation to form mitosene, and results in DNA cross-linking (190). 5-FU is a pyrimidine analogue that inhibits cellular proliferation as it interferes with DNA synthesis by inhibiting thymidylate synthetase, which is an enzyme that catalyses the synthesis of thymidine, a DNA nucleotide. Both medications interfere with DNA synthesis and lead to cellular apoptosis.

MMC and 5-FU are both administered at the site of surgery in GFS and GDD implantation either alone or with other anti-inflammatory drugs to reduce fibroblast proliferation and formation of scar tissue. MMC and 5-FU are administered either topically by soaking a sponge with the drug and placing it in the subconjunctival space (site of surgery) for five minutes or by injecting them into the subconjunctiva (127,192).

The evidence available for the efficacy of MMC includes the Tube Versus Trabeculectomy (TVT) study (ClinicalTrials.gov Identifier: NCT00306852)(193). This was a multicentre, randomised, interventional clinical trial that compared GFS with MMC (0.4 mg mL^{-1} for 4 minutes), with a Baerveldt® GDD (350 mm^2 end plate) over five years. The GDD was associated with the use of more medications than GFS during the first two years of follow-up, but this levelled with longer follow-up. GFS was associated with more early postoperative complications, but vision loss, rates of late postoperative complications and serious complications were similar between both procedures (194).

Although augmentation of the wound healing process with off-label antimetabolites is pervasive in glaucoma treatment, there are significant risks associated with their use, such as filtration bleb infections, leaks from tissue thinning, hypotony, suprachoroidal haemorrhaging, and necrosis due to the nonspecific toxicity of these drugs (195,196). These toxic effects are due to the suppression of cellular RNA and protein syntheses, as well as apoptosis and necrosis at high concentrations (0.4 mg mL^{-1}). In a case study, a one year follow up after a high-dose MMC injection displayed

toxic effects to the ocular tissues and atrophy of the iris, ciliary body, and retina were observed (197). Because higher concentrations of MMC may be preferred for cases of repeat GFS (198), close monitoring is required after surgery (80,127,199).

There is one MMC formulation for ophthalmic that has been available as an FDA-approved formulation in the US since 2012 (Mitosol Kit; Mobius Therapeutics). This formulation can be stored at room temperature for extended periods while maintaining a reliable dose (200). However, there have been no randomised clinical trials comparing the Mitosol kit to MMC prepared in a compounding pharmacy, and the FDA approval was based on the efficacy of MMC documented in existing literature (190,201,202). Furthermore, the cost of one Mitosol kit is reportedly $359 (190), whereas the current cost of an existing MMC preparation used in GFS is less than £10 in the UK (203).

Other strategies with less-toxic agents have been investigated to temper the scarring process in glaucoma by targeting components in one or more of the wound healing phases (204). Various anti-inflammatory or antifibrotic drugs have been evaluated preclinically for subconjunctival use after GFS, such as ilomastat (205), doxycycline (206), pirfenidone (207), and rosiglitazone (208); however, none of these are available for use in the clinic.

1.4. Challenges of ophthalmic drug delivery

The aim of any therapy is to deliver the drug molecule or active ingredient at a relevant therapeutic concentration to the site of action for an optimal period. However, drug design is contingent on the notion that key disease targets are isolated from the diseased tissue (209). Compartmental sites of disease, such as the eye, contain biological barriers that intrinsically obstruct access of systemically administered drugs (210). Systemic drug distribution is often accompanied by side effects due to off-target interactions, whereas localised drug delivery efforts have the potential to minimise these deleterious side effects by reducing the amount of drug needed for the desired effect.

Treatment administration to the eye presents several drug delivery challenges and requires a basic understanding of the structure and function of each part of the eye. Since the eye is exposed to the outside environment, there are numerous protective structures in place to keep foreign particles and pathogens from entering, see **Figure 1-5**

(211). The eye is externally protected by the eyelids, eyelashes, conjunctiva, and the tear film of the cornea (212). The cornea is a transparent window, covered by the tear film, and is situated at the front of the sclera, and connected to the sclera via the corneal limbus. The sclera is composed of collagen fibres and encompasses the eyeball. Covering the inside of the eyelids and the anterior sclera, excluding the cornea, lies the conjunctiva. It is a thin, clear, mucous membrane enriched with blood vessels and provides lubrication through the production of mucus and tears (213).

Internally, the eyeball is divided into two segments. The first one-third of the eye is classified as the anterior segment, while the remaining two-thirds are called the posterior segment. The anterior segment of the eye incorporates the cornea, iris, ciliary body, and lens. The cornea is a convex structure with highly innervated tissue and no blood supply. Thus, it is extremely sensitive to pain and requires support for nourishment and removal of waste products from the aqueous humour. The surface of the cornea is covered with a tear film consisting of five tissue layers: the corneal epithelium, Bowman's membrane, stroma, Descemet's membrane, and endothelium (214). Directly posterior to the cornea is the anterior chamber, a cavity between the

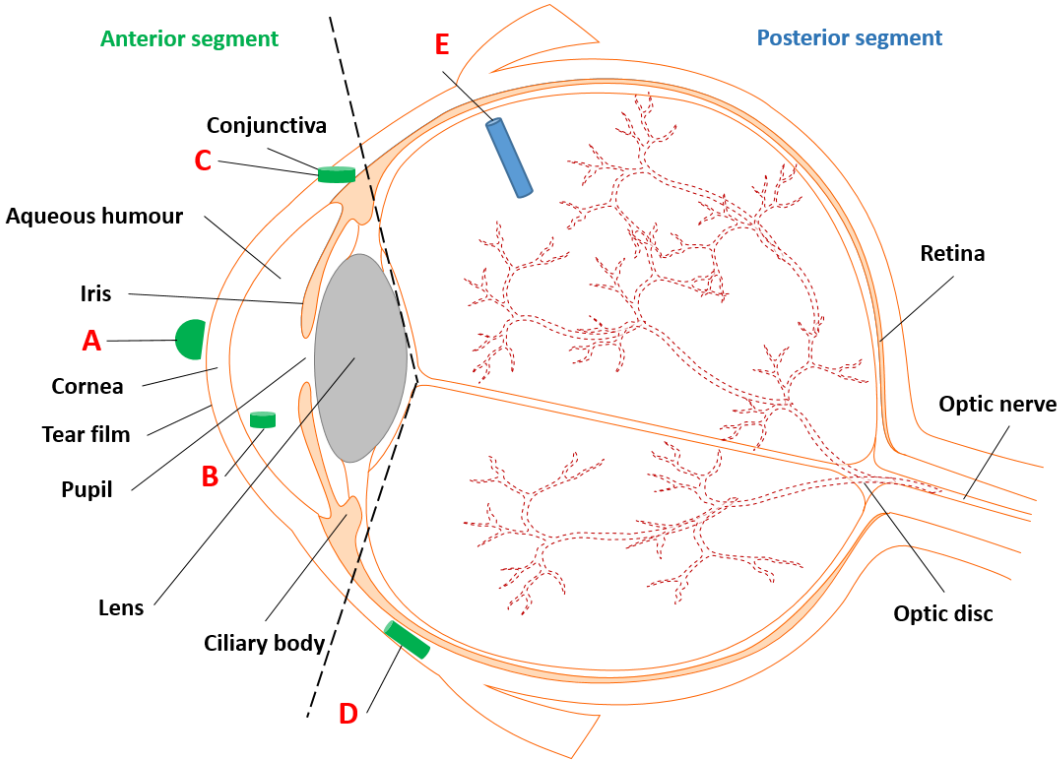

Figure 1-5. A diagram of the eye, which shows the location of the anatomy of the anterior and posterior segments. Green and blue shapes represent the routes of ophthalmic drug delivery; including **(A)** topical **(B)** intracameral **(C)** subconjunctival **(D)** intrascleral **(E)** intravitreal.

cornea and the iris containing aqueous humour. The iris is the pigmented fibrovascular portion of the eye that contains and controls an aperture known as the pupil. Between the iris and lens lies the posterior chamber. The lens itself is a clear, flexible structure and is surrounded by the ciliary body, which contains ciliary muscles that control the shape of the lens, and the ciliary epithelium (215).

These anatomical structures signify static and dynamic barriers that limit drug entry and distribution into the anterior segment. In addition to systemic administration, the main routes of administration in ocular drug delivery related to glaucoma include topical, intracameral, intravitreal, subconjunctival, and intrascleral (216). Topical drug delivery through eye drops is the most common route for the treatment of glaucoma in the anterior segment due to the non-invasive nature of the route; however, several factors affect the pharmacokinetics of drug molecules in anterior segment tissues (217).

Topically administered drugs are absorbed either through permeation across the cornea or through systemic absorption through local capillaries. The cornea is considered a key static barrier for drug absorption, and the corneal tear film layers contain different polarities (218,219). The human corneal epithelium is 52 µm thick, and the tight junctions of the lipoidal corneal epithelium limit drug transport through the cornea, especially for large and/or polar molecules (220). In contrast, the corneal stroma has a large water content, making it conducive to solubilising hydrophilic molecules (217). The blood-aqueous barrier is another static barrier that has tight junctions of the non-pigmented epithelium of the ciliary body and iridial tissues that also limit drug absorption (221).

The pre-corneal tear film can only accommodate approximately 30 µL of volume, yet many commercially available eyedroppers deliver volumes in the range of 30–70 µL to the tear film (222). Moreover, the tear volume in human eyes under normal conditions is 7–9 µL with a turnover rate of 0.5–2.2 µL per minute, making it a dynamic barrier to drug absorption (217). Topical administration abruptly increases the total tear volume, and since there is not enough space to hold the liquid, this causes reflex blinking and rapid dilution and removal of the medication via tearing and drainage through the nasolacrimal ducts (47). It has been estimated that 70–95% of the drug in eye drop formulations is lost to these pre-corneal factors, and that only 5% reaches the periocular and intraocular tissues (223). Efforts to improve bioavailability and drug release times

of drugs administered topically have been attempted by using drug-loaded contact lenses, but these lenses can decrease oxygen permeability and decrease the lens transparency (224).

Another route that is relevant to current glaucoma treatment strategies is subconjunctival drug delivery, where drugs are injected, inserted, or implanted underneath the conjunctiva. The human subconjunctiva is 42 µm thick with tight junctions that can allow molecules up to 5 kDa in size to pass (220,225). As typical injection volumes are 0.1–0.6 mL (226), a portion of the injected solution might seep into the tear fluid and become absorbed through the cornea (227). The injected drug can also absorb into the sclera, which allows drug diffusion to other structures like the iris and ciliary body to occur (226). The majority of the injected drug will absorb into lymphatic and blood circulation and rapidly clear into the systemic circulation, which necessitates repeated dosing (228). As a result, the bioavailability, while generally higher than topically administered drugs, is limited in the subconjunctival delivery route (226). The counter directional convection of the aqueous humour from the ciliary body hinders drug distribution into the posterior segment of the eye (229). Additionally, the subconjunctival route is invasive, which carries the possibility of infection or hypotony. (230–233).

1.5. Implantable drug delivery systems

Due to the selective functionality of the biological barriers in ocular tissues, ocular drug delivery is a challenging task that traditionally leads to suboptimal drug concentrations at the target sites. Consequently, the eye has been a target organ of interest for the development of prolonged drug delivery systems within the past decade. Specifically, implantable delivery systems for prolonged release of pharmacological treatment of glaucoma (**Table 1-3**) have been extensively investigated as a replacement of viscoelastic depot delivery injections (ClinicalTrials.gov identifier NCT02129673, NCT01408472, NCT01845038, NCT01016691, NCT01229982, NCT01915940, NCT03868124, NCT04060758)(92,109,181,233–254). An ideal ocular delivery implant must not interfere with vision, is able to achieve a high drug bioavailability, and can prolong the release of a drug to the specific compartment of the eye without any complications arising at the site of administration. Since this route of drug

administration bypasses the biological barriers of the eye, intraocular bioavailability will be enhanced, while minimising drug waste and maximising the efficacy of treatment (90,253).

Implantable drug delivery systems in ophthalmology can be characterised by the drug-polymer arrangement in the system. In theory, an open system (**Figure 1-6A-C**) would have a steady flow of biological fluid, and the release of the drug would be diffusion controlled. This system is passive, bidirectional, and requires a difference in the concentration of drug in the surrounding environment to drive drug release. This open system includes both reservoir and matrix-based drug distribution (255).

In a matrix-based drug delivery system (**Figure 1-6B**), the drug is dissolved or dispersed inside a polymer matrix. In theory, if the drug distribution in the polymer matrix is homogenous, a steady drug release with zero-order release kinetics, where the drug release concentration is independent of time, can be achieved. However, in practice, the rate of drug release from the matrix system usually is not steady and decreases over time due to the decreased drug concentration in the surrounding polymer membrane. The solubility of the drug partially dictates the drug-release rate. The primary driver for drug mass-transfer is the surrounding biological fluid. In implant form, the thickness of the polymer membrane and drug-release area also affect the drug-release kinetics (256).

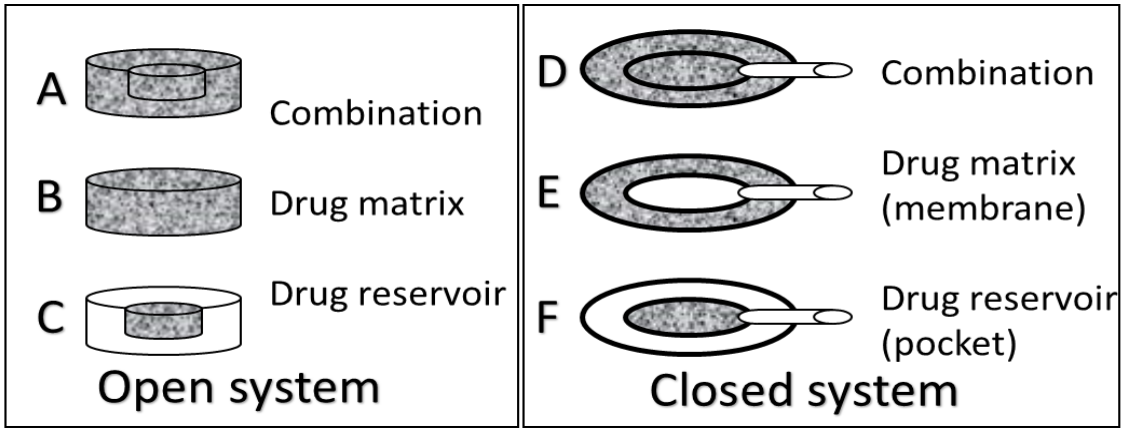

Figure 1-6. Drug delivery systems can be classified into two main types based on the drug-polymer arrangement, such as open **(A, B, C)** and closed **(D, E, F)** systems. The rate and mechanism of drug release is influenced by the system.

In reservoir-based drug delivery systems (**Figure 1-6C**), a drug core is surrounded by a polymer, and the drug-release rate is controlled by the properties of the polymer such as polymer composition, molecular weight and thickness (257,258). The

physicochemical properties of the enclosed drug, such as solubility, drug particle size, and molecular weight also affect the drug-release kinetics from these systems (257).

In contrast, a closed system (**Figure 1-6D–F**) is a theoretical system where the drug is enclosed in a non-permeable or slightly permeable membrane, and the release of the drug is controlled and unidirectional, i.e. the drug flows from the system to the site of action. This system is active and requires an energy source for drug release. This energy source could be in the form of magnetic energy, electricity, heat, liquid pressure or air pressure, which is converted into motion to drive drug release (259–261). In theoretical closed matrix-based systems (**Figure 1-6E**), the drug is dissolved or dispersed within the membrane, and the drug release rate is controlled by an internal or external stimulus, such as utilising the energy stored in the space between the membranes. In reservoir-based systems (**Figure 1-6F**), the drug is enclosed within a pocket formed using non-permeable membranes, and the elastic energy of the membranes would dictate the drug release rate.

Most implantable drug delivery systems in ophthalmology that are currently under clinical development are open systems, which means that the drug release is controlled by diffusion. Some of these examples of implantable drug-release systems under clinical development for glaucoma are listed in **Table 1-3.**

There is only one FDA-approved implantable drug delivery device for glaucoma treatment. The biodegradable intracameral implant, Durysta™, was approved in March 2020 and is indicated to reduce IOP in patients with OAG by providing a sustained release of 10 μg of bimatoprost, a prostaglandin analogue (262). The VS101 (Eye-D) is a subconjunctival insert intended for patients with OAG or ocular hypertension. The latanoprost-loaded insert recently completed a Phase 1/2a multicentre randomised controlled study, which found that the insert demonstrated a reduction in IOP for 12 weeks with a favourable safety profile (263). ENV515 is a PLGA-based intracameral implant for sustained travoprost delivery that has shown clinically meaningful reductions in IOP for 11 months in a Phase 2 cohort study (264). Bimatoprost SR is also a PLGA-based intracameral implant that is currently undergoing a Phase 3 study and has demonstrated favourable efficacy and safety for up to six months in a Phase 1/2 clinical study (92,246,265).

Table 1-3. Examples of sustained-release delivery implants for glaucoma that are in clinical development.

Delivery location	Implant name/description	Drug	Delivery system	Reference
Inserted into canaliculus of the eyelid	Sustained-release punctal plug	Bimatoprost	Open matrix	(250)
		Latanoprost		(249)
		Travoprost		(242,251)
		Dexamethasone		(266)
Pars plana implantation	Non-biodegradable NT 501	Ciliary neurotrophic factor	Closed combination	(240,267)
Subconjunctival implantation	Biodegradable slow release insert	Bimatoprost	Open reservoir	(268)
	VS101 (Eye-D)	Latanoprost		(234)
Fornix-based ocular insert	Silicone matrix	Bimatoprost	Open combination	(246)
Intracameral implantation	G2TR (iDOSE™)	Travoprost	Open reservoir	(248)
	Durysta™*	Bimatoprost	Open matrix	(262)
	PA5108	Latanoprost		(247)
	ENV515	Travoprost		(264)
	Bimatoprost SR	Bimatoprost		(265)

*Durysta™ was approved by the FDA in March 2020 and is the only FDA-approved sustained-release implant indicated to reduce IOP.

Non-degradable ocular implants that have been approved by the FDA for intravitreal drug delivery could potentially be adapted in glaucoma management. Vitrasert, approved for cytomegalovirus retinitis, and Retisert, approved for chronic non-infectious uveitis, are both polyvinyl alcohol-based inserts that deliver ganciclovir over a period of five to eight months (269), and the corticosteroid, fluocinolone acetonide, for about 2.5 years, respectively directly in the vitreous (270). Iluvien® (Durasert™), designed to deliver fluocinolone acetonide for a duration of 36 months, has been approved for diabetic macular oedema (253). Due to its small size (cylinder, 3.5 x 0.37 mm), it can be injected into the vitreous directly using a 25-gauge trans-conjunctival injector system, which eliminates the need for an invasive procedure (271,272). Ozurdex® is a biodegradable PLGA-based implant loaded with corticosteroid, dexamethasone, that is approved for intravitreal implantation in the treatment of

uveitis and macular oedema, which affect the posterior segment of the eye. This implant was also investigated for intravitreal delivery of neuroprotective agents (*e.g.* Brimonidine) in glaucoma; however, this trial was completed in 2013 and failed to meet its primary endpoint (273).

Much of the implantable drug delivery systems to manage glaucoma have been investigated to improve the efficacy and decrease the administration frequency of pharmacological therapies (*i.e.* eye drops). The high cost and discomfort of administration have been established as concerns for patients who require lifelong use (86). Low patient compliance is common, particularly in the case of developing countries, where a large proportion of patients need to travel long distances to collect the treatment and potentially cannot afford the medications due to their high cost relative to income (274). It was discovered that in Ghana, only 17% of patients that were prescribed eye drops complied with the therapy (274). Therefore, in developing countries where patients might not be anticipated to comply fully with medical treatment, a cost-effective, "one-time" treatment along with standard glaucoma surgery is a preferred approach. Implantable drug delivery systems have the potential to relieve issues with patient compliance, overcome the ocular delivery challenges, and improve glaucoma treatments.

1.6. Hydrogels as a material for drug delivery systems

Hydrogels are three-dimensional (3D) viscoelastic structures composed of hydrophilic polymeric chains that can hold large amounts of fluids, up to thousands of times their dry weight, by swelling reversibly in liquids without changing their chemical structures (275–277), see **Figure 1-7**. Hydrogels can behave in this way due to the presence of physical cross-links, including inter-polymer entanglements of long polymeric chains, hydrogen bonding, van der Waals forces, or chemical cross-links, such as strong covalent bonds that form a solid polymer matrix (278). The expansion and contraction of the 3D cross-linked polymer network of the hydrogel, which is also referred to as a mesh, provide elasticity and prevents the hydrogel structure from completely solubilising into a liquid state (278–281).

The polymer chains in hydrogels are held together by cross-links, which allow hydrogels to behave like solids rather than liquids, despite containing at least 20% and often greater than 90% water by weight (282). Water transport through hydrogels is essential for their use as soft contact lenses (283), in drug release (284), and as stimuli-sensitive hydrogels (285). The swelling behaviour of hydrogels is their most critical property because it allows them to absorb and hold high amounts of liquid, giving them broad possibilities of applications. Both the swelling and absorption capacity of hydrogels is attributed to the degree of cross-linking, which also known as the number of junction points. The degree of cross-linking is altered by varying the ratio of cross-linker to solvent during the hydrogel preparation. A higher number of junction points hinders the mobility of the polymer chains, which results in a more rigid structure of the hydrogels and hence swell less than those with a lower number of junction points (277).

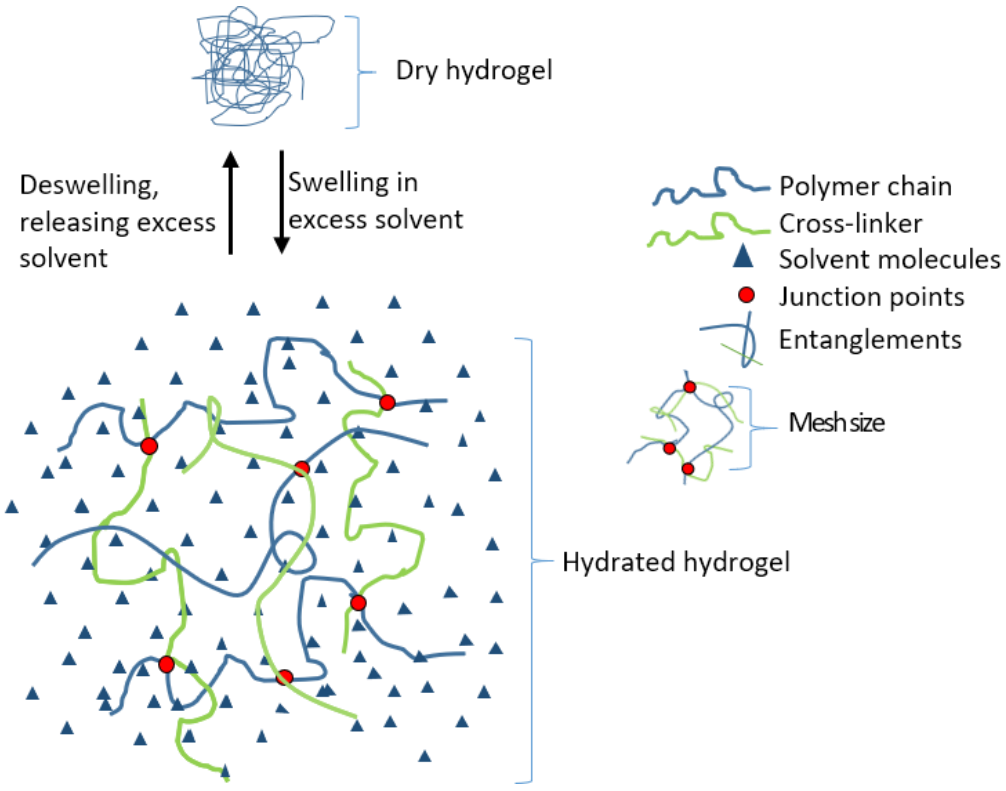

Figure 1-7. An illustration of the expansion of polymeric strands in a dry hydrogel (known as a xerogel) upon the addition of excess solvent (water in this case) to form hydrated hydrogels. The junction points allow for the cross-linking of molecules to attach to the polymer chain. The expansion and contraction of the 3D cross-linked polymer network (known as a mesh) in the hydrogel provides elasticity and prevents the hydrogel structure from completely solubilising into a liquid state.

The chemical composition of the hydrogels also governs hydrogel swelling. To minimise exposure to water, hydrophobic groups in the polymer chains tend to aggregate and collapse in the presence of an aqueous environment (276). As a result, the hydrogels with a higher amount of hydrophilic groups in them tend to swell more (279). The swelling kinetics of the hydrogels can be classified into either diffusion-controlled (Fickian), where the transport of the solvent into the polymeric structure of hydrogels is concentration-dependent; or relaxation controlled, where the rigidity of the hydrogel, or the ability of the polymeric chains to relax, limits the capacity of swelling of the hydrogel (286–288).

1.6.1 Types of hydrogels

When the hydrogel network is made by covalent bonds cross-linking different polymers chains; the hydrogels formed are classified as permanent or chemical hydrogels (289). Chemical hydrogels may be synthesised by cross-linking two existing polymer chains in the solid-state or in solution, copolymerisation of monomer/cross-linker reactive in solution/multi-functional macromer or polymerisation of a monomer inside a different solid polymer (289). When the inter-polymer molecular entanglement in the hydrogel structure is derived from secondary forces such as ionic bonds, hydrogen bonds, or hydrophobic forces, a reversibility is imparted to the hydrogel. These hydrogels are commonly named reversible or physical hydrogels (290). Hydrogels containing charged functional groups present in their structure may undergo changes in shape and swelling, when exposed to different stimuli, such as pH or electrical fields (290). Physical hydrogels may be synthesised by heating or cooling a polymer solution to form a gel, changing pH to promote the appearance of hydrogen bonds that form a gel between two different polymers, or mixing solutions of polyelectrolytes of different charges, forming a coacervate gel (289).

First described over 120 years ago (291), hydrogels have been used in numerous applications in medicine and industry (292). Hydrogels prepared from hydrophilic polymers have been studied extensively in biomedical research because of their ability to interact with water through hydrophilic functional groups such as -OH, -CONH, -CONH2, -COOH and -SO3H (280). As hydrophobic polymers cannot be used alone for hydrogel preparation, they are either co-polymerised with hydrophilic polymers or a

hydrophilic group is added to their structure to modify their properties and improve their interaction with water (293).

The first work of hydrophilic hydrogels was published on cross-linked 2-hydroxyethyl methacrylate (HEMA) hydrogels (294). It was based on this work that the first spun-cast contact lenses were made that ushered in a new era of the modern contact lens industry (295). HEMA monomers are acrylates containing double bonds that undergo free-radical polymerisation to form the poly (2-hydroxyethyl methacrylate)(pHEMA) polymer (280). HEMA can be covalently cross-linked using a diacrylate, such as ethylene glycol dimethacrylate (EGDMA), which prevents solubilisation of the polymer chains, and results in a non-degradable polymer network (296). Hydrogel contact lenses are hydrophilic, which allows for increased tear wettability over their surface (297).

The hydrophilicity of pHEMA is due to the presence of hydroxyl groups (-OH) in the primary chains, which results in contact lenses with a 38–40% water content once fully hydrated (298). The development of these hydrogel lenses resulted in the refinement of several functional characteristics of contact lenses, including the optimisation of the lens fitting profile, which reduces the mechanical effects of lens placement, and the definition of the 'material flexibility' range for improved comfort and durability (299). pHEMA hydrogels are also considered biocompatible because there is a reduction of protein adsorption onto pHEMA surfaces and improved biocompatibility with blood cells, when compared with alternative materials, such as acrylates and silicones used for manufacturing contact lenses (300).

Polymers used for hydrogel synthesis can be either natural, semisynthetic, or synthetic. Polymers from natural sources include polysaccharides like cellulose, starch, chitin, gelatine and hyaluronic acid, which are widely used in food and pharmaceutical applications as they tend already be biocompatible and safe (301). Gelatine, a hydrolysed form of collagen, is used in food, tablet coating and in the synthesis of hard and soft gelatine capsules. Hyaluronic acid (in the form of sodium hyaluronate) is used in various applications including cosmetic formulations, Healon® surgical aid for cataract extraction, as a raw material in tissue engineering, and in eye drops for the treatment of dry eyes (301,302). Semisynthetic polymers are derived from modified natural polymers. An example of a semisynthetic polymer is chitosan, which is the deacetylated

derivative of the natural polymer chitin. While chitin is poorly soluble in both aqueous and organic solvents, chitosan has been widely investigated and is much more commonly used in drug delivery due to its improved solubility, biocompatibility, low toxicity, and biodegradability (303). Examples of common synthetic polymers include pHEMA, phosphorylcholine (PC), acrylic acid and its derivatives, poly (vinyl) alcohol (PVA) and poly (N-vinyl pyrrolidone)(PVP), which also display biocompatibility, low toxicity, but resist degradation (304).

Hydrogels can be further classified based on the method of preparation. When preparing hydrogels, one of the most versatile forms of polymerisation for preparing chemically cross-linked hydrogels is free radical polymerisation, where polymer chain propagation occurs by the addition of free radical building blocks with monomer units (305). A water-soluble monomer is polymerised with a small amount of a second co-monomer/cross-linker to form a 3D hydrophilic network (306). The reaction can be facilitated by several different initiator systems, such as ultraviolet photo-polymerisation, thermally-initiated, and chemically-initiated polymerisation, with the reaction conditions based around the final intended application of the polymer (307,308). Variation in the amount of cross-linker, polymerisation temperature, and pH leads to a change in the properties of the prepared hydrogel (309).

Hydrogels can be prepared by cross-linking a single species of monomer (homo-polymer), co-monomers (co-polymer), multiple monomers (multi-polymer), interpenetrating networks (IPN), or semi-IPNs. A co-polymer hydrogel is composed of two types of monomer where at least one is hydrophilic in nature. An IPN is a hydrogel with a combination of two polymers, where one polymer is chemically cross-linked in the presence of the other (310). A semi-IPN is a hydrogel where one polymer is linear and entangles with a cross-linked network in the presence of another monomer. The two monomers can be polymerised together in the same sample or polymerised sequentially, but the two resulting polymer chains are entangled in the matrix without any chemical cross-linking occurring between them (311), see **Figure 1-8**. IPN hydrogels impart superior mechanical properties such as strength than non-IPN hydrogels, but they mixing two different polymers can be difficult to achieve, so semi-IPNs offer the chance for two polymers to be more intimately entangled (312).

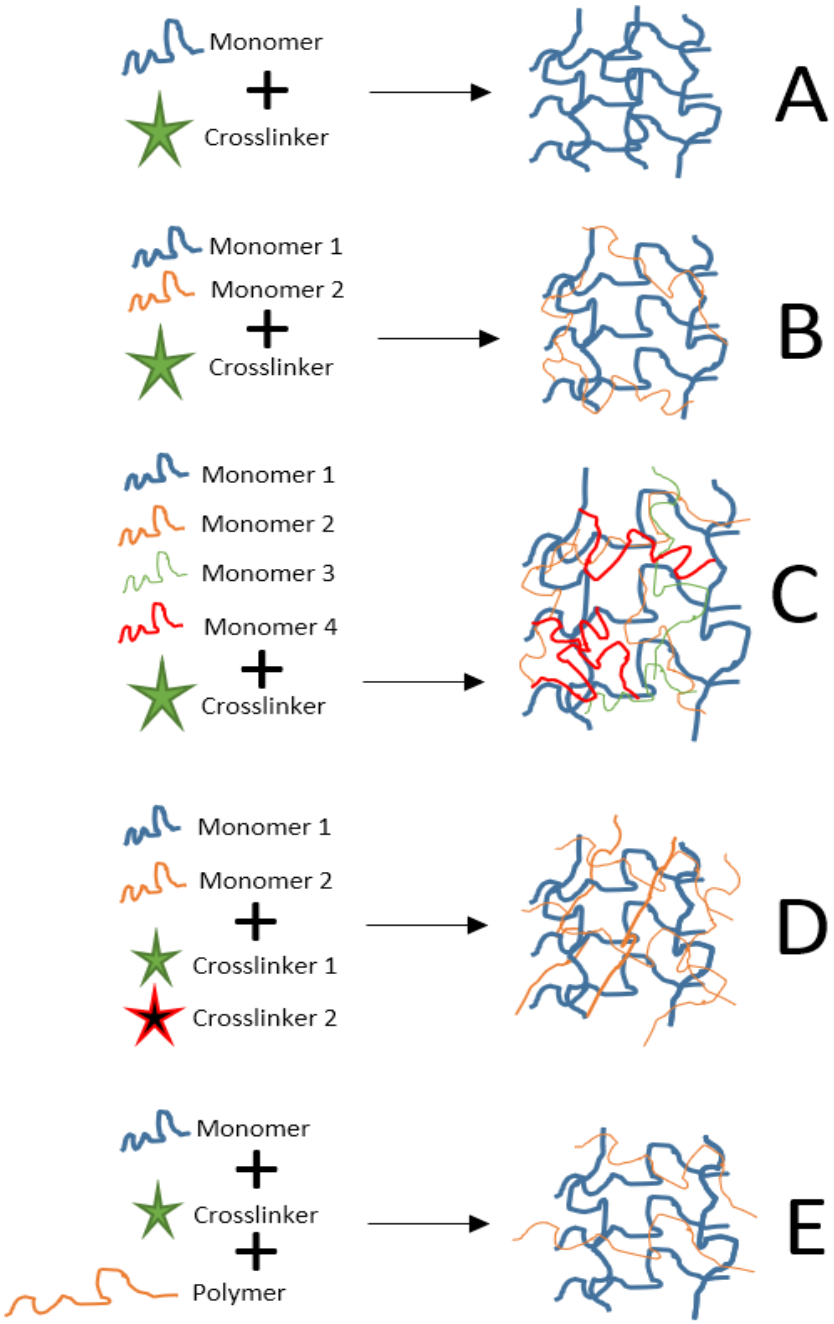

Figure 1-8. Classification of hydrogels based on hydrogel preparation method. Hydrogels can be classified as **(A)** homo-polymer, **(B)** co-polymer, **(C)** multi-polymer, **(D)** IPN and **(E)** semi-IPN hydrogels based on the number of monomers, cross-linkers, and polymers added.

1.6.2 Hydrogel applications

Due to their ability to retain fluids, soft texture and high flexibility, hydrogels have the ability to mimic the mechanical properties of the native extracellular matrix of many tissues, with minimal irritation to the surrounding tissues when applied *in vivo* (289,313). Their biocompatibility and the ability to absorb and release fluids have resulted in the extensive investigation of hydrogels as a material in applications such as

tissue engineering, artificial replacement of organs, coating of implantable devices, drug delivery, gene delivery, scaffolding and wound dressings (314–318).

Hydrogels with high chemical stability can be synthesised to be non-degradable, with the different polymer chains cross-linked with covalent bonds to maintain the structure of the hydrogel. Alternatively, hydrogels may be engineered such that the polymer chains include cross-links that can either degrade hydrolytically or enzymatically into smaller degradation products after a specific period (275,276,317,319). This ability to tailor the hydrogel degradation according to the intended application bolsters their use in implantable devices, implant coatings, soft contact lenses and wound dressings (319,320). One of their primary biomedical applications is their use as wound dressings to absorb exudates from wounds and are useful to treat necrotic wounds. Examples of the available hydrogel wound dressings are ActiFormCool, Coolie, Geliperm, Novogel, Algisite®, AlgiDerm®, Sorbsan®, Kaltostat®, Intrasite®, Neoheal®, Purilon® and Aquaflo™ (321,322). Hydrogels are also used in different medical devices such as keratoprosthesis, intraocular lenses, smart drug-delivery systems and bio-sensors (275,276,317,323,324).

Hydrogels, while extremely versatile in the context of drug delivery, have been associated with burst release profiles and poor drug loading efficiencies. A burst drug release is especially problematic with drugs that have a narrow therapeutic index, and their rapid release may cause toxicity in the surrounding tissues. Poor drug loading efficiencies particularly affect hydrophobic drugs due to their limited solubility and the high water content in hydrogels, which makes loading therapeutic doses challenging (325).

1.7. Elastic pursed pockets as drug delivery systems

Elastic pursed pockets represent another option for controlled ocular drug delivery. An elastic pocket is created by introducing a fluid between two elastic membranes that are fixed together along a common edge (326,327). Elastic pursed pockets are commonly used in technological applications, including as pressure-sensitive buttons, to strain cells in a controlled manner, and as infusion pumps for cost-effective ambulatory care for patients (328–330).

When the fluid inside exerts pressure on the elastic membranes, they purse, or inflate, and form a pocket. Understanding how elastic membranes undergo the process of deformation is of significance to many biological systems, from cellular replication and motility to the pathogenesis of cardiovascular diseases (331,332). Previous research has focussed on studying the inflation of axisymmetric (symmetrical around a common axis) balloons, particularly in the context of how stent placements interact with arteries (333–335), electro-elastomers used in prosthetic blood pumps (336), endoscopic devices (337), and urinary sphincters for patients suffering from severe stress incontinence (338). Today, the majority of coronary stents are expandable elastomeric pockets and are deployed using an elastomeric-tipped catheter, which is a thin tube made of medical-grade materials. To improve stent implantation, the biocompatible elastomeric membranes of the angioplasty pocket is typically folded around the catheter in a pleated configuration. As such, the deployment of the angioplasty pocket is governed by the material properties of the elastomeric membrane, its folded configuration, and its attachment to the catheter (333,335).

For nearly 70 years, the principle of delivering drugs using elastomeric pockets has been mostly used in the form of ambulatory infusion pumps (339), but it was only around the mid-1990s that there were changes introduced in the design to make them compact and cost-effective. These later designs of compact elastomeric pockets are used to deliver fluids into a patient's body in a systematically controlled fashion. Although there are various mechanisms behind the controlled rate of the drug delivery from these pumps, *e.g.* electronic, mechanical, or osmotically driven, the non-electronic elastomeric infusion pumps, such as shown in **Figure 1-9**, are easier to use, more compact (smaller in size and lighter in weight), portable, and cost-effective compared with electronic pumps (340). Elastomeric infusion pumps are now widely used in clinical and home settings because they are reliable and comparatively cheaper than electronic medication pumps and of course, hospital care itself (341). These elastomeric infusion pumps are being used for various indications mentioned in **Table 1-4**.

Figure 1-9. Commonly used elastomeric infusion pumps have two designs; the first is composed of two connected elastomeric membranes encased in a protective shell such as **(A)** Baxter INFUSOR, **(B)** PCA infusor, **(C)** Canox MYFUSER, **(D)** Baxter INTERMATE, and the second does not include the protective shell such as **(E)** SMARTeZ pump, **(F)** B.Braun Easypump, and **(G)** ON-Q pump.

Table 1-4. Commercially approved portable infusion pumps and their clinical indications. Please note, these pumps are not implanted in the body but used for ambulatory delivery of medication to the patient by using the elastic energy stored in the stretched membrane of their drug reservoir.

Elastomeric pump	Application	References
ReadyMED	Antivirals	(342)
Accufuser® (Woo Young Medical Co.)	Oncology	(343)
Advance Silicone Infuser, Baxter LV™, Baxter Two Day Infusor™, Multirate™ Infuser LV, Homepump E-Series® (Block Medical), ReadyMED (Alaris)	Antibiotics	(341–347)
Intermate™	Antimicrobials	(346)
Accufuser ®, Baxter LV™, Baxter PCA Infusor™™ (Baxter Healthcare), Baxter Two Day Infusor™, Intermate™ (Baxter Healthcare), Multirate™ Infuser LV (Baxter Healthcare), C-Bloc (I-Flow Corp.), Eclipse®, Homepump®, Homepump C-Series® (Block Medical), MedFloII™ (MPS Acacia), Surefuser+™ (NIPRO)	Analgesia	(328,341–352)
Baxter LV™, Baxter Two Day Infusor™, Multirate™ Infuser LV, Singleday Infusor™	Chemotherapy	(343–347,350)
Homepump C-Series®	Iron chelation therapy	(346)
Baxter LV, Baxter Two Day Infusor™, Multirate™ Infuser LV, Singleday Infusor™, Homepump C-Series®	Desferrioxamine	(343–347,350)
Advance Silicone Infuser, Surefuser+™ (NIPRO)	Cystic fibrosis, Thalassemia, Heparin	(341,343,350)

Elastomeric pumps consist of single or multiple elastomeric membranes that can be manufactured using either natural or synthetic elastomers, *e.g.* silicone, latex, or isoprene rubber. The properties of the material, such as stiffness, as well as the geometry such as size, shape, and material thickness of the elastomeric pocket, determine the pressure exerted on the fluid when the pocket is filled. Multiple-layer elastomeric membranes can exert higher pressures than single-layer membranes. The elastomeric pocket is protected by an outer shell that can either be a rigid plastic (*e.g.* Infusor [Baxter Healthcare, Deerfield, IL]) or a more flexible elastomer (*e.g.* Homepump Eclipse [I-Flow Corporation, Lake Forest, CA]). Elastomeric pumps currently available operate with a driving pressure of 260–520 mmHg and infuse drug at rates of 0.3–500 mL $hour^{-1}$.

1.8. Thesis overview

This thesis will explore novel strategies that have the potential to match the unmet clinical need to improve current glaucoma therapy. There were two primary objectives for the work described in this thesis:

- **Firstly**, to investigate methods for localised and sustained delivery of drugs that modulate post-surgical wound healing. To realise this objective, stand-alone, non-refillable drug delivery spacer systems, such as hydrogels, electrospun fibres, and solvent cast matrices were explored. Refillable drug delivery systems, such as elastomeric pockets were also investigated.
- **Secondly**, to evaluate the potential of hydrogels as an alternative material for aqueous flow modulation that could be used to develop a novel GDD. The primary focus was on the characterisation of aqueous permeability and mechanical integrity of novel and established hydrogel formulations.

Chapter 2 describes an experimental assessment of two main approaches for formulating an implantable drug delivery spacer system assessed using *in vitro* drug release chambers. Chapter 3 elucidates the major variables that affect the function of elastomeric pumps and establishes their relationships. Based on experimental and modelling data, recommendations for designing an implantable pump for localised subconjunctival drug delivery are provided. Chapter 4 investigates the performance of aqueous flow modulation by hydrogels using established and novel formulations with chemical and physical modifications. The general discussion, conclusions, and future work are stated in Chapter 5.

Chapter 2 Investigating spacers for prolonged drug release for the subconjunctiva

Abstract

This Chapter describes an investigation into drug-eluting spacers that were formulated using established biocompatible materials. The aim was to prolong drug release for at least five weeks critical to postoperative fibrosis, in conditions representing the subconjunctival space post-GFS or GDD implantation. The drug-eluting spacers that were investigated were formulated using non-degradable and degradable polymers. Of these formulations, the spacer containing non-ionic surfactant, Brij 98, at a concentration of 1.25% w/v was able to prolong the release of dexamethasone from poly(2-hydroxyethyl methacrylate) pHEMA hydrogels significantly longer (>30 days) than hydrogels containing no surfactant (<7 days) at therapeutically relevant drug concentrations *in vitro*. The degradable formulations failed to prolong the release of Doxycycline for five weeks *in vitro*.

2.1. Background

The wound healing process after any surgery comprises of a series of complex events, starting with inflammation and haemostasis and ending with tissue remodelling and scar formation (see **Section 1.3.5**) (130). The first five weeks are regarded as the critical period of maximum postoperative fibrosis (353–355). In the eye, the postoperative fibrosis leads to scar formation, posing a significant challenge to the success of surgery as it may close the channel formed during GFS or GDD implantation. Different drugs, including the use of anti-scarring agents in different dosage forms, such as injections and implantable films, have been investigated to modulate the wound healing process and reduce scar formation (131,353). Use of hydrogel spacers at the site of the surgery has shown promising results in bleb survival and surgery success in both preclinical models and humans (see **Section 1.6.2**) (356,357).

Antimetabolites, *e.g.* MMC and 5-FU, are routinely used at the time of GFS to lower the chance of postoperative fibrosis and improve the outcome of the surgery (354). However, use of these antimetabolites carries several risks, and these risks, along with the intrinsic toxicity of these drugs, require close monitoring of the patient after surgery (127,199). Less toxic anti-fibrotic drugs might be used as alternatives. An example is the anti-fibrotic drug ilomastat, which has been demonstrated to promote bleb survival with minimal scarring when injected into the subconjunctiva in rabbit models (231,239,358). The anti-fibrotic activity; however, was reversible and repeated injections were needed to maintain efficacy (358,359). A slow-release implant may be a way of increasing drug bioavailability at the site of surgery, overcoming the need for repeated drug administration during and after surgery. However, when anti-fibrotic drugs have been implanted directly (in powder or tablet form) at the time of surgery, they may themselves elicit a fibrotic response. Previous work conducted in the Brocchini research group has demonstrated a significant antagonistic effect of a solid anti-fibrotic drug implanted at the site of surgery (GFS in animal model, New Zealand albino rabbits)(356).

Currently, no anti-fibrotic drug-release implants for the subconjunctiva have been licensed for human use, and subconjunctival injections are routinely required to modulate postoperative wound healing. Biocompatible polymers, instead of powders or

drug tablets, offer the versatility to tailor drug-release kinetics for specific drugs without triggering a foreign body response (360–363). Ocular implants that are currently in preclinical development include non-degradable and degradable designs. Preclinical research on implantable drug delivery systems for the subconjunctiva has emerged within the last ten years (244,364,365), with the current state of the art sustained-release implants for glaucoma listed in **Table 1-3**. The safety and clinical effectiveness of a drug delivery system determine its practical use and require extensive *in vitro* and *in vivo* studies before a potential product can be translated to the clinic.

2.1.2 Using spacers for drug delivery

The concept of using spacers to promote surgical success is common when it comes to GDDs. The principal of a spacer is most commonly used by GDDs such as the Ahmed®, the Baerveldt® and Molteno® tubes (see **Section 1.3.4**). Their structure consists of a flexible plate attached to a tube and relies on foreign body encapsulation around the plate to create a reservoir of aqueous humour in a subconjunctival capsule (180,366).

The Ologen implant (also named iGen) uses the spacer effect as its underlying principle to decrease postoperative fibrosis. It is a biodegradable cylinder made of a 3D collagen matrix manufactured using highly purified pepsin-treated type-I collagen (>90%) and glycosaminoglycan (<10%). Its dimensions are 4.00 mm ± 0.3 mm (height) × 7.0 mm ± 0.5 mm ×7 mm (diameter), allowing for easy insertion into the subconjunctival space. Placed between the scleral and conjunctival flap, Ologen pushes on the scleral flap to control postoperative hypotony until a bleb is formed (367). A study of 63 eyes of 44 patients compared trabeculectomy with the Ologen implant (31 eyes) *versus* trabeculectomy with MMC without the implant (32 subjects). The Ologen group were found to have a significantly lower IOP at three months, six months, one year, three years, and five years follow up (367). In preclinical research, several methods have been described to prolong the release of drugs to enable controlled wound healing, including the use of drug-releasing spacers (199). Such spacers can be implanted in the subconjunctival space during the surgery to release drugs over an extended period and improve the outcomes of GFS and GDD implantations (279).

Because hydrogels have a unique capability of absorbing a large amount of water, hydrogels have many advantages as implantable materials because they are considered biocompatible and can be exploited to load and release drugs. Drug-loaded hydrogel contact lenses have been developed to increase tear film residence times of numerous drugs such as β-blockers, antibiotics, steroids, antihistamines and antimicrobials (368). The most simple method of hydrogel drug loading is called 'drug-imbibing', in which the hydrogels are soaked into saturated drug solutions with the aim of drug absorption into the hydrogel (369,370). However, this method leads to a poor drug loading efficiencies, and since the only resistance to drug transport is diffusion through the gel matrix, burst drug release profiles are observed in aqueous environments, characterised by spikes of high concentrations of drug released (371–374). Previous studies have reported that commonly used topical drugs when loaded in hydrogel contact lenses using the imbibition technique, released drug amounts that were lower or comparable to those of eye-drops (375–377).

Another method to embed the drug within a hydrogel is called '*in-situ* loading' which involves solubilising the drug into a polymer solution prior to the polymerisation of the xerogel (dry hydrogel) (287,378). This method ensures a 100% drug entrapment efficiency within the polymer matrix but is limited in application due to the requirement for post-fabrication processing (379). Unreacted monomer often needs to be removed but is also accompanied by the loss of drug during this post-fabrication step. Another potential disadvantage of directly dissolving the drug in the polymerisation mixture is the possibility of drug molecules interfering with the polymerisation process or losing their efficacy as a result of the polymerisation reaction (380). *In-situ* loading might increase the bioavailability of the drug in hydrogels but does not prolong the drug residence time in an aqueous environment, limiting the potential of these hydrogels for prolonged delivery of drugs (381).

The successful use of a non-degradable pHEMA spacer in combination with AGD to release MMC at the site of surgery has previously been demonstrated *in vivo* (382). The MMC-containing pHEMA spacer decreased the postoperative fibrosis and inflammation from bleb formation in a rabbit model. Another recent *in vivo* study in New Zealand albino rabbits confirmed that MMC-loaded pHEMA discs prevent postoperative

fibrosis and inflammation around the bleb (355). Both studies showed excellent biocompatibility of pHEMA in the subconjunctival space.

2.1.3 Use of dexamethasone in ophthalmology

Corticosteroids are anti-inflammatory agents that have been used to treat ocular inflammatory conditions for decades (370,383–388). They suppress inflammation by inhibiting the adherence of vascular endothelial cells (EC) and the migration of neutrophils through blood vessel walls to tissue sites of inflammation, inhibiting the presence of macrophages and decreasing the number of T and B lymphocytes at the site of tissue damage (389). Another mechanism of action is through the inhibition of phospholipase A2, and thus the arachidonic acid pathway, which decreases the production of pro-inflammatory mediators, such as prostaglandins, thromboxanes and leukotrienes (387,389).

Dexamethasone (DEX) is an inexpensive, highly potent glucocorticoid steroid (390) that is approved for use in steroid-responsive inflammatory conditions of the anterior eye, and it is most commonly used in eye drops and subconjunctival injections to reduce inflammation following eye surgery, such as GFS, cataract surgery and corneal operations (ClinicalTrials.gov identifiers NCT02006888, NCT03751059, NCT00825864, NCT04075227, NCT02875158)(391–397), the chemical structure of DEX shown in **Figure 2-1**. This drug is poorly soluble in water and has an aqueous solubility of approximately 100 µg mL^{-1} at 25°C, and has a low molecular weight of 392.5 g mol^{-1}. DEX is potent at micromolar concentrations (398) and has been shown to have a dissociation constant (K_d) of 3.47 ±0.38 nM, which correlates with the EC_{50} value (2.77 nM) determined from DEX regulation of glucocorticoid receptors (β-adrenergic) in fibroblasts (385,399,400). DEX has been shown to inhibit the proliferation of fibroblasts *in vivo* (401). It has also demonstrated a partial inhibitory effect on cytokine-induced upregulation of MMPs (2

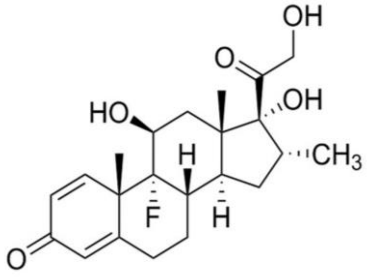

Figure 2-1. Chemical structure of dexamethasone (DEX).

and 9) in human vascular endothelial cells (402) and the inhibition of cytokine induction in human retinal microvascular pericytes at 2 nM (385). Additionally, DEX does not cause the complications that are frequently associated with the application MMC and 5-FU.

However, after topical administration of DEX, only about 1% reaches the ocular anterior segment (385). The dosing schedule for DEX-containing eye drops is generally 1–2 drops per eye every 2 hours for the first 24–48 hours, with 1–2 drops every 4–6 hours afterwards (371). Prolonged systemic administration of steroids can cause serious side effects, such as diabetes, haemorrhagic ulcers, skin atrophy, myopathies, osteoporosis, and psychosis (403,404). DEX utilisation, while being remarkably effective at reducing ocular inflammation, has been associated with increased IOP, defects in visual acuity and fields of vision, and posterior subcapsular cataract formation and thinning of the cornea or sclera with prolonged use (387,405–407).

In order to overcome the potential for side effects associated with corticosteroid application, a controlled release of DEX from a biocompatible implant would be clinically useful (408). Also, a site-specific, sustained release formulation is desirable that would eliminate the need for multiple postoperative injections and prolonged eye-drop administration that are required to maintain therapeutic concentrations. Recent investigations further reflect this clinical need into prolonging DEX release from hydrogels for one month (ClinicalTrials.gov identifier NCT04403516, NCT04200651)(266,409).

2.1.4 Use of doxycycline in ophthalmology

Doxycycline (DOX) is a common, inexpensive, antibiotic that has shown promising results as an anti-scarring agent in ophthalmology (410–412), see **Figure 2-2**, for the chemical structure of DOX. It is a broad-spectrum antibiotic of the tetracycline family that has been used for the treatment of conditions caused by bacterial infections

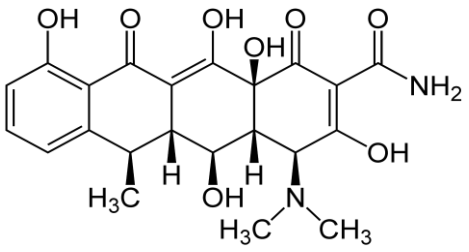

Figure 2-2. Chemical structure of doxycycline (DOX).

such as acne, urinary tract infections, intestinal infections, eye infections, gonorrhoea, chlamydia and periodontitis (413). DOX is used in the clinic in several dosage forms including injections, suspensions, capsules and tablets for the treatment of inflammatory, autoimmune and granulomatous diseases, and even in the form of a hydrogel (Atridox®) for the treatment of periodontal disease (414,415).

Some properties such as regulation of cytokines, antioxidation, inhibition of protease-activated receptor 2 (PAR2), MMP inhibition, inhibition of collagen breakdown and chemotaxis of leukocytes have been reported as being responsible for its anti-inflammatory effect (410,412,415–418). DOX is commercially available as a slightly water-soluble monohydrate form, and as water-soluble forms, hyclate and hydrate. DOX hyclate has been shown to be useful as an anti-scarring agent to modulate wound healing after GFS (419). Considering the efficacy of DOX in modulating post-surgical tissue repair (ClinicalTrials.gov identifier NCT00064766)(420), a spacer formulated with biocompatible materials for the site-specific release of DOX at therapeutically relevant concentrations for five weeks would help to modulate wound healing post-GFS or GDD implantation.

2.1.5 Surfactants

Surfactants are compounds that lower the surface tension (or interfacial tension) between two phases (fluid: fluid/fluid: solid)(421). They contain both hydrophobic groups (tails) and hydrophilic groups (heads), which give them the unique quality of being both water-soluble and insoluble (422,423), see **Figure 2-3A**. According to the Surface-tension theory, surfactants reduce the interfacial tension between two phases, whereas according to the Repulsion theory, they create a film over one phase that forms globules that repel each other (422). Surfactants aggregate together, creating physical barriers between the two phases. In water, surfactant molecules adsorb at the air-water interface, decreasing the cohesion between the water molecules on the surface. Below a certain concentration threshold, known as critical micelle concentration (CMC), individual surfactant molecules adsorbing at the air-water interface increases with increasing concentration of surfactants. This linearly decreases the surface tension with the increasing surfactant concentration (424). At the CMC, both the bulk solution and the interface are saturated, and any additional surfactant associates together to form

micelles, which is driven entropically via the expulsion of ordered water molecules into the bulk aqueous phase (425).

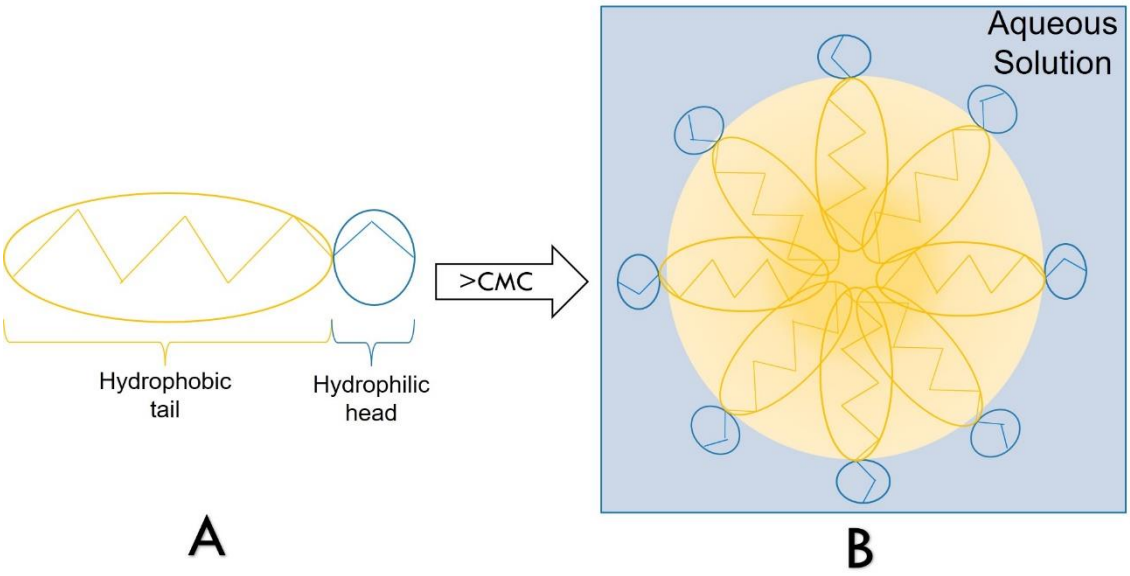

Figure 2-3. (A) Surfactants contain both hydrophobic (tails, shown in yellow) and hydrophilic (heads, shown in blue) groups that adsorb between interfaces, decreasing the surface tension in a mixed solution. Above the CMC (critical micelle concentration), **(B)** the hydrophobic blocks of the surfactants assemble to form hydrophobic core (shown in yellow) sites surrounded by hydrophilic shells. These cores can be utilised as drug depots for hydrophobic drugs in hydrophilic environments.

Above the CMC, the hydrophobic blocks of surfactants assemble to form hydrophobic core sites, shown in yellow in **Figure 2-3B**. There is a rapid drop in surface tension when the surfactant concentration is increased further above the CMC (424). The hydrophilic segments of the surfactant lie between the hydrophobic core and the external aqueous medium, stabilising the core and serving as an interface between the bulk aqueous phase and the hydrophobic core. This process is driven by the hydrophobic attraction between the hydrocarbon chains of the surfactants and the electrostatic repulsion between the polar head group of the surfactant (424). Tanford proposed that the hydrophobic affinities are responsible for the cooperative growth of micelles, while the interactions between the polar head groups of surfactants provide the anti-cooperativity that limit the aggregates to finite sizes (426).

It is possible that poorly soluble drugs can enter into these hydrophobic cores and the drug-entrapped micelles can act as drug depots, which could potentially increase drug-loading efficiencies and extend drug release times in a biomaterial such as hydrogels (427). The transport of the drug and surfactant through the hydrogel is

controlled by the bulk and surface diffusion of water. As water diffuses into the hydrogel matrix, it forms a depletion zone near the micellar-aggregate surface (428). As the concentration of the surfactant decreases, the drug-depot micelles dissociate or rupture and release the drug into the hydrogel matrix, and the rate in which the drug diffuses out of the hydrogel matrix depends primarily on the matrix composition that allows for greater water diffusion (429,430).

Most commonly, surfactants are classified according to their polar head group. Ionic surfactants carry a net positive (anionic), or negative (cationic) charge. Non-ionic surfactants have no charged groups in its hydrophilic head. The head of zwitterionic surfactants contains two oppositely-charged groups (422,423,425). Non-ionic surfactants have become increasingly influential in pharmaceutical preparations due to the implementation of high throughput screening techniques (430,431). In the past few decades, the search for new pharmacologically active compounds using hit strategies has led to a higher number of low solubility drug candidates belonging to Class II (high permeability) and Class IV (low permeability) of the biopharmaceutical classification scheme (BCS)(432,433). The poor aqueous solubility of these drugs is a significant barrier to forming an effective drug-delivery system.

The Brij family of non-ionic surfactants, which contain a hydrophilic chain of oxyethylene groups and a distinct hydrophobic hydrocarbon chain, are of specific interest. Brij surfactants are non-toxic surfactants can form micellar carriers for hydrophobic drugs (434), are FDA approved and are widely utilised in pharmaceutical applications (435). Several of these surfactants have been shown to have little to no ocular toxicity (430,436–438).

Surfactant-containing soft contact lenses have been shown to extend the delivery of hydrophobic ophthalmic drugs (430). Brij 78 has been previously reported as a promising carrier for extended-release of cyclosporine A (CyA) from pHEMA contact lenses (429,430,436). Moreover, in addition to being non-toxic, these surfactants act as permeation enhancers over the corneal surface and have shown to increase the drug bioavailability (438). Brij 98 is of particular interest due to its low CMC value, 0.6% w/v (439) and its safety on ocular surfaces (Kapoor & Chauhan 2008a; Kapoor, Howell, et al. 2009; Kapoor, Thomas, et al. 2009; Sahoo et al. 2014; Saettone et al. 1996).

2.2. Hypothesis and aims

The hypothesis for this chapter was that it was possible to incorporate a known non-toxic, anti-fibrotic drug into a spacer system formulated with biocompatible materials and achieve a prolonged drug release profile. If drug release at therapeutically-relevant concentrations can be maintained for a five-week period critical to postoperative fibrosis (353–355), then this spacer has the potential to modulate subconjunctival wound healing following a GFS or GDD implantation. The rationale behind formulating a drug-release spacer with biocompatible materials is that the spacer could either act as a stand-alone controlled drug-release implant or in combination with a GDD to modulate wound healing.

The two main aims of the work described in this chapter were:

- Firstly, to formulate and characterise a non-degradable hydrogel spacer incorporating a model hydrophobic drug and assess its drug-release profile in conditions mimicking the subconjunctival space. DEX was chosen as the model drug due to is low molecular weight, poor water-solubility, its widespread use in anti-inflammatory formulations (*e.g.* eye drops for inflammation following eye surgery), and its ability to represent other low MW hydrophobic drugs used in ophthalmic indications. A non-ionic surfactant, Brij 98 was utilised to form micelles to entrap the DEX within non-degradable hydrogels and characterise its release using an in-house *in vitro* drug-release set-up. The rationale was that increasing surfactant concentrations would increase the micellar aggregates available for the preferential partitioning of the hydrophobic drug in them. These micelles would act as drug-depots, and higher drug-loading would prolong the release of DEX.
- Secondly, to formulate a degradable drug-polymer spacer to achieve prolonged drug release for five weeks. The rationale for using degradable polymers for the spacer was due to their potential to degrade into smaller, biocompatible constituents, allowing the spacer to clear from the subconjunctival space into the systemic circulation after the drug-payload has been delivered. DOX monohydrate and hyclate were chosen as two forms of the model drug due to their low molecular weight, water-solubility, widespread use in the clinic for the treatment of eye infections, and its promising effect as an anti-scarring agent. Three different spacer

materials and methods were investigated: chitosan hydrogels loaded with DOX monohydrate and hyclate, electrospun poly(ε-caprolactone)-poloxamer fibres containing DOX monohydrate, and formulating solvent-cast poly(ε-caprolactone)-poloxamers with DOX monohydrate.

2.3. Optimal Device Requirements

The requirements for an optimal spacer device include fabrication of the spacer with biocompatible materials and the ability to release drugs at pharmacologically relevant concentrations for at least five weeks, which is a critical period for postoperative fibrosis following GFS or GDD implantation in glaucoma.

2.4. Materials and Methods

Materials used in this Chapter are listed in **Table 2-1** (list of chemicals and solvents) and **Table 2-2**. (list of materials and equipment). Reagents were all used as received without further purification. Instruments and experimental set-ups used are all described in relevant sections below.

Table 2-1. List of chemicals and solvents used in this Chapter.

Material (MW, density*)	Supplier	CAS; Catalogue/Lot number
2-hydroxyethyl methacrylate (HEMA) (MW: 130.14 g mol^{-1}, density: 1.073 g mL^{-1})	Sigma Aldrich, UK	868-77-9; 525464
Ethylene glycol dimethacrylate (EGDMA)(MW: 198.22 g mol^{-1}, density: 1.051 g mL^{-1})	Sigma Aldrich, UK	97-90-5; 335681
2,2'-Azobis(2-methylpropionitrile) (AIBN)(MW: 164.21 g mol^{-1})	Sigma Aldrich, UK	78-67-1; 441090
2-Hydroxy-4'-(2-hydroxyethoxy)-2-methylpropiophenone (HMPN)(MW: 224.25 g mol^{-1})	Sigma Aldrich, UK	106797-53-9; 410896
Dexamethasone (MW: 392.46 g mol^{-1})	VWR International, UK	50-02-2; 10173165
Brij™ 98 (Polyoxyethylene(20) oleyl ether) (density: 1.07 g mL^{-1})	Fisher Scientific, UK (Acros Organics™)	9004-98-2; 10117553-100
Doxycycline hyclate (MW: 512.94 g mol^{-1})	VWR International, UK	24390-14-5; J60579.14
Doxycycline monohydrate (MW: 462.46 g mol^{-1})	VWR International, UK	17086-28-1, J63805.06
Acetone (MW: 58.08 g/mol; density: 0.791 g mL^{-1})	Sigma Aldrich, UK	67-64-1; 179124
Chitosan (MW: 190,000-310,000 Da)	Sigma Aldrich, UK	9012-76-4; 448877
Hydrochloric acid solution (MW: 36.46 g mol^{-1})	Sigma Aldrich, UK	7647-01-0
Poly(ε-caprolactone) (PCL) (MW: ~14,000 g mol^{-1}) (Mn: ~10,000)	Sigma Aldrich, UK	440752
di-Sodium β-glycerophosphate pentahydrate (MW: 306.11 g/mol)	VWR International, UK	13408-09-8; 2765890
Poloxamer 188 (average MW: ~7680-9510 g mol^{-1})	Sigma Aldrich, UK	9003-11-6; 188-15759
Poloxamer 407 (average MW: ~7680-9510 g mol^{-1})	Sigma Aldrich, UK	9003-11-6; 407-P2443
Acetonitrile (HPLC grade) (MW: 41.05 g mol^{-1})	Sigma Aldrich, UK	75-05-8; 34851
Water (HPLC grade) (MW: 18.02 g mol^{-1})	Sigma Aldrich, UK	7732-18-5; 270733
Trifluoroacetic acid (MW: 114.02 g mol^{-1})	Sigma Aldrich, UK	76-05-1; 302031
Sodium azide (MW: 65.01 g mol^{-1})	Sigma Aldrich, UK	26628-22-8; 769320

*density at 25°C.

Table 2-2. List of materials and equipment used in this Chapter.

Material	Supplier	Catalogue/Lot number
Silicone sheets	Polymax, UK	Silona
Glass microscope slides	Sigma Aldrich, UK	BR474702-2500EA
21 gauge needles	Terumo, UK	21G AN-2138R
5 mL syringes	Terumo, UK	SS05SE1
3 mL slip top plastic syringes	BD Plastics, UK	309656

Thin wall stainless steel tubing	Coopers Needle Works Ltd, UK	16 gauge
20 gauge stainless steel needle	Nordson EDF, UK	7018169
Clear cast acrylic rods	RS Components Ltd., UK	RS PRO Clear 824-626
Silicone tubing	VWR International, UK	Tygon® 3350
Sealing film	Cole-Palmer, UK	P7543-1EA
PTFE tape	RS Components Ltd., UK	Klinger 228-687
Water purifier	VWR International, UK	Purite Select Fusion 80
Weighing balance	Sigma Aldrich, UK	Ohaus® Explorer® Pro
pH meter	Hanna Instruments Ltd, UK	HI-2210-02
Universal oven	Fisher Scientific, UK	Memmert™ UN110plus Universal 50
UV lamp	Fisher Scientific, UK	95020102
Peristaltic pump	Cole-Palmer, DE	Ismatec® IPC-N
Syringe pump	KD Scientific, UK	KDS100
Dynamic light scattering	Malvern Panalytical, UK	Zetasizer Nano ZS
Laser diffraction	Malvern Panalytical, UK	Mastersizer 3000
Micro Cuvettes	VWR International, UK	MSPP-ZEN0040
DC power supply	FuG Elektronik, DE	HCP35-35000
HPLC-UV	Agilent, UK	1200 series
Stationary phase columns	Thermo Fisher Scientific, UK	Hypersil BDS C18
	Supleco/Sigma Aldrich, USA	Ascentis RP-amide
Digital microscopy	Thermo Fisher Scientific, UK	EVOS XL cell imaging system
Scanning electron microscopy (SEM)	FEI Company, NL	Quanta 200 ESEM FEG
Dynamic Scanning Calorimetry (DSC)	TA Instruments, USA	DSC Q2000
Thermogravimetric analysis (TGA)	TA Instruments, USA	Discovery TGA 5500
Freeze dryer	SP Scientific, USA	VirTis AdVantage

2.4.1 Non-degradable spacers

2.4.1.1 Micelle preparation and size characterisation

Micellar solutions were prepared by adding different quantities of polyoxyethylene (20) oleyl ether (Brij 98) in water. Amounts of Brij 98 (125 mg, 375 mg, 750 mg, and 1000 mg) were added to 5 mL of deionised (DI) water and were left to stir overnight at 800 rpm at room temperature to achieve 2.5%, 7.5%, 15%, and 20% w/v solutions. These solutions were at least four times as concentrated as the reported CMC (0.6% w/v) of Brij 98 to ensure complete micellisation (434). After overnight stirring, 100 µL of each micellar solution was added to a micro-cuvette and were analysed for micellar size by dynamic light scattering (DLS). Average particle size was analysed by a Zetasizer Nano ZS with the following specifications: automatic sampling time of 12 measurements per sample, measurements were carried out at 25°C with an equilibration time of 120 seconds and a 173° scattering angle. The particle size was calculated automatically by

the Zetasizer Nano software v7.12, using the Stokes-Einstein relationship. At least three samples for each concentration of surfactant were analysed, and the values were reported as average ±SD. The measurements were pre-calibrated using pure DI water as a baseline.

2.4.1.2 pHEMA hydrogel preparation and drug loading

The hydrogel preparation protocol was optimised based on published protocols (430,436,441). To prepare drug-entrapped hydrogels, 70 mg of DEX powder was added to 2.1 mL of HEMA monomer. Then, 2 mL of the Brij 98 solutions were added to the DEX-HEMA mixture along with 100 µL (2.5% v/v) of ethylene glycol dimethacrylate (EGDMA) cross-linker. This resulted in a total volume of 4.1 mL (final concentration of 1.7% w/v DEX) of the HEMA-DEX-Brij 98 mixture, and this mixture was left to stir at 600 rpm for 15 hours to ensure complete dissolution.

Because the limit of solubility of DEX in micellar HEMA is unknown, additional DEX was added in increments of 0.1 mg to the HEMA-DEX-Brij 98 mixture and was stirred for 2 hours until the solution turned clear and no precipitates were observed. DEX solubility was visually confirmed by observing the mixture against a diffused light source (442,443). A clear solution indicated the partitioning of DEX into micelles. The maximum concentration of additional DEX that allowed for complete solubilisation in the HEMA-DEX-Brij 98 mixture was recorded, and this solubility method was repeated. The highest concentration of DEX that produced a clear solution; 28.1 mg mL^{-1}, 28.4 mg mL^{-1}, 29.7 mg mL^{-1}, and 30.5 mg mL^{-1} DEX for 1.25%, 3.75%, 7.5%, and 10% w/v Brij 98 mixtures, respectively, were added to new vials of all four HEMA-DEX-Brij 98 mixtures. For pHEMA hydrogels without Brij 98, 8 mg of DEX was dissolved in 2.1 mL of HEMA monomer. Brij 98 was substituted by 2 mL of DI water and was added to make a total HEMA-DEX mixture of 4.1 mL (0.2% w/v DEX). This mixture was stirred at 600 rpm for 15 hours to ensure complete dissolution.

Thermal curing for the fabrication of pHEMA hydrogels is common; however, in this study, hydrogels were created using UV-initiated polymerisation to promote a rapid polymerisation and prevent segregation of DEX aggregates of insoluble pHEMA that could give rise to a heterogeneous hydrogel structure (373).

To initiate free radical polymerisation via UV light, 4.92 mg of UV initiator, 2-Hydroxy-4'-(2-hydroxyethoxy)-2-methylpropiophenone (HMPN), was added (0.12% w/v) to the HEMA-DEX-Brij 98 mixture (**Figure 2-4**), and the polymer mixture was degassed with argon for 10 minutes to avoid oxygen inhibiting the radical polymerisation of HEMA (444). Meanwhile, polymer casting moulds were prepared by cutting out a 2.7 cm x 1.0 cm area from silicone gaskets with a 1 mm thickness. Glass microscope slides were placed on either side of the silicone gasket, and the slides and gasket were secured by placing binder clips on three sides of the casting mould to seal a cavity inside, see **Figure 2-5A**.

Immediately after degassing, the polymer mixture was drawn into a 1 mL plastic syringe using a 21G needle, which then pierced the silicone at the top of the casting

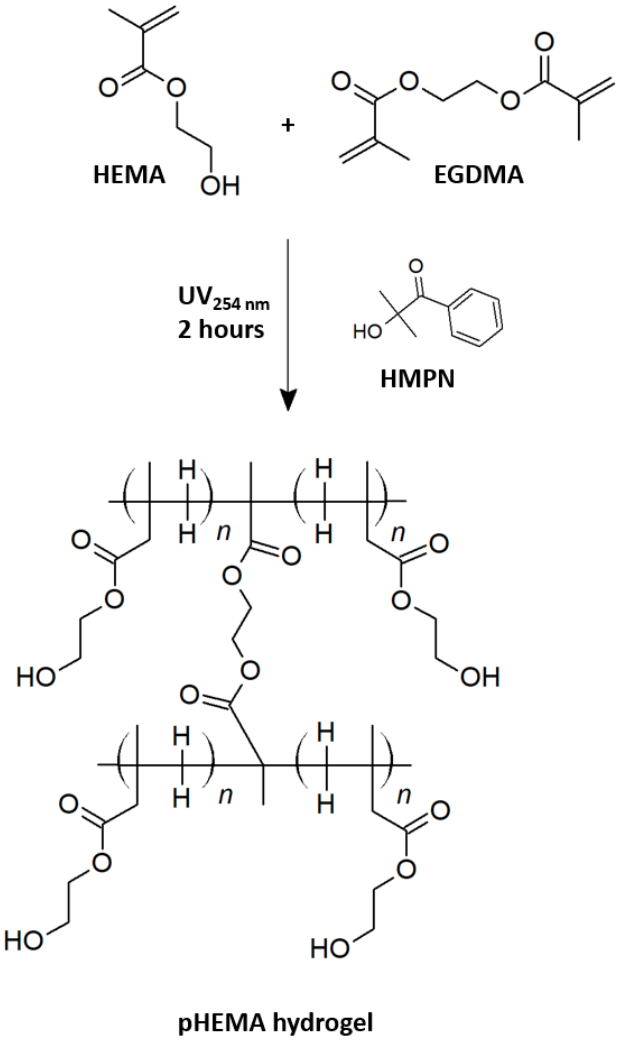

Figure 2-4. Chemical synthesis of HEMA hydrogel films by UV-initiated free radical polymerisation. The monomer (HEMA) was mixed with cross-linker EGDMA to form a clear solution. The initiator HMPN then added and placed under an 8W for at least 2 hours.

mould between the glass slides and was injected to fill the cavity. The moulds were completely filled with the polymer mixture before transferring them beneath an 8W UV lamp (**Figure 2-5B**). The samples were laid flat under the UV lamp with a wavelength of 254 nm. After 2 hours, the casting moulds were held up to a light source, where it was obvious if there was any remaining liquid polymer mixture, which implied polymerisation was not complete.

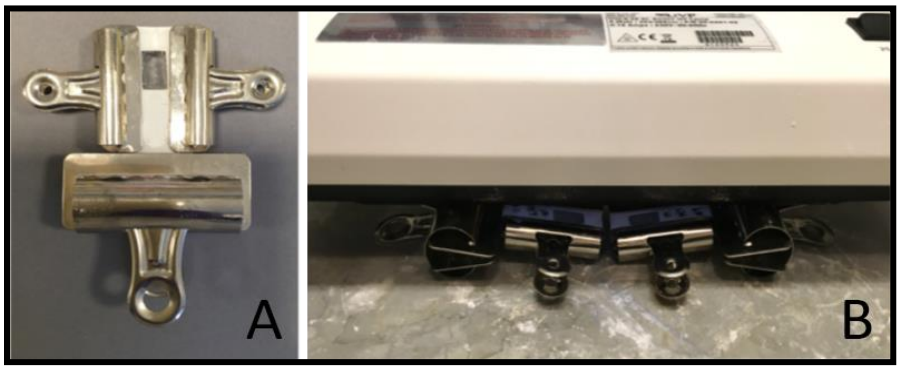

Figure 2-5. For UV-initiated polymerisation, **(A)** casting moulds were prepared using glass microscope slides and a silicone gasket to hold the polymer mixture and were **(B)** placed under a UV lamp (8 W) at 254 nm for at least 2 hours.

2.4.1.3 Post-fabrication processing

Using a custom-made punch, discs 5 mm in diameter were punched out of the polymerised (1 mm thick) xerogels and weighed. These discs were then washed in 10 mL of DI water at 50°C, the DI water was replaced every five minutes, and this step was repeated five times to remove unreacted monomer and surface-adsorbed DEX before conducting release experiments. The amount of drug lost during the washing step was quantified using HPLC (explained further in **Section 2.4.9**) and taken into considering when calculating final drug release. The encapsulation efficiency and loading capacity of DEX in the DEX-pHEMA-Brij 98 hydrogel discs were calculated using the following equations;

$$Encapsulation\ efficiency\% = \frac{drug\ amount\ added - drug\ lost\ in\ washing}{drug\ amount\ added} \times 100 \quad (2.1)$$

$$Loading\ capacity\% = \frac{drug\ amount\ added - drug\ lost\ in\ washing}{hydrogel\ disc\ weight} \times 100 \quad (2.2)$$

The amount of drug added to the discs was determined by the concentration of DEX added to the polymer mixture, the volume of polymer mixture added to the casting moulds and the weights of the resulting individual xerogels and individual discs.

2.4.1.4 Scanning electron microscopy

An FEI Quanta 200 FEG Scanning Electron Microscopy (SEM) maintained at the UCL School of Pharmacy was used for the examination of the surface and inner structure of the hydrogels. The acceleration potential used for imaging was 5 kV, and the working distance was 5–17 mm. The hydrogel samples were freeze-dried prior to SEM analysis. The fully hydrated gels were frozen at -40°C and freeze-dried using VIRTIS-Advantage freeze-dryer for three days. The dried samples were cut and adhered onto aluminium SEM stubs using carbon-coated double-sided tape. In order to make the samples electrically conductive, they were sputter-coated with gold prior to imaging.

2.4.1.5 Cross-linked hydrogel tablet preparation and particle characterisation

Another option for a non-degradable spacer was a compressed hydrogel tablet. A study demonstrated that an ilomastat-polymer mini-tablet achieved sustained drug release and prolonged bleb survival in a rabbit model for several weeks (445). Given the promise of this drug delivery system, a formulation of HEMA with a biocompatible comonomer MPC, also known as the 1015 formulation, utilised in manufacturing contact lenses, was prepared according to a heat-initiated free radical polymerisation method. Fully hydrated 1015 hydrogels were dried in an oven at 60°C for 2 hours and then ground using a mortar and pestle until a fine powder of cross-linked pHEMA-MPC was achieved. The fine powder was further dried in an oven for 5 hours at 50°C before characterising for particle size using laser diffraction (Mastersizer 3000 with AERO attachment, Malvern Panalytical, UK). The laser obscuration during the measurement was within 1-10%, which was the acceptable range of the instrument. The system was auto-cleaned between measurements to reduce the carry-over effect. A minimum of 10 measurements were made, and the average median particle size ±SD (Dv50) was analysed using the Mastersizer software version 3.63.

The hydrogel tablets were formulated using direct-compression method without excipients using a custom-made punch and die set (Holland, Nottingham, UK). Three different punch and dies created mini-tablets of 2 mm and 3 mm in diameter. A diagram illustrating the apparatus for the tablet punch and die set is shown in **Figure 2-6**.

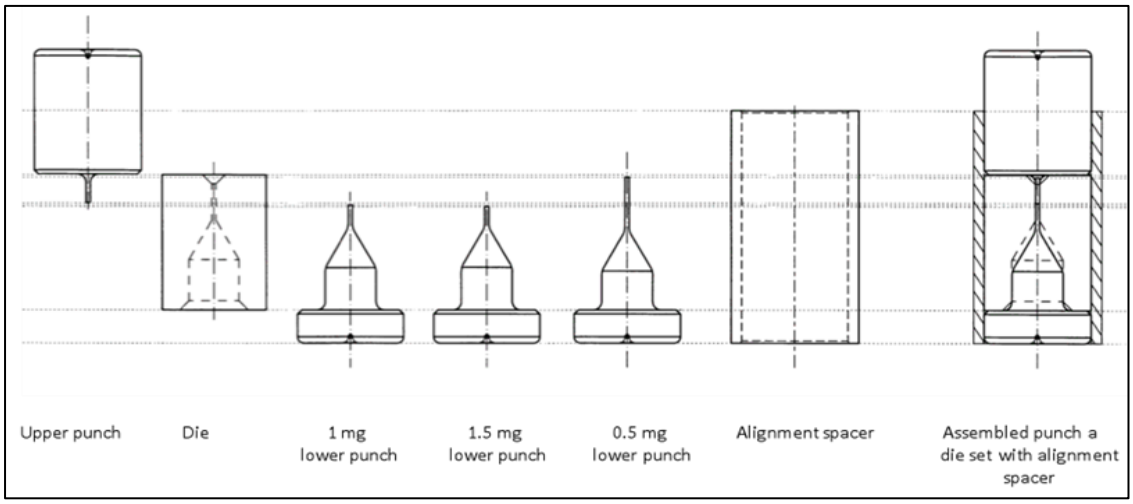

Figure 2-6. The different components of the punch and die set. For each size of the intended mini tablet, a specific upper and corresponding lower punch would be used to punch a known amount of drug polymer mixture. An alignment spacer was used to ensure the symmetrical distribution of compression force during tablet pressing.

To lubricate the parts, micro grade Poloxamer 188 (Lutrol F68, BASF, Germany) 0.1% in acetone was applied, and the solvent was allowed to evaporate before tablet compression. The FDA has approved the use of Poloxamer 188 in ophthalmic drops (446). The tablets were pressed using a Specac IR press. Cross-linked pHEMA powder was mixed with DEX (75% w/w) and poured into the die for the 2 mm tablet. The punch was placed with the pin inside the die and compression applied (0.3 MPa for 10 minutes).

For preparing the 3 mm tablet, firstly, an excipient-less DEX tablet was fabricated using a punch and die (2 mm diameter) set with no lubricant. DEX (1.5 mg) was weighed and placed into the die and compressed (0.3 MPa for 10 minutes). The tablet was ejected from the die, and its weight was recorded. The DEX tablet was placed individually into tared Eppendorf tubes (1.5 mL) and stored at 4°C. Next, cross-linked pHEMA powder (1.5 mg) was emptied into the 3 mm die. The excipient-less DEX tablet was carefully centred in the middle of the 3 mm die on top of the cross-linked pHEMA powder. To this, the cross-linked pHEMA powder was added from a second vial (1.5 mg). Fitting the punch into the die, this combination of solids was compressed (0.5 MPa for 20 minutes)

to yield a cross-linked pHEMA coated DEX tablet (33% w/w drug/polymer) that was ejected from the punch. The tablet heights were measured using a micrometre screw gauge.

2.4.2 Degradable spacers

2.4.3 Chitosan hydrogel preparation

Chitosan is an amino-polysaccharide obtained by alkaline deacetylation of chitin that is naturally found in Crustacean shells (447). Chitosan was investigated as a degradable drug hydrogel spacer because it is both biocompatible and biodegradable (448), readily dissolving in acidic solutions through protonation of its amine groups. Once dissolved, chitosan remains in solution up to a pH of 6.2. In the presence of β-glycerophosphate at 37°C, the pH value reaches the physiological range, and electrostatic attractions between the ammonium and phosphate groups form, chitosan interchain hydrogen bonding increases, and chitosan-chitosan hydrophobic interactions occur, which leads to the formation of a hydrated gel-like precipitate (**Figure 2-7**).

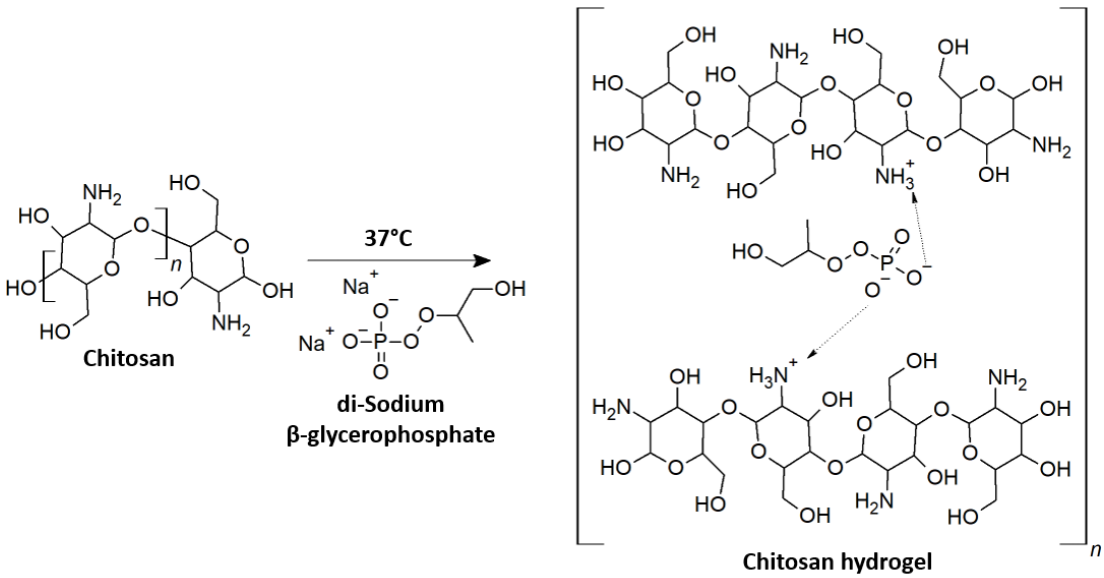

Figure 2-7. Synthesis of chitosan hydrogels in the presence of β-glycerophosphate. Chitosan dissolves in pH <6.2 via protonation of its amine groups. In the presence of β-glycerophosphate salt at physiological, neutral pH and at 37°C, chitosan transitions from a solution to a hydrogel by chitosan interchain hydrogen bonding, electrostatic attractions between the ammonium and phosphate groups, and chitosan-chitosan hydrophobic interactions.

A polymer solution was prepared by dissolving 200 mg of chitosan (with medium viscosity and a >80% degree of deacetylation) in 10 mL of 0.1N HCl to a final concentration of 2% w/v. The solution was stirred for 6 hours at 600 rpm with a magnetic

stirrer to ensure complete mixing and was then cooled to 4°C. di-Sodium β-glycerophosphate pentahydrate (500 mg) was dissolved in 1 mL of DI water, and drops of this solution were carefully added to the cooled chitosan-HCl solution to obtain a clear and homogeneous liquid solution. The chitosan solution was split into two 5 mL portions, and 110 mg of DOX monohydrate (2.2% w/v) was added to one portion, and 110 mg of DOX hyclate (2.2% w/v) was added to the other portion. The pH values of the two DOX-chitosan solutions were determined as 7.12 and 7.19 for DOX monohydrate and DOX hyclate, respectively. The solutions were heated to 37°C while stirring 600 rpm on a heating plate. Chitosan hydrogels were used without any further modification for *in vitro* drug release of DOX (monohydrate and hyclate) using the same set-up and method described in 2.4.9.

2.4.4 Electrospinning polymers to formulate poly(ε-caprolactone) fibres

Fibres were explored as a potential degradable drug-delivery spacer for DOX monohydrate. The rationale was that a polymer should encapsulate DOX monohydrate, which is a poorly-water soluble form of DOX, and prolong its release whilst preventing its degradation by photolysis. Poly(ε-caprolactone)(PCL) and poloxamers have been approved by the FDA for ophthalmic formulations and were used to formulate fibres by electrospinning, using a vertical set-up.

Electrospinning works by applying a high voltage (typically 0–30 kV) to a capillary tube with the polymer and drug mixture. Once the voltage is applied to the liquid mixture, the liquid droplets become charged with the same polarity (449). When these charged polymer droplets at the tip of the capillary tube are sufficient for the electrostatic repulsion to counteract the confinement of liquid surface tension, a droplet elongates to form a Taylor cone (450–454). Because the liquid is subjected to a high electric field, the charged droplets become unstable and emerge as a single jet, travelling straight down, decreasing in diameter, until it starts to bend. The jet then enters the “whipping instability” regime, in which it accelerates and fluctuates rapidly in a “whipping” motion (449,455). As the solvent evaporates, the jet solidifies to form continuous fibres that are collected on a grounded collector plate, see **Figure 2-9**.

First, a polymer solution was prepared by adding 1 gram of low molecular weight PCL (M_n ~10,000) and 1 gram of poloxamer 407 (PPO units of 4000 kDa and a 70% PEO content) to 10 mL of acetone to obtain a final solution concentration of 20% w/v (**Figure 2-8**). Another solution of PCL and poloxamer 188 (PPO units of 1800 kDa and an 80% PEO content) in acetone at the same concentration was prepared. DOX monohydrate (250 mg) was added to each of these PCL-poloxamer solutions, with final a drug concentration of 12.5% w/w with respect to the polymer mixture and was used to estimate the final drug loading in the fibres. To ensure complete mixing, both solutions were stirred at 800 rpm for 6 hours at room temperature.

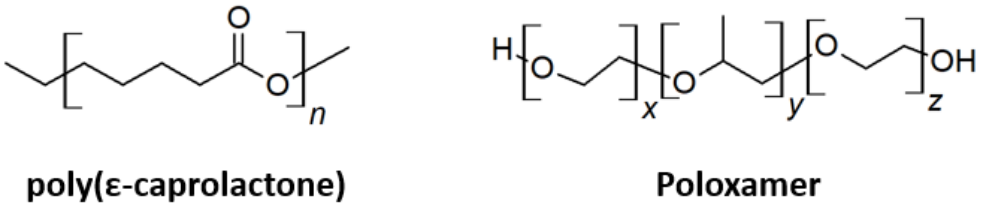

poly(ε-caprolactone) **Poloxamer**

Figure 2-8. Chemical structures of poly(ε-caprolactone) and poloxamer, a co-block polymer of polyethylene oxide and polypropylene oxide.

Second, the PCL-poloxamer-DOX solutions were transferred into a 5-mL syringe, and a stainless-steel needle with an inner diameter of 0.6 mm was attached to the syringe. The syringe was mounted on a syringe pump, and a flow rate of 1 mL $hour^{-1}$ was maintained. The applied positive voltage was 18 kV using a DC power supply (HCP35-35000, FuG Elektronik, Germany). The resulting fibres were collected on a grounded plate covered in aluminium foil for easy collection and storage (**Figure 2-9**). The distance between the needle tip and the grounded target was 18 cm. Electrospinning processes were conducted under ambient conditions, with a temperature of ~21°C and relative humidity of ~45%. Optimisation of the electrospinning parameters was first performed to find the most appropriate flow rate, voltage, and needle to collector distance. The range of parameters explored, and optimal processing conditions identified are detailed in **Table 2-3**.

Table 2-3. Range of electrospinning processing parameters explored and identified optimised values.

Parameter	Range	Optimised
Flow rate (mL h^{-1})	0.5-1.5	1
Voltage (kV)	14-24	18
Distance from needle to collector (cm)	12-20	18

Finally, PCL nanofibre preparation was confirmed by visual inspection using a digital microscope (EVOS XL cell imaging system, Thermo Fisher Scientific, UK). Diameter distribution analysis of the fibres was carried out using the digital microscope images by making manual measurements at 50 different points, using the ImageJ 1.53a software (National Institutes of Health, USA)(456). The collected fibres were stored in darkness at room temperature and were used without any further modification for *in vitro* drug release of DOX (monohydrate) using the same set-up and method described in **Section 2.4.9**.

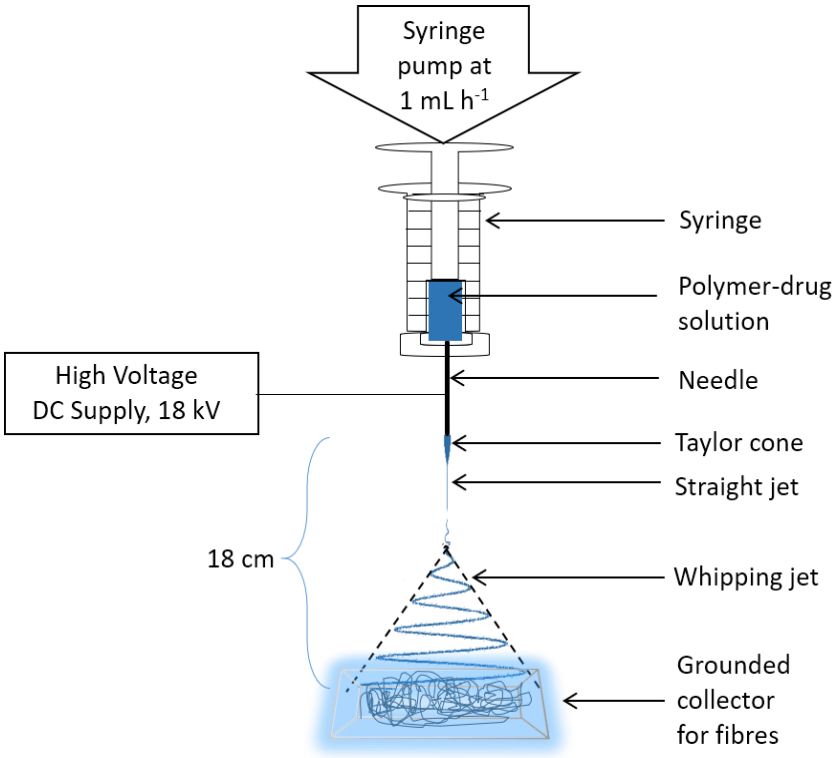

Figure 2-9. Schematic of the set-up used for electrospinning PCL fibres. Polymer-drug liquid mixture was drawn in a syringe with a needle of 0.6 mm inner diameter attached to it. The syringe was mounted on a syringe pump and flow rate was maintained at 1 mL hour^{-1}. A positive voltage of 18 kV was applied using a DC power supply. A grounded target was covered in aluminium foil for easy fibre collection and storage. The distance between the needle tip and the grounded target was 18 cm. Electrospinning processes were conducted under ambient conditions (temperature: ~21°C, relative humidity: ~45%). Fibre preparation was confirmed by visual inspection using digital microscopy.

2.4.5 Solvent-casting polymers

In this method, a drug is dissolved in a suitable solvent and mixed with a polymer carrier, which is followed by solvent removal and solidification to form solid dispersions. The advantage of this method is that the temperature and the mixing time are lower

than traditional melting methods of polymer processing, thus protecting the drug from potential thermal degradation (457).

Solvent casting was used to encapsulate DOX monohydrate in PCL. PCL-poloxamer 407 and PCL-poloxamer 188 (20% w/v) solutions were prepared by adding 1 gram of low molecular weight PCL (M_n ~10,000) and 1 gram of either poloxamer 407 or 188 to 10 mL of acetone. DOX monohydrate (250 mg) was added to the polymer solutions with a concentration of 12.5% w/w (DOX/PCL-poloxamer) and was used to estimate the final drug loading in the solvent-cast PCL spacers. To ensure complete mixing, both solutions were stirred at 800 rpm for 6 hours at room temperature. Since the solvent vapour pressure of acetone is 25.1 kPa at ~20°C (information from supplier), the DOX-PCL-poloxamer solutions were poured into glass Petri dishes and were placed in a standard laboratory fume hood for solvent vapour extraction, and were left in the fume hood for 9 hours. The dry DOX-PCL-poloxamer spacers were weighed and used without any further modification for *in vitro* drug release of DOX monohydrate using the same set-up and method described in **Section 2.4.9**.

2.4.6 Swelling ratio measurements of hydrogels

The type of binding of water in a hydrogel can determine the overall exchange of solute from the hydrogel. The maximum percentage of water absorbed by the hydrogel to reach full hydration is termed as equilibrium water content per cent measurements (EWC%)(458). To calculate the EWC% of pHEMA hydrogels, 5 mm discs were cut from fully hydrated pHEMA hydrogels and weighed, which was considered the weight of the disc in equilibrium with water (W_e). The discs were then completely dried by placing them in a vacuum oven at 70°C until they reached constant weight (W_d).

Chitosan hydrogels were weighed after polymerisation, and this weight was considered the equilibrium with water (W_e) weight. The hydrogels were then dried in a vacuum oven at 70°C until they reached a constant weight (W_d). The equation below was used for the calculation of EWC% (458,459).

$$\text{EWC}\ (\%) = \frac{(W_e - W_d)}{W_e} \times 100 \tag{2.3}$$

Swelling ratio (SR) refers to the ratio between the weight of solvent absorbed by the hydrogel and the dry weight of the xerogel. It gives an indication of the increase in the size of the xerogel when fully hydrated. It was calculated as;

$$\mathrm{SR} = \frac{(W_e - W_d)}{W_d} \tag{2.4}$$

2.4.7 Differential scanning calorimetry

To measure the free water to bound water ratio in pHEMA hydrogels, differential scanning calorimetry (DSC) was utilised. The principle behind DSC is that only free water and lightly-bound water molecules are frozen, so the endotherm obtained from DSC represents the amount of frozen water only. The heat of fusion of freezable water in hydrogels was assumed to be the same as ice. The amount of bound water is the difference between the total water content and freezable water (317,460). The melting enthalpies achieved from DSC were used to calculate the bound to free water ratio. As given in the equations below, W_b is the amount of bound water, W_f is the amount of free water, W_{fb} is the amount of lightly bound water, Q_{endo} is the melting enthalpies derived from the DSC chart and Q_f is the melting enthalpies of free water which is the same as ice; 79.9 cal g^{-1} (458).

$$W_b(\%) = EWC\% - (W_f + W_{fb}) \times 100 \tag{2.5}$$

$$W_b(\%) = EWC\% - (\frac{Q_{endo}}{Q_f}) \times 100 \tag{2.6}$$

DSC measurements were performed with a DSC Q2000 equipped with a refrigerated cooling system. Nitrogen with a flow rate of 50 mL min^{-1} was used as a purge gas for all the experiments. Fully hydrated hydrogel samples were weighed into TA zero aluminium hermetic pans. All samples weighed between 15–20 mg. An empty hermetically sealed pan was used as a reference for all samples. Calibration with indium (Tm =156.6; ΔHf =28.71 J g^{-1}) was performed according to the manufacturer instructions. Samples were cooled from 25°C to -35°C at a cooling rate of 5°C min^{-1}, then were held for 3 minutes at -35°C, and then were heated to 150°C at a rate of 10°C min^{-1}. All measurements were performed at least in triplicate for all hydrogels, and the mean values were used in data analysis with TA Universal Analysis software version 4.5A (TA Instruments, USA).

2.4.8 Thermogravimetric analysis

To evaluate the thermal stability and degradation profiles of micellar pHEMA hydrogels, thermogravimetric analysis (TGA) was carried out on a Discovery TGA 5500. Nitrogen was used as a purge gas for the furnace at 50 mL min^{-1}. Fully hydrated hydrogel samples were weighed into open TA aluminium pans. All samples weighed between 15–20 mg. The samples were heated to 50°C, were held at 50°C for 5 minutes, and then were heated to 500°C at a rate of 20°C min^{-1}. The sample weight remaining (%) and the rate of thermal decomposition data as a function of temperature (°C) were plotted using OriginPro b9.5 Academic (Origin Lab Cooperation, USA).

2.4.9 *In vitro* drug release studies

2.4.9.1 Design of *in vitro* drug release flow chamber

Because the drug delivery spacers are intended for use in the subconjunctiva, a two-piece, closed-top drug-release rig was fabricated from clear cast acrylic rods by Mr John Frost UCL School of Pharmacy workshop to mimic the subconjunctival space. Each rig consisted of two acrylic parts and a silicone-ring that were sealed securely with three screws, see **Figure 2-10**. To minimise water evaporation, all junctions were secured using

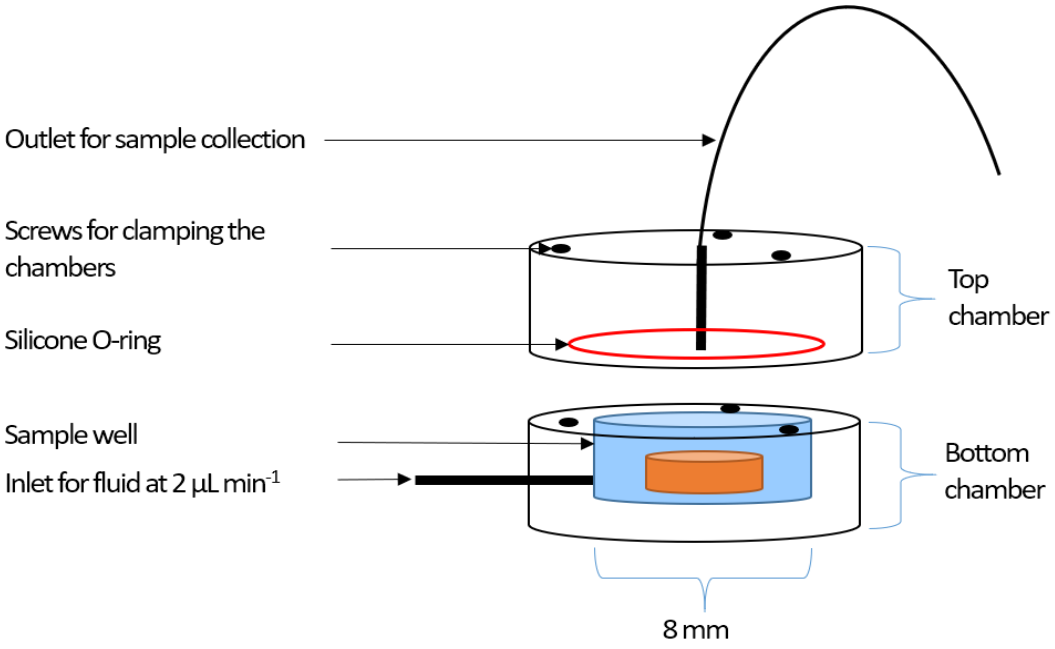

Figure 2-10. Schematic diagram of the *in vitro* flow rig used for drug release studies was designed to mimic the bleb formed in the subconjunctival space after GFS. It had an inlet for aqueous flow through the spacers and an outlet to collect the drug-release aliquots for quantification using HPLC-UV.

tie locks and thread sealing PTFE tape. The bottom part of the drug-release rig was 8 mm in diameter and contained an inlet for fluid into a small well with a 250 µL capacity, which is the estimated volume for a filtration bleb in the subconjunctiva (239,461,462). A constant flow of water at 2 µL per minute was maintained across the drug-polymer spacers to assess drug release using a pharmaceutical dispensing pump. The top part of the release rig had an outlet tube for sample collection.

2.4.9.2 *In vitro* drug-release set-up

All drug-loaded spacers were tested for drug release, and the schematic of the set-up is shown in **Figure 2-11**. Since there were no visually-observable aggregates in the hydrogels or fibres, the drug distribution was assumed to be homogenous and represented the drug distribution profile in the entire material.

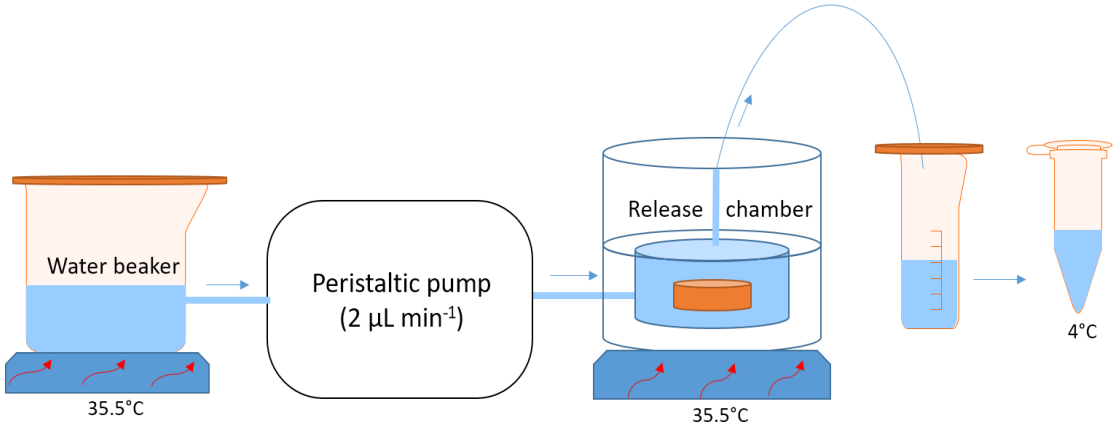

Figure 2-11. Schematic of the *in vitro* drug-release set-up used. Hydrogel discs (shown as an orange disc) were placed in drug-release chambers (maintained at 35.5°C), connected to a peristaltic pump which pumped warm water (maintained at 35.5°C) at the physiological rate (2 µL/min) of aqueous production. Drug-release aliquots were stored 4°C until quantified using High Pressure Liquid Chromatography with a UV detector (254 nm).

After any post-fabrication processing, spacers were seated in the well of the bottom chamber of the *in vitro* drug-release rigs and were screwed shut. The drug-release rigs were placed on a heated oil bath, so a constant temperature of 35.5°C was maintained, which is an estimate of the subconjunctival temperature (463). DI water supplemented with 0.02% sodium azide, maintained at 35.5°C, was pumped through the rigs using an eight-channel peristaltic pump (Ismatec, Germany) at the physiological rate of aqueous production in the eye (2 µL min^{-1})(52,53,64). The flow rig apparatus was calibrated and checked by collecting and weighing effluent over a set period of time. Calibration took place at the start and the end of the experiment. Drug-release samples

were collected in glass vials and were covered with a parafilm. Samples were collected every two hours on the first day, every day for the next four weeks and once every three days until 35 days (end of five weeks). The eluted samples from drug release experiments were stored at 4°C until quantified using HPLC.

2.4.9.3 HPLC methods for drug quantification

DEX samples were analysed by an HPLC-UV system Agilent 1200 series equipped with Chemstation software (Agilent, Wokingham, Berkshire, UK). The stationary phase was a Hypersil BDS C18 (250 x 4.6 mm, 5 µm) column maintained at 25°C. The mobile phase was composed of 32% (v/v) acetonitrile and 0.1% (v/v) trifluoroacetic acid in water. The separation method included a mobile phase flow rate of 1.1 mL min^{-1} for a 10 minute run time. The injection volume was 25 µL, and the detection wavelength was 254 nm. The retention time for DEX was 7.4 minutes.

DEX samples for the calibration curve were prepared using the mobile phase as the solvent. The first sample in the calibration curve was prepared by adding 1 mg of DEX to 8 mL of mobile phase and stirred at 600 rpm for 15 minutes with a magnetic stirrer to ensure that DEX was dissolved. This sample was diluted 1:1 in the mobile phase, and a concentration range was created by further 1:1 dilution. To increase the reliability of measures, this process was repeated three times, and an average of each concentration was plotted on the calibration curve. The correlation coefficient of the calibration curve was R^2: 0.9996 for a concentration range of 125–0.031 µg mL^{-1}, indicating acceptable linearity. The deviation between replicate samples was <1%, and the limit of detection for DEX in the mobile phase was ~0.1 µg mL^{-1}.

DOX monohydrate and hyclate samples were also analysed by an HPLC-UV system Agilent 1200 series equipped with Chemstation software. The stationary phase was an Ascentis RP-amide column (150 x 4.6 mm, 5 µm) maintained at 40°C. The mobile phase was composed of 25% (v/V) acetonitrile and 0.1% (v/v) trifluoroacetic acid in water. The separation method included a mobile phase flow rate of 1 mL min^{-1} over a 10 minute run time. The injection volume was 25 µL, and the detection wavelength was 273 nm. The retention time for DOX monohydrate was 3.4 minutes.

A calibration curve for DOX monohydrate was prepared using the mobile phase as the solvent; the first sample was prepared by adding 1.1 mg of DOX monohydrate to

8 mL of mobile phase and stirred at 600 rpm for 15 minutes with a magnetic stirrer to ensure that DOX was dissolved. This sample was diluted 1:1 in the mobile phase, and a concentration range was created by further 1:1 dilution. To increase the reliability of measures, this process was repeated three times, and an average of each concentration was plotted on the calibration curve. The correlation coefficient of the calibration curve was R^2: 0.9989 for a concentration range of 137.5-0.03 µg mL^{-1}, indicating acceptable linearity. The deviation between replicate samples was <1%. The limit of quantification for DOX in solvent was ~0.1 µg mL^{-1}.

A calibration curve for DOX hyclate was also prepared using the mobile phase as the solvent; the first sample was prepared by adding 32.0 to 8 mL of mobile phase and stirred at 600 rpm for 15 minutes with a magnetic stirrer to ensure that DOX was dissolved. This sample was diluted 1:1 in the mobile phase, and a concentration range was created by further 1:1 dilution. To increase the reliability of measures, this process was repeated three times, and an average of each concentration was plotted on the calibration curve. The correlation coefficient of the calibration curve was R^2: 0.9999 for a concentration range of 4000-0.03 µg mL^{-1}, indicating acceptable linearity. The deviation between replicate samples was <1%. The limit of quantification for DOX hyclate in solvent was ~0.2 µg mL^{-1}.

The concentrations of DEX and DOX were determined from the area under the release rate curve (AUC) using the trapezoidal rule to approximate the definite integral (signed area of the region in XY-plane that is bounded by the graph). The concentration of drug in each sample analysed on a given day was determined by a standard curve prepared on the same day. If the concentration of drug release in a sample fell outside the linearity range of the calibration curve, appropriate dilutions were made using the mobile phase, and the dilution factor was accounted for in the concentration estimation.

Next, the volume that was collected from drug-release chambers between each time point was calculated using equation 2.7;

$$volume = flow\ rate \times time \tag{2.7}$$

with the flow rate set as 2.0 µL min^{-1}. From there, the mass of drug in each sample was calculated using equation 2.8;

$$mass = concentration \times volume \tag{2.8}$$

and then the cumulative mass for each time point was calculated. Next, the cumulative drug release (total drug released) for each time point was calculated using the total drug content in a hydrogel disc using equation 2.9;

$$Cumulative\ drug\ release\% = \frac{cumulative\ mass}{drug\ amount\ in\ disc - \ drug\ washed} \times 100 \quad (2.9)$$

Average cumulative drug released (%) and standard deviation for each time point were calculated. The time required for half of the drug amount in the spacer to be released, or the elimination half-life, $T_{1/2}$ was estimated using the following equations:

$$k_t t = lnQ_0 - lnQ_t \quad (2.10)$$

$$T_{1/2} = \frac{0.693t}{k_t} \quad (2.11)$$

where Q_t is the amount of drug released in time t, Q_0 is the initial amount of drug in the spacer and k_t is the first order release constant (464,465).

2.4.10Mathematical modelling of drug release kinetic data

To evaluate the kinetics of *in vitro* release data from the pHEMA hydrogel discs, mathematical models such as zero order, first order, Higuchi's, Hixson-Crowell's, Weibull and Korsmeyer-Peppas models were applied (465–470). The criterion for selecting the most appropriate model was based on matching the assumption criteria of the model: goodness-of-fit test (R^2) and the smallest sum of squares of residuals (SSR) value (471–473). Korsmeyer-Peppas model was found to be the best fit for studying the mechanism of drug release. According to this model, to find out the mechanism of drug release from a polymeric system, the first 60% of the drug-release data is fitted to the equation using the following equation;

$$\frac{M_t}{M_\infty} = kt^n \quad (2.12)$$

where $\frac{M_t}{M_\infty}$ is the fraction of drug released at time, t, k is the rate constant, and *n* is the diffusion exponent. The *n* value is used to characterise different release mechanisms for cylindrical shaped matrices (474,475).

2.4.11Statistical analysis

All results are presented as the average (arithmetic mean) and standard deviation (± SD) of at least three samples, and data were plotted using Origin Pro 2018 Academic (OriginLab, USA). For the analysis of variance, one-way and repeated measure ANOVA with Tukey's post hoc test was carried out to evaluate statistical differences between the mean values of experimental data. Probability value descriptive data were generated for all variables and values less than 0.05 ($p<0.05$) were considered as indicative of statistically significant differences.

2.5. Results

2.5.1 Non-degradable pHEMA spacers

The aim of these experiments was to formulate DEX-loaded pHEMA spacers using a non-ionic surfactant, Brij 98, and evaluate *in vitro* release kinetics and duration of release. DEX was used as the model hydrophobic drug due to its widespread use as an anti-inflammatory drug in ophthalmic formulations. A range of Brij 98 surfactant concentrations (1.25-10% w/v), well above the CMC (0.6% w/v) was investigated to achieve maximum drug-loading and prolong drug release.

2.5.1.1 Micelle characterisation

As the concentration of Brij 98 was increased (2.5–20%) in aqueous solution, the mean particle size of the micelles decreased, see **Figure 2-12**. For a 2.5% w/v Brij 98 solution, the mean size of the micelles was 8.8 ±0.08 nm with a poly-dispersity index (PDI) of 0.1. For 7.5% w/v Brij 98 concentration, the mean size of the micelles decreased to 7.69 ±0.08 nm with a PDI of 0.2. For 15% w/v Brij 98 solution, the mean size of the micelles further decreased to 6.21 ±0.07 nm with a PDI of 0.2. For 20% Brij 98 concentration, the mean size of the micelles was observed to be the smallest of the four concentrations of Brij 98 solutions analysed by DLS. The mean size of the micelles was 5.67 ±0.07 nm, with a PDI of 0.2. These results suggest that as the concentration of Brij

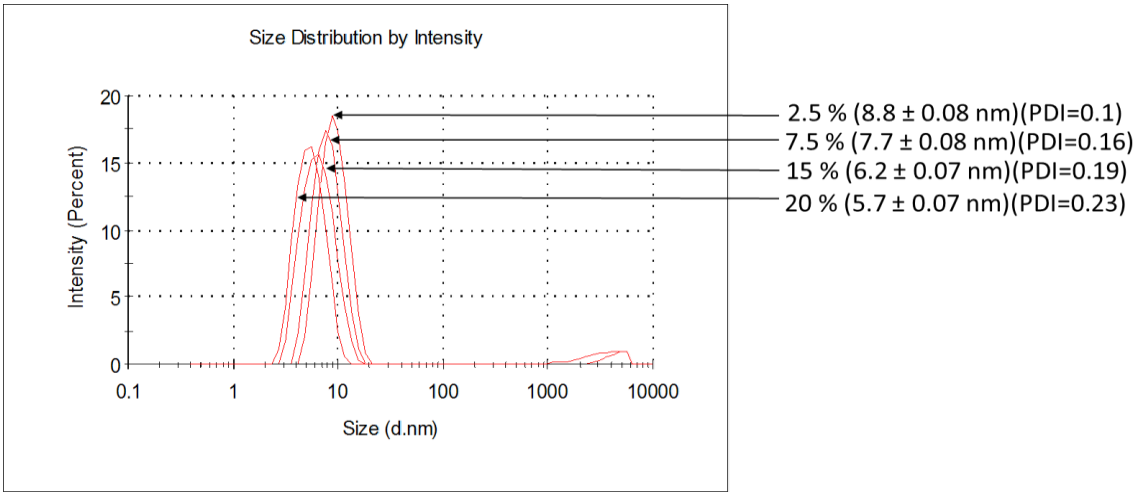

Figure 2-12. Dynamic light scattering showed that as the concentration of Brij 98 in water increased, the average size of the micelles decreased (n=6). The range of average micelle particle sizes was 8.8 ±0.08–5.7 ±0.07 nm. The poly-dispersity index increased as the concentration of Brij 98 increased, suggesting small, moderately polydisperse micelles at higher concentrations of Brij 98.

98 increases, the resulting micelles are smaller and are moderately polydisperse in solution, while lower concentrations of Brij 98 result in monodisperse particle distributions.

2.5.1.2 Visual characterisation

The UV-polymerised DEX-pHEMA-Brij 98 xerogels were transparent and glossy with no precipitates observed during the visual inspection, see **Figure 2-13**. They were also pliable to the touch. The absence of particulates suggested that the majority of DEX was entrapped in micelles within the xerogels. Importantly, heterogeneous DEX distribution would affect the accuracy of the drug release results. Additionally, a non-encapsulated drug can trigger the immune system resulting in foreign body response and ultimately adversely affect the therapeutic efficacy of the implantable spacer disc (356,476,477). The inclusion of Brij 98 and DEX did not appear to interfere in the polymerisation process of pHEMA hydrogels.

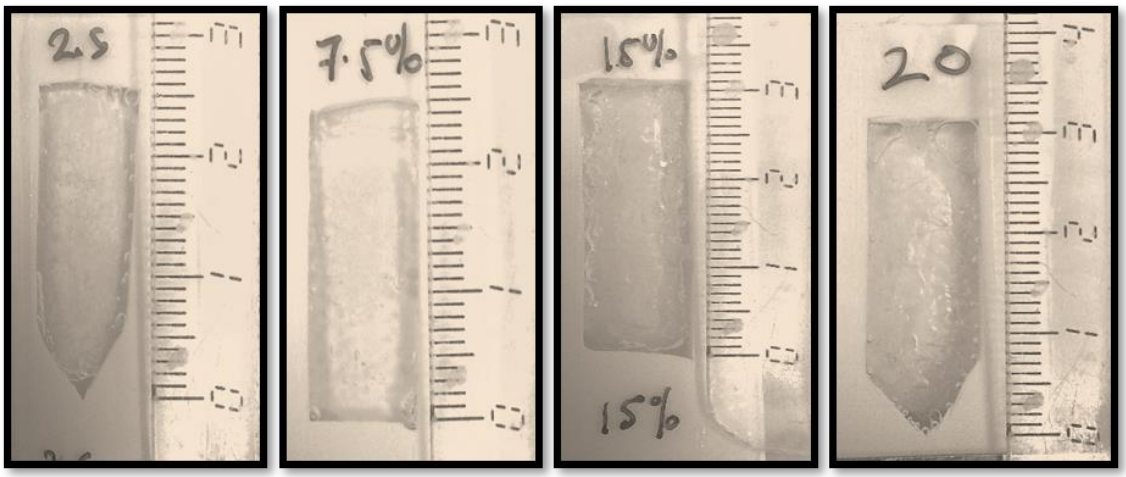

Figure 2-13. UV-initiated polymerisation resulted in pHEMA xerogels loaded with DEX. (L-R) DEX-pHEMA hydrogels containing 1.25%, 3.75%, 7.5% and 10% w/v Brij 98. The xerogels did not show particulate aggregates, indicating that majority of the drug was entrapped in micelles.

2.5.1.3 Post-fabrication processing

After recording the observations of pHEMA xerogel visual inspection, circular discs were punched out (**Figure 2-14**) and weighed to calculate the drug loading efficiencies and drug loading capacities. DEX loading increased from 0.2% w/v in DEX-pHEMA xerogels (103.3 ±6.4 µg $disc^{-1}$) without Brij 98 to >2.5% w/v for Brij 98-loaded DEX-pHEMA xerogels, see **Table 2-4**. Drug loading was determined based on the

maximum solubility of DEX in the system (with or without Brij 98), which was confirmed by repeated evaluations, the volume of polymer mixture added to the casting moulds, and weights of individual xerogels and discs. Post-fabrication of the xerogel discs included a washing step with hot water (50 mL at 50°C).

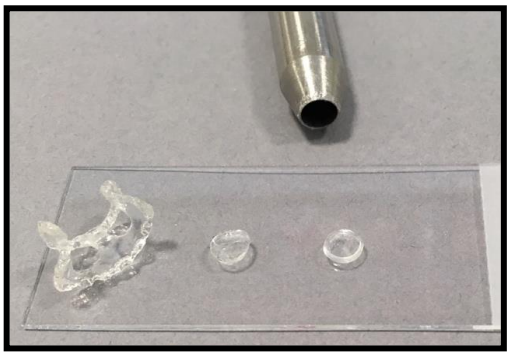

Figure 2-14. Discs with a diameter of 5 mm were created from xerogel films using a custom-made punch for characterisation and drug release studies.

Table 2-4. The amount of DEX lost during post-fabrication processing, the final amount of DEX loaded per disc, drug-loading capacities, and drug-loading efficiencies of the hydrogels.

Brij 98 concentration in hydrogel discs (% w/v)	Amount of DEX lost in washing (µg)	Final amount of DEX loaded* (µg disc^{-1})	Loading capacity (%)	Encapsulation efficiency (%)
0	24.8 ±4.1	78.5 ±4.2	0.3 ±0.03	75.9 ±1.5
1.25	165.2 ±27.0	718.4 ±12.3	2.8 ±0.3	81.2 ±1.6
3.75	201 ±32.8	667.1 ±6.0	2.8 ±0.3	76.7 ±1.9
7.5	180 ±29.4	884.0 ±23.7	3.6 ±0.4	83.0 ±1.4
10	182.7 ±29.8	1230.3 ±25.1	4.6 ±0.4	87.0 ±1.1

*Calculated by subtracting the amount of drug lost in the washing step from the theoretical amount of DEX (in µg) added to the discs. The theoretical amount of DEX was derived from the concentration of DEX added to the polymer mixture, the volume of polymer mixture injected into the casting moulds and the weight of the individual hydrogels and hydrogel discs.

This method is commonly utilised while manufacturing soft contact lenses to remove unreacted monomer after polymerisation is complete (436). This method also washed out some drug from the xerogel discs and the drug lost was quantified using HPLC and subtracted from the total drug per disc for estimation of final drug loading, see **Table 2-4**. As the concentration of Brij 98 increased, there was an increase in the calculated per cent loading capacities of the hydrogels; however, there was no clear difference in the calculated per cent encapsulated efficiencies between all the hydrogels. This indicates that hydrogels with higher Brij 98 concentrations are able to hold high drug amounts.

2.5.1.4 Scanning electron microscopy

Scanning electron microscopy (SEM) imaging was employed to qualitatively assess the microstructure of drug-loaded hydrogels because it enabled a closer inspection of their bulk homogeneity (internal structure) as well as their surface. In UV-initiated polymerisation, the surface of the xerogel is first to polymerise followed by the bulk of the xerogel. Hydrogels examined included both DEX-pHEMA hydrogels (0% Brij 98) and Brij 98-loaded DEX-pHEMA hydrogels. DEX-pHEMA hydrogels without Brij 98 showed a uniform glossy surface with folds presumably formed during the polymerisation process, see **Figure 2-15**.

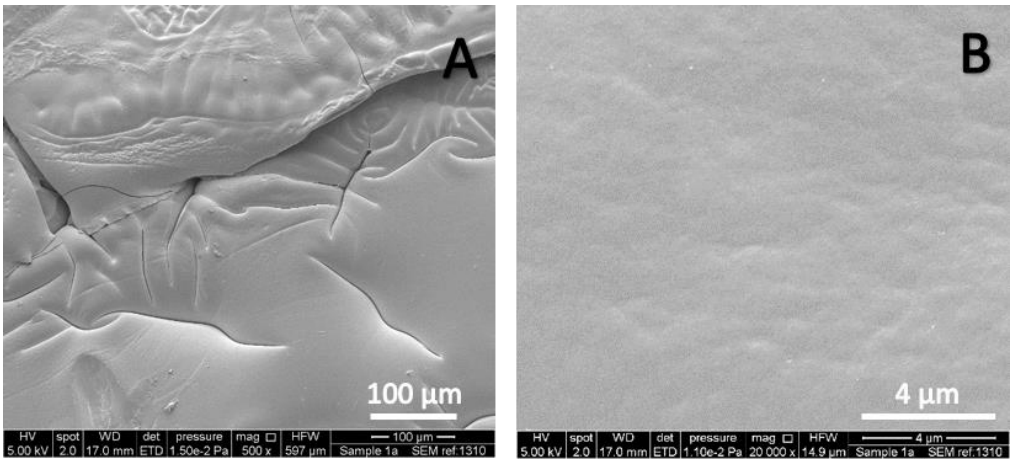

Figure 2-15. SEM images of DEX-pHEMA hydrogels with no added Brij 98 of **(A)** the surface at 500x magnification and **(B)** the bulk structure at 20,000x magnification. The surface had visible folds caused by swelling in the casting mould during polymerisation. The bulk structure did not show any visible aggregates, suggesting homogeneity across the hydrogel. The scales bars are 100 µm for the surface and 4 µm for the bulk.

SEM images of the Brij 98-loaded DEX-pHEMA hydrogels revealed some noticeable structural differences compared with DEX-pHEMA hydrogels without Brij 98, see **Figure 2-16**. All Brij 98-loaded DEX-pHEMA hydrogels were characterised by rougher surfaces with the presence of complex aggregates and cavities in the bulk structures, indicating varying pore distributions, whereas DEX-pHEMA hydrogels displayed a uniform structure with no visible aggregates.

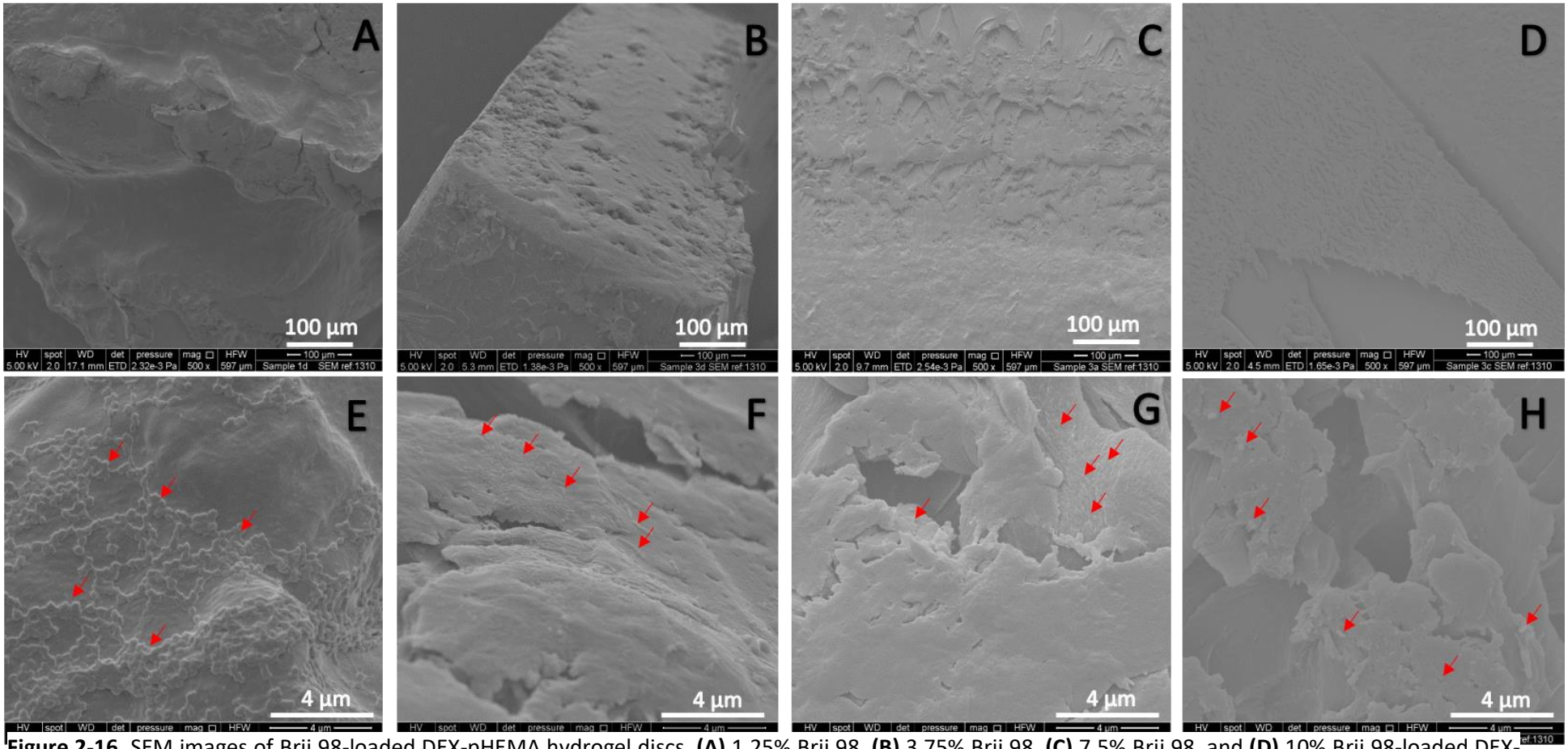

Figure 2-16. SEM images of Brij 98-loaded DEX-pHEMA hydrogel discs. **(A)** 1.25% Brij 98, **(B)** 3.75% Brij 98, **(C)** 7.5% Brij 98, and **(D)** 10% Brij 98-loaded DEX-pHEMA hydrogels at 500x magnification. Increasing the magnification to 20,000x for **(E)** 1.25% Brij 98, (F) 3.75% Brij 98, **(G)** 7.5% Brij 98, and **(F)** 10% Brij 98-loaded DEX-pHEMA hydrogels revealed spherical aggregates (red arrows) with complex shapes as well as cavities within the bulk structures.

2.5.1.5 Water in DEX-loaded pHEMA hydrogels

Understanding how Brij 98-loaded DEX-pHEMA hydrogels swell in water was important to understand the effect of surfactant concentration on drug loading and drug release from the hydrogel discs. The effect of the Brij 98 concentration on the EWC% and the SR of the DEX-pHEMA hydrogels were measured. The results are shown in **Figure 2-17**. Brij 98 had an impact on EWC% and SR as there was a significant decrease in the EWC% and SR in the Brij 98-loaded DEX-pHEMA hydrogel discs as compared with DEX-pHEMA hydrogel discs (0% Brij 98)($p<0.0001$). However, no significant correlation was observed between the different surfactant concentrations and EWC% of the hydrogels ($p<0.5$). Brij 98-loaded DEX-pHEMA hydrogels showed a minimum EWC% greater than 38.5%; 1.25%, 3.75%, 7.5%, and 10% Brij 98-loaded hydrogels displayed EWC% of 38.8%, 43.6%, 43.1%, and 40%, respectively. In comparison, DEX-pHEMA hydrogels (0% Brij 98) resulted in an EWC% of 69.6%. Brij 98-loaded DEX-pHEMA hydrogels all showed a minimum SR less than 0.63%. 1.25%, 3.75%, 7.5%, and 10% Brij 98-loaded hydrogels

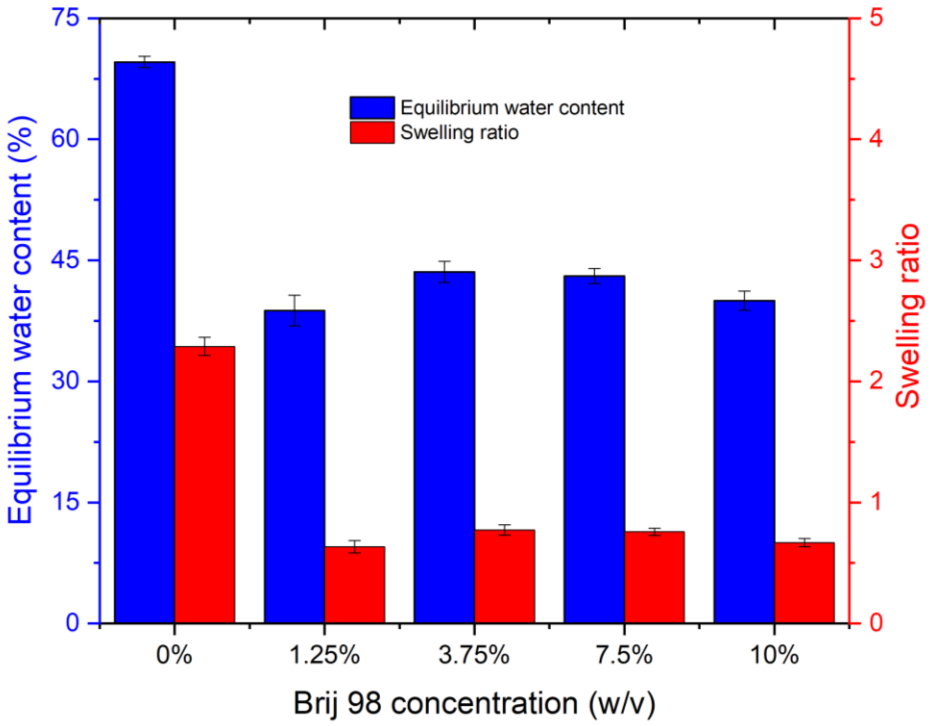

Figure 2-17. The effect of surfactant concentration on the EWC% and SR of Brij 98-loaded DEX-pHEMA hydrogels. There was a significant difference between the DEX-pHEMA hydrogels without Brij 98 (0%) and all the DEX-pHEMA hydrogels containing Brij 98 ($p<0.0001$). However, no significant correlation between the surfactant concentrations and EWC nor SR was observed ($p>0.5$).

displayed SR values of 0.64, 0.77, 0.76, and 0.67, respectively. In comparison, DEX-pHEMA hydrogels (0% Brij 98) exhibited an SR value of 2.3.

2.5.1.6 Differential Scanning Calorimetry and Thermogravimetric Analysis

Diffusion of drugs from hydrogels is related to the bulk water percentage in the hydrogel; the higher the free + lightly bound water content, the faster the drug release will be (478). Relative to the EWC%, the proportion of the non-freezing water content, *i.e.* bound water increased and the proportion of freezing water content, *i.e.* free + lightly bound water decreased as the surfactant concentration increased, see **Figure 2-18**. DEX-pHEMA hydrogels (0% Brij 98), 1.25% Brij 98 and 3.75% Brij 98-loaded DEX-pHEMA hydrogels contained a statistically lower proportion of bound water compared with the 10% Brij 98-loaded DEX-pHEMA hydrogel, ($p<0.05$, $p<0.001$, and $p<0.05$, respectively). Additionally, the proportion of bound water in 1.25% Brij 98 and 7.5% Brij

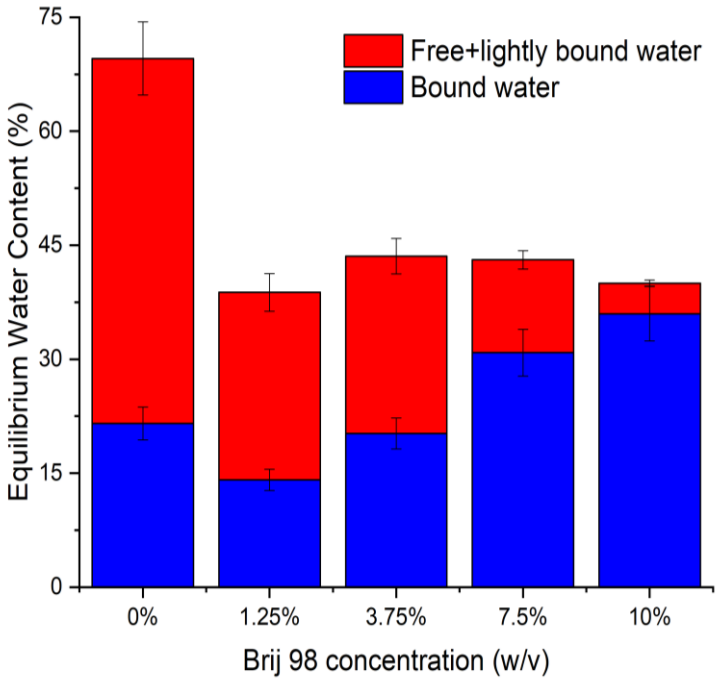

Figure 2-18. The effect of surfactant concentration on the proportion of bound water to free and lightly bound-water in Brij 98-loaded DEX-pHEMA hydrogels. The proportion of free and lightly-bound water generally decreased as the concentration of Brij 98 increased, whereas the proportion of bound water increased as the concentration of Brij 98 increased. For the proportion of bound water, there was a significant difference between 10% Brij 98 and 0% Brij 98, 1.25%, and 3.75% Brij 98 ($p<0.05$, $p<0.001$, and $p<0.05$). 1.25% and 7.5% Brij 98-loaded DEX-pHEMA hydrogels also were significantly different ($p<0.01$). For free and lightly-bound water, all Brij 98-loaded DEX-pHEMA hydrogels were significantly lower than 0% Brij 98 ($p<0.001$ for 1.25% and 7.5% Brij 98; $p<0.0001$ for 7.5% and 10% Brij 98).

98-loaded hydrogels were statistically different ($p<0.01$). For the proportion of free and lightly bound water in the hydrogels, all the Brij 98-loaded hydrogels contained significantly lower amounts of free and lightly bound water ($p<0.001$ for 1.25% and 3.75% Brij 98; $p<0.0001$ for 7.5% and 10% Brij 98). Comparing the surfactant-loaded hydrogels revealed that the free and lightly-bound water in 1.25% and 3.75% Brij 98-loaded hydrogels was significantly higher than 10% Brij 98 ($p<0.01$).

Table 2-5. Endotherms from DSC analysis of Brij 98-loaded DEX-pHEMA hydrogels.

Brij 98 concentration (%)	1st endotherm		2nd endotherm*	
	T_{onset} (°C)	$T_{maximum}$ (°C)	$T_{maximum}$ (°C)	$T_{maximum}$ (°C)
0	0.05	2.67	111.53	-
1.25	0.34	3.65	103.3	108.8
3.75	-0.29	3.65	104.2	113.6
7.5	-0.83	4.04	104.87	116.6
10	-1.65	0.28	112.9	N/A

* The second endotherm was composed of two fused peaks in all Brij 98-loaded hydrogels and two values for $T_{maximum}$ are reported.

DSC examination of Brij 98-loaded DEX-pHEMA hydrogels exhibited two clear endothermic peaks, see **Table 2-5**. The first peak was around 0°C for the melting temperature of ice, which reflected free and lightly bound water as they are able to freeze, and the second peak was around 100°C, which reflected the evaporation of water and volatiles from Brij 98. Comparing TGA data along with DSC thermograms can give some useful information regarding volatiles, including water, carbon monoxide (CO) and carbon dioxide (CO_2), and the influence of surfactant concentration on thermal stability by measuring the change in weight of hydrogels as a function of temperature.

During the TGA analysis, a three-step degradation process was observed in all the DEX-pHEMA hydrogels, with and without Brij 98. The first step was between 50–150°C, the second step was between 150–380°C, and the third step was between 380–500°C and is typically attributed to main chain breakdown. The data for the maximum rate of thermal decomposition (ΔT_{dec} in °C) in each of these three steps and the amount of sample decomposed at ΔT_{dec} is shown in **Table 2-6**.

In the case of DEX-pHEMA (0% Brij 98) hydrogels, the DSC data (**Figure 2-19–A**) indicated the first endothermic peak, composed of two fused peaks at 0.05°C and 2.67°C, corresponded to the melting of ice. The second broad endothermic peak at 111.53°C corresponded to the evaporation of water from the hydrogels. TGA analysis

(**Figure 2-19–B**) revealed that although approximately 50% of the sample weight was lost during the first step (50–150°C), the rate of thermal decomposition (ΔT_{dec}) peaked at 95.4°C, where 30.1% of the sample had decomposed.

Table 2-6. TGA analysis of Brij 98-loaded DEX-pHEMA hydrogels showing the temperature (°C) at peak rates of thermal decomposition (ΔT_{dec}) and amount of sample decomposed (%) at the ΔT_{dec} peak during the 3-step degradation of the hydrogels.

Brij 98 concentration (%)	First step		Second step		Third step		Residual ash (%)
	ΔT_{dec} (°C)	Sample lost (%)	ΔT_{dec} (°C)	Sample lost (%)	ΔT_{dec} (°C)	Sample lost (%)	
0	95.4	30.1	342.8	60.1	423.4	81.8	<1.0
1.25	109.3	7.2	378.5	40.6	435.1	76.3	<2.0
3.75	114.6	19.6	365.1	46.4	436.8	83.4	<1.3
7.5	108.0	12.4	373.8	43.4	436.7	80.7	<1.3
10	108.7	10.3	350.2	34.5	442.9	86.7	<1.5

ΔT_{dec} refers to the peak rate of thermal decomposition during each step, and the per cent sample lost corresponds to that ΔT_{dec}.

These observations were in agreement with the DSC data that showed the free and lightly-bound water was about 50% of the total EWC% (**Figure 2-18**). The second step, 150–380°C, resulted in a loss of 60.1% of the total sample weight, and the ΔT_{dec} peaked at 342.8°C. The third step, 380–500°C, resulted in 81.8% sample loss, and the ΔT_{dec} peaked at 423.4°C. The amount of residual ash content was <1%.

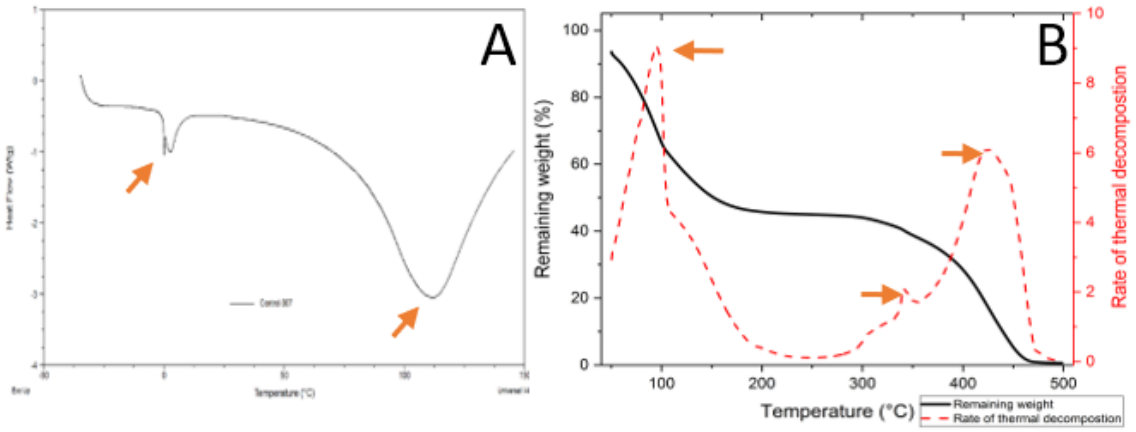

Figure 2-19. DSC and TGA thermograms for DEX-pHEMA hydrogels without surfactant. **(A)** In the DSC endotherm, orange arrows indicate the melting (1st peak) and evaporation of free and lightly-bound water (2nd peak). **(B)** In the TGA thermogram, orange arrows indicate a three-step degradation process.

For 1.25% Brij 98-loaded DEX-pHEMA hydrogels, the DSC data (**Figure 2-20–1A**) indicated that the first endothermic peak onset (T_{onset}) was 0.34°C and peak maximum ($T_{maximum}$) was 3.65°C. The second broad endothermic peak comprised two fused peaks at 103.3°C and 108.8°C, which corresponded to the evaporation of water and volatiles,

such as CO and CO_2, from Brij 98. TGA analysis (**Figure 2-20–1B**) revealed that although 8.6% of the sample was lost during the first step, ΔT_{dec} peaked at 109.3°C, where 7.2% of the sample had decomposed. These data were in agreement with DSC data that showed the free and lightly-bound water in the hydrogel was approximately 24% of the total EWC% (**Figure 2-18**). During the second step, 40.6% of the sample weight was lost, and ΔT_{dec} peaked at 378.5°C. During the third step, ΔT_{dec} peaked at 435.1°C and represented a substantial loss in sample weight (76.3%). The amount of residual ash content was <2%.

For 3.75% Brij 98-loaded DEX-pHEMA hydrogels, the DSC data (**Figure 2-20–2A**) indicated T_{onset} for the first endothermic peak was at -0.29°C, and $T_{maximum}$ was 3.65°C. The second broad endothermic peak was also two fused peaks at 104.2°C and 113.6°C, which corresponded to the evaporation of water and volatiles from Brij 98. TGA analysis (**Figure 2-20–2B**) revealed a 24% sample loss during the first step, and ΔT_{dec} peaked at 114.6°C, where 19.6% of the sample had decomposed. Even though the DSC data showed the free and lightly-bound water in the hydrogel was approximately 26% of the total EWC%, the extra 10% loss in sample weight may be attributed to release of residual water, CO, or CO_2 (from Brij 98) from the hydrogels. During the second step, 46.4% of the sample weight was lost, and ΔT_{dec} peaked at 365.1°C. During the third step, ΔT_{dec} peaked at 436.8°C and represented a substantial loss in sample weight of 83.4%. The amount of residual ash content was <1.3%.

For 7.5% Brij 98-loaded DEX-pHEMA hydrogels, the DSC data (**Figure 2-20–3A**) indicated the first endothermic T_{onset} was at -0.83°C, and $T_{maximum}$ was 4.04°C. The second broad endothermic peak were fused peaks at 104.87°C and 116.6°C, and corresponded to the evaporation of water and volatiles from Brij 98. TGA analysis (**Figure 2-20–3B**) revealed an 18% sample loss during the first step, and ΔT_{dec} peaked at 114.6°C, where 12.4% of the sample had decomposed. Even though the DSC data showed the free and lightly-bound water in the hydrogel was approximately 14% of the total EWC%, the additional 10% weight loss may be attributed to the residual release of water, CO, and CO_2 (from Brij 98) from the hydrogels. During the second step, 43.4% of the sample weight was lost, and ΔT_{dec} peaked at 373.8°C. During the third step, ΔT_{dec} peaked at 436.7°C and represented a substantial loss in sample weight of 80.7%. The amount of residual ash content was <1.3%.

For 10% Brij 98-loaded DEX-pHEMA hydrogels, the DSC data (**Figure 2-20–4A**) indicated the first endothermic T_{onset} was -1.65°C with $T_{maximum}$ at 0.28°C. The second broad endothermic peak observed at 112.9°C and corresponded to the evaporation of water and volatiles from Brij 98. TGA analysis (**Figure 2-20–4B**) revealed a 15% sample loss during the first step, and ΔT_{dec} peaked at 108.7°C, where 10.3% sample had decomposed. Even though the free and lightly-bound water in these hydrogels was around 5% of the total EWC%, the additional 12% weight loss may be attributed to the release of residual water and the increase in CO, and CO_2 volatilisation. During the second step, 34.5% of the sample weight was lost, and ΔT_{dec} peaked at 350.6°C. During the third step, ΔT_{dec} peaked at 442.9°C, representing a substantial loss in sample weight of 86.7%. The amount of residual ash content was <1.5%.

Overall, TGA data revealed an increase in the ΔT_{dec} peak for all Brij 98-loaded hydrogels compared with hydrogels without Brij 98, which suggests that the addition of surfactant improved the thermal stability of the hydrogels. The sample weight lost in the first step during TGA was more than the estimated free and lightly-bound water (from DSC and EWC data). The volatiles escaping from Brij 98 had minimal impact on the total weight loss of the hydrogel.

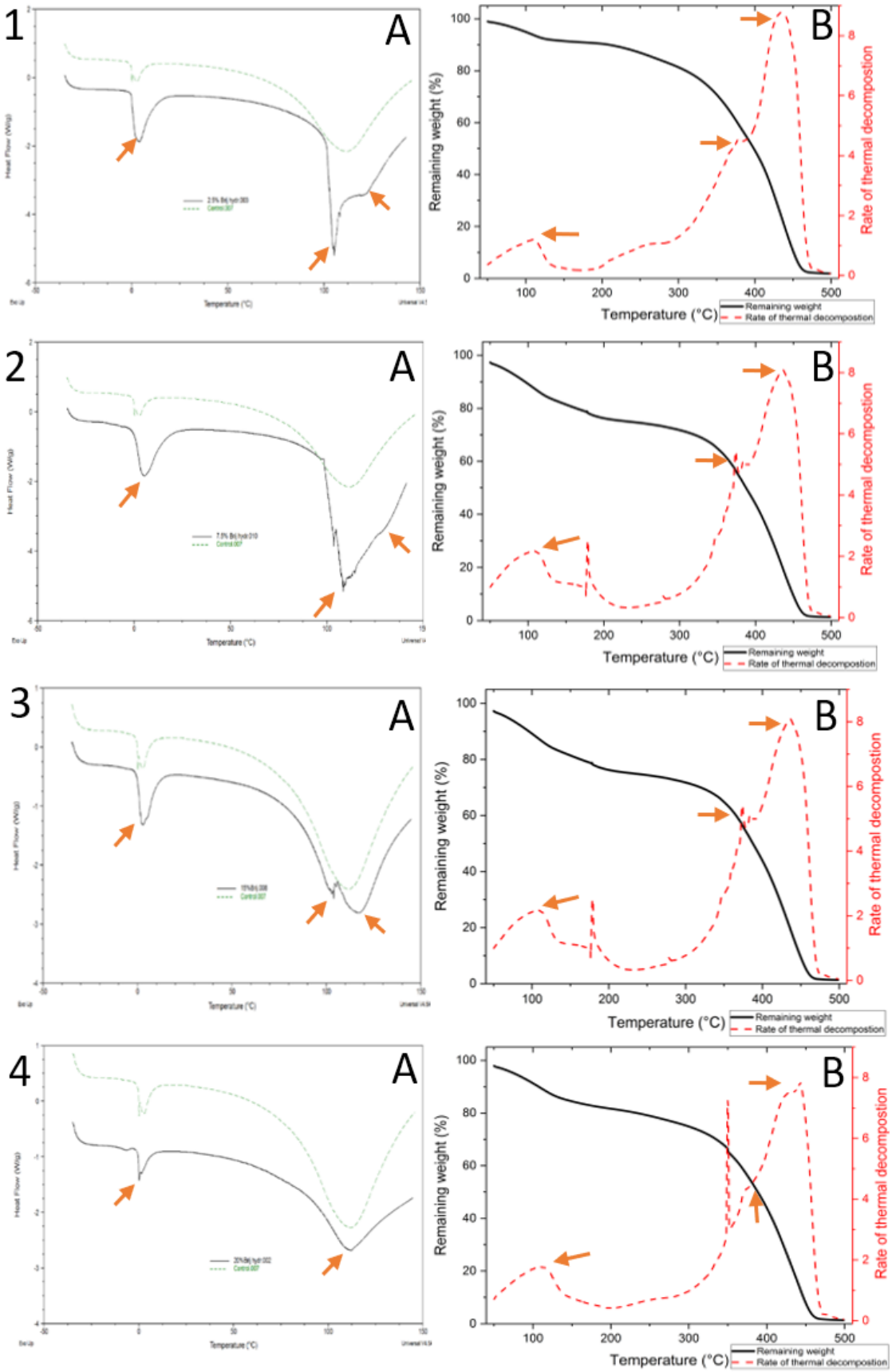

Figure 2-20. DSC and TGA thermograms for DEX-pHEMA hydrogels loaded with **(1)** 1.25% Brij **(2)** 3.75% Brij 98, **(3)** 7.5% Brij 98, and **(4)** 10% Brij 98. In the **(A)** DSC thermograms, orange arrows indicate the melting (1st peak) and evaporation of free and lightly-bound water (2nd peak). In the **(B)** TGA thermograms, orange arrows indicate a three-step degradation process.

2.5.1.7 *In vitro* drug release of DEX-pHEMA hydrogels

The experiments described in this section examined the drug-release profiles of DEX-loaded pHEMA hydrogel discs using different concentrations of micelles in conditions mimicking the subconjunctiva. A flow rate of 2 µL minute^{-1} and a temperature of 35.5°C (52,53,64,463), representing subconjunctival conditions in a healthy eye, were maintained for the duration of the experiments. DEX appeared to be unaffected by the polymerisation process because the DEX released from the hydrogel spacers eluted at the same retention time as pure DEX during HPLC analysis.

DEX loading into the pHEMA hydrogel discs was 78.5 ±4.2 µg, 718.4 ±12.3 µg, 667.1 ±6.0 µg, 884.0 ±23.7 µg, and 1230.3 ±25.1 µg per hydrogel disc for 0%, 1.25%, 3.75%, 7.5%, and 10% Brij 98, respectively. All Brij 98-loaded DEX-pHEMA hydrogel discs showed a sustained release of DEX at therapeutically-relevant concentrations for an anti-inflammatory agent (>2 µM) over the course of 35 days, see **Figure 2-21**. All Brij 98-loaded hydrogels released the maximum concentration of DEX within four hours; however, higher surfactant concentrations seemed to lower the amount of drug lost during the initial burst release. The maximum concentration of DEX released by all the

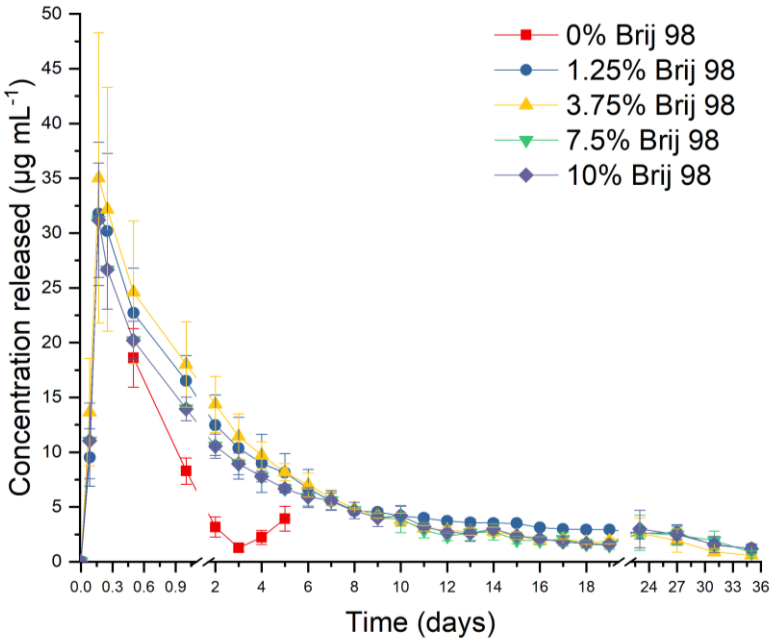

Figure 2-21. DEX was released at concentrations >2 µM from Brij 98 (1.25-10%)-loaded DEX-pHEMA hydrogel discs, a concentration adequate for effective anti-scarring agents. There was a burst release of the drug in the first 4 hours, but all surfactant-loaded hydrogels sustained the release of DEX for 35 days. In contrast, DEX-pHEMA hydrogels (0% Brij 98) released most of their drug content in under a week.

Brij 98-loaded hydrogel discs at one time during the experiments was 31.8 ±6.5 μg mL^{-1}, 35.0 ±13.3 μg mL^{-1}, 31.2 ±5.2 μg mL^{-1}, and 31.2 ±5.2 μg mL^{-1} for 1.25%, 3.75%, 7.5% and 10% Brij 98, respectively at 4 hours (0.2) days (**Figure 2-21**). DEX-pHEMA hydrogels (0% Brij 98) released the highest concentration of DEX during the experiment, 18.6 ±2.7 μg mL^{-1}, at 12 hours (0.5 days). The half-lives ($T_{1/2}$) of DEX release were extended with higher concentrations of Brij 98 added in each hydrogel disc, and $T_{1/2}$ for DEX were 1.6 ±0.3, 27.5 ±4.6, 27.9 ±6.6, 46.9 ±10.0, 68.9 ±14.0 days for 0%, 1.25%, 3.75%, 7.5%, and 10% Brij 98, respectively, see **Table 2-7**.

After 35 days, the total amount of DEX released was 69.2 ±3.0 μg, 425.5 ±28.1 μg, 395.0 ±20.5 μg, 365.9 ±18.7 μg, and 374.9 ±19.1 μg for 0%, 1.25%, 3.75%, 7.5%, and 10% Brij 98-loaded pHEMA hydrogels, respectively. This corresponded to 88.2%, 59.2%, 59.2%, 41.4%, and 30.5% of DEX released for 0%, 1.25%, 3.75%, 7.5%, and 10% Brij 98-loaded pHEMA hydrogels, respectively (**Table 2-7**). The cumulative percent DEX released between all concentrations of surfactant were statistically significant ($p<0.05$), except for 1.25% and 3.75% Brij 98 ($p=0.09$). All Brij 98-loaded hydrogels exhibited percent DEX releases that were statistically different from the 0% Brij 98 hydrogels ($p<0.05$).

Table 2-7. Drug release of DEX-loaded pHEMA hydrogel discs after 35 consecutive days.

Brij 98 concentration in hydrogel discs (% w/v)	DEX loaded (μg $disc^{-1}$)	DEX released (μg)	$T_{1/2}$ (days)	Cumulative DEX release (%)
0	78.5 ±4.2	69.2 ±3.0	1.6 ±0.3	88.2 ±4.3
1.25	718.4 ±12.3	425.5 ±28.1	27.5 ±4.6	59.2 ±6.6
3.75	667.1 ±6.0	395.0 ±20.5	27.9 ±6.6	59.2 ±5.2
7.5	884.0 ±23.7	365.9 ±18.7	46.9 ±10.0	41.4 ±5.1
10	1230.3 ±25.1	374.9 ±19.1	68.9 ±14.0	30.5 ±5.1

The results in **Figure 2-22** demonstrate a significant reduction in DEX release rate and a concurrent increase in the duration of release upon addition of Brij 98 micelles to the pHEMA hydrogels. DEX-pHEMA hydrogels containing no surfactant (0% Brij 98), released most of the drug (88.2 ±4.3%; 69.2 ±3.0 μg) in fewer than seven days. The cumulative amount of drug release was Brij 98 concentration-dependent ($p<0.05$) in the case of 3.75%, 7.5% and 10% Brij 98-loaded hydrogels. The cumulative drug-release data indicate that Brij 98 was successful in prolonging the release of the hydrophobic drug,

DEX, significantly longer than non-micelle entrapped DEX-pHEMA hydrogels, **Figure 2-22**.

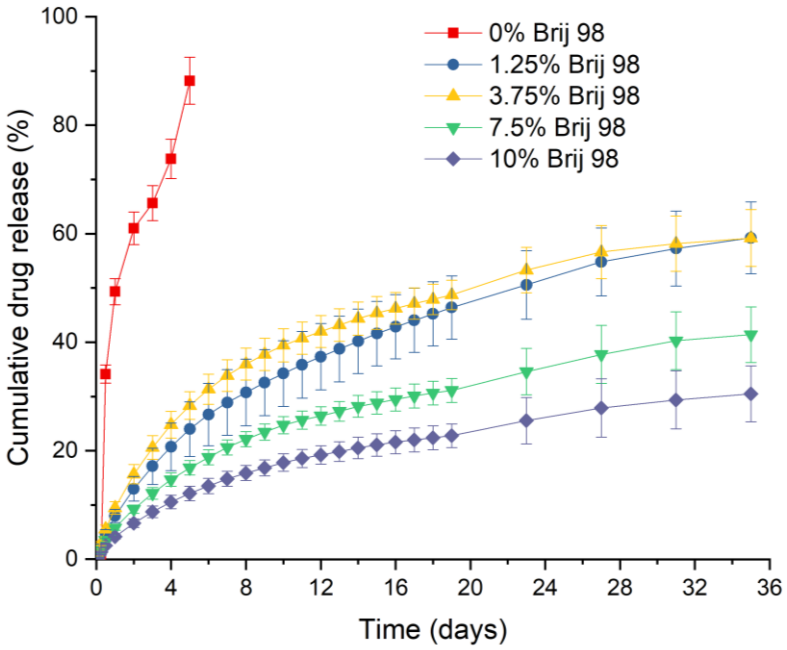

Figure 2-22. DEX-loaded pHEMA hydrogel discs demonstrated a sustained release over 35 days at all four concentrations of Brij 98. DEX-pHEMA hydrogels with 1.25%, 3.75%, 7.5%, and 10% Brij 98-loaded hydrogels released 59.2%, 59.2%, 41.4% and 30.5% of DEX at the end of the experiment, respectively, whereas DEX-pHEMA hydrogels without Brij 98 (0%) released 88.2% of DEX loaded in fewer than 7 days. There was a significant difference in drug release between all Brij 98-loaded DEX-pHEMA hydrogels and the hydrogels without Brij 98 ($p<0.05$), and there was a significant difference in drug release between all Brij 98 concentrations ($p<0.05$), except for between 1.25% and 3.75% Brij 98 ($p=0.09$).

2.5.1.8 Mathematical model fitting of *in vitro* drug-release data

To evaluate the kinetics of DEX *in vitro* release data from the pHEMA hydrogel discs, mathematical models such as zero order, first order, Higuchi's, Hixson-Crowell's, Weibull and Korsmeyer-Peppas models were used. The criterion for selecting the most appropriate model was based on matching the assumption criteria of the model, goodness-of-fit test (R^2) and the smallest sum of squares of residuals (SSR) value (471–473). The R^2/SSR ratio was the smallest for kinetic data modelled using Korsmeyer-Peppas model, indicating that the data best fit this model, see **Figure 2-23**. The value for the diffusion exponent *n* was obtained from the slope of the linear graph, see **Table 2-8**.

Table 2-8. The parameters obtained when *in vitro* drug release data were fitted using the Korsmeyer-Peppas model.

Parameter	Brij 98 concentration				
	0%	**1.25%**	**3.75%**	**7.5%**	**10%**
Intercept	1.7 ±0.02	0.85 ±0.02	0.92 ±0.2	0.71 ±0.02	0.57 ± 0.02
Slope (n)	0.42 ±0.07	0.7 ±0.02	0.67 ±0.02	0.67 ±0.02	0.67 ±0.02
SSR	7.61E-04	0.07	0.08	0.06	0.05
Pearson's r	0.988	0.99	0.99	0.99	0.99
R^2	0.98	0.98	0.98	0.98	0.999

Because the *n* values for all Brij 98-loaded DEX-pHEMA hydrogels were all between 0.45–0.89, the model suggests the mechanism of drug release from these hydrogels was via Anomalous transport, following non-Fickian diffusion, and is characterised by both diffusion of the molecules and swelling of the polymer matrix (474,475). Furthermore, it must be noted that there was no increase in the *n* values when Brij 98 concentration was increased. For 3.75%, 7.5%, and 10% Brij 98-loaded DEX-pHEMA hydrogels, *n* = 0.67 ±0.02. For 1.25% Brij 98, *n* = 0.70 ±0.02. For DEX-pHEMA hydrogels (0% Brij 98), *n* = 0.42 ±0.07.

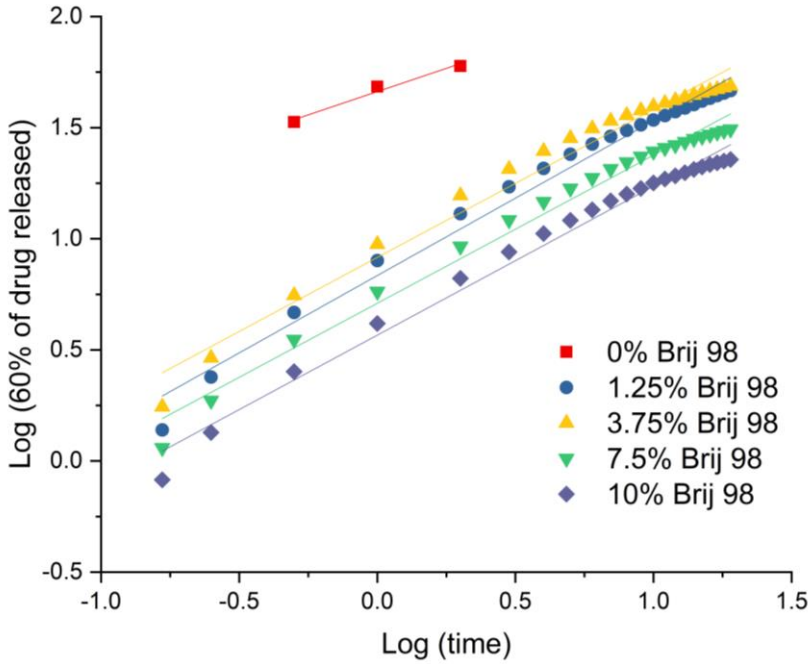

Figure 2-23. Data from *in vitro* drug-release experiments using DEX-loaded pHEMA hydrogel discs containing varying concentrations of Brij 98 (0%, 1.25%, 3.75%, 7.5%, 10%) were transformed and plotted to fit the Korsmeyer-Peppas model. This graph shows data fitting to log [data for ≤60% drug released] *versus* log [time (days)].

2.5.1.9 Cross-linked hydrogel tablet

Before compression of pHEMA hydrogel tablets, the fine cross-linked xerogel powder was characterised for particle size using particle laser diffraction. Results obtained showed the average ±SD median particle diameter (Dv50) for the powder was 64.2 ±0.6 µm, which was within the range for Quality Audit Standard Measurement Protocol (479). The distribution of the particle size was unimodal, *i.e.* the particles were uniformly distributed around the median value, see **Figure 2-24** (480).

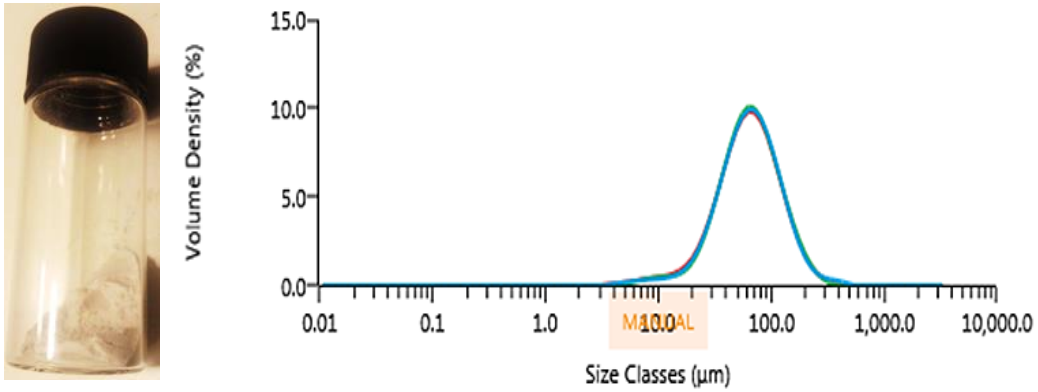

Figure 2-24. Laser diffraction results (R) showed a unimodal particle size distribution of the fine cross-linked pHEMA powder (L) with the average ±SD median particle diameter (Dv50) for the powder was 64.2 ±0.6 µm.

Compression forces of 0.3 MPa (for 10 minutes) and 0.5MPa (for 20 minutes) were found suitable for making tablets 2 mm and 3 mm in diameter that could withstand their weight, respectively, see **Table 2-9**. The source of DEX (Alfa Aesar, UK) used consisted of fine powder that poured easily into the press and resulted in less than 10% loss between weighing the powder and the resulting tablet. The approximate drug loading efficiency for 2 mm and 3 mm tablets were 50% and 33%, respectively.

Table 2-9. Dimensions of fine cross-linked pHEMA tablets.

Tablet diameter (mm)	Tablet height (mm)	Tablet mass (mg)	Tablet surface area (mm^2)	Tablet volume (mm^3)
2	0.7	2.9	10.68	2.2
3	1.55	4.9	28.75	10.96

Before testing the tablets for drug release, post-fabrication processing to remove excess monomer, as described earlier for hydrogel discs, caused the tablets to disintegrate entirely within seconds. As shown in **Figure 2-25**, when water was added to the Eppendorf tubes containing the 2 mm diameter hydrogel tablets, they disintegrated in under 5 minutes, leading to the formation of gel-like microstructures surrounding the insoluble DEX.

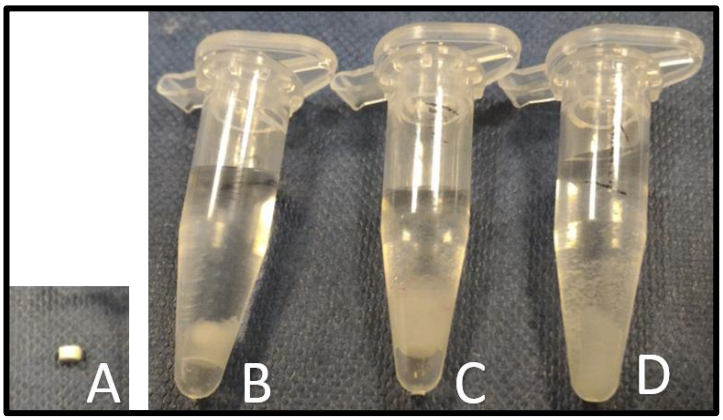

Figure 2-25. Upon adding water to the Eppendorf tubes containing 2 mm hydrogel tablets, they disintegrated quickly, forming gel like microstructures surrounding the insoluble DEX. This figure shows the 2 mm tablet **(A)** after being ejected out of the tablet die. Disintegration of the tablet is shown at 10 seconds **(B)**, 1 minute **(C)** and 5 minutes **(D)**.

The 3 mm tablet completely disintegrated too (<3 minutes), forming gel-like microstructures similar to the 2 mm tablet, as shown in **Figure 2-26**. The gel granules were more heterogenous for the 3 mm tablet with drug particles visible in the Eppendorf tube as compared to the 2 mm tablet.

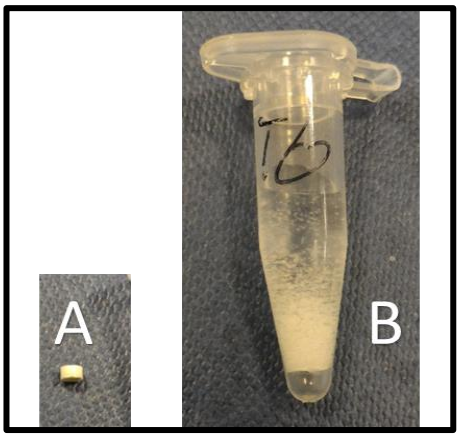

Figure 2-26. Upon adding water to the Eppendorf tubes containing 3 mm hydrogel tablets, they too disintegrated quickly forming heterogeneous, gel like microstructures surrounding the insoluble DEX. The figure above shows the 3 mm tablet **(A)** after being ejected out of the tablet die. Disintegration of the tablet is shown at 3 minutes **(B)**.

2.5.2 Degradable spacers

These experiments aimed to encapsulate DOX into a biocompatible and degradable polymer spacer and evaluate the *in vitro* drug release. DOX monohydrate and DOX hyclate were used as the model hydrophilic drug because, in addition to its antibacterial activity, DOX has shown potential as an anti-inflammatory and anti-scarring

agent in ophthalmic formulations. Three different approaches were explored to formulate degradable polymer spacers to prolong DOX release; chitosan hydrogels, electrospun PCL fibres, and solvent-cast PCL.

2.5.2.1 DOX-encapsulated chitosan hydrogels

It was possible to formulate DOX-chitosan solutions that transitioned to hydrogels at 37°C. **Figure 2-27** (left) shows a solution of chitosan after addition of β-glycerophosphate (GP) during agitation, and **Figure 2-27** (right) shows the transition to a viscous hydrogel after heating the solution to 37°C with the magnetic stirrer suspended in the hydrogel.

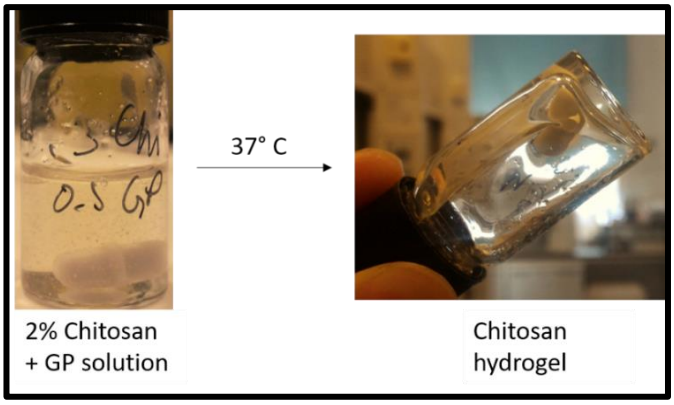

Figure 2-27. DOX-chitosan solutions transitioned to hydrogels at 37°C. The solution of chitosan after the addition of GP during agitation (left) transitioned to a viscous hydrogel after the solution was heated to 37°C, and the same stirrer can be seen suspended in the hydrogel (right).

The EWC% for the chitosan hydrogels were 55.7% and 60.0% for DOX monohydrate and DOX hyclate, respectively. The swelling ratios were 1.26 and 1.50 for DOX monohydrate and DOX hyclate, respectively, see **Table 2-10**.

Table 2-10. The EWC% and SR values for DOX-chitosan hydrogels.

Spacer	EWC (%)	SR
$DOX_{monohydrate}$	55.7 ±1.4	1.26 ±0.04
$DOX_{hyclate}$	60.0 ±2.1	1.50 ±0.1

SEM images of the DOX-chitosan hydrogels analysed under vacuum revealed that $DOX_{monohydrate}$-chitosan hydrogels were characterised by mostly smooth surfaces with raised bumps that could be macroporous vacuoles underneath the surface. At a higher magnification, a few small aggregates were observed on the surfaces, which could be attributed to either chitosan or $DOX_{monohydrate}$ phase-separating from the bulk hydrogel structure. $DOX_{hyclate}$-chitosan hydrogels were characterised by uniform surfaces with small, undulating striations on the surfaces, see **Figure 2-28**. Additionally, $DOX_{hyclate}$-chitosan hydrogels displayed no visible aggregates, which suggested that the

drug was evenly distributed within the hydrogels. No macroporous holes were visible in either of the hydrogels, perhaps due to the application of vacuum during SEM imaging.

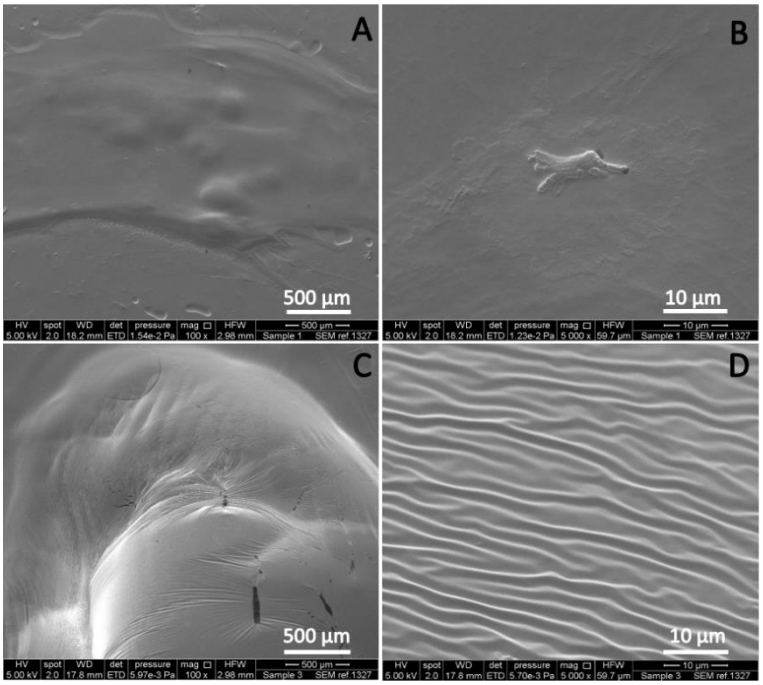

Figure 2-28. SEM images of $DOX_{monohydrate}$-encapsulated chitosan hydrogels at **(A)** 500x magnification and **(B)** at 5,000x magnification, and $DOX_{hyclate}$-encapsulated chitosan hydrogels at **(C)** 500x magnification and **(D)** at 5,000x magnification performed under a vacuum. $DOX_{monohydrate}$ –chitosan hydrogels contained a few small aggregates on the surfaces, which could be attributed to either chitosan or $DOX_{monohydrate}$ phase-separating from the bulk hydrogel structure. $DOX_{hyclate}$-chitosan hydrogels displayed no visible aggregates.

These DOX-chitosan hydrogels were not processed further before evaluation for *in vitro* drug release. DOX monohydrate loading into the chitosan hydrogels (250 µL in volume) was 5.5 mg hydrogel^{-1}. The $DOX_{monohydrate}$-chitosan hydrogels showed a burst release of $DOX_{monohydrate}$ with maximum drug concentration of 1.96 ±0.2 mg mL^{-1} released within 24 hours, see **Figure 2-29A**. The $T_{1/2}$ of $DOX_{monohydrate}$ was 26.3 ±6.0 hours. The $DOX_{monohydrate}$-chitosan hydrogels released 51.2 ±4.1% of the total amount of drug-loaded over 24 hours and showed a sustained release of $DOX_{monohydrate}$ for a further 144 hours, releasing 77.3 ±8.2% of total drug amount and the end of the 168-hour experiment, see **Figure 2-29B** and **Table 2-11**.

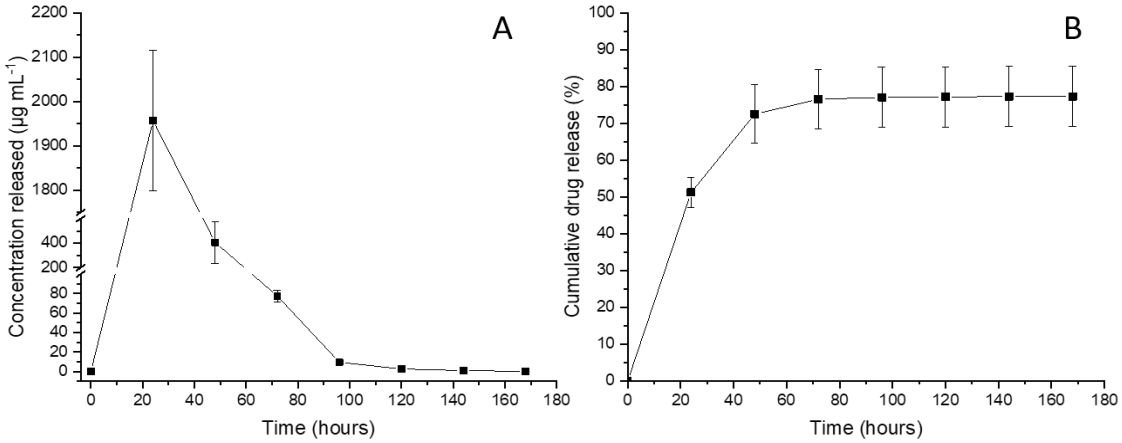

Figure 2-29. The concentration of DOX monohydrate released **(A)** and cumulative percent release **(B)** of DOX monohydrate from 2.5% w/w chitosan hydrogels over time. Chitosan hydrogels released 77.3 ±8.2% of the total DOX monohydrate amount added in seven days.

DOX hyclate loading into the chitosan hydrogels (250 µL in volume) was also 5.5 mg hydrogel^{-1}. Chitosan hydrogels showed a burst release of DOX hyclate with a maximum concentration of 8.3 ±0.5 mg mL^{-1} released at 4 hours, see **Figure 2-30A**. The $T_{1/2}$ of $DOX_{hyclate}$ was 2.5 ±0.3 hours. Chitosan hydrogels released 72.8 ±4.3% of the total drug amount loaded within four hours and demonstrated a sustained release of DOX hyclate for 72 hours, releasing 90.8 ±2.7% of the total drug amount loaded into the hydrogels, see **Figure 2-30B**.

Table 2-11. Drug release after seven and three days from $DOX_{monohydrate}$ and $DOX_{hyclate}$-chitosan hydrogels, respectively.

Chitosan spacer	Drug loaded (mg spacer^{-1})	Drug released (mg)	$T_{1/2}$ (hours)	Cumulative drug release (%)
$DOX_{monohydrate}$	5.5	4.25 ±0.5	26.3 ±6.0	77.3 ±8.2
$DOX_{hyclate}$	5.5	5.00 ±0.2	2.5 ±0.3	90.8 ±2.7

*Half-life calculations estimated based on the assumption of drug diffusion following first-rate kinetics.

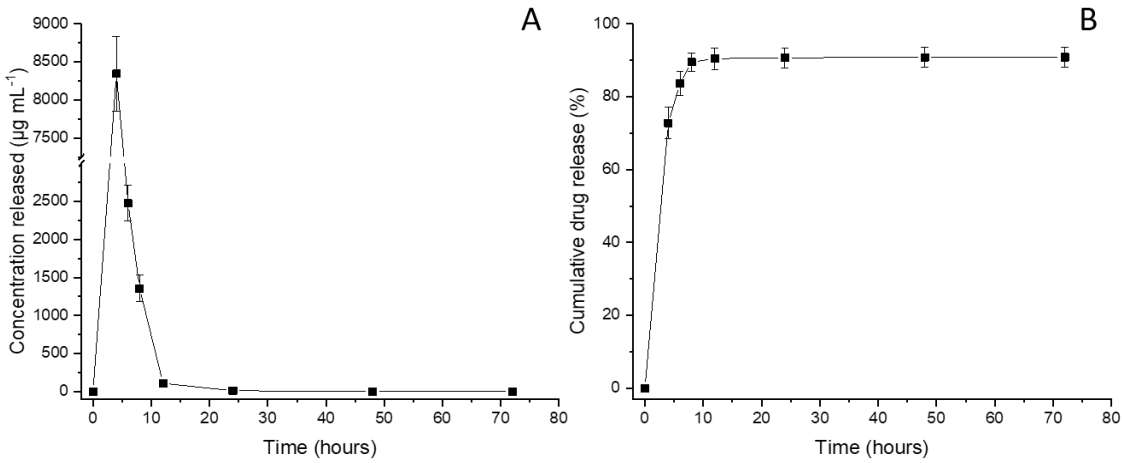

Figure 2-30. The **(A)** concentration released and **(B)** cumulative release percent of DOX hyclate from 2.5% w/w chitosan hydrogels over time. Chitosan hydrogels released 90.8 ±2.7% of the total DOX hyclate amount added in 72 hours.

2.5.2.2 Electrospun DOX-PCL fibres

DOX-incorporated fibres were successfully formulated from PCL and two types of poloxamer using electrospinning as a technique. The resulting DOX-loaded fibres were confirmed using a digital microscope, see **Figure 2-31**. Diameter distribution analysis suggested that PCL-DOX fibres formulated with 407 were larger (2.58 ±0.4 µm) as compared with those formulated using 188 (1.78 ±0.51 µm). The fibres had a white to a slightly yellow hue, and while the fibres used in assessing *in vitro* drug release were stored in darkness, the fibres maintained this colour even when exposed to light for three weeks on the lab bench (not shown). This confirmed that DOX was loaded in the fibres and suggested they had a prolonged resistance to DOX photosensitisation. These DOX-PCL-poloxamer fibres were not processed further before evaluation for *in vitro* drug release.

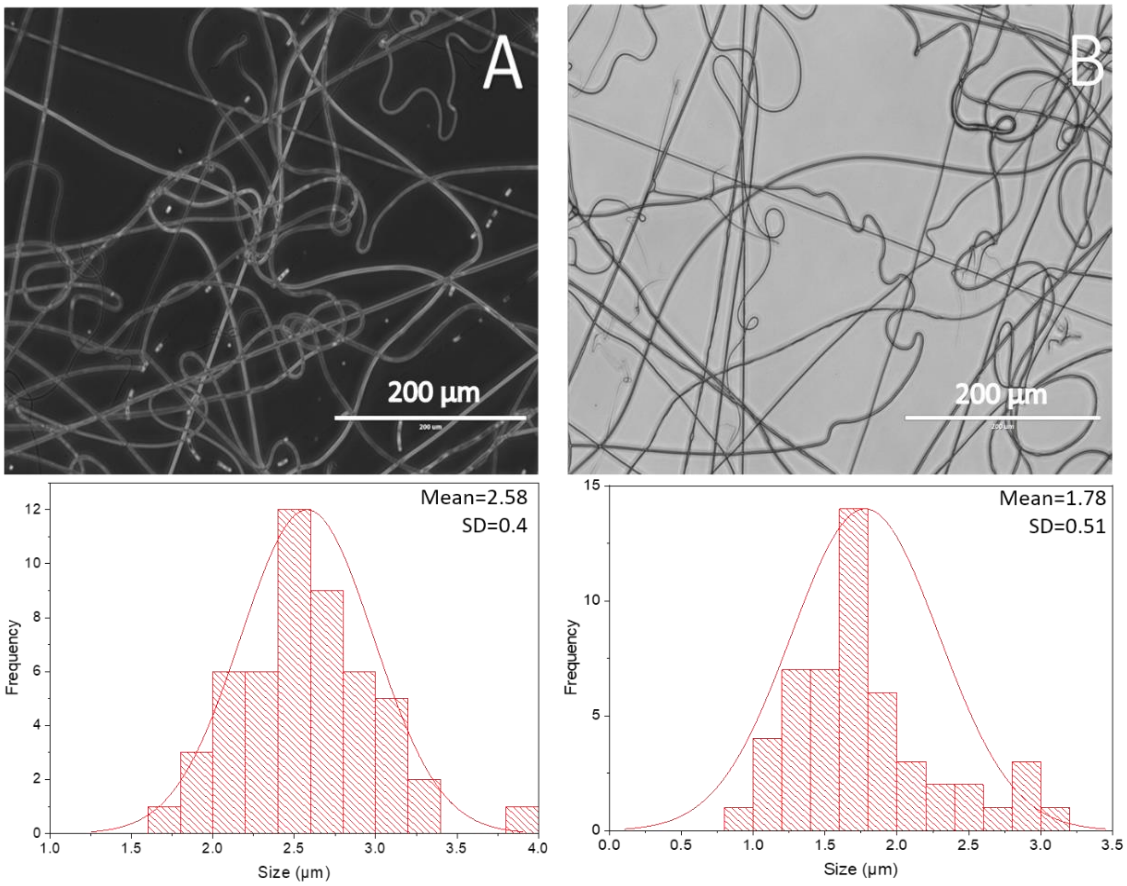

Figure 2-31. Digital microscope images of electrospun fibres formulated with 20% w/w PCL and DOX monohydrate with poloxamer 407 **(A)** and 188 **(B)**.The scale bars are 200 µm. Diameter distribution analysis suggested that PCL-DOX fibres formulated with 407 had a larger average diameter (2.58 ±0.4 µm) as compared with those formulated using 188 (1.78 ±0.51 µm).

DOX monohydrate loading into the PCL-poloxamer 188 and PCL-poloxamer 407 fibres was 2.5 mg per 20 mg of fibres. DOX-PCL fibres with poloxamer 188 showed a burst release of DOX monohydrate with a maximum concentration of 3.4 ±0.3 mg mL^{-1} released within four hours, see **Figure 2-32A**. Electrospun PCL fibres with poloxamer 407 showed a burst release of DOX monohydrate with a maximum concentration of 2.3 ±0.9 mg mL^{-1} released at four hours, see **Figure 2-32A**. The concentration of drug released between PCL-poloxamer 188 and PCL-poloxamer 407 fibres was not statistically significant ($p>0.05$).

Table 2-12. Drug release of DOX monohydrate-loaded PCL-poloxamer fibres after seven days.

Fibres	Drug loaded (mg 20 mg fibres^{-1})	Drug released (mg)	$T_{1/2}$ (hours)	Cumulative drug release (%)
PCL-poloxamer 188	2.5	2.2 ±0.2	2.7 ±0.5	88.1 ±4.2
PCL-poloxamer 407	2.5	2.0 ±0.1	4.0 ±0.3	78.3 ±2.7

*Half-life calculations were estimated on the assumption of drug diffusion following first-rate kinetics.

Electrospun DOX-PCL-poloxamer 188 fibres released 64.3 ±4.4% of the total drug amount loaded within four hours, and showed a sustained release of DOX monohydrate for five days (120 hours), releasing 88.1 ±4.2% of the total amount of DOX loaded at the end of the experiment, see **Figure 2-32B**. The $T_{1/2}$ of DOX monohydrate was 2.7 ±0.5 hours and 4.0 ±0.3 hours for PCL-poloxamer 188 fibres and PCL-poloxamer 407 fibres,

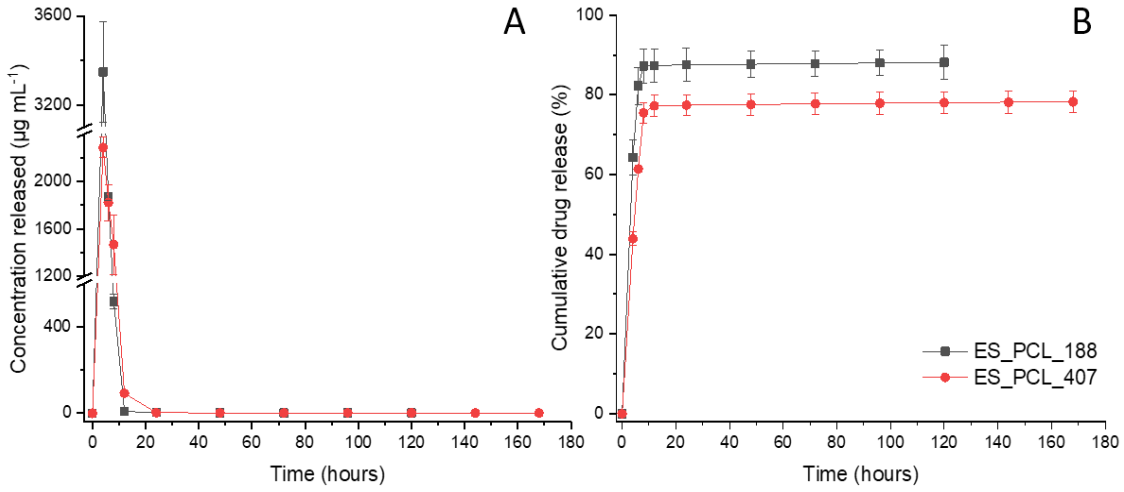

Figure 2-32. The concentration released **(A)** and cumulative release percent **(B)** of DOX monohydrate from electrospun fibres of PCL with poloxamer 188 and 407 over time. Drug release experiments using electrospun PCL with poloxamer 188 and 407 showed a sustained release of DOX monohydrate for five and seven days, respectively. Concentration of drug release between PCL-poloxamer 188 fibres and PCL-poloxamer 407 fibres was not statistically significant ($p>0.05$). PCL-poloxamer 188 fibres released significantly more DOX monohydrate than PCL-poloxamer 407 fibres ($p<0.05$).

respectively, see **Table 2-12**. Electrospun DOX-PCL-poloxamer 407 fibres released 43.9 ±1.7% of the total drug amount loaded in four hours, and showed a sustained release of DOX monohydrate for seven days, releasing 78.3 ±2.7% of the total DOX amount loaded (**Figure 2-32B**). PCL-poloxamer 188 fibres released significantly ($p<0.05$) more cumulative per cent DOX monohydrate than PCL-poloxamer 407 fibres at the end of the experiment.

2.5.2.3 Solvent-cast DOX-PCL spacers

After the acetone solvent evaporated, solvent-cast DOX-PCL spacers had a yellow hue, which turned darker in colour when exposed to light for two weeks (data not shown). This observation indicated that spacers formulated by loading DOX in PCL using solvent casting did not provide a prolonged resistance to DOX photosensitisation. These solvent cast DOX-PCL-poloxamer spacers were not processed further before punching into discs for evaluation of *in vitro* drug release.

DOX monohydrate loading into the PCL-poloxamer 188 and PCL-poloxamer 407 spacers was 2.5 mg per 20 mg of the spacer. Solvent cast PCL-poloxamer 188 spacers showed a burst release of DOX monohydrate with a maximum concentration of 1.59 ±0.6 mg mL^{-1} released within four hours, see **Figure 2-33A**. Solvent cast PCL-poloxamer 407 spacers with showed a burst release of DOX monohydrate with a maximum concentration of 0.74 ±0.1 mg mL^{-1} released within four hours, see **Figure 2-33A**. The $T_{1/2}$ of DOX monohydrate was 35.9 ±14.8 hours and 57.8 ±5.0 hours for PCL-poloxamer 188 spacers and PCL-poloxamer 407 spacers, respectively, see **Table 2-13**. The concentration of drug release between solvent cast PCL spacers with poloxamer 188 and solvent cast PCL spacers with poloxamer 407 was not statistically significant ($p>0.05$).

Table 2-13. Drug release of DOX monohydrate-loaded, solvent-cast PCL-poloxamer spacers after ten days.

Spacers	Drug loaded (mg 20 mg spacer^{-1})	Drug released (mg)	$T_{1/2}$ (hours)*	Cumulative drug release (%)
PCL-poloxamer 188	2.5	1.6 ±0.4	35.9 ±14.8	65.1 ±15.7
PCL-poloxamer 407	2.5	1.1 ±0.1	57.8 ±5.0	45.5 ±2.4

*Half-life calculations were estimated on the assumption of drug diffusion following first-rate kinetics.

Solvent-cast PCL-poloxamer 188 spacers released 30.54 ±10.6% of the total drug amount loaded within four hours and showed a sustained release of DOX monohydrate for ten days, releasing 65.1 ±15.7% of the total amount of DOX monohydrate loaded at the end of the experiment, see **Figure 2-33B**. Solvent case PCL-poloxamer 407 spacers

released 14.2 ±0.9% of the total drug amount loaded within four hours, and showed a sustained release of DOX monohydrate over the course of ten days, releasing 45.5 ±2.4% of their total drug amount, see **Figure 2-33B**. Solvent cast PCL-poloxamer 188 released significantly more DOX monohydrate than solvent cast PCL-poloxamer 407 ($p<0.05$).

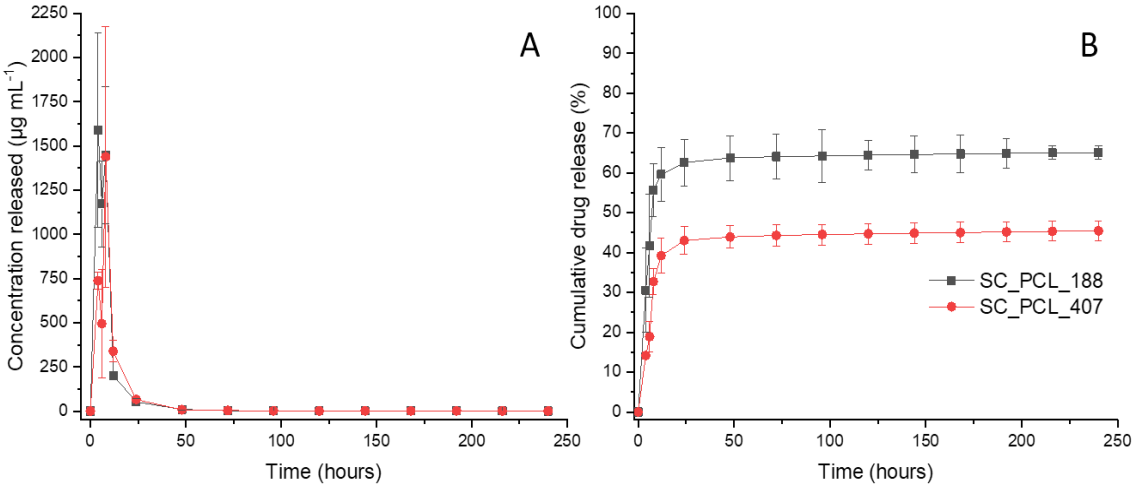

Figure 2-33. The concentration released **(A)** and cumulative release percent **(B)** of DOX monohydrate from solvent cast PCL-poloxamer 188 and PCL-poloxamer 407 spacers over time. Drug release experiments using solvent cast PCL-poloxamer 188 and PCL-poloxamer 407 spacers showed a sustained release of DOX monohydrate (<11 days). Concentration of drug release between solvent cast PCL-poloxamer 188 and solvent cast PCL-poloxamer 407 was not statistically significant ($p>0.05$). Solvent cast PCL-poloxamer 188 spacers released significantly more DOX monohydrate than solvent cast PCL-poloxamer 407 spacers ($p<0.05$).

2.6. Discussion

Utilising hydrogels to formulate spacers for use in the human body is of much clinical interest. SpaceOAR™ is a recent FDA approved hydrogel that consists primarily of water and polyethylene glycol (PEG) in a liquid form (ClinicalTrials.gov identifier NCT01538628, NCT02353832, NCT04004312)(481–483). It is used to reduce rectal injury in men receiving prostate cancer radiation therapy (RT) by acting as a spacer pushing the rectum away from the prostate. Upon injection, the liquid precursor solidifies to form a hydrogel that maintains space between the rectum and prostate during radiation therapy to protect the rectum from acute and long-term toxicity caused by the high dose radiation field. It then gradually liquefies to clear out from the body (484).

Ozurdex® (Allergan), a biodegradable copolymer D, L lactide-co-glycolide (PLGA) which contains 700 µg DEX, has been approved by the FDA to be used as a sustained-release, free-floating intravitreal implant (0.46 x 6 mm cylinder). It has been approved for the management of macular oedema following retinal vein occlusion, diabetic macular oedema or non-infectious uveitis, and its use is increasing, especially where other therapies have been unsuccessful. The PLGA co-polymer used to fabricate Ozurdex® slowly undergoes hydrolysis to form carbon dioxide and water, while DEX is slowly released into the vitreous cavity over the course of six months (385,485). A study done on New Zealand albino rabbits concluded that Ozurdex-treated GFS blebs had significantly prolonged bleb survival compared to untreated blebs (485). Moreover, Ozurdex®-treated blebs exhibited a favourable bleb histology (<50% avascularity) compared with the MMC treated blebs. However, authors of the same study also reported that MMC treated blebs had significantly longer survival compared to Ozurdex®-treated blebs (485). These results indicate that DEX was unable to improve bleb survival as compared to MMC but was a much safer alternative.

More recently, DEXTENZA®, a 3 mm cylindrical-shaped, resorbable, ophthalmic insert, containing 400 µg dexamethasone in a polyethylene glycol (PEG) based hydrogel conjugated with fluorescein was approved by the FDA for the treatment of ocular inflammation and pain following ophthalmic surgery (486,487). In three randomized, multicentre, double-masked, parallel-group, vehicle-controlled trials, a higher proportion of patients were pain-free, as compared to the vehicle alone. On postoperative day 14, in two of the three studies, DEXTENZA® had a significantly higher

proportion of patients than the vehicle group who had an absence of anterior chamber cells (486). More recently, a Phase IV clinical trial investigating the safety and efficacy of DEXTENZA®, following concomitant minimally invasive glaucoma surgery (ClinicalTrials.gov identifier NCT04200651)(266) and another investigating the use of DEXTENZA® for the treatment of post-surgical pain and inflammation compared to standard of care (topical prednisolone acetate 1%) in patients undergoing conjunctival surgery is underway (ClinicalTrials.gov identifier NCT04403516)(409).

2.6.1 Non-degradable pHEMA spacers

2.6.1.1 Micelles

In the work described in this chapter, DEX-pHEMA hydrogels (0% Brij 98) resulted in a loading capacity of 0.3 ±0.03%, which was limited by the solubility of dexamethasone in the HEMA solution pre-polymerisation. Moreover, considering that some drug was lost during the post-fabrication of DEX-pHEMA hydrogels, the adjusted loading efficiencies reported here are comparable with the literature. A previous study has demonstrated that loading values of DEX in pHEMA hydrogels as 0.1–0.6% w/w using an *in situ* entrapment method (488). This study did not investigate phase separation of DEX from the final pHEMA hydrogels; however, it reported comparatively significantly lower loading capacities when DEX was loaded in the pHEMA hydrogels using the imbibing method (488).

It has been previously reported that pre-soaking hydrogel contact lenses in a drug solution, for a period from 2 minutes to 24 hours, resulted in drug uptake varying from 0.02 to 2.3 mg lens^{-1} for ionic materials and 0.01–5.53 mg lens^{-1} for non-ionic materials (489,490). Ketorolac tromethamine, a hydrophobic drug, exhibited poor drug loading of 106 µg lens^{-1} and a significantly poorer average drug release of 21 µg lens^{-1} when loaded in pHEMA hydrogels (369). Using the entrapment method, a comparatively higher amount of drug (69.2 ±3.0 µg disc^{-1}) was released from the DEX-pHEMA hydrogel spacers in this study. However, this amount is not therapeutically relevant for more than a week in the subconjunctival space. To achieve a prolonged release of DEX from pHEMA hydrogel spacers, use of micelles was investigated.

Varying the concentrations of Brij 98 were added in the polymer mixture, and a direct dissolution method was used to prepare Brij 98 micelles. Brij 98 is a non-ionic

surfactant, containing a hydrophilic head, with 20 polyoxyethylene (POE) groups and a distinct hydrophobic tail consisting of an 18-carbon polymethylene chain, see **Figure 2-34**. The CMC values of Brij 98 have been reported in the literature from 0.2–2.5% w/v using iodine solubilisation and fluorescence techniques (368,429,434,439). However, some of these studies defined micellisation to represent the completion of the micellisation process, rather than the initiation of micelle formation. To ensure complete micellisation, the smallest concentration of Brij 98 used (1.25%) was at least two times larger than its reported CMC value (0.6% w/v)(434).

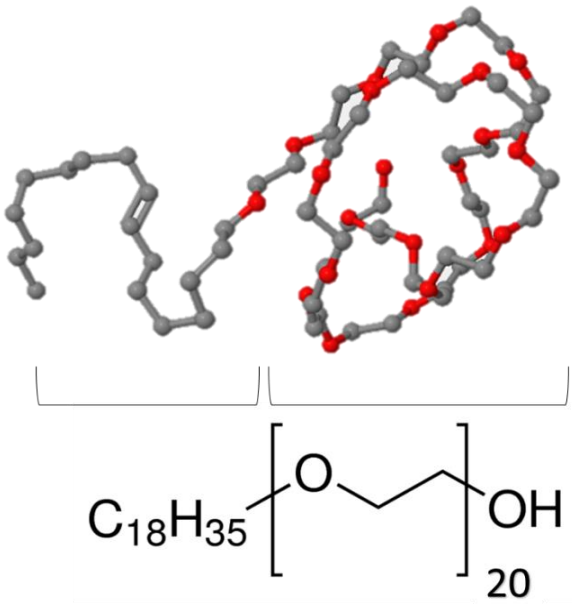

Figure 2-34. Brij 98 has a hydrophobic tail made of 18 carbon polymethylene chain and a hydrophilic head made of 20 polyoxyethylene groups. Above the CMC value, the oxyethylene head groups form a barrier between the hydrophobic core and aqueous environment (3D model generated using JSmol).

Brij 98 micelles resulted in an overall increase in DEX solubility in HEMA. Subsequently, this resulted in increased DEX loading capacities of pHEMA hydrogels. Based on the classic packing model by Tanford (426), Israelachvili *et al.* estimated that the prediction of micelle shape is governed by the packing parameter, P which can be calculated as;

$$P = \frac{V_0}{a_0 I_0}$$

Where V_0 is the surfactant tail volume, a_0 is the equilibrium area per molecule at the aggregate interface and I_0 is the tail length of the surfactant molecule (491). Since Brij 98 has a single polymethylene chain with a large polyoxyethylene (POE) headgroup made of 20 units (manufacturer's datasheet), the value of P is <1/3. Based on this model, it can be predicted that Brij 98 would form spherical micelles with some ellipsoidal and cylindrical aggregates present in the system (491,492). It has been suggested that only

headgroup (POE) controls the aggregate structure via a_0 and the tail (polymethylene) does not have any influence on the shape and size of the aggregate (426). However, the latter has been contested in the literature by Nagarajan *et al.,* who suggested an additional consideration of the tail packing constraint (422).

The large poly(oxyethylene oxide) head group of Brij 98 means the area per surfactant molecule at the micellar aggregate interface would be large enough to have significant repulsive forces between their headgroups (423,426). The repulsive forces would favour a positive curvature of the micellar interface, with the increasing surfactant concentration (491,493). This further suggests the formation of more spherical shaped micelles at higher surfactant concentrations. This observation was in agreement with the predicted model based on surfactant packing perimeter, P and taking into account the surfactant tail constraint (422,491,494).

PDI values <0.1 are considered as monodisperse and between 0.1–0.4 as moderately disperse (368). Using DLS for micelle characterisation, a slight increase in polydispersity was observed with the increase in Brij 98, indicating the presence of free surfactant molecules and larger micellar aggregates. This is expected due to the decrease in the thermodynamic stability of the surfactant solutions, and the tendency of the micelles to aggregate to counter the change in entropy as the concentration of surfactant increases (422,423). Moreover, Brij 98 solutions have been reported to begin micellisation at concentrations as low as 0.025% w/v. The increase in pre-micellar aggregates could further explain the increase in poly-dispersity with the increase in Brij concentration (434).

Another reason for the increase in PDI values could be attributed to the presence of ellipsoidal and elongated micelles at higher concentration. The true shape of globular micelles, to accommodate a larger number of hydrocarbon chains (>10), leads to a distortion in the micellar shape (426). This includes oblate and prolate ellipsoids (426). This distortion of the globular shape of micelles has previously been reported in the case of non-ionic micellar aggregates made of large oxyethylene headgroups (>10 groups)(422). In addition, when the surface concentration of surfactants exceeds a critical surfactant concentration, known critical aggregation concentration (CAC), the surfactant may form complexes with the polymer itself. CAC for homologous surfactants such as Brij 98, is primarily dependent on the hydrophobic moiety (polymethylene chain)

and not on the PEO chain length. CAC is generally lower than CMC for non-ionic surfactants as the hydrogel-surfactant system thermodynamically favours aggregation rather than micellisation (495–497).

The utilisation of Brij 98 micelles significantly improved DEX solubility in HEMA and resulted in significantly higher DEX loading as compared to DEX-pHEMA hydrogels without Brij 98. Consequently, the increased amount of DEX loaded in pHEMA hydrogel discs after post-fabrication processing (667.1 ±6.0–1230.3 ±25.1 µg) was comparable with the only FDA approved DEX containing ophthalmic implants, Ozurdex® (700 µg) and DEXTENZA® (400 µg), the only FDA approved intracameral DEX injection DEXYCU® (517 µg), and the subconjunctival injection of DEX (500 µg) used during conventional TSC laser treatment for refractory glaucoma (ClinicalTrials.gov identifier NCT02875158)(397,486,498,499).

2.6.1.2 Visual analysis

There are several other potent ophthalmic drugs that are hydrophobic and have a similar size to DEX, and thus it was considered as a model drug to study the release of small, hydrophobic molecules from hydrogel spacers. Initially, heat-initiated polymerisation was investigated to entrap DEX loaded Brij 98 micelles in pHEMA hydrogel spacers. However, irregularly distributed small spots were observed during a visual inspection of the xerogels, indicating that DEX phase-separated and precipitated on the xerogel surface. This observation suggested a heterogenous drug distribution in the xerogel with the majority of DEX distributed within the polymer matrix, instead of within the hydrophobic cores of micellar aggregates. A possible explanation could be the evaporation of free water from the polymer solution due to the high temperature and long time required for polymerisation. This heterogeneity of drug distribution would give unreliable pharmacokinetic data of pHEMA spacer discs, which were representative of the drug amount in the hydrogel. Moreover, solid particulate matter is known to elicit an immune response when implanted in the body (356,500,501).

In comparison, the UV-initiated hydrogels were clear with no visible aggregates. This could be due to the higher water content in the hydrogels as UV-initiated polymerisation was much faster than heat-initiated hydrogels and evaporated less water from the polymer mixture. The absence of particulates suggested that majority of

DEX was still entrapped in the micelles and distributed homogenously within the hydrogels.

SEM was used to characterise the hydrogels for their internal structure and specifically compare differences between drug-loaded hydrogels containing Brij 98 and pure pHEMA hydrogels (0% Brij 98). However, a major drawback of this characterisation technique is the drying of hydrogels that is needed for sample preparation. Since the pore structure of the aqueous samples collapses in the dry state, this could introduce artefacts and skew the representation of the true internal structure of a hydrogel. Bearing this limitation in mind, the SEM results were only assumed to indicate the hydrogel structure and were used in support of other characterisation techniques to get a better understanding of the drug-loaded hydrogels.

Characteristic folds were observed in the pHEMA hydrogel structure during SEM characterisation. This observation has also been shown in previous studies in the literature (502,503). The folds in the hydrogels are formed due to the high degree of swelling of the polymer network in a confined space, during polymerisation in the presence of water. Some additional artefacts such as minor holes and blemishes are commonly produced on the exposure of hydrogels to the beam in the microscope (504).

As polymerisation progresses, there is a dramatic decrease in the solubility of pHEMA, resulting in the amorphous solid material. However, pHEMA is able to absorb a high amount of water, nearly 45% (w/w), and this water remains and fills the intermolecular spaces of the polymer network (505). The water-soluble monomer HEMA, filled with pHEMA, aggregates together into small droplets. By the end of the polymerisation process, pHEMA becomes fixed in a network filled with larger spaces which could be interconnected to form channels. These channels are occupied by the water phase, which in the meantime has also separated (503,504). From SEM images in this study, the porous nature of the pHEMA hydrogels and the formation of cavities in the bulk structure was evident. Due to the polymer (pHEMA) property of being able to hold up large amounts of water, the empty spaces observed between polymer networks suggest that these might be filled with water upon hydrogel swelling. Similar cavities have been observed in previous studies of pHEMA hydrogels (506). It may be possible for a drug to access these empty spaces, and when placed in sink conditions where the volume of solvent about 5–10 times greater than the volume present in the saturated

solution of drug, this can cause a burst drug release due to the absence of any additional rate-limiting step (*e.g.* micelle dissociation)(427,464,507).

The increased roughness (as compared with pure pHEMA hydrogels) of the bulk structure of Brij 98-loaded DEX-pHEMA hydrogels may be attributed to the presence of a higher degree of porosity as free, and polymer-adsorbed surfactants create water-rich environments and might increase pore size distribution (430). However, these individual pores would not be visible as they are only a few nanometres in size. If the water content were to be increased in the pre-polymerisation mix, it would increase phase separation to form larger interconnected pores that form a sponge-like hydrogel which is mechanically fragile (503,504).

The presence of complex aggregates was another striking observation that was noticed in the SEM micrographs of Brij 98-loaded DEX-pHEMA hydrogels. These aggregates were much larger than the Brij 98 micelle size, suggesting the formation of complex vesicular structures, which could be due to the confining effects of the hydrogels (436). Increased globule sizes, on the addition to the pre-polymer mixture, has previously been reported in a recent study (508). The authors reported a 4–5 fold increase in micro-emulsion globule size on dilution by the pre-polymer mixture.

Although the possible collapse of porous structure and formation of artefacts are significant limiting factors to the use of SEM as a tool in gel porosimetry, this procedure can provide useful insight into the morphology of the gels (503). Environmental SEM is a technique, capable of analysing 'wet' samples, eliminating the high-vacuum requirement of conventional SEM (509,510). It could be utilised for future studies, to reduce the introduction of artefacts caused by drying of hydrogel samples. However, this technique was unavailable at the time this research was conducted.

2.6.1.3 Water in hydrogels

As drug release from hydrogels is governed by the transport of molecules in the soluble fraction (or solvent), it was thought that the water content of the hydrogel might affect the rate of drug release through the hydrogel; such that the more water that was present, the better diffusion and the faster the release would be (224,511). From the DSC data acquired in this study, low EWC% were observed in surfactant-containing hydrogels indicated that the drug-release rates from pure DEX-pHEMA hydrogels (0% Brij 98), which had a significantly higher EWC%, would be significantly faster than the

Brij 98-loaded hydrogels. This faster release was evident in the drug-release studies where DEX-pHEMA hydrogels (0% Brij 98) released most of their drug content significantly faster than the pHEMA hydrogels that utilised Brij 98 micelles to entrap DEX.

Additionally, the amount of water at the surface and inside the polymer networks can play a vital role in implant biocompatibility by avoiding platelet and protein adhesion (512). When a protein molecule is adsorbed on a polymer surface, water molecules between the protein and polymer need to be replaced (459). Protein adsorbed on the surface loses the bound water at the surface-contacting portion. This exposes the hydrophobic part of the protein to the polymer surface, leading to conformational changes in the protein (513). If the water state at the surface is similar to an aqueous solution, proteins do not release bound water molecules, even if protein molecules contact the surface. This means that the hydrophobic interaction between proteins and the polymer surface is restricted. Moreover, conformational changes during protein adsorption upon contact with the surface are also suppressed. This reversible nature of protein binding associated with hydrated surfaces causes fewer conformational changes in the proteins (513). Softer hydrogels with high water content (>50%) have less effect on the surrounding tissues (less inflammation and foreign body response)(300,514). The presence of water reduces the interaction between polymer and protein by reducing the non-reversible protein adsorption on the surface of the hydrogel device leading to increased biocompatibility (513).

Brij 98-loaded pHEMA hydrogels showed a decrease in the EWC%, but DSC data revealed the ratio of bound/free water increased on the addition of Brij 98. The amount of bound water was the same or increased on the addition of Brij 98 (except 1.25% Brij 98, which showed a decrease in the amount of bound water). This suggests that there would be some difference in the platelet adhesion ability to the pHEMA hydrogels with the addition of Brij 98. However, this was not characterised in the present work but would be of significant interest for future studies. Shi *et al.* have reported that free or bulk water is mainly responsible for the improvement in biocompatibility (515). Tanaka and Mochizuki reported that the slightly bound water on the polymer surface is the type of water responsible for the reduction in protein adsorption while He *et al.* suggested that bound water is the key player (512,516,517). Although there is some disagreement on which type of water is responsible for biocompatibility; free, slightly bound or bound

water, in general, the biocompatibility of a hydrogel matrix is directly proportional to the total water content (518–520).

Furthermore, the amount and type of binding of water in a hydrogel can determine the overall exchange of solute from the hydrogel (290,317). In the present work, the addition of Brij 98 significantly decreased the amount of bulk water as compared with the pure pHEMA hydrogel (0% Brij 98). This would further contribute to decreasing the rate of drug release due to a significant decrease in the availability of free-moving water molecules inside the Brij 98-loaded hydrogels. When a xerogel (dry hydrogel) begins to absorb water, the first water molecules entering the matrix will hydrate the hydrophilic polar groups, leading to 'bound water' (458). This 'bound water' represents the water molecules that are immobilised by hydrogen bonding to the polymer chains of the hydrogels (521). Bound water does not freeze within the temperature range investigated using DSC, remaining unfrozen even at temperatures lower than -100°C (522). This causes the hydrogel network to swell, exposing hydrophobic groups, which also interact with water molecules, leading to hydrophobically-bound water, or 'lightly bound water' (460). Bound and lightly bound water are often combined and simply called the 'total bound water' (317,458).

DSC analysis of DEX-pHEMA hydrogels revealed a lowering of $\mathbf{T_{onset}}$ for the first endothermic peak corresponding to the melting of frozen water with the increase of Brij 98 (3.75, 7.5 and 10%). This could be attributed to an overall increase in the hydrogen bonding ability of pHEMA. The presence of higher fractions of non-freezable bound water on the addition of Brij 98 indicated that the water molecules were likely strongly hydrogen-bonded to the hydrophilic hydroxyl and carbonyl groups of the pHEMA polymer, inhibiting the mobility of the water molecules from nucleating and forming ice crystals at cooling temperatures. This observation was consistent with the findings in the literature (522,523).

For Brij 98-loaded DEX-pHEMA hydrogels, the DSC data showed a peak shift of the first endotherm for melting of bulk water (free + lightly bound), when compared with DEX-pHEMA hydrogels (0% Brij 98). This was expected as frozen lightly bound water melts at temperatures lower than frozen free water (524). It was observed that the free water content decreased in the pHEMA hydrogels with the addition of Brij 98. Similar results have been previously reported in the literature (523). A further peak shift for the

melting of bulk water was observed with the increased concentration of the surfactant. This could be attributed to the plasticising nature of the Brij 98 surfactant. After the polar and non-polar (hydrophobic) sites in the polymer network have interacted with water molecules, hydrogels imbibe additional water, which is driven by the osmotic force of the hydrogel chains. This additional swelling is opposed by the crosslinks (physical or covalent), thus bringing the hydrogel to an equilibrium swelling level (290). The additional water that is imbibed after the ionic, polar and hydrophobic groups become saturated with bound water, is called 'free water' or 'bulk water', and is assumed to fill the space between the network chains, and/or the centre of larger pores or voids. These water molecules exhibit increased mobility due to the absence of hydrogen bonding with the polymer chains.

It should be noted that DSC gives information about the bulk structure of water in the polymer, not the structure of the polymer surface. The reader must also bear in mind that the calculation of the relative amounts of free and bound water in the pHEMA hydrogels was approximate, since exact heats of melting are required for the calculation of the amount of free water from the peak area and the measured heat/g of a wet sample. It has been observed that in polymers showing multiple endotherms, a portion of the water melting below 0°C would have a lower heat of fusion than pure water (460,525). Consequently, for the results presented in the current work, the use of the heat of fusion of pure water (the upper limit) for the calculation of the amounts of free water would have lead to a slight overestimation of the amount of bound water.

With the addition of Brij 98 to the hydrogels, the bound surfactant around the hydrophobic parts of pHEMA will require more energy to dismantle the micellar structures and polymer chain alignment. This would raise the energy requirement of the system, the magnitude of which is primarily governed by the electrostatic repulsion and its strength. However, it is known that interactions between non-ionic surfactants and neutral polymers are hydrophobic interactions and hydrogen bonding (496,526). This does not create significant difficulties to dismantle polymer-non-ionic surfactant systems as compared with pure pHEMA hydrogels (527), and this was evident from the TGA analysis of Brij 98-loaded DEX-pHEMA hydrogels.

It is worth noting that similar to the DSC method, TGA results are changeable and depend on the conditions of sample and experimental process, making it rather

challenging to compare the experimental results with published literature (528). The TGA thermograms for the pHEMA hydrogels analysed showed a three-step thermal degradation process. This can be explained as follows; firstly, the bulk water (free + lightly bound) present in the structure of the hydrogels (adsorbed and absorbed moisture) was eliminated via dehydration and evaporation between ~50–150°C. In the second step, the weight loss was characterised by the volatilisation of bound water, decomposition in the side groups and the branches of pHEMA hydrogel, between ~150–380°C. Volatiles from Brij 98 were mainly carbon monoxide (CO) and carbon dioxide (CO_2), according to the manufacturer's supplied datasheet. The final step was attributed to the breakdown of the primary polymer chain, between 380–500°C. These degradation results corresponded well with previous findings in the literature investigating pHEMA hydrogels (529,530).

2.6.1.4 Drug release and modelling

Encapsulating DEX into a hydrogel for sustained release is of particular interest for formulating prolonged drug-release ophthalmic formulations (531). Incorporating surfactants into the gel matrix can alter the interaction of the drug with the hydrogels and significantly affect drug-release. This effect was investigated and utilised to formulate non-degradable pHEMA hydrogel spacers.

Results from drug-release experiments confirmed that there was a significant ($p<0.05$) decrease in cumulative drug release and drug-release rates when Brij 98 was used to entrap DEX in pHEMA hydrogels at all four concentrations (1.25–10%). Furthermore, this decrease was found to be significantly ($p<0.05$) inversely related to the concentration of Brij 98, except 1.25% and 3.75%, which were found to be not statistically significant ($p>0.05$). The primary rate-limiting step for drug release from hydrogels is considered to be the rate of drug diffusion through the polymer matrix into the surrounding environment (532). In the matrix of Brij 98-loaded DEX-pHEMA hydrogel spacers, surfactants may exist in three different forms (a zoomed-in schematic of the hydrogel spacer arrangement is shown in **Figure 2-35**), a free form that constitutes of surfactants that do not interact with the polymer or other molecules of surfactants. The second form is where they interact with polymer, and the third is where they exist as micelle aggregates with hydrophobic cores. Similarly, drug exists in three forms inside

the hydrogel matrix: free form, adsorbed on to the polymer or inside micelle aggregates (430).

Since the hydrophobic cores of micelles provide thermodynamically stable sites for DEX, the majority of the drug lies in the hydrophobic micellar aggregates. For this drug to be released, it needs to partition out of the hydrophobic micellar cores into the hydrogel matrix by disassociation of micelles, followed by diffusion out of the hydrogel (428). This two-step release process decreases the total drug-release rate. The remaining amount of free DEX present inside the hydrogel matrix can readily diffuse through the hydrogel. The obvious question is 'which of the two mechanisms play a greater role in slowing the release of DEX'. By using mathematical models to analyse the drug-release kinetics data, further conclusions may be drawn to get a better idea about the underlying dominant mechanism for the drug-release.

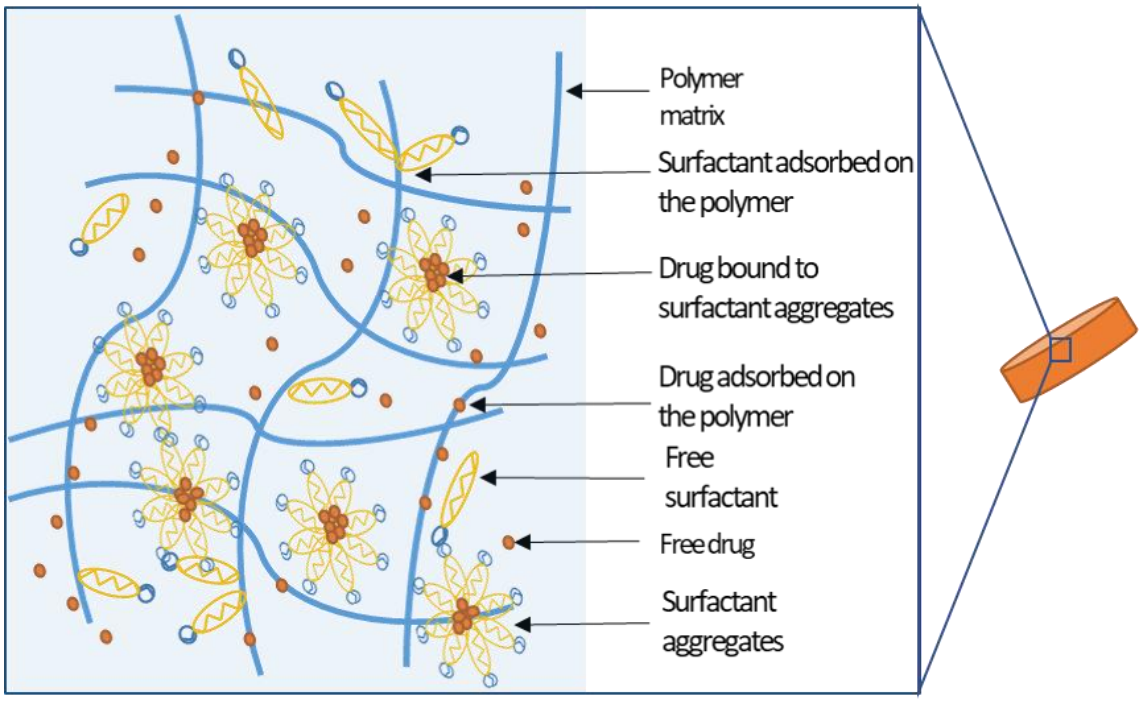

Figure 2-35. A schematic of the Brij 98-loaded DEX-pHEMA hydrogel spacer. In the matrix of hydrogels, surfactants may exist in three different forms; a free form that constitutes of surfactants that do not interact with the polymer or other surfactant molecules, a second form where the surfactant molecules interact with polymer and a third form is where they exist as micelle aggregates with hydrophobic cores. Similarly, DEX exists in three forms inside the hydrogel matrix; free form, adsorbed on to the polymer and inside the hydrophobic cores of the micelle aggregates. Since the hydrophobic cores of micelles provide thermodynamically stable sites for DEX, the majority of the drug lies in the hydrophobic micelle aggregates. This added barrier to drug diffusion would prolong drug-release from the hydrogel spacer.

DEX-pHEMA hydrogels did not release 100% of the drug initially loaded into the polymer solution. This could be caused by drug degradation during the polymerisation

process. However, this is unlikely as during HPLC analysis, no change in DEX chromatograms were observed, as compared with native DEX, confirming that the drug being released was in fact unaltered. This suggests that the reason for the discrepancy in drug release amount would be irreversible entrapment of DEX within the hydrogel. In the literature, irreversible entrapment of 17% DEX in pHEMA has been reported, which was estimated using the difference in drug loading and release (488). The mechanism of entrapment, *i.e.* physical or chemical entrapment has not been investigated and could be pursued in future work.

DEX loaded Brij 98 DEX-pHEMA hydrogels were clear and free from particulate matter which indicated that majority of the drug was inside the micellar aggregates. Results from the drug release experiments further indicated that the two-step release process decreased the total drug-release rate of DEX from Brij 98-loaded pHEMA hydrogels as comparatively, DEX-pHEMA hydrogels (0% Brij 98) released most of their drug content under a week. For a micelle-entrapped drug to be released, the influx of water must decrease the surfactant concentration in the hydrogel below the CMC value, disassociating the micelle and releasing the drug into the hydrogel matrix. It is only then possible for this drug to diffuse out of the hydrogel. This added step of micelle to matrix partition of the drug creates a depot effect and extends drug release from the pHEMA hydrogels. The effect of this rate-limiting step (micelle to matrix partitioning of the drug) was also evident in the prolonged drug-release from Brij 98 micelle-entrapped hydrogels. However, it was somewhat surprising that I did not observe a correlation between the increase in surfactant concentration and the prolonging of the drug-release time. This could be due to the higher drug entrapment efficiency of micelles at higher surfactant concentrations, slowing down the rate of drug release even further.

In both *in vitro* and *in vivo* studies, a pulse-like (burst) or dose-dumping release of the drug has generally been observed for drug-loaded hydrogels (370,533). In the present work, SEM characterisation of pure pHEMA hydrogels (0% Brij 98) revealed empty spaces in the hydrogel matrix that the drug may access when the hydrogel would be placed in sink conditions. This would lead to a characteristic burst release due to the absence of any additional added rate-limiting step to the diffusion of DEX. In another *in vitro* study, the corticosteroid triamcinolone acetonide, commonly used in ocular therapy (including intraoperative augmentation supplementing MMC for GFS), was

loaded into non-degradable pHEMA contact lenses by the soaking method (0.05% w/w). These contact lenses released 80% of the drug in 24 hours (373). In the present work, comparable findings were reflected in the pHEMA hydrogel drug-release data as Brij 98-loaded DEX-pHEMA hydrogels, even though have a much higher loading than pure pHEMA hydrogels (0% Brij 98), exhibited a smaller burst release (amount of drug released <one day).

All drug release experiments were carried out using DI water rather than PBS, which is considered as a suitable model fluid for aqueous humour. DEX is a non-ionic drug and so its diffusion into the aqueous environment from the hydrogel is not expected to depend significantly on the salt concentration. It has been previously reported in a comparative study that there is a negligible effect on the partition (ratio of the drug concentration in the hydrogel and the concentration in the aqueous phase at equilibrium) and diffusivity of DEX loaded in pHEMA hydrogels, when comparing release using DI water and PBS (488).

In the case of hydrogels, progressive swelling of the polymer particles is observed on hydration, leading to considerable structural changes. These include a change of the mobility of the macromolecular chains, macromolecular relaxations, and alterations in the porous structure (534). These changes induce alteration of the shape and size distribution of pores, modifying the overall porosity during hydrogel swelling and increased diffusion (474,535). To get a better understanding of the underlying dominant mechanisms of action of drug release from pharmaceutical dosage forms, mathematical modelling is often applied to the drug-release kinetics data. It aids in the measurement of important physical parameters, such as the drug diffusion coefficients based on model fitting of experimental release data (468). These parameters aid in predicting the drug-release rates and mechanisms involved when comparing dosage forms with a similar active drug, polymer, adjuvants, as well as the geometry (size and shape)(469).

For studying the release kinetics of DEX from pHEMA hydrogels, I found the R^2/SSR ratio to be the smallest for drug release data modelled using the Korsmeyer-Peppas model. The criterion for selecting the most appropriate mathematical model for drug-release kinetics from pHEMA hydrogels was based on matching the assumption criteria of the model, goodness-of-fit test (R^2) and smallest SSR value (471–473). The mathematical model used, needs to have the ability to transform the drug-release curve

in function of some other parameter related to the dosage form under analysis (465). The R^2 value, also known as the coefficient of determination, has been used in the literature as the goodness of fit parameter in linear relationships (467,536–538). The sum of squares of residuals (SSR) and R^2 as final criteria have also been utilised to predict the mechanism of drug release (472). However, the deviation predicted on the basis of drug release, SSR and R^2 as individual entities may result in error up to 16% from ideal release (473). As R^2 mainly reports variability in the data that is accounted for the model, and its calculation involves the use of mean value, an increasing number of data points increases the value of R^2. Therefore, R^2 alone cannot be considered as an accurate indicator of goodness of fit statistics in either linear or non-linear relationships (539,540).

The *n* values of the slope obtained graphically (**Figure 2-23** and **Table 2-8**) using the Korsmeyer-Peppas model can be compared with the values in the literature to predict the mechanism of DEX release from pHEMA hydrogels. The *n* value for DEX-pHEMA hydrogels without Brij 98 was found to be ~0.45 and Brij loaded DEX-pHEMA hydrogels was found to be between 0.45 and 0.89. Thus, this model suggested that the mechanism of drug release from DEX-pHEMA hydrogels without Brij was diffusion-controlled, which includes contributions from both bulk and surface diffusion. This finding was comparable with the literature (488).

On the other hand, the mechanism of drug release from Brij 98-loaded DEX-pHEMA hydrogels was found to be Anomalous transport, following non-fickian diffusion which is characterised by both, diffusion of the molecules and swelling of the matrix (474,475). This can be explained due to the slow rearrangement of pHEMA polymer chains and the simultaneous diffusion of DEX and water molecules, causing the time-dependent anomalous effects (465). In Anomalous transport, the velocity of solvent diffusion and the polymeric relaxation process have similar magnitudes. At $n > 0.89$, there is a significant change in the mechanism of drug release as the velocity of chain relaxation significantly increases diffusion velocities. This shift in the mechanism of drug release has been shown to correspond to zero-order kinetics. The diffusion of a solvent through the drug-polymer system is much faster, compared to the polymeric chain relaxation process (465). The increase in the *n* value on the addition of Brij 98 indicates

that Brij 98 increased the role of polymer chain relaxation as compared to solvent diffusion alone, significantly increasing the time of DEX release from the hydrogels.

After any surgical intervention, the first five weeks are regarded as the critical period of maximum postoperative fibrosis (353–355). In the eye, the postoperative fibrosis leads to scar formation, posing a significant challenge to the success of surgery as it may close the newly formed channel during GFS or GDD implantation. The *in vitro* drug-release results presented here suggest that Brij 98-loaded pHEMA hydrogels released DEX at a release profile that matches the post-surgical inflammation response profile. This indicates the that Brij 98 at concentrations as low as 1.25% w/v might be a suitable surfactant for optimal DEX loading in pHEMA hydrogels to extend drug release over a month while maintaining an optimal therapeutic dose. Moreover, the initial high concentration of DEX release, followed by a taper in the present may be beneficial to mimic the regimen of DEX eye drops currently used in the clinic (ClinicalTrials.gov identifier NCT02873806, NCT00825864)(392,541). The pHEMA hydrogel discs have the potential be used as a standalone implant at the site of surgery as shown in **Figure 2-36**, for localised drug release of an anti-fibrotic to modulate wound healing for approximately a month. Once the drug has been released, this spacer would stay permanently implanted at the site to support the space for a diffused filtration bleb.

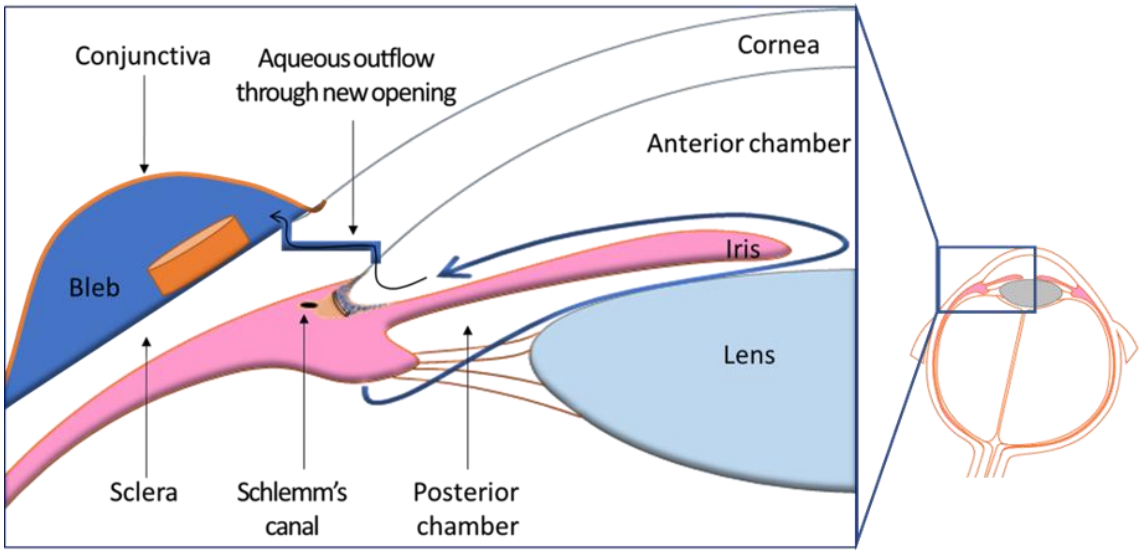

Figure 2-36. A schematic showing a hydrogel disc spacer implanted at the site of surgery after GFS (or GDD). If optimal drug-release kinetics were to be achieved *in vivo* from this drug-surfactant-hydrogel spacer, the spacer has the potential to modulate wound healing and improve the success of the surgery.

It must be noted that even though the biocompatibility of pHEMA is well established in the front of the eye, the DEX-Brij entrapped pHEMA hydrogel spacer described in this chapter has never been characterised in the subconjunctival space. The release of surfactant from these spacers might be an important factor to consider as surfactants at large concentrations may cause ocular irritation (438). Brij surfactants have been investigated as ocular permeation enhancers, and their ocular toxicities on the corneal surface have been reported in the literature to be minimal. Saettone *et al*. have reported that Brij 98, tested as a permeation enhancer at 0.5% w/v for β-blockers, in male New Zealand white rabbits exhibited negligible irritant effects in the lower conjunctival space (438).

Moreover, since this Brij 98-loaded DEX-pHEMA hydrogel spacer would be implanted in the subconjunctival space, the releasing surfactant should clear into the systemic circulation without causing any harm to the corneal tissue (438). This Chapter is unable to encompass the effect of surfactant on the surrounding tissues in the subconjunctival space. For this purpose, a reasonable approach for future work would be the quantification of Brij released from these hydrogel systems for an extended period, or until no more surfactant is detected in the release media.

The *in vitro* drug-release results from Brij 98 loaded DEX-pHEMA hydrogel spacers suggest the viability of this drug delivery system to deliver DEX at therapeutic concentrations for more than a month. However, given the hydrophobic nature of DEX, it was considered to be a model hydrophobic drug for alternative anti-fibrotic drugs. An ideal example of such an alternative drug is an MMPi called ilomastat (GM6001). It is a poorly water-soluble (~140 µg/mL at 25°)(542) broad spectrum MMPi that has successfully shown to promote bleb survival and reduce postoperative scarring in preclinical evaluation (231,358). Initially designed as an inhibitor of human skin collagenase for the treatment of the invasive phase of rheumatoid arthritis, later studies indicated ilomastat's potential to treat corneal ulcers by reducing the infiltration of inflammatory cells in alkali-burned rabbit corneas (543).

Ilomastat is a potent anti-scarring agent that unlike other MMPis such as DOX, has shown to be extremely effective even in nanomolar concentrations (358,543). The inflammatory inhibition of ilomastat was shown to be reversible, and it was non-toxic to cells in both *in vitro* and *in vivo* models (358,359). Removing ilomastat two days after

application in cultured fibroblasts initiated gel contraction, which indicated the reversible nature of its effect. To translate such a drug to the clinic, a sustained release drug delivery system would be suitable that can be implanted in the subconjunctival space at the time of GFS. This would prolong optimal drug concentration directly at the site without the inconvenience of repeated injections and 'spikes' of concentration. To achieve this, the drug would need to be encapsulated in a biocompatible material to minimise foreign body response by the surrounding tissue. Future studies can be aimed at exploring the encapsulation of ilomastat in Brij 98-loaded pHEMA hydrogels.

The reader must bear in mind that the findings in this chapter cannot be extrapolated to all anti-fibrotic drugs as the micelles prepared using Brij surfactants preferentially encapsulate hydrophobic drugs into their cores. I used DEX as a model drug due to its anti-inflammatory efficacy at mico-molar concentrations, widespread use in the clinic, significant clinical interest for a prolonged-release formulation and its hydrophobic nature. The generalisation that this system would prolong the release of hydrophobic drugs should be approached with some caution due to two main reasons. First, the drug-release kinetics observed from a relatively small sample size in the *in vitro* experiments (n=3) might not necessarily correlate *in vivo*. Second, Brij 98 might not encapsulate a hydrophobic drug with a much larger molecular weight into its core with similar encapsulation efficiency, thereby decreasing the drug-loading in the pHEMA hydrogel spacer.

The *in vitro* drug release chamber utilised in the current work provides valuable information regarding drug release from spacers in an open flow system. It does, however, have limitations as a model of the bleb. The chamber to hold the spacer implant was of a fixed volume (250 µl) whereas as blebs may vary in their internal volume in every patient. Using optical coherence tomography, a functioning bleb has been reported to have a fluid volume as small as 6.3 µL (544). Moreover, in the current *in vitro* set-up, the aqueous fluid drains through one exit point as opposed to diffusely through episcleral veins. The aqueous flow rate used for the drug release experiments was 2 µl/min. A range of values for the production rate of aqueous humour by the ciliary body has been reported in the literature depending upon the method of assessment, ranging from 1.5 µL/minute at night to 3.0 µL/minute in the morning (52–54,545). Although the value of 2.0 +/- 0.4 µL/minute is generally accepted (52,55), this value may

significantly vary in patients and conversely translate to varying pharmacokinetics of the drug-eluting spacer.

Additional factors involved in the pharmacokinetics of release would be the interplay of cells and tissue around the spacer, and to be able to test this, experimental work involving animal models is needed. Investigating the effect of different sterilisation methods on drug release from micelle-entrapped pHEMA spacers is warranted, prior to any meaningful *in vivo* studies.

2.6.1.5 Cross-linked tablet

DEX's low solubility would enable the prolonged concentration over therapeutic levels of the drug in the subconjunctival space for a significant duration. Additionally, the drug loading of DEX could be adjusted according to the tablet size. Furthermore, by not using anything other than pure drug and polymer, there would be no 'by-product' that remains that might cause toxic or inflammatory side effects. In an *in vivo* experiment with 24 rabbits, it has been demonstrated that an anti-fibrotic drug "tablet" prolonged bleb survival significantly longer than MMC with significantly less collagen deposition than either MMC or negative control (application of water in the same way as MMC at the time of surgery)(546,547).

The average median particle size (Dv50) of the cross-linked pHEMA-MPC was found to be in the nanometre range with a unimodal distribution. The Dv50 was found to be within the range for Quality Audit Standard Measurement Protocol (Malvern, 2016). The literature suggests that small particles yield stronger tablets with homogenous distribution of pores due to the increase in bonding surface area (548). Moreover, spread in particle size has been shown in the literature, to have little influence on tablet porosity during compression but can significantly influence the short-term post-compression increase in tablet tensile strength (548,549). This is primarily due to capillary forces restructuring the surface in the presence of humidity (550). In pharmaceutical manufacturing, particle size distribution plays a vital role in filtration and product purity, making it an essential parameter in shipping and handling of the powder (549,551).

During post-fabrication processing, the crosslinked pHEMA-MPC tablets disintegrated rapidly, and particulate matter was observed. Such non-solubilised particulate matter is well known to cause an immune response when implanted in the

body. In the acute inflammation stages, this response consists predominantly of neutrophil recruitment and infiltration (500,501). These cells are limited in their ability to reconstitute the proteases needed to eliminate pathogens, and if a foreign material persists, recruitment of macrophages in great numbers occurs during the stages of chronic inflammation (356). Cannon & Swanson have demonstrated that macrophages are capable of ingesting particles of more than their own size (552). The larger particles can cause the macrophages to contain the stimulus (latex beads in this particular case) in a foreign body granuloma. Even micro-fragments of surgical-grade cotton retained from gauze used in surgery can cause a significant foreign body reaction (500). Specifically in the conjunctiva, this has been explicitly demonstrated by the retention of particles of methylcellulose sponge (501).

Assessing these findings in the literature, I concluded that the hydrogel tablet would trigger a foreign body response, resulting in the tablet becoming enclosed in a granuloma. This would inhibit drug diffusion, and thus the tablet would fail to provide the anti-inflammatory or anti-scarring effect. Considering these findings, it was decided not to pursue this strategy further.

2.6.2 Degradable spacers

DOX is another anti-inflammatory drug that has been investigated to improve the success rate of surgery to treat trachoma. This study reported favourable results of DOX treatment suppressing the contractile phenotype of fibroblasts and matrix degradation. DOX significantly altered MMP expression associated with the profibrotic phenotype (411). DOX hydrogels have shown promising results for MMP inhibition in a double-blind, placebo-controlled trial, assessing the use of low dose DOX (1.5 mg g^{-1}) in a hydrogel (553). Another study found no statistical difference in the clinical outcomes for the management of periodontitis, when comparing PCL-DOX controlled release implants with *in situ* controlled release gels containing DOX (554). There was a statistically significant difference in the release of DOX from the gel, when compared with the implant on the 10th and 30th days, more DOX being released from the gel (554).

The same UV-initiated Brij 98-loaded pHEMA spacer system was initially investigated to incorporate DOX in a hydrogel. A similar drug-loading method and polymerisation process was carried out with the aim to formulate Brij 98-loaded DOX-pHEMA hydrogels. I found that in all concentrations of Brij 98 (1.25–10%), as well as the

pure pHEMA hydrogels (0% Brij), the hydrogel failed to polymerise. Furthermore, the polymer mixture, when removed from under the UV lamp, had completely turned black, see **Figure 2-37**. A significant problem with DOX is its photosensitivity. It has been reported that DOX degrades by photolysis under UVC light at 100–280 nm (555). Other researchers have previously reported that DOX molecules absorb UV energy at a higher wavelength than the photoinitiator and that DOX likely blocks the generation of active free radicals and thus decreases the overall conversion rate from monomer to polymer (556). The ability DOX to act as a UV absorber against the photoinitiator explains the inability for the DOX-pHEMA hydrogels to polymerise.

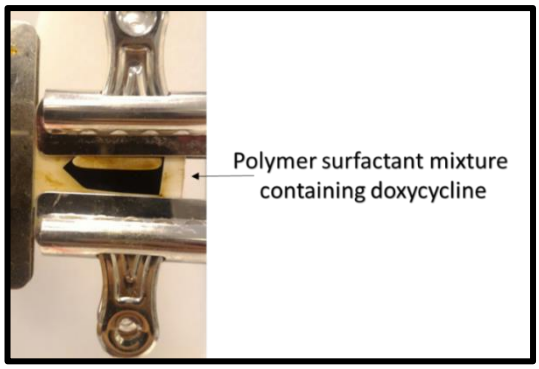

Figure 2-37. The Brij 98-DOX-HEMA mixture failed to polymerise when initiated by UV.

2.6.2.1 DOX-encapsulated chitosan hydrogels

To overcome the inability to carry free radical polymerisation with entrapped DOX in pHEMA hydrogels, an alternative hydrogel system using chitosan was explored for DOX encapsulation. Chitosan has gained significant interest for drug-loaded hydrogel preparation, largely due to its biocompatibility, biodegradability and cost-effectiveness (557–564). Due to the presence of the free amino groups in its chemical structure, chitosan can be dissolved in aqueous acidic solutions in the ionized state. Most importantly, a chitosan solution, on the addition of glycerophosphate (GP), becomes thermo-responsive at physiological pH and temperature (565). Additionally, anionic nature of most human tissues due to the presence of glycosaminoglycans in the extracellular matrix, and the cationic character of chitosan allows for adherence of chitosan hydrogels to tissue sites (566).

In the present work, chitosan in the presence of GP was investigated as a biocompatible and degradable material for formulating a spacer to encapsulate DOX monohydrate and DOX hyclate. Chitosan DOX solutions transitioned to hydrogels at 37°

C. Chitosan hydrogels released most of their drug content, DOX monohydrate in seven days which was significantly longer than DOX hyclate, which was released in three days. This difference in release duration was expected as DOX hyclate is more hydrophilic and would solubilise into the surrounding aqueous environment more readily than DOX monohydrate. However, in both cases, chitosan hydrogels were unable to prolong the release of DOX for five weeks. A possible explanation for this could be a potential reverse sol-gel transition, leading to the disintegration of chitosan hydrogels as the temperature in the *in vitro* release chamber was set at 35.5°C. The constant flow rate would have expedited the release of the chitosan from the release chamber, leading to a short release duration. Considering these results, utilising chitosan for formulating a prolonged drug-release degradable spacer was deemed unsuitable, as this formulation would fail to achieve a prolonged concentration release of DOX at therapeutic levels, in the subconjunctival space. These results however, further exemplify the requirement for added barriers to drug release, when utilising hydrogels.

2.6.2.2 Electrospun DOX-PCL fibres

Next, electrospinning was explored as a potential polymer processing technique to load DOX in a degradable PCL-based delivery system. “Electrospinning” derived from “electrostatic spinning” refers to a fibre production method, which uses electric force to draw charged drops of visco-elastic polymer solutions to form fibres. The main advantage of this technique relates to the extremely high surface area per unit mass of fibres, which facilitates the fast and efficient solvent evaporation, leading to the formation of amorphous dispersions (567). The utilisation of this technique was first published in 1887, and the term ‘electrospinning’ was coined in 1897 by Rayleigh, and the first patent describing an experimental set-up for the production of polymer filaments using an electrostatic force was published in 1934 (568–570).

During the electrospinning process, the diameter and morphology of the fibres are affected by solution surface tension, the polymer solution dielectric constant, feeding rate, the electric field strength, tip-to-collector distance as well as some environmental parameters such as temperature, humidity and air velocity in the spinning chamber (571). In addition to solid fibres with a smooth surface, electrospinning has also been adapted to generate fibres with several secondary structures, including those characterised by a porous, hollow, or core-sheath structures.

All of these attributes make electrospun fibres well-suited for encapsulation of bioactive species, drug delivery, tissue engineering, and regenerative medicine (449). More importantly, for formulating DOX spacers, electrospinning involves electrical evaporation rather than using elevated temperatures to remove the solvent, thus avoiding thermally-induced drug-degradation (572).

In the case of degradable implants, the degradation products should be non-toxic and should completely clear the body. PCL is a highly hydrophobic and semi-crystalline polymer with well-established biocompatibility. It is widely used as biomedical material for manufacturing FDA-approved sutures (Monocryl™ and Ethicon), subcutaneous contraceptive implants (Capronor™), medical devices for use in bone voids in craniofacial defects (Osteomesh™ and Osteoplug™) and dental fillings (573,574). PCL degrades in aqueous media or when in contact with microorganisms and thus can be used to make degradable polymeric devices (507).

Bulk degradation of PCL occurs when water penetrates the entire polymer bulk, causing hydrolysis throughout the entire polymer matrix (575,576). In the literature, degradation studies have concluded that PCL undergoes a two-stage degradation process; first, the non-enzymatic random hydrolytic scission of ester groups, and second, when the polymer is reduced to a lower molecular weight (less than 3000), it is shown to undergo intracellular degradation. Hydrolysis intermediates are formed, which are metabolised intracellularly via the tricarboxylic acid cycle or are eliminated from the body by direct renal secretion (577). This mechanism of degradation is concluded by the observation of PCL hydrolysing to 6-hydroxyl caproic acid and acetyl coenzyme A, which are uptaken by macrophages and fibroblasts (575,578).

In the present work, low molecular weight PCL (M_n ~10,000) was chosen for spacer formulation to decrease the degradation time of the bulk material. However, PCL alone was found to be unsuitable for electrospinning as the solution viscosity was too low to form fibres, and rather the polymer was sprayed as droplets on the collector plate, see **Figure 2-38**. Moreover, due to the presence of five hydrophobic -CH_2 moieties in its repeating units, PCL degrades slowest among all the polyesters (3–4 years *in vivo*)(579). Addition of poloxamers to PCL materials have been shown to decrease the overall degradation time of the overall bulk material. Poloxamers are block co-polymers of ethylene oxide (EO) and propylene oxide (PO), synthesized by sequential addition of

propylene oxide first to the two hydroxyl groups of a low molecular weight, water-soluble propylene glycol, and then ethylene oxide is added at both ends of the PPO block to form the PEO end-blocks (507,580). The ability to change from individual block copolymer chains (unimers) to self-assembling micelles has enabled the use of poloxamers to increase the solubility and dissolution of hydrophobic drugs (581,582). Fluorescence probe studies have found that the micelle core is hydrophobic and made by PPO blocks, while the micelle corona, in contact with the bulk aqueous environment, is comprised of hydrated PEO blocks (583). Poloxamers increase the viscosity of the final formulation and increase the hydrophilicity, thus are frequently investigated in combination with PCL for implant formulation (584–587).

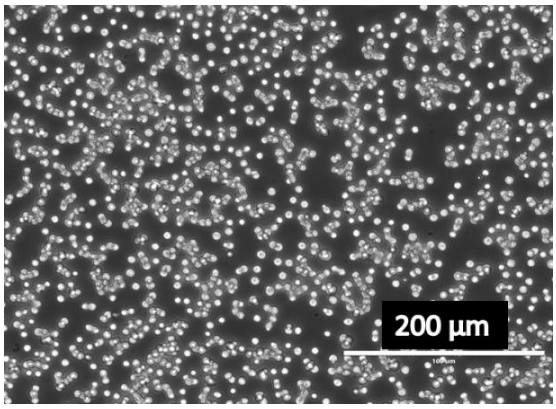

Figure 2-38. Electrospun DOX-PCL droplets without the addition of poloxamers, observed using digital microscopy. After electrospinning, droplets of DOX-PCL solution were deposited on the collector plate, and it appears that poloxamers are required to increase the viscosity in order to form fibres in the electrospinning conditions used in the present work.

Digital microscopy indicated that PCL fibres formulated using poloxamer 188 had a thinner average diameter than fibres formulated using poloxamer 407. This would lead to an increase in the surface area of the spacer available for drug diffusion. During drug-release experiments, PCL fibres released most of their drug content in under seven days. Fibres formulated using poloxamer 188 released significantly more DOX in a shorter time with shorter $T_{1/2}$, as compared with fibres formulated using poloxamer 407. This could be attributed to the increased surface area available for drug diffusion as a direct result of thinner fibres (576). In addition, the resulting materials from electrospinning technique generally contain the drug molecules randomly distributed throughout the polymer, and thus can significantly increase the solubility and dissolution rate of poorly water-soluble drugs, by nanosizing and amorphisation (588). This would explain rapid DOX release from the electrospun fibres.

2.6.2.3 Solvent-cast DOX-PCL spacers

I utilised solvent casting method to formulate PCL-poloxamer spacers containing DOX. In a solvent casting method, the solidification rate can determine the physical state of drugs in solid dispersions. Ideally, a fast solidification method is preferred to ensure the amorphous state of drugs (457). Commonly utilised methods for fast solvent removal are heating on a hot plate (589), vacuum drying (590), rotary evaporation (591), spray drying (592), freeze-drying (593), spray freeze drying (594) and ultra-rapid freezing (595). However, these methods have their own associated disadvantages that include drug degradation, poor scalability, and high processing costs. To overcome these disadvantages, I utilised a less harsh and significantly more cost-effective technique of solvent evaporation using a standard laboratory fume hood.

During drug-release experiments, solvent cast PCL spacers released most of their drug content in under 11 days. Similar to what was observed with fibres, solvent cast spacers formulated using poloxamer 188 released significantly more DOX in a shorter time with shorter $T_{1/2}$, as compared with spacers formulated using poloxamer 407. The difference in cumulative drug release between electrospun fibres and solvent cast spacers was significant, with the latter releasing a lower amount of DOX with significantly longer $T_{1/2}$. This difference could be attributed to the differences in the surface area available for drug diffusion.

Even though using implantable drug delivery systems have shown promise in improving the efficacy and safety of ocular therapies, a number of factors limit their use. The polymer-drug interaction is essential as the molecular weight and the type of polymer system used determines the rate and mechanism of drug release from the implant (252). Poloxamer 188 has a higher ratio of PEO:PPO units (206:39) as compared with poloxamer 407 (200:65), making the latter more hydrophobic and have a larger polymer chain size (582). Both these factors would translate to a faster drug release from spacers formulated using poloxamer 188. This difference in drug release was evident from the results in the *in vitro* release experiments.

Additionally, the high concentration of poloxamers used in the preparation of DOX loaded PCL spacers would have rapidly leached out during the *in vitro* testing, increasing the porosity of the PCL spacer, thus increasing the rate of DOX release. Previous studies in the literature from PCL-poloxamer spacers have found similar results,

reporting a significant increase in drug release with the increase in poloxamer concentration used in implant formulation (585–587). Another study found comparable burst release profiles and significantly faster release of the poorly water-soluble drug docetaxel from PCL-poloxamer matrices, as compared to PCL alone (586). A preclinical evaluation of levonorgestrel implants made of PCL-poloxamer blend reported that poloxamer molecules leached out rapidly because of surrounding body fluids, creating micropores in the implant matrices, thus enhancing the drug release from the implant. The authors also reported the PCL-Poloxamer implants to be biologically safe and nontoxic after a two-year follow up (587).

A plausible explanation for these phenomena could be derived using the Percolation theory. According to Percolation theory, few and isolated pores created in matrices are not favourable for generating the interconnected open pore structures. Once the porosity increases above the percolation threshold (the critical porosity), the interconnecting pathways in porous matrices would be formed easily and became more ‘‘filled-in’’ by release medium, facilitating drug to diffuse and release from the matrices (596–599). Addition of equal amounts of PCL and poloxamer led to the formation of a large number of interconnected pores by the rapid leaching out poloxamers from the spacers. The significant difference in cumulative DOX release suggests that poloxamer 188 formed larger and more interconnected pores in the PCL-poloxamer spacers, as compared to those formed by poloxamer 407. This effect was pronounced in the DOX release profile from solvent cast spacer.

Moreover, the leaching poloxamers from the PCL spacers would form micelles that would significantly improve the solubility of DOX in the release samples. It has been shown previously that poloxamers (P9200, P10300, P10400 and P10500) at 5% w/w were able to increase in the solubilization of the water-insoluble drug, fenofibrate over 100-fold at 25°C (600). Nuclear Overhauser effect spectroscopy (NOESY)-NMR experiments indicated that the protons from fenofibrate interacted exclusively with PPO, enhancing the drug solubility (600). The effect of poloxamer micelle formation on DOX solubility was not investigated in the present work, but future studies could involve utilising this effect to improve drug loading in hydrophilic spacers.

The degradation products of the non-permanent spacers should ideally be biocompatible, safe and must completely exit the body to make them suitable for tissue

engineering and smart drug-delivery devices (292,601–603). I was unable to formulate a prolonged DOX-release formulation of 1:1 PCL-poloxamer spacers using electrospinning and solvent cast techniques. In the absence of poloxamers, PCL shows extremely slow degradation profiles (575) which would be unsuitable for the intended purpose of formulating a degradable spacer for prolonged drug release at therapeutic levels.

2.6.2.4 Trachoma

In addition to subconjunctival scarring caused by surgeries to lower the IOP in glaucoma patients, trachoma, a bacterial infection of the eyelid, conjunctiva, and cornea, is also strongly associated with subconjunctival scarring. Trachoma is caused by *Chlamydia trachomatis*, leading to chronic conjunctivitis and scarring of the upper conjunctiva (604). At present, trachoma is the leading infectious cause of blindness worldwide, affecting large populations of patients in developing countries (604,605). It is considered an endemic disease that affects poor communities in Central and South America, Africa, the Middle East, Asia, and large populations in Australia (606–610). It is estimated that trachoma remains endemic in 44 countries, has blinded or visually impaired around 1.9 million people with 142 million people at risk of trachoma, responsible for 1.4% of all blindness worldwide (609). In earlier stages, tetracycline ointments are used to treat trachoma, but severe scarring can cause the eyelid to in turn, which requires corrective surgery (605).

Trachoma surgery involves rotating the eyelid outwards and making an incision through the scarred tissue and suturing the tissue to the margin of the eyelid. Sutures are removed after two weeks and to prevent infection, antibiotic treatment in the form of ointment is required throughout the process (611) Unsurprisingly, low patient adherence to the antibiotic treatment, potential for systemic side-effects caused by antibiotics (604,612), combined with post-surgical scarring pose a significant challenge to the success of the treatment (613).

The amine groups in chitosan make it antibacterial, haemostatic, antifungal, and mucoadhesive in nature (564,614–617). PCL is frequently used to formulate implantable delivery systems for wound healing applications and has been utilised for making ophthalmic implants (618–621). Poloxamers have been shown to be mucoadhesive, and are utilised to encapsulate drugs with high loading efficiencies using thin-film hydration

and lyophilisation techniques, which can significantly improve the shelf-life of the final formulation (622–626).

DOX is frequently prescribed either topically or orally to prevent infection, but a two-week sustained release formulation implanted under the eyelid would benefit patients undergoing trachoma surgery. In the present work, DOX containing degradable spacers released most of their drug content in 10 days or less, when tested *in vitro* at a flow rate of aqueous humour production (2 µL min^{-1}). However, tear turnover rate has been reported to be comparatively significantly lower (0.2 ±0.2-1.2 ±0.5 µL min^{-1}), which would decrease the rate of drug diffusion from the degradable spacers, translating to a slower release of DOX (627–630). DOX containing spacers might be potentially useful for trachoma, both as an antibiotic and as an MMPi to reduce post-surgical scarring. At the time of writing this thesis, there is currently no prolonged-release formulation for DOX that could be used after trachoma surgery in the clinic or in development. Thus, the degradable DOX spacers could be a viable solution to improve success rate after the trachoma surgery.

2.7. Summary and conclusions

There is a clinical need to develop a sustained release anti-scarring drug-eluting spacer fabricated from biocompatible materials that can be used after GFS, with or without a GDD to modulate wound healing. This spacer should deliver optimal doses of an anti-scarring agent to the subconjunctival space to modulate post-surgical wound healing. The site of surgery is prone to eliciting a significant foreign body response, making it harder to implant a drug-eluting tablet. This chapter aimed to investigate spacer formulation strategies to prolong drug release of clinically used anti-fibrotic drugs for five weeks.

It was possible to formulate pHEMA hydrogel spacers with a significantly higher DEX loading by using Brij 98 surfactant, as compared with pHEMA hydrogels prepared without the surfactant. Results from *in vitro* drug-release experiments over a period five weeks suggest that Brij 98-loaded pHEMA hydrogels released DEX at therapeutically efficacious concentrations that could potentially match the post-surgical inflammation response profile. Mathematical modelling revealed the underlying mechanisms of drug release to be diffusion for DEX-pHEMA hydrogels and anomalous transport for Brij 98-loaded DEX-pHEMA hydrogels, with both diffusion and relaxation of polymer chains playing a significant role in drug release from the hydrogel spacer. These findings indicate Brij 98-loaded pHEMA hydrogels to be suitable candidates for encapsulating anti-fibrotic drugs for prolonged drug release. Future work could investigate the reproducibility of this spacer system *in vivo.*

It was also possible to formulate DOX-loaded polymer spacers, using chitosan hydrogels that transitioned from solution to hydrogel at physiological pH and temperatures. It was also possible to formulate electrospun fibres and solvent cast spacers using PCL in combination with poloxamers 188 and 407. However, *in vitro* drug-release experiments revealed burst drug release profiles and the spacers were unable to prolong the release of DOX over ten days. For this purpose, formulating spacers using chitosan and PCL was concluded to be an unsuitable strategy for prolonging drug release.

Drug releasing spacers formulated with pHEMA and chitosan hydrogels, and PCL-poloxamers have a significant advantage of having optimal biocompatibility and regulatory approval for use in the human body. However, once the drug has been

released, no effective methods exist currently to replenish the depleted drug reserves in the spacer successfully. Elastomeric pumps are a cost-effective approach to deliver drugs with the added option of refill-ability. In the next chapter, I will explore the use of elastomeric pumps for prolonged ophthalmic drug delivery.

Chapter 3 Evaluating elastic pockets for their potential as subconjunctival drug delivery systems

Abstract

In this Chapter, engineering principles were applied to inflated elastomeric membranes, with the aim to provide novel insights into considerations needed to design a novel ophthalmic drug delivery pump. Inflation, compression and deflation of elastic pockets of different geometries and varying material properties were investigated to elucidate relationships that govern the discharge of fluid from elastic pockets. A novel optical method developed for experimental fluid mechanics was successfully applied to determine the displacement of elastomeric membranes of a pursed pocket when a fluid exerts pressure. Pocket geometry and material properties had a significant impact on internal pressure and subsequent pocket function as a pump for fluid release. Modelling data supports the feasibility of elastomeric pockets for prolonged subconjunctival drug delivery.

3.1. Background

Topical drug delivery to the eye poses a number of challenges, including systemic side effects and low bioavailability in the ocular tissues. Patients have to be treated quite frequently, which creates a burden for physicians, health systems and the patients themselves. Poor patient compliance has become another important variable in determining the treatment outcome of glaucoma therapy. Sustained ocular drug delivery therapies are sought to decrease repeated hospital visits in an attempt to improve patient compliance and disease management (see **Section 1.5**).

For example, Genentech recently revealed favourable results at the 2018 ASRS annual meeting of a Phase 2 clinical trial (ClinicalTrials.gov identifier NCT02510794) of the Port Delivery System (PDS) with Lucentis (631). Ranibizumab, the active ingredient of Lucentis, is a monoclonal antibody fragment that was designed to bind to and inhibit VEGF (vascular endothelial growth factor), a protein that is believed to play a critical role in the formation of new blood vessels (angiogenesis) and the hyperpermeability (leakiness) of the vessels. Currently, to maintain clinical efficacy, patients suffering from neovascular age-related macular degeneration (nAMD) require a monthly intraocular injection of ranibizumab (0.5 mg)(632) or bi-monthly injections of aflibercept (633), costing the National Health Service (NHS) in the UK around £550 and £880 per injection, respectively (634). However, a gap is observed between clinical trial results and clinical practice outcomes of vision gains from the current treatment. The difficulty with maintaining office visit and treatment (injection) frequency is a major problem as it increases the burden for the cost-effective management and treatment of disease, adversely impacting patient outcomes (635).

Acute volume-related IOP elevation is commonly observed after intraocular injections (232,636–638). Repeated acute IOP spikes may contribute to cumulative, non-specific and permanent damage to the retina (638). A recent systematic literature review analysing 15 randomised clinical trials found that patients receiving monthly anti-VEGF injections were at an increased risk of endophthalmitis (639). After glaucoma surgery, subconjunctival injections of anti-inflammatory drugs are often used to maintain drug concentrations at the site surgery and manage post-surgical fibrosis. However, the amount of drug delivered is limited by the volume and concentration of drug injected. Moreover, subconjunctival injections also result in poor bioavailability

because they are cleared rapidly into the systemic circulation, necessitating repeated administration (230–233).

Several degradable intravitreal implants for sustained release of small molecule anti-inflammatory agents are already approved but require repeated surgical interventions to implant and replace the implant, causing similar side effects to those observed in injection therapies (634,640–643). Moreover, no devices have yet been approved for localised delivery of anti-fibrotic drugs in the sub-conjunctival space. Results from this work (**Chapter 2**) suggest that hydrogels have the potential to deliver anti-fibrotic drugs directly at the site of surgery in a sustained manner. Once the drug has been released from a hydrogel implant, the hydrogel, if biocompatible, might act as a spacer in the subconjunctival space. The favourable effect of hydrogel spacers in promoting the success of glaucoma surgery (356,357,367) along with the exploitation of their biocompatibility for alternative indications (484) is well documented in the literature (see **Section 2.1.2**). However, a significant limitation for using hydrogels as implantable materials for long-term drug delivery is their inability to be refilled and reused after the drug has eluted.

3.1.2 Elastomeric pockets for ophthalmic delivery

Implantable micropumps have been investigated to overcome the need for repeated localised injections and the challenge of rapid drug clearance. The principles of microelectromechanical systems (MEMS) engineering have been utilised to design and fabricate, manually and electrically controllable refillable pockets that act as drug reservoirs, and have a tube attached for drug outflow (644). Saati *et al.* have previously demonstrated the ability of such a micropump to deliver micro-doses in animal models, with the potential for repeated fillings (up to 24 refills) of the drug reservoir (7 × 7 × 1.58 mm)(645). The flow rates demonstrated by this first generation device were as low as 438 pL min^{-1} at 5 µA to 7 µL min^{-1} (645).

Recent advances in micropump technology have led to more progress by delivering small quantities of the drug in a precise manner (646). A study demonstrated the use of a refillable micropump fabricated with polydimethylsiloxane *in vitro*. The volume dispensed by the pump and the duration of pressure was found to be linearly proportional for both applied pressures (250 and 500 mmHg), resulting in a consistent flow. *In vivo* experiments in male Dutch Belted pigmented rabbits demonstrated

delivering 100 µL of phenyl epinephrine, resulting in the corresponding physiological response of pupil dilation during the dosing period. (647). A one-year feasibility study using Replenish micro-pumps (13 x 16 x 5 mm), implanted episclerally in Beagle dogs demonstrated good biocompatibility of this device (648). Another safety and surgical feasibility study assessing the feasibility of implanting the Replenish micro-pumps in patients reported favourable results of the implantation procedure. Furthermore, no serious adverse events were reported during the 90 day follow-up period.

Refillable implantable micropumps have the potential to replace the conventional therapy of subconjunctival injections. Using an implantable pocket to deliver drugs at a controlled rate might be a viable solution for treating diseases at the front of the eye. The pocket of such a device would act as a reservoir, storing a saturated drug solution. After completion of the drug-release process, the emptied reservoir would be refilled easily in a minimally invasive manner through a refill port. This implantable pocket could be placed in the superotemporal quadrant under the conjunctiva, similar to how and where a GDD is currently implanted (see **Section 1.3.4**). Furthermore, these pumps may be filled with a combination of potent anti-fibrotic drugs that could be delivered at the site of surgery, at controlled and sustained rates. This type of a controlled drug delivery system in the eye would be a novel closed-system (see **Section 1.5**) and could potentially modulate the wound healing process after GFS or GDD implantation.

However, the use of moving parts for fluid release actuation and valve membranes or flaps to control the rate of outflow pose significant drawbacks to current implantable micropumps under development. These moving parts increase the possibility of device malfunction due to risk of wear and fatigue of the parts, which require post-implantation manipulation and ultimately hinder the long term reliability of these implantable devices (649–651). Additionally, all pumps require a source of energy to generate a driving force for fluid release. This energy in the form of magnetic energy, electricity, heat, liquid pressure or air pressure is converted into motion within the pump (259–261). This necessitates the requirement of a means for energy storage within the pump in the form of a battery that would need replacement or implementing additional mechanisms for contactless re-charging. Both scenarios increase the number of parts needed for the pump function and significantly reduces an already limited space

available for the fluid (drug) reservoir (652). Additionally, the need for parts-miniaturisation and post-implantation manipulation would increase the associated manufacturing costs, ultimately passing the cost burden on to the patients and the healthcare services.

Elastomeric pumps, commonly used for ambulatory infusions, provide the advantage of being essentially maintenance-free, using no mechanical moving parts for fluid actuation as they utilise the potential energy stored in the membrane for fluid release (see **Section 1.7**) (653,654). This significantly reduces the cost burden for the patients as compared to electronic medication pumps (329). However, the reliability of drug-release dynamics, offered by elastomeric pumps is debatable, with variations in drug-release rate and duration (340,342,348,654–665). The functional reliability of an elastomeric pump could be improved by closely controlling the major parameters that govern pump function, the current state of the art portable elastomeric pumps for drug delivery are listed in **Table 1-4**.

The performance of an elastomeric pump is influenced by the internal pressure of the drug reservoir (666). This internal pressure is influenced by the elastomeric pump's material properties, e.g. stiffness, and the pump's pocket geometry, e.g. thickness, shape, and size. When an elastomeric material is inflated, it undergoes characteristic deformations, known as bending and stretching. Bending is a deformation that is smaller than the material's thickness, and stretching is a deformation that is larger than the material's thickness (667). In the literature, previous analysis of the deformations of clamped, or closed, elastomeric pockets have all been theoretical, using numerical or computational techniques (668–673). However, a systematic experimental comparison analysing the differences between the two deformations and their implications for designing an elastomeric pump has never been performed.

For the sake of clarity, there are a number of terms in this Chapter which are used based on their significance in the field of mechanical engineering. The terms 'deformation,' 'displacement,' and 'deflection' in this Chapter refer to the same phenomenon defined as a temporary change of shape that is self-reversing after an applied force has been removed so that the object returns to its original shape. The term 'pursing' has been used in this Chapter to describe the process of inflating connected elastomeric membranes when pressure is exerted on these membranes by a fluid. This

pressure increases the displacement height of the elastomeric membranes and forms a 'pursed' chamber. This chamber is referred to as an elastomeric pocket or purse. In the context of drug delivery, these pockets are also called elastomeric pumps.

When the amount of the deflection (height, H) is smaller than or approximately equal to the thickness (T) of the material, the deformation of the pocket shape follows a bending regime ($\frac{H}{T} \leq 1$). When the amount of deflection is greater than the thickness of the material, then the deformation of the pocket shape follows a stretching regime ($\frac{H}{T} > 1$)(667). These regimes follow different dynamics, such as pressure exerted on the fluid, height of deflection from the original non-pursed state, and their combined effects on the flow rate of the liquid released when the pocket deflates. Investigating these changes is necessary to understand their contribution to the design of an elastomeric pump for localised drug delivery.

3.2. Hypothesis and Aims

The hypothesis for this Chapter is that it is possible to elucidate engineering principles in a system using elastomeric membranes and then design a mini elastomeric pump so that prolonged release of at least five weeks in the subconjunctival space using commercially available materials could be achieved. The transition from bending to stretching regimes in pursed (inflated) elastic pockets is dependent on the geometry and the material properties. These regimes would theoretically influence the functionality of the pursed pocket and thus, have important implications for an ophthalmic drug delivery pump-design.

The three main aims of the work described in this chapter were:

- Firstly, to characterise pursed elastic pockets and their deformation profiles (bending and stretching) to explore the relationship between purse deformation, material properties, pocket geometries and internal pocket pressure. This would be helpful to estimate the change in internal pump pressure as a function of key variables involved in the design of an ophthalmic elastomeric pump.
- Secondly, to evaluate the relationship between the application of a compressive force and the resulting change in the internal pressure of a pursed elastic pocket. This would be helpful to estimate the change in pump performance (fluid release rate) when subjected to the compressive forces applied by the conjunctiva after implantation.
- Thirdly, to characterise the relationship between the rate of fluid released from a pursed pocket, internal pocket pressure and volume.

Finally, the evaluation of these relationships will be used to model drug release profiles from hypothetical single-chamber elastic pockets, within the constraints of feasible dimensions for subconjunctival implantation and commercially available materials. The decision to characterise the design of an elastomeric pump that utilises stored elastic energy of the membranes to drive the drug out was made due to the simplicity of the mechanism of mass transfer. The rate of drug flow can be controlled with precision by adding additional resistance at the outlet of the pump.

3.3. Optimal Device Requirements

While there are many different types of elastomeric pumps that are available commercially, the size constraint of the site of implantation in the eye is a major challenge for an implantable drug delivery device to be successful. The requirements for an optimal elastic pursed pocked device include fabrication of the pursed pocket with biocompatible materials, dimensions that do not exceed 20 mm in length and 6 mm in displacement height, and the theoretical suitability for implantation in the subconjunctival space. The elastic pursed pocket should prolong the drug release for at least five weeks, which is a critical period for postoperative fibrosis following GFS or GDD implantation in glaucoma.

3.4. Materials and Methods

Materials used in this Chapter are listed in **Table 3-1**. Reagents were all used as received without further purification. Instruments and experimental setups used for characterisation are all described in the Methods section below.

Table 3-1. List of materials used in this Chapter.

Material	Supplier	CAS; Catalogue/Lot number
Methylene blue	Sigma Aldrich, UK	122965-43-9; M9140
Silicone sheets	Silex, UK	SuperClear
Electromagnetic linear actuator	Bose Corporation – ElectroForce Systems Group, USA	ElectroForce® 3220 Series III
Stainless steel sheets	Metals4U Ltd., UK	3066
3-way stop valve	Fisher Scientific, UK	4201634503
Camera (Pixel density 1280 × 960, 8-bit)	Allied Vision Technologies GmbH, Germany	Prosilica GC 1290
Clear acrylic sheets	Displaypro, UK	DP0015
Glass Burette for water column	Aimer Products Limited, UK	1567/BT
Silicone tubing	VWR International, UK	Tygon® 3350
PTFE tape	Sigma Aldrich, UK	20808-U
Peek tubing	IDEX Health & Science, UK	1569
20 gauge needles	Terumo, UK	NN-2038S
Leur-Lok tip syringe	BD Plastic, UK	309657
Pressure transducer	Honeywell, USA	162PC01D
Syringe pump	Harvard Apparatus, USA	PHD 22/2000
Weighing balance	A & D Company, Japan	GX series

Commercially available silicone membranes were used in this work due to their material reproducibilities such as uniform thickness and stiffness, relatively low cost, and the similarity of their stiffness with subconjunctival tissue (~1 MPa)(674,675). To gather more information on the behaviour of how a pursed elastomeric pocket would behave in a clinical situation, the structural and functional changes caused by inflation and deflation of the pocket with different geometries (circles and squares of varying thicknesses) and sizes, taking into account the changes in the internal pressure exerted by fluid and material properties (stiffness) needed to be assessed. To do this, it was essential to characterise the materials used for pocket formation for their stiffness.

3.4.1 Measuring the physical properties of elastic materials

The term that is used for the quantitative determination of mechanical strength, or stiffness, is called Young's modulus or elastic modulus (E). The stiffness of any material depends on the dimensions of the specimen being analysed. This makes the

deformation harder to compare because of the applied force in different materials. To overcome this problem, a material's strain, rather than deformation, and stress, rather than applied force, are reported.

The silicone membranes for the current work were characterised using an electromagnetic linear actuator (Bose Electroforce 3220 Series III, USA). Each silicone sample was cut into a dog-bone shape (**Figure 3-1**) that is typical for tensile testing so that the deformation was confined to the narrow centre region and not to the ends of the sample, and the dimensions of the centre were 15 mm long by 4 mm wide. The maximum load applied to the samples was 225 N with a uniaxial displacement (stretching) of 6.5 mm and a resolution of 1 nm. Each uniaxial tensile test (n=3 for each membrane) was performed at a rate of 0.1 mm s^{-1}. These range of displacements were large enough to determine the engineering stress, δ and engineering strain, ε which were calculated using equation 3.1;

$$\delta = \frac{F}{A_0}, \qquad \varepsilon = \frac{\Delta L}{L_o} \tag{3.1}$$

where F was the force applied on the material, A_0 was the initial cross-sectional area of the material tested, ΔL was the change in sample length during the test and L_o is the initial non-deformed length of the sample (674,676,677).

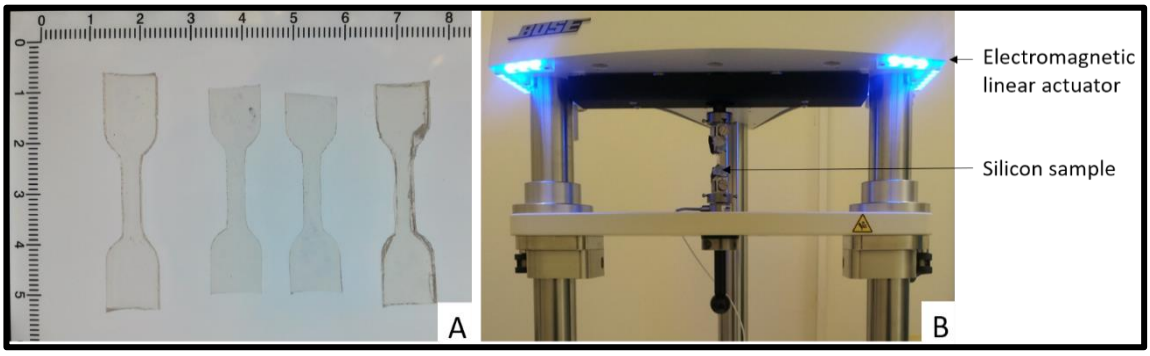

Figure 3-1. Each silicone membrane sample was cut into a dog-bone shape **(A)** before being placed into the electromagnetic actuator **(B)** for tensile testing. The tested samples were 4 mm wide and 15 mm long. The maximum load applied was 225 N with a uniaxial displacement (stretching) of 6.5 mm and a resolution of 1 nm. Each uniaxial tensile test (n=3 for each membrane) was performed at a rate of 0.1 mm s^{-1}

The data was exported as a text file to obtain the values of the engineering stress, δ and the engineering strain, ε for the silicone membranes. The ratio of the material's stress to strain (when strains are small, less than 10%) gives the value of Young's

modulus, E (modulus of elasticity) calculated as the initial linear slope of the stress-strain graph. Young's modulus was calculated using equation 3.2 ;

$$E = \frac{\delta}{\varepsilon} \tag{3.2}$$

3.4.2 Determining pocket displacement using an optical method

An optical method was used to determine the displacement of the elastic membranes to an applied pressure using a technique developed for experimental fluid mechanics (678). This technique exploited the translucent nature of the silicone membranes. The membrane deformation was determined using a dilute methylene blue solution at a concentration of 33 mg L^{-1}. This optical technique correlates the height of the membrane to the attenuation of light intensity caused by dyed water. The intensity of the methylene blue solution was recorded by a camera. MATLAB version R2017b (The MathWorks, Inc., USA) was used to measure the average intensity of each pixel in each image and correlated this with the average height of the fluid. This intensity of the dyed water was pre-calibrated against thin layers of dyed water that were created by successively adding 0.5 mL of dyed water to a measuring cylinder from a height of 0.82 mm up to 19.8 mm. As the intensity increased with fluid height, a greyscale value corresponding to fluid height was converted attributing a 0–255 greyscale to all areas in an image. No dye was attributed as 255 and the upper limit of detection of the dye intensity was 0. To ensure reproducibility, the optical intensity calibration was performed each day before starting the experiment.

This optical technique was used to accurately determine the deformation in elastic membranes when the internal fluid exerted pressure on them, see **Figure 3-3**. Each image was first converted into red, green, and blue colours (RGB) using MATLAB version 2017b (The MathWorks Inc., USA) and the conversion from RGB to greyscale was done using MATLAB, with the help of Dr Yann Bouremel (Research Associate at UCL Institute of Ophthalmology).

3.4.3 Inflation of elastic pockets

Elastic pockets were created using six clear silicone membranes of thicknesses, 0.32, 0.5, 1.6, 1.72, 3.2, and 3.25 mm, clamped between two clear acrylic plates, an upper plate, and a base plate of dimensions 162 x 162 mm. These formed simply connected elastomeric pockets, meaning that the point of contact was along a single continuous boundary at the outer edge. There was a diffusive light source below the membranes, and an 8-bit camera with a pixel density of 1280 × 960, using a 16 mm lens (Allied Vision technology, Germany) was placed perpendicularly above the membranes and was used to record the optical images, see **Figure 3-2**.

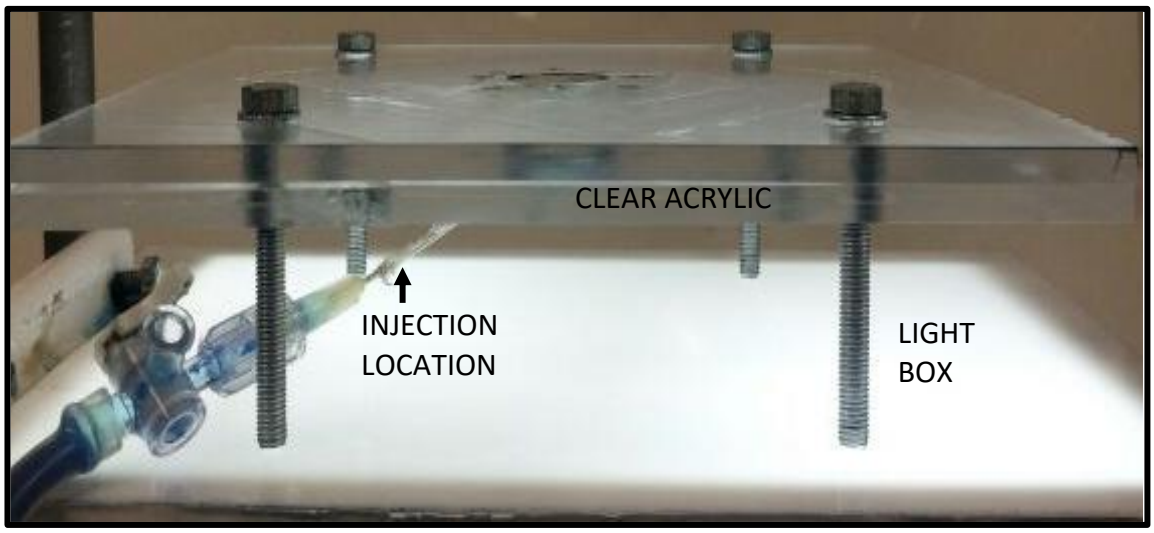

Figure 3-2. The experimental set-up for inflation of elastomeric sheets using dyed water clamped between clear acrylic plates. The top plate had a hole cut for inflation, the bottom plate had an injection for inlet of liquid.

Different pocket geometries; a circle with radii (R) of 10 and 20 mm, and a square with sides (a) 20 and 40 mm long were cut in the upper plate using a laser (by technicians at UCL Department of Mechanical Engineering Workshop) to fix the outer edge of the pockets. The pockets were pressurised by injecting dyed water under the clamped membrane through a hole drilled in the base plate, as shown in **Figure 3-2** and **Figure 3-3**. In order to apply a uniform hydrostatic pressure over the membrane, water columns of different heights were connected to the pocket. Since the height of the water column was significantly greater than deflection, ΔH, the pressure, ΔP , applied over the membrane was uniform.

For the case of inflation of different shapes of elastomeric membranes, the experimental results were non-dimensionalised to obtain the value of the coefficient γ for inflation. With the scaling analysis, the characteristics of interest were the dependences of membrane displacement, H, thickness, T, Young's modulus, E, shape and size (R for circular and a for square-shaped pockets) of the pocket and the internal pocket pressure, P. An in-depth assessment of how the variables would determine fluid release from pursed pockets was performed.

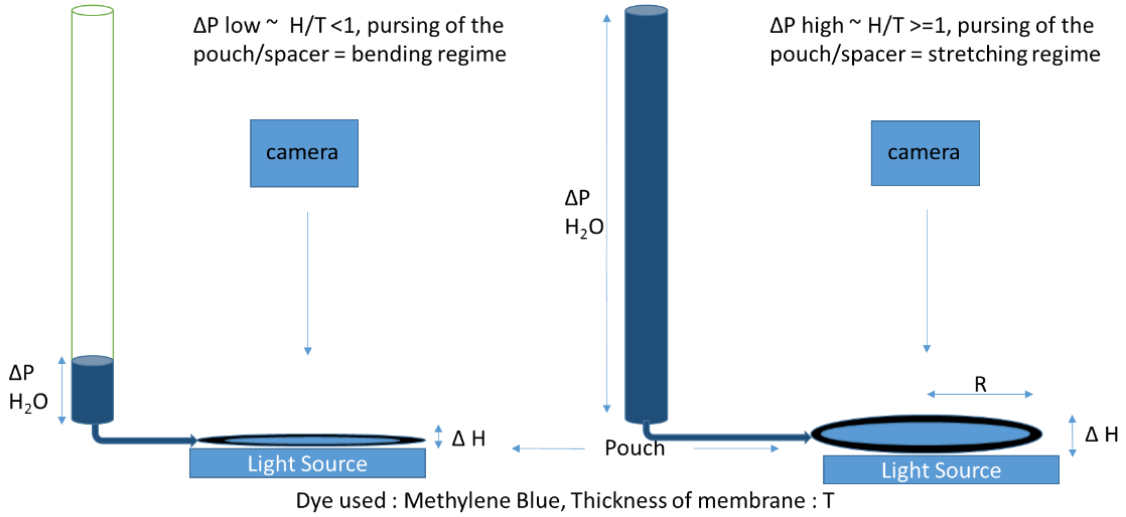

Figure 3-3. A schematic of the experiment analysing the deflection in the pocket height, ΔH, of a fixed radius, R, when a pressure head of water is changed, ΔP, with time. When ΔP is low (**left**), there is smaller pursing of the pouch, and when ΔP is higher (**right**), there is larger pursing of the pouch. Dyed water is used to image the deflection using a diffused light source kept under the pocket.

3.4.3.1 Finite Element Analysis model

To complement the experimental results obtained from inflation experiments, a finite element model of the three-dimensional elastic pocket was created and solved by Dr Yann Bouremel (Research Associate at UCL Institute of Ophthalmology), using Abaqus version 6.12-3 (Dassault Systèmes , France)(667).

During the simulations, the pressure was applied uniformly on the lower surface of the pocket. Newton's method was used to calculate solutions for pressure values in sequence, covering five orders of magnitude. After each solution was found, the pressure was increased by step ranging from 0.0001 to 10 pascal, depending on the pressure range of the simulation. The current solution was used as an initial guess for the next solution. For a solution to be accepted as 'converging', the largest correction of

the solution for one increment was less than 1% of the incremental change for the corresponding solution variable, and a residual error of less than 0.5%. The edges of the pockets were set to be clamped. A three-dimensional mesh with 8-node linear hexagonal brick elements was generated by extruding a 2D grid. The optimal number of elements was determined with the convergence of the maximum deflection, H and was usually around 50000. The numerical results obtained from the finite element analysis were plotted using MATLAB version 2017b (The MathWorks Inc., USA) to complement experimental results.

3.4.4 Compression of inflated elastic pockets

Most of the elastomeric pumps used in the clinic currently are enclosed in a hard casing, presumably to protect it from damage during handling and avoid altering the intended rate of drug delivery. Once implanted, the pump would experience a compressive force exerted by the conjunctiva. However, the relationship between the compression of the elastomeric pocket when subjected to external force and the change in the internal pressure of the pocket has not been studied in the literature.

For the compression of pursed pockets, four elastic silicone membranes of thicknesses, 0.25, 0.5, 0.8, and 1.6 mm were sandwiched between a clear base acrylic plate and a steel upper plate. A circular hole radius, a=20 mm was cut into the upper plate (by technicians at UCL Department of Mechanical Engineering Workshop) so that introducing water beneath the sheet enabled it to be pressurised to an initial pressure, P, and form a purse, see **Figure 3-4**. The inlet to the circular pocket was connected via a three-way control tap with one end to a column of glass capillary with an inner diameter of 3 mm, that enabled the initial pressure of the pocket to be set using a column of water. After setting the initial pressure of the inflated pocket, the connection to the water column was sealed, and the other end of the three-way control tap was connected to a calibrated pressure transducer (Honeywell, USA). The water column height varied from 20 to 50 cm, which was significantly larger than the deflection height of the purse (<10 mm) so that the pressure variation with the height in the purse is negligible. A static compressive force, F_c was applied uniformly over the top of the purse by using custom-made weights. After applying a compressive force, F_c, the pressure in the purse

increased to P_c. The contact between the applied force F_c and the elastic membrane generates an area of the purse A_c and is related through equation 3.3;

$$A_c = \frac{F_c}{P_c} \tag{3.3}$$

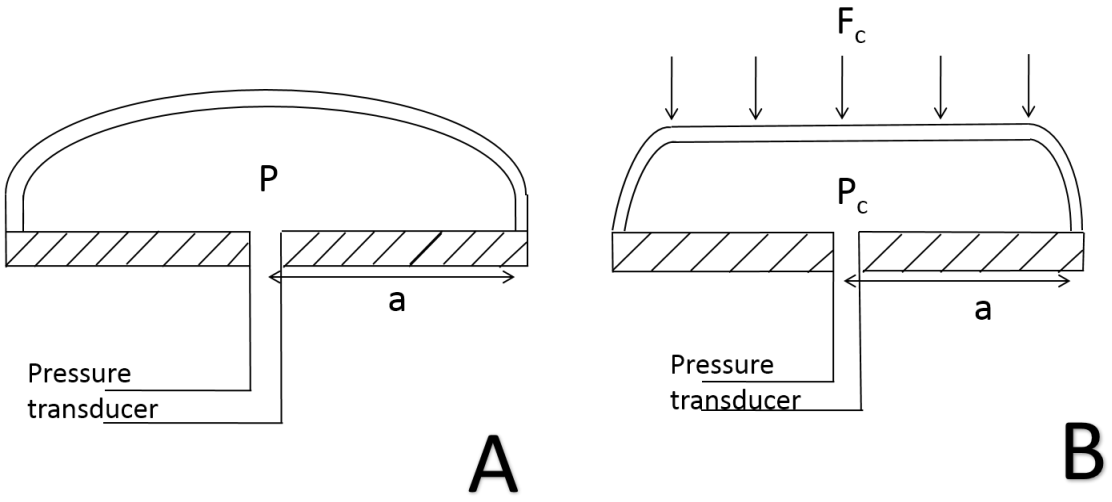

Figure 3-4. A schematic of an elastic pocket of radius $\boldsymbol{a}$ in the initial pursed state **(A)** with a uniform internal pressure $\boldsymbol{P}$, which is compressed **(B)** by uniformly applying a static force $\boldsymbol{F_c}$ on the top of the pocket, changing the internal pressure of the pocket, $\boldsymbol{P_c}$.

3.4.5 Deflation of elastic pockets

The aim for this part of the experimental work was to understand the relationship between the rate of fluid release, internal pocket volume and pressure, when deflating an elastomeric pocket. Experiments focussed characterising release of liquids from a circular purse made of silicone sheet in terms of internal pressure, volume and flow rate of liquid released. A silicone sheet of 0.5 mm thickness and Young's modulus of 1.241 MPa was used as they closely match to Young's modulus of the sclera which has been reported to be in the range of 1–2.9 MPa (674,675,679,680). Also, the pressure to inflate these pockets was low enough to be between the linear ranges of our experimental calibration.

For this purpose, an elastomeric purse made of a simply connected silicone sheet, clamped in between two acrylic plates was inflated by filling water. The top acrylic plate had a hole (radius 10 mm) cut out to let the pocket purse during inflation. The bottom acrylic plate had an inlet tube attached to a three-way control tap connected to a pressure transducer (Honeywell, USA). The bottom plate also had an outlet tube

attached to a three-way control tap to release the liquid that would empty from the pursed pocket. A tube with an internal diameter of 500 µm and a length of 10 cm was attached on the outlet three-way tap to provide additional resistance to the outflow of water, see **Figure 3-5**.

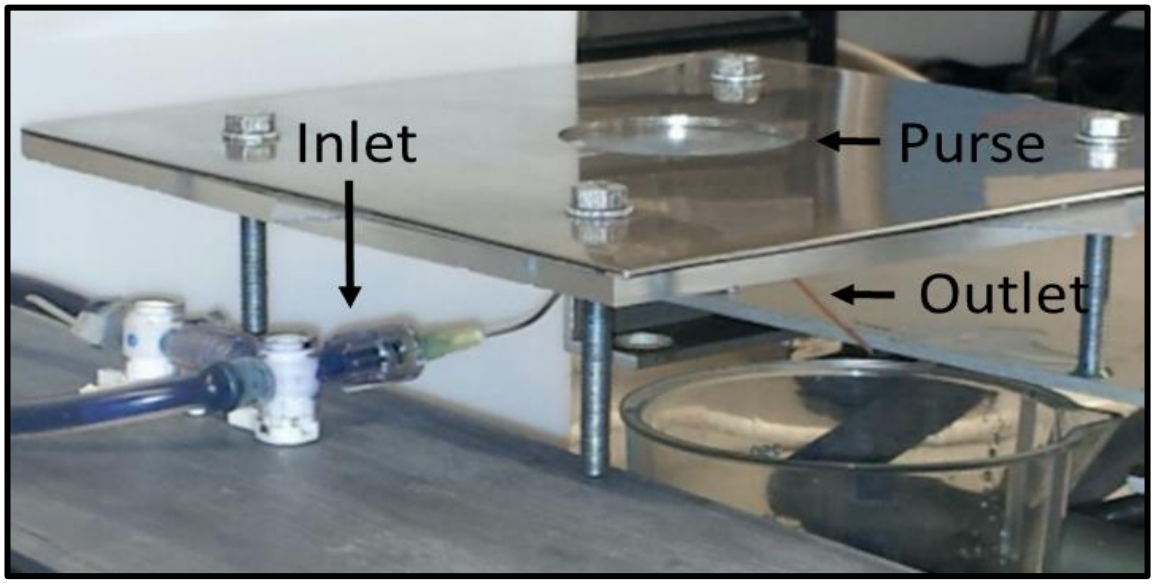

Figure 3-5. The experimental setup for deflation of pursed elastomeric sheets, clamped between clear acrylic plates. The top plate had a hole (radius 10 mm) cut for inflation, the bottom plate had an injection for inlet and outlet of liquid). The inlet tube was connected to a pressure transducer to measure the internal pressure of the elastomeric purse. The outlet tube would empty into a beaker placed on a weighing balance to measure the volume of liquid released.

The internal pressure (back-pressure) of the inflated pocket was recorded by the pressure transducer (Honeywell, USA) in mV, which was converted to Pa with the help of a calibration curve made against a water column, described in **Section 3.4.6.** To begin the experiment, the outlet with the resistance tube was opened and the released water was collected in a beaker, placed on a weighing balance (A&D Company, Japan), to measure the simultaneous change in back-pressure, the internal volume of the pocket, rate of fluid release, as a function of time.

3.4.6 Pressure measurements

A one-metre-high glass column of water was attached to a pressure transducer (Honeywell, USA) and a syringe pump (Harvard Apparatus, UK) using a three-way control tap, a schematic of the experimental setup was shown previously in **Figure 3-3**. The pressure transducer was powered by an external voltage source at 5V and was attached to a laptop with Velleman software to measure the change in pressure output as a change in mV. The change in mV as a function of the change in the height of the water

column (measured using a fixed ruler) was recorded to calculate a calibration curve for the transducer ($R^2 > 0.999$). To ensure reproducibility, the calibration was performed each day before starting the experiment. To perform the experiments, the elastomeric pockets were connected to the pressure transducer and the back-pressure was recorded in mV and was converted to Pa using the calibration curve.

3.4.7 Flow rate and volume measurements

For the inflation and deflation of the elastomeric membranes, a syringe pump (Harvard Apparatus) was used to control the flow rate and volume of water with precision. For the deflation experiments, the elastomeric pumps were connected to a three-way control valve, one outlet connected to a tube of 500 µm internal diameter and 10 cm length, that would empty into a beaker kept on a weighing balance. The weighing balance was connected to a laptop using a standard RS-232-to-USB cable, and the change in weight was recorded using WinCT401 software provided on the manufacturer website (A&D Company).

The flow rate, Q (mL s^{-1}), for time point, T (s), was calculated using the change in weight, $W_2 - W_1$ (mg), as a function of time using equation 3.4;

$$Q = \frac{W_2 - W_1}{T_2 - T_1} \tag{3.4}$$

The third outlet was connected to a pressure transducer (Honeywell, USA) and the change in pressure was recorded as a function of time using the method described in **Section 3.4.6**.

A general schematic for the experimental setup used in the experimental work is given in **Figure 3-6**.

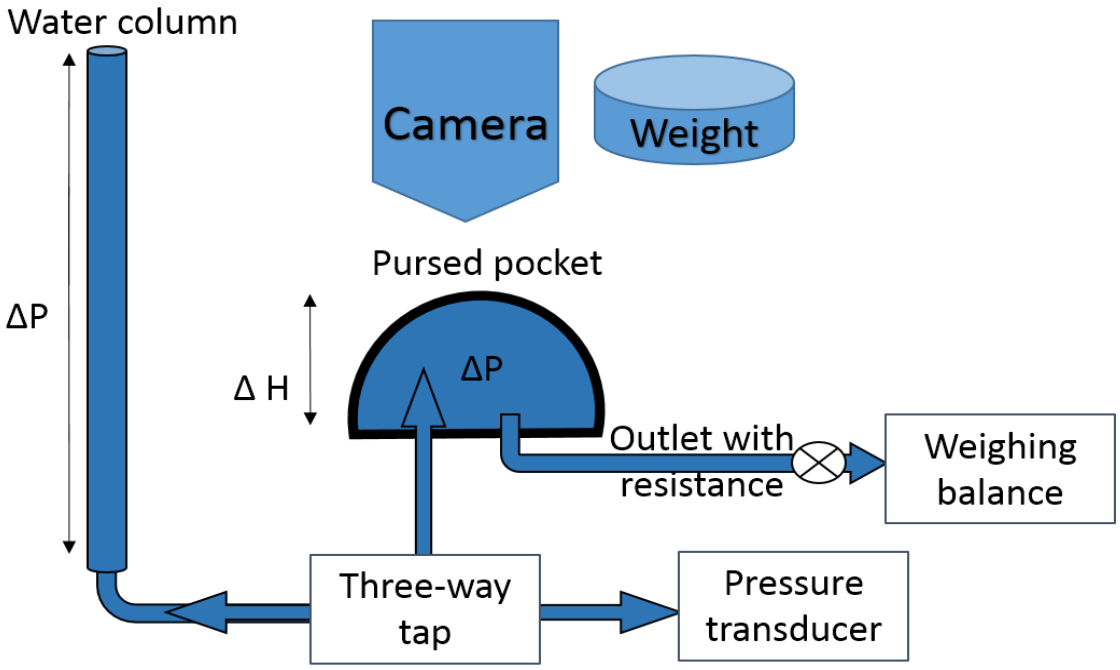

Figure 3-6. A general schematic for the experimental setup used in the experimental work for this chapter. After the silicone membranes were characterised for stiffness, the experimental work was undertaken in three main parts. 1. Inflation of pockets (circles and squares of varying sizes) with dyed water to study the deformation in the pocket height (using an optical photographic method) and internal pocket pressure (using a pre-calibrated pressure transducer). 2. Compression of inflated pockets (circles) to study the relationship between compressive forces (applied uniformly on the top of the pocket using custom made cylindrical weights) and the change in internal pocket pressure (using a pre-calibrated pressure transducer). 3. Deflation of pockets (circle) to understand the relationship between internal pocket pressure (using a pre-calibrated pressure transducer) and flow rate of fluid released (using a weighing balance) through an outlet attached with a known resistance. Please note; the pocket outlet with resistance was open only in the case of deflation experiments.

3.4.8 Modelling drug release from hypothetical single-chamber elastic pockets

This part of the work was aimed at modelling the effect of material properties such as Young's modulus (E), material thickness (T) and the diameter of the outlet tube on drug release from proof-of-concept single-chamber hypothetical elastic pockets with small volumes (~1 mL). According to the Hydrodynamics principle, flow rate (Q) of fluid is dependent on the resistance (R) to fluid flow. This can be re-written as equation 3.5;

$$P = RQ \tag{3.5}$$

This resistance generates pressure, P, which acts as the driving force for fluid flow. In an inflated elastomeric pocket, this pressure is applied by the displaced (deflection height, H) elastomeric sheet that drives the fluid out of the pocket.

The drug release (fluid) from the hypothetical pockets would be slowed with the help of additional resistance provided a micro-tube. The resistance, R offered by the micro-tube was calculated using the Hagen-Poiseuille's equation (equation 3.6) that calculates the fluid flow through a cylindrical pipe of length, L and diameter, D $(2r)$, the dynamic viscosity of the fluid at 37°C, μ (681);

$$R = \frac{128\mu L}{\pi D^4} \tag{3.6}$$

Using the results described in **Section 3.5.3**, we know the pressure exerted by a circular elastomeric membrane of a fully pursed drug reservoir, rearranging for P;

$$P = \frac{4.63ETH^3}{R^4} \tag{3.7}$$

The volume (V) of fluid inside the hypothetical single-chamber pockets with radii, R of 10 mm and maximum displacement, H of 6 mm was calculated using the formula (equation 3.8) for the volume of spherical domes (682,683);

$$V = \frac{1}{6}\pi h(3R^2 + H^2) \tag{3.8}$$

The fluid release results from hypothetical single-chamber pockets with known parameters for E, H, T, R, and the dimensions of the outlet tube, D and L were plotted and compared using MATLAB version R2017b (The MathWorks Inc., USA). The time required for release of 50% ($T_{1/2}$) of the total fluid released was also calculated. The fluid release results were modelled with a cut-off pressure value to match the IOP of a healthy eye, such that the fluid would be released until a minimum internal pressure of the hypothetical pocket reached 15 mm Hg. A maximum and minimum value of E (E*max* and E*min*) and T (T*max* and T*min*) for elastomeric sheets, and D (D*max* and D*min*) for an outlet tube was fixed based on commercially available materials. Pocket dimensions of H and R were fixed based on the optimal size of a pump that could be implanted in the superotemporal quadrant of the eye.

In a hypothetical pocket with R as 0.01 m, a square shape with a side of 0.01 m can easily fit on the circular bottom plate. If a tube of D=25 µm were to be arranged inside the pocket, along a square serpentine shape with a separation of 100 µm apart,

the total L of the tube would be 8 m. However, it would not be possible to arrange the tube using 100% of the area of the square as some area would be used for bending the tube. For this reason, a conservative estimate of 50% space used by the tube would make the equivalent length of the tube to be 4 m.

Finally, a hypothetical optimal pump with same dimensions (H and R) and optimal values (Optimal) for E, T, D and L for prolonging drug release was modelled for fluid release. Pump efficiency was calculated using equation 3.9;

$$Efficiency\% = \frac{Volume\ released}{Initial\ volume} X\ 100 \tag{3.9}$$

Table 3-2. Parameters for modelling drug release from hypothetical single-chamber elastic pockets. The changes for each condition have been highlighted in grey.

Variable	Young's modulus		Thickness		Diameter		Optimal
	E*max*	E*min*	T*max*	T*min*	D*max*	D*min*	
E **(MPa)**	5.25	0.525	1.25	1.25	1.25	1.25	5.25
T **(m)**	1.0E-04	1.0E-04	0.0016	2.0E-05	1.0E-04	1.0E-04	2.0E-05
H **(m)**	0.006	0.006	0.006	0.006	0.006	0.006	0.006
R **(m)**	0.01	0.01	0.01	0.01	0.01	0.01	0.01
D **(m)**	5.0E-05	5.0E-05	5.0E-05	5.0E-05	2.5E-04	2.5E-05	2.5E-05
L **(m)**	4	4	4	4	4	4	4

A schematic of the seven hypothetical single chamber pockets that were used for modelling the fluid release is presented in **Figure 3-7**.

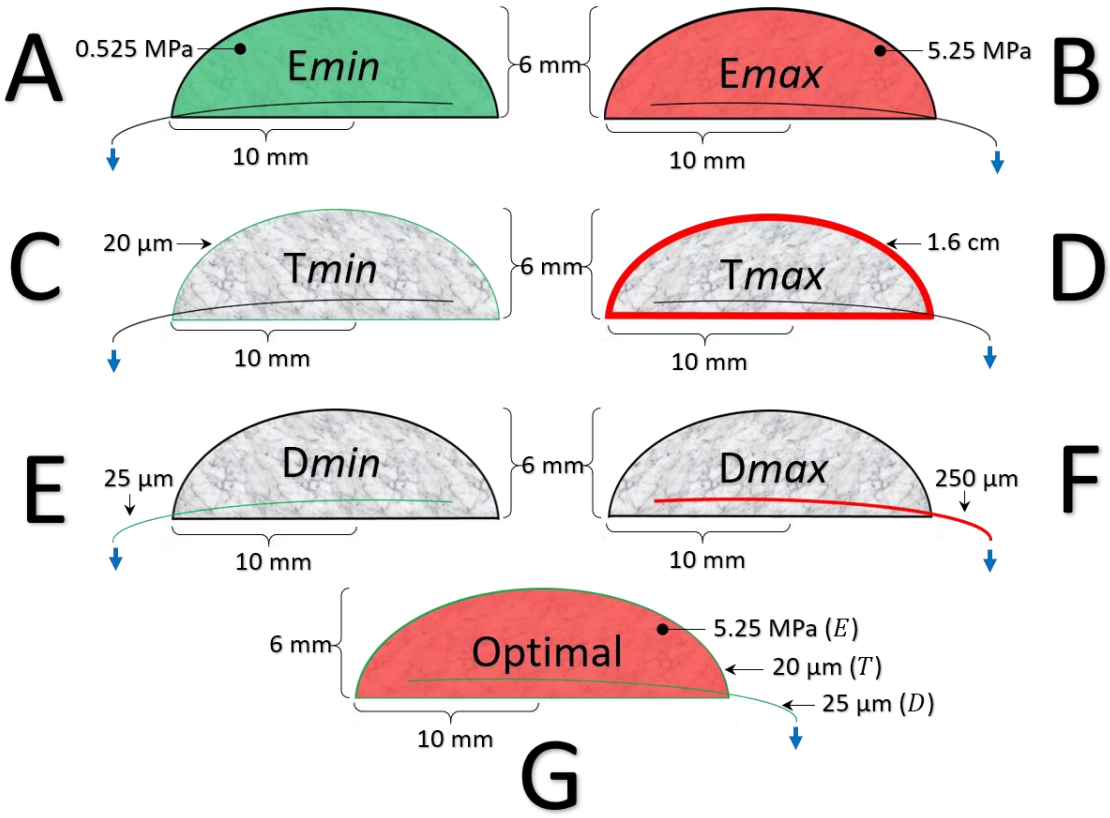

Figure 3-7. Seven hypothetical single-chamber elastic pockets of radius $\boldsymbol{R}$ = 10 mm and maximum displacement $\boldsymbol{H}$ = 6 mm were used for modelling fluid release from a hypothetical pump. The maximum (*max* change depicted in red) and minimum (*min* change depicted in green) values of material young's modulus $\boldsymbol{E}$ (E*max* and E*min*) (**A, B**) and thickness $\boldsymbol{T}$ (T*max* and T*min*)(**C, D**) of elastomeric sheets, and diameter $\boldsymbol{D}$ (D*max* and D*min*) (**E, F**) of an outlet tube was fixed based on commercially available materials. Finally, a hypothetical optimal pump with same dimensions ($\boldsymbol{H}$ and $\boldsymbol{R}$) and optimal values (Optimal) (**G**) for $\boldsymbol{E}, \boldsymbol{T}, \boldsymbol{D}$ and $\boldsymbol{L}$ for prolonging drug release was modelled for fluid release. The blue arrows indicate direction of fluid release from the outlet tube.

3.5. Results

3.5.1 Material characterisation

Engineering stress, δ and engineering strain, ε were calculated from the force applied on a known area of the sample and the displacement in sample length in comparison with original sample length. The initial linear slope of the equilibrium engineering stress-strain curve was used to calculate Young's modulus (E) for the silicone membranes, data points shown in **Figure 3-8**.

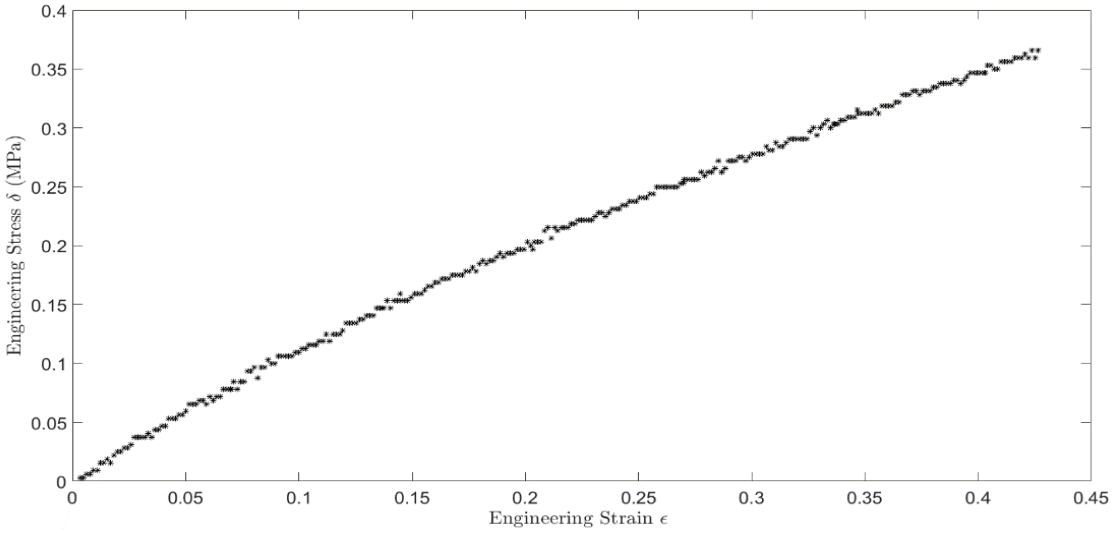

Figure 3-8. Engineering stress, $\boldsymbol{\delta}$, and engineering strain, $\boldsymbol{\varepsilon}$, were measured for 0.8 mm thick silicone sample. The linear slope of the data points shown above was used to calculate the value for Young's modulus, $\boldsymbol{E}$ (MPa).

For the silicone sheets tested, the values of E were found to be between 1–2.5 MPa. The material properties tested using the electromagnetic linear actuator for different samples are given in **Table 3-3.** Summary of silicone samples used in the experimental study; the sheet thickness, $\boldsymbol{T}$ Young's modulus, $\boldsymbol{E}$ length ($\boldsymbol{R}$ for circles or $\boldsymbol{a}$ for squares), and symbols are listed below. Silicone membranes were characterised using uniaxial tests to give Young's modulus E.

Table 3-3. Summary of silicone samples used in the experimental study; the sheet thickness, T Young's modulus, E length (R for circles or a for squares), and symbols are listed below.

Thickness T (mm)	Young's modulus E (MPa)	Length R or a (mm)	Symbol used in the results
0.25	1.241	20	
0.32	2.628	20	
0.5	1.241	10	
0.5	1.241	20	
0.8	1.241	20	
1.6	1.241	10	
1.6	1.241	20	
1.72	1.112	10	
1.72	1.112	20	
3.2	1.241	20	
3.25	1.083	20	

These samples were further used for inflation and compression experiments, as described in **Sections 3.4.3** and **3.4.4**.

3.5.2 Optical method for displacement determination

For an accurate 3D estimate of the height of the pursed pockets, a novel experimental method was used to correlate the optical intensity of dyed water with height. **Figure 3-9** shows an example of the images used for calibration of the height (mm) of dyed water optical intensity (greyscale). For height 0 mm, the greyscale was 135 ±4.1, for height 1.65 mm, the greyscale was 120.5 ±4.3, and for height 3.3 mm, the greyscale was 106.2 ±3.8.

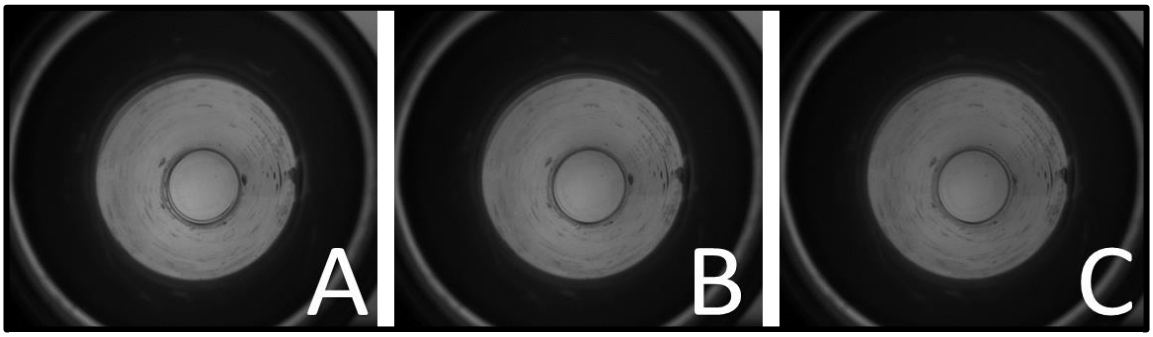

Figure 3-9. Images used for calibration of the height (in mm) of dyed water optical intensity (greyscale). For **(A)** height 0 mm, the greyscale was 135 ±4.1, for **(B)** height 1.65 mm, the greyscale was 120.5 ±4.3, and for **(C)** height 3.3 mm, the greyscale was 106.2 ±3.8.

The optical intensity calibration was found to be linear with error <3.5%, and data is shown in **Figure 3-10**.

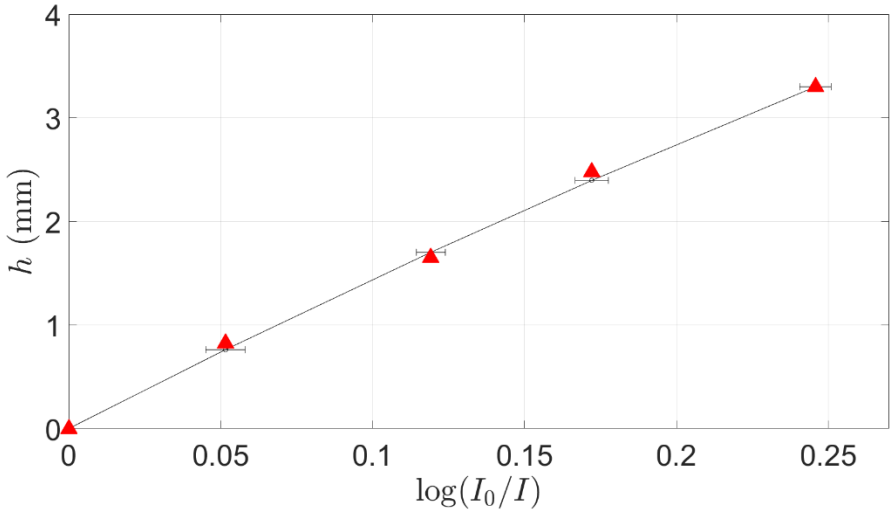

Figure 3-10. Calibration test showing the correlation between height and light intensity determined optically, the error was less than 3.5%.

Figure 3-11 shows an example of a circular elastomeric pocket with a radius of 10 mm with a silicone sheet of thickness 0.5 mm and Young's modulus of 1.241 MPa, pursed with a pressure of 6005.7 Pa showing a colour photograph of the pocket. In the black-and-white image recorded by the camera and post-processing are shown, respectively. The same processing technique was used to correlate the images from pockets with the height to give an accurate value for the 3D displacement of the elastomeric membranes.

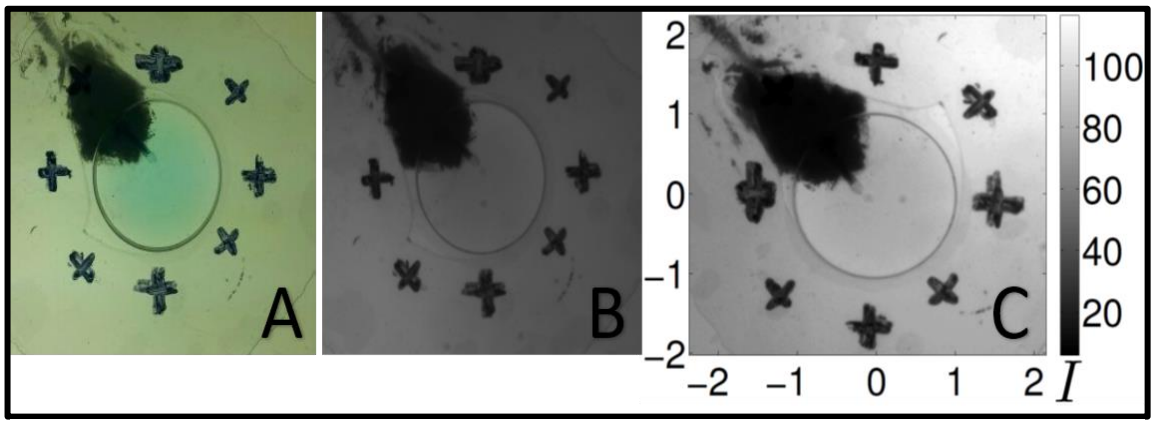

Figure 3-11. Images of the circular elastomeric pockets with a silicone sheet (thickness 0.5 mm and Young's modulus of 1.241 MPa) pursed with pressure of 6005.7 Pa showing **(A)** a colour photograph of the pocket. In **(B)** and **(C)** the black-and-white image recorded by the camera and the post-processed image with the greyscale are shown.

Figure 3-12 shows a typical 3D elevated and 2D plane views of the deflection obtained experimentally using the optical method for the silicone sheet with a thickness of 0.5 mm and Young's modulus of 1.241 MPa, fitted in a circle of radius 10 mm. The sample was clamped using acrylic plates at a single continuous boundary to form a circular pursed pocket (radius 10 mm and internal pressure 4500.5 Pa).

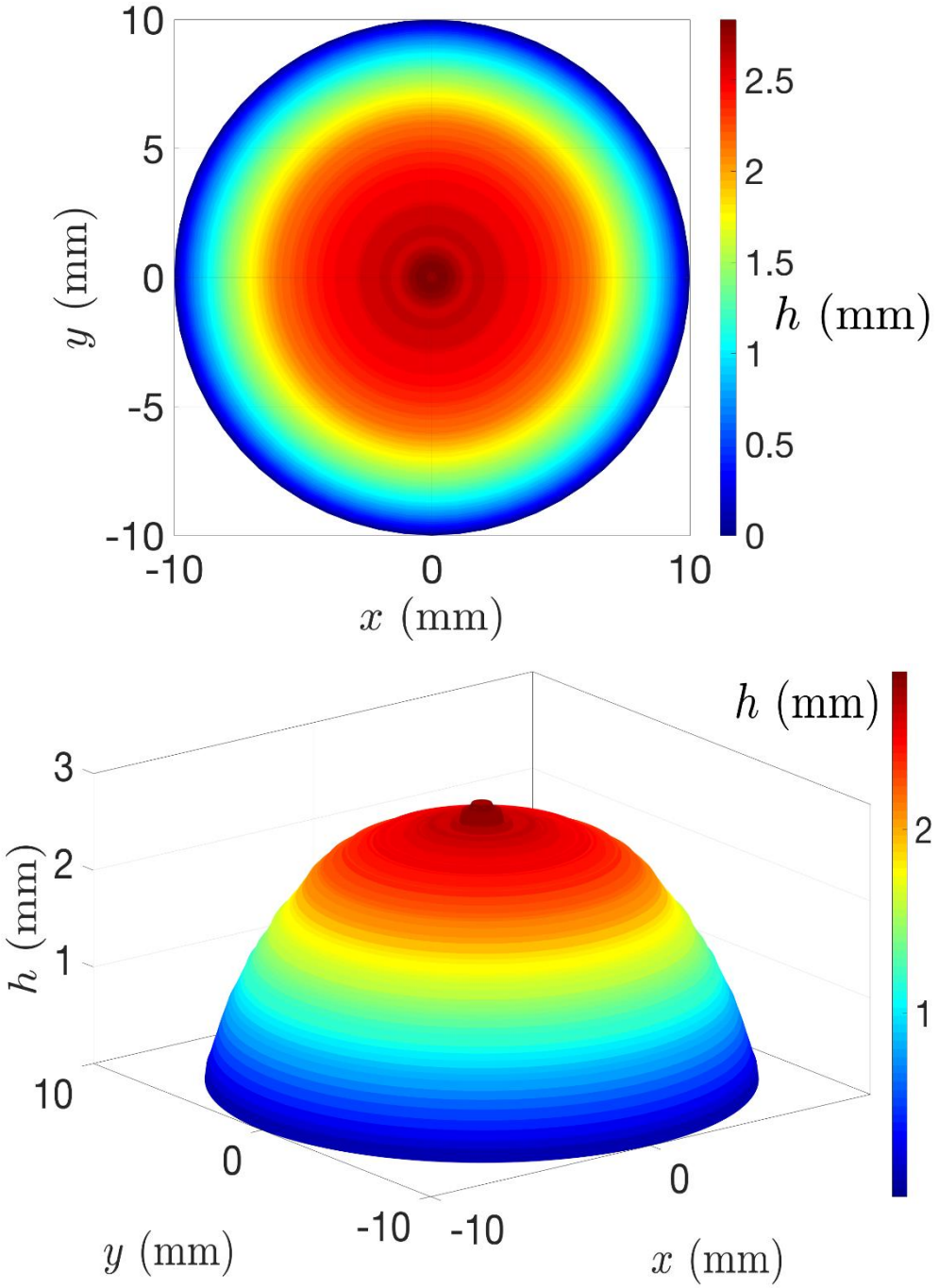

Figure 3-12. The 2D planar (top panel) and the 3D elevated view (bottom panel) of the experimental deflection profile of a silicone sample (thickness 0.5 mm and Young's modulus of 1.241 MPa) obtained using the optical method. The silicone sheet was clamped to form circular pursed pocket (radius 10 mm and internal pressure 4500.5 Pa).

Figure 3-13 shows the typical 3D elevated and 2D plane views of the deflection obtained experimentally using the optical method for the silicone sheet with thickness 0.5 mm and Young's modulus of 1.241 MPa, fitted in a square of side 40 mm. The sample was clamped using acrylic plates at a single continuous boundary to form a square pursed pocket (side 40 mm and internal pressure 1070.8 Pa). This method allowed to

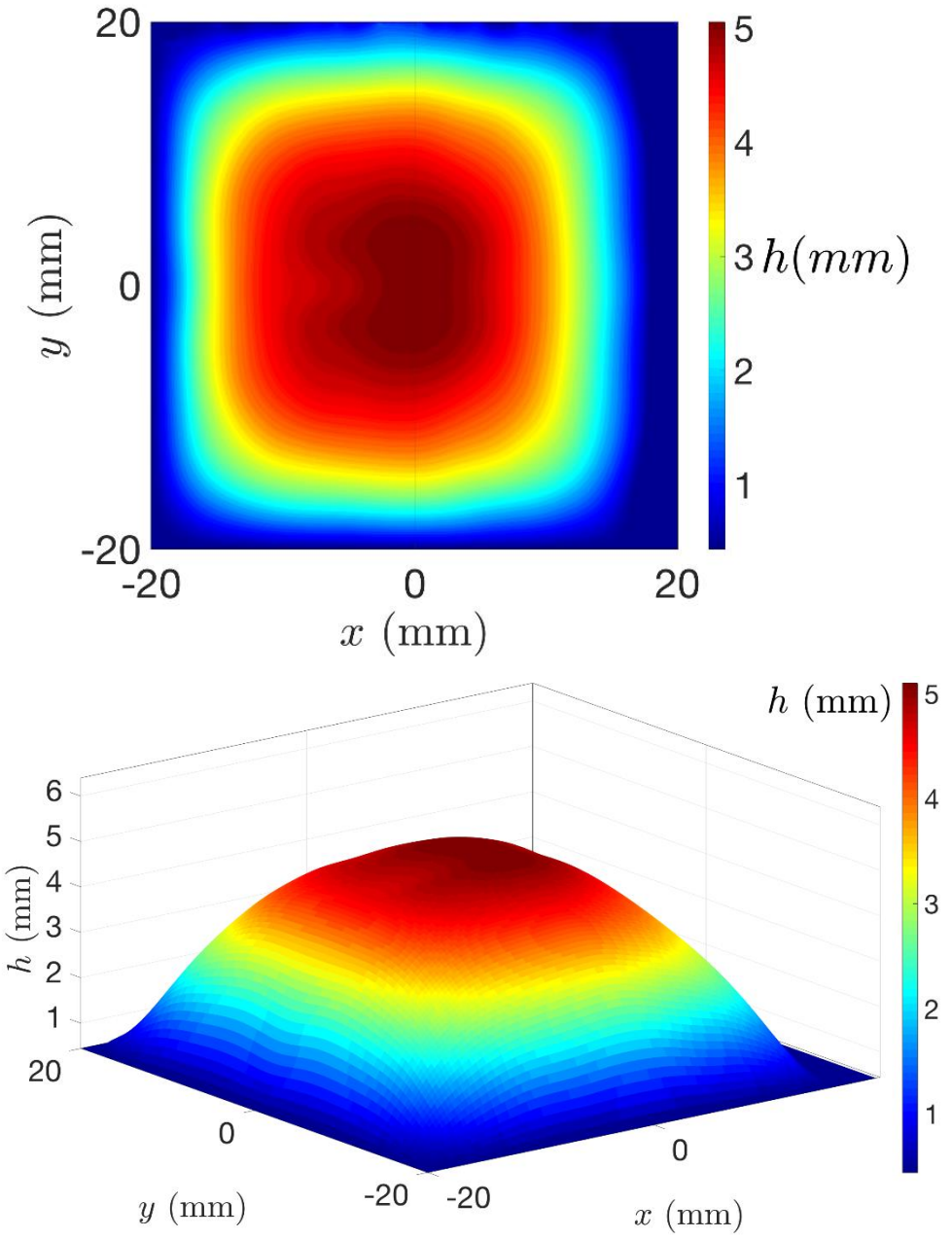

Figure 3-13. The 2D planar (Top) and the 3D elevated view (bottom) of the experimental deflection profile of a silicone sample (thickness 0.5 mm and Young's modulus of 1.241 MPa) obtained using the optical method. The sample was clamped to form a square pursed pocket (side 40 mm and internal pressure 1070.8 Pa).

accurately plot a 3D deformation profile based on the deformation planes of the pursed pockets while comparing the 2D deformation distribution along pocket width.

3.5.3 Inflation of elastic pockets

The static profiles of an elastic membrane that is clamped to a rigid base when the pocket between them is inflated by a fluid with uniform pressure were studied. Simply connected (point of contact along a single continuous boundary) circular and square pocket shapes were considered for the inflation experiments. These pockets were pinched on the edges with acrylic plates allowing no boundary rotation. Experiments were performed for the simply-connected cases in which the attenuation of light passing through the dyed fluid was measured to infer the thickness of the fluid layer and hence the deflection of the membrane. Both the bending regime (pocket deformations smaller than the membrane thickness) and the stretching regime (pocket deformations larger than the membrane thickness) were considered.

3.5.3.1 Circular pockets

From the energy balance equation (684), when an elastomeric circular pocket is in bending regime such that, $\frac{H}{T} \leq 1$, the relationship between membrane displacement, H; membrane thickness, T; pressure, P; pocket radius, R; Young's modulus, E; and Poisson's ratio, σ, has been analytically calculated (685) using equation 3.10 as ;

$$\frac{H}{T} = \frac{3(1-\sigma^2)}{16}\left(\frac{PR^4}{ET^4}\right) \tag{3.10}$$

Poisson's ratio is a measure of the deformation in the material in a direction perpendicular to the direction of the applied force, value for silicone/rubber membranes is estimated to be 0.5 (686). Landau *et al*. determined that the transition from bending to stretching of a membrane in a pursed pocket occurs when $\frac{H}{T} \sim 1$ (Landau and Lifshitz, 1975). In case of stretching of the elastomeric membranes, ($\frac{H}{T} > 1$), the relationship between membrane displacement H and pressure P, pocket size L, membrane thickness T and Young's modulus E was estimated (684,687) using equation 3.11 as ;

$$\frac{H}{T} \sim \left(\frac{PL^4}{ET^4}\right)^{\frac{1}{3}} \tag{3.11}$$

While the scaling analysis gives an estimate of the purse response in the two regimes, experimental data is required to determine the pre-multiplying coefficient. With the scaling analysis, the characteristics of interest were the dependencies of both membrane displacement, H, and pressure, P, on the membrane (circle) with thickness, T, radius, R, and Young's modulus, E. Elastomeric (silicone) membranes were used to objectively measure Young's modulus, the influence of membrane thickness, shape, the pressure under the pursed pocket. A qualitative assessment of how the variables determine release from pursed pockets was performed.

The changes in the deformation height, H (mm) with the change in internal pressure, P (Pa), of the circular purse of radius 20 mm using silicone sheets of Young's modulus, E 1.241 MPa and different thickness, T of 0.5, 1.6 and 3.2 mm are plotted in **Figure 3-14**.

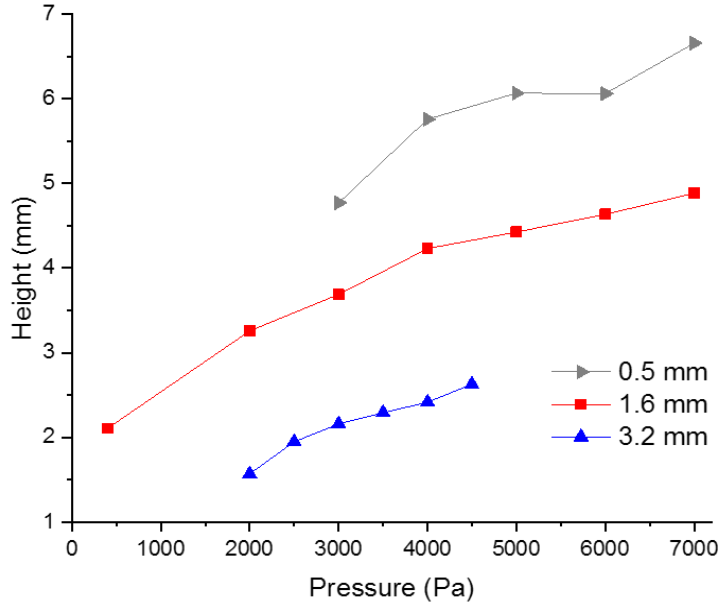

Figure 3-14. Differences in the deflection, $\boldsymbol{H}$ at different pressures, $\boldsymbol{P}$ using silicone sheets off different thicknesses, $\boldsymbol{T}$ for pursing circular shaped pockets with radius 20 mm and Young's modulus, $\boldsymbol{T}$ 1.241 MPa. The displacement height, $\boldsymbol{H}$ decreased with the increase in material thickness, $\boldsymbol{T}$ at similar pressure, $\boldsymbol{P}$ and pocket size.

The changes in the deformation height, H (mm) with the change in internal pressure, P (Pa), of circular purses of radii 10 (R1) and 20 (R2) mm using silicone sheets of Young's modulus, E 1.241 MPa and thickness, T of 0.5 **(A)** and 1.72 mm **(B)** are plotted in **Figure 3-15**.

For a circular pocket of radius 20 mm, made using a material with Young's modulus 1.241 MPa, an inverse correlation was found between the thickness, T of the membrane used and maximum deformation height, H of the pocket when compared under similar internal pressure during inflation. The observed height (maximum deformation) for the thicker membranes was lower than the observed height for thinner membranes. For similar material thickness and Young's modulus, the displacement height, H increased with the increase in pocket size at similar pressure, P and material thickness, T.

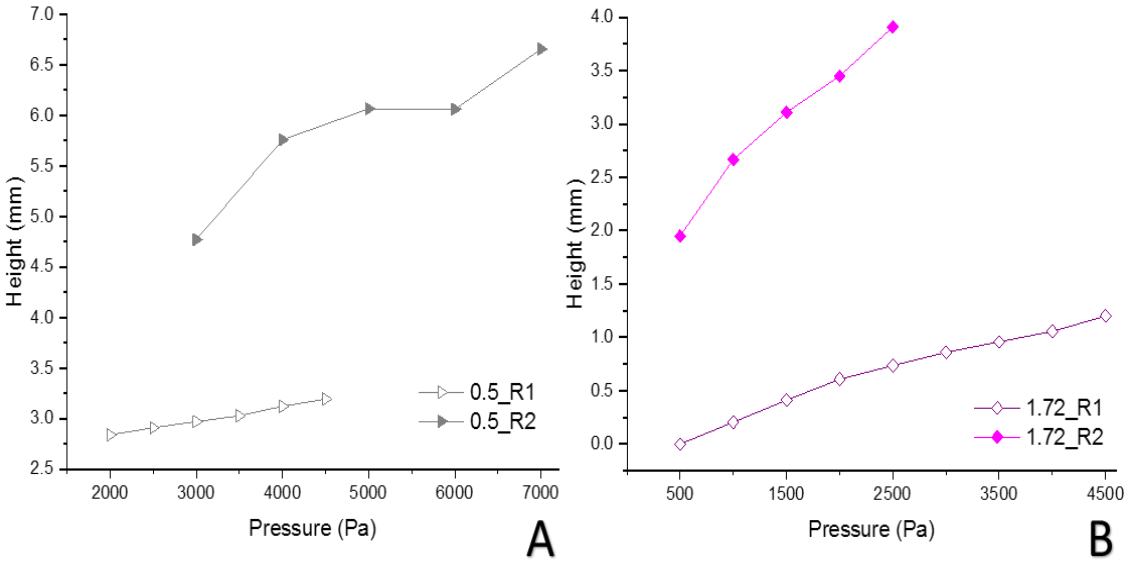

Figure 3-15. Differences in the deflection. $\boldsymbol{H}$ at different pressure, $\boldsymbol{P}$ using silicone sheets for pursing circular shaped pockets with radii of 10 (R1) and 20 mm (R2) at Young's modulus, $\boldsymbol{E}$ 1.241 MPa for 0.5 mm thickness **(A)** and 1.72 mm thickness **(B)**. Deflection increased with the size of the pocket.

From the above results, the data were non-dimensionalised to obtain the value of the coefficient γ for inflation for a pursed circular pocket in the stretching regime $\frac{H}{T} > 1$. **Figure 3-16** shows the dimensionless maximum deflection $\frac{H}{T}$ of circular elastic pockets over six orders of magnitude of $\frac{PR^4}{ET^4}$. The experimental data matches very well with the analytical bending solution (667) for the circle plotted with black curves up to the maximum deflection of $\frac{H}{T} \approx 1$. Above $\frac{H}{T} \approx 1$, the silicone pocket undergoes stretching and the data obtained numerically through finite element analysis (**Section 3.4.3.1**) can be fitted (667), in the case of the circular shapes, using equation 3.12 ;

$$\frac{H}{T} \approx \gamma \left(\frac{PR^4}{ET^4}\right)^{\frac{1}{3}} \tag{3.12}$$

The value of γ was calculated from the experimental data to be 0.60.

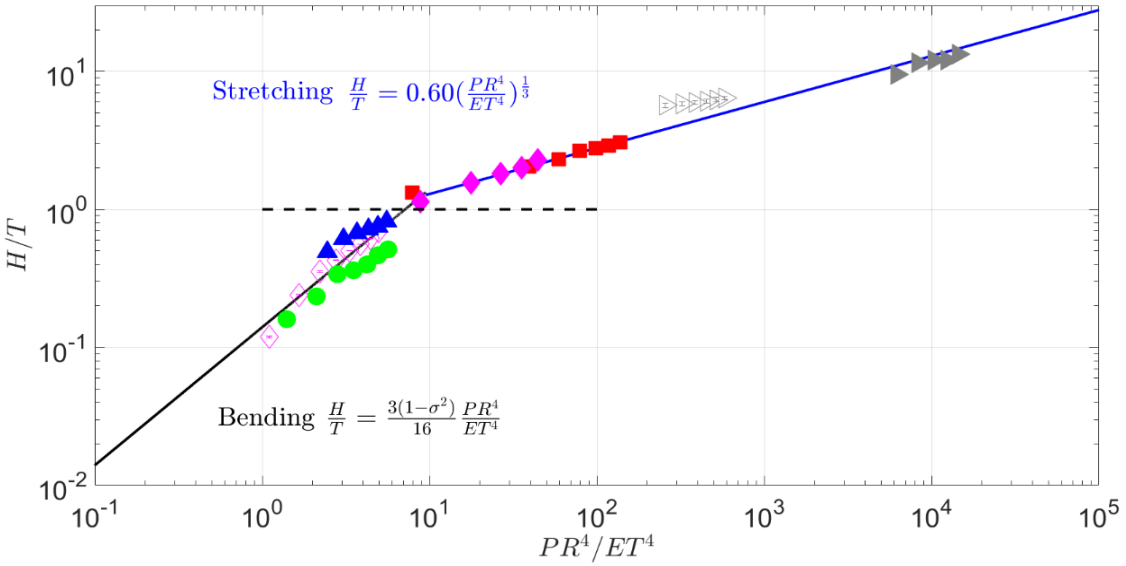

Figure 3-16. Variation of the dimensionless maximum deflection $\frac{H}{T}$ with the dimensionless pressure $\frac{PR^4}{ET^4}$ for simply connected circular shapes obtained experimentally for a range of silicone samples (see **Table 3-3** for legend). The black curve is the analytical result (published data, Bouremel et al 2017) for the bending regime and the blue curve is the numerical result for stretching regimes, obtained using finite element analysis (published data, Bouremel et al 2017). Each experimental data point is reported as average ±error (n=3).

3.5.3.2 Square pockets

As mentioned in the previous section, to simplify the relationships between variables, scaling analysis is commonly used where the values of variables are non-dimensionalised. From the energy balance equation (684), when an elastomeric square pocket is in bending regime such that, $\frac{H}{T} \leq 1$, the relationship between membrane displacement, H; membrane thickness, T, pressure, P; pocket side length, a; Young's modulus, E; and Poisson's ratio, σ, has been analytically calculated (688) using equation 3.13 as ;

$$\frac{H}{T} = 0.245(1-\sigma^2)\left(\frac{Pa^4}{ET^4}\right) \tag{3.13}$$

Similar to the case of circles, for inflated square pockets, stretching of the elastomeric membranes, $\frac{H}{T} > 1$, the relationship between membrane displacement, H,

and pressure, P, pocket-size, L, membrane thickness, T, and Young's modulus, E, was estimated (684,687) from equation 3.11. With the scaling analysis, the characteristics of interest were the dependencies of both membrane displacement, H, and pressure, P, on the membrane (square) with thickness, T, side length, a, and Young's modulus, E. Elastomeric (silicone) membranes were used to objectively measure Young's modulus, the influence of membrane thickness, shape, the pressure under the pursed pocket. A qualitative assessment of how the variables determine release from pursed pockets was performed.

The changes in the deformation height, H (mm) with the change in internal pressure, P (Pa), of square purses of sides 20 and 40 mm using silicone sheets of Young's modulus, E 1.241 MPa and thickness, T of 0.5 and 1.6 mm are plotted in **Figure 3-17**.

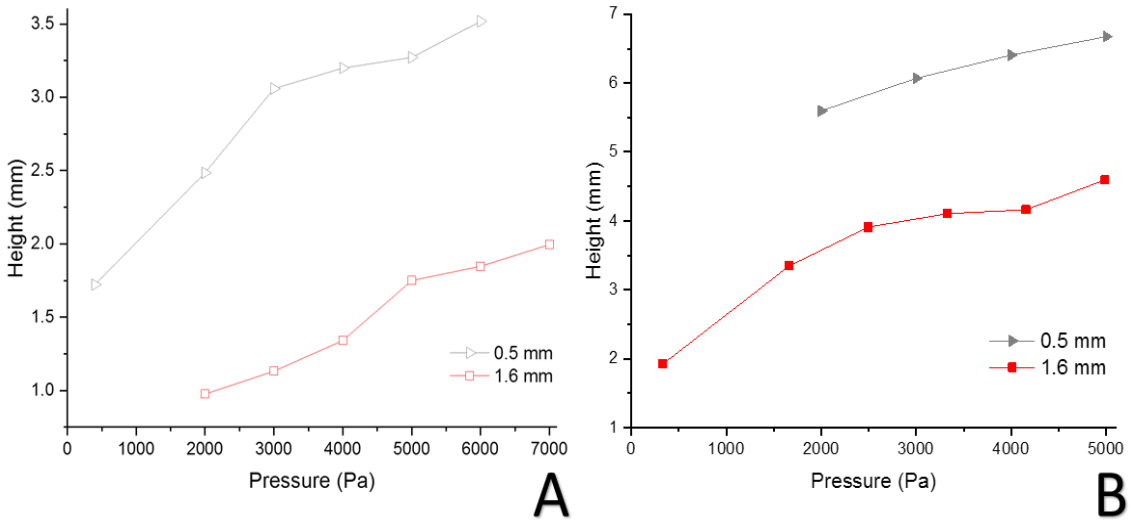

Figure 3-17. Differences in the deflection, $\boldsymbol{H}$ at different pressure, $\boldsymbol{P}$ using silicone sheets for pursing square shaped pockets of membrane thickness 0.5 mm, 1.6 mm, Young's modulus, $\boldsymbol{E}$ 1.241 MPa for sides 20 mm **(A)** and 40 mm **(B)**. The displacement height, $\boldsymbol{H}$ decreased with the increase in material thickness, $\boldsymbol{T}$ at similar pressure, $\boldsymbol{P}$ and pocket size.

The changes in the deformation height, H (mm) with the change in internal pressure, P (Pa), of square purses of sides 20 (S20) and 40 mm (S40) using silicone sheets of Young's modulus, E 1.241 and 1.112 MPa and thickness, T of 0.5 and 1.6 mm and 1.72 mm are plotted in **Figure 3-18**.

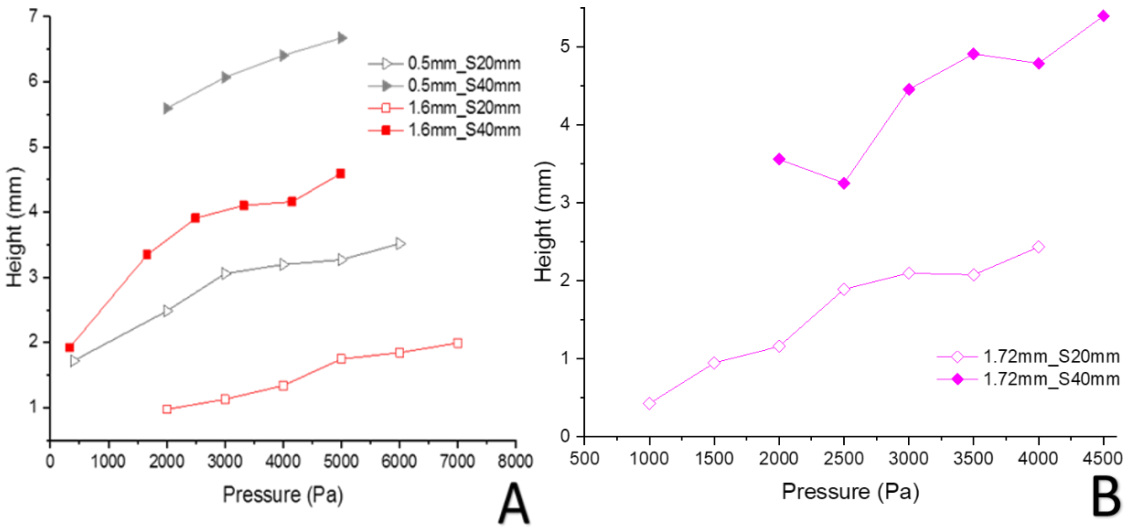

Figure 3-18. Differences in the deflection, $\boldsymbol{H}$ at different pressure, $\boldsymbol{P}$ using silicone sheets for pursing square shaped pockets with sides, $\boldsymbol{a}$ 20 (S20), 40 mm (S40), Young's modulus, $\boldsymbol{E}$ 1.241 MPa for 0.5 mm, 1.6 mm sheet thickness **(A)** and Young's modulus 1.112 MPa for 1.72 mm sheet thickness **(B)**. The displacement height, $\boldsymbol{H}$ increased with the increase in pocket size at similar pressure, $\boldsymbol{P}$, and material thickness, $\boldsymbol{T}$, and Young's modulus $\boldsymbol{E}$.

For a square pocket of similar size (20 mm and 40 mm) made using a material with Young's modulus. E 1.241 MPa, an inverse correlation was found between the thickness. T of the membrane and maximum deformation height, H of the pocket when compared under similar internal pressure, P during inflation. The observed height (maximum deformation) for the thicker membranes was lower than the observed height for thinner membranes. The displacement height, H increased with the increase in pocket size at similar pressure, P, material thickness, T and Young's modulus, E.

From the above results, the data were non-dimensionalised to obtain the value of the coefficient γ for inflation for a pursed square pocket in the stretching regime, $\frac{H}{T} > 1$. **Figure 3-19** shows the dimensionless maximum deflection $\frac{H}{T}$ of square elastic pockets over six orders of magnitude of $\frac{Pa^4}{ET^4}$. The experimental data matches very well with the analytical bending solution (667) for the square plotted with black curves up to the maximum deflection of $\frac{H}{T} \approx 1$. Above $\frac{H}{T} \approx 1$, the silicone pocket undergoes stretching and

the data obtained numerically, using a finite element analysis model (Abaqus version 6.12-3) can be fitted (667), in the case of the square shapes, using equation 3.14;

$$\frac{H}{T} \approx \gamma \left(\frac{Pa^4}{ET^4}\right)^{\frac{1}{3}} \tag{3.14}$$

The value of γ was calculated from the experimental data to be 0.70.

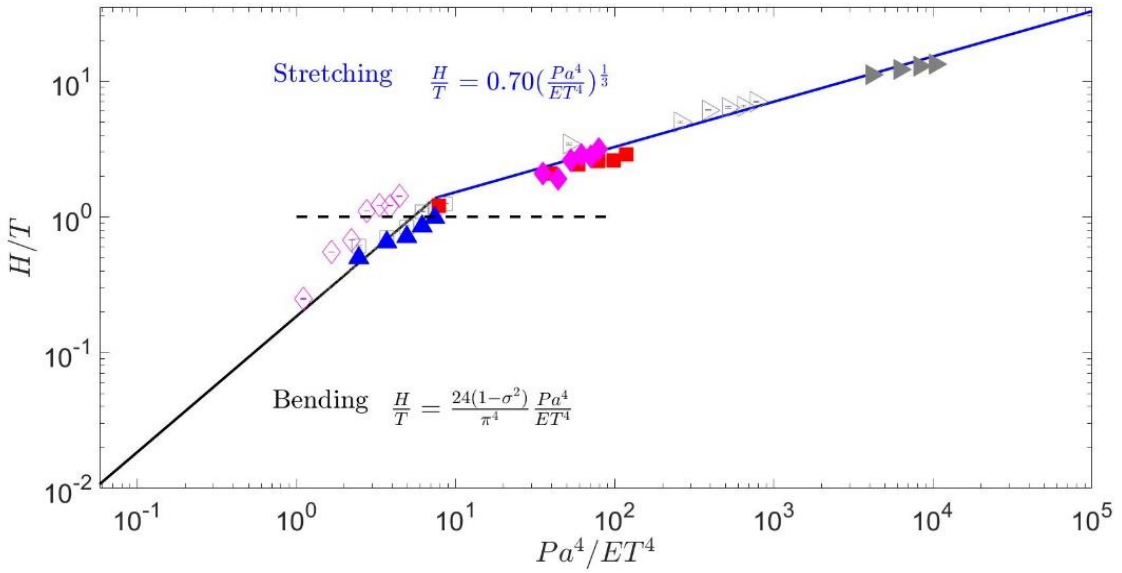

Figure 3-19. Variation of the dimensionless maximum deflection $\frac{H}{T}$ with the dimensionless pressure ($\frac{Pa^4}{ET^4}$) for simply connected square shapes obtained experimentally for a range of silicone samples (see **Table 3-3** for legend). The black curve is the analytical results for bending regimes and the blue curve is the numerical results for stretching regimes, obtained using finite element analysis, verifying the experimental values (published data, Bouremel et al 2017). Each experimental data point is reported as average ±error (n=3)

In the present work, the transition from bending to stretching has been studied in detail. It was shown that the maximum deflection varies linearly with P in the bending regime but to the power $\frac{1}{3}$ in the stretching regime once the maximum deflection reaches approximately the thickness of the pocket and continues to increase. Both analytical and numerical approaches validated the optical methods to obtain the dimensionless maximum deflection ($\frac{H}{T}$) of pursed silicone pockets for a range of dimensionless pressure $\frac{Pa^4}{ET^4}$ ranging from 10^{-1} to 10^{5}. The profile widths of bent pockets compared to stretched pockets were also found to be narrower as expected and quantified at different dimensionless pressures (667).

3.5.4 Compression of inflated elastic pockets

For the case of subconjunctival implantation, the inflated elastic pocket of an ophthalmic pump would be subjected to compression by the conjunctiva. This compressive force applied on an inflated pocket can have significant effects on the internal pressure of the purse. We know from equation 3.5, the internal pressure, P of the purse is directly proportional to the flow rate, Q of liquid being released from such a pocket through a tube of known resistance, R.

To understand the effects of compressive forces on a pressurised pocket affecting the flow rate of liquid released, elastomeric pockets of different internal pressures, P, radii, a, and material thicknesses, T, were pursed. Increasing weights were placed on top of pursed pockets. The change in the internal pressure of the pocket, P_c was measured as a function of the successive application of weight as compressive force, F_c on the top of the pocket, as shown in **Figure 3-20**.

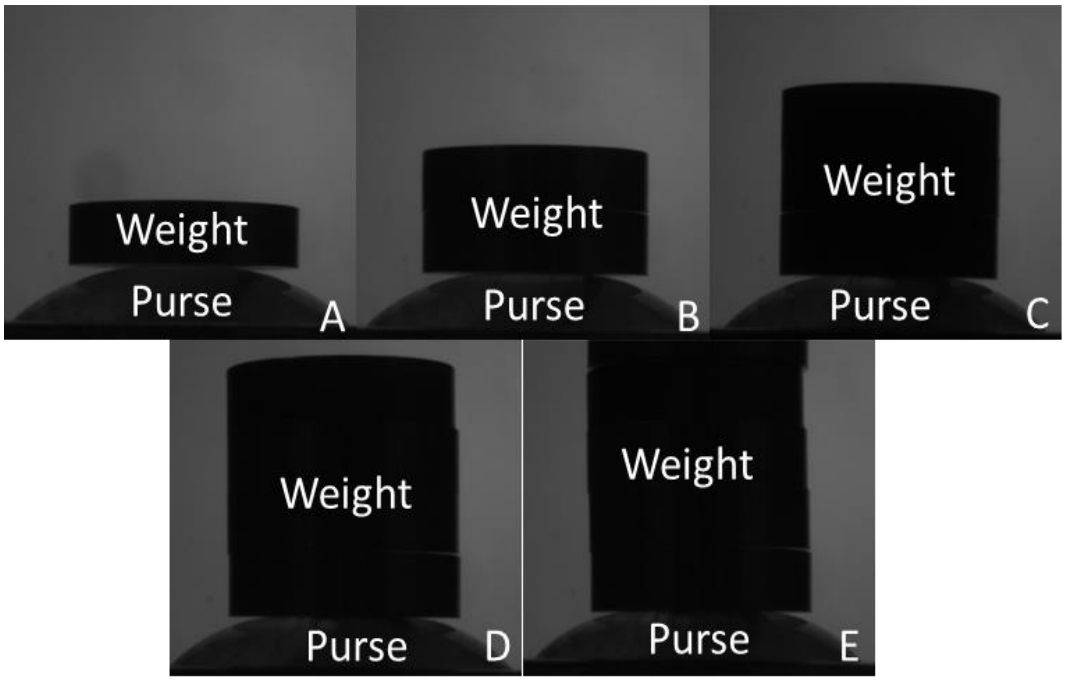

Figure 3-20. Pressurised pocket at 4903 Pa with radius, $\boldsymbol{a}$=20 mm, $\boldsymbol{T}$=0.5 mm, $\boldsymbol{E}$=1.241 MPa. Applied compressive force $\boldsymbol{F_c}$ for **(A)** 0.24 N **(B)** 0.48 N, **(C)** 0.72N, **(D)** 0.95N, **(E)** 1.19N.

The data were non-dimensionalised to find the relationship between the change in internal pressure, P_c/P of the pursed pockets, when a compressive force F_c was applied on the pressurised pockets. The relationship, β between increased compressive forces, $F_c/P\pi a^2$ and changes in the internal pressure P_c/P of the squashed inflated

pocket was calculated through the linear fitting of the data, as shown in **Figure 3-21**. Using the line of best fit, β was calculated from equation 3.15

$$\frac{P_c}{P} = \frac{\beta F_c}{P\pi a^2} + 1 \qquad (3.15)$$

The value of β was calculated from the slope as ≈ 1.85 (689). This equation is plotted with a black line in **Figure 3-21**.

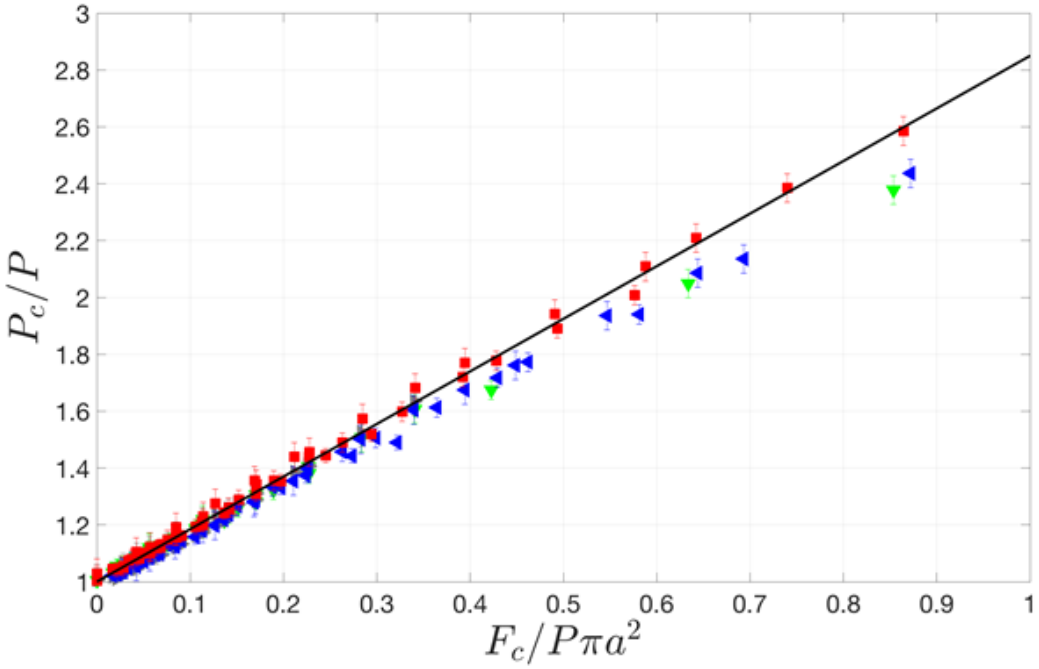

Figure 3-21. Variation of the internal pressure $\boldsymbol{P_c/P}$ of pursed pockets (see Table 14 for legend) of different thickness when under increasing compressive forces $\boldsymbol{F_c/P\pi a^2}$. The relationship constant, **β** was calculated using the slope of the graph.

3.5.5 Deflation of elastic pockets

A circular pocket with a radius of 20 mm was made by clamping a silicone sheet of thickness, T 0.5 mm with Young's modulus, E 1.241 MPa, to understand the mechanism of fluid release from an elastomeric pocket. A tube with an internal diameter, $(2r)$ of 500 µm and length of 10 cm was attached at the outlet, to provide additional resistance to the outflow of water, as shown in **Figure 3-22**.

Deflation experiments were undertaken, as mentioned previously (see **Section 3.4.5**). The results from inflation of pursed pockets confirm that the deflection for a pocket made of elastomeric sheets with similar material properties (Young's modulus) and material thickness increases with the increase in pocket size. For deflation

experiments, the size of a 20 mm radius was used to increase the amount of fluid that could be filled in the pocket at a given pressure.

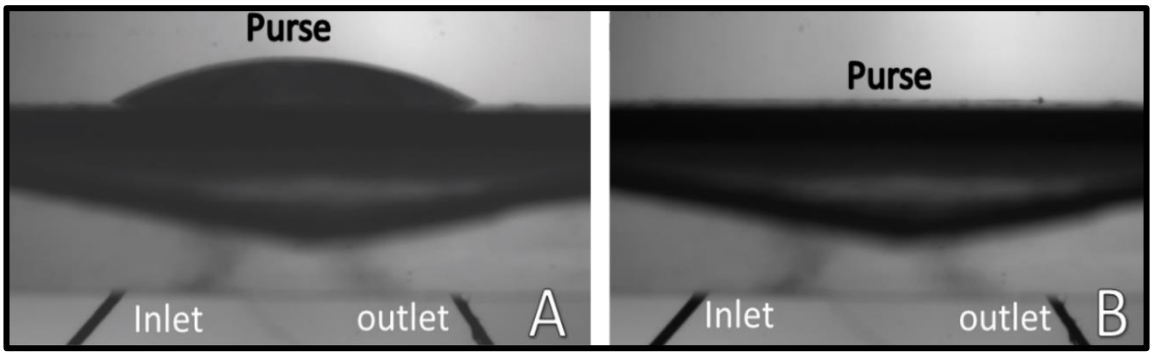

Figure 3-22. A circular pocket with radius 20 mm, 0.5 mm thick silicone membrane and Young's modulus 1.241 MPa was used for the deflation experiments. At the start of the experiment, inflated purse a with internal pressure 3000 Pa shows a deflection of purse height to 4.75 mm, **(A)** at the end of the experiment, empty purse with no internal pressure has no deflection in height **(B)**.

Figure 3-23 shows the relationship between the flow rate Q (mL s^{-1}) of liquid released and the internal pressure (Pa) of the pocket. The flow rate Q of liquid released was found to be linearly proportional to the internal pressure of the pocket when a tube of an internal diameter of 500 µm and length of 10 cm was attached on the outlet, as plotted in **Figure 3-23**.

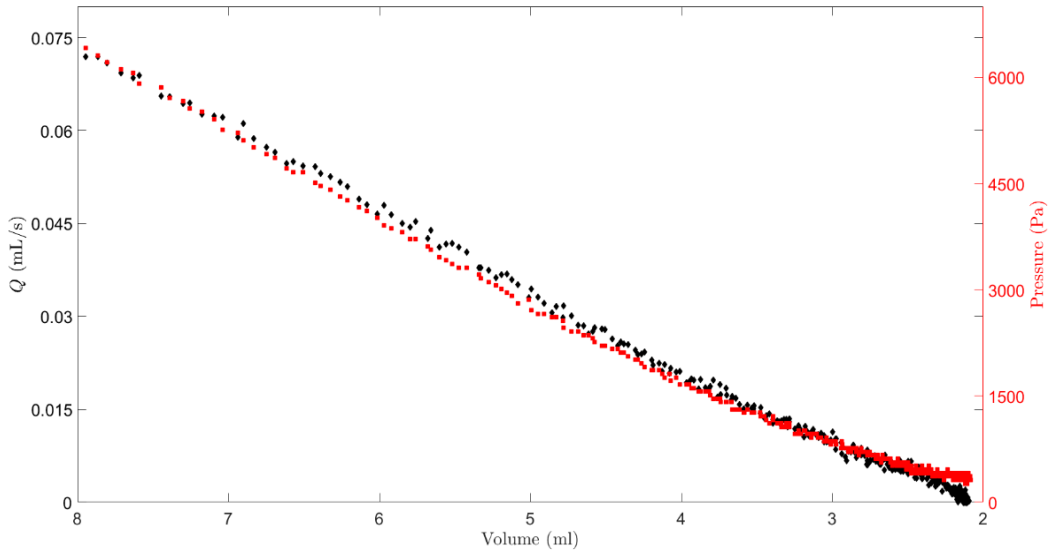

Figure 3-23. The deflation profile of a purse shaped elastomeric pocket is shown. Flow rate, $\boldsymbol{Q}$ (mL s^{-1}) and pressure, $\boldsymbol{P}$ (Pa) as a function of internal volume (mL). For circular pocket with radius 20 mm, 0.5 mm thick, $\boldsymbol{T}$ silicone membrane and Young's modulus, $\boldsymbol{E}$ 1.241, the flow rate, $\boldsymbol{Q}$ was linearly proportional to the internal pressure, $\boldsymbol{P}$ of the pocket.

3.5.6 Modelling fluid release from hypothetical single-chamber elastic pockets

The effect of an elastomeric material's Young's modulus, material thickness and the diameter of the outlet tube on drug release amount and duration from proof-of-concept single-chamber hypothetical elastic pockets with small volumes (~1 mL) was modelled. The fluid volume inside the pocket was calculated to be 1055.58 µL. The results for the modelling data are presented in **Table 3-4**, and the volume of fluid released and the release profiles for the seven conditions modelled are plotted in **Figure 3-24** and **Figure 3-25**.

Table 3-4. Modelling data of fluid release from hypothetical single-chamber elastic pockets of a fixed dimension of radius 10 cm and maximum displacement height of 0.6 cm.

Variable	Condition	Time (hours)	Volume released (µL)	$T_{1/2}$ (hours)	Flow rate	Efficiency (%)
Young's modulus	E*max*	364.5	738.7	49.2	0.24–0.007*	70.0
	E*min*	502.1	372.9	171.4	24.4–6.6+	35.3
Thickness	T*max*	247	852.7	17.18	0.93–0.007*	80.8
	T*min*	347.2	181.4	149.3	11.6–6.6+	17.2
Tube diameter	D*max*	0.8	544.3	0.2	36.2–4.1*	51.6
	D*min*	7915	544.8	1980	3.63–0.4+	51.6
$\boldsymbol{E, T, D}$	Optimal	8072	513.7	2154	3.05–0.4+	48.7

*Release rate was in µL min^{-1}, + Release rate was in nL min^{-1}

Amongst the different hypothetical single-chamber elastic pockets modelled, T*max* released the largest volume of fluid, 852.7 µL and took 247 hours (10.3 days) with a decreasing flow rate, 0.93–0.007 µL min^{-1} with the highest pump efficiency of 80.8%. E*max* released the next largest volume of fluid, 738.7 µL and took 364.5 hours (15.2 days) with a narrower range of decreasing flow rate, 0.24–0.007 µL min^{-1} with a pump efficiency of 70%. E*min* released, 372.9 µL of fluid and took 502.1 hours (20.9 days) with a narrow range of decreasing flow rate, 24.4–6.6 nL min^{-1} with a pump efficiency of 35.5%. T*min* released the smallest volume of fluid, 181.4 µL and took 347.2 hours (14.5 days) with a decreasing flow rate, 11.6–6.6 nL min^{-1} with the lowest pump efficiency of 17.2%. D*max* showed the fastest release rate of fluid, 544.3 µL released in 0.8 hours, the smallest value for $T_{1/2}$= 0.2 hours with a decreasing flow rate, 36.2–4.1 µL min^{-1} with a pump efficiency of 51.6%. Optimal showed the slowest release rate of fluid, 513.7 µL released in 8072 hours (336.3 days), largest value for $T_{1/2}$=2154 hours (89.8 days) with a decreasing flow rate, 3.05–0.4 nL min^{-1} with a pump efficiency of 48.7%. The next

slowest release of fluid was from D*min*, 544.8 µL released in 7915 hours (329.8 days), second largest value for $T_{1/2}$=1980 hours (82.5 days) with a decreasing flow rate, 3.63–0.4 nL min^{-1} with a pump efficiency of 51.6%.

The results from the modelling data of fluid release from hypothetical single-chamber pockets further revealed that the efficiency of the pump was proportional to Young's modulus (E) and thickness (T) of the elastic material. Decreasing Young's modulus (E) of the material by a factor of 10 (E*max*/E*min*) decreased the pump efficiency by 49.5% but increased the time taken for fluid release by 37.8% and increased $T_{1/2}$ by a 248.4%. A similar trend was observed when the thickness of the material was decreased by a factor of 80 (T*max*/T*min*), pump efficiency was decreased by 78.7% but the time taken for fluid release increased by 40.6% and $T_{1/2}$ increased by 769%.

Changing the diameter of the outlet tube had the most significant impact on the performance of the hypothetical pump. Decreasing the diameter of the outlet tube by a factor of 10 (D*max*/D*min*) had a negligible impact on the efficiency of the pump (efficiency decreased by 0.1%) but increased the time taken for fluid release by a factor of 9,893.8 (0.8/7915) and $T_{1/2}$ by a factor of 9,899 (0.2/1980 hours).

Finally, increasing to maximum values of E and minimum values of T and D, the Optimal pump compared with D*min* showed a decrease in efficiency of the pump by 5.7% but increased the time taken for fluid release by 2% and increased $T_{1/2}$ by 8.8%.

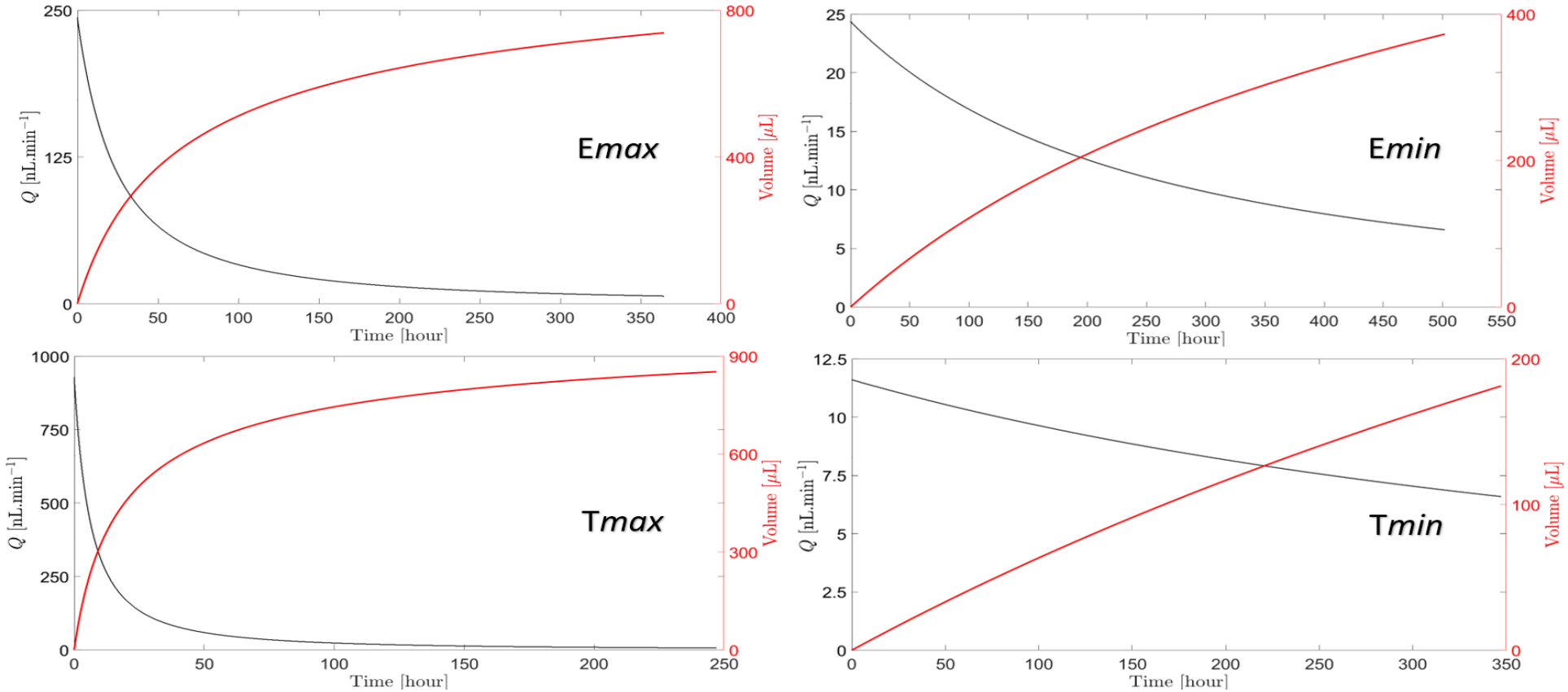

Figure 3-24. Fluid release was modelled from hypothetical single chamber pockets with fixed dimensions of $\boldsymbol{R}$= 10 mm, $\boldsymbol{H}$= 6 mm. For **E*max*,** the parameters for sheet were $\boldsymbol{T}$= 0.1 mm, maximum $\boldsymbol{E}$= 5.25 MPa, and the dimensions of the outlet tube were $\boldsymbol{D}$= 0.05 mm and **L**= 4 m. The maximum volume released was 738.7 µL in 364.5 hours. For **E*min*** the parameters for sheet were $\boldsymbol{T}$= 0.1 mm, minimum $\boldsymbol{E}$= 0.525 MPa, and the dimensions of the outlet tube were $\boldsymbol{D}$= 0.05 mm and **L**= 4 m. The maximum volume released was 372.9 µL in 502.1 hours. For **T*max***, the parameters for sheet were maximum $\boldsymbol{T}$= 1.6 cm, $\boldsymbol{E}$= 1.25 MPa, and the dimensions of the outlet tube were $\boldsymbol{D}$= 0.05 mm and **L**= 4 m. The maximum volume released was 852.7 µL in 247 hours. For **T*min*** the parameters for sheet were minimum $\boldsymbol{T}$= 0.02 mm, $\boldsymbol{E}$= 1.25 MPa, and the dimensions of the outlet tube were $\boldsymbol{D}$= 0.05 mm and **L**= 4 m. The maximum volume released was 347.2 µL in 181.4 hours.

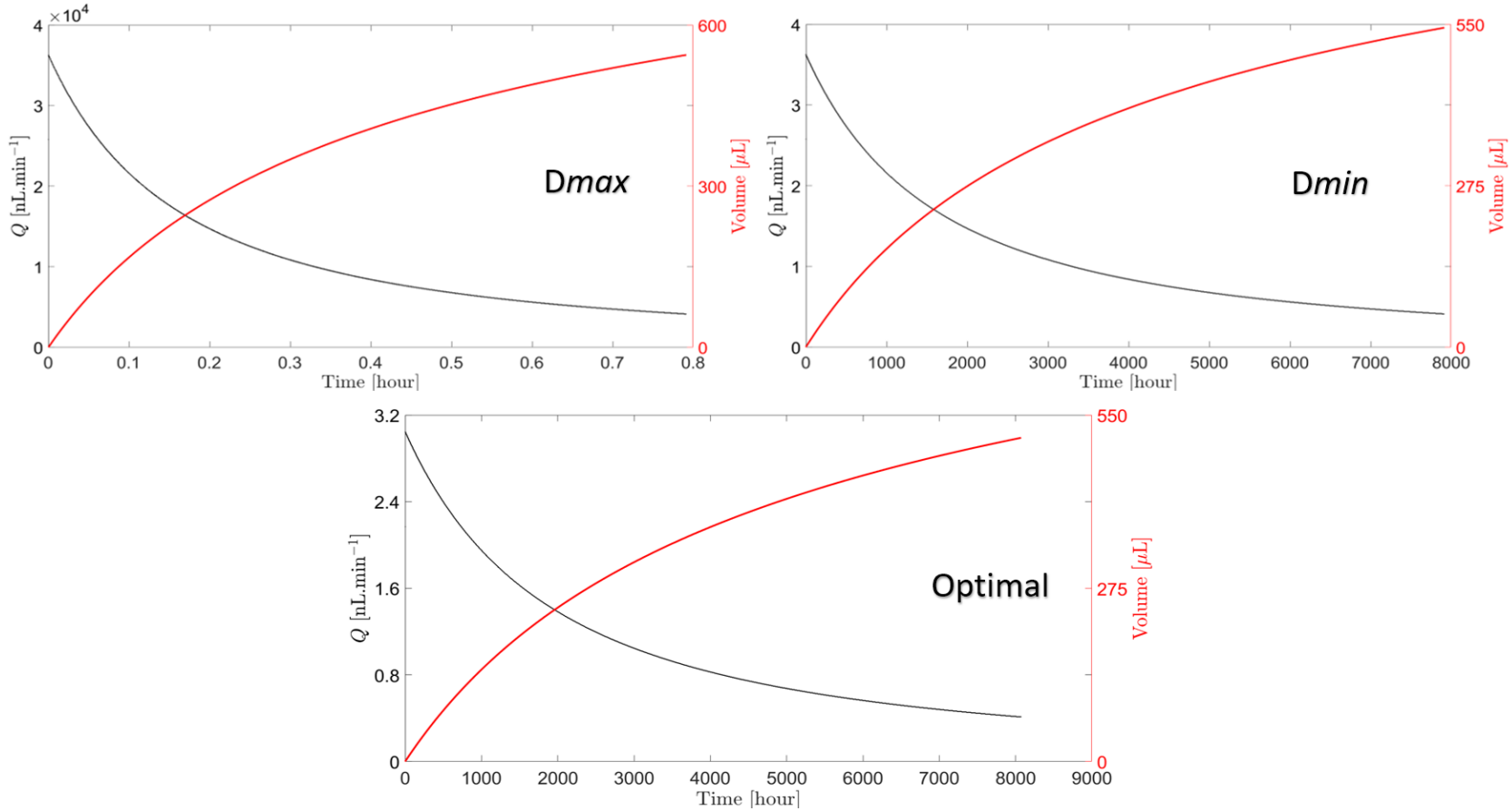

Figure 3-25. Fluid release was modelled from hypothetical single chamber pockets with fixed dimensions of $\boldsymbol{R}$= 10 mm, $\boldsymbol{H}$= 6 mm. For **D*max*,** the parameters for sheet were $\boldsymbol{T}$= 0.1 mm, $\boldsymbol{E}$= 1.25 MPa, and the dimensions of the outlet tube were maximum $\boldsymbol{D}$= 0.25 mm and **L**= 4 m. The maximum volume released was 544.3 µL in 0.8 hours. For **D*min*** the parameters for sheet were $\boldsymbol{T}$= 0.1 mm, $\boldsymbol{E}$= 1.25 MPa, and the dimensions of the outlet tube were minimum $\boldsymbol{D}$= 0.025 mm and **L**= 4 m. The maximum volume released was 544.8 µL in 7915 hours. For **Optimal**, the parameters for sheet were minimum $\boldsymbol{T}$= 0.02 mm, $\boldsymbol{E}$= 5.25 MPa, and the dimensions of the outlet tube were minimum $\boldsymbol{D}$= 0.025 mm and **L**= 4 m. The maximum volume released was 513.7 µL in 8072 hours.

3.6. Discussion

Post-operative wound management remains a major challenge for the success of glaucoma surgery. Anti-inflammatory drugs are frequently dosed using eye-drops, which provide poor bioavailability in the subconjunctival space. Intra-ocular injections are often needed, but the drug is rapidly cleared into the systemic circulation, requiring repeated administration. Elastomeric pumps could potentially be a viable solution for prolonged drug delivery in the subconjunctival space. However, a systematic analysis of different variables governing pump function has previously not been experimentally assessed. To this end, an in-depth analysis was conducted, assessing the relationships between material properties and pocket geometry, and the internal pressure of pocket, when an elastomeric pump transitions from bending to stretching regimes.

3.6.1 Material and Methods

For the work described in this Chapter, commercially available silicone membranes were used due to their material reproducibility, relatively low cost, and the similarity of their stiffness with subconjunctival tissue (~1 MPa). To be used as medical implants, it is often crucial for the material to match the properties of the surrounding tissue to avoid physical damage caused by hard materials, thus reduce localised inflammation. Moreover, these silicone sheets are considered to be biocompatible (manufacturer's guidelines).

The ratio of the material's stress to strain (when strains are small, less than 10%) gives the value of Young's modulus, E (modulus of elasticity), calculated as the initial linear slope of the stress-strain graph (674,676,677). It gives the measure for a material's property to resist deformation, see **Figure 3-26** (690). A typical stress-strain curve can define elastic and plastic regions of the material being tested. In the elastic region, the material obeys Hooke's law (691), published by Robert Hooke in 1678 as a solution to his previously published Latin anagram (692). Hooke's law states that the force applied (stress) is proportional to the change in surface area (strain) of a material. The law also states that when force is no longer applied to the material, it returns to its original shape and size without deformation. In the stress/strain curve, the straight line represents Hooke's behaviour of the material in the elastic region and the slope of the line is

Young's modulus E (691). Materials that behave according to Hooke's Law are called elastic materials (693). If the material deformation is permanent under an applied force, it is called plastic material (694).

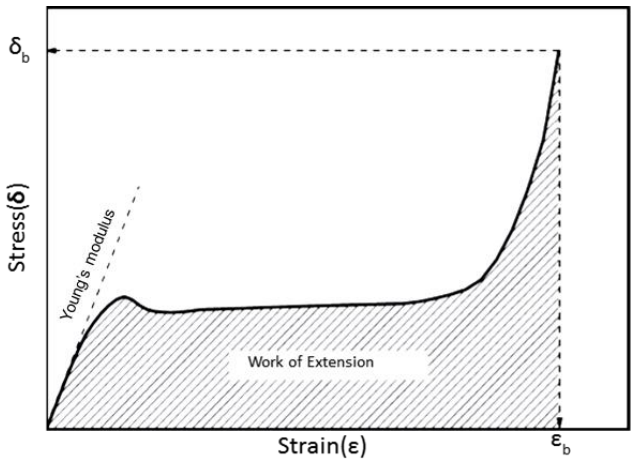

Figure 3-26. Typical stress-strain curve for a tough gel illustrating Young's modulus ($\boldsymbol{E}$), breaking strength ($\boldsymbol{\delta_b}$), elongation at break ($\boldsymbol{\varepsilon_b}$) and work of extension ($\mathbf{W_{ex}}$), figure adapted from (675)

Elastic behaviour is required for an implant or a device to withstand pressure during implantation without deforming. Elongation at break (ε_b), also known as fracture strain, expresses the capability of a material to resist changes of shape without crack formation. It is the ratio between changed length and initial length after breakage of the material being tested, see **Figure 3-26** (676).

(676)Moduli have units of stress (N m^{-2} = Pa) and cover a wide range from kPa to MPa. Stiffer materials have higher values for the elastic modulus. Typical Young's modulus values for ceramics and metals are >10 GPa, for un-orientated polymers is 1–3 GPa, for elastomers is about 1 MPa, and for highly swollen gels are 10–100 kPa (676). The soft tissue in the human heart have moduli in the range of 10–500 kPa, which is similar to highly swollen hydrogels (695). Another important parameter is fracture energy (Jm^{-2}), defined as the energy required for breaking the material in an infinitely large specimen. This parameter can be used to assess the toughness as a function of molecular mechanisms in different materials and the energy absorbed in creating a unit area of a crack in the material (676,696,697).

For the silicone sheets tested in the present work, the values of E were found to be between 1–2.5 MPa. These values are comparable to the reported scleral values of 1.2–1.3 MPa (674,675) and 1.8–2.9 MPa (679,680). This is particularly important for matching the pump material stiffness to the biological tissue to avoid foreign body

response (698,699). However, for a final pump design, a well-established biocompatible polymer (such as a double network HEMA or medical grade silicon) could be used to fabricate the pocket of the pump that acts as a reservoir for the drug.

A novel optical method developed for experimental fluid mechanics, using methylene blue dye, was successfully applied for the first time to accurately plot a 3D deformation profile based on the deformation planes of the pursed pockets while comparing the 2D deformation distribution along pocket width. This technique can be applied to any sheet provided the material is clear and the deflection of the pockets being analysed is relatively low.

3.6.2 Inflation of elastic pockets

Initially, to evaluate pursing of elastomeric membranes, simply (single point of contact along a continuous boundary) and doubly (two separate continuous boundaries) connected pockets were made by joining two silicone membranes of varying thickness and radius with silicone glue, see **Figure 3-27**. A 5 mL Terumo syringe was used to accurately apply a known amount of silicone glue to avoid variances in the joining boundary conditions of the pocket. A 26-gauge Terumo needle was used (ID 0.45 mm) as the inlet for fluid. The pockets were analysed for changes in deflection at varying internal pressures and material thickness. A major advantage of this approach was rapid prototyping of different variables (material thickness, size and joining boundary

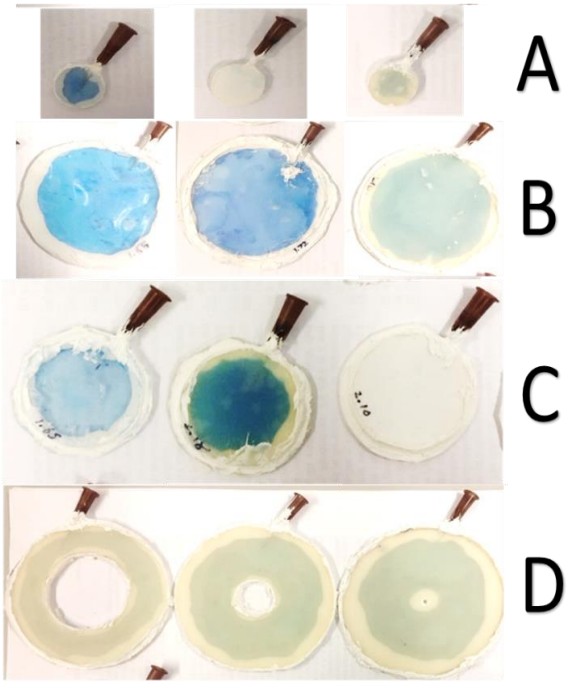

Figure 3-27. Simply connected circular elastomeric pockets were initially made by joining two silicone membranes of varying thickness and radius with silicone glue. A 26-gauge Terumo needle was used (ID 0.45 mm) as inlet for fluid. Row **A** shows circular pockets with radius 10 mm, row **B** shows pockets of radius 22 mm **C** with radius 35 mm and row **D** shows doubly connected pockets of radius 45 mm with varying area of central clamping (internal diameter).

conditions) to gain a preliminary understanding of the impact by each variable on pump design.

However, it was difficult to control the joining boundary between the silicone sheets accurately. Moreover, the shapes that could be fabricated using this method lacked precision due to the clamping effects of the boundary. The variance in inflated pocket height, H (deflection) versus internal pressure between similar pockets (similar material properties and geometry) was over 20%. For this purpose, a more robust methodology of pursing elastic pockets was required. Acrylic and stainless-steel plates with holes of different shapes and sizes cut for pocket formation were used to improve the robustness of the experimental setup and was used subsequently for all inflation, compression, and deflation experiments.

In order to simplify the relationships between variables, scaling or dimensional analysis is a commonly used technique where the values of variables being studied are non-dimensionalised. This is a technique that is commonly used in fluid mechanics for changing units, determining a convenient arrangement of variables of a physical relationship, and calculating the pre-multiplying co-efficient for the parameters of interest. It frequently aids in making a more natural description of the phenomena being investigated and the influences of all the variable involved. However, a reference to experimental data needs to be made to obtain the necessary constants or coefficients for a complete numerical expression. With the scaling analysis, the characteristics of interest were the dependencies of both membrane displacement, H, and pressure, P, on the membrane (circles and squares) with thickness, T, radius, R, and Young's modulus, E. Elastomeric (silicone) membranes were used to objectively measure Young's modulus, the influence of membrane thickness, shape, the pressure under the pursed pocket. The experimental data provided further insight into these relationships. The data were non-dimensionalised to obtain the value of the coefficient γ for inflation for pursed pockets in the stretching regime $\frac{H}{T} > 1$.

For circles, the value for coefficient γ was calculated from the experimental data to be 0.60. The coefficient γ obtained with the current experimental approach is comparable with previous findings in the literature (667). Chien, Dickey, Kao and Perrone, Christensen and Feng and Kelkar *et al.* found out the same value of 0.595 with different computing and numerical techniques (700–705). Christensen and Feng

reported the value of γ as 0.572 (706). The current value of 0.60 is within 1% of the values reported in the literature. For squares, the value of γ was calculated from the experimental data to be 0.70. The coefficient γ obtained with the current approach is comparable with previous findings in the literature (667). Jones found numerically a value of γ = 0.71 which is within 1.5% of our current values (707).

It was observed that the experimental data did not exactly match, as well, the analytical results (plotted with a black line in **Figure 3-16** and **Figure 3-19**) in the bending regime. This may be due to the compression of the sheets by the acrylic plates when tightened to create a seal. The clamping can cause the sheet to be raised, which would more prominently affect the dynamics of pursing for smaller deflections in the bending regime, when compared to larger deflections in the stretching. The deflection of elastomeric pockets on inflation follows different dynamics from bending to stretching. In further work where doubly-connected (silicone membranes connected at two points of a continuous boundary) pockets were studied using Finite Element Analysis, it was observed that the maximum deflection of doubly-connected pockets is greatly reduced compared to simply-connected shapes with similar outer shapes (circle or square). The results compared favourably with analytical results from the literature (667).

3.6.3 Compression of elastic pockets

Most of the elastomeric pumps currently used in the clinic are enclosed in a hard casing, presumably to protect them from being squashed and changing the intended rate of drug delivery. However, the relationship between the deformation of inflated elastomeric pockets when subjected to compressive forces and the resulting change in internal pocket pressure has not been studied previously. This deformation due to compression and change in internal pressure is critical to understand how an ophthalmic pump would function when subjected to a compressive force applied by the conjunctiva, after implantation.

If a pursed pocket were to be compressed, the increase in internal pressure, P_c , is associated with increased flow rate, Q, of liquid released, as the flow rate can be re-written as $Q = P/R$, as explained from equation 3.5. This relationship also has an additional significance when considering the design of an ophthalmic pump requiring more than a single chamber (pocket), made of elastomeric materials with known

material properties and geometry. The primary chamber(s) would act as a drug reservoir that could be easily refilled when depleted. The secondary chamber(s) could be controlled by an external stimulus to inflate when needed, applying a known amount of compressive force on the drug reservoir. From the estimated value of $\beta \approx 1.85$ calculated in the present work studying compression of inflated elastic pockets (**Section 3.5.4**), in combination with the coefficient of stretching calculated in the inflation experiments (**Section 3.5.3**), it is possible to accurately predict the effect of compression by the stimuli sensitive chamber on the rate of drug released from an elastomeric pump.

3.6.4 Deflation of elastic pockets

For the work mentioned in this Chapter, water was the fluid used for both inflation and deflation experiments. In the real-world application of an elastomeric pump, however, this is seldom the case. If we assume that, an elastomeric pump made using a membrane of E 1.241 MPa and thickness, T of 0.5 mm was to be filled with a saturated drug solution with a dynamic viscosity similar to that of water (10^{-3} Pa s at 20°C), the evolution of Q as a function of volume released in the deflation of circular elastic pockets experimental results suggest a first order release rate. However, the change in viscosity of the drug solution can be easily taken into account using the Hagen-Poiseuille's equation (equation 3.6) that calculates the fluid flow through a cylindrical pipe of length L and diameter D, dynamic viscosity of the fluid (681). According to the Hydrodynamics principle (equation 3.5), flow rate (Q) of fluid is dependent on the resistance (R) to fluid flow. This resistance generates a pressure, P, which acts as the driving force for fluid flow. In an inflated elastomeric pocket, this pressure is applied by the displaced (deformed height, H) elastomeric sheets that drives the fluid out of the pocket. As mentioned earlier, for a simply connected pursed pocket made with elastomeric membranes, the relationship between membrane material thickness (T), pursed deformation height (H), internal pressure (P), pocket size (L) and Young's modulus (E) is given by equation 3.12. The values for pre-multiplying coefficients (γ) was found to be 0.6 and 0.7 for circle and square shaped pockets, respectively (667). For deflation, to calculate the resistance, R, provided by an outlet tube, of length,L diameter, D, the volumetric flow rate, Q, may be calculated according to Hagen-Poiseuille's equation (equation 3.6).

Currently, to manage retinal diseases such as AMD, intravitreal injection of a bolus of anti-VEGF into the vitreous cavity is administered on a frequent basis. Endophthalmitis and retinal detachment are the major side effects, linked to delivering a large bolus of the drug (708). In addition, this administration creates a typical curve of a large peak of drug with rapid decay. The literature supports that the half-life of anti-VEGFs, such as ranibizumab, a humanised monoclonal antibody fragment, administered as a single IVT bolus is indeed very short (2.2 days in the retina, 2.5 days in the aqueous humour and just under 4.0 days in the vitreous cavity)(709). This makes it necessary to use a higher initial dose in order to exceed therapeutic levels to allow a longer treatment interval (709).

Humayun *et al.* demonstrated the use of a micropump (13x16x5 mm, volume 60 µL) to deliver ranibizumab in patients suffering from diabetic macular oedema (646). The materials of the pump that were in contact with the ocular tissue included a titanium hermetic package on the bottom, a polycarbonate top surface to protect the pump, and a hybrid silicone-parylene cannula with suture tabs (648). The pump was prefilled with 8.5 µL ranibizumab and implanted into the subconjunctival space of 11 patients, delivering the entire drug within 90 minutes of loading the drug into the pump. The micropump successfully delivered the programmed dose in seven subjects with no adverse events reported during the 90 day follow-up period. However, it must be noted that this was a relatively small study (11 subjects) and the long term efficacy on the micropump was not evaluated (follow up period ended after 90 days)(646).

For deflation of elastic pockets in the current work, the flow rate of a liquid released from a single geometry (circle) of elastomeric pocket composed of silicone membrane was investigated. The flow rate Q of liquid released was found to be linearly proportional to the internal pressure of the pocket when a tube of an internal diameter of 500 µm and length of 10 cm was attached on the outlet. This tapered release profile would be particularly useful in the case of delivering initial high doses of a drug and tapering the amount of drug delivered as a function of time while prolonging the duration of therapy. A previous study validated a micro-electronic mechanical device with the volume dosed and the duration of pressure were found to be linearly proportional for both applied pressures, resulting in a consistent flow (647). However, this device used a different mechanism of dose release that needed to be actuated

externally. The pursed pockets studied in the present work utilise only elastic energy stored in the stretched pocket membrane to release the internal liquid over a period of time. It must be noted that the release rate of liquid can be precisely controlled by utilising a variable resistance at the outlet of the pocket.

Post-operative inflammation is a major challenge for the success of glaucoma surgery (355). There is increasing evidence to support the view that angiogenesis and inflammation are mutually dependent. In addition to the appearance of newly formed blood vessels in granulation tissue, the angiogenic factors exhibit both pro-inflammatory and pro-angiogenic effects (710,711). Angiogenesis results from a cascade of multiple signals acting on the EC layer of blood vessels (712). These cells are surrounded by pericytes that regulate blood vessel function (712). During inflammatory reactions, immune cells synthesise and secrete pro-angiogenic factors that promote neovascularisation. The vascular endothelial growth factor (VEGF) receptor (VEGF-R1 and VEGF-R2) system is deeply involved in angiogenesis (711). VEGF-A directly stimulates EC proliferation by engaging with the VEGF-R2 to activate tyrosine kinase and initiate the sprouting of new vessels from existing micro-vessels, destabilising existing micro-vessels. This leads to pericyte dropout, diminished cell–cell adhesion, dissolution of the basement membrane and increased vascular permeability (710). Even though inflammation and angiogenesis can potentiate each other, these processes are distinct and separable. There is evidence in the literature that the angiogenesis that accompanies chronic inflammation tends to prolong and intensify the inflammatory response (710).

Results from deflation experiments, in correlation with the relationships calculated from inflation experiments, provides further insight into a proposed design for the miniaturisation of a pump for ocular drug delivery. Before designing a pursed planar pocket that can efficiently deliver drugs to the site of action (such as the site of surgery in the subconjunctival space), one must consider and assess the various limiting factors and constraints of size, shape, and thickness of the material. As mentioned previously in Chapter 1, the site of surgery in the conjunctiva is an incredibly challenging place to implant a device. In addition to delivering the required dose, a pursed pocket needs to be robust and biocompatible. A circular or “button-shaped” pump is the appropriate shape to achieve the maximum volume in the pocket for the minimum

amount of material. A hypothetical pursed pocket with a diameter of a 10 mm and height of 6 mm should hold a total volume of about 1.1 mL of a saturated drug solution. Another consideration when designing an optimal drug delivery pump is the ability of the pump to maintain close contact with the sclera while still being able to hold a sufficient amount of drug. In order to achieve this balance, the pump should have varying thicknesses to allow for deflection at the top but no deflection at the bottom, which lies in contact with the sclera.

3.6.5 Modelling fluid release from hypothetical single-chamber elastic pockets

The maximum implant size is a significant limitation when considering the design of an elastic pump for localised ocular drug delivery. The size of a human adult eye is approximately 24.2 mm (transverse) × 23.7 mm (sagittal) × 22.0–24.8 mm (axial)(713). The optic nerve's exit point from the eyeball measures 28 mm from the limbus (where the cornea meets the sclera) in the superonasal quadrant and 33 mm in the superotemporal quadrant (714), see **Figure 3-28**. Ayyala *et al.* reported nerve changes in rabbits with GDD implantation closer than 2 mm to the nerve. Thus, an implant placed closer than 2 mm to the optic nerve might impinge on the optic nerve and may compromise the nerve function. This may especially be true in eyes with shorter axial lengths (715). Also, if the patient develops severe inflammation, the fibrous reaction involved may adversely affect the optic nerve.

Thus, for an implantable pocket to be used in the superotemporal quadrant of the eye, the maximum length of the device must not exceed 20 mm. This is a significant challenge that limits the amount of drug that can be stored in an elastomeric pocket and the duration between the refilling. Currently, the Baerveldt® 350 GDD which is 15 mm long and 32 mm wide with a total surface area of 350 mm^2, is the largest implant

approved for use in the subconjunctival space (715). Comparatively, AGD has a much smaller surface area of 184 mm^2, but a slightly increased length of 16 mm (715).

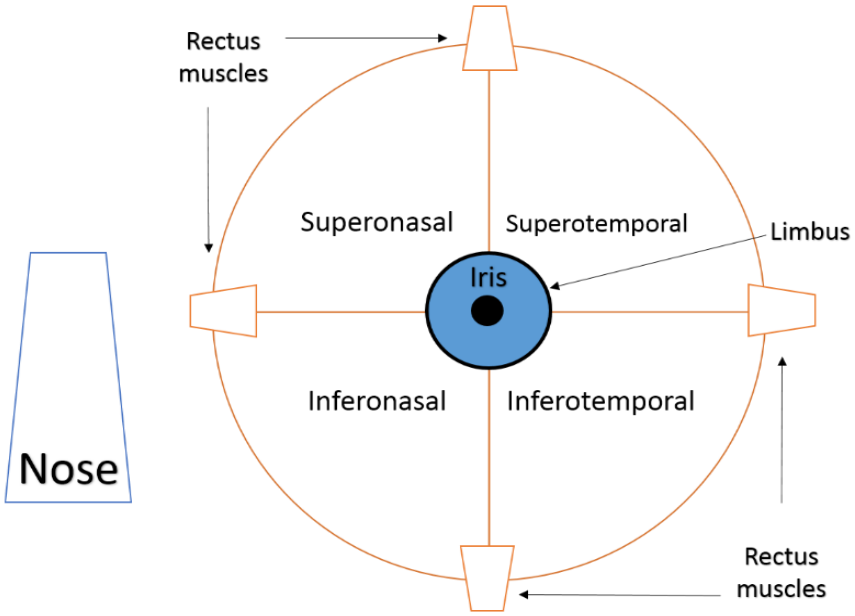

Figure 3-28. Relative to the nose, the eyeball can be divided into four main quadrants, superonasal, superotemporal, inferonasal and inferotemporal. The rectus muscles (as shown in this schematic diagram) are responsible for the movement of the eye.

From the results of the modelling data of fluid release from hypothetical single-chamber elastic pockets, it was evident that to increase the duration of drug (fluid) release, changing the diameter of the outlet tube would have the most significant impact. D*max* released 51.6% of its total fluid volume in 0.8 hours whereas D*min* released a similar amount of fluid (51.6%) in about 330 days (~11 months). Decreasing the diameter (D) of the outlet tube would result in a significantly longer $T_{1/2}$, which would potentially translate *in vivo* to a significantly prolonged drug release from a pump, when compared with a pump with an outlet tube of a larger diameter. It is worth noting that the biggest surprise in the application of Poiseuille's law to fluid flow is the dramatic effect of changing the radius as compared to the length of the pipe. According to Hagen-Poiseuille's law, (equation 3.6) the dependence on the resistance to fluid flow provided by a tube is directly proportional to the tube length, L, but a power of $\frac{1}{R^4}$ to the radius of the tube. Furthermore, from the Hydrodynamics principle (equation 3.5), we know that the resistance provided by a tube to fluid flow is inversely proportional to the rate of

fluid flow, we can calculate that by decreasing the radius of the outlet tube by a mere 20%, it is possible to reduce the flow rate of the liquid released by 50%.

The results from the modelling data of fluid release from hypothetical single-chamber pockets further revealed that the efficiency of the pump increased with the decrease in Young's modulus (E) and thickness (T) of the elastic material of the pocket. A closer inspection of the modelling results reveals a narrower range and lower average values of fluid release rates when E and T were decreased (E*max*, T*max*/E*min*, T*min*). An interesting result was that the E*min* pocket displayed an almost 33% wider range of flow rate, as compared to T*min.* These trends can be explained by the direct dependence of $T_{1/2}$ on the fluid release rate of the pump. Decreasing Young's modulus (E) and thickness (T) of the elastic material resulted in a longer $T_{1/2}$, which would potentially translate *in vivo* to a steadier amount of drug released for a prolonged period, when compared with a pump made with thicker and stiffer elastic materials.

Finally, increasing to maximum values of E and minimum values of T and D, the Optimal pump compared with D*min* showed a slight decrease in pump efficiency (5.7%) but increased the time taken for fluid release and $T_{1/2}$ (2% and 8.8%, respectively). This further supports the result that within the current limitation of commercially available elastomeric materials and tubes, the dimensions (diameter in particular) of the outlet tube have the most significant impact on the performance of the pump.

Currently, it is unknown if a steadier delivery of a drug in the subconjunctival space might improve clinical outcomes as compared with a pulsatile delivery, which is commonly observed with intraocular injections. However, there is significant merit in reducing concentration spikes and maintaining higher drug bioavailability by a continuous delivery of the drug (635,708). Moreover, an ophthalmic pump should improve patient outcome as the adherence to the therapeutic regimen would be significantly improved. Several studies and clinical trials have demonstrated that uninterrupted IVT injections improve patient outcomes, as compared to patients who are less compliant to their dosage regimen (716–720).

Recent results from the Ladder trial (ClinicalTrials.gov identifier NCT02510794), reported favourable outcomes for extended intervals of time required between drug refills for the PDS delivery device (635). The median time to first implant refill was reported to be 8.7, 13.0, and 15.0 months in the PDS 10 mg ml^{-1}, PDS 40 mg ml^{-1}, and

PDS 100 mg ml^{-1} arms, respectively. Active ranibizumab was reported to be measurable (with a lower limit of quantification of 15 pg/ml) in serum for 15 months or more after insertion of the PDS implant filled with ranibizumab 100 mg ml^{-1} (631,635). The authors of the study asserted that the results suggested the PDS to be a good candidate to change the current treatment paradigm in nAMD and respond to the current unmet need to reduce treatment burden without sacrificing clinical efficacy (635).

The Ladder results provided a proof of concept that biologics or small molecules can be delivered safely to the eye for months at a time through a permanent refillable intraocular reservoir. Currently, two Phase 3 clinical trials are ongoing to study the efficacy, safety, and pharmacokinetics of the PDS with ranibizumab in patients with, nAMD (ClinicalTrials.gov. identifier NCT03677934)(721) and diabetic macular oedema (ClinicalTrials.gov. identifier NCT04108156)(722). Another Phase 3 clinical trial to evaluate the long-term safety and tolerability of the PDS is ongoing (ClinicalTrials.gov. identifier NCT03683251)(723).

For the present work, results from the modelling of fluid release from hypothetical single-chamber elastic pockets suggest an extended time (D*min* and Optimal ~11 months) before a refill would be needed, which is comparable to that of the PDS implant. After the completion of fluid release, the pocket would be refilled using a dual-lumen needle that would simultaneously withdraw the pre-existing drug solution remaining in the pocket, ensuring total fluid exchange of old drug with new drug in the reservoir, similar to the way the PDS was refilled in the clinic using standard aseptic techniques and local anaesthesia (635). Moreover, in experimental testing, the single-chamber elastic pockets might show even extended release times, as has been noted in preliminary testing of these devices (ongoing work, data not shown).

Currently used stored-energy disposable pumps show a varying drug release performance which depends on their power source and mechanism of flow control. Elastomeric pumps typically deliver at higher flow rates at the beginning and end of an infusion cycle whereas pressure-actuated pumps deliver at higher flow rates at the beginning of an infusion and much lower flow rates at the end of an infusion (724). Clinical evaluations of elastomeric pumps have shown that the variations in flow rates were not clinically significant and did not present a hazard to patients (725). Data from modelling fluid-release results from hypothetical single-chamber elastic pockets were in

good agreement with clinical performance data of commercially used elastomeric pumps.

Based on the experimental findings and modelling data from this Chapter, two mechanisms of action for an elastomeric pump for ophthalmic drug delivery can be suggested. Firstly, a single-pocket elastomeric pump, utilising the kinetic energy stored in the stretched membranes due to the uniform internal pressure exerted by the stored fluid. A schematic of this proposed mechanism is shown in **Figure 3-29**. It would be implanted in the superotemporal quadrant of the eye, in the subconjunctival space. The pump should be enclosed in a hard-protective casing to avoid having variable flow rates, caused by accidental compression of the pump.

Pumps working on a similar principle are commercially available but are much larger in size with shorter duration of drug delivery as compared with the proposed design for an implantable elastomeric ophthalmic pump (340,350,661,726,727). Such a pump would be simple, cost-effective and would not need any external stimuli to deliver the stored drug in a saturated solution form. Moreover, a drug refill port may be added to the protective casing of the pump to make the refilling of the pump easy, much like the way an IVT or subconjunctival injection is currently administered.

The effect of material thickness, Young's modulus, pocket-size, internal pocket pressure and volume of the reservoir on the flow rate of liquid released from the single pocket elastomeric pump can be estimated using the relations developed from the results of inflation (667) and deflation of the pocket experiments. In indications where the rate of drug delivery required is low, additional resistance to the pump outflow would be necessary, which can be easily estimated using equation 4.10. The modelling data of fluid release from hypothetical single-chamber pockets of fixed dimensions suggested a wide range of pump efficiencies (17.2–80.8%) and $T_{1/2}$ (0.2–2154 hours). However, this data is by no means an exhaustive estimate of all the probable values for pump efficiency and $T_{1/2}$, as we now know that these values can change based on changes in material properties (E), material thickness (T) and outlet tube diameter (D).

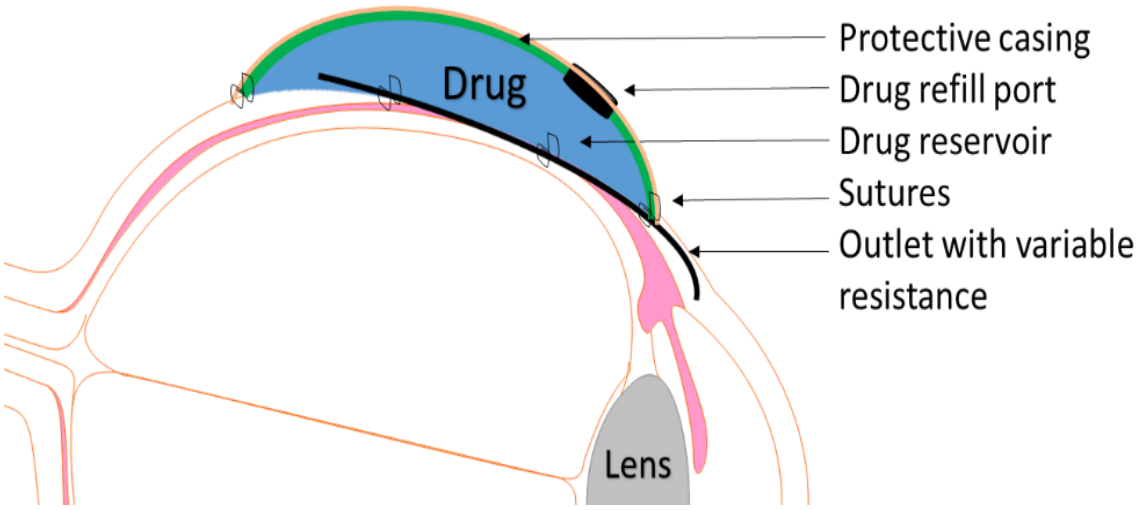

Figure 3-29. A proposed schematic of a single pocket elastomeric pump that could be implanted under the conjunctiva, much like the current surgical technique used for GDD implantation. The rate of drug delivery could be controlled by changing the dimensions of the pump outlet and could be refilled once the drug reservoir has been emptied. Pump is not drawn to scale.

Secondly, based on the principles and the observations from studying the compression of inflated elastomeric pockets (689), I propose that the rationale behind the single pocket pump could be extended to double or multi-pocket elastomeric pumps. Such a pump would utilise the compressive forces generated by single or multiple pockets to expel out the stored drug, at a controlled flow rate. These pumps would be relatively more complicated than single pocket pumps and would often require some external stimuli to deliver the stored drug fluid. A schematic of this proposed mechanism is shown in **Figure 3-30.** One or more pockets inside the pump could be externally controlled, causing them to 'swell'. This would be the pressure exerting chamber (C_1). This systematic swelling would apply compressive forces on the drug reservoir (C_2), squeezing the drug out of the pump. This option to tailor the drug release according to a variable requirement of the drug concentrations needed would be a significant added advantage over single pocket pumps.

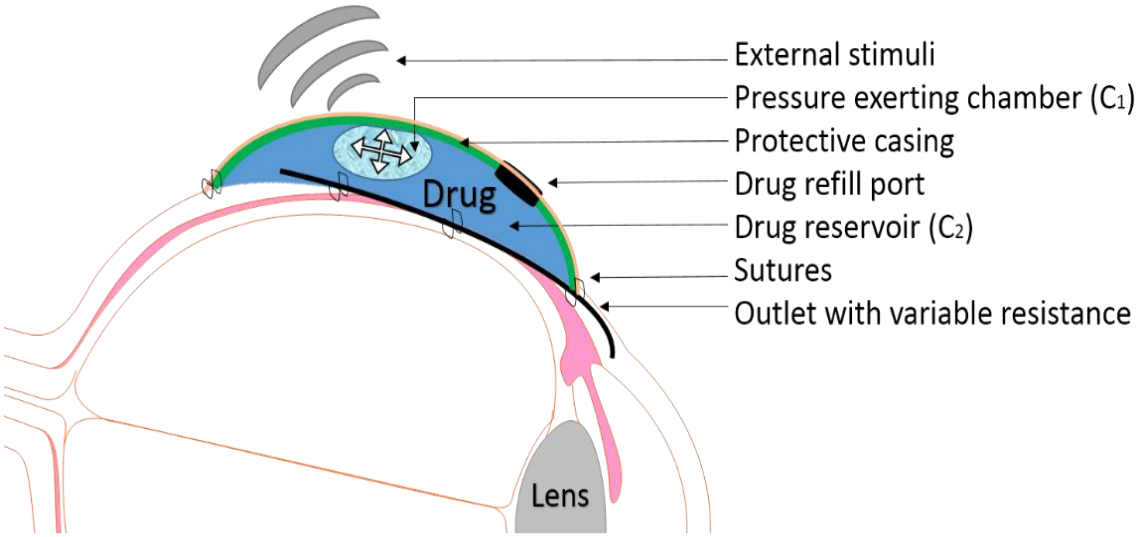

Figure 3-30. A proposed schematic of a double-pocket elastomeric pump that could be implanted under the conjunctiva, much like the current surgical technique used for GDD implantation. This pump would have the added advantage of being able to respond to external stimuli to tailor the drug release according to the therapeutic requirement. Pump is not drawn to scale.

The experimental results for compression of elastic pockets (**Section 3.5.4**) indicate that the internal pressure of a pocket is proportional to the compressive force applied, across a range of elastomeric material properties and material thickness. The externally controllable pumps might offer a precisely tailored control of the drug delivery rates. Pumps employing this multi-pocket design approach could potentially have improved pump efficiencies as compared to single-chamber pumps by increasing the internal pressure of the pump as it approaches nearer to the cut off pressure value of the pump. Additionally, it may be possible to fill different pockets of a multi-pocket ophthalmic pump with different concentrations of single or multiple drugs and achieve a complex delivery of a patient-specific combination dose. The potential for a tailored delivery regimen would significantly improve on the fixed-dose combination eye drops that are currently available for glaucoma management. Additionally, to improve the long-term stability of the drug in a multi-pocket pump, different pockets could be filled with separate drug and stabilisers that could be eluted at the same time. It has been shown previously that the stability of the anti-VEGF drug, bevacizumab was improved with the addition of DEX sodium phosphate (728).

In our previous work from the Brocchini lab, we have shown *in vivo* that a coated implant of the potent MMPi, ilomastat was delivered at desirable concentrations in the conjunctival (719.13 ± 267.68 pg/mg tissue) and scleral tissues (3818.18 ± 351.17 pg/mg

tissue) of rabbits (239). In another study using rabbits, it was shown that ilomastat could be successfully formulated as eye drops with cyclodextrins (CD) to achieve therapeutic doses (10–100 nM) in conjunctival and scleral tissues (205). This ilomastat eye drop formulation could potentially be stored and delivered at the site of surgery, using the proposed implantable elastomeric pocket.

However, a proof-of-concept investigation with a saturated drug solution within an elastomeric pocket is warranted. This design concept would need to be scaled down to the size of the superotemporal quadrant of the eye, which would be an accurate estimation of 'real-world application' of such a device. Future work at scaling down the pocket size of the pump and optimisation of flow rate is underway.

3.7. Summary and conclusions

The work described in this Chapter elucidated the relationships between key parameters involved in the functioning of simply connected (connected across a single boundary) elastomeric pockets.

First, the effect of the pressure exerted by a fluid on elastomeric membranes was characterised in terms of pressure applied, membrane thickness, Young's modulus, and the shape and size of the elastomeric pockets. Significant differences between pursed regimes of two different shaped elastic pockets in terms of maximum deflection. The results indicate that the maximum deflection varies linearly with internal pressure in the bending regime (maximum deflection $\leq$ thickness of the pocket). However, maximum deflection varies to the power $\frac{1}{3}$ with internal pressure in the stretching regime (maximum deflection $>$ thickness of the pocket). Finally, the release of fluid from these pressurised elastomeric pockets as a function of time, internal pressure, and internal fluid volume was analysed. Material properties, such as Young's modulus, and material thickness proved to be important factors in the bending regime whereas, in the stretching regime, the size and shape of the pocket itself had drastic implications on the results obtained. The relationship between applied compressive forces and changes in the internal pressure of an inflated pocket was found to be approximately linear.

Results from analysing compression and deflation of elastic pockets were utilised to provide recommendations for pump design for localised ophthalmic delivery. Modelling of drug release from a single-chambered hypothetical pump made with commercially available materials of varying properties was undertaken using MATLAB. Modelling results indicate that it is possible to prolong the release of drugs from a single chamber elastic pocket using the elastomeric pocket designs, D*min* and Optimal, which released 544.8 and 513.7 µL, respectively, over approximately 11 months with ~50% efficiencies and without the need for replenishing the drug reservoir of the pocket, making these pockets ideal candidates for future investigation.

The original contribution of this work is in elucidating the relationships between the key variables involved in the design and function of elastomeric pumps and applying them to ophthalmic drug delivery. Further work would focus, first, on the *in vitro* optimisation of the maximum dimensions of the reservoir that would be allowed for

placement in the eye (*i.e.* diameter and height) for maximum drug volume and drug release duration. Second, further work should focus on the optimisation the pump's dimensions, including outlet tube dimensions, to obtain maximum drug release over a duration of several months. Finally, optimisation of drug viscosity and validation of drug stability, *e.g.* small molecules versus biologics, within the pump should be undertaken for maintaining a steady concentration of drug released by a pump over prolonged periods.

Chapter 4 Optimising pHEMA hydrogels for aqueous flow control

Abstract

This chapter reports an investigation into an alternative mechanism of IOP control by modulation aqueous flow. Novel and established hydrogel formulations were evaluated for their aqueous permeability and mechanical integrity while simulating the *in vivo* environment of the eye and the endurance to clinician handling during GDD implantation. Chemical and physical modifications to hydrogel formulations were investigated with the aim of achieving optimal aqueous permeability for IOP control. Despite evidence to suggest the feasibility of hydrogels to modulate aqueous flow, the *in vitro* permeability of hydrogel candidates was determined to be too low to maintain optimal IOP. Furthermore, hydrogel permeability tended to negate its mechanical integrity, making them unsuitable candidate materials for GDD development

4.1. Background

Glaucoma drainage devices (GDDs) are progressively becoming a primary surgical intervention to halt the progression of glaucoma due to a better understanding of controlling flow in the early postoperative phase by clinicians (729). The current state of the art GDDs are listed in **Table 1-2**. However, the long-term success of a GDD implantation is dependent upon controlling the rate of postoperative fibrosis (see **Section 1.3.5)**. Initially, fibrous encapsulation around the GDD end plate modulates aqueous humour flow to regulate IOP levels and prevent hypotony; but as the encapsulation increases, the aqueous is unable to drain properly, IOP increases, and disease progression proceeds. It is understood that the GDD material affects the postoperative inflammatory response. Improvements in GDD development are needed to reduce the foreign body response that often results in fibrous encapsulation around a device (see **Section 1.3.4**). Developing a device composed of a biocompatible material that reduces the foreign body response, and allows for fluid transport at a controlled rate, similar to what is required to maintain a healthy level of IOP (10–12 mmHg), could improve the outcomes of GDD implantation. Hydrogels are good candidates for this purpose because their biocompatibility is well-established and they readily swell to absorb large quantities of water (see **Section 1.6.1**).

4.1.1 pHEMA-MPC hydrogels

Hydrogels from hydrophilic polymers are soft and transparent due to high concentrations of water, but they often lack mechanical strength (518). Hydrogels composed of synthetic polymers also have the advantage of controlling properties, such as pore size and degradation time. Specifically, pHEMA, a synthetic, hydrophilic polymer, is known for its use in the synthesis of soft contact lenses (SCL), intraocular lenses (IOL), wound dressings and ophthalmic implants, such as the Esnoper-V2000® and Esnoper clip® (563). These implants were created to improve the outcome of deep sclerectomy surgery in glaucoma patients (730). pHEMA has also been modified by co-polymerisation with other polymers for hydrogel synthesis to improve water uptake, mechanical properties and modify the drug-releasing properties when used for drug delivery (see **Section 1.6.1**) (731,732).

Efforts to improve the biocompatibility of hydrogels have focussed on using phosphorylcholine (PC) as polymers. PC is the polar head group found in many cell membrane phospholipids (520). PC is zwitterionic, so has both negative and positive charges with an overall neutral charge (361). The highly polar nature of the chemical structure results in the hydration of the PC group. The resulting water layer is tightly bound, making the interaction with proteins energetically unfavourable due to an increase in Gibbs energy (733). Additionally, the overall neutral charge on the PC group helps to reduce the electrostatic charge on the surface of the polymer chains, further reducing interactions between proteins and the polymer. This impedes the proteins and cells from binding irreversibly to a PC polymer, thus increasing the biocompatibility and anti-biofouling nature of the polymer system (513,520,734).

Hydrogels prepared using these zwitterionic polymers have been confirmed as biocompatible, and they have also been used as coating materials for clinically-approved medical devices such as drug-eluting stents, urology and otology devices. The issue of biocompatibility is important during passive interactions between proteins and the surface of a hydrophobic material. When exposed to a hydrophobic surface, proteins tend to rearrange their structure and favour adsorption to the surface to decrease Gibbs energy (735). When exposed to a hydrophobic surface, proteins favour adsorption to the surface, resulting in a decrease in Gibbs free energy (735). During this process, proteins lose their outer shell of hydration, causing changes in conformation, and the proteins then irreversibly bind to the surface of the foreign body. *In vivo*, these conformational changes expose binding sites and recruit other proteins and cells, leading to a 'foreign body response' that can result in blood clot formations, fibrous capsules or an excessive inflammatory response (520,736).

In the case of a PC-coated surface, a surface layer of water is bound to the hydrophilic surface. Although proteins can still interact with the PC-coated surface, it is no longer energetically favourable for irreversible binding to occur, see **Figure 4-2**. The conformation of proteins adsorbed on non-PC-coated materials changes considerably from their native state, compared with proteins adsorbed on polymers containing a PC group, such as 2-methacryloyloxyethyl phosphorylcholine (MPC) (**Figure 4-1**), which differed little from their native state (513). Studies have shown that PC polymers reduce protein deposition and activation, thrombus formation, bacterial adhesion and biofilm

deposition, inflammatory and fibrotic response (363,737–741). PC polymers have been used in the manufacture of various clinical devices, such as PC polymer-based SCL containing 20% MPC (Proclear R, omafilcon A), commercially available from CooperVision (300), a drug-eluting PC coating in coronary stents such as Sorin and Endeavor (742), PC-coated urological devices (743) and a PC-coated grafted hip joint system (744). Vertellus Biomaterials specialises in the synthesis of PC-based polymers and currently holds a patent for PC (745). Several PC-based polymers are commercially available, and their nomenclature is related to product numbers such as PC-1015, which is used to make contact lenses. Each number represents a co-polymer derived from a different 'formulation' of monomers in which MPC is always included (746), see **Table 4-1**.

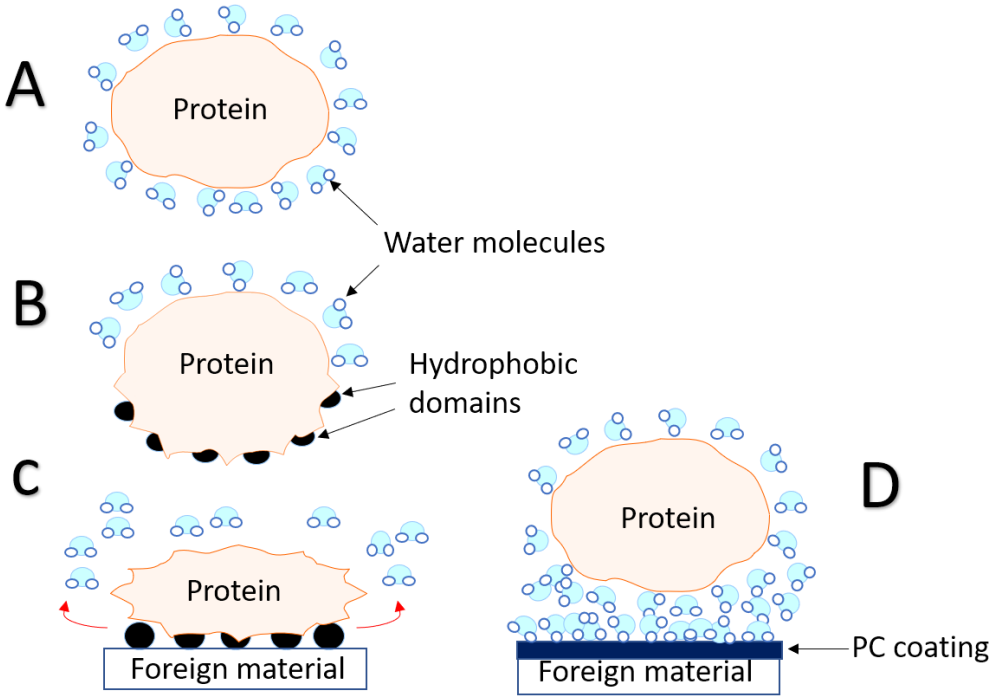

Figure 4-2. Schematic diagram indicating how a protein **(A)** interacts with a foreign body. After an interaction with the surface, proteins may lose their own shell of hydration, denature and irreversibly bind to the surface, **(B** and **C)**. In the case of a PC coated substrate, (D) the protein can still interact but the surface layer of water bound to the PC, but now it is energetically unfavourable for irreversible binding to occur, and the protein does not denature and activate an inflammatory response.

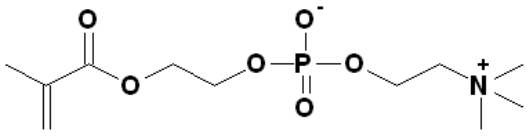

Figure 4-1. Chemical structure of 2-Methacryloyloxyethyl phosphorylcholine (MPC).

Table 4-1. Most commonly used PC formulations (745,746).

Polymer	Description	Characteristic	Typical Applications
PC-1036	Cross-linked PC coating	High durability, drug-delivery matrix	Drug-eluting stents, urology, otology devices
PC-1059	'Standard' non-cross-linked PC coating	Easily applied, stable coating	Guidewires, CPB systems, blood processing devices
PC-2118	Cross-linked PC coating with instant wettability	High surface energy, self-priming surfaces	Blood filtration and processing
PC-1062	Cross-linked PC coating with a low level of positive charge	Binds heparin to form an anti-thrombogenic coating	Blood filtration and processing
PC-2028	Cross-linked PC coating with a high level of positive charge	Matrix for delivery of high Mw drugs	Drug-eluting stents
PC-1071	Vinyl functional in-mould PC coating	Applied to curable materials, e.g. silicones	Otology devices
PC-1015	Cross-linked PC hydrogel	Bulk material for moulding	Contact lenses
PC-2083	Flexible PC hydrogel with high refractive index	Bulk material for moulding	Contact lenses

4.1.2 Hydraulic conductivity and permeability

Hydraulic conductivity (L) is a term used to describe the fluid transport characteristics of a given semi-permeable membrane (747). It is the rate of fluid transported (in m s^{-1}) across a permeable membrane divided by the pressure (in Pascals) that causes fluid flow and has units of m s^{-1} Pa^{-1}. Hydraulic conductivity reflects the intrinsic transport characteristics of the material. Permeability (K) is arguably one of the most important properties of any porous medium as it describes the conductivity concerning fluid flow through connected voids within the medium (748). Since the rate of fluid transport is dependent on the thickness of the membrane (T), multiplying L by T gives K of the membrane. In contrast to hydraulic conductivity, hydraulic permeability describes the transport characteristics across a membrane as a function of path length or thickness.

4.1.3 Permeability studies of hydrogels and study rationale

Hydrogels have been reported in the literature to show permeability to aqueous flow, and glycidyl methacrylate (GMA), as well as pHEMA hydrogels with varying initiators and cross-linkers, were reported to have aqueous permeability values in the range of 0.075 to 42.04 x 10^{-16} m^2 s^{-1} pas^{-1}. Cross-linked pHEMA hydrogels have also been reported to have a range of values for aqueous permeability which were affected by their cross-linker density; 0.1 to 1.5 x 10^{-16} m^2 s^{-1} pas^{-1}, solvent concentration; 0.03 to 1.5 x 10^{-16} m^2 s^{-1} pas^{-1} and cross-linker concentration (ethylene dimethacrylate, EDMA); 2.0

x 10^{-13} to 1.7 x 10^{-18} m^2 s^{-1} pas^{-1} (749), which indicates that pHEMA hydrogels generally allow some degree of water flow. However, a more recent study reported that collagen type I (0.3% w/v) hydrogels showed a higher aqueous permeability of 1 x 10^{-9} m^2 s^{-1} pas^{-1} (750). Previous preliminary work in the Brocchini research group found that pHEMA-MPC hydrogels display permeability values of approximately 1-9 ×10^{-14} m^2 s^{-1} pas^{-1}. These same hydrogels, when frozen and visualised under SEM, revealed a structural that was remarkably similar to a healthy trabecular meshwork in the eye. The size and density of pores in the pHEMA-MPC hydrogels increased with the concentration of added MPC (613). Another study conducted previously in the Brocchini research group demonstrated that a commercially available contact lens did not elicit a fibrotic response in New Zealand albino rabbits after 14 days (356). Considering the promising findings in the literature and work from previous PhD students, hydrogels demonstrate the potential to modulate aqueous flow as an appropriate biomaterial for a GDD fabrication.

An ideal GDD to address the unmet need in glaucoma should appropriately control the flow of aqueous humour to regulate the intraocular pressure at 10 mmHg while being able to withstand the implantation procedure. Equally, for a hydrogel to be deemed fit for GDD fabrication, it must restrict aqueous flow at a rate of 2 µL min^{-1} at a steady pressure of 10 mmHg. It is possible that this flow control may be achieved by either chemical or physical modifications to the hydrogel formulations, provided that the mechanical integrity of the hydrogel is not hindered by such changes.

4.2. Hypothesis and aims

The hypothesis for this chapter was that a novel, alternative strategy to modulate aqueous flow using a hydrogel material would be possible. This hydrogel would collect the aqueous and allow it to slowly diffuse through the hydrogel matrix, mimicking how the aqueous humour flows through the TM into the subconjunctival space, maintaining the IOP in a healthy eye.

The work described in this Chapter thus aimed to investigate if the chemical formulation of pHEMA-MPC hydrogels could be fine-tuned to control the flow of water at the same rate of aqueous humour production rate of 2 µL min^{-1} in the eye. Secondary aims were to determine if the flow of water could be controlled through physical modifications to the hydrogels pre- and post-polymerisation, as well as to measure the mechanical integrity in order to ensure that hydrogels could withstand handling by a clinician. If these aims can be achieved, it is possible that a novel GDD composed of hydrogels can progress into clinical development.

The two main objectives of the work described in this chapter were:

- Firstly, to create an experimental method and characterise the aqueous permeability of non-degradable pHEMA hydrogels relative to the theoretical optimal aqueous permeability needed to regulate IOP at normal levels. The hydrogels were formulated with varying monomer concentrations, polymerisation temperatures and durations, co-monomer concentrations and types, cross-linking densities, initiator concentrations, and the addition of various diluents to the hydrogels.
- Secondly, to devise a protocol and evaluate mechanical integrity to comply with clinician handling of the hydrogel materials, and third, to explore the viability of alternative methods to increase pHEMA hydrogel permeability. These methods included femtosecond laser augmentation and hydrogel polymerisation around physical spacers.

4.3. Optimal Device Requirements

The requirements for an optimal GDD material include the identification of biocompatible materials with the ability to restrict aqueous flow a rate of 2 µL min^{-1} at

a steady pressure of 10 mmHg. The GDD material should also be mechanically resilient to withstand clinician handling while undergoing subconjunctival implantation.

4.4. Materials and Methods

Chemicals and solvents used in this chapter are listed in **Table 4-2** and **Table 4-3**. Reagents were all used as received without further purification. Instruments and experimental setups used for characterisation are all described in the Methods section below.

Table 4-2. List of chemicals and solvents used in this chapter.

Material (MW, density*)	Supplier	CAS; Catalogue/Lot number
2-hydroxyethyl methacrylate (HEMA)(MW: 130.14 g mol^{-1}, density: 1.073 g mL^{-1})	Sigma Aldrich, UK	868-77-9; 525464
2-Methacryloyloxyethyl phosphorylcholine (MPC) (MW: 295.27 g mol^{-1})	Vertellus Biomaterials, UK	67881-98-5; 84A4108P
Ethyl methacrylate (EMA) (MW: 114.14 g mol^{-1}, density: 0.917 g mL^{-1})	Sigma Aldrich, UK	97-63-2; 234893
Hydroxypropyl methacrylate (HPMA) (MW: 144.17 g mol^{-1}, density: 1.066 g mL^{-1})	Sigma Aldrich, UK	27813-02-1; 268542
1-Vinyl-2-pyrrolidinone (VP) (MW: 111.14 g mol^{-1}, density: 1.04 g mL^{-1})	Sigma Aldrich, UK	88-12-0; V3409
Poly-n-vinylpyrrolidone (PVP) (MW: 40,000 g mol^{-1})	Sigma Aldrich, UK	9003-39-8; PVP40
PC1059	Vertellus Biomaterials, UK	http://www.pcbiomaterials.com/Products.html
Ethylene glycol dimethacrylate (EGDMA) (MW: 198.22 g mol^{-1}, density: 1.051 g mL^{-1})	Sigma Aldrich, UK	97-90-5; 335681
Poly(ethylene glycol) dimethacrylate (PEGDMA) (MW: 700 g mol^{-1}, 2000 g mol^{-1})	Sigma Aldrich, UK	25852-47-5; Mn 700 - 437468 Mn 2000 - 687529
N, N-methylenebisacrylamide (MBAM) (MW: 154.17 g mol^{-1})	Sigma Aldrich, UK	110-26-9; M7279
Ammonium persulfate (APS) (MW: 228.18 g mol^{-1})	Sigma Aldrich, UK	7727-54-0; A3678
2,2'-Azobis(2-methylpropionitrile) (AIBN) (MW: 164.21 g mol^{-1})	Sigma Aldrich, UK	78-67-1; 441090
Tert-butanol (MW: 74.12 g mol^{-1}, density: 0.7800 g mL^{-1})	Fisher Scientific, UK	75-65-0; 194701L
Tetrarahydrofuran (THF) (MW: 72.11 g mol^{-1}, density: 0.8876 g mL^{-1})	Fisher Scientific, UK	109-99-9; 34865
Ethanol (MW: 46.07 g mol^{-1}, density: 0.789 g mL^{-1})	Sigma Aldrich, UK	64-17-5; 459828
Phosphate buffered saline tablets (PBS)	Fisher Scientific, UK	18912014
Sodium chloride (MW: 58.44 g mol^{-1})	Fisher Scientific, UK	7647-14-5

*density at 25°C. PC1059 was a proprietary PC-based polymer gifted by Vertellus Biomaterials.

Table 4-3. List of materials used in this chapter.

Material	Supplier	Catalogue/Lot number
Silicone sheets	Polymax, UK	Silona
Polypropylene sheets	RS Components, UK	682-551
3-way stop valve	Fisher Scientific, UK	4201634503
Luer to ¼-28 adapter	Sigma Aldrich, UK	58722
Clear cast acrylic rods	RS Components, UK	RS PRO Clear 824-626
3 mL slip top plastic syringes	BD Plastics, UK	309656
21 gauge needles	Terumo, UK	NN-2116R
Silicone tubing	VWR International, UK	Tygon® 3350
PTFE thread seal tape	Sigma Aldrich, UK	20808-U
Large bulldog binder clips	Staples, UK	WW-297959053
Universal oven	Fisher Scientific, UK	Memmert™ UN110plus Universal 50
Water purifier	VWR International, UK	Purite Select Fusion 80
Weighing balance	Sigma Aldrich, UK	Ohaus® Explorer® Pro
Titanium-Sapphire femtosecond laser	Coherent, USA	Legend
Laser beam shaper	AdlOptica, DE	π-shaper - model 6_6
Beam splitter	Thorlabs, USA	UBS21
Auto-correlator	Thorlabs, USA	FSAC
Variable neutral density filter	Thorlabs, USA	NDK1
Microscope objective lens	Mitutoyo, UK	50x
Charge-coupled device camera	Brunel Microscopes Ltd., UK	Brunel Toupcam Fluor1
Dichroic mirror	Thorlabs, USA	DMBP740B

4.4.1 General hydrogel preparation

All hydrogels were either supplied pre-made by industrial collaborator, Vertellus Biomaterials (Basingstoke, UK) or were formulated by Dr Tamara Alhilfi and Dr Clare Haeysman, polymer chemists at UCL School of Pharmacy. Hydrogels were synthesised using a free-radical polymerisation method using either heat or UV-initiation following the protocol provided by Vertellus Biomaterials, UK. Pre-synthesised hydrogels supplied by Vertellus have been mentioned in the appropriate sections. All hydrogel formulations are reported in percentage by weight and complete details of the weights and volumes of hydrogel components are reported in **Appendix 2.**

All components were weighed using an analytical balance and were added to a glass vial and stirred at 600 rpm for 2 hours using a magnetic stirrer until the solution was clear. Meanwhile, polymer casting moulds were prepared by cutting out a 7.5 cm x 2.5 cm area from silicone gaskets with a 1 mm thickness. A 2.5 cm x 7.5 cm area was cut out of two 3 mm polypropylene sheets, which were placed on either side of the silicone gasket, and the sheets and gasket were secured by placing binder clips on all four sides of the casting mould to seal a cavity inside, see **Figure 4-3**.

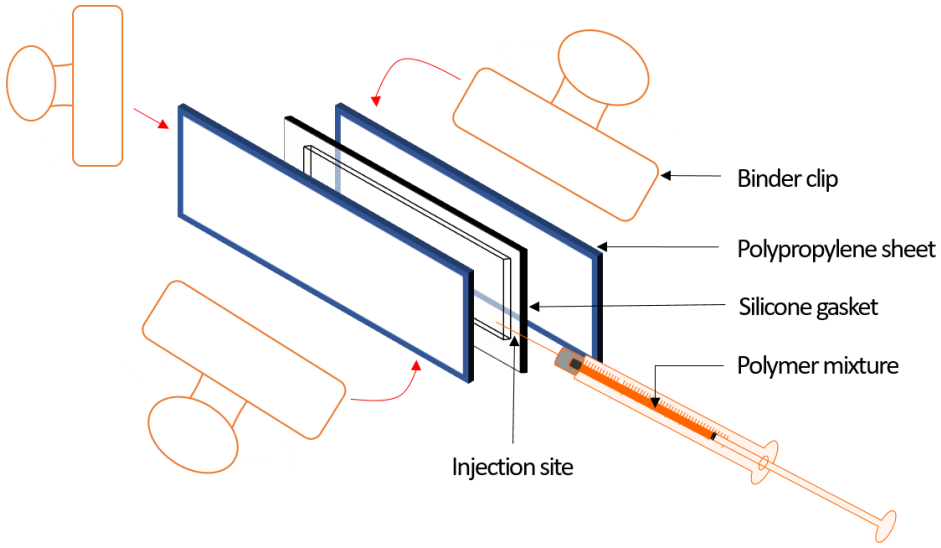

Figure 4-3. Diagramme of the casting mould used for hydrogel preparations. The mould consisted of two 3 mm polypropylene sheets and a 1 mm thick silicone sheet between them. The mould was held together with binder clips and the polymer mixture was injected into the mould after degassing.

The polymer mixture was degassed with argon for 10 minutes to avoid oxygen inhibiting the radical polymerisation of HEMA (444). Immediately after degassing, the polymer mixture was drawn into a 5 mL plastic syringe using a 21G needle, which then pierced the silicone at the top of the casting mould and was injected to fill the cavity. The moulds were filled with the polymer mixture before transferring them to an oven for polymerisation to avoid trapping any air bubbles that may have hindered polymerisation. The samples were laid flat, and the oven was maintained at 70°C for 7 hours. Polypropylene sheets are rigid and translucent, which were optimal for easy handling and ensuring that the moulds were not overfilled with the polymer mixture. The use of a 21G needle to fill the polymer mixture in the mould significantly reduced the chances of cavity overspill.

After 7 hours, a polymeric xerogel formed. The term xerogel is used to describe the hydrogel in a dried, unhydrated state. The polypropylene sheets were separated, and the xerogels were removed from the silicone gasket and were placed in 50 mL of purified deionised (DI) water for hydration and to remove any unreacted monomer or oligomeric species. The DI water was changed an average of five times over 24 hours in a polypropylene tube until the xerogels were fully hydrated. The washing water was saved and scanned by a UV spectrophotometer over a range of $A_{180–400\ nm}$ to check for any residual unreacted monomer.

4.4.1.1 1015 formulation

The polymer composition used for manufacturing of contact lenses (CooperVision) is known as the 1015 formulation (**Figure 4-4**). 1015 hydrogels were prepared according to a protocol provided by Vertellus Biomaterials. HEMA was added as the primary monomer, MPC was added as a co-monomer to enhance biocompatibility and improve the hydrophilicity of the hydrogels, ethylene glycol dimethacrylate

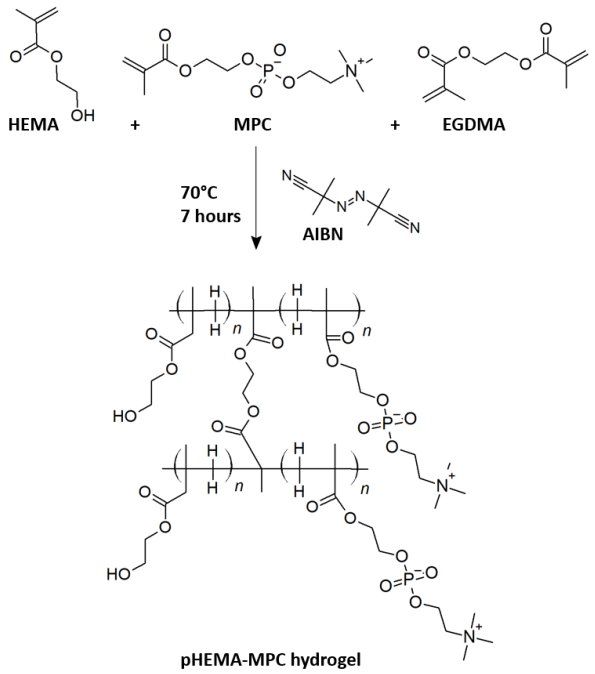

Figure 4-4. Chemical synthesis of pHEMA-MPC hydrogel films by free radical polymerisation. The monomer, HEMA, and co-monomer, MPC, were mixed with cross-linker, EGDMA, to form a clear solution. The initiator, AIBN, was added, the formulation was degassed with argon, was injected into the casting moulds, and was placed in the oven at 70°C for 7 hours. Figure was made using ACD's ChemSketch.

(EGDMA) was added as a cross-linker, and 2,2'-Azobis(2-methylpropionitrile)(AIBN) was used as the thermal initiator, see **Table 4-4**.

Table 4-4. 1015 hydrogel formulation.

Component	Material	Mass per preparation (g)	% per hydrogel (w/w)
Primary monomer	HEMA	8.46	84.7
Co-monomer	MPC	1.41	14.1
Cross-linker	EGDMA	0.07	0.7
Thermal initiator	AIBN	0.05	0.5

HEMA mass was calculated using its density, 1.073 g mL^{-1}. EGDMA mass was calculated using its density, 1.051 g mL^{-1}. **Abbreviations:** AIBN, 2,2'-Azobis(2-methylpropionitrile); EGDMA, ethylene glycol dimethacrylate; HEMA, 2-hydroxyethyl methacrylate; MPC, 2-methacryloyloxyethyl phosphorylcholine.

4.4.1.2 Swelling ratio

To quantify swelling ratios (SR), and the time required to reach equilibrium swelling (EWC%) by 1015 hydrogels, freshly prepared xerogel membranes were weighed, W_d, and submerged in centrifuge tubes containing either 50 mL DI water; a PBS solution; 9% saline solution or 100% ethanol (EtOH). At various time points, the membranes were removed from the centrifuge tubes and patted dry with a filter paper to remove the excess adsorbed water and were weighed, W_t $\mathrm{EWC}\%$ and SR was calculated for each time point using equations 4.1 and 4.2;

$$\mathrm{EWC}\ (\%) = \frac{(W_t - W_d)}{W_t} \times 100 \tag{4.1}$$

$$\mathrm{SR} = \frac{(W_t - W_d)}{W_d} \tag{4.2}$$

4.4.1.3 Monomer concentrations

The concentration of HEMA monomer relative to the amounts of co-monomer, cross-linker, initiator, and water was changed to determine the effects on aqueous permeability, see **Table 4-5.** HEMA compositions of different pHEMA hydrogel films prepared by free radical polymerisation. Ammonium persulfate (APS) was used as an initiator of free radical polymerisation whenever water was used in the formulation as it was more water-soluble than AIBN (**Figure 4-5**).

Table 4-5. HEMA compositions of different pHEMA hydrogel films prepared by free radical polymerisation.

Hydrogel	% HEMA	% MPC	% EGDMA	% AIBN	% APS	% H_2O
M1	91.7	7.7	0.4	0.5	0.0	0.0
M2	73.4	24.5	1.3	0.5	0.0	0.0
M3	79.6	0.0	0.5	0.5	0.0	19.4
M4	79.6	0.0	0.5	0.0	0.5	19.4
M5	59.7	0.0	0.5	0.0	0.5	39.3
M7	30.3	2.6	0.5	0.0	0.5	66.1
M9	19.8	0.8	0.5	0.0	0.5	78.5

Components are reported in % w/w. HEMA mass was calculated using its density, 1.073 g mL^{-1}. EGDMA mass was calculated using its density, 1.051 g mL^{-1}. **Abbreviations:** AIBN, 2,2'-Azobis(2-methylpropionitrile); APS, ammonium persulfate; EGDMA, ethylene glycol dimethacrylate; HEMA, 2-hydroxyethyl methacrylate; MPC, 2-methacryloyloxyethyl phosphorylcholine. pHEMA, poly(2-hydroxyethyl methacrylate).

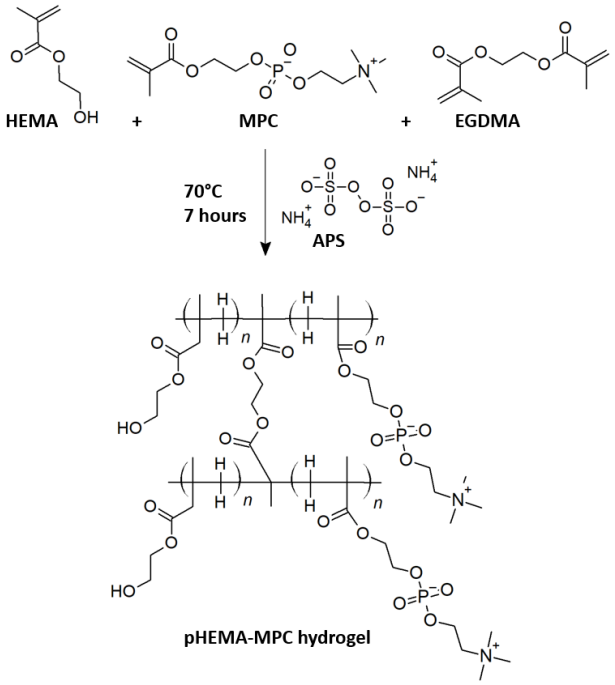

Figure 4-5. Chemical synthesis of pHEMA-MPC hydrogel films by free radical polymerisation. The monomer, HEMA, and co-monomer, MPC, were mixed with cross-linker, EGDMA, to form a clear solution. The water-soluble initiator, APS, was added, the formulation was degassed with argon and injected into the casting moulds, and was placed in the oven at 70°C for 7 hours. Figure was made using ACD's ChemSketch.

4.4.1.4 Curing conditions

The effect of different curing temperatures and durations on the aqueous permeability of hydrogels was also investigated, see **Table 4-6**. Conditions of increased heat duration, such as heating from ambient temperature to 70°C, then holding the heat constant at 70°C for 7 hours; increasing the polymerisation duration at lower

temperatures, *e.g.* 12 hours at 40°C, 20 hours at 50°C; adding an annealing step after a prolonged duration at lower temperatures, *e.g.* 12 hours at 40°C, followed by 4 hours at 120°C or 20 hours at 50°C, followed by 2 hours at 90°C; and using high temperatures, *e.g.* 7 hours at 70°C followed by 2 hours annealing at 120°C were explored. UV polymerisation for 1 hour at 60°C was also investigated with hydrogels made by industrial partner, Vertellus, see **Table 4-7.**

Table 4-6. Curing cycles for pHEMA hydrogels with formulations containing 85%, 60%, 50%, 40%, and 30% w/w HEMA.

Formulations						Curing cycle 1		Curing cycle 2		Curing cycle 3	
Hydrogel	**%HEMA**	**%MPC**	**%EGDMA**	**%APS**	**%H_2O**	**Temp. (°C)**	**Time (h)**	**Temp. (°C)**	**Time (h)**	**Temp. (°C)**	**Time (h)**
M19	59.7	0.0	0.5	0.5	39.3	40	12	-	-	-	-
M20	49.8	0.0	0.5	0.5	49.3	40	12	-	-	-	-
M21	39.8	0.0	0.6	0.5	59.2	40	12	-	-	-	-
M22	29.4	0.0	0.5	0.5	69.6	40	12	-	-	-	-
M23	59.7	0.0	0.5	0.5	39.3	40	12	120	4	-	-
M24	49.8	0.0	0.5	0.5	49.3	40	12	120	4	-	-
M25	39.8	0.0	0.6	0.5	59.2	40	12	120	4	-	-
M26	29.4	0.0	0.5	0.5	69.6	40	12	120	4	-	-
M27	59.7	0.0	0.5	0.5	39.3	70	7	-	-	-	-
M28	49.8	0.0	0.5	0.5	49.3	70	7	-	-	-	-
M29	39.8	0.0	0.6	0.5	59.2	70	7	-	-	-	-
M30	29.4	0.0	0.5	0.5	69.6	70	7	-	-	-	-
M31	59.7	0.0	0.5	0.5	39.3	50	20	-	-	-	-
M32	49.8	0.0	0.5	0.5	49.3	50	20	-	-	-	-
M33	39.8	0.0	0.6	0.5	59.2	50	20	-	-	-	-
M34	29.4	0.0	0.5	0.5	69.6	50	20	-	-	-	-
M35	59.7	0.0	0.5	0.5	39.3	50	20	90	2	-	-
M36	49.8	0.0	0.5	0.5	49.3	50	20	90	2	-	-
M37	39.8	0.0	0.6	0.5	59.2	50	20	90	2	-	-
M38	29.4	0.0	0.5	0.5	69.6	50	20	90	2	-	-
M39	84.6	14.1	0.7	0.5[a]	0.0	23–70	15	70	7	-	-
M40	84.6	14.1	0.7	0.5[a]	0.0	23–70	15	70	7	120	2
M41	84.6	14.1	0.7	0.5[a]	0.0	70	7	120	2	-	-

[a]AIBN was used as an initiator instead of APS in these hydrogel formulations. Components are reported in % w/w. HEMA mass was calculated using its density, 1.073 g mL^{-1}. EGDMA mass was calculated using its density, 1.051 g mL^{-1}. **Abbreviations:** AIBN, 2,2'-azobis(2-methylpropionitrile); APS, ammonium persulfate; EGDMA, ethylene glycol dimethacrylate; HEMA, 2-hydroxyethyl methacrylate; MPC, 2-methacryloyloxyethyl phosphorylcholine; pHEMA, poly(2-hydroxyethyl methacrylate).

Table 4-7. UV curing conditions for pHEMA hydrogels with formulations containing 85%, 60%, and 30% w/w HEMA with and without MPC added, and a 1015 formulation diluted with 60%, 70%, 80% and 90% DI water.

	Formulations						Curing conditions	
Hydrogel	**%HEMA**	**%MPC**	**%EGDMA**	**%AIBN**	**%APS**	**%H_2O**	**Temp. (°C)**	**Time (h)**
V1	84.8	14.1	0.7	0.0	0.0	0.0	60	1
V2	60.0	0.0	0.7	0.0	0.5	38.8	60	1
V3	30.0	0.0	0.7	0.0	0.5	68.8	60	1
V4	30.0	5.0	0.7	0.0	0.5	63.8	60	1
V5	84.8	14.0	0.7	0.5	0.0	0.0	60	1
V6	33.9	5.6	0.3	0.0	0.2	60.0	60	1
V7	25.4	4.2	0.2	0.0	0.2	70.0	60	1
V8	17.0	2.8	0.1	0.0	0.1	80.0	60	1
V9	8.5	1.4	0.07	0.0	0.05	90.0	60	1

Components are reported in % w/w. AIBN was used as an initiator instead of APS when no water was added to the hydrogel formulations. HEMA mass was calculated using its density, 1.073 g mL^{-1}. EGDMA mass was calculated using its density, 1.051 g mL^{-1}. **Abbreviations:** AIBN, 2,2'-azobis(2-methylpropionitrile); APS, ammonium persulfate; EGDMA, ethylene glycol dimethacrylate; HEMA, 2-hydroxyethyl methacrylate; MPC, 2-methacryloyloxyethyl phosphorylcholine.

4.4.1.5 Co-monomer concentration and types

Concentrations of MPC were altered from 4–24% w/w to manipulate the amount of water that could be held by the hydrogels, see **Table 4-8**. The change in MPC concentration was made up with the concentration of HEMA, such that MPC + HEMA formed ~99% w/w of the hydrogel. Other co-monomers were added in addition to MPC to determine their effect on aqueous permeability.

Table 4-8. Compositions of different pHEMA hydrogel films containing varying co-monomer types and concentrations prepared by free radical polymerisation.

Hydrogel	% HEMA	% MPC	% EMA	% HPMA	% VP	% PVP	% PC1059	% EGDMA	% AIBN	% H_2O
CM1	94.6	4.1	0.0	0.0	0.0	0.0	0.0	0.7	0.5	0.0
CM2	89.6	9.1	0.0	0.0	0.0	0.0	0.0	0.7	0.5	0.0
CM4	79.6	19.1	0.0	0.0	0.0	0.0	0.0	0.7	0.5	0.0
CM5	74.7	24.1	0.0	0.0	0.0	0.0	0.0	0.7	0.5	0.0
CM6	84.0	14.0	0.0	0.0	0.0	0.8	0.0	0.7	0.5	0.0
CM10	83.2	13.9	0.0	0.0	0.0	0.0	1.8	0.7	0.5	0.0
CM11	98.0	0.0	0.0	0.0	0.0	0.0	0.8	0.7	0.5	0.0
CM12	42.3	14.1	0.0	42.3	0.0	0.0	0.0	0.7	0.5	0.0
CM13	42.3	14.1	42.3	0.0	0.0	0.0	0.0	0.7	0.5	0.0
CM17	68.8	15.0	0.0	0.0	15.0	0.0	0.0	0.7	0.5	0.0
CM18	58.8	15.0	0.0	0.0	25.0	0.0	0.0	0.7	0.5	0.0
CM19	48.8	15.0	0.0	0.0	35.0	0.0	0.0	0.7	0.5	0.0
CM20	38.8	15.0	0.0	0.0	45.0	0.0	0.0	0.7	0.5	0.0
CM21	28.8	15.0	0.0	0.0	55.0	0.0	0.0	0.7	0.5	0.0

Components are reported in % w/w. HEMA mass was calculated using its density, 1.073 g mL^{-1}. EGDMA mass was calculated using its density, 1.051 g mL^{-1}. **Abbreviations:** AIBN, 2,2'-Azobis(2-methylpropionitrile); EGDMA, ethylene glycol dimethacrylate; EMA, ethyl methacrylate; HEMA, 2-hydroxyethyl methacrylate; HPMA, hydroxypropyl methacrylamide; MPC, 2-methacryloyloxyethyl phosphorylcholine; PC, phosphorylcholine; PVP, poly-n-vinyl pyrrolidone; VP, vinylpyrrolidone.

The addition of a highly hydrophilic, non-immunogenic polymer, 2-hydroxypropyl methacrylamide (HPMA) to HEMA in a 1:1 ratio was also investigated to increase the hydrophilic nature of the hydrogel. The addition of ethyl methacrylate (EMA) to HEMA in a 1:1 ratio was also investigated to introduce hydrophobicity to the hydrogels.

IPN and semi-IPN hydrogels with HEMA and poly-n-vinyl pyrrolidone (PVP) and 1-Vinyl-2-pyrrolidinone (VP) were also investigated to increase the macroscopic pores in the polymer network. To increase the porosity of the hydrogels, 20 mg of PVP was stirred in 1 mL of 1015 mixture to make semi-IPN hydrogels. Varying the ratios of VP:HEMA such as 15:69%, 25:59%, 35:49%, 45:39% and 55:39% w/w with a constant

concentration of 15% w/w MPC in the formulations to increase the pore size in the hydrogel structure was also investigated.

PC1059 is a proprietary PC-based polymer from Vertellus Biomaterials, which specialises in the synthesis PC polymers. PC1059 was added to hydrogel formulations with and without MPC to assess any effect on aqueous permeability.

4.4.1.6 Cross-linker concentrations

The concentration of EGDMA was altered to manipulate the number of cross-links in the 1015 hydrogel structure. PEGDMA of two different chain lengths (700 and 2000 M_n) was also investigated as a co-monomer the concentration of 0.7% w/w to form polymer chains with larger spaces between them, see **Table 4-9**.

Table 4-9. Compositions of different pHEMA hydrogel films with varying types and concentrations of cross-linkers prepared by free radical polymerisation.

Hydrogel	% HEMA	% MPC	% EGDMA	% PEGDMA 700	% PEGDMA 2000	% MBAM	% AIBN	% APS	% H_2O
CX1	85.0	14.2	0.4	0.0	0.0	0.0	0.5	0.0	0.0
CX2	84.0	14.0	1.5	0.0	0.0	0.0	0.5	0.0	0.0
CX3	79.4	13.3	6.9	0.0	0.0	0.0	0.5	0.0	0.0
CX4	84.7	14.1	0.0	0.7	0.0	0.0	0.5	0.0	0.0
CX5	84.7	14.1	0.0	0.0	0.7	0.0	0.5	0.0	0.0
CX6	84.9	14.2	0.0	0.0	0.0	0.4	0.5	0.0	0.0
CX7	84.0	14.0	0.0	0.0	0.0	1.5	0.5	0.0	0.0
CX10	79.9	13.3	2.1	0.0	0.0	0.0	4.6	0.0	0.0
CX11	85.4	14.2	0.2	0.0	0.0	0.0	0.2	0.0	0.0
CX13	29.9	0.0	0.5	0.0	0.0	0.0	0.0	0.5	64.2
CX15	29.7	2.5	0.5	0.0	0.0	0.5	0.0	0.5	66.3
CX16	29.9	5.0	0.0	0.0	0.0	2.5	0.0	0.5	62.2

Components are reported in % w/w. HEMA mass was calculated using its density, 1.073 g mL^{-1}. EGDMA mass was calculated using its density, 1.051 g mL^{-1}. **Abbreviations:** AIBN, 2,2′-Azobis(2-methylpropionitrile); APS, ammonium persulfate; EGDMA, ethylene glycol dimethacrylate; HEMA, 2-hydroxyethyl methacrylate; MBAM, N, N-methylenebisacrylamide; MPC, 2-methacryloyloxyethyl phosphorylcholine; PEGDMA, poly(ethylene glycol) dimethacrylate.

The addition of N, N-methylenebisacrylamide (MBAM) at 0.4%, 0.5%, 1.5%, and 2.5% w/w were also investigated (**Figure 4-6**) with the idea that the heterogeneous cross-linking densities formed by the use of more rigid MBAM (as compared with EGDMA) would result in micro-gels, enhancing the overall aqueous permeability of the hydrogel (751).

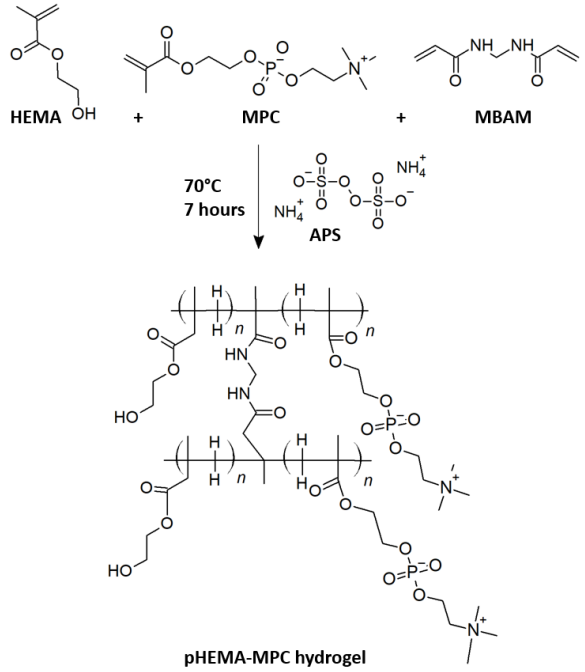

Figure 4-6. Chemical synthesis of pHEMA-MPC hydrogel films by free radical polymerisation. The monomer, HEMA, and co-monomer, MPC, were mixed with rigid cross-linker, MBAM, to form a clear solution. The water-soluble initiator, APS, was added, the formulation was degassed with argon and injected into the casting moulds, and was placed in the oven at 70°C for 7 hours. Figure was made using ACD's ChemSketch.

4.4.1.7 Initiator concentrations

The concentration of the thermal initiator from the 1015 formulation, AIBN, was altered from 0.5% to 0.2% and 1.0% w/w to manipulate the number of oligomers in the 1015 hydrogel structure, see **Table 4-10**. APS is a water-soluble oxidising agent used frequently in the synthesis of SDS-PAGE gels (in combination with Tetramethylethylenediamine). APS, while used in previous hydrogel formulations with large amounts of water present, was used to carry out a direct comparison with AIBN at the same concentration. For the formulation with APS, 100 µM of water was added to ensure it solubilised before degassing and injecting the formulation into the casting mould.

Table 4-10. Compositions of different pHEMA hydrogel films with varying types and concentrations of initiators prepared by free radical polymerisation.

Hydrogel	% HEMA	% MPC	% EGDMA	% AIBN	% APS	% H_2O
I1	84.9	14.1	0.7	0.2	0.0	0.0
I2	84.3	14.0	0.7	1.0	0.0	0.0
I3	82.9	13.9	0.7	0.0	0.5	2.0

Components are reported in % w/w. HEMA mass was calculated using its density, 1.073 g mL^{-1}. EGDMA mass was calculated using its density, 1.051 g mL^{-1}. **Abbreviations:** AIBN, 2,2'-Azobis(2-methylpropionitrile); APS, ammonium persulfate; EGDMA, ethylene glycol dimethacrylate; HEMA, 2-hydroxyethyl methacrylate; MPC, 2-methacryloyloxyethyl phosphorylcholine.

4.4.1.8 Addition of diluents

The addition of diluents before polymerisation to increase hydrogel permeability was also investigated. Phase separation occurs in pHEMA hydrogels with diluents at >60% w/w, forming macroporous structures and thus potentially increasing the aqueous permeability of hydrogels (752). Varying concentrations of t-butanol, glycerol, and tetrahydrofuran (THF) were added as diluents to the 1015 formulation before polymerisation would lead to phase separation, see **Table 4-11**.

Table 4-11. Compositions of different pHEMA hydrogel films containing added diluents and prepared by free radical polymerisation.

Hydrogel	% HEMA	% MPC	% VP	% EGDMA	% MBAM	% AIBN	% APS	% t-but	% THF	% GLY	% H_2O
D1	63.5	10.6	0.0	0.5	0.0	0.4	0.0	25.0	0.0	0.0	0.0
D2	42.3	7.1	0.0	0.4	0.0	0.2	0.0	50.0	0.0	0.0	0.0
D3	19.1	3.2	0.0	0.2	0.0	0.1	0.0	33.8	0.0	0.0	43.6
D4	39.1	7.6	0.0	0.4	0.0	0.3	0.0	0.0	0.0	52.7	0.0
D12	68.8	13.2	0.0	0.0	0.7	0.0	0.1	0.0	16.3	0.0	0.9
D14	46.1	8.8	0.0	0.0	0.4	0.0	0.1	0.0	43.9	0.0	0.6
D15	40.3	8.8	8.8	0.4	0.0	0.3	0.1	0.0	41.3	0.0	0.0
D16	34.4	8.8	14.7	0.4	0.0	0.3	0.0	0.0	41.4	0.0	0.0
D17	28.7	8.8	20.6	0.4	0.0	0.3	0.0	0.0	41.2	0.0	0.0
D20	24.6	8.2	24.6	0.4	0.0	0.3	0.0	0.0	41.8	0.0	0.0
D21	45.3	7.6	0.0	0.4	0.0	0.3	0.0	0.0	46.7	0.0	0.0

Components are reported in % w/w. HEMA mass was calculated using its density, 1.073 g mL^{-1}. EGDMA mass was calculated using its density, 1.051 g mL^{-1}. **Abbreviations:** AIBN, 2,2'-Azobis(2-methylpropionitrile); APS, ammonium persulfate; EGDMA, ethylene glycol dimethacrylate; EMA, ethyl methacrylate; GLY, glycerol; HEMA, 2-hydroxyethyl methacrylate; HPMA, hydroxypropyl methacrylamide; MBAM, N, N-methylenebisacrylamide; MPC, 2-methacryloyloxyethyl phosphorylcholine; PC, phosphorylcholine; t-but, t-butanol; THF, tetrahydrofuran; VP, vinylpyrrolidone.

THF was added to the 1015 formulation before polymerisation to final concentrations of 16.3% w/w (D12) and 43.9% w/w (D14), as well as added to a formulation without MPC (D21) to a final concentration of 46.7% w/w to create phase-separated hydrogels. Combining THF (~41% w/w final concentration) with varying ratios

of VP:HEMA, such as 8.8:40.3%, 14.7:34.4%, 20.6:28.7%, and 24.6:24.6% w/w, to dilute the co-monomer concentrations of semi-IPN hydrogels were also explored. Hydrogel preparations with THF were degassed with argon for 5 minutes rather than 10 minutes due to THF's volatility before being injected into the casting moulds.

4.4.1.9 Coating mesh with PC1059 polymer

Nylon mesh with average pore sizes of 1 µm and 0.2 µm were coated by dipping in a polymer solution of PC1059 (Vertellus biomaterials, UK), a non-cross-linked polymer used for coating blood processing devices. PC1059 (1.59 g) was dissolved in 10 mL of ethanol and diluted to the following concentrations: 30 mg mL^{-1}, 50 mg mL^{-1}, 75 mg mL^{-1}, 90 mg mL^{-1}, 100 mg mL^{-1}, and 110 mg mL^{-1}. The meshes were submerged in the polymer mixture and left to air dry (by hanging with binder clips) overnight. The coated mesh was fully hydrated for aqueous permeability analysis.

4.4.2 Introducing physical channels into the hydrogels

Because xerogels swell considerably when fully hydrated, an alternative approach to fabricate a pouch and tubing in hydrogels was explored. Two approaches were used to attempt to create physical channels in the pHEMA-MPC hydrogels: polymerisation around physical objects, and ablation using a femtosecond laser to create channels, pouches or holes in the hydrogel material.

The 1015 mixture was polymerised around physical spacers such as glass capillaries (outer diameter = 200 µm) and stainless steel wires (diameter = 120 µm) to fabricate tubes in the hydrogel. A stainless steel spatula with a thickness = 0.5 mm, width = 5 mm, and length = 2.5 cm was used as a physical spacer to create a pouch in the hydrogel. The xerogels (thickness 1 mm except for the xerogel that was moulded around the glass capillary, which was 2 mm in thickness) were fully hydrated to form hydrogels, and the physical spacers were gingerly removed before visual inspection, see **Figure 4-7**.

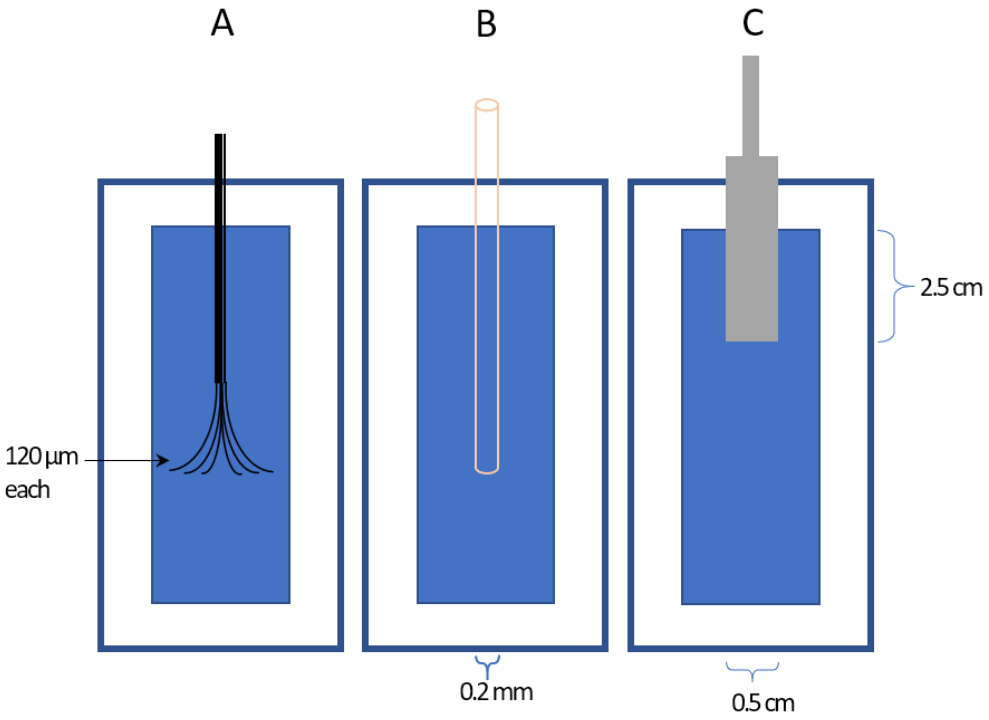

Figure 4-7. Schematic of the experimental design used for introducing physical channels into the hydrogels via the addition of spacers. **(A)** Stainless steel wires 120 µm in diameter, **(B)** a glass capillary 0.2 mm thick, and **(C)** a stainless steel spatula with 0.5 cm x 2.5 cm dimensions were inserted into the casting mould before injecting 1015 polymer mixture and placing in the oven to polymerise.

4.4.2.1 Using femtosecond laser augmentation to create pouches, holes and tubes

The unique characteristics of ultrafast lasers, such as ultra-short pulse widths and high peak intensities, allow for high precision and high-resolution materials processing. Ultrafast lasers that emit optical pulses with durations as low as picoseconds (10^{-12} s) and femtoseconds (10^{-15} s) have a smaller heat-affected zone (HAZ) than longer pulses

due to a reduced thermal diffusion around the processed areas, and this improves the quality of materials processing in terms of resolution (753–756).

A tuneable Titanium-Sapphire amplifier was utilised to produce 150 fs, 800 nm wavelength laser pulses (FAST Lab at the Optoelectronics Research Centre, Southampton, UK) in order to determine if creating physical channels in hydrogels was possible with laser augmentation. The pulses were spatially homogenized using a π-shaper model 6_6 to produce a 'top-hat' spatial intensity distribution. A variable neutral density filter was used to tune the laser power precision, and the exposure time was controlled by a mechanical shutter. A beam splitter was employed to split the input laser beam into two with a fixed intensity ratio in order to monitor the stability of the input laser power during fabrication. One of the split beams was monitored using a power meter, and an auto-correlator was used to evaluate the pulse duration (<8 femtoseconds). The second split beam was passed through a 50x de-magnification microscope objective lens (Mitutoyo, UK) to produce a tightly focused spot for ablation.

The sample was placed on a high-precision XYZ translation stage controlled by a computer for 3D translation. A dichroic mirror and a charge-coupled device camera connected to the computer were installed above the focusing lens, enabling the fabrication process to be monitored in real-time.

Pouch and hole fabrication tests were performed on a high-precision XYZ 3D translation stage which had a positional accuracy of ~1µm and 50 mm total travel in each direction. This allowed for precise control of the sample positioning. Hydrogel and xerogel samples were sandwiched between two glass sides and were held by the translation stage vertically, with the longest side of the sample perpendicular to the ground. This exposed the area for laser targeting at the edge of the glass slides. Several tests were performed on the xerogel and hydrogel samples using one pulse, five pulses, 10 pulses, and 50 pulses with a maximum energy of one mJ at a one kHz repetition rate.

A similar set-up as above was used for fabricating tubes using the femtosecond laser. The xerogel (0.5 mm thick) was sandwiched between two glass slides and positioned on the XYZ 3D stage laterally, with the longest side parallel to the ground. This allowed the thickness of the xerogel exposed to the laser beam at the edge of the glass slides.

4.4.3 Dynamic-flow approach to measure aqueous permeability

The purpose of the dynamic-flow approach was to measure the relationship between pressure and flow of the hydrogel samples when exposed to a decreasing pressure gradient in an aqueous environment (145). A pressure head, or a fluid exerting a known pressure, was applied to the hydrogel sample to instigate aqueous flow, and the fall in pressure was followed as a function of time.

The equations used for determining hydraulic conductivity are derived from first principles from measuring the porosity measurement of soils (748). A schematic representation of the apparatus used for the dynamic-flow analysis is shown in **Figure 4-9**. The analysis was based on D'Arcy's law, which is a constitutive equation describing the flow of fluid through porous media (757,758). It states that flow $\mathbf{F}$ is proportional to the applied pressure. Thus, for a membrane disc of radius $\mathbf{a}$ (m), flow per unit area is designated by;

$$\frac{\mathbf{F}}{\boldsymbol{\pi}\,\mathbf{a^2}} = \mathbf{L} \times \mathbf{P} \tag{4.1}$$

where $\mathbf{L}$ is the hydraulic conductivity of the membrane (in m s^{-1} Pa^{-1}) and $\mathbf{P}$ is the applied pressure (in Pa). Hydraulic conductivity, $\mathbf{L}$ is given by;

$$\mathbf{L} = -\frac{\mathbf{r^2}}{\mathbf{a^2}\ \mathrm{p}\ \mathbf{g}} \times \mathbf{G} \tag{4.2}$$

where $\boldsymbol{r}$ is the radius of the water column, p is the density of water (1000 Kg m^{-3}), $\mathbf{g}$ is the gravitational constant, 9.81 m s^{-2}, and gradient $\mathbf{G}$ (change in column height over time) can be obtained by linear regression. Then, experimental aqueous permeability, $\mathbf{K_e}$ (m^2 s^{-1} Pa^{-1}) is calculated using $\mathbf{L}$, such that;

$$\mathbf{K_e} = \mathbf{L} \times \mathbf{T} \tag{4.3}$$

where $\mathbf{T}$ is the thickness (in m). The following equation was used to calculate the optimal permeability (759);

$$\mathbf{K} = \frac{\mathbf{QT}}{\mathbf{\Delta PA}} \tag{4.4}$$

where $\mathbf{Q}$ is the flow rate (in m^3 s^{-1}), $\mathbf{\Delta P}$ is the equilibrium pressure in Pascal, $\mathbf{T}$ is the thickness of the sample (in m), and $\mathbf{A}$ is the area of the sample (in m^2) and is equal to πr^2. To calculate the optimal permeability of a healthy eye, $\mathbf{K_{optimal}}$, T = 1 mm = 1×10^{-3} m and A = 2 cm^2 = 2×10^{-4} m^2 with an estimated flow rate = 2 µL min^{-1} = 3.3×10^{-11} m^3 s^{-1} to maintain IOP at 10 mmHg. To simplify the experimental change

measured in permeability, the pressure of water applied was increased to 30 cm of water (22.5 mmHg). Therefore, $\mathbf{P}$, the pressure applied = 22.5 mmHg = 3000 Pa. By substituting these values into equation (4.4), the following value can be obtained for $\mathbf{K_{optimal}}$;

$$\mathbf{K_{optimal}} = \frac{(\mathbf{3.3 \times 10^{-11}\,\frac{m^3}{s}}) \times (\mathbf{1 \times 10^{-3}\ m})}{(\mathbf{3000\ Pa}) \times (\mathbf{2 \times 10^{-4}\ m^2}\ )} \qquad (4.5)$$

$$\mathbf{K_{optimal} = 5.56 \times 10^{-14}\ m^2\ s^{-1}\ Pa^{-1}}$$

4.4.4 Design of a flow chamber to assess hydrogel permeability

To assess aqueous permeability of the different candidate hydrogels, a two-part closed-top flow chamber (FC) that was modified from a Franz diffusion cell commonly used in skin permeation studies was designed to test the flux of water through the hydrogel samples. The FC was manufactured by Mr John Frost, UCL School of Pharmacy workshop. The FC was fabricated from clear cast acrylic rods and had a 16 mm internal diameter, which was theoretically small enough to fit in the eye (760–763). The two-part closed-top acrylic chamber was designed to reduce any error caused by evaporation of water, see **Figure 4-8**. Rubber O-rings were used in the FC to seal the hydrogel sample shut using three screws, and all junctions were secured using tie locks and thread sealing polytetrafluoroethylene (PTFE) tape to prevent micro-leaks. The bottom part of the FC contained a dedicated seat to place the hydrogel sample and prevent damage while sealing the FC. The depth of the seat was 2 mm, and a silicone washer was also placed

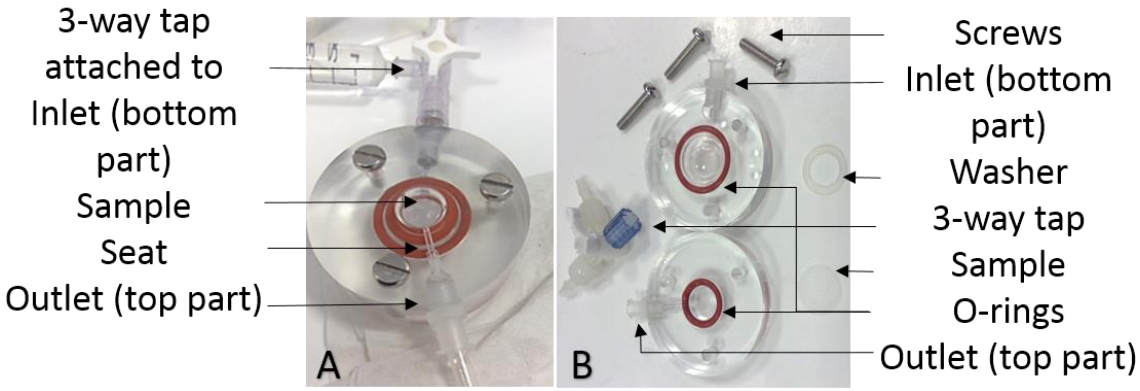

Figure 4-8. The two-piece closed-flow chamber that was used to test hydrogel discs for aqueous permeability is shown in use **(A)**, and the different parts of the chamber **(B)**. The design of the flow chamber was modified on the base of Franz cells' design, which is commonly used for skin permeation studies.

in the seat to make the total thickness (hydrogel + silicone washer) 2 mm, further preventing any micro-leaks. The bottom part of the FC also hosted an inlet that was eventually connected to a water column, and the top-part had an outlet that emptied into a water bath, as shown in **Figure 4-8**.

4.4.5 Aqueous permeability testing

Hydrogels samples were analysed for their aqueous permeability using the dynamic flow approach. To fit the dimensions of the FC, 16 mm diameter discs were punched out of the hydrogels using a custom-designed punch fabricated by Mr John Frost, UCL School of Pharmacy workshop.

A glass capillary with an internal diameter of 3.2 mm was connected to a Tygon connector tube with a cable tie and sealant. A 'tube to Luer' lock adapter was connected to the other end of the tubing with a cable tie and sealant. A three-way tap to the capillary tube was secured to the FC using a Luer to ¼–28 adapter (Sigma Aldrich, UK) and thread sealing PTFE tape. Inside the well of the FC, silicone washers were placed on either side of the sample to prevent mechanical damage to the sample's edges sample. The FC was filled up to the first washer with DI water, and the hydrogel disc was placed in the sample seat of the FC, followed by the second washer. The FC was submerged in a beaker containing DI water and then closed by screwing into position. This avoided trapping any air bubbles in the system. The FC was then transferred to a water bath with the outflow tube from the top part of the FC placed into a reservoir container, see **Figure 4-9.** The system used to apply a dynamic hydrostatic pressure across the hydrogel samples using a water column and the tube connecting it to the flow chamber kept in a water bath. The direction of flow of water is shown with navy blue arrows.

The glass capillary was filled to 30 cm (22.5 mmHg) above the height of the hydrogel disc (tubing and equipment included) with DI water, ensuring there were no air bubbles in the system. The system was allowed to stabilise for 15 minutes, and then the change in the height of the water column was recorded in millimetres after two hours to calculate the gradient, G (**Equation 4.2**). Using G, hydraulic conductivity (L) was calculated using **Equation 4.3**. **Equation 4.4** was then used to calculate experimental aqueous permeability (in $m^2/s/Pa$). Data were reported as the relative difference in aqueous permeability (K_{diff}), calculated as ($K_{experimental}/K_{optimal}$).

Validation of the test set-up was performed by using a 16 mm disc punched out of 1 mm and 0.5 mm thick impermeable silicone sheets. The discs were placed in the sample seat, and the drop in the height of the water column (in mm) was recorded over a testing period of two hours, during which, there was no change in the height of the water column. The set-up was left in place overnight. After 24 hours, the final permeability was considered negligible; there was a <1 mm drop in water column height due to water evaporation. This confirmed that FC was completely sealed and no water leaked.

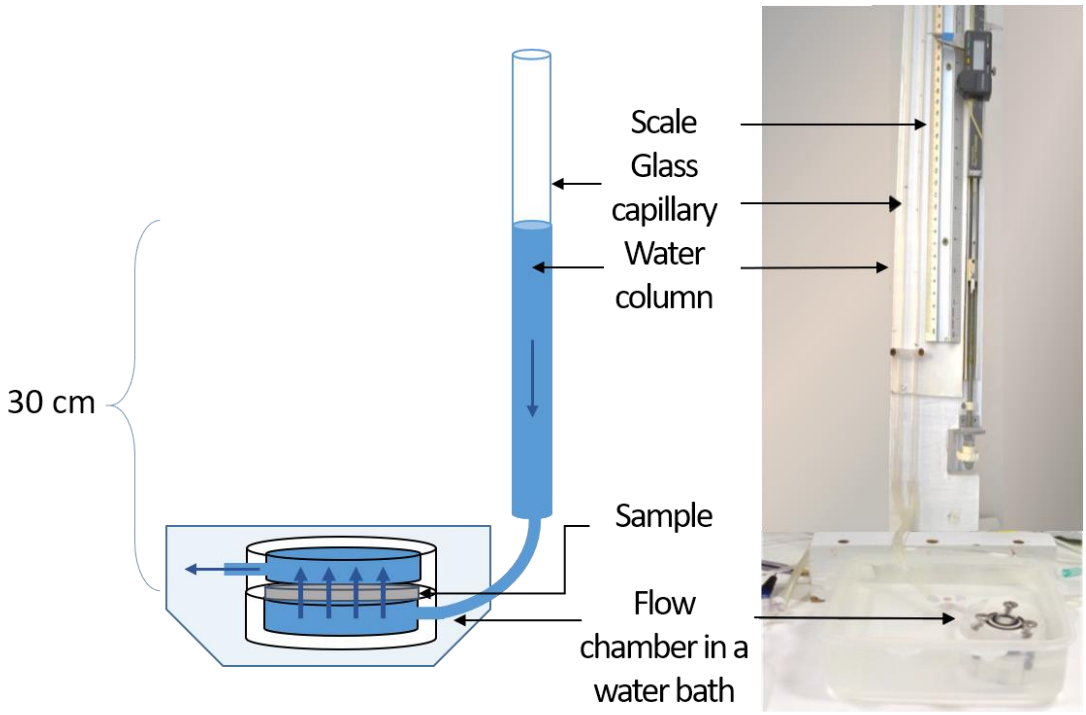

Figure 4-9. The system used to apply a dynamic hydrostatic pressure across the hydrogel samples using a water column and the tube connecting it to the flow chamber kept in a water bath. The direction of flow of water is shown with navy blue arrows.

4.4.6 Environmental scanning electron microscopy

Hydrogel samples were examined using environmental scanning electron microscopy (ESEM) Quanta TM Scanning Electron Microscopy (FEI Quanta200 FEGESEM, The Netherlands), which is maintained at the UCL School of Pharmacy. All ESEM imaging was carried out by Dr Clare Heaysman. The ESEM was operated at a pressure of 200 Pa in the chamber. Hydrogel samples were maintained at 5°C, creating a water-saturated environment in the specimen chamber at 200 Pa. In these conditions, no dehydration of

the samples occurred. Pieces of approximately 1 mm in size were cut from each sample using a scalpel, then were sprayed with DI water to avoid dehydration during the initial evacuation of the chamber. The acceleration potential used for imaging was 20 kV, and the working distance was 0.1–10 mm. No deterioration of the samples was noticed. Both top surface and cross-section specimens from each hydrogel were examined.

4.4.7 Characterising mechanical integrity of hydrogels

When evaluating the efficacy of biomaterials, the material cannot be divorced from the intended device, and it is recommended that the characterisation methods should be employed with the final intended application in mind (290). During GFS or implantation of GDD, the surgeon will push the implant into the subconjunctival space using surgical instruments such as forceps and clamps. For hydrogels to be used as biomaterials for device/implant development, they need to be mechanically resilient to withstand this clinical handling. In order to mimic the common handling procedures in the clinic (as advised during personal communication with Professor Sir Peng T. Khaw), a qualitative method was devised to rank the hydrogels for their mechanical resilience.

Hydrogel discs (16 mm in diameter), were cut 3 mm from the edges using a scalpel so that a 10 mm width remained, as shown in **Figure 4-10.** Special care was given to ensure the hydrogel samples were free from any visible cuts, slits or defects at the edges. Sample hydration during testing was maintained by soaking in 50 mL DI water between repeated tests. Hydrogel structural resilience to twisting, stretching and

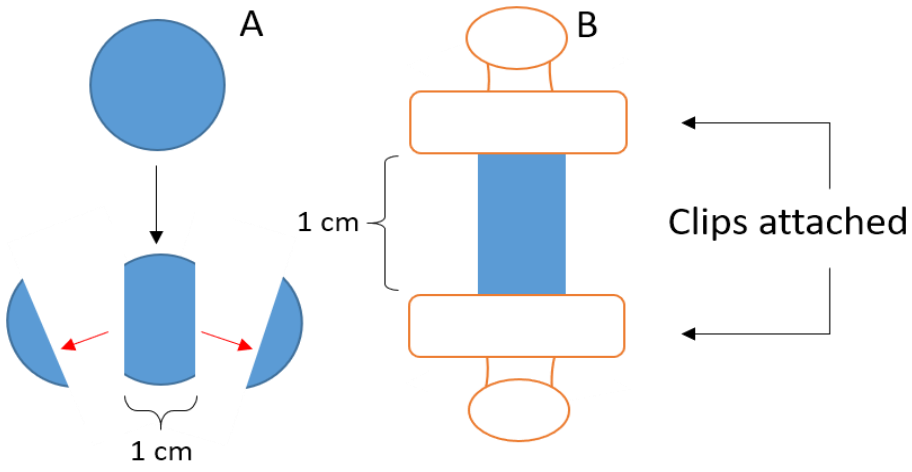

Figure 4-10. The hydrogel discs were cut 3 mm from the edges to obtain a disc sample with 1 cm width for mechanical testing **(A)**. For twisting and stretching tests, the samples were clamped on the top and bottom with binder clips **(B)**.

bending was tested. For twisting and stretching tests, the samples were attached on the top and bottom with large Bulldog binder clips. The edges of the clamping part of these binder clips were covered with anti-slip tape to avoid damaging and prevent slipping of hydrogel samples. The tests were done as described in the following subsections.

4.4.7.1 Folding (compression and tension)

The limits of hydrogel compression were tested by folding the hydrogel sample, so the short edges meet. The sample 'failed' the test if cracking or fracture was observed after manual-folding, see **Figure 4-11**. A grading system (0–3+) was created and applied to the hydrogel samples based on visual assessment of how well they could fold. Grading was assigned as follows: 1 = a single fold in both directions, so the ends meet; 2 = a single fold in both directions flattened with 50 g weight applied; 3 = double folds in both directions; 3+ = double folds in both directions flattened with 50 g weight applied.

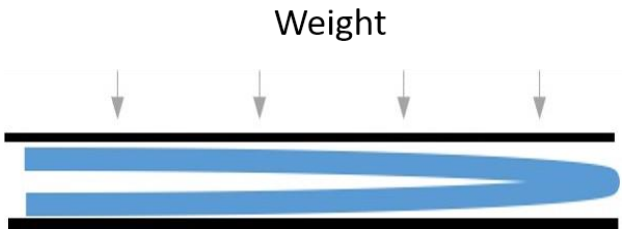

Figure 4-11. Hydrogel samples were folded so the sort edges would meet, sample would 'fail' the test if cracking or fracture was observed after manual folding.

4.4.7.2 Twisting (shear strength)

Twisting was performed by holding the hydrogel sample at both ends using a binder clip, leaving a 1 cm of hydrogel sample in between the clips to be tested, see **Figure 4-12**. The sample 'failed' the test if cracking or fractures were observed after

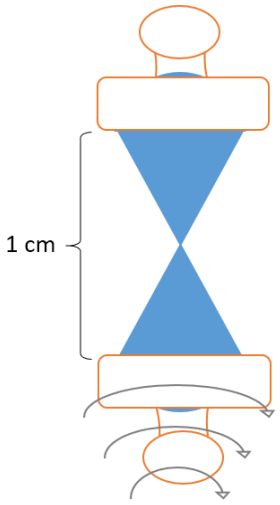

Figure 4-12. The twisting test was performed by holding the hydrogel sample at both ends using a binder clip, leaving a 1 cm of hydrogel sample in between the clips to be tested. The sample 'failed' the test if cracking or fractures were observed after manual twisting in both directions and returning to normal (untwisted) position.

manual twisting in both directions and returning to normal (untwisted) position. A grading system (0–3+) was applied to the hydrogel samples based on visual assessment. Grading was assigned as follows; 1 = 0–90° twist; 2 = 90–180° twist; 3 = 180–360° twist; 3+ = >360° twist.

4.4.7.3 Stretching (tensile strength)

Binder clips were weighed after covering the edges of their clamping part with anti-slip tape. One of the binder clips covered with tape and was fixed onto a stand to minimise movement during the test procedure. The top end of the disc was clamped 0.3 cm from the top edge, see **Figure 4-13.** Photograph of the experimental set-up used for tensile testing of the hydrogel samples. The sample 'failed' the test if cracking or fractures were observed under 50 g of weight applied to stretch the sample. In the same way, binder clips were attached to the bottom end of the disc, leaving about 1 cm x 1 cm area of the hydrogel visible. Additional clips were carefully attached to the bottom clip until the hydrogel film tore. Grading was done as follows: 1 = 0–50g of added weight; 2 = 50–100g of added weight; 3 = 100–150g of added weight. For reference, according

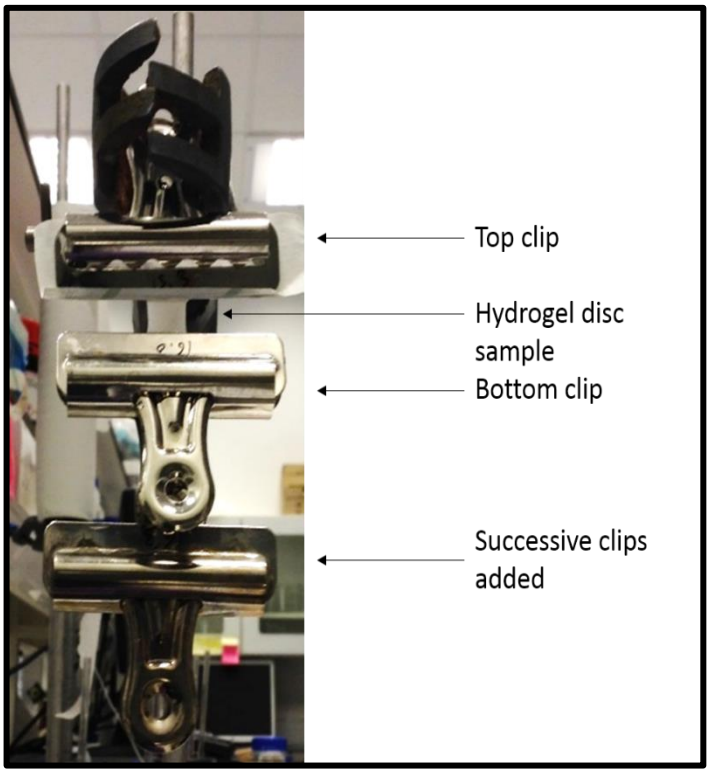

Figure 4-13. Photograph of the experimental set-up used for tensile testing of the hydrogel samples. The sample 'failed' the test if cracking or fractures were observed under 50 g of weight applied to stretch the sample.

to the FDA guidelines for the structural integrity of Aqueous Shunts (145), hydrogels scoring above one are considered to 'pass' the tensile test.

4.4.8 Statistical analysis

All results are presented as the average (arithmetic mean) and standard deviation (± SD) of at least three samples, and data were plotted using Origin Pro 2018 Academic (OriginLab, USA). For the analysis of variance, one-way ANOVA with Tukey's post hoc test was carried out to evaluate statistical differences between the mean values of experimental data. Probability value descriptive data were generated for all variables and values less than 0.05 ($p<0.05$) were considered as indicative of statistically significant differences.

4.5. Results

4.5.1 Assessing aqueous permeability of pHEMA-MPC hydrogels

pHEMA hydrogels were tested for their aqueous permeability based on manipulating the concentrations of components in hydrogel formulations. This involved varying the monomer concentration, polymerisation types, temperatures and durations, co-monomer concentrations and co-monomer types, cross-linker concentrations and cross-linker types, initiator concentrations and initiator types, as well as the addition of diluents to the hydrogels. Prior to the permeability experiments, the 16 mm hydrogel discs, as shown in **Figure 4-14**, were visually inspected for obvious physical artefacts such as pits, cracks and holes to avoid spurious results caused by these artefacts, and hydrogels that passed initial visual inspection were then subjected to aqueous permeability analysis. By substituting the physical dimensions of the hydrogel discs (radius = 8 mm, thickness = 1 mm) into the variables of **Equations 4.2–4.4**, the optimal permeability, K_o, was calculated. To effectively balance the physiological rate of aqueous humour production (at 2 µL min^{-1}), the K_o was calculated as 5.56×10^{-14} m^2 s^{-1} Pa^{-1} for a 1 mm thick hydrogel film.

Figure 4-14. For assessing the aqueous permeability of hydrogel films, discs of 16 mm diameter each were punched out, as shown here. Discs were then placed in the flow chamber (FC) with appropriately-sized silicone washers to ensure no leakage. A column of water of 30 cm was attached to the FC containing the disc and the drop in the column height was recorded over two hours to estimate the experimental permeability (K_e) of the hydrogel. All measurements were taken in triplicate.

4.5.1.1 1015 formulation

pHEMA hydrogels prepared using the Vertellus Biomaterials 1015 formulation for contact lenses were successfully reproduced, see **Figure 4-15**. The resulting hydrogels were transparent, soft and flexible. For the 1015 formulation, experimental

permeability (K_e) was determined as 8.90×10^{-15} $m^2 s^{-1} Pa^{-1}$ for a 1 mm thick film. Dividing this value by optimal permeability (K_o), yielded an average K_{diff} value of 0.16 ±0.07. Acuvue contact lenses (n=1) were also tested for permeability as a qualitative comparison, resulting in a K_{diff} value of 0.27. Even though the permeability values for the 1015 formulation are well documented (for contact lenses), to maintain the IOP at 10 mmHg by allowing transport of water at 2 µL min^{-1}, the 1015 did not meet the necessary aqueous permeability.

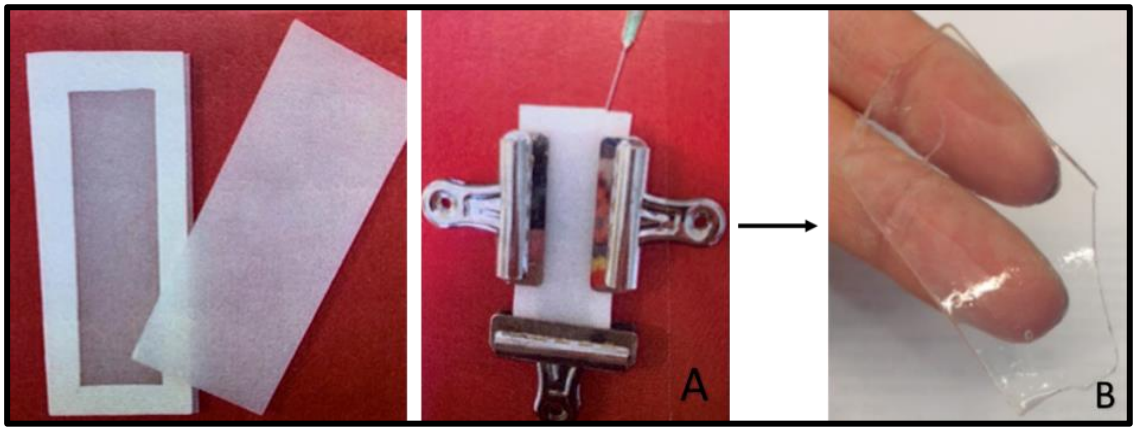

Figure 4-15. The hydrogel casting mould after injecting the 1015 polymer mixture **(A)** was made of two 3 mm thick polypropylene sheets, used to seal silicone gaskets around an empty cavity where the polymer mixture could be filled in using a syringe. After the polymerisation was complete, the xerogels were soaked in purified water to remove any unreacted monomer and to form a fully hydrated hydrogel **(B)**.

Measuring the equilibrium water content per cent (EWC%) and swelling ratio (SR) of the 1015 hydrogel films was important to understand the ability of the hydrogel to hold water and other solvents. In this study, EWC% and SR were quantified to understand if the method of hydration of xerogels produced was adequate. The 1015 films absorbed the maximum EWC% when soaked for 24 hours in PBS, 56.92 ±0.03% followed closely by water, 54.13 ±0.03%. The 1015 films when soaked for 24 hours in EtOH showed an EWC% of 16.73 ±0.06% but the standard 1015, when soaked in 9% saline, showed the maximum EWC of 49.3% at 6 hours but slightly decreased to 48.4% at 24 hours of soaking, see **Figure 4-16A**. 1015 films in water, PBS, and 9% saline show >90% equilibrium swelling after six hours, while films soaked in EtOH exhibited a much lower swelling and continue to swell for up to 24 hours, see **Figure 4-16B**. Chemical

modifications were made to the 1015 hydrogel composition in an attempt to improve aqueous permeability.

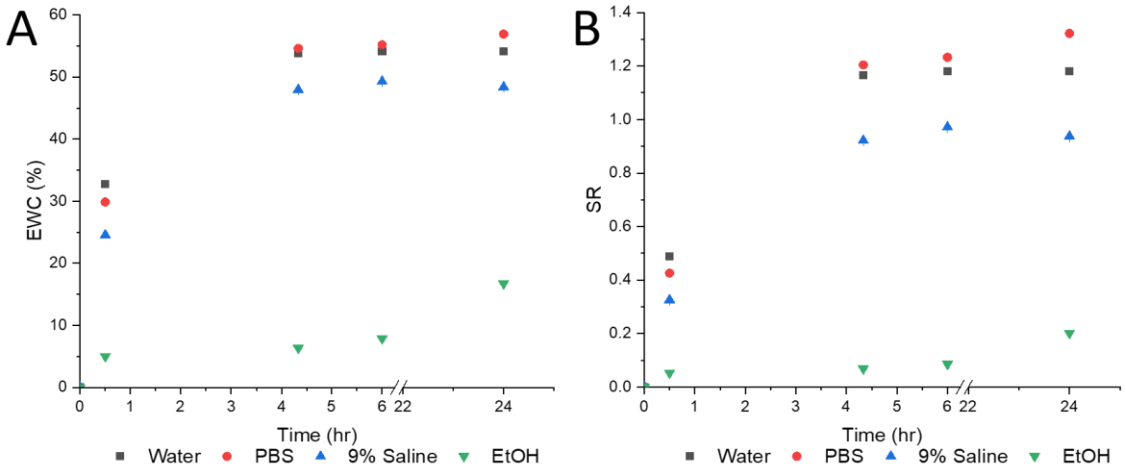

Figure 4-16. The effect of solvent on **(A)** EWC% and **(B)** swelling ratio (SR) of the 1015 hydrogel films. Samples in water, PBS, and 9% saline show >90% of their equilibrium swelling after six hours. 1015 films soaked in EtOH continued to swell for up to 24 hours

4.5.1.2 Effect of monomer concentration on aqueous permeability

Hydrogels with HEMA concentrations of 60% (M5), and 80% w/w (M4) resulted in transparent, flexible hydrogels similar to the 1015 hydrogels. Decreasing the concentration of HEMA to 30% w/w (M7) resulted in a translucent hydrogel. Further decreasing HEMA to 20% w/w (M9) resulted in a white and opaque hydrogel, indicating phase separation occurred during the polymerisation process, see **Figure 4-17**.

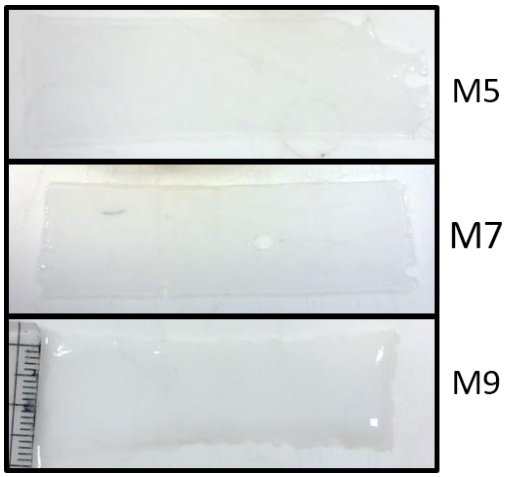

Figure 4-17. HEMA concentrations of 60% w/w (M5) resulted in transparent hydrogel films similar to 1015. Decreasing the concentration of HEMA to 30% w/w (M7) resulted in translucent and 20% w/w (M9) in opaque hydrogels, indicating phase separation during the polymerisation process.

Increasing the HEMA content to 91.7% w/w (M1) showed a decrease in relative aqueous permeability compared with the 1015; however, decreasing the concentration of HEMA to 79.6% w/w (M4) or 73.4% w/w (M3) resulted in no statistically significant ($p>0.05$) difference from M1, **Figure 4-18**. A formulation with 59.7% w/w HEMA (M5) showed a comparable K_{diff} value to the 1015 formulation, although there was a considerable variation between the replicates. Similarly, 30% w/w HEMA (M7) showed a slight improvement in aqueous permeability with a K_{diff} value of 0.34 ±0.06. This improvement was statistically significant ($p<0.05$) as compared with M1, M2, and M4. When the concentration of HEMA was decreased to 20% w/w, the resulting hydrogel (M9) exhibited a significantly ($p<0.05$) increased relative permeability with a K_{diff} value of 0.72 ±0.12, as compared with the rest of the hydrogels represented in **Figure 4-18**. This increased permeability to water flow was fairly close to the optimum permeability (K_{diff} = 1.0) required to modulate aqueous humour theoretically.

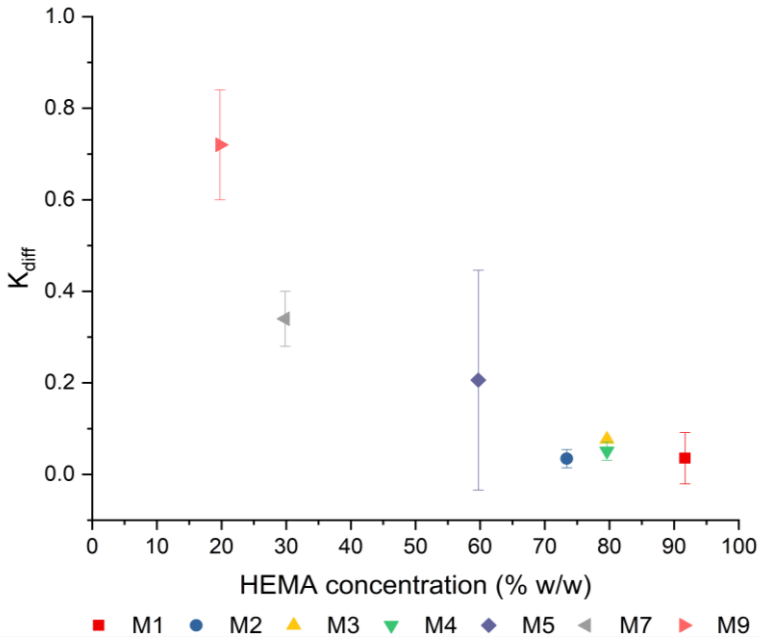

Figure 4-18. Relative aqueous permeabilities of pHEMA hydrogels with varying concentrations of HEMA monomer. (M1) contained 91.7% w/w HEMA, 7.7% MPC, 0.4% w/w EGDMA, 0.3% w/w AIBN; (M2) contained 73.4% w/w HEMA, 24.5% w/w MPC, 1.3% w/w EGDMA, and 0.9% w/w AIBN; (M3) contained 79.6% w/w HEMA, 0.5% w/w EGDMA, 19.4% w/w water, and 0.5% w/w AIBN; (M4) contained 79.6% w/w HEMA, 0.5% w/w EGDMA, 19.4% w/w water, and 0.5% w/w APS; (M5) contained 59.7% w/w HEMA, 0.5% w/w EGDMA, 39.3% w/w water, and 0.5% w/w APS; (M7) contained 30.3% w/w HEMA, 2.6% w/w MPC, 0.5% w/w EGDMA, 66.1% w/w water, and 0.5% w/w APS; (M9) contained 19.8% w/w HEMA, 0.7% w/w MPC, 0.5% w/w EGDMA, 78.5% w/w water, and 0.5% w/w APS. As the concentration of HEMA increased, the relative aqueous permeability generally decreased. pHEMA hydrogels could be synthesised containing approximately 20–92% w/w HEMA, and M9 20% w/w pHEMA hydrogels with mostly water yielded a K_{diff} value of 0.72 ±0.12. K_{diff} values are reported as mean ±SD.

4.5.1.3 Effect of curing conditions on aqueous permeability

The effect of different polymerisation temperatures using different concentrations of HEMA 30%, 40%, 50%, and 60% w/w on the relative aqueous permeability of the hydrogels was investigated. Formulations M19–M22 were cured at 40°C for 12 hours, but polymerisation was incomplete, resulting in sticky gels (not shown). Films M23–M26 cured at 40°C for 12 hours and then annealed at 120°C for 4 hours fully polymerised, but the resulting xerogels were coloured beige and had shrunk within the casting mould, see **Figure 4-19** for an example.

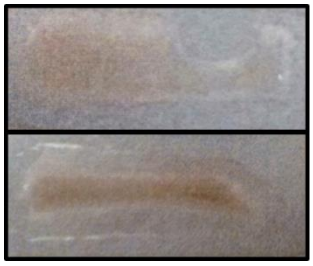

Figure 4-19. Xerogels containing 50% (M24) and 40% w/w HEMA (M25) cured for 40°C for 12 hours and then annealed at 120°C for 4 hours fully polymerised, but the resulting xerogels were coloured beige and had shrunk within the casting mould.

Films M27–M30 cured at 70°C for 7 hours successfully polymerised. M27 (60% w/w HEMA) resulted in a transparent xerogel, whereas M28–M30 (50–30% w/w HEMA) produced white xerogels, presumably due to phase separation that occurred as a result of high amounts of water present in the polymer mixture. Films M31–M34 cured at 50°C for 20 hours resulted in a transparent, flexible film (M31) and phase-separated, white films (M32–M34). M30 and M34 films were further characterised using ESEM to evaluate whether the appearance of hydrogels resulted in changes to the microstructures of the films. When fully hydrated, resulting hydrogels were transparent (M31), phase-separated to appear translucent (M32), and white hydrogels (M33), see **Figure 4-20**. Films M35–M38 cured at 50°C for 20 hours and at 90°C for 2 hours polymerised, but resulted in beige and shrunken films, which could be discolouration from the silicone washers, which also had a beige colour. When fully hydrated, resulting slightly beige hydrogels were transparent (M35), phase-separated to appear translucent (M36), and white hydrogels (M37), see **Figure 4-20**.

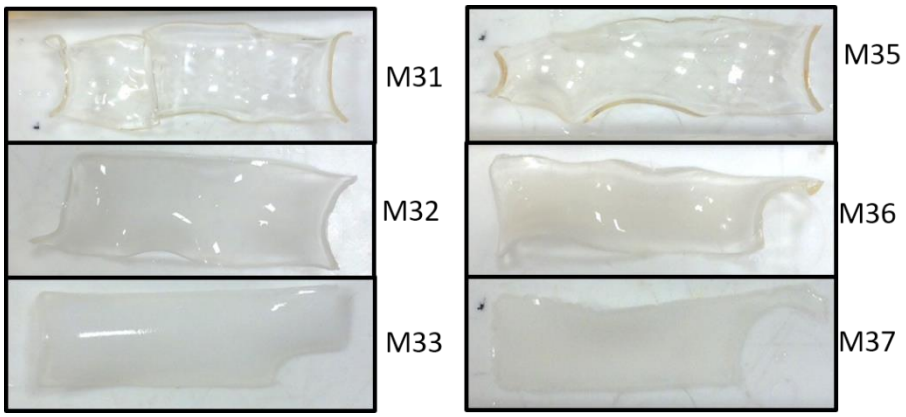

Figure 4-20. Hydrogels containing 60% (M31, M35), 50% (M32, M36) and 40% w/w HEMA (M33, M37), when cured at 50°C for 20 hours resulted in a transparent, film (M31) and phase separated, translucent (M32), and opaque films (M33). When cured at 50°C for 20 hours and then at 90°C for 2 hours, it resulted in slightly beige hydrogels, that were transparent (M35) and phase separated, translucent (M36), and opaque films (M37).

Finally, multiple curing cycles (*e.g.* increasing from 23°C to 70°C over 15 hours, then held at 70°C for 7 hours, then held at 120°C for 2 hours) resulted in transparent, bubbly xerogels, see **Table 4-12**.

Table 4-12. Effects of curing times and temperatures on polymerisation, xerogel appearance, and aqueous permeability. The polymerisation was assessed for completeness based on the visual appearance of the xerogels and how easily the xerogels could be removed from the casting moulds.

Hydrogel	Polymerisation competed?	Xerogel visual appearance	Permeability (K_{diff} ±SD)
M19	N	-	-
M20	N	-	-
M21	N	-	-
M22	N	-	-
M23	Y	Beige, shrunken films	n.d.
M24	Y	Beige, shrunken films	n.d.
M25	Y	Beige, shrunken films	n.d.
M26	Y	Beige, shrunken films	n.d.
M27	Y	Transparent film	n.d.
M28	Y	White film	n.d.
M29	Y	White film	n.d.
M30	Y	White film	n.d.
M31	Y	Transparent film	0.08 ±0.03
M32	Y	White film	0.10 ±0.04
M33	Y	White film	0.00 ±0.04
M34	Y	White film	n.d.
M35	Y	Slightly beige films	0.04 ±0.36
M36	Y	Slightly beige films	0.72 ±0.36
M37	Y	Slightly beige films	0.04 ±0.10
M38	Y	Slightly beige films	n.d.
M39	Y	Transparent film, with bubbles	0.04 ±0.06
M40	Y	Transparent film, with bubbles	0.04 ±0.06

M41	Y	Transparent film	n.d.

n.d. not determined. M23–M26 and M35–M38 did not punch evenly and were not tested for aqueous permeability. M30 and M34 films were further characterised using ESEM.

Overall, the transparent films tested resulted in low aqueous permeability, while there was high variability in the K_{diff} values of the beige, shrunken films. One of these films, M36, resulted in a K_{diff} of 0.72 ±0.36, but because the xerogel surface appeared uneven after polymerisation, it was possible that the hydrogel punching created an uneven disc that allowed more water to pass through the flow chamber during the aqueous permeability analysis.

Hydrogels M30 and M34 were further characterised using ESEM, see **Figure 4-21**, to evaluate whether the appearance of hydrogels resulted in changes to the microstructures of the films. M34 polymerised at a slower rate and a lower temperature (50°C for 20 hours) than M30, polymerised at 70°C for 7 hours. The surfaces of both 30% w/w HEMA hydrogels appeared as agglomerations of small particles at the same magnification; however, M30 seemed to have a smaller microstructure than M34, which suggests that curing conditions have an impact on hydrogel structure.

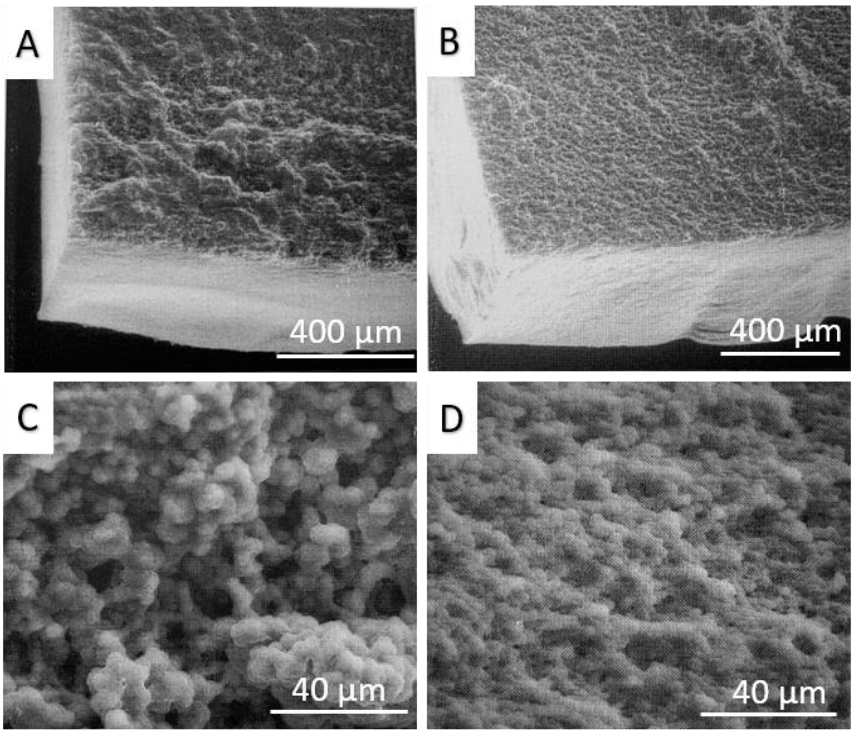

Figure 4-21. ESEM micrographs of M30 and M34 hydrogel films. (A & C) M34 was polymerised at a slower rate and at a lower temperature (50°C for 20 hours) than (B & D) M30, which was polymerised at 70°C for 7 hours. The surfaces of both 30% w/w HEMA hydrogels at 2,500x magnification (C & D) appeared as an agglomeration of small particles, however M30 seemed to have a smaller microstructure than M34.

The effects of UV curing on polymerisation and aqueous permeability were also explored. Industrial collaborator, Vertellus Biomaterials, supplied fully-hydrated films that were UV-cured at 60°C for 1 hour, see **Figure 4-22** and **Table 4-13.** Effects of UV curing for 1 hour at 60°C on polymerisation and aqueous permeability. Hydrogels discs were supplied pre-cut from industrial partner, Vertellus Biomaterials.

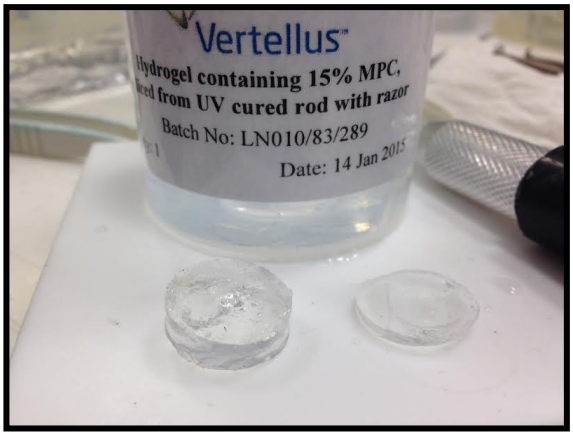

Figure 4-22. UV-polymerised 1015 hydrogels supplied by Vertellus Biomaterials.

There was no difference in the visual appearance between V1 (1015), V2 (60% w/w HEMA), or V3 (30% HEMA); however, V2 exhibited the best relative aqueous permeability, with a K_{diff} value of 0.45 ±0.09. The presence of 5% w/w MPC in a 30% w/w pHEMA hydrogel (V4) resulted in a transparent, glossy film. V5–V9 hydrogels were all 1015 formulations diluted with 60%, 70%, 80%, and 90% w/w DI water. Films V8 and V9 failed to polymerise. Vertellus reported that a significant increase in the energy involved in UV polymerisation was required to polymerise these more dilute hydrogel formulations. There was no significant difference in the relative aqueous permeabilities in the UV-cured hydrogels containing MPC, see **Table 4-13.**

Table 4-13. Effects of UV curing for 1 hour at 60°C on polymerisation and aqueous permeability. Hydrogels discs were supplied pre-cut from industrial partner, Vertellus Biomaterials.

Hydrogel	Polymerisation competed? (Y/N)	Hydrogel visual appearance	Permeability (K_{diff} ±SD)
V1	Y	Transparent film	0.07 ±0.06
V2	Y	Transparent film	0.45 ±0.09
V3	Y	Transparent film	0.13 ±0.04
V4	Y	Transparent, glossy film	0.20 ±0.08
V5	Y	Transparent, glossy film	0.13 ±0.10
V6	Y	Transparent, glossy film	0.14 ±0.08
V7	Y	Transparent, glossy film	0.14 ±0.02
V8	N	-	-
V9	N	-	-

4.5.1.4 Effect of co-monomer concentration on aqueous permeability

Varying the concentration of MPC from the 1015 formulation down to 4.1% and 9.1% w/w resulted in brittle xerogels and were clear and flexible when fully hydrated (not shown). Increasing the MPC concentration from 15% w/w to 19.1% and 24.1% w/w resulted in transparent, smooth, and glassy hydrogel films. Increasing the concentrations of MPC generally increased the average K_{diff} values, see **Figure 4-23**.

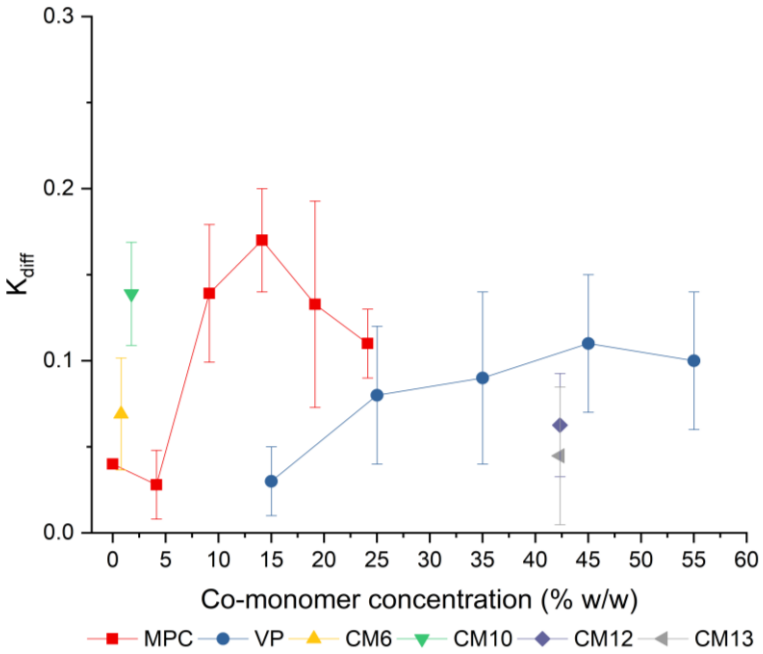

Figure 4-23. Relative aqueous permeabilities of pHEMA hydrogels with varying types and concentrations of co-monomers. The 1015 formulation was modified by (MPC) creating a gradient of 0–25% w/w MPC (red squares), (VP) adding a gradient of 15–55% VP (blue circles), (CM6) adding 0.8% w/w PVP, (CM10) adding 1.76% w/w of PC1059, (CM12) adding HPMA in a 1:1 HEMA:HPMA ratio, (CM13) adding EMA in a 1:1 HEMA:EMA ratio. Increasing the concentrations of MPC and VP generally increased K_{diff} values. Adding PC10159 to the 1015 formulation yielded the highest K_{diff} value compared to the additions of co-monomers, VP, HPMA, and EMA. K_{diff} values are reported as mean ±SD.

There was a significant difference ($p<0.05$) between hydrogels containing 4.1% and 9.1%, and 4.1% and 14.1% w/w MPC, an increase in relative aqueous permeability observed between these formulations. MPC concentrations >10% w/w resulted in no statistically significant ($p>0.05$) change between the films.

Hydrogel films composed of 15% (CM17), 25% (CM18) and 23% w/w VP (CM19) were transparent and glassy, see **Figure 4-24**. Hydrogels containing 45% w/w VP (CM20) were translucent, and 55% w/w VP-containing hydrogels (CM21) appeared fragile and opaque, requiring extra care to place in the flow chamber during analysis. Increasing concentrations of VP generally increased the average K_{diff} values; however, this trend was not statistically significant ($p>0.05$). Using PVP to form an IPN with components in

the 1015 formulation resulted in hydrogels that showed a statistically significant ($p<0.05$) decrease in permeability as compared with the 1015 formulation. The K_{diff} for 20 mg PVP (0.79% w/w)(CM6) dissolved in 1 mL of polymer mixture was found to be 0.07 ±0.03.

Figure 4-24. Hydrogel films composed of 15% (CM17), 25% (CM18) and 35% w/w VP (CM19) were transparent and glassy. Hydrogels containing 45% w/w VP (CM20) were translucent, and 55% w/w VP-containing hydrogels (CM21) appeared fragile and opaque.

The addition of other co-monomers did not improve the relative aqueous permeability either. Hydrogels containing HEMA:EMA::1:1 (CM13) showed virtually no permeation to water (K_{diff} = 0.04 ±0.04). In comparison, hydrogels with HPMA:HEMA::1:1 (CM12) showed a very slight increase in permeability (K_{diff} = 0.06 ±0.03), but again, this was not significantly different from the permeability of the 1015 formulation, suggesting that HPMA and EMA had a negligible effect on water permeation. Adding PC10159 to the 1015 formulation yielded the highest K_{diff} value (0.14 ±0.03) compared to the additions of other co-monomers. Not only did any of these hydrogels not meet the requirement for optimal permeability, but they also did not offer an improvement in relative aqueous permeability compared with the 1015 formulation.

4.5.1.5 Effect of cross-linker concentration on aqueous permeability

Increasing the amount of cross-linker EGDMA had no visual effect on xerogel or hydrogel appearance from 1015. Overall, increasing the concentration of EGDMA displayed a general increase in aqueous permeability, but only up until 1.46% w/w EGDMA, after which there were no changes observed in average relative aqueous permeability values, see **Figure 4-25**.

There was a slight decrease in hydrogel permeability from K_{diff} = 0.06 ±0.02 to K_{diff} = 0.04 ±0.02 with the cross-linker chain length increased using PEGDMA 700 g mol^{-1} (CX4) and PEGDMA 2000 g mol^{-1} (CX5), respectively, after 2 hours at 30 cm water pressure, see **Figure 4-25**. However, these differences in K_{diff} values were not statistically significant from one another or EGDMA at a similar concentration (p>0.05).

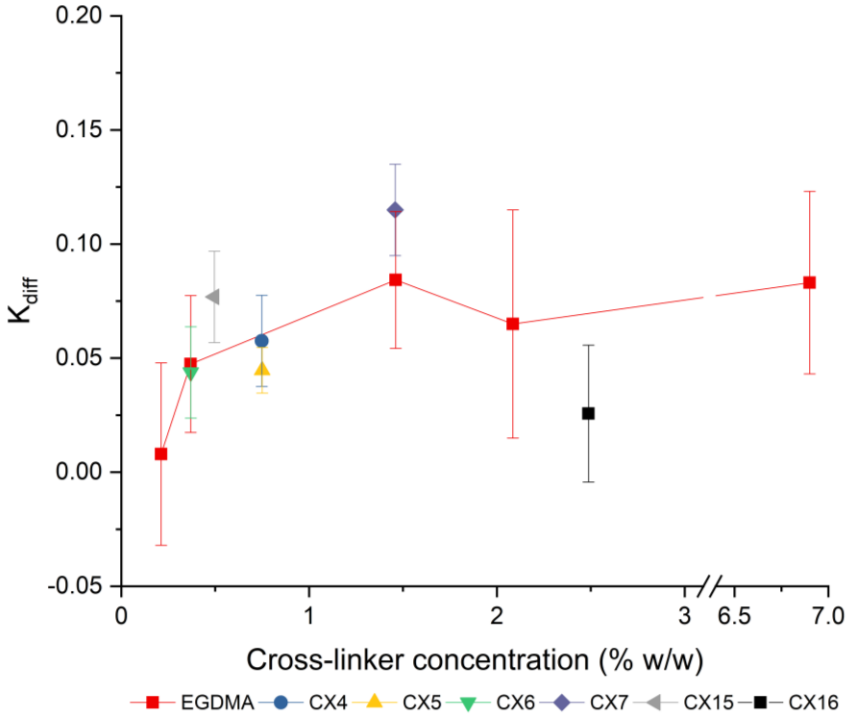

Figure 4-25. Relative aqueous permeabilities of pHEMA hydrogels with varying types and concentrations of cross-linkers. The 1015 formulation was modified by creating a gradient of 0.2–6.9% w/w EGDMA (red squares); (CX4) contained 84.7% w/w HEMA, 14.1 % w/w MPC, 0.75% w/w PEGDMA 700 g mol^{-1}, and 0.5% w/w AIBN; (CX5) contained 84.7% w/w HEMA, 14.1 % w/w MPC, 0.75% w/w PEGDMA 2000 g mol^{-1}, and 0.5% w/w AIBN; (CX6) contained 84.9% w/w HEMA, 14.2% w/w MPC, 0.4% w/w MBAM, and 0.5% w/w AIBN; (CX7) contained 84.0% w/w HEMA, 14.0% w/w MPC, 1.4% w/w MBAM, and 0.5% w/w AIBN; (CX15) contained 29.7% w/w HEMA, 2.5% w/w MPC, 0.5% w/w EGDMA, 0.5% w/w MBAM, 0.5% w/w APS and 66.3% w/w water; (CX16) contained 29.9% w/w HEMA, 5.0% w/w MPC, 2.5% w/w MBAM, 0.5% w/w APS and 62.2% w/w water. Changing the type and concentration of cross-linkers resulted in no significant change to relative aqueous permeability. K_{diff} values are reported as mean ±SD.

The addition of 0.37% w/w (CX6) and 1.46% w/w (CX7) MBAM replaced EGDMA in the 1015 formulation to form more rigid cross-linking was tested. There were no observable differences in the hydrogel films with MBAM compared with EGDMA (not shown). CX6 and CX7 resulted in K_{diff} values of 0.04 ±0.02 and 0.11 ±0.02, respectively which were not significantly (p>0.05) different to comparable to hydrogel formulations containing similar EGDMA concentrations. The addition of 0.5% w/w (CX15) and 2.5% w/w (CX16) MBAM with water, APS, and reduced concentrations of HEMA and MPC, resulted in hydrogels with K_{diff} values of 0.08 ±0.11 and 0.03 ±0.03, respectively.

Increasing the water content decreased the permeability of these hydrogels, but there was a wide variation in the test results. Despite all these changes, none of the hydrogels with MBAM as a cross-linker could statistically improve the aqueous permeability ($p>0.05$).

4.5.1.6 Effect of initiator concentration on aqueous permeability

The concentration of the thermal initiator AIBN was altered (0.25% w/w [I1] and 1% w/w [I2]) to manipulate the number of oligomers in the hydrogel structure. There was no statistically significant ($p>0.05$) difference in the K_{diff} values between these formulations, see **Figure 4-26**. A formulation with 0.5% w/w APS was created to compare with AIBN directly, and there was a slight but statistically insignificant ($p>0.05$) difference in relative aqueous permeability, which suggests that they are interchangeable as initiators in terms of water permeation through hydrogels.

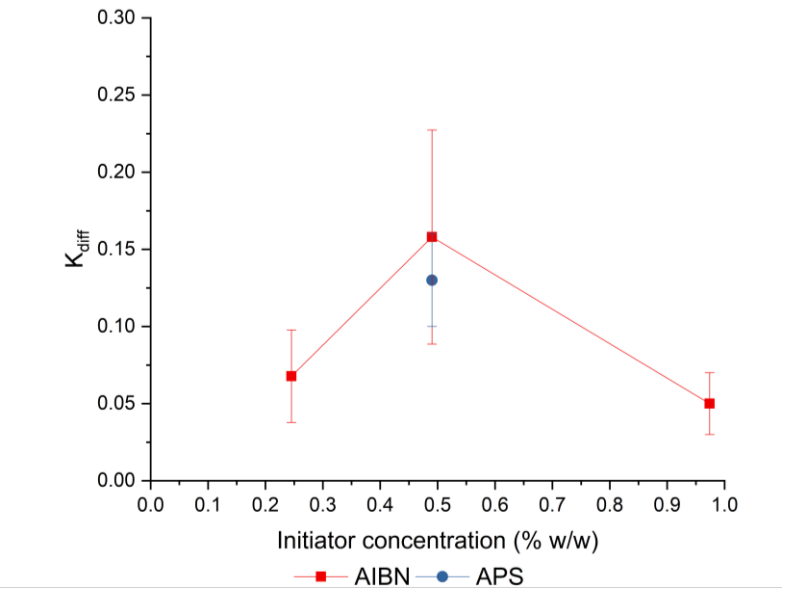

Figure 4-26. Relative aqueous permeabilities of pHEMA hydrogels with varying types and concentrations of initiators. The 1015 formulation was modified by creating a gradient of 0.25–1.0% w/w AIBN (red squares); and 0.5% w/w APS (blue circle) was used as an alternative initiator. Changing the type and concentration of initiators resulted in no change to relative aqueous permeability, except that 1% AIBN produced a more rigid, less-permeable hydrogel. K_{diff} values are reported as mean ±SD.

4.5.1.7 Effect of addition of diluents on aqueous permeability

Hydrogels with t-butanol, glycerol, and THF were used as diluents to the 1015 polymer mixture, formed hydrogels. Hydrogels with 25% (D1), 33.8% (D3), and 50% (D2) w/w t-butanol resulted in transparent, glassy films that curled and contained bubbles,

see **Table 4-14.** As the concentration of t-butanol increased, relative aqueous permeability values increased, see **Figure 4-27**. Despite this, the highest concentration of t-butanol tested (50% w/w) only reached a relative aqueous permeability value of 0.22 ±0.05, which was significantly ($p<0.05$) more than D1 and D3 but not significantly ($p>0.05$) more than the 1015.

Table 4-14. Hydrogel formulations that incorporated diluents in a fully hydrated state prior to permeability testing.

Hydrogel	Hydrogel film visual appearance	Diluent
D3		33.8% w/w t-butanol
D2		50% w/w t-butanol
D4		50% w/w glycerol
D14		43.9% w/w THF

Adding 50% glycerol (D4) produced hydrogel films that were similar to t-butanol-containing films in that they were transparent and glassy, but also fragile and curled. However, these films resulted in an average K_{diff} value of 0.09 ±0.02, only about 10% of the necessary permeability to theoretically control IOP. This value was significantly less than D12, D21 and D2 ($p<0.05$).

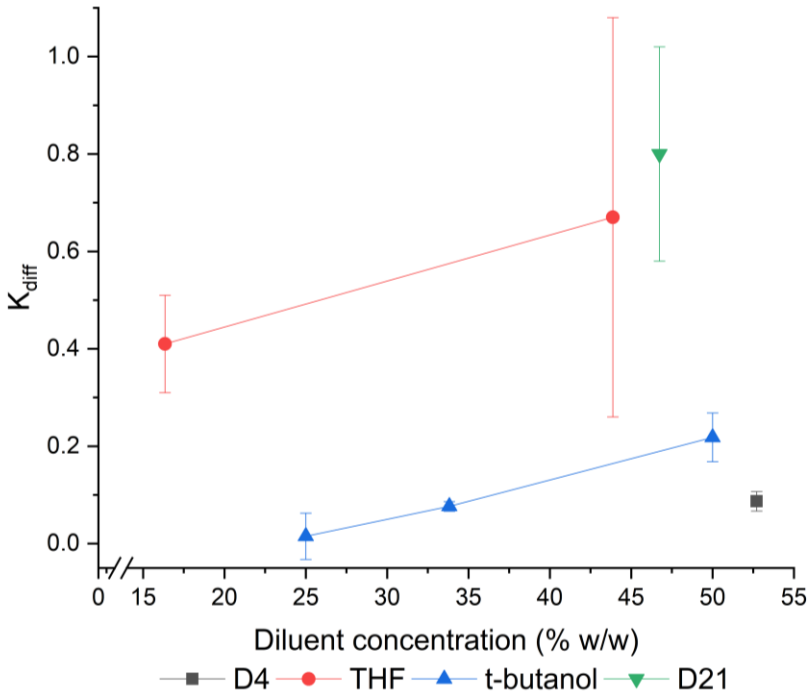

Figure 4-27. Relative aqueous permeabilities of pHEMA hydrogel with added diluents. The 1015 formulation was diluted by adding 25% w/w, 33.8% w/w, and 50% w/w of t-butanol (blue triangles); (D4) was diluted with glycerol (52.7% w/w); D12 and D14 (THF) were modified 1015 formulations that contained 46.2% and 68.8% w/w HEMA, 0.7% and 0.4% w/w MBAM cross-linker (instead of EGDMA), and 16.4% and 43.9% w/w THF (red circles); (D21) was 1015 formulation diluted with THF (46.7 % w/w final concentration). Further addition of THF (>50% w/w) created hydrogels that were extremely permeable to water. The addition of THF created hydrogels permeable to water close to the desired range, with an average K_{diff} value of 0.67. There was a slight increase in relative aqueous permeability as the concentration of t-butanol increased, but it was not significant. Glycerol did not increase the permeability. K_{diff} values are reported as mean ±SD.

The addition of THF (16.4% and 43.9% w/w in a final concentration of D12 and D14, respectively) to a modified 1015 formulation containing 0.7% and 0.4% w/w MBAM, and 0.11% and 0.07% w/w APS resulted in milky, phase-separated hydrogels that were fragile when handling. These hydrogel discs resulted in an average K_{diff} value of 0.41 ±0.1 and 0.67 ±0.41, which were significantly ($p<0.05$) more than K_{diff} values of hydrogels containing t-butanol and glycerol. Replacing MBAM with a similar concentration of EGDMA (D21) increased ($p>0.05$) the K_{diff} value to 0.8 ±0.22. THF was also used to dilute semi-IPN hydrogel films (D15–D20) that had a varying ratio of

VP:HEMA and a fixed concentration (~ 8% w/w final concentration) of MPC. Combining THF (~41% w/w final concentration) with VP:HEMA ratios of 8.8:40.3%, 14.7:34.4%, 20.6:28.7%, and 24.6:24.6% w/w (final concentrations) formed hydrogels with a gradual increase in opacity, see **Figure 4-28.**

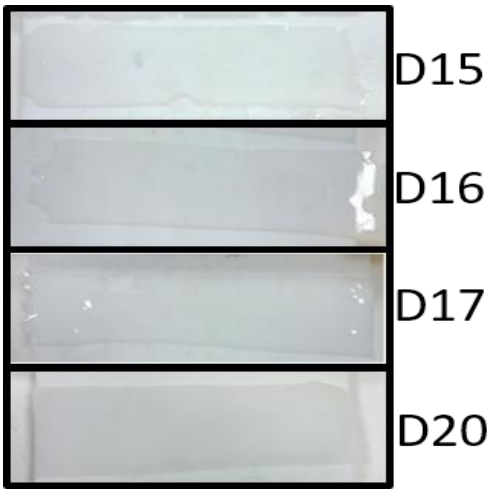

Figure 4-28. D15, D16, D17, D20. The addition of THF (~41% w/w final concentration) ratios of VP:HEMA ratios of 8.8%:40.3% (D15), 14.7%:34.4% (D16), 20.6%:28.7% (D17), and 24.6%:24.6% (D20) w/w final concentrations resulted in a gradual increase in opacity in the fully hydrated films as the concentration of VP increased, suggesting an increase in phase separation in the semi-IPN films.

The K_{diff} significantly ($p<0.05$) increased with increasing VP concentration and constant THF concentrations, resulting in values of 707.1 ±109.7, 1216.3 ±175.0, 9199.80 ±1182.8 for 8.8%, 14.7%, 20.6% w/w VP, respectively, see **Figure 4-29**. These

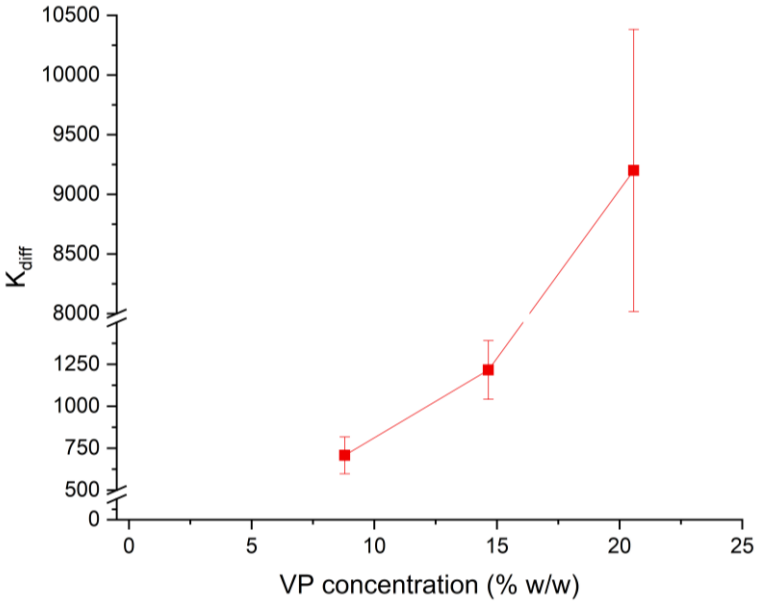

Figure 4-29. Relative aqueous permeabilities of pHEMA hydrogels with VP and THF. The 1015 formulation was modified by creating a gradient of 8.8–24.6% w/w (final concentration) VP and diluting the formulation with THF (~40% w/w final concentration) (red). Increasing the concentrations of VP resulted in increased K_{diff} values. K_{diff} values are reported as mean ±SD.

hydrogels were significantly ($p<0.05$) more permeable when compared to hydrogels that had no THF (CM17 and CM18), plotted in **Figure 4-24.**

4.5.1.8 Effect of coating nylon mesh with PC 1059 on aqueous permeability

Nylon meshes with 0.2 and 1 µm average pore sizes were coated with a range of concentrations of PC1059. These coated meshes, while not hydrogels, were subjected to aqueous permeability testing because they possessed rigid pores and were coated in a biocompatible polymer. There was a significant ($p<0.05$) decline in relative aqueous permeabilities as the concentration of PC1059 increased in the meshes with 0.2 µm pores, see **Figure 4-30**. However, the 1 µm-pores nylon mesh coated with 90, 100 and 110 mg mL^{-1} PC1059 provided some resistance to water flow, resulting in K_{diff} values of 11.68 ±0.38, 5.92 ±0.96 and 5.96 ±0.87, respectively, providing permeability that was at least 6-fold higher than required for IOP control (1)`. The difference in permeability between 100 and 110 mg mL^{-1} PC1059 coated was not statistically significant ($p>0.05$) but both were significantly less permeable than 90 mg mL^{-1} PC1059 coated ($p<0.05$).

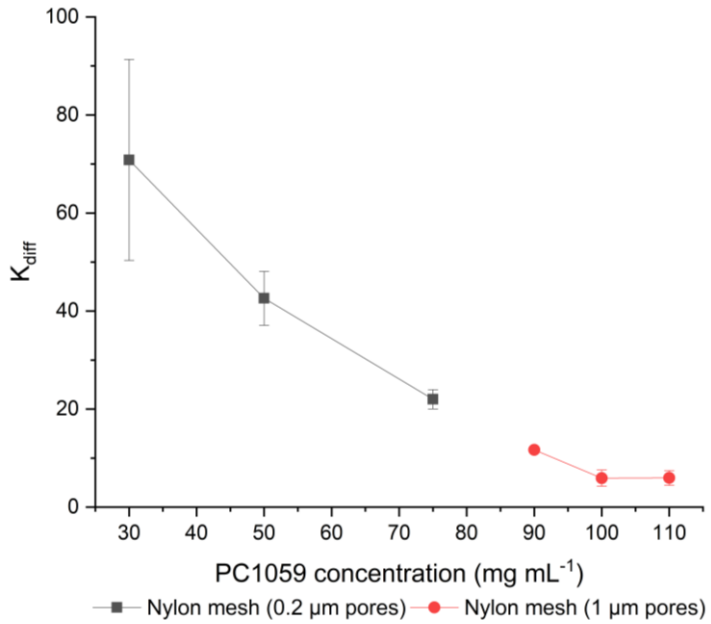

Figure 4-30. Relative aqueous permeabilities of nylon meshes with 0.2 µm (grey squares) and 1 µm (red circles) sized pores coated in different concentrations of PC1059 mixtures. The coated meshes exhibited large relative aqueous permeabilities compared with permeabilities observed with pHEMA hydrogels, and the relative aqueous permeability decreased as the concentration of PC1059 increased. K_{diff} values are reported as mean ±SD.

4.5.1.9 Further characterisation of most permeable hydrogel candidates

Of the hydrogel candidates, M9, D14, and D21 exhibited relative aqueous permeability values closest to the optimal aqueous permeability requirement (0.80 ±0.22 for D21, 0.72 ±0.12 for M9, and 0.67 ±0.41 for D14). Therefore, hydrogels M9 and D14 (D21 was not tested) were further characterised using ESEM to visualise the film microstructures. The ESEM micrographs are shown for a UV-cured 1015 hydrogel as a point of reference (**Figure 4-32**), for D14 (**Figure 4-31**), and M9 (**Figure 4-33**). There was a clear difference between the surfaces of 1015, D14, and M9 at high magnifications (100x and 250x). The 1015 hydrogel was smooth and gel-like with only blemishes present from preparing the sample using a scalpel. The surfaces of M9 and D14

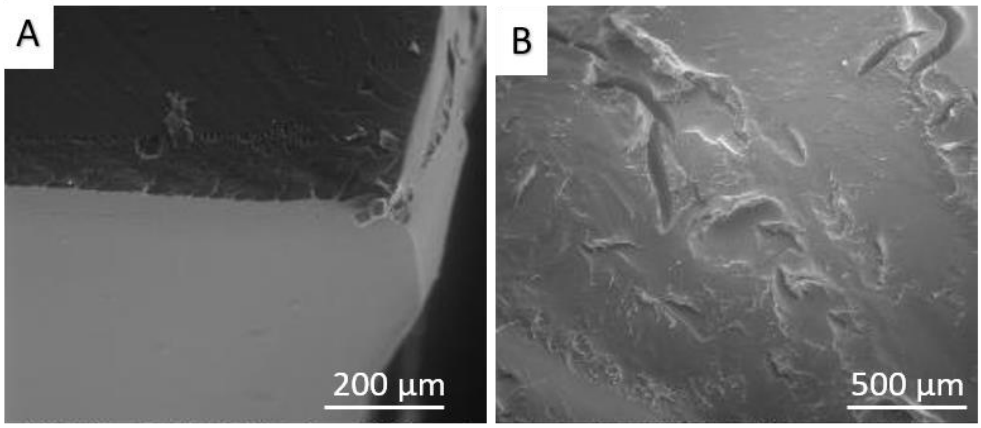

Figure 4-32. ESEM micrographs showing 1015 formulation hydrogel UV-cured for 1 hour at 60°C. **(A)** shows the surface of the cut corner of the hydrogel disc at 500x magnification, and **(B)** shows the surface at 100x magnification. The surface is smooth showing striations from being cut with a scalpel during sample preparation.

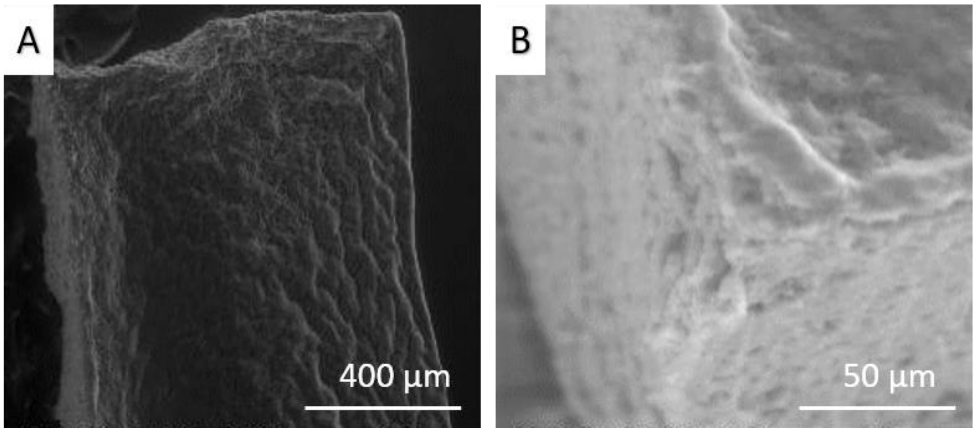

Figure 4-31. ESEM micrographs are shown of D14 (43.9% w/w THF, 46.2% w/w HEMA, 8.8% w/w MPC, 0.4% w/w MBAM, and 0.1% APS). **(A)** shows the surface area of the hydrogel at 250x magnification. **(B)** shows the structure at a corner cut with a scalpel to expose the internal microstructure at 1600x magnification. The surface is characterised by phase separation.

appeared to have a more complex microstructure, with small agglomerates as a result of phase separation. This microstructure appears to correlate with the opacity observed in the hydrogels.

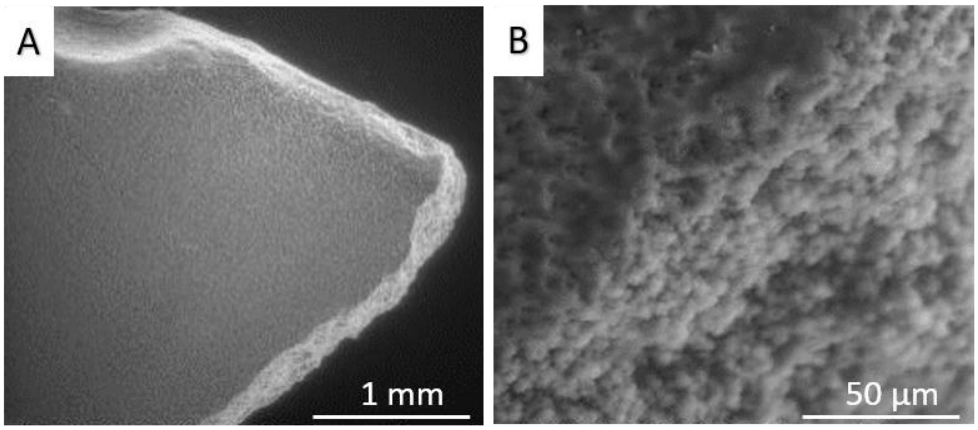

Figure 4-33. ESEM micrographs are shown of M9 (19.7% HEMA, 0.8% MPC, 0.5% w/w EGDMA, 0.5% w/w APS, and 78.5% w/w water). **(A)** shows a 100x magnification of the corner of the cut hydrogel. **(B)** shows the structure at the edge and surface of the film at 2000x magnification. The porous-like microstructure correlates with the opacity observed in the hydrogels.

4.5.2 Introducing physical channels to pHEMA hydrogels

4.5.2.1 Fabricating pHEMA hydrogels around physical spacers

As the results assessing relative aqueous permeability did not result in a clear candidate hydrogel formulation to pursue further, an alternative strategy to use hydrogels to control the aqueous flow that would not rely on the flow through the entire hydrogel film was explored. Physical spacers were placed in 1015 polymer mixtures before polymerisation to attempt to introduce physical channels that could be assessed for their control of aqueous permeability. After polymerisation, there was a clear discolouration around a stainless-steel wire in the xerogel suggesting that some oxidation of the metal occurred during polymerisation. This would be caused by the free radicals released by AIBN at 70°C. During hydration, the hydrogel completely split in half

near the entry point of the wires. Upon removal of the wires, clear channels could be seen, but parts of the hydrogel surface were completely damaged, see **Figure 4-34**.

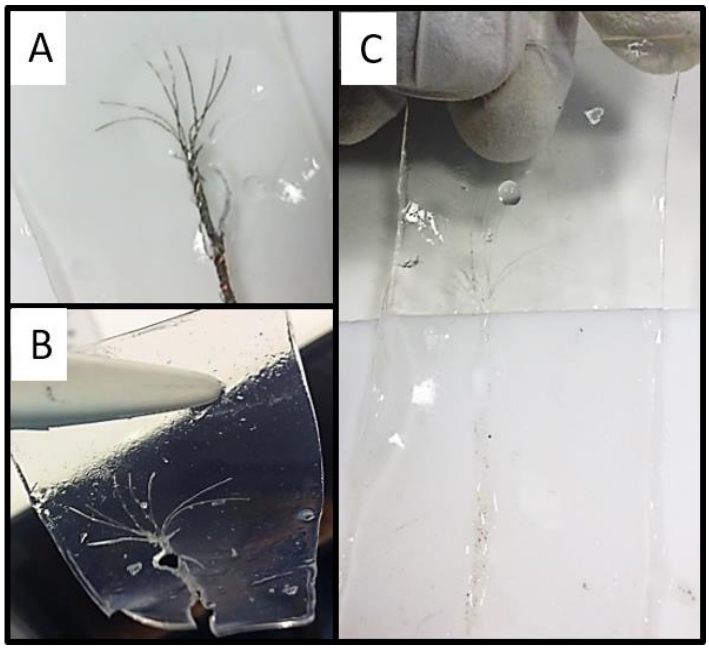

Figure 4-34. A standard 1015 xerogel was polymerised around **(A)** metal wires (diameter 120 µm) which were carefully pulled out of the hydrogel **(B)** causing visible damage at the entrance points **(C)**.

When 1015 xerogels polymerised around a different spacer material, a glass capillary, the capillary could be easily removed from the hydrogel. However, the newly formed tube space significantly compromised the mechanical strength of the hydrogel, causing it to tear during simple handling of the material (**Figure 4-35**). Another noteworthy observation was the opacity of this hydrogel. This could be attributed to partial polymerisation of the hydrogel. As previously mentioned, oxygen can inhibit the radical polymerisation of HEMA (444). As the capillary tube was polymerised within the

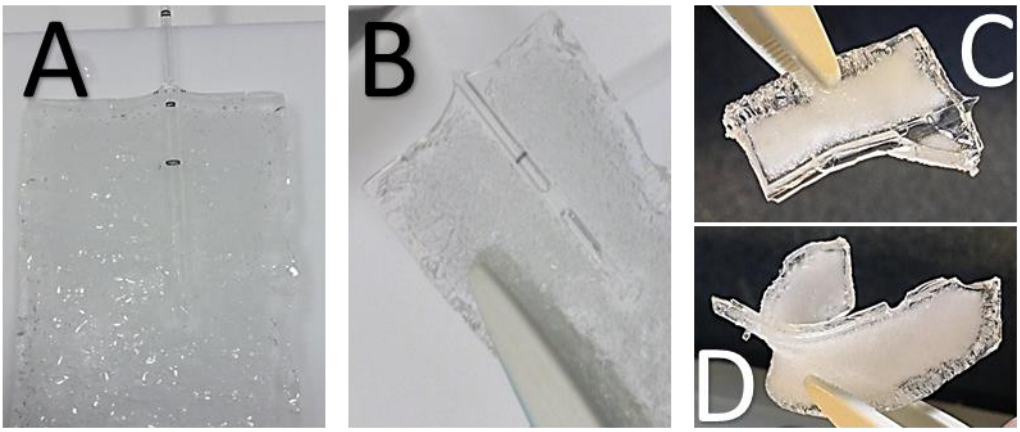

Figure 4-35. Standard 1015 was polymerised around glass capillaries **(A)** (outer diameter 100 µm), the capillary could be easily pulled out of the hydrogel **(B)** but the hydrogels were mechanically weak and tore apart even with gentle physical manipulation **(C, D)**.

hydrogel, it could have transferred reactive oxygen species that inhibited the polymerisation of HEMA.

A final attempt to introduce a physical spacer into the 1015 was with a 0.5 µm-thick stainless steel spatula. Once fully hydrated, the stainless steel spatula could be removed, leaving a 'pocket' in the hydrogel. However, this pocket was delicate and compromised the integrity of the hydrogel, causing it to tear at the entry site of the newly created pocket, see **Figure 4-36**.

Figure 4-36. Standard 1015 polymerised around a stainless steel spatula (thickness 0.5 µm, width 5 mm and; length 2.5 cm) formed a spacer that made the hydrogel mechanically weak and ripped during gentle physical handling of the hydrogel.

4.5.2.2 Femtosecond laser augmentation of pouches, holes or tubes

Femtosecond lasers were explored for the fabrication of pouches, tubes, and holes in 1015 hydrogels. The femtosecond laser was able to create a small (approximately 5 mm radius) irregular pouch in the xerogel without any visible damage to the surrounding xerogel surface. Upon hydration, this hydrogel surface above the pouch disintegrated, forming a pit in the hydrogel. This indicated that the laser was unable to create a pouch in the hydrogel, even though it might have appeared to do so in the xerogel. The significant difficulty in focussing the laser beam inside the xerogel prevented the formation of the pouch. Significant damage to the hydrogel surface was evident under the microscope.

Further, it was attempted to fabricate 50 µm diameter holes on a 0.5 mm in a 1015 xerogel. This was done to maintain the optimal aspect ratio that the laser could utilise for between the hole and the thickness of the xerogel, 1:10. Due to the low power setup of the standard femtolaser, only partial-thickness (superficial) holes were developed, see **Figure 4-38**. The diameter of the hole was about 63 µm, and reducing the diameter was not possible at lower wattages. Increasing the duration of the laser at

the same spot increased melting of the surrounding xerogel (**Figure 4-38A**) but did not make a full-thickness hole (**Figure 4-38B**).

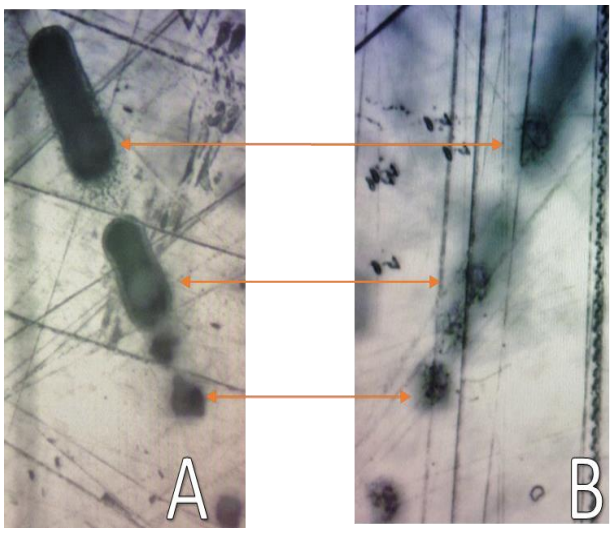

Figure 4-38. Holes made by increasing the duration of femtolaser at same spot (front **A** and back **B**).

An automated platform was used to create a trench instead of a hole, but the edges were tapered to 5 µm on either side of the processed area. It was also observed that debris splashed and stuck near the processed area, possibly due to the high temperature in the Heat-affect Zone (HAZ). The HAZ increased in size with the number of shots.

A single shot of the femtolaser fabricated a partial thickness hole with a diameter of 95 µm on the xerogel sample. Full-thickness holes seemed to be produced with 50 shots, but under a microscope, it was also confirmed to be superficial. Although proper holes (full thickness of the xerogel) were successfully fabricated using additional lenses, the holes were tapered, and fracture damage occurred at the other end of the hole, see **Figure 4-39**. Given the aspect ratio of the diameter of the hole (50 µm) versus the thickness of the material (0.5 mm), it is difficult to produce a non-tapered hole using this technique. Additional lenses were used to reduce the intensity of the laser to reduce the risk of fracture damage to the xerogel. Using the additional lens, fracture lines and the

diameter of the holes were reduced in the xerogel. The diameter of the hole was about 90 µm despite the reduced intensity.

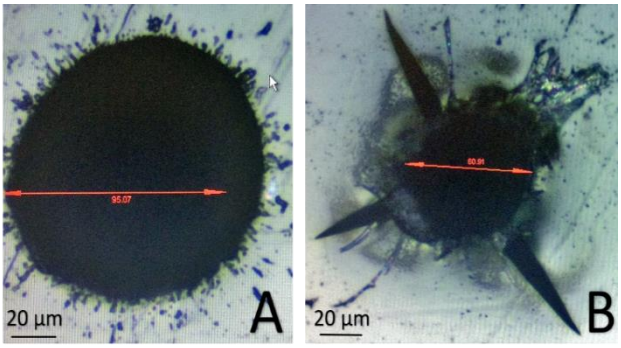

Figure 4-39. Hole formed by 50 shots using an additional lens **(A)**-front **(B)**-back showed visible damage to the xerogel. The scale bar is 20 µm.

Using the hydrogel material to form holes also helped to reduce the risk of fracture lines at the back of the hole, see **Figure 4-40**. This was due to improved heat distribution HAZ caused by the volatilisation of water in the hydrogels. This effect is commonly observed when processing biological tissues using lasers (764).

These results show that it was possible to create partial-thickness and full-thickness holes in hydrogel and xerogel states. Development of holes smaller than 50 µm proved challenging although further optimisation may be possible using varying lenses with different focal power and distance.

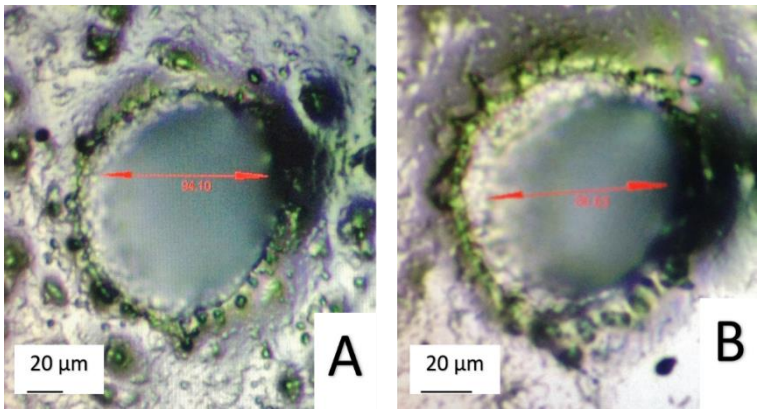

Figure 4-40. Holes created in hydrogels with reduced fractures due to improved heat distribution caused by volatilisation of water. The scale bar is 20 µm

Finally, it was not possible to create a uniform tube through a hydrogel and instead, a funnel with tapered edges was formed, as shown in **Figure 4-41**. The entrance appeared to be damaged although this may have been due to misalignment of the test apparatus. Developing a tube using the femtosecond laser was challenging and did not

provide uniform results. Achieving aspect ratios >100:1 is difficult and commercially not a feasible method to develop holes and tubes.

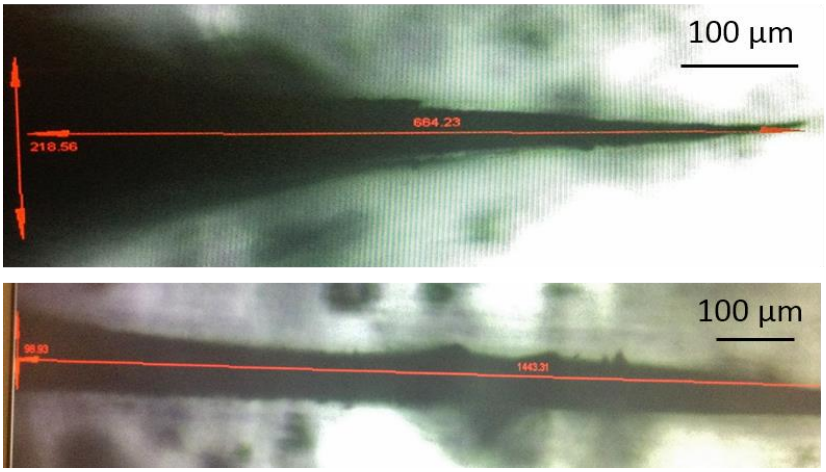

Figure 4-41. Tapered end of the tube in the xerogel with irregular interior. The scale bar is 100 µm.

The femtolaser works optimally with materials of a few hundred nanometers in thickness. Developing an accurate pocket could not be guaranteed in the case of xerogels, given that the material properties such as transparency may allow for light scattering and therefore affect the laser's cutting ability. While an opaque material would allow for better cutting ability, it would not be possible to fashion a pocket in an opaque material as the laser cannot focus inside the material for ablation. These above results indicate that while it might be possible to make holes in the hydrogel using a femtolaser, it is not the optimal method in terms of feasibility and practicality. Given this above findings, no permeability tests were undertaken to test the permeability through laser augmented hydrogels.

4.5.3 Mechanical integrity characterisation

Because part of the rationale behind this experimental work included clinical input, a protocol for mechanical testing of hydrogel samples was devised for rapid preliminary measurement of the structural integrity of hydrogels. As shown previously, changing the concentration and types of monomers, co-monomers and diluents resulted in noticeable physical changes in the hydrogels. A typical 1015 xerogel was clear and physically resembled an acrylic sheet. The xerogel was fully hydrated to form a hydrogel before subjecting to mechanical integrity measurements. Visually, the 1015 hydrogels resembled soft contact lenses, and they also resembled contact lenses in their

durability, as they were delicate and easily prone to tearing. The 1015 formulation failed all three tests for mechanical integrity and endured “grade 2” folding and twisting and <16 g of weight in the stretching test, see **Table 4-15**. 1015, therefore, failed the qualitative mechanical integrity grading system and was too weak to be suitable for further development. UV polymerisation of 1015 (V1) offered no improvement over heat polymerisation (1015).

Table 4-15. Results from the mechanical integrity characterisation of hydrogels.

Hydrogel	Folding (0-3+)	Twisting (0-3+)	Stretching (g)
1015	Fail (2)	Fail (2)	Fail (<16 g)
V1	Fail (1)	Fail (1)	Fail (<32.3 g)
M33	Pass	Pass	Fail (<16 g)
M32	Pass	Pass	Pass (60.8 g)
M31	Pass	Pass	Pass (88.5 g)
M9	Fail (3)	Fail (2)	Fail <49 g)
CM1	Fail (3)	Fail (2)	Fail (<49 g)
CM2	Fail (2)	Fail (2)	Fail (<32.3 g)
CM4	Fail (3)	Fail (2)	Fail (<16 g)
CX7	Fail (2)	Fail (2)	Fail (<16 g)
CX5	Fail (3)	Pass	Pass (60.8 g)
CX4	Fail (3)	Fail (3)	Pass (60.8 g)
I2	Fail (2)	Fail (1)	Fail (<16 g)
D12	Fail (2)	Fail (1)	Fail (<16 g)
D14	Fail (2)	Fail (1)	Fail (<16 g)
D15	Fail (3)	Fail (1)	Fail (<16 g)
D16	Fail (2)	Fail (1)	Fail (<16 g)
D17	Fail (2)	Fail (1)	Fail (<16 g)
D20	Fail (1)	Fail (1)	Fail (<16 g)

Grades refer to the point of failure of the films. “Pass” refers to a grade of “3+” for the folding and twisting tests and >50 grams for the stretching test.

However, longer curing durations at lower temperatures than required in the 1015 procedure resulted in much more mechanically-resilient hydrogels. M31–M33 films passed the folding test and twisting test, while M31 and M32 passed the stretching test, see **Table 4-15**. These films also contained a reduced amount of HEMA and higher amounts of water from the 1015 formulation; 40%, 50% and 60% w/w HEMA for M33, M32, and M31, respectively.

The concentration of MPC had an impact on mechanical integrity. Higher amounts of MPC resulted in weaker hydrogels. For example, CM2 (10% w/w MPC) was able to withstand less weight in the stretching test than CM1 (5% w/w MPC) or M9 (0.7 % w/w MPC). This correlates with the mechanical integrity of the 1015 formulation, which contains 14–15% w/w MPC. M9, which was one of the hydrogels close to optimal

aqueous permeability, failed all three tests, indicating it was too fragile for the type of clinical handling required for a GDD.

The highest concentration of EGDMA tested (6.7% w/w) also failed all three tests to similar grades as the 1015 formulation. However, PEGDMA 700 g mol^{-1} (CX4) and 2000 g mol^{-1} (CX5) displayed more mechanical resilience, passing the stretching test. Additionally, CX5 passed the twisting test, showcasing superior flexibility to CX4. No improvement was observed in hydrogel mechanical integrity when the concentration of AIBN was doubled. D12, which was the other hydrogel formulation that revealed a relative aqueous permeability near to the theoretical optimum, also failed all three tests. Semi-IPN hydrogels containing VP and THF (D12–D20) failed all three mechanical tests as well, indicating that THF decreases the mechanical strength of the hydrogels. It seems that there was a slight trend among these films, that with an increase in VP (THF was held constant), but the point of failure for folding tests decreased, and the hydrogel samples failed each of the tests.

Finally, all coated mesh samples passed the qualitative mechanical integrity grading system.

4.6. Discussion

Poor biocompatibility and inadequate aqueous flow control remain the most significant challenges faced in GDD development. The two mechanisms for flow control in current GDDs is either by diffusion through a fibrovascular capsule around the end plate or through a pressure-controlled valve. In this Chapter, a novel mechanism for aqueous flow modulation and IOP management using known biocompatible hydrogel materials was proposed. The main rationale for investigating hydrogels as a candidate material for flow modulation was based on work done by previous students in the Brocchini research group; one that showed the similarity between the internal structures of pHEMA-MPC hydrogels and a healthy trabecular meshwork, and another that demonstrated that a commercially available pHEMA contact lens did not elicit a fibrotic response in rabbit eyes. It was then hypothesised that by varying the components of pHEMA-MPC hydrogel formulations, optimal permeability to maintain IOP in healthy range would be achievable. As compared to the materials that are currently used in most GDDs, *i.e.* silicone and polypropylene, hydrogels may display better biocompatibility. Using the 1015 formulation as a starting point, the components of pHEMA hydrogels were manipulated before polymerisation. Because it was clear at the outset what the capacity for water flow was for hydrogels, so for hydrogels that polymerised were then subjected to testing for aqueous permeability and mechanical integrity. Discussion of the permeability and mechanical testing methods and best-performing hydrogels will be given first, followed by a discussion of the categorical changes made to the hydrogel formulations.

4.6.1 Permeability testing

Permeability testing was conducted on all hydrogel samples using an *in vitro* test that mimicked the pressure and flow conditions of the subconjunctiva, and permeability reflects the transport characteristics of water through a material. Initially, a two-part open-top acrylic chamber was designed based on Franz cells that are commonly used to assess drug diffusion in skin permeation studies (765). However, preliminary testing revealed a significant drawback of this open-top chamber in that there was enormous variation in the permeability data for similar samples tested on different days. This variation was likely due to evaporation and the absence of a dedicated seat for the

hydrogel sample. Since this chamber did not actually mimic the physiological conditions of the subconjunctival space (where the hydrogel would not be exposed to air), an improved closed-top flow chamber was designed with a seat for the hydrogel sample to be placed during testing without damaging the hydrogel and without any evaporation occurring. This flow chamber did not leak and showed less variability and was thus used in the permeability studies.

The FDA Aqueous shunt 501(k) guidance was published in 1998 and is a document that refers to devices intended to reduce IOP in patients with glaucoma when medical or surgical treatments have failed (145). The guidance is structured around recommendations for appropriate pre-clinical testing, such as pressure/flow characteristics, structural integrity, biocompatibility, and quality assessment, as well as recommendations for clinical testing, packaging, and labelling. The guidance outlines approaches for testing the flow characteristics of a GDD *in vitro*, with the caveat that the pressure/flow characteristics should be "substantially equivalent to that of a predicate device" (145). Predicate devices include Molteno®, Ahmed®, Baerveldt®, and Krupin. One of the approaches for characterising aqueous flow is the constant flow test, which evaluates the pressure versus flow characteristics of the device when exposed to a constant flow rate (mimicking the physiological flow rate of aqueous production of 2 µL min^{-1} in the eye) in an aqueous environment (145).

Following this guidance, a constant flow system was initially used to determine the aqueous permeability of hydrogel samples. A three-way tap was used to connect the sample holder, the flow rate controller, and the transducer that was attached to a laptop with a software (Velleman, UK) to measure the pressure, see **Figure 4-42**. When the flow rate controller was fixed at a specific rate, the change in pressure was recorded with respect to time, and the calibration curve for the transducer was calculated. Once the flow control apparatus was fixed at a specific flow rate, readings from the transducer were monitored over time. Some publications utilise a syringe pump and pressure transducer to record similar data (766–768), but it was not possible to obtain any meaningful results using the fixed-flow approach as the permeability of the hydrogels was too low to match the 2 µL min^{-1} flow used for the tests. The pressure transducer would saturate the upper limit of pressure detection and eventually, the hydrogel disc would rupture.

The constant flow method required pressures greater than what is normally expected in the anterior chamber of the eye, and for these reasons, it was decided to continue testing the aqueous permeability of the hydrogels using only the dynamic approach (glass column method). In this method, a pressure head using a column of water was applied to the sample to activate flow and the fall in pressure is followed as a function of time. Also, by calculating the theoretical permeability value for water flow through hydrogels, the opening pressure of a valved GDD could be obtained from this test method (145). A similar method has been used to determine the changes in hydraulic conductivity of human Bruch's membrane in the eye with age to correlate how these changes contribute to the development of acute macular degeneration (769).

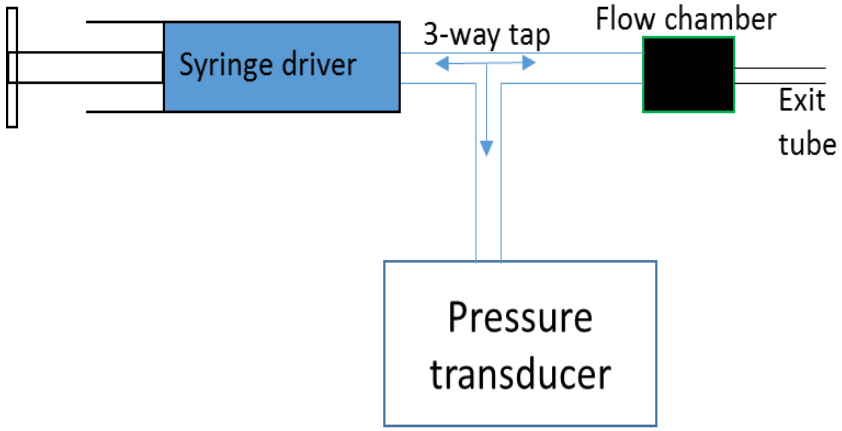

Figure 4-42. Schematic diagram for the system used for measuring permeability using a constant flow approach according to FDA guidelines for testing of aqueous shunts. The syringe driver was used at 2 µL min^{-1} to mimic the rate of aqueous flow in the eye.

In the literature, similar methods that have been used to assess pHEMA hydrogel permeability to water by using Franz cell-like apparatuses (typically with clamped metal or glass cells, in which the sample was placed between supportive materials); however, these studies applied pressures to the samples that were 52 times, 68 times, and 1,323 times as large as the pressure used this study (30 cm water/22.5 mmHg), but report permeability values of 2 x 10^{-13}–1.5 x 10^{-16} m^2 s^{-1} Pa^{-1} (749), 0.8–14 x 10^{-17} m^2 s^{-1} Pa^{-1} (752), and 2.9 x 10^{-17} m^2 s^{-1} Pa^{-1} (770), respectively. All of these studies used supportive materials, such as filter papers and a metal mesh to prevent the samples from buckling under the high pressures used for the analysis.

4.6.2 Mechanical testing

To address the limitations of currently used GDDs, an ideal GDD would be easily and quickly implanted into the subconjunctiva with only a small incision needed, as opposed to the time- and skill-intensive GFS. A GDD needs to be mechanically robust enough to be folded for implantation and maintain general structural integrity for an extended period while exhibiting minimal foreign body response. It also needs to be effective in reliable IOP control without the requirement of any post-surgical manipulation.

Initially, hydrogel samples were tested for Young's Modulus using an Instron Universal testing instrument. Films were cut into a dog bone shape and placed in the clamps of the machine and were pulled apart at a rate of 10 mm min 1 and 100 N (2 kg) static load; however, the films were too weak, and the results were not reproducible between samples. For this reason, a protocol for mechanical testing of hydrogel samples was devised for rapid preliminary measurement of the structural integrity of hydrogels. The testing was done keeping in mind the practical advice given by clinicians regarding the handling of GDDs in the clinic (personal communication with Professor Sir Peng T. Khaw). The stretching part of the protocol was based on the 510K FDA guidelines for Aqueous Shunts, where the recommendation for structural integrity is that any of the components of the device should withstand a force of 0.5 N (~51 grams) without breaking or causing leakage (CDRH, 1998).

Of the hydrogels that were resilient enough to subject them to mechanical testing, all failed except hydrogels M31–M33, which passed the folding test and twisting test, while M31 and M32 passed the stretching test. These hydrogels contained reduced amounts of HEMA from the 1015 and higher amounts of water but were polymerised at 50°C for 20 hours. The degree of cross-linking in the polymer network plays an important part in a hydrogel strength, as closely linked chains are more resilient to mechanical stresses. There seems to be an optimal ratio of monomer to cross-linker concentration. The hydrogels can be weak if the ratio is too high, as the polymer chains are held too close together, causing decreased network flexibility and forming brittle hydrogels (502). If the ratio is too low, the polymer chains have a greater degree of mobility due to being further apart (due to fewer cross-links), forming softer hydrogels that are mechanically weak (771). Physical hydrogels are not homogeneous, since clusters of

molecular entanglements, or hydrophobically or ionically associated domains, can create inhomogeneity. The free chain ends, or chain loops also represent transient network defects in physical gels (317).

The main reason for the lack of mechanical strength of a hydrogel is its solution-like nature, *i.e.* low density of polymer chains and small friction between the polymer chains (772). Another reason is the heterogeneity of the network structure of the hydrogel formed during the gelation (773). When a force is applied to a gel with a heterogeneous structure, stress is concentrated around the shortest chain, and this leads to a failure of the sample at a very low force (772). An increase in the mechanical strength of hydrogels comes at the price of further losing the permeability of the hydrogels to solvents (774), making them an unsuitable raw material for GDD development. An ideal GDD would have reliable material properties so it can survive being manipulated by a clinician and stay inside the body for a long time without disintegrating into smaller fragments.

Over the past several years, strategies have been investigated to increase the mechanical strength of conventional hydrogels (319,677,775–782). The literature suggests that homogenous networks produce tougher hydrogels as compared to heterogeneous networks with equivalent cross-link density. These homogenous networks overcome the problem of the applied load being concentrated to fewer sites by uniformly distributing the strain to a larger fraction of chains, providing fewer sites for crack formation (676,783). Slip link hydrogels that were introduced in 2001 have been reported to be more robust in comparison to conventional heterogeneous hydrogels (784). The increased extensibility in these 'topological gels' is provided due to the ability of the (α-CD) cross-linkers to slide along the PEG polymer chains like a pulley (784,785). These sliding cross-links may enable all network strands between the cross-links to carry equal force, leading to very high elongations at the break above 1000% (784).

However, double network (DN) gels are the strongest synthetic hydrogels, with compression strengths >15 MPa as compared to ~0.5 MPa of a conventional single network hydrogel (786). Introduced in 2003, the DN hydrogels consist of two interpenetrating networks that are independently and sequentially prepared. The first network is soaked in a solution containing the monomer of the other second network, which is subsequently polymerised. The DN formed from poly(2-acrylamido-2-

methylpropanesulfonic acid)(PAMPS), and polyacrylamide gels (PAA) gave a compression strength of 17 MPa as compared to 0.4 and 0.8 MPa of the single network gels of PAMPS and PAA, respectively (787). It appears that having a high molar ratio of the second network to the first (>10 times) and a very low degree of cross-linking in the second network is essential to achieve high toughness (786). The structural compromise caused by the micro-cracks in the first network (PAMPS) is compensated by the loose strands of the second network (PAA), stopping the crack propagation in the DN gel (788,789). However, these gels have demonstrated a large hysteresis in the first tensile load-unload cycle which seems to be absent in the subsequent cycles. This shows that even though these DN gels are much stronger than conventional hydrogel systems, the scission of the short strands in the structure can irreversibly deform them (751).

It has been noted that a balanced stoichiometry of reacting groups, increased cross-linking efficiency and optimal reaction conditions (pH, salt concentrations) also can dramatically improve the mechanical properties of these DN hydrogels (772,790). A DN alginate-polyacrylamide gel system was made by a similar technique of sequential polymerisation of loosely interpenetrating networks (781). These gels contain ~90% water, can be stretched beyond 20 times their initial length (781). Other classes of hydrogels that seem to have more robustness as compared to the conventional hydrogel systems are nanocomposite hydrogels. They contain nano-particulate fillers like clay particles acting as multifunctional cross-linking sites (777).

In this work, the method for characterising mechanical integrity to analyse hydrogels for their 'clinic handling' fit was validated by assessing technical replicates to reduce experimental error. However, the level of precision and accuracy could be significantly improved by using Dynamic Mechanical Analysers that employ linear motors and high-resolution displacement sensors that provide much better control over a wider range of force, displacement, and frequency. This would significantly improve the overall data quality and could be used to quantify the hydrogel materials for their moduli values. This could provide further insight into the underlying structural changes (polymer chain arrangement) as a function of hydrogel chemistry.

4.6.3 Monomer

To manipulate the primary chain length of the polymer, the concentration of HEMA monomer was altered in the 1015 hydrogel formulation, which utilises about 85%

w/w of HEMA. Increasing the HEMA content to 91.7% w/w (M1) showed a decrease in relative aqueous permeability compared with the 1015. Decreasing the concentration generally showed an increase in aqueous permeability of the hydrogel films. Decreasing the concentration of HEMA to 20% w/w (M9) exhibited a significantly ($p<0.05$) increased relative aqueous permeability with a K_{diff} value of 0.72 ±0.12. This increased permeability to water flow was fairly close to the optimum permeability (K_{diff} = 1.0) required to modulate aqueous humour theoretically.

These results suggest that decreasing the concentration of HEMA monomer generally improves the relative permeability of the hydrogels to water flow. This finding is consistent with previous reports that found that increasing the amount of monomer available for polymerisation results in more polymer chains that produce additional network structures. These additional structures may hinder the entry of water into the polymer network and decrease the overall aqueous permeability (791). Moreover, HEMA monomer is water-soluble, but the newly formed pHEMA polymer is insoluble in water. Additionally, it has been determined that HEMA influences the arrangement of water within the hydrogel and that there are three types of water; water close to the polymer, the interstitial water in regions or cavities surrounded by polymer chains, and the bulk water in the environment (792). It is likely that higher amounts of HEMA have a lower proportion of interstitial water due to the additional network structures and a lower proportion of bulk water. Since the hydrogels were fully hydrated before testing for permeability, this decrease in bulk water could also explain the decrease in aqueous permeability as the concentration of HEMA increased (524).

The total hydrogel formulations with decreased a HEMA concentration from the 1015 were adjusted to 100% w/w by adding water. Hydrogels with lower concentrations of HEMA (*e.g.* M9) were opaque, which was a reflection of the heterogeneous nature of the polymer structure (793). This correlates with what is reported in the literature as pHEMA hydrogels with a water content in the polymer solution >50% lose transparency (794). Indeed, the surface of M9, when visualised using ESEM, appeared to have a more complex microstructure than the 1015 hydrogel film, with small agglomerates at 2000x magnification as a result of phase separation. With the decrease of HEMA (<50% w/w) and the resulting pHEMA phase separation, there could be an increase in the overall porosity of the hydrogel structure. While this is useful in characterising a material for permeability with a GDD application in mind, this also resulted in mechanically weak

hydrogels. The propagation of tears and cracks in the hydrogel films even at relatively low amounts of applied stress (<49 grams) occurred. Personal communication with ophthalmologists indicated that the material's capacity for clinical handling is essential as GDDs require manual manipulation during implantation into the subconjunctiva.

4.6.4 Hydrogel curing

To slow the rate of polymerisation, UV curing and lower temperature polymerisation conditions were intended to slow the rate of phase separation and produce a homogenous polymer network (795–797). It was anticipated that adding an annealing step would relax the polymer chains and reduce polymer chain movement during the hydraulic permeability testing. The effect of different polymerisation temperatures using different concentrations of HEMA, 30%, 40%, 50%, and 60% w/w, on aqueous permeability was investigated. Hydrogels that were cured at 40°C for 12 hours (M19–M22) resulted in incomplete polymerisation, whereas hydrogel films cured at 40°C for 12 hours and then annealed at 120°C for 4 hours (M23–M26) fully polymerised, but the resulting xerogels were discoloured and shrunken.

Films M31–M34 cured at 50°C for 20 hours resulted in a transparent, flexible film (M31) and phase-separated, white films (M32–M34). M30 (70°C for 7 hours) and M34 films (both 30% w/w HEMA), when characterised using ESEM, appeared as agglomerations of small particles at the same magnification. M34 polymerised at a slower rate and a lower temperature than M30, and M30 seemed to have a smaller microstructure than M34, which suggests that curing conditions have an impact on hydrogel structure. A study characterising phase-separated pHEMA hydrogels for drug release found a remarkably similar macroporous structure of a hydrogel sponge with 30% w/w HEMA polymerised for 50°C for 20 hours (798). Cases of incomplete polymerisation also affected the structural integrity of the hydrogels causing them to be more prone to physical damage under mechanical stress (such as the column of water at 30 cm, used for permeability testing).

Increasing polymerisation temperatures and duration also formed tougher hydrogels. The hydrogels that were cured at lower temperatures (50°C) for longer durations (20 hours) exhibited the greatest mechanical strength. This could be attributed to the increase in the reaction sites (due to increased initiator to monomer ratio), forming an increased amount of smaller primary chains. The increased

temperature has also been associated with more branching of the polymer chain due to increased primary to secondary chain ratios (799).

UV initiation resulted in transparent films with no significant difference in the relative aqueous permeabilities between the UV-cured 1015 hydrogels that were diluted with water. V2 (60% w/w HEMA without MPC); however, exhibited the highest relative aqueous permeability of the samples provided from Vertellus, with a K_{diff} value of 0.45 ±0.09.

4.6.5 Co-monomers

MPC was used in the hydrogel formulations because it is zwitterionic and is highly biocompatible. MPC is also a hydrophilic molecule that attracts a large amount of water compared to HEMA, which could influence the amount of water and the distribution of water within the hydrogel matrix. Increasing the concentrations of MPC generally increased the average K_{diff} values, and there was a significant difference ($p<0.05$) between hydrogels containing 4.1% and 9.1%, and 4.1% and 14.1% w/w MPC, an increase in relative aqueous permeability observed between these formulations. MPC concentrations >10% w/w resulted in no statistically significant ($p>0.05$) change between the films. Upon increasing the MPC concentration, hydrogels absorb increased amounts of water, making them soft. This causes the weakening of the polymer network due to reduced density of polymer chains and smaller friction between the polymer chains, caused due to water molecules arranging themselves around the hydrophilic groups in the polymer chain (772,800)

Numerous MPC polymers having a wide variety of molecular architectures, such as random co-polymers, block-type co-polymers, graft-type co-polymers, and terminal-functioned polymers are being utilised today in the clinic (363,746). It has been shown that homogeneously prepared MPC polymer surfaces normally have low water contact angles (0–20°), displaying a non-cell-adhesive surface nature. It was reported that a heterogeneously prepared poly(dimethylsiloxane) surface coated with MPC (highly hydrophilic, with a water contact angle of less than 20°) induced a large number of plasma proteins to adhere onto its surface even though the MPC monomer composition was around 45% (801). This result emphasises the importance of surface morphologies in designing a biomaterial. Heterogeneously segregated hydrophobic domains can have

a significant effect on cellular responses, even with a hydrophilic MPC polymer surface (801).

Increasing concentrations of co-monomer VP generally increased the average K_{diff} values; however, this trend was not statistically significant ($p>0.05$). Using PVP to form an IPN with components in the 1015 formulation resulted in hydrogels that showed a statistically significant ($p<0.05$) decrease in permeability as compared with the 1015 formulation. The K_{diff} for 20 mg PVP (0.79% w/w)(CM6) dissolved in 1 mL of polymer mixture was found to be 0.07 ±0.03. PVP is a hydrophilic polymer that has been used as a pore-forming additive in membranes for ultrafiltration and synthesising IPN hydrogels for drug release (802). IPNs are based on polymer blends in which linear or branched polymers are embedded into one or more polymer networks during the polymerisation reaction without any chemical reaction occurring between them (289,312). PVP is also used in the pharmaceutical and food industry and has been found to be non-toxic *in vivo* (802). PVP was stirred in a HEMA mixture to make semi-IPN hydrogels where the free chains of PVP macromolecules would be embedded into the pHEMA network (803). As expected, the hydrogels showed an overall decrease in permeability as compared to the 1015 formulation. In the presence of water, the hydrocarbon chains increase the hydrophobicity, leading the gel to collapse rather than swell. This minimises the number of hydrophobic groups that can be exposed to water and allows less transport of water as a consequence (804).

Adding PVP to HEMA mixtures resulted in hydrogels that felt tougher as compared to 1015. This could be due to the hydrogel being less hydrophilic than 1015, leading to less water content, feeling less slippery and hence, tougher than 1015. Furthermore, water has been previously well established in various industrial applications to act as a plasticiser, decreasing the interactions between polymer chains in that context (805). If water is present during the polymer network synthesis, some water molecules remain entrapped and strongly bonded to the polymer cross-linked structure, decreasing the friction between the polymer chains, making the hydrogel weaker (773).

Given the assumption that the hydrophilic nature of HEMA could be responsible for the 'holding' of water and therefore a lack of hydrogel permeability, EMA was used to introduce hydrophobicity to the hydrogels. Hydrogels containing HEMA:EMA::1:1 (CM13) showed virtually no permeation to water, which can potentially be explained by

the hydrophobic EMA migrating to the outer surface in the hydrogel (simultaneously as the polymerisation of hydrophobic pHEMA) creating a barrier to water entry. The addition of other co-monomers, HPMA, and PC105 did not improve the relative aqueous permeability either.

4.6.6 Cross-linkers

A cross-linker has been reported to play a major role in modifying the properties of hydrogels in terms of permeability and mechanical properties. The chemical structure of a cross-linker can affect absorption properties by providing more/fewer cross-linking sites. Hydrophilic cross-linkers enhance the aqueous permeability of hydrogels (806). Cross-linkers have been reported to have an ideal, and usually short, concentration range with respect to the polymer, below and above which, the absorption capacities of hydrogels decreases (807–809). Cross-linked pHEMA hydrogels have previously been reported to have a range of values for aqueous permeability which have been reported to be affected by their cross-linker density; 0.1 to 1.5 x 10^{-16} m^2 s^{-1} pas^{-1}, solvent concentration (ethylene glycol); 0.03 to 1.5 x 10^{-16} m^2 s^{-1} pas^{-1} and cross-linker concentration (ethylene dimethacrylate, EDMA); 2.0 x 10^{-13} to 1.7 x 10^{-18} m^2 s^{-1} pas^{-1} (749).

In this study, increasing the concentration of EGDMA up until 1.46% w/w displayed a general increase in aqueous permeability. Increasing the concentration of EGDMA further resulted in decreased average relative aqueous permeability values. However, no significant changes in the aqueous permeability were observed. This was perhaps due to the increase in the cross-linking density within the bulk structure of the hydrogel. Cross-linking density of hydrogels is controlled by the fraction of cross-linking agent present during the polymerisation and the double bond conversion process. Low concentrations of cross-linking agents lead to heterogeneous cross-linking degrees in the polymer network. This disrupts the active formation of the three-dimensional polymer network, and consequently, the water molecules cannot be held, decreasing the ability of the hydrogel polymer chains to hold water (804). This would also explain the increased variability that was observed in relative aqueous permeability at 0.2% w/w EGDMA.

At high concentrations of cross-linkers, cross-linking sites are more readily available, facilitating the formation of more closely-bound polymer chains that preclude

water entry and could decrease the aqueous permeability of the hydrogels (810). Moreover, at higher cross-linker concentrations, a large number of growing polymer chains are involved in producing an additional network structure. This dense concentration of additional network further impedes water penetration into the network, decreasing the overall aqueous permeability (791,806). Using EGDMA at 2.1% and 6.8% w/w, hydrogels exhibited an increased variation in their aqueous permeability. This suggests the formation of increased polymer networks with the increase in cross-linker density and a more macroporous network (804,811). Increased concentrations of EGDMA lead to poorer water solubility of the polymer mixture, leading to phase-separation during polymerisation, which is responsible for this macroporous structure. Haldon and Lee reported that the mechanism of aqueous permeability at such a high concentration of the cross-linker would exclusively be through viscous flow (749). This macro-porosity has also been reported to form weaker hydrogels that may disintegrate (usually with micro-cracks) which skews the results from permeability measurements. This observation was also confirmed in the present work when hydrogels formulated using 6.8% w/w of EGDMA failed all three mechanical tests.

MBAM is a more rigid and shorter cross-linker compared to EGDMA because there are two amide functional groups in MBAM's structure, whereas EGDMA has two esters that allow an easier degree of chain movement. In the present work, at similar low concentrations, MBAM (0.5% w/w)(CX15) slightly increased hydrogel permeability but decreased permeability at increased (2.5% w/w)(CX16) concentrations. The hydrogels formed were mechanically weak and failed all three tests during mechanical characterisation. MBAM is most frequently used for cross-linking PAA gels, which are widely used in industry and academia. These gels have regions with varying cross-linking densities (812,813). Where the density of cross-linker is higher, the rate of polymerisation and monomer to polymer turnover rates are higher, forming micro-gels within the hydrogel. This inhomogeneity of the polymer network leads to the formation of low strength brittle hydrogels (751). Previous studies have observed that PAA gels most likely show low toughness, as only a few strands between microgels need to be fractured in order for crack propagation. This can initiate micro-cracks that act as stress concentrating sites, aiding in macro-crack propagation and hence a weaker gel (676,773).

The use of PEGDMA has been reported in the literature to improve the aqueous absorption capacity of hydrogels due to the increase in the hydroxyl groups (814). Even if this might be the case, in present work, hydrogels prepared with PEGDMA 700 g mol^{-1} (CX4) and 2000 g mol^{-1} (CX5), the aqueous permeability decreased as compared to the EGDMA used at the same concentration, suggesting that increased water absorption may not necessarily mean increased water transport. However, an interesting result was the increased mechanical resilience of CX4 and CX5, passing the stretching test. Additionally, CX5 passed the twisting test, indicating that a longer cross-linker was better suited to improve the flexibility of hydrogel films. It is worth noting that when a hydrogel is thinner, it is easier to compact the hydrogel pores when pressure is applied by a column of water, blocking the flow of water through the hydrogel. This was further confirmed when for a similar concentration of EGDMA (0.5% w/w), thinner hydrogels exhibited lower aqueous permeability.

4.6.7 Initiators

The amount of initiator affects the molecular weight of the primary polymer chains in the system. At low initiator concentrations, the monomer to polymer conversion reaction does not proceed completely due to lack of free radicals supplied by the initiators. This decreases the water absorption capacities of hydrogels. Increasing initiator concentration has been linked to the increased monomer to polymer conversion rates by providing more initiating species (sites) for polymerisation (276,815).

Use of APS with other initiators has been shown in the literature to improve the polymer reaction by improving the monomer to polymer conversion rate (Zhang et al., 2006). It was hypothesised that since APS begins the polymerisation process much faster than AIBN, this would form smaller pores in the hydrogel, and would lead to a mixed pore size distribution, thus would increase aqueous hydrogel permeability. This was not the case when only APS was changed (I3), but the combination of APS in other formulations with high water content, resulted in improved aqueous permeability (M9).

Increasing the AIBN to a maximum limit in terms of solubility (I2)(1% w/w) produced rigid, but crumbling hydrogels that failed all three tests for mechanical integrity. This could be due to the presence of excess radicals in the system which created small dimers or oligomers of HEMA, increasing the formation of heterogeneous

micro-gel structures with decreased cross-linked network size that reduced the overall mechanical integrity in the hydrogel (808).

4.6.8 Diluents

The addition of t-butanol, glycerol, and THF to hydrogel formulations was tested for their effect on aqueous permeability. Solvent concentration affects the hydrogel network properties by affecting the dynamics of free radical propagation. At low solvent concentration, the double bond concentration surrounding the free radical is relatively high. This leads to a faster propagation step and less opportunity for the free radicals to cycle (react intra-molecularly with its own pendant double bond), losing the opportunity to cross-link. The higher the extent of this cyclisation, the less cross-linked the polymer will be and the larger the mesh size (771). Solvent type and quality also have been reported to affect the hydrogel network properties. The result of using a less viscous solvent is a loose network structure, and firm networks result from using more viscous solvents. Increasing the concentration of diluents in the polymerisation mixture leads to phase separation as the polymerisation process progresses (793). The solubility differences between the monomer and cross-linker in the solvent is another important factor in governing the final polymer structure. The difference in solubility determines the rate and extent of cyclisation of the cross-linker (771).

The hydrogels containing THF were semi-opaque, suggesting the irregular formation of the primary polymer chains, caused by phase separation during polymerisation. The addition of 16% (D12) and 43.9% w/w THF (D14) created hydrogels permeable to water that were closer to the desired permeability, with an average K_{diff} value of 0.41 ±0.1 and 0.67 ±0.41, respectively. Replacing MBAM with a similar concentration of EGDMA (D21) increased ($p>0.05$) the K_{diff} value to 0.8 ±0.22. However, the amount of THF used for formulating these hydrogels was not safe as the lower explosive limit of THF is much lower, 0.2% (816). Hydrogels with a high content of diluents (>30%) were structurally weak and tore easily, which indicates that some of the samples could have been damaged while being screwed in the flow-chamber for the tests. Hydrogels with a higher content of diluents (>50%) were too fragile to be tested, and after a few attempts with ruptured discs, these permeability tests were not continued to avoid spurious results.

Compared with no THF used (CM17 and CM18), the K_{diff} values significantly ($p<0.05$) increased when THF was used with increasing VP concentrations. The near-negligible water resistance was possibly caused by the formation of micro-tears in the structure when subjected to the water column for permeability testing. Adding a diluent to the formulation caused phase separations to occur, which indicates that larger pores within the hydrogel microstructure were formed. The permeability seemed to be concentration-dependent in the case of both THF ($p>0.05$) and VP ($p<0.05$), suggesting an increase in the hydrogel porosity when increasing diluent concentration. It is worth noting that these gels were mechanically fragile and subjecting them to pressure (even as low as the testing pressure of 30 cm water) could have caused micro-tears in the hydrogels that were not noticeable by visual inspection.

4.6.9 Mesh

Mesh with different average pore sizes were coated with a solution of a different biocompatible non-cross-linked polymer PC 1059 using the dip-coating method. Unsurprisingly, there was a significant increase in permeability when compared with the 1015. All mesh samples tested using the mechanical characterisation methods passed all three tests (data not shown). However, these formulations did not provide enough resistance to flow to match the ideal IOP regulation required for managing glaucoma. Additionally, coating mesh could provide with additional challenges such as coating reproducibility, surface texture, coating efficiency and additional cost involved. This might be a viable area for future studies where a mesh could be used as a scaffold to reinforce hydrogel strength.

4.6.10Laser

Because all hydrogels exhibited low relative aqueous permeability values an alternative approach was considered for a hydrogel GDD: that a pouch or tube could be fabricated using femtosecond laser from a hydrogel so that water did not have to flow through the entire hydrogel. The pouch could potentially be engineered (by depressurising the pouch before implantation) to exert pressure from inside the hydrogel to improve flow. Femtosecond lasers are routinely used in cataract surgery where the cloudy lens is removed and replaced with a synthetic intraocular lens (IOL). In the surgery, an incision is created where the cornea and sclera meet, to remove and

insert the new IOL. Precise incisions are produced by the use of femtosecond laser machines. The laser eliminates variability due to surgical skills and produces incisions without damage to surrounding tissues (817,818).

The laser could also be used to fabricate holes, increasing the porosity of the hydrogel, without affecting the surface of the hydrogel, surrounding the pouch to control the rate of aqueous diffusion with better precision.

It was confirmed that creating micrometre-sized holes in xerogels and hydrogels via femtolaser augmentation is not feasible since the material properties of hydrogels required for an optimal GDD interfere with the technical processes of the femtosecond lasers. In addition to subpar permeability, the hydrogel compositions were too fragile to be practically handled and manipulated by a clinician. The introduction of physical spacers to create drainage channels, although rudimentary, also supported these results that permeable hydrogels made from biocompatible materials were too weak for practical manipulation.

4.6.11 Overall hydrogel performance

A range of aqueous permeability values for other types of hydrogels have been previously reported in the literature, **Table 4-16**. In permeability analysis, fluid flow through pHEMA hydrogels is like that of a rubber-like material. It shows an initial strong decrease in permeability due to membrane compaction, eventually attaining a constant value of water flow after a period of time, as mentioned previously in the literature (752). These permeability values are generally comparable to the experimental results presented in the present work, but these values also do not suffice to match the outflow rate of the aqueous needed to match the production rate of the eye to prevent the increase in pressures as seen in glaucoma patients.

Table 4-16. Comparison of permeability values of various hydrogels in the literature.

Permeability reported ($m^2 s^{-1} Pa^{-1}$)	Materials	Source
1×10^{-9}	Collagen hydrogels	(750)
0.8 to 14×10^{-17}	pHEMA cross-linked with EDMA, prepared with PVP, glycerol or diacetin	(752)
1 to 5×10^{-15} and 2.8×10^{-17}	Acuvue contact lens, a co-polymer of HEMA and MMA	(819)
1.2×10^{-13} and 6.5×10^{-15}	Fibrin hydrogels	(820)
0.1–59 x 10^{-5}	pMEMA, pMEEMA, and their co-polymers with pHEMA with water ranging 3–63%	(821)
3.56×10^{-10}	With sacrificial additives	(810)

4–9 x 10^{-18}	Soft contact lenses	(822)
1.8 x 10^{-14}	0.686-mm thick Etafilcon-A hydrogel membrane (58 wt% water)	(823)
Cross-linker density: 0.1– 1.5 x 10^{-16} Solvent concentration: 0.03– 1.5 x 10^{-16} EDMA concentration: 2.0 x 10^{-13}–1.7 x 10^{-18}	pHEMA	(749)
0.075–42.04 x 10^{-16}	GMA, HEMA and PGMA hydrogels. Some had cross-linker TEGDMA, initiators APS, sodium metabisulfate	(824)
2.9 x 10^{-17}	Monomer (GMA or HEMA or MMA), solvent (water, water/formic acid for GMA, water-ethylene glycol for HEMA), TEGDMA as cross-linker for some membranes, initiator $K_2S_2O_8$ and $Na_2S_2O_5$)	(770)
99/1: 2.0x 10^{-16} 90/10: 1.9 x 10^{-16}	AAM/MBAM as a fraction 99/1 and 90/10	(825)

Abbreviations: APS, Ammonium persulfate; EDMA, ethylene glycol dimethacrylate; GMA, glycidyl methacrylate; MMA, methyl methacrylate; PGMA, poly(glyceryl methacrylate); pHEMA, poly(2-hydroxyethyl methacrylate); pMEEMA, poly(methoxyethoxyethyl methacrylate); pMEMA, poly(methoxyethyl methacrylate; PVP, poly-n-vinyl pyrrolidone; TEGDMA, tetraethyleneglycol dimethacrylate.

In the present work, out of all the hydrogels tested for aqueous permeability using the dynamic flow approach, hydrogel D21 exhibited a relative aqueous permeability closest to the optimal permeability value, with a K_{diff} value of 0.80 ±0.22. Other hydrogels that displayed relative aqueous permeability values close to the optimal permeability value were M9 and D14. Overall, these hydrogels were opaque, suggesting phase separation occurred, and they were fragile, performing poorly in qualitative mechanical testing. M9 contained a very low HEMA concentration (20% w/w), with the majority of the remaining formulation made up of water. D21 contained 45.3% w/w HEMA, 7.6% w/w MPC, and 46.7% w/w THF, while D14 contained 46.2% w/w HEMA, 8.8% MPC, and 43.9% THF. Both formulations contained no water. Although these relative aqueous permeability values were close to the required optimal permeability, it was still not sufficient for modulating aqueous flow in a glaucomatous eye. In the clinic, their use would translate to an elevated IOP (>10 mm Hg), and the disease progression would not be halted. For this purpose, the hydrogel formulations investigated in this chapter were deemed unfit for GDD development, and an optimised formulation was ultimately not identified.

Another reason for the low permeability to water flow may have been due to gel blocking. In this case, it is possible that under the pressure of water flow, hydrogel chain conformations change, which results in polymer chains blocking any liquid flow. Höhne and Tauer suggested gel-blocking in a confined geometry is responsible for the reduction

in the water inflow with increased hydrogel swelling in direct contact with water (826). Wack and Ulbricht have suggested a diffusion-relaxation model for estimating the swelling pressure responsible for gel blocking effect in hydrogels (827). Compared with an osmotic driving force that is determined only by the number of solute molecules, swelling pressure additionally takes into account the elastic force of the gel, making it more reflective of the sorption (relating to both absorption and adsorption as a single process) process for polymer-solvent systems (828). Berg *et al.* suggested that the surface area to mass ratio of the polymer plays a significant role in water uptake and decreasing the mass average particle size can increase water uptake (829). However, counterintuitively, these small polymer particles may coagulate due to the fluid tension forces, forming a barrier to fluid flow within the hydrogel mass, decreasing their permeability. This phenomenon is termed as 'gel blocking' (829).

Flory and Rehner have proposed that water molecules (solvent) penetrate the cross-linked polymer networks to produce 3D molecular network at the same time expanding the primary polymer chains between the cross-linked junction points (830). The osmotic pressure is the primary driving force for the expansion of the polymer network. The polymer network also has a counteracting elastic force that tries to make the networks contract. When these opposing forces reach an equilibrium, the expansion and contraction also reach a balance (831). pHEMA hydrogels are highly hydrophilic, and once equilibrium swelling by water absorption is reached, any additional uptake of water is unfavourable as there is no osmotic pressure to counteract the elastic contractive force of the polymer network. This explains why xerogels (dry hydrogels) readily swell up in water. When hydrogels are placed on a dry surface, such as a lab bench, the water quickly evaporates, much like what happens in a contact lens that is left exposed to air. This further indicates the role of an osmotic gradient on the aqueous permeability of hydrogels.

However, to understand the effects of "pore-compacting" in various hydrogel systems, the permeability measurements should be taken for more extended periods under varying pressure gradients. A major limitation of this study was that the aqueous permeability of hydrogels was only tested over a two-hour window as the aim of this research was to achieve optimal 'water transport' at a fixed pressure and as a function of hydrogel chemistry. Conventional gravity flow and constant flow tests proved not to be precise enough to assess flow rates at a microliter scale properly. However, it would

be interesting to investigate an ‘optimal pressure‘ for water transport through hydrogels or utilise a microfluidic approach to measuring flow control at smaller volumes more precisely.

4.7. Summary and conclusions

The original contribution of this research indicates that even though hydrogels allow some permeation of aqueous flow under applied pressure, their permeability was far lower than the values required for efficient aqueous humour drainage and IOP management by an ideal GDD. It was further established that there was an apparent compromise between aqueous permeability and mechanical strength of the hydrogels. Formulating permeable hydrogels was possible, but it seemed that any increase in permeability resulted in fragile hydrogels, unsuitable for 'clinic handling'. Improving the aqueous permeability through other engineered means, such as femtosecond laser drilling and moulding around physical spacers was also investigated but were unsuccessful in fabricating a mechanically-robust hydrogel that could be further characterised for aqueous permeability.

The investigations described in this Chapter were unable to optimise a hydrogel formulation suitable to be used as a good candidate for GDD development. Future work could involve conducting permeability experiments for a longer period to understand the effects of pressure on water flow through hydrogels and exploring techniques to formulate tougher hydrogels that can withstand physical modification and 'clinic handling'. The primary conclusion of this experimental work that permeation of water does not necessitate flow through hydrogels is obviously practical but is also of fundamental importance.

Chapter 5 General discussion, conclusions and future work

Glaucoma is the leading cause of irreversible blindness, affecting over 70 million people worldwide (4). Currently, the only clinically modifiable risk factor in halting the progression of glaucomatous neuropathy of the optic nerve is lowering the IOP. Almost all treatment modalities aim to achieve lowering of the IOP by either reducing aqueous humour production or by increasing aqueous drainage. The first line of treatment is using eye drops, but poor-patient compliance, sub-optimal therapeutic efficacy, and the risk of systemic side effects pose significant challenges to the success of this therapy.

To provide an effective lowering of the IOP, surgical interventions such as GFS or GDD implantation are required to create a new channel for the aqueous humour to drain into the subconjunctival space and lower the IOP. However, postoperative fibrosis leads to scar formation, posing a significant challenge to the success of these surgeries as it may close the channel formed during GFS or GDD implantation. Anti-metabolites are applied locally or injected at the site of surgery to improve outcomes, but these drugs may have blinding complications stemming from hypotony and infections. This necessitates close monitoring of the patient after surgery. Additionally, frequent medications are required after surgery in the form of repeated subconjunctival injections or as dexamethasone (DEX) eye drops to reduce local ocular inflammation. Despite significant research into drug delivery implants, no prolonged-release subconjunctival implants have been approved to control post-surgical inflammation. There is an unmet clinical need to improve current glaucoma therapy.

The objective of the work described in this thesis was to investigate potential approaches to improve current glaucoma management via surgical interventions. Two main strategies were pursued; First, to explore methods for prolonged site-specific delivery of anti-inflammatory drugs that are commonly used ophthalmology. To this end, the primary strategy was to use drug-eluting spacers to prolong drug release in the subconjunctival space. Surfactant loaded pHEMA non-degradable hydrogels containing DEX were formulated. Degradable chitosan hydrogels, as well as electrospun fibres and solvent cast spacers, using PCL and poloxamers, were formulated with doxycycline (DOX) were also formulated. Second, the potential of elastomeric pockets for prolonging

drug release in the subconjunctival space was investigated. Finally, the use of biocompatible materials for the regulation of aqueous flow and their feasibility as raw materials for GDD development was assessed. To investigate this further, novel and established hydrogel formulations were characterised for their ability to modulate aqueous flow while being able to endure 'clinical' handling that would be required during implantation in the eye.

An ideal implantable drug delivery system would be biocompatible and would deliver an anti-fibrotic over approximately five-weeks, which is the critical period of maximum postoperative fibrosis. Bearing these considerations in mind, well-established biocompatible materials were utilised to formulate spacers with the aim to prolong the release of anti-fibrotic drugs for at least five weeks. Previous work conducted in the Brocchini research group and by researchers in other labs has demonstrated that using a 'spacer' can promote bleb survival, better IOP control and a lower rate of postoperative complications to the same degree or better than MMC, when combined with GFS. The potential for using hydrogels as a spacer for site-specific drug delivery has also been demonstrated favourably in the literature. However, poor drug loading efficiencies, dose-dumping and consequently, short maintenance of the therapeutic window are the significant challenges in using hydrogels for developing effective drug delivery spacer systems.

To overcome these hurdles, a non-ionic surfactant, Brij 98, was used to form micellar aggregates in pHEMA hydrogels. The rationale behind this work was that if the micelles could be loaded with a drug and entrapped within the hydrogels, a depot effect would occur, prolonging the drug release from these surfactant-drug combination hydrogels. A model hydrophobic drug, DEX, which is most commonly used in ophthalmology to control post-surgical inflammation, was loaded in the pHEMA hydrogels. For drug-release analysis, an *in vitro* setup was used which mimicked the subconjunctival space bleb volume, temperature and aqueous humour flow rate. Drug release results confirm that Brij 98 (1.25% w/v)-containing pHEMA hydrogel spacers could be loaded with DEX at a significantly higher drug loading efficiency and can release DEX for a significantly extended period (over a month), as compared with DEX loaded pure (no surfactant) pHEMA hydrogel spacers.

Despite the numerous improvements made to the traditional GFS and the advent of new GDDs, scarring is the prime cause of suboptimal pressure control and surgical

failure in all forms of surgery. As a general principle, the duration and severity of post-surgical inflammation correlate well with the extent of fibrosis (353). If a prolonged drug delivery system of an anti-inflammatory agent could be translated to the clinic, it would improve the current failure rate of glaucoma surgery. The main potential advantages of such an implant would include, but not be limited to; localised drug delivery, improved patient compliance by eliminating eye drop usage, minimised systemic side effects by reducing off-target effects, lower drug doses by avoiding first-pass metabolism, improved drug stability by avoiding the gastrointestinal and the hepatobiliary systems, and in the case of an adverse reaction, a facile termination of drug delivery. Drug release results from the *in vitro* experiments indicated that it is possible to prolong DEX release from Brij 98-loaded pHEMA hydrogel spacers at a therapeutic concentration, for over a month.

It could be argued that the prolonged release of DEX was observed due to the higher drug loading in Brij 98-loaded pHEMA hydrogels and that a similar drug release profile might be achieved by using a mini DEX tablet. It is worth noting that DEX has very poor solubility in water, and indeed, the rate of drug release from a tablet might be slow in the subconjunctival space. However, one cannot dismiss the fact that any particulate matter excites a foreign body response characterised by inflammation and scarring when placed in the subconjunctival space. DEX, when used alone or in combination with other potent anti-fibrotic drugs, still elicits a significant antagonistic effect due to the non-solubilised drug. Using a hydrogel would potentially be a viable method to mask the particulate drug matter while maintaining a therapeutic concentration at the site of surgery.

Furthermore, this drug delivery system could be loaded with other potent anti-fibrotic drugs, such as ilomastat, which has shown to be a highly effective anti-scarring agent at nanomolar concentrations. The contribution of the work presented here has been to demonstrate a proof-of-concept that pHEMA hydrogels, when loaded with Brij 98 micelles, can prolong the release of DEX for over a month at therapeutically relevant levels. Future work to establish the viability of Brij 98-loaded pHEMA spacer system for prolonged drug delivery could involve, in the first instance, an investigation into candidate drugs with similar chemical and physical properties to DEX.

Next, the aim was to formulate a degradable spacer system that could prolong the release of DOX for five weeks. DOX, a broad-spectrum antibiotic has shown promise

as an anti-scarring agent in ophthalmology. DOX is also known to undergo photolysis and thermally-induced-degradation. Therefore, all the materials chosen for spacer formulation had well-established biocompatibility, and the techniques investigated for spacer formulation did not involve high temperatures. Chitosan-glycerophosphate solutions containing DOX (monohydrate and hyclate) were formulated that turned to gels at physiological pH and temperature. The advantage of such a spacer system would be the ability to be injected at the site of surgery and then transition into a mucoadhesive gel, that would prolong the release of DOX and modulate post-surgical wound healing. The majority of $DOX_{hyclate}$ was released in three days while $DOX_{monohydrate}$ was released in one week when assessed using the *in vitro* drug release setup.

Next, PCL was used in combination with poloxamers (188 and 407) to formulate degradable spacers, encapsulating $DOX_{monohydrate}$. It was possible to formulate DOX-PCL-poloxamer fibres, using the electrospinning technique, and DOX-PCL-poloxamer spacer matrices, using the solvent cast technique. Diameter distribution analysis revealed that fibres formulated using poloxamer 188 were on average thinner than fibres formulated using poloxamer 407. During *in vitro* drug release characterisation using the same setup, the majority of $DOX_{monohydrate}$ was released in five days when using poloxamer 188 and was released in seven days when using 407 for fibre formulation. Results also indicate that the former released significantly more drug than the latter. Similar results were observed when characterising drug-release from solvent cast spacers; $DOX_{monohydrate}$ was released in 10 days, but a significantly more amount of the drug was released when using poloxamer 188 compared with using 407 for spacer formulation. The difference in the cumulative drug-release amounts was primarily attributed to the chemical differences between the two poloxamers, poloxamer 188 being a smaller and more hydrophilic co-polymer as compared with poloxamer 407.

Additionally, the difference in drug release profiles with the change in surface area available for drug diffusion was evident, thinner fibres providing a larger surface area as compared with thicker fibres and thicker solvent cast spacers. These kinetics are based on both diffusive and convective flow of molecules (832). Finally, the differences in drug release achieved from the same formulation but different processing techniques further exemplified the importance of choosing an appropriate drug-polymer processing method.

While the release of DOX from degradable spacers was not prolonged for five weeks, these drug delivery systems could be used to modulate post-surgical wound healing in Trachoma patients, where the target duration for drug release would be approximately two weeks. The tear turn-over rate is slower than the aqueous humour production rate, which could further prolong the release of DOX from these spacers. Future considerations to bear in mind would primarily be the intended application of the drug delivery spacer system, which would dictate the target drug release and implant degradation profiles. Additionally, drug-polymer interactions, polymer-polymer interactions and finally, choosing an appropriate setup for *in vitro* drug-release to mimic the physiological conditions is imperative to make appropriate conclusions of the feasibility of a drug delivery spacer.

While using a spacer for prolonged site-specific delivery of potent anti-fibrotic drugs would be beneficial in modulating post-surgical wound healing, the spacers would be limited in the amount and type of drug that could be delivered. Specifically, hydrophilic drugs, when delivered using hydrogels, display significant burst release profiles and release most of their drug in a short time. Additionally, these spacers, once exhausted of their drug stores, cannot be replenished without significant surgical intervention. A refillable device with the capability of delivering potent drugs at precisely controlled release profiles would benefit patients who require frequent or long-term ocular medication.

With the aim of a refillable, localised and prolonged drug delivery system in the subconjunctival space, the use of an implantable elastomeric pump was proposed. The use of elastomeric pumps is reasonably common for patient-controlled analgesia and chemotherapy primarily due to their ease of use and economic benefit. These pumps rely solely on utilising the elastic energy stored in their stretched membranes for drug delivery. However, patients using elastomeric pumps have reported significant variability in drug delivery rates and duration, sometimes up to twice that of the present time asserted by the manufacturers. Moreover, these pumps are bulky, and the idea of a smaller pump being implanted inside the human body has not gained much success in the clinic. One exception to this is the Replenish Micro Pump that was proven to be safe in the first human clinical trial for NAMD while delivering a small dose of ranibizumab.

What was not clear at the outset was the impact of material properties and pump geometry on the intended pump applications of flow rate, pocket pressure and

deflection. Previous work in the literature has been limited to analytical and numerical solutions, exploring small or large deformations clamped inflatable elastomeric membranes. For this purpose, a systematic experimental analysis of simply connected pursed pockets was performed. Circular and square pursed pockets made with elastic silicone membranes of varying thicknesses and Young's modulus were analysed to infer relationships between different variables governing pump function. An experimental optical method developed for fluid mechanics was applied for the first time to study the pursing of elastic pockets made with silicone sheets. Additionally, the effect of compressive forces applied by the conjunctiva on an inflated elastomeric pocket and the change in internal pocket pressure was investigated.

Experimental results highlight that there were significant differences between different pursed regimes of the pocket studied under no outflow. When pocket deflection was smaller than or approximately equal to the thickness of the pocket material, the pocket was in the bending regime, and the maximum deflection varied linearly with internal pocket pressure. However, when the deflection was larger than the material thickness and continued to increase, the pocket was in the stretching regime, and the maximum deflection was to the power of $\frac{1}{3}$ of the internal pocket pressure. Furthermore, when comparing materials with similar Young's modulus values, the deflection of pursed silicone pockets increased with the pocket size but decreased with the increase in the thickness of the material for a range of dimensionless pressures 10^{-1} to 10^{5}. The coefficient of inflation, γ, for circular pursed pockets was found to be 0.6 and for square pursed pockets was found to be 0.7. The observations from these results were also the basis of analytical and numerical solutions derived by Bouremel *et al.* for the qualitative comparison between pursed regimes of different simply and doubly connected pocket shapes, in terms of maximum deflections and profiles of pockets (667).

Next, the relationship, β, between compression of pursed elastic pockets with no outflow and the changes to their internal pressure was analysed by compressing circular pockets using varying compressive forces. Through linear regression of the results, the value of β was estimated to be ≈ 1.85. This relationship significantly adds to the considerations involved when designing a circular elastomeric pump to be implanted in the subconjunctival space. Further, this principle could be applied while designing a

double-chambered pump. Such a pump would have one chamber that could be controlled by external stimuli to inflate when needed, applying a known amount of compressive force on the drug reservoir, hence increasing the outflow from the elastomeric pump. Next, the release of fluid from simply connected circular elastic pockets was studied. For deflating pockets, the flow rate of liquid released was found to be linearly proportional to the internal pressure of the pocket. This functionality is unique to the geometry (dome-shaped simply connected pursed pocket) and could be useful in achieving a tapered drug dose to the eye using a pursed pocket.

Finally, building on the results obtained during the assessment of inflating, compressing and deflating elastic pockets, drug release from implantable hypothetical pockets for site-specific ophthalmic delivery was modelled. Within the constraints of feasible dimensions for subconjunctival implantation and commercially available materials, it is possible to slow the release of drugs from single-chamber elastic pockets significantly. Specifically, for D*min* and Optimal, drug release could be maintained for almost 11 months before a refill would be needed. Based on the results for inflation, compression, deflation and modelling release from hypothetical single-chamber pockets, two recommendations were provided for designing ophthalmic pumps. Firstly, a simply connected single-pocket elastomeric pump that would require no moving parts such as valves or for energy to be stored in the form of a battery. Secondly, multi-pocket elastomeric pumps that could potentially be externally actuated to deliver a fixed or combination of drugs, at a specific time. This design might offer a more tailored approach to disease management and could improve patient compliance and the quality of therapy. The findings from this work will be of specific interest when considering the design of an implantable elastomeric pump for confined spaces, such as the subconjunctiva. The engineering principles of pump function elucidated in the current work may further be extended to design implantable elastomeric pumps for other indications where a prolonged release of drugs is sought. Further work is being conducted to optimise a scaled-down version of the elastomeric pumps to match the pump design, efficiency, and flow control mechanisms, setup shown in **Figure 5-1**. Microfluidic flow sensors are being utilised to improve the accuracy and precision of the pocket pressure and flow rate measurements.

Finally, the use of biocompatible materials for the regulation of aqueous flow and investigated their feasibility as raw materials for GDD development was proposed. The 1015 hydrogel formulation, developed by Vertellus Biomaterials, UK and manufactured as contact lenses by CooperVision, was considered as the primary biomaterial candidate for GDD development. The rationale for this work was the favourable biocompatibility of the 1015 hydrogel formulation at the front of the eye, the ability of this hydrogel to absorb and hold large amounts of water, and the microscopic structural similarity of this hydrogel to the trabecular meshwork, all of which is supported in the literature and previous work done in the Brocchini research group. Furthermore, in previous experiments, the biocompatibility and improvement in the outcome of bleb survival post-GFS have been demonstrated due to the 'spacer' effect of an implanted hydrogel (contact lens) in the subconjunctival space. It was hypothesised that their structural similarity to TM, structural flexibility and high water-absorption capacity would make hydrogels an ideal biocompatible aqueous flow regulator that could be folded and inserted with a small incision into the subconjunctival space with relative ease.

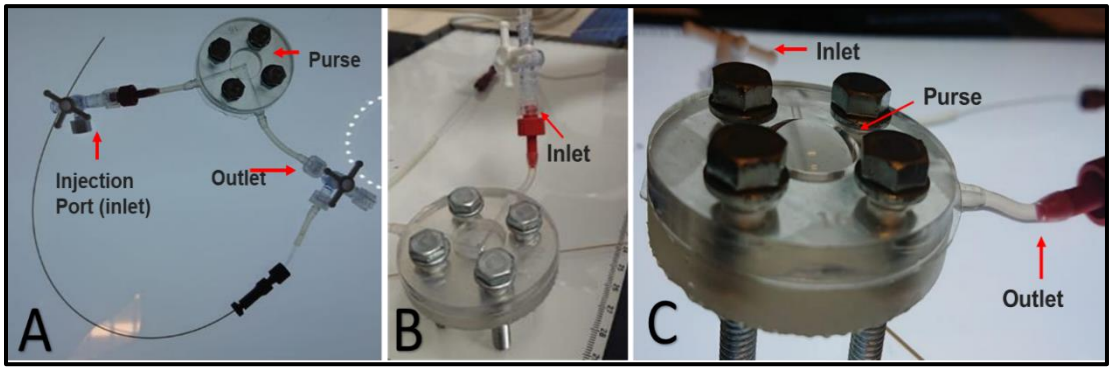

Figure 5-1. Scaled-down elastic pockets are created using a clear silicone membrane clamped between two clear acrylic plates, an upper plate and a base plate. The upper plate has a hole of radius 10 mm, cut out for the silicone membrane to purse and form a pocket. The bottom plate has an inlet injection port that is used to fill up the elastomeric pocket, and an outlet port that is used to externally attach micro-tubes that provide varying resistance to the flow of liquid from the pocket. The outlet micro-tube is attached to a microfluidic flow sensor and measurements of flow rate of liquid released from the inflated pockets are taken every 0.1 second.

If this could be achieved, it is possible to develop a GDD that can be implanted by a clinician within 10 minutes requiring less surgical skill, and no post-surgical manipulation would be necessary for at least 10 years. This non-degradable hydrogel GDD would also maintain the IOP at 10 mmHg, which is vital to stop the progression of glaucoma. If this 10 minutes-10 years-10 mmHg "challenge" can be met, then this device has the potential to revolutionise the treatment of glaucoma worldwide as most

patients could be treated using a one-time surgery to implant this improved GDD. This strategy could be realised in much the same way as patients are now treated for cataracts, characterised by high success rates and the ease of the surgical procedure.

To this end, aqueous permeability of hydrogels was assessed in line with the recommendation provided by the FDA for Aqueous Shunts (145) and qualitative assessment of mechanical resilience was carried out following expert advice to assess the ability of hydrogels in enduring clinical-handling procedures, used during GDD implantation. The optimum aqueous permeability value necessary to maintain IOP in a healthy eye was calculated to be 5.56×10^{-14} m^2 s^{-1} Pa^{-1}, and all hydrogels were measured against this criterium. The aqueous permeability investigation revealed that the 1015 hydrogel formulation (used for making contact lenses) was significantly less permeable to water flow at the physiological rate of aqueous humour production (2 µL min^{-1}) than the desired permeability value for optimal IOP control. Furthermore, these hydrogels were not sufficiently resilient to clinical-handling procedures. To improve the aqueous permeability, chemical changes were made to the hydrogel formulations by changing the concentrations and types of crosslinkers, co-monomers, initiators, diluents and polymerisation conditions (*e.g.* temperature and duration).

The most significant effect on increasing permeability was found to be the addition of water to the 1015 formulation. The modified 1015 formulation containing almost 80% water added to the pre-polymer mixture achieved a relative permeability of 0.72 ±12. Other hydrogels that displayed relative aqueous permeability values close to the optimal permeability value used almost 50% THF instead of water as an added diluent to the modified 1015 formulation. This amount of THF used for hydrogel formulations was well above the lower explosive limit of THF (816). Overall, these hydrogels were opaque, suggesting phase separation occurred, and they were fragile, performing poorly in qualitative mechanical testing.

While it was possible to increase the aqueous permeability of the hydrogels, it was observed that a higher aqueous permeability led to a decrease in structural integrity and resulted in weaker hydrogels. The mechanical resilience of hydrogels could be increased by using a longer curing duration of 20 hours at a lower curing temperature of 50°C. Unfortunately, these hydrogels proved to be even less permeable than the standard 1015 formulation. These hydrogels were deemed unfit for ‘clinical use’ as they

would not be able to withstand the necessary handling procedures currently used during GDD implantation.

The permeability results were somewhat counterintuitive and raised intriguing questions regarding the nature and extent of water flow through hydrogels and the distinct separation of two phenomena; water flow and water absorption. Once equilibrium swelling by water absorption is reached in the hydrophilic pHEMA hydrogels, additional uptake of water is unfavourable as there is no osmotic pressure to counteract the elastic contractive force of the polymer network. This further indicated the role of an osmotic gradient on the aqueous permeability of hydrogels. Another plausible reason for the low permeability to water flow may have been due to gel blocking, caused by the change in polymer network confirmations when pressure was applied by the column of water, effectively blocking water transport (826–828). Berg *et al.* suggested that decreasing the mass average particle size of the polymer chains can increase water uptake (829). However, counterintuitively, these small polymer particles may coagulate due to the fluid tension forces, forming a barrier to fluid flow within the hydrogel mass, decreasing their permeability (829).

It is worth noting that the potential of pHEMA hydrogels to be used as a carrier for drug delivery is still promising. While the low aqueous permeability proved disadvantageous for GDD development, it would benefit in prolonging drug-release from spacers. Moreover, the dimensions of the spacer are significantly smaller than a GDD, and would not require the same level of surgical manipulation of the material during implantation. To develop a sustained released formulation delivering anti-fibrotic drugs at the site of surgery, alternative approaches such as the use of micelles may be viable in manipulating the drug release kinetics through the gels.

Alternatively, a drug delivery spacer could be used in combination with GDDs to improve treatment outcomes. The GDD end plate could be made of a pocket for storing drugs; the tube would have an adjustable resistance to tailor the drug-delivery rate and finally, a resilient elastomer that would not perforate when the pouch is refilled with the drug. The pocket would release the drug via the resistance tube to either the anterior or posterior chamber. The results from deflating pursed pockets indicated that that the amount of drug delivered from a purse is pressure-dependent and the modelling data suggested that dosing may be adjusted by manipulating the pocket geometry, material properties and the external resistance provided by the outlet tube. Therefore, there is

promise in the concept of developing a combination drainage device system to deliver drugs as well as drain the aqueous humour into the subconjunctival space. Such a combination device warrants pursuing in future studies.

Chapter 6 Bibliography

1. Quigley HA. Glaucoma. The Lancet. 2011 Apr;377(9774):1367–77.
2. Quigley HA, Broman AT. The number of people with glaucoma worldwide in 2010 and 2020. The British journal of ophthalmology. 2006 Mar;90(3):262–7.
3. Bourne RRA, Stevens GA, White RA, Smith JL, Flaxman SR, Price H, et al. Causes of vision loss worldwide, 1990-2010: A systematic analysis. The Lancet Global Health. 2013;1(6):339–49.
4. WHO. World report on vision. Geneva; 2019.
5. Weinreb RN, Aung T, Medeiros FA. The Pathophysiology and Treatment of Glaucoma. JAMA. 2014 May 14;311(18):1901.
6. Cook C, Foster P. Epidemiology of glaucoma: What's new? Canadian Journal of Ophthalmology. 2012;47(3):223–6.
7. Flaxman SR, Bourne RRA, Resnikoff S, Ackland P, Braithwaite T, Cicinelli M V., et al. Global causes of blindness and distance vision impairment 1990–2020: a systematic review and meta-analysis. The Lancet Global Health. 2017;5(12):e1221–34.
8. Tham YC, Li X, Wong TY, Quigley HA, Aung T, Cheng CY. Global prevalence of glaucoma and projections of glaucoma burden through 2040: A systematic review and meta-analysis. Ophthalmology. 2014;121(11):2081–90.
9. Song P, Wang J, Bucan K, Theodoratou E, Rudan I, Chan KY. National and subnational prevalence and burden of glaucoma in China: A systematic analysis. Journal of Global Health. 2017 Dec;7(2).
10. Cheng J-W, Zong Y, Zeng Y-Y, Wei R-L. The Prevalence of Primary Angle Closure Glaucoma in Adult Asians: A Systematic Review and Meta-Analysis. Acott TS, editor. PLoS ONE. 2014 Jul 24;9(7):e103222.
11. Rein DB, Zhang P, Wirth KE, Lee PP, Hoerger TJ, McCall N, et al. The economic burden of major adult visual disorders in the United States. Archives of ophthalmology. 2006;124(12):1754–60.
12. Taylor HR. The economic impact and cost of visual impairment in Australia. British Journal of Ophthalmology. 2006 Mar 1;90(3):272–5.
13. Minassian D, Reidy A. Future sight loss in the decade 2010 to 2020: an epidemiological and economic model. 2009.
14. Rahman MQ, Beard SM, Discombe R, Sharma R, Montgomery DMI. Direct healthcare costs of glaucoma treatment. British Journal of Ophthalmology. 2013;97(6):720–4.
15. Poulsen PB, Buchholz P, Walt JG, Christensen TL, Thygesen J. Cost analysis of glaucoma-related-blindness in Europe. International Congress Series. 2005 Sep;1282:262–6.
16. Lee PP, Walt JG, Doyle JL, Kotak S V., Evans SJ, Budenz DL, et al. A Multicenter, Retrospective Pilot Study of Resource Use and Costs Associated With Severity of Disease in Glaucoma. Archives of Ophthalmology. 2006 Jan 1;124(1):12.
17. Traverso CE. Direct costs of glaucoma and severity of the disease: a multinational long term study of resource utilisation in Europe. British Journal of Ophthalmology. 2005 Oct 1;89(10):1245–9.

18. Varma R, Lee PP, Goldberg I, Kotak S. An Assessment of the Health and Economic Burdens of Glaucoma. American Journal of Ophthalmology. 2011 Oct;152(4):515–22.
19. McKean-Cowdin R, Varma R, Wu J, Hays RD, Azen SP. Severity of Visual Field Loss and Health-related Quality of Life. American Journal of Ophthalmology. 2007 Jun;143(6):1013–23.
20. McKean-Cowdin R, Wang Y, Wu J, Azen SP, Varma R. Impact of Visual Field Loss on Health-Related Quality of Life in Glaucoma: The Los Angeles Latino Eye Study. Ophthalmology. 2008 Jun;115(6):941-948.e1.
21. Muratov S, Podbielski DW, Kennedy K, Jack SM, Pemberton J, Ahmed IIK, et al. Preference-based Glaucoma-specific Health-related Quality of Life Instrument. Journal of Glaucoma. 2018 Jul;27(7):585–91.
22. King A, Azuara-Blanco A, Tuulonen A. Glaucoma. BMJ. 2013 Jun 11;346(jun11 1):f3518–f3518.
23. Nuzzi R, Marolo P, Nuzzi A. The Hub-and-Spoke Management of Glaucoma. Frontiers in Neuroscience. 2020;14(March).
24. Coleman AL, Miglior S. Risk Factors for Glaucoma Onset and Progression. Survey of Ophthalmology. 2008;53(6 SUPPL.):3–10.
25. Wislicki L. Factors affecting intraocular pressure. Proceedings of the Royal Society of Medicine. 1977;70(5):372.
26. Khaw PT, Shah P, Elkington AR. Glaucoma--1: Diagnosis. BMJ. 2004 Jan 10;328(7431):97–9.
27. Hu CX, Zangalli C, Hsieh M, Gupta L, Williams AL, Richman J, et al. What Do Patients With Glaucoma See? Visual Symptoms Reported by Patients With Glaucoma. The American Journal of the Medical Sciences. 2014 Nov;348(5):403–9.
28. Crabb DP, Smith ND, Glen FC, Burton R, Garway-Heath DF. How Does Glaucoma Look? Ophthalmology. 2013 Jun;120(6):1120–6.
29. Lockwood AJ, Kirwan JF, Ashleigh Z. Optometrists referrals for glaucoma assessment: A prospective survey of clinical data and outcomes. Eye. 2010;24(9):1515–9.
30. Topouzis F, Coleman AL, Harris A, Koskosas A, Founti P, Gong G, et al. Factors Associated with Undiagnosed Open-Angle Glaucoma: The Thessaloniki Eye Study. American Journal of Ophthalmology. 2008;145(2):327–36.
31. Kumar Singh M. Challenges in diagnosis and management of glaucoma: Indian scenario. Indian Journal of Clinical and Experimental Ophthalmology. 2020 Mar 28;6(1):3–4.
32. Lee DA, Higginbotham EJ. Glaucoma and its treatment: a review. American journal of health-system pharmacy : AJHP : official journal of the American Society of Health-System Pharmacists. 2005 Apr 1;62(7):691–9.
33. Almasieh M, Wilson AM, Morquette B, Cueva Vargas JL, Di Polo A. The molecular basis of retinal ganglion cell death in glaucoma. Progress in Retinal and Eye Research. 2012;31(2):152–81.
34. Burgoyne CF, Crawford Downs J, Bellezza AJ, Francis Suh J-K, Hart RT. The optic nerve head as a biomechanical structure: a new paradigm for understanding the role of IOP-related stress and strain in the pathophysiology of glaucomatous optic nerve head damage. Progress in Retinal and Eye Research. 2005 Jan;24(1):39–73.
35. Morgan-Davies J, Taylor N, Hill AR, Aspinall P, O'Brien CJ, Azuara-Blanco A. Three

dimensional analysis of the lamina cribrosa in glaucoma. The British journal of ophthalmology. 2004 Oct;88(10):1299–304.
36. Grieshaber MC, Flammer J. Blood flow in glaucoma. Current Opinion in Ophthalmology. 2005;16(2):79–83.
37. Fechtner R, Weinreb R. Mechanisms of optic nerve damage in primary open angle glaucoma. Survey of Ophthalmology. 1994;39(1):23–42.
38. Quigley HA. Optic Nerve Damage in Human Glaucoma. Archives of Ophthalmology. 1981 Apr 1;99(4):635.
39. Morgan JE. Circulation and axonal transport in the optic nerve. Eye. 2004 Nov 8;18(11):1089–95.
40. Fahy ET, Chrysostomou V, Crowston JG. Impaired Axonal Transport and Glaucoma. Current Eye Research. 2015 Jun 30;3683:1–11.
41. Calkins DJ, Horner PJ. The Cell and Molecular Biology of Glaucoma: Axonopathy and the Brain. Investigative Opthalmology & Visual Science. 2012 May 3;53(5):2482.
42. Quigley HA, McKinnon SJ, Zack DJ, Pease ME, Kerrigan-Baumrind LA, Kerrigan DF, et al. Retrograde axonal transport of BDNF in retinal ganglion cells is blocked by acute IOP elevation in rats. Investigative Ophthalmology and Visual Science. 2000;41(11):3460–6.
43. Chidlow G, Ebneter A, Wood JPM, Casson RJ. The optic nerve head is the site of axonal transport disruption, axonal cytoskeleton damage and putative axonal regeneration failure in a rat model of glaucoma. Acta Neuropathologica. 2011;121(6):737–51.
44. Harwerth RS, Wheat JL, Rangaswamy N V. Age-Related Losses of Retinal Ganglion Cells and Axons. Investigative Opthalmology & Visual Science. 2008 Oct 1;49(10):4437.
45. Leydhecker W, Akiyama K, Neumann HG. Intraocular pressure in normal human eyes (Der intraokular Druck gesunder menschlicher Augen). Klinische Monatsblatter fur Augenheilkunde und fur augenarztliche Fortbildung. 1958;133(5):662–70.
46. Davanger M, Hotter Ö. THE STATISTICAL DISTRIBUTION OF INTRAOCULAR PRESSURE IN THE POPULATION. Acta Ophthalmologica. 1965 May 27;43(2):314–22.
47. Rawas-Qalaji M, Williams C-A. Advances in Ocular Drug Delivery. Current Eye Research. 2012 May 17;37(5):345–56.
48. Chowdhury UR, Madden BJ, Charlesworth MC, Fautsch MP. Proteome analysis of human aqueous humor. Investigative ophthalmology & visual science. 2010 Oct;51(10):4921–31.
49. Yadav KS, Sharma S. Implantable drainage devices in glaucoma: Quo vadis? European Journal of Pharmaceutical Sciences. 2019;133(February):1–7.
50. Ophthalmics I. Osmed | IOP Ophthalmics [Internet]. 2013 [cited 2015 Sep 10]. Available from: https://www.iopinc.com/store/osmed/
51. Pizzirani S, Gong H. Functional Anatomy of the Outflow Facilities. Veterinary Clinics of North America: Small Animal Practice. 2015 Nov;45(6):1101–26.
52. Brubaker RF. The flow of aqueous humor in the human eye. Transactions of the American Ophthalmological Society. 1982;80:391–474.
53. Brubaker RF. Flow of aqueous humor in humans. Investigative Ophthalmology and Visual Science. 1991;32(13):3145–66.

54. Goldmann H. Das Minutenvolumen der menschlichen Vorderkammer bei Normalen und bei Fallen von primärem Glaukom [Minute Volume of the Aqueous in the Anterior Chamber of the Human Eye in Normal State and in Primary Glaucoma]. Ophthalmologica. 1950;120(1–2):19–21.
55. Kiel JW, Hollingsworth M, Rao R, Chen M, Reitsamer HA. Ciliary blood flow and aqueous humor production. Progress in Retinal and Eye Research. 2011 Jan;30(1):1–17.
56. Abu-Hassan DW, Acott TS, Kelley MJ. The Trabecular Meshwork: A Basic Review of Form and Function. Journal of Ocular Biology. 2014;2(1).
57. Goel M, Picciani RG, Lee RK, Bhattacharya SK. Aqueous humor dynamics: a review. The open ophthalmology journal. 2010 Jan;4:52–9.
58. Oterendorp C Van. Bildgebung der intraskleralen Kammerwasserabflusswege – neue Einblicke für die Trabekelwerkschirurgie Imaging of the Intrascleral Aqueous Drainage System – New Insights for Glaucoma Surgery Targeting the Trabecular Meshwork Einführung. 2016;
59. Tektas OY, Lütjen-Drecoll E. Structural changes of the trabecular meshwork in different kinds of glaucoma. Experimental Eye Research. 2009;88(4):769–75.
60. Chowdhury UR, Hann CR, Stamer WD, Fautsch MP. Aqueous humor outflow: Dynamics and disease. Investigative Ophthalmology and Visual Science. 2015;56(5):2993–3003.
61. Keller KE, Acott TS. The Juxtacanalicular Region of Ocular Trabecular Meshwork: A Tissue with a Unique Extracellular Matrix and Specialized Function. Journal of ocular biology. 2013;1(1):3.
62. Buller C, Johnson D. Segmental variability of the trabecular meshwork in normal and glaucomatous eyes. Investigative ophthalmology & visual science. 1994;35(11):3841–51.
63. Flocks M. The anatomy of the trabecular meshwork as seen in tangential section. AMA archives of ophthalmology. 1956 Nov;56(5):708–18.
64. Siggers JH, Ethier CR. Fluid Mechanics of the Eye. Annual Review of Fluid Mechanics. 2012 Jan;44(1):347–72.
65. Kapetanakis V V., Chan MPY, Foster PJ, Cook DG, Owen CG, Rudnicka AR. Global variations and time trends in the prevalence of primary open angle glaucoma (POAG): A systematic review and meta-analysis. British Journal of Ophthalmology. 2016;100(1):86–93.
66. Weinreb RN, Leung CKS, Crowston JG, Medeiros FA, Friedman DS, Wiggs JL, et al. Primary open-angle glaucoma. Nature Reviews Disease Primers. 2016;2.
67. Kesav N, Palestine AG, Kahook MY, Pantcheva MB. Current management of uveitis-associated ocular hypertension and glaucoma. Survey of Ophthalmology. 2020 Jul;65(4):397–407.
68. Khazaeni B KL. Acute Closed Angle Glaucoma. In: StatPearls [Internet]. Treasure Island (FL): StatPearls Publishing; 2020.
69. Wiggs JL, Pasquale LR. Genetics of glaucoma. Human Molecular Genetics. 2017;26(R1):R21–7.
70. Wright C, Tawfik MA, Waisbourd M, Katz LJ. Primary angle-closure glaucoma: An update. Acta Ophthalmologica. 2016;94(3):217–25.
71. Jin Hui Goh E, Neelam K, Sangtam T, Stanley P. A case of bilateral acute angle closure glaucoma secondary to systemic decongestants. Acta Ophthalmologica. 2019 Dec 19;97(S263):j.1755-3768.2019.5362.

72. Garway-Heath DF, Crabb DP, Bunce C, Lascaratos G, Amalfitano F, Anand N, et al. Latanoprost for open-angle glaucoma (UKGTS): a randomised, multicentre, placebo-controlled trial. The Lancet. 2015 Apr;385(9975):1295–304.
73. Hyman L, Heijl A, Leske MC, Bengtsson B, Yang Z. Natural history of intraocular pressure in the early manifest glaucoma trial: A 6-year follow-up. Archives of ophthalmology. 2010;128(5):601–7.
74. Chang EE, Goldberg JL. Glaucoma 2.0: Neuroprotection, neuroregeneration, neuroenhancement. Ophthalmology. 2012;119(5):979–86.
75. Kass MA, Heuer DK, Higginbotham EJ, Johnson CA, Keltner JL, Miller JP, et al. The Ocular Hypertension Treatment Study: a randomized trial determines that topical ocular hypotensive medication delays or prevents the onset of primary open-angle glaucoma. Archives of ophthalmology (Chicago, Ill : 1960). 2002 Jun;120(6):701–13; discussion 829-30.
76. Musch DC, Gillespie BW, Lichter PR, Niziol LM, Janz NK, CIGTS Study Investigators. Visual field progression in the Collaborative Initial Glaucoma Treatment Study the impact of treatment and other baseline factors. Ophthalmology. 2009 Feb;116(2):200–7.
77. Heijl A, Leske MC, Bengtsson B, Hyman L, Bengtsson B, Hussein M, et al. Reduction of intraocular pressure and glaucoma progression: results from the Early Manifest Glaucoma Trial. Archives of ophthalmology (Chicago, Ill : 1960). 2002 Oct;120(10):1268–79.
78. The Agis Investigators. The advanced glaucoma intervention study (AGIS): 7. the relationship between control of intraocular pressure and visual field deterioration. American Journal of Ophthalmology. 2000 Oct;130(4):429–40.
79. Occhiutto ML, Maranhão RC, Costa VP, Konstas AG. Nanotechnology for Medical and Surgical Glaucoma Therapy—A Review. Advances in Therapy. 2020;37(1):155–99.
80. Mohamed NG, Yap TE, Almonte M, Susanna FN, Crawley L, Cordeiro MF. Focusing on surgical and laser advances in glaucoma management. Expert Review of Ophthalmology. 2020 Jan 2;15(1):27–41.
81. Winfield AJ, Jessiman D, Williams A, Esakowitz L. A study of the causes of non-compliance by patients prescribed eyedrops. British Journal of Ophthalmology. 1990 Aug 1;74(8):477–80.
82. Maurice DM, Mishima S. Handbook of Experimental Pharmacology. In: Sears, M.L. Berlin-Heidelberg: Springer: Berlin-Heidelberg, Germany; 1984. p. 16–119.
83. Balendra SI, Zollet P, Cisa Asinari Di Gresy E Casasca G, Cordeiro MF. Personalized approaches for the management of glaucoma. Expert Review of Precision Medicine and Drug Development. 2020;00(00):1–20.
84. Dahlmann-Noor AH, Vijay S, Limb GA, Khaw PT. Strategies for optic nerve rescue and regeneration in glaucoma and other optic neuropathies. Drug Discovery Today. 2010;15(7–8):287–99.
85. Metoki T, Ohguro H, Ohguro I, Mamiya K, Ito T, Nakazawa M. Study of effects of antiglaucoma eye drops on N-methyl-D-aspartate-induced retinal damage. Japanese Journal of Ophthalmology. 2005;49(6):453–61.
86. Sambhara D, Aref A a. Glaucoma management: relative value and place in therapy of available drug treatments. Therapeutic advances in chronic disease. 2014;5(1):30–43.
87. Lichter PR, Musch DC, Medzihradsky F, Standardi CL. Intraocular pressure effects

of carbonic anhydrase inhibitors in primary open-angle glaucoma. Vol. 107, American journal of ophthalmology. 1989.
88. Babić N. Fixed combinations of glaucoma medications. Srpski Arhiv za Celokupno Lekarstvo. 2015;143(9–10):626–31.
89. ClinicalTrials.gov. NCT03310580 Study of Netarsudil Ophthalmic Solution in Japanese/Japanese-American Subjects With Open-angle Glaucoma or Ocular Hypertension [Internet]. NIH U.S. National Library of Medicine. 2017. Available from: https://clinicaltrials.gov/ct2/show/NCT03310580?term=optimed&cond=glaucoma&draw=2&rank=1
90. Kolko M. Present and New Treatment Strategies in the Management of Glaucoma. The open ophthalmology journal. 2015;9:89–100.
91. Radhakrishnan S, Iwach A. Glaucoma Medications and their Side Effects [Internet]. Glaucoma Research Foundation. 2018. Available from: https://www.glaucoma.org/gleams/glaucoma-medications-and-their-side-effects.php
92. Craven ER, Walters T, Christie WC, Day DG, Lewis RA, Goodkin ML, et al. 24-Month Phase I/II Clinical Trial of Bimatoprost Sustained-Release Implant (Bimatoprost SR) in Glaucoma Patients. Drugs. 2020 Feb 28;80(2):167–79.
93. ClinicalTrials.gov. NCT02087085 A Safety and Efficacy Study of Brimonidine Intravitreal Implant in Geographic Atrophy Secondary to Age-related Macular Degeneration (BEACON) [Internet]. NIH U.S. National Library of Medicine. 2018. Available from: https://clinicaltrials.gov/ct2/show/NCT02087085
94. Doucette LP, Walter MA. Prostaglandins in the eye: Function, expression, and roles in glaucoma. Ophthalmic Genetics. 2017 Mar 4;38(2):108–16.
95. Mulvihill A. Medical management of glaucoma. Irish medical journal. 1998;91(3):84.
96. Lang JC. Ocular drug delivery conventional ocular formulations. Advanced Drug Delivery Reviews. 1995;16(1):39–43.
97. Inoue K. Managing adverse effects of glaucoma medications. Clinical Ophthalmology. 2014;8:903–13.
98. Noecker R. Effects of common ophthalmic preservatives on ocular health. Advances in Therapy. 2001;18(5):205–15.
99. Konowal A, Morrison JC, Brown SVL, Cooke DL, Maguire LJ, Verdier D V., et al. Irreversible corneal decompensation in patients treated with topical dorzolamide. American Journal of Ophthalmology. 1999;127(4):403–6.
100. Muir KW. Glaucoma Medication Adherence. Archives of Ophthalmology. 2011 Feb 14;129(2):243.
101. Okeke CO, Quigley HA, Jampel HD, Ying G, Plyler RJ, Jiang Y, et al. Adherence with Topical Glaucoma Medication Monitored Electronically. Ophthalmology. 2009 Feb;116(2):191–9.
102. Kass MA, Gordon M, Morley RE, Meltzer DW, Goldberg JJ. Compliance With Topical Timolol Treatment. American Journal of Ophthalmology. 1987 Feb;103(2):188–93.
103. Kass MA, Meltzer DW, Gordon M, Cooper D, Goldberg J. Compliance with Topical Pilocarpine Treatment. American Journal of Ophthalmology. 1986 May;101(5):515–23.
104. Tse AP, Shah M, Jamal N, Shaikh A. Glaucoma treatment adherence at a United

Kingdom general practice. Eye (Basingstoke). 2016;30(8):1118–22.
105. Sleath B, Robin AL, Covert D, Byrd JE, Tudor G, Svarstad B. Patient-reported behavior and problems in using glaucoma medications. Ophthalmology. 2006;113(3):431–6.
106. Sleath BL, Krishnadas R, Cho M, Robin AL, Mehta R, Covert D, et al. Patient-reported barriers to glaucoma medication access, use, and adherence in southern India. Indian journal of ophthalmology. 2009;57(1):63–8.
107. NICE. Glaucoma: brinzolamide/brimonidine combination eye drops Evidence summary [ESNM56]. 2015.
108. Barnebey HS, Robin AL. Adherence to Fixed-Combination Versus Unfixed Travoprost 0.004%/Timolol 0.5% for Glaucoma or Ocular Hypertension: A Randomized Trial. American Journal of Ophthalmology. 2017 Apr;176:61–9.
109. Manickavasagam D, Oyewumi MO. Critical assessment of implantable drug delivery devices in glaucoma management. Journal of drug delivery. 2013;2013:895013.
110. Heijl A, Peters D, Leske MC, Bengtsson B. Effects of argon laser trabeculoplasty in the Early Manifest Glaucoma Trial. American journal of ophthalmology. 2011 Nov;152(5):842–8.
111. GLAUCOMA LASER TRIAL RESEARCH GROUP. The Glaucoma Laser Trial (GLT): 6. Treatment Group Differences in Visual Field Changes. American Journal of Ophthalmology. 1995 Jul;120(1):10–22.
112. Martinez-de-la-Casa JM, Garcia-Feijoo J, Castillo A, Matilla M, Macias JM, Benitez-del-Castillo JM, et al. Selective vs argon laser trabeculoplasty: Hypotensive efficacy, anterior chamber inflammation, and postoperative pain. Eye. 2004;18(5):498–502.
113. Mahdy M a-MS. Efficacy and safety of selective laser trabeculoplasty as a primary procedure for controlling intraocular pressure in primary open angle glaucoma and ocular hypertensive patients. Sultan Qaboos University medical journal. 2008 Mar;8(1):53–8.
114. Kramer TR, Noecker RJ. Comparison of the morphologic changes after selective laser trabeculoplasty and argon laser trabeculoplasty in human eye bank eyes. Ophthalmology. 2001 Apr;108(4):773–9.
115. Ansari E, Gandhewar J. Long-term efficacy and visual acuity following transscleral diode laser photocoagulation in cases of refractory and non-refractory glaucoma. Eye (London, England). 2007 Jul;21(7):936–40.
116. Roberts MA, Rajkumar V, Morgan G, Laws D. Sympathetic ophthalmia secondary to cyclodiode laser in a 10-year-old boy. Journal of American Association for Pediatric Ophthalmology and Strabismus. 2009 Jun;13(3):299–300.
117. Tay E, Aung T, Murdoch I. Suprachoroidal haemorrhage: a rare complication of cyclodiode laser therapy. Eye. 2006 May 3;20(5):625–7.
118. Wise JB. Ten year results of laser trabeculoplasty. Does the laser avoid glaucoma surgery or merely defer it? Eye (London, England). 1987 Jan;1 (Pt 1)(1):45–50.
119. Bar-David L, Blumenthal EZ. Evolution of Glaucoma Surgery in the Last 25 Years. Rambam Maimonides Medical Journal. 2018;9(3):e0024.
120. Yu D-Y, Morgan WH, Sun X, Su E-N, Cringle SJ, Yu PK, et al. The critical role of the conjunctiva in glaucoma filtration surgery. Progress in retinal and eye research. 2009 Sep;28(5):303–28.
121. Cairns JE. Trabeculectomy. Preliminary report of a new method. American journal

of ophthalmology. 1968 Oct;66(4):673–9.
122. Rulli E, Biagioli E, Riva I, Gambirasio G, De Simone I, Floriani I, et al. Efficacy and safety of trabeculectomy vs nonpenetrating surgical procedures: A systematic review and meta-analysis. JAMA Ophthalmology. 2013;131(12):1573–82.
123. Boland M V., Ervin A-M, Friedman DS, Jampel HD, Hawkins BS, Vollenweider D, et al. Comparative Effectiveness of Treatments for Open-Angle Glaucoma: A Systematic Review for the U.S. Preventive Services Task Force. Annals of Internal Medicine. 2013 Feb 19;158(4):271.
124. Lee RMH, Bouremel Y, Eames I, Brocchini S, Khaw PT. Translating Minimally Invasive Glaucoma Surgery Devices. Clinical and Translational Science. 2020;13(1):14–25.
125. Team A project. Experimental flow studies in glaucoma drainage device development. Ophthalmol, Br J. 2001;1231–6.
126. Dhingra S, Khaw PT. The moorfields safer surgery system. Middle East African journal of ophthalmology. 2009 Jul;16(3):112–5.
127. Khaw PT, Chiang M, Shah P, Sii F, Lockwood A, Khalili A. Enhanced Trabeculectomy: The Moorfields Safer Surgery System. In 2017. p. 15–35.
128. Aref AA, Gedde SJ, Budenz DL. Glaucoma Drainage Implant Surgery. In: Bettin P, Khaw PT, editors. Glaucoma Surgery. 2nd ed. Basel: Karger; 2017. p. 43–52.
129. Lockwood A, Khaw PT. The Impact of Wound Healing on Glaucoma Therapy. Glaucoma Today. 2013;(October):1–3.
130. Skuta GL, Parrish RK. Wound healing in glaucoma filtering surgery. Survey of ophthalmology. 1987;32(3):149–70.
131. Seibold LK, Sherwood MB, Kahook MY. Wound modulation after filtration surgery. Survey of ophthalmology. 2012 Nov;57(6):530–50.
132. Gedde SJ, Schiffman JC, Feuer WJ, Herndon LW, Brandt JD, Budenz DL. Treatment outcomes in the tube versus trabeculectomy study after one year of follow-up. American journal of ophthalmology. 2007 Jan;143(1):9–22.
133. Kim J, Allingham RR, Hall J, Klitzman B, Stinnett S, Asrani S. Clinical Experience With a Novel Glaucoma Drainage Implant. Journal of Glaucoma. 2014 Feb;23(2):e91–7.
134. Lim KS, Allan BDS, Lloyd AW, Muir A, Khaw PT, LIM KS, et al. Glaucoma drainage devices; past, present, and future. British Journal of Ophthalmology. 1998 Sep 1;82(9):1083–9.
135. Porter JM, Krawczyk CH, Carey RF. In Vitro Flow Testing of Glaucoma Drainage Devices. Ophthalmology. 1997 Oct;104(10):1701–7.
136. Singh P, Kuldeep K, Tyagi M, Sharma P, Kumar Y. Glaucoma drainage devices. Journal of Clinical Ophthalmology and Research. 2013;1(2):77.
137. Molteno a C, Straughan JL, Ancker E. Long tube implants in the management of glaucoma. South African medical journal = Suid-Afrikaanse tydskrif vir geneeskunde. 1976 Jun;50(27):1062–6.
138. Riva I, Roberti G, Oddone F, Konstas AG, Quaranta L. Ahmed glaucoma valve implant: surgical technique and complications. Clinical Ophthalmology. 2017 Feb;Volume 11:357–67.
139. Schwartz KS, Lee RK, Gedde SJ. Glaucoma drainage implants: a critical comparison of types. Current opinion in ophthalmology. 2006 Apr;17(2):181–9.
140. Krupin T, Podos SM, Becker B, Newkirk JB. Valve implants in filtering surgery. American journal of ophthalmology. 1976 Feb;81(2):232–5.

141. Wang J, Barton K. Aqueous shunt implantation in glaucoma. Taiwan Journal of Ophthalmology. 2017;7(3):130.
142. Kramer G. EDITOR Molten0 Implant Surgery in Refractory Glaucoma. 1990;34(6).
143. Molteno AC, Polkinghorne PJ, Bowbyes JA. The vicryl tie technique for inserting a draining implant in the treatment of secondary glaucoma. Australian and New Zealand journal of ophthalmology. 1986 Nov;14(4):343–54.
144. Molteno a C. The dual chamber single plate implant--its use in neovascular glaucoma. Australian and New Zealand journal of ophthalmology. 1990 Dec;18(4):431–6.
145. CDRH. Guidance for Industry and for FDA Reviewers / Staff Guidance on 510 (k) Submissions for Aqueous Shunts. Vol. 510, World. 1998.
146. Ayyala RS, Zurakowski D, Monshizadeh R, Hong C-H, Richards D, Layden WE, et al. Comparison of double-plate Molteno and Ahmed glaucoma valve in patients with advanced uncontrolled glaucoma. Ophthalmic surgery and lasers. 2002;33(2):94–101.
147. Patel S, Pasquale LR. Glaucoma drainage devices: A review of the past, present, and future. Seminars in Ophthalmology. 2010;25(5–6):265–70.
148. Dietlein T, Neugebauer A, Fricke J, Lappas A, Rosentreter A. Nachsorge von epibulbären Glaukomdrainageimplantaten. Klinische Monatsblätter für Augenheilkunde. 2016 May 17;233(05):606–12.
149. Choudhari NS, Badakere SV, Richhariya A, Chittajallu SNSH, Senthil S, Garudadri CS. Is Ahmed Glaucoma Valve Consistent in Performance? Translational Vision Science & Technology. 2018 Jun 22;7(3):19.
150. Luong QM, Shang L, Ang M, Kong JF, Peng Y, Wong TT, et al. A New Design and Application of Bioelastomers for Better Control of Intraocular Pressure in a Glaucoma Drainage Device. Advanced Healthcare Materials. 2014 Feb;3(2):205–13.
151. Chaudhry M, Grover S, Baisakhiya S, Bajaj A, Ms B. Review article Artificial drainage devices for glaucoma surgery : an overview. 2012;4(8):295–302.
152. Wilson-Holt N, Franks W, Nourredin B, Hitchings R. Hypertropia following insertion of inferiorly sited double-plate Molteno tubes. Eye (London, England). 1992 Jan;6 (Pt 5):515–20.
153. Siegner SW, Netland P a., Urban RC, Williams a. S, Richards DW, Latina M a., et al. Clinical Experience with the Baerveldt Glaucoma Drainage Implant. Ophthalmology. 1995 Sep;102(9):1298–307.
154. Ceballos EM, Parrish RK, Schiffman JC. Outcome of Baerveldt glaucoma drainage implants for the treatment of uveitic glaucoma. Ophthalmology. 2002 Dec;109(12):2256–60.
155. Good TJ, Kahook MY. Assessment of bleb morphologic features and postoperative outcomes after Ex-PRESS drainage device implantation versus trabeculectomy. American journal of ophthalmology. 2011 Mar;151(3):507-13.e1.
156. Nyska A, Glovinsky Y, Belkin M, Epstein Y. Biocompatibility of the Ex-PRESS miniature glaucoma drainage implant. Journal of glaucoma. 2003 Jun;12(3):275–80.
157. Rivier D, Roy S, Mermoud A. Ex-PRESS R-50 miniature glaucoma implant insertion under the conjunctiva combined with cataract extraction. Journal of cataract and refractive surgery. 2007 Nov;33(11):1946–52.
158. Hille K, Ruprecht KW. The Ahmed Glaucoma Valve – a new implant for high

intraocular pressure. Der Ophthalmologe. 1999 Oct 1;96(10):653–7.
159. Ayyala RS, Zurakowski D, Smith JA, Monshizadeh R, Netland PA, Richards DW, et al. A clinical study of the Ahmed glaucoma valve implant in advanced glaucoma. Ophthalmology. 1998 Oct;105(10):1968–76.
160. ClinicalTrials.gov. NCT01563237 Safety and Performance of Miami InnFocus Drainage Implant (MIDI Arrow) Glaucoma Drainage Implant [Internet]. NIH U.S. National Library of Medicine. 2012. Available from: https://clinicaltrials.gov/ct2/show/NCT01563237
161. Acosta AC, Espana EM, Yamamoto H, Davis S, Pinchuk L, Weber BA, et al. A newly designed glaucoma drainage implant made of poly(styrene-b-isobutylene-b-styrene): biocompatibility and function in normal rabbit eyes. Archives of ophthalmology. 2006 Dec;124(12):1742–9.
162. Hueber A, Roters S, Jordan JF, Konen W. Retrospective analysis of the success and safety of Gold Micro Shunt Implantation in glaucoma. BMC ophthalmology. 2013 Jul;13(1):35.
163. Höh H, Grisanti S, Grisanti S, Rau M, Ianchulev S. Two-year clinical experience with the CyPass micro-stent: Safety and surgical outcomes of a novel supraciliary micro-stent. Klinische Monatsblatter fur Augenheilkunde. 2014;231(4):377–81.
164. ClinicalTrials.gov. NCT03065036 Safety and Efficacy Study of the Hydrus Aqueous Implant in Subjects With POAG (POAG) [Internet]. NIH U.S. National Library of Medicine. 2017. Available from: https://clinicaltrials.gov/ct2/show/NCT03065036?term=hydrus&draw=2&rank=2
165. FDA. Recently-Approved Devices - Glaukos iStent® Trabecular Micro-Bypass Stent (Models: GTS-100R, GTS-100L) and Inserter (GTS-100i) - P080030. Center for Devices and Radiological Health; 2012.
166. ClinicalTrials.gov. NCT02024464 Comparing Hydrus Microstent(TM) to the iStent for Lowering IOP in Glaucoma Patients Undergoing Cataract Surgery [Internet]. NIH U.S. National Library of Medicine. 2013. Available from: https://clinicaltrials.gov/ct2/show/NCT02024464?term=hydrus&draw=2&rank=4
167. Tetz M, Knowlton P. New Glaucoma Devices. Eurotimes. 2009;16/17(12/1):36–7.
168. Lewis R a. Ab interno approach to the subconjunctival space using a collagen glaucoma stent. Journal of Cataract and Refractive Surgery. 2014 Aug;40(8):1301–6.
169. FDA. Recently-Approved Devices - AquaFlow™ Collagen Glaucoma Drainage Device - Model CGDD-20 - P000026. Center for Devices and Radiological Health; 2001.
170. Pourjavan S, Collignon N, De Groot V. STARflo™ Glaucoma Implant: 12 month clinical results. Acta Ophthalmologica. 2013 Aug;91.
171. Kammer J, Mundy K. Suprachoroidal devices in glaucoma surgery. Middle East African Journal of Ophthalmology. 2015;22(1):45.
172. Samsudin A, Eames I, Brocchini S, Khaw PT. Evaluation of Dimensional and Flow Properties of ExPress Glaucoma Drainage Devices. Journal of Glaucoma. 2016 Jan;25(1):e39–45.
173. Huerva V, Soldevila J, Ascaso FJ, Lavilla LM, Muniesa J, Sánchez MC. Evaluation of the Ex-PRESS® P-50 implant under scleral flap in combined cataract and glaucoma surgery. International Journal of Ophthalmology. 2016 Apr 18;9(4):546–50.

174. Dada T, Angmo D, Sharma R, Temkar S. Evaluation of ExPress glaucoma filtration device in Indian patients with advanced glaucoma. Indian Journal of Ophthalmology. 2015;63(5):459.
175. Malvankar-Mehta MS, Chen YN, Iordanous Y, Wang WW, Costella J, Hutnik CML. iStent as a Solo Procedure for Glaucoma Patients: A Systematic Review and Meta-Analysis. Pasquale LR, editor. PLOS ONE. 2015 May 27;10(5):e0128146.
176. Ayyala RS, Michelini-Norris B, Flores a, Haller E, Margo CE. Comparison of different biomaterials for glaucoma drainage devices: part 2. Archives of ophthalmology. 2000;118(8):1081–4.
177. El Sayed Y, Awadein A. Polypropylene vs silicone Ahmed valve with adjunctive mitomycin C in paediatric age group: a prospective controlled study. Eye. 2013 Jun 12;27(6):728–34.
178. Ishida K, Netland PA, Costa VP, Shiroma L, Khan B, Ahmed IIK. Comparison of Polypropylene and Silicone Ahmed Glaucoma Valves. Ophthalmology. 2006;113(8):1320–6.
179. Ichhpujani P, Moster M. Novel Glaucoma Surgical Devices. Glaucoma-Basic and clinical …. 2011;417–42.
180. Rao K, Ahmed I, Blake D a, Ayyala RS. New devices in glaucoma surgery. Expert Review of Ophthalmology. 2009 Oct;4(5):491–504.
181. Pinchuk L, Wilson GJ, Barry JJ, Schoephoerster RT, Parel JM, Kennedy JP. Medical applications of poly(styrene-block-isobutylene-block-styrene) ("SIBS"). Biomaterials. 2008;29(4):448–60.
182. Ayyala RS. Comparison of Different Biomaterials for Glaucoma Drainage Devices. Archives of Ophthalmology. 1999 Feb 1;117(2):233.
183. Ayyala RS. Comparison of Different Biomaterials for Glaucoma Drainage Devices<subtitle>Part 2</subtitle>. Archives of Ophthalmology. 2000 Aug 1;118(8):1081.
184. Hong CH, Arosemena A, Zurakowski D, Ayyala RS. Glaucoma drainage devices: A systematic literature review and current controversies. Survey of Ophthalmology. 2005;50(1):48–60.
185. Heuer DK, Lloyd MA, Abrams DA, Baerveldt G, Minckler DS, Lee MB, et al. Which Is Better? One or Two? A Randomized Clinical Trial of Single-plate versus Double-plate Molteno Implantation for Glaucomas in Aphakia and Pseudophakia. Ophthalmology. 1992;99(10):1512–9.
186. Gonzalez AC de O, Costa TF, Andrade Z de A, Medrado ARAP. Wound healing - A literature review. Anais Brasileiros de Dermatologia. 2016 Oct;91(5):614–20.
187. Barišić A, Dević Pavlić S, Ostojić S, Pereza N. Matrix metalloproteinase and tissue inhibitors of metalloproteinases gene polymorphisms in disorders that influence fertility and pregnancy complications: A systematic review and meta-analysis. Gene. 2018 Mar;647:48–60.
188. Bruno CA, Fisher GJ, Moroi SE. Is 'scarless wound healing' applicable to glaucoma surgery? Expert Review of Ophthalmology. 2007 Feb 9;2(1):79–90.
189. Yamanaka O, Kitano-Izutani A, Tomoyose K, Reinach PS. Pathobiology of wound healing after glaucoma filtration surgery. BMC Ophthalmology. 2015 Nov 17;15(S1):157.
190. Edward D, Al Habash A, Aljasim L, Owaidhah O. A review of the efficacy of mitomycin C in glaucoma filtration surgery. Clinical Ophthalmology. 2015 Oct;9:1945.

191. Amoozgar B, Lin SC, Han Y, Kuo J. A role for antimetabolites in glaucoma tube surgery. Current Opinion in Ophthalmology. 2016 Mar;27(2):164–9.
192. Zada M, Pattamatta U, White A. Modulation of Fibroblasts in Conjunctival Wound Healing. Ophthalmology. 2018 Feb;125(2):179–92.
193. ClinicalTrials.gov. NCT00306852 Tube Versus Trabeculectomy (TVT) Study [Internet]. NIH U.S. National Library of Medicine. 2006. Available from: https://clinicaltrials.gov/ct2/show/NCT00306852
194. Gedde SJ, Schiffman JC, Feuer WJ, Herndon LW, Brandt JD, Budenz DL. Treatment Outcomes in the Tube Versus Trabeculectomy (TVT) Study After Five Years of Follow-up. American Journal of Ophthalmology. 2012 May;153(5):789-803.e2.
195. Kwong TQ, Mahroo O, Scoppettuolo E, Ansari E. Outcomes of Trabeculectomy With Transconjunctival Application Versus Subconjunctival Application of Mitomycin C. Journal of Glaucoma. 2016 Jun;25(6):467–71.
196. Dada T, Midha N, Shah P, Sidhu T, Angmo D, Sihota R. Innovations in glaucoma surgery from Dr. Rajendra Prasad Centre for Ophthalmic Sciences. Indian Journal of Ophthalmology. 2017;65(2):103.
197. Mirshahi A, Lashay A, Mehrabi Bahar MR, Abrishami M. Consequences of inadvertent intravitreal Mitomycin C injection. International Journal of Retina and Vitreous. 2018 Dec 12;4(1):7.
198. Maquet JA, Dios E, Aragón J, Bailez C, Ussa F, Laguna N. Protocol for mitomycin C use in glaucoma surgery. Acta ophthalmologica Scandinavica. 2005 Apr;83(2):196–200.
199. Wu Z, Li S, Wang N, Liu W, Liu W. A comparative study of the safety and efficacy effect of 5-fluorouracil or mitomycin C mounted biological delivery membranes in a rabbit model of glaucoma filtration surgery. Clinical Ophthalmology. 2013 Mar;7:655–62.
200. Stiles M. Glaucoma Today - Filtration Surgery: Indications and Improvements (July/August 2014) [Internet]. 2014 [cited 2015 Sep 10]. p. 48–9. Available from: http://glaucomatoday.com/2014/08/filtration-surgery-indications-and-improvements/
201. FDA. Summary review of Mitosol for glaucoma surgery. Application Number:0225720rig1S000. 2012.
202. Mitomycin solution (Mitosol) for glaucoma surgery. The Medical letter on drugs and therapeutics. 2013 Mar 18;55(1412):24.
203. NIHR Horizon Scanning Research & Intelligence Centre. Mitomycin ophthalmic (Mitosol) for glaucoma surgery. 2016.
204. Schlunck G, Meyer-ter-Vehn T, Klink T, Grehn F. Conjunctival fibrosis following filtering glaucoma surgery. Experimental Eye Research. 2016 Jan;142:76–82.
205. Mohamed-Ahmed AHA, Lockwood A, Li H, Bailly M, Khaw PT, Brocchini S. An ilomastat-CD eye drop formulation to treat ocular scarring. Investigative Ophthalmology and Visual Science. 2017;58(9):3425–31.
206. Yi Q, Zou W. The Wound Healing Effect of Doxycycline after Corneal Alkali Burn in Rats. Journal of Ophthalmology. 2019 Oct 10;2019:1–10.
207. Jung KI, Park CK. Pirfenidone inhibits fibrosis in foreign body reaction after glaucoma drainage device implantation. Drug Design, Development and Therapy. 2016;10:1477–88.
208. Zhang F, Liu K, Cao M, Qu J, Zhou D, Pan Z, et al. Rosiglitazone Treatment Prevents Postoperative Fibrosis in a Rabbit Model of Glaucoma Filtration Surgery.

Investigative Opthalmology & Visual Science. 2019 Jun 27;60(7):2743.
209. Wen H, Jung H, Li X. Drug Delivery Approaches in Addressing Clinical Pharmacology-Related Issues: Opportunities and Challenges. The AAPS Journal. 2015 Nov 15;17(6):1327–40.
210. Cima MJ, Lee H, Daniel K, Tanenbaum LM, Mantzavinou A, Spencer KC, et al. Single compartment drug delivery. Journal of Controlled Release. 2014 Sep;190:157–71.
211. Kobayashi H, Kohshima S. Unique morphology of the human eye and its adaptive meaning: comparative studies on external morphology of the primate eye. Journal of human evolution. 2001;40(5):419–35.
212. McCaa CS. The eye and visual nervous system: anatomy, physiology and toxicology. Environmental health perspectives. 1982 Apr;44(April):1–8.
213. Willoughby CE, Ponzin D, Ferrari S, Lobo A, Landau K, Omidi Y. Anatomy and physiology of the human eye: effects of mucopolysaccharidoses disease on structure and function - a review. Clinical & Experimental Ophthalmology. 2010 Aug;38(May):2–11.
214. Molokhia S a, Thomas SC, Garff KJ, Mandell KJ, Wirostko BM. Anterior eye segment drug delivery systems: current treatments and future challenges. Journal of ocular pharmacology and therapeutics : the official journal of the Association for Ocular Pharmacology and Therapeutics. 2013 Mar;29(2):92–105.
215. Sridhar MS. Anatomy of cornea and ocular surface. Indian Journal of Ophthalmology. 2018;66(2):190–4.
216. Novack G. Ophthalmic Drug Delivery: Development and Regulatory Considerations. Clinical Pharmacology & Therapeutics. 2009 May 18;85(5):539–43.
217. Gaudana R, Ananthula HK, Parenky A, Mitra AK. Ocular drug delivery. The AAPS journal. 2010;12(3):348–60.
218. Agrahari V, Mandal A, Agrahari V, Trinh HM, Mitra AK. A comprehensive insight on ocular pharmacokinetics. Drug Delivery and Translational Research. 2016;735–54.
219. Davies NM. Biopharmaceutical Considerations In Topical Ocular Drug Delivery. Clinical and Experimental Pharmacology and Physiology. 2000 Jul;27(7):558–62.
220. Hämäläinen KM, Kananen K, Auriola S, Kontturi K, Urtti A. Characterization of paracellular and aqueous penetration routes in cornea, conjunctiva, and sclera. Investigative Ophthalmology and Visual Science. 1997;38(3):627–34.
221. Cholkar K, Dasari SR, Pal D, Mitra AK. Eye: anatomy, physiology and barriers to drug delivery. In: Ocular Transporters and Receptors. Elsevier; 2013. p. 1–36.
222. Durairaj C. Ocular Pharmacokinetics. In: Whitcup SM, Azar DT, editors. Pharmacologic Therapy of Ocular Disease, Handbook of Experimental Pharmacology. Springer International Publishing Switzerland; 2016. p. 31–55.
223. Urtti A. Challenges and obstacles of ocular pharmacokinetics and drug delivery. Advanced Drug Delivery Reviews. 2006 Nov;58(11):1131–5.
224. Maulvi FA, Soni TG, Shah DO. A review on therapeutic contact lenses for ocular drug delivery. Drug Delivery. 2016;23(8):3017–26.
225. Hosoya K, Lee VHL, Kim K-J. Roles of the conjunctiva in ocular drug delivery: a review of conjunctival transport mechanisms and their regulation. European Journal of Pharmaceutics and Biopharmaceutics. 2005 Jul;60(2):227–40.
226. Kim SH, Csaky KG, Wang NS, Lutz RJ. Drug Elimination Kinetics Following

Subconjunctival Injection Using Dynamic Contrast-Enhanced Magnetic Resonance Imaging. Pharmaceutical Research. 2008 Mar 3;25(3):512–20.
227. Delplace V, Payne S, Shoichet M. Delivery strategies for treatment of age-related ocular diseases: From a biological understanding to biomaterial solutions. Journal of Controlled Release. 2015 Dec;219:652–68.
228. Gaudana R, Ananthula HK, Parenky A, Mitra AK. Ocular Drug Delivery. The AAPS Journal. 2010 Sep 1;12(3):348–60.
229. Malhotra M, Majumdar DK. Permeation through cornea. Indian Journal of Experimental Biology. 2001;39(1):11–24.
230. Cui L, Sun N, Li X, Huang J, Yang J. Subconjunctival sustained release 5-fluorouracil for glaucoma filtration surgery. Acta pharmacologica Sinica. 2008 Sep;29(9):1021–8.
231. Wong TTL, Mead AL, Khaw PT. Matrix metalloproteinase inhibition modulates postoperative scarring after experimental glaucoma filtration surgery. Investigative Ophthalmology and Visual Science. 2003 Mar;44(3):1097–103.
232. Kotliar K, Maier M, Bauer S, Feucht N, Lohmann C, Lanzl I. Effect of intravitreal injections and volume changes on intraocular pressure: clinical results and biomechanical model. Acta Ophthalmologica Scandinavica. 2007 Jun 16;85(7):777–81.
233. Yasukawa T, Ogura Y, Sakurai E, Tabata Y, Kimura H. Intraocular sustained drug delivery using implantable polymeric devices. Advanced drug delivery reviews. 2005 Dec 13;57(14):2033–46.
234. ClinicalTrials.gov. NCT02129673 A Phase 1/2 Multicenter, Randomized, Study to Evaluate the Safety and Efficacy of VS101 Subconjunctival Latanoprost Insert in Subjects With Open-Angle Glaucoma or Ocular Hypertension [Internet]. NIH U.S. National Library of Medicine. 2017. Available from: https://clinicaltrials.gov/ct2/show/NCT02129673
235. Weng Y, Liu J, Jin S, Guo W, Liang X, Hu Z. Nanotechnology-based strategies for treatment of ocular disease. Acta Pharmaceutica Sinica B. 2017;7(3):281–91.
236. Walters TR, Lee SS, Goodkin ML, Whitcup SM, Robinson MR. Bimatoprost Sustained-Release Implants for Glaucoma Therapy: 6-Month Results From a Phase I/II Clinical Trial. American Journal of Ophthalmology. 2017;175:137–47.
237. Franca JR, Foureaux G, Fuscaldi LL, Ribeiro TG, Rodrigues LB, Bravo R, et al. Bimatoprost-loaded ocular inserts as sustained release drug delivery systems for glaucoma treatment: In Vitro and in Vivo evaluation. PLoS ONE. 2014;9(4):1–11.
238. Nguyen T, Kim H, Mielke C, Momont AC, Brandt JD, Liu Y. Combined Dexamethasone Intravitreal Implant and Glaucoma Drainage Device Placement for Uveitic Glaucoma. Journal of Glaucoma. 2020 Apr;29(4):252–7.
239. Mohamed-Ahmed AHA, Lockwood A, Fadda H, Madaan S, Khaw PT, Brocchini S, et al. LC–MS analysis to determine the biodistribution of a polymer coated ilomastat ocular implant. Journal of Pharmaceutical and Biomedical Analysis. 2018;157:100–6.
240. ClinicalTrials.gov. NCT01408472 NT-501 CNTF Implant for Glaucoma: Safety, Neuroprotection and Neuroenhancement [Internet]. NIH U.S. National Library of Medicine. 2011. Available from: https://www.clinicaltrials.gov/ct2/show/NCT01408472?term=NCT01408472&rank=1
241. Kim J, Kudisch M, Rosa N, Asada H, Aya-shibuya E, Bloomer MM, et al. Long-term

intraocular pressure reduction with intracameral polycaprolactone glaucoma devices that deliver a novel anti-glaucoma agent. Journal of Controlled Release. 2018;269(June 2017):45–51.
242. ClinicalTrials.gov. NCT01845038 Multi-Arm Feasibility Study Evaluating OTX-TP Compared to Timolol in Treatment of Subjects With Open Angle Glaucoma [Internet]. NIH U.S. National Library of Medicine. 2016. Available from: https://clinicaltrials.gov/show/NCT01845038
243. Brandt JD, Sall K, DuBiner H, Benza R, Alster Y, Walker G, et al. Six-Month Intraocular Pressure Reduction with a Topical Bimatoprost Ocular Insert: Results of a Phase II Randomized Controlled Study. Ophthalmology. 2016;123(8):1685–94.
244. Manickavasagam D, Wehrung D, Chamsaz EA, Sanders M, Bouhenni R, Crish SD, et al. Assessment of alkoxylphenacyl-based polycarbonates as a potential platform for controlled delivery of a model anti-glaucoma drug. European Journal of Pharmaceutics and Biopharmaceutics. 2016;107:56–66.
245. Utkhede D, William R. Improving Retention Rates for Sustained Therapeutic Delivery Through Punctal Plugs. Investigative Ophthalmology & Visual Science. 2018 Jul 13;59(9):5675.
246. ClinicalTrials.gov. NCT01915940 Bimatoprost Ocular Insert Compared to Topical Timolol Solution in Patients With Glaucoma or Ocular Hypertension [Internet]. NIH U.S. National Library of Medicine. 2018. Available from: https://clinicaltrials.gov/ct2/show/NCT01915940
247. ClinicalTrials.gov. NCT04060758 Open Label, Sequential-dose Study of PA5108 Latanoprost FA SR Ocular Implant for Mild-moderate Glaucoma [Internet]. NIH U.S. National Library of Medicine. 2020. Available from: https://clinicaltrials.gov/ct2/show/NCT04060758?term=latanoprost&cond=implant&draw=2&rank=1
248. ClinicalTrials.gov. NCT03868124 Clinical Study Comparing Two Models of a Travoprost Intraocular Implant [Internet]. NIH U.S. National Library of Medicine. 2019. Available from: https://clinicaltrials.gov/ct2/show/NCT03868124?term=EVA&cond=Glaucoma&draw=2&rank=1
249. ClinicalTrials.gov. NCT01229982 A Study Evaluating the Latanoprost Punctal Plug Delivery System (L-PPDS) in Subjects With Ocular Hypertension or Open-Angle Glaucoma [Internet]. NIH U.S. National Library of Medicine. 2013. Available from: https://www.clinicaltrials.gov/ct2/show/NCT01229982?term=NCT01229982&rank=1
250. ClinicalTrials.gov. NCT01016691 Safety and Efficacy of a Drug Delivery System in Glaucoma [Internet]. NIH U.S. National Library of Medicine. 2015. Available from: https://www.clinicaltrials.gov/ct2/show/NCT01016691?term=NCT01016691&rank=1
251. Perera S, Nongpiur M, Chew P, Aquino MC, Sng C, Ho S-W, et al. Feasibility study of sustained-release travoprost punctum plug for intraocular pressure reduction in an Asian population. Clinical Ophthalmology. 2016 Apr;10:757.
252. Thrimawithana TR, Young S, Bunt CR, Green C, Alany RG. Drug delivery to the posterior segment of the eye. Drug discovery today. 2011 Mar;16(5–6):270–7.
253. Del Amo EM, Urtti A. Current and future ophthalmic drug delivery systems. A shift to the posterior segment. Drug Discovery Today. 2008 Feb;13(3–4):135–43.

254. Parkinson G, Gaisford S, Ru Q, Lockwood A, Khalili A, Sheridan R, et al. Characterisation of ilomastat for prolonged ocular drug release. AAPS PharmSciTech. 2012 Dec;13(4):1063–72.
255. Dubashynskaya N, Poshina D, Raik S, Urtti A, Skorik YA. Polysaccharides in Ocular Drug Delivery. Pharmaceutics. 2019 Dec 24;12(1):22.
256. Bourges JL, Bloquel C, Thomas A, Froussart F, Bochot A, Azan F, et al. Intraocular implants for extended drug delivery: Therapeutic applications. Advanced Drug Delivery Reviews. 2006;58(11):1182–202.
257. Langer R. New methods of drug delivery. Science. 1990 Sep 28;249(4976):1527–33.
258. Yang WW, Pierstorff E. Reservoir-based polymer drug delivery systems. Journal of Laboratory Automation. 2012;17(1):50–8.
259. Kwon JO, Yang JS, Chae JB, Chung SK. A novel drug delivery method by using a microrobot incorporated with an acoustically oscillating bubble. In: 2013 IEEE 26th International Conference on Micro Electro Mechanical Systems (MEMS). IEEE; 2013. p. 1157–60.
260. Ashraf MW, Tayyaba S, Afzulpurkar N. Micro Electromechanical Systems (MEMS) based microfluidic devices for biomedical applications. International Journal of Molecular Sciences. 2011;12(6):3648–704.
261. Eluru G, Adhikari JV, Chanda P, Gorthi SS. Hand-powered elastomeric pump for microfluidic point-of-care diagnostics. Micromachines. 2020;11(1).
262. FDA. DURYSTA (bimatoprost implant), for intracameral administration-Full Prescribing Information [Internet]. Drugs At FDA. 2020. Available from: https://www.accessdata.fda.gov/drugsatfda_docs/label/2020/211911s000lbl.pdf
263. BOLT. BioLight Reports Successful Results in Phase 1/2a Clinical Trial for Glaucoma Insert. Tel-AVIV; 2017.
264. ClinicalTrials.gov. NCT02371746 Safety and Efficacy of ENV515 Travoprost Extended Release (XR) in Patients With Bilateral Ocular Hypertension or Primary Open Angle Glaucoma [Internet]. NIH U.S. National Library of Medicine. 2019. Available from: https://clinicaltrials.gov/ct2/show/study/NCT02371746
265. ClinicalTrials.gov. NCT01157364 Safety and Efficacy of a New Ophthalmic Formulation of Bimatoprost in Patients With Open Angle Glaucoma and Ocular Hypertension [Internet]. NIH U.S. National Library of Medicine. 2010. Available from: https://clinicaltrials.gov/ct2/show/NCT01157364?term=NCT01157364&draw=2&rank=1
266. ClinicalTrials.gov. NCT04200651 Prospective Study on DEXTENZA® Safety And Efficacy Following Concomitant MIGS and Cataract Surgery (SUSTAIN) [Internet]. NIH U.S. National Library of Medicine. 2020. Available from: https://clinicaltrials.gov/ct2/show/NCT04200651?term=Dextenza&draw=2&rank=5
267. ClinicalTrials.gov. NCT02862938 Study of NT-501 Encapsulated Cell Therapy for Glaucoma Neuroprotection and Vision Restoration [Internet]. NIH U.S. National Library of Medicine. 2019. Available from: https://clinicaltrials.gov/ct2/show/NCT02862938
268. ClinicalTrials.gov. NCT03850782 Evaluation of the Duration of Effect of Bimatoprost SR in Participants With Open-angle Glaucoma or Ocular

Hypertension [Internet]. NIH U.S. National Library of Medicine. 2020. Available from: https://clinicaltrials.gov/ct2/show/NCT03850782?term=pavia&cond=Glaucoma&draw=2&rank=2
269. Lee SS, Hughes P, Ross AD, Robinson MR. Biodegradable Implants for Sustained Drug Release in the Eye. Pharmaceutical Research. 2010 Oct 10;27(10):2043–53.
270. Driot J-Y, Novack GD, Rittenhouse KD, Milazzo C, Pearson PA. Ocular pharmacokinetics of fluocinolone acetonide after Retisert intravitreal implantation in rabbits over a 1-year period. Journal of ocular pharmacology and therapeutics : the official journal of the Association for Ocular Pharmacology and Therapeutics. 2004 Jun 29;20(3):269–75.
271. Conway B. Recent Patents on Ocular Drug Delivery Systems. Recent Patents on Drug Delivery & Formulation. 2008 Jan 1;2(1):1–8.
272. Bailey C, Chakravarthy U, Lotery A, Menon G, Talks J, Group for the MA, et al. Real-world experience with 0.2 μg/day fluocinolone acetonide intravitreal implant (ILUVIEN) in the United Kingdom. Eye. 2017 Jul 24;31:1707.
273. ClinicalTrials.gov. Safety and Efficacy of Brimonidine Intravitreal Implant in Patients With Geographic Atrophy Due to Age-related Macular Degeneration (AMD) (NCT00658619) [Internet]. NIH U.S. National Library of Medicine. 2008 [cited 2015 Sep 6]. Available from: https://clinicaltrials.gov/ct2/show/study/NCT00658619?term=NCT00658619&rank=1
274. Rotchford A. What is practical in glaucoma management? Eye. 2005;19(10):1125–32.
275. Peppas NA, Bures P, Leobandung W, Ichikawa H. Hydrogels in pharmaceutical formulations. 2000;50.
276. Laftah WA, Hashim S, Ibrahim AN. Polymer Hydrogels: A Review. Polymer-Plastics Technology and Engineering. 2011 Oct;50(14):1475–86.
277. Buwalda SJ, Boere KWM, Dijkstra PJ, Feijen J, Vermonden T, Hennink WE. Hydrogels in a historical perspective: From simple networks to smart materials. Journal of controlled release : official journal of the Controlled Release Society. 2014 Apr 16;190:254–73.
278. Rubinstein M, Panyukov S. Polymer Entanglements. Annual Review of Condensed Matter Physics. 2011;3(1):110301095507029.
279. Smolensky MH, Peppas NA. Chronobiology, drug delivery, and chronotherapeutics. Advanced Drug Delivery Reviews. 2007 Aug;59(9–10):828–51.
280. Omidian H, Park K. Introduction to Hydrogels. In: Ottenbrite RM, Park K, Okano T, editors. Biomedical Applications of Hydrogels Handbook. New York, NY: Springer New York; 2010. p. 1–16.
281. Ullah F, Othman MBH, Javed F, Ahmad Z, Akil HM. Classification, processing and application of hydrogels: A review. Materials Science and Engineering: C. 2015 Dec;57:414–33.
282. López-Alemany A, Compañ V, Refojo MF. Porous structure of Purevision versus Focus Night&Day and conventional hydrogel contact lenses. Journal of biomedical materials research. 2002 Jan;63(3):319–25.
283. Council NR. Considerations in Contact Lens Use under Adverse Conditions. Pamela Ebert Flattau, editor. Washington, D.C.: National Academy Press; 1991.

178 p.
284. Censi R, Di Martino P, Vermonden T, Hennink WE. Hydrogels for protein delivery in tissue engineering. Journal of controlled release : official journal of the Controlled Release Society. 2012 Jul 20;161(2):680–92.
285. Gupta P, Vermani K, Garg S. Hydrogels: from controlled release to pH-responsive drug delivery. Drug Discovery Today. 2002 May;7(10):569–79.
286. Holmes MH. A THEORETICAL ANALYSIS FOR DETERMINING THE NONLINEAR HYDRAULIC PERMEABILITY OF A SOFT TISSUE FROM A PERMEATION EXPERIMENT. Bulletin of Mathematical Biology. 1985;47(5):669–83.
287. Peppas NA, Colombo P. Analysis of drug release behavior from swellable polymer carriers using the dimensionality index. J Control Release. 1997;45:35–40.
288. Williams MMR. The mathematics of diffusion. Annals of Nuclear Energy. 1977;4(4–5):205–6.
289. González Calderón JA, Contreras López D, Pérez E, Vallejo Montesinos J. Polysiloxanes as polymer matrices in biomedical engineering: their interesting properties as the reason for the use in medical sciences. Polymer Bulletin. 2020 May 2;77(5):2749–817.
290. Rosiak JM, Yoshii F. Hydrogels and their medical applications. Nuclear Instruments and Methods in Physics Research, Section B: Beam Interactions with Materials and Atoms. 1999;151(1–4):56–64.
291. van Bemmelen JM. Das Hydrogel und das krystallinische Hydrat des Kupferoxyds. Zeitschrift f�r anorganische Chemie. 1894;5(1):466–83.
292. Jin R, Dijkstra PJ. Hydrogels for Tissue Engineering Applications. Biomedical Applications of Hydrogels Handbook. 2010;101(7):203–25.
293. Volkmer E, Leicht U, Moritz M, Schwarz C, Wiese H, Milz S, et al. Poloxamer-based hydrogels hardening at body core temperature as carriers for cell based therapies: in vitro and in vivo analysis. Journal of materials science Materials in medicine. 2013 Sep;24(9):2223–34.
294. Wichterle O, LÍm D. Hydrophilic Gels for Biological Use. Nature. 1960 Jan 9;185(4706):117–8.
295. Wichterle O. Method of manufacturing soft and flexible contact lenses. US: United States Patent Office; US3496254A, 1965.
296. Han YA, Mi E, Chul B. the Physical Properties of Poly (2-Hydroxyethyl Methacrylate) Copolymer Hydrogels Used As Intravaginal Rings. Chinese Journal of Polymer Science. 2009;27(3):359–66.
297. Musgrave CSA, Fang F. Contact lens materials: A materials science perspective. Materials. 2019;12(2):1–35.
298. Efron N. Hydrogel Lenses – Materials and Manufacture : A Review. 2003;4:101–15.
299. Lloyd AW, Faragher RGA, Denyer SP. Ocular biomaterials and implants. Biomaterials. 2001;22(8):769–85.
300. Goda T, Ishihara K. Soft contact lens biomaterials from bioinspired phospholipid polymers. Expert Review of Medical Devices. 2006 Jan 9;3(2):167–74.
301. Kadajji VG, Betageri G V. Water soluble polymers for pharmaceutical applications. Polymers. 2011;3(4):1972–2009.
302. Kaushik K, Sharma RB, Agarwal S. Natural polymers and their applications. Vol. 37, International Journal of Pharmaceutical Sciences Review and Research. 2016. p. 30–6.

303. Bhattarai N, Gunn J, Zhang M. Chitosan-based hydrogels for controlled, localized drug delivery. Advanced Drug Delivery Reviews. 2010 Jan;62(1):83–99.
304. Gong M, Zhang L, Zuo Y, Zou Q, Wang Y, Wang L, et al. Investigation on the interpenetrating polymer networks (ipns) of polyvinyl alcohol and poly(N-vinyl pyrrolidone) hydrogel and its in vitro bioassessment. Journal of Applied Polymer Science. 2012 Aug;125(4):2799–806.
305. Odian G. Principles of Polymerization, 4th Edition. New York: Wiley-Interscience; 2004. 832 p.
306. Erman B, Mark JE. Rubber-Like Elasticity. Annual Review of Physical Chemistry. 1989 Oct;40(1):351–74.
307. Thakur VK, Thakur MK. Recent trends in hydrogels based on psyllium polysaccharide: a review. Journal of Cleaner Production. 2014 Nov;82:1–15.
308. Brazel CS, Peppas NA. Synthesis and Characterization of Thermo- and Chemomechanically Responsive Poly(N-isopropylacrylamide-co-methacrylic acid) Hydrogels. Macromolecules. 1995 Nov;28(24):8016–20.
309. Gelfi C, Righetti PG. Polymerization kinetics of polyacrylamide gels II. Effect of temperature. Electrophoresis. 1981 Feb;2(4):220–8.
310. Lipatov Y. Polymer blends and interpenetrating polymer networks at the interface with solids. Progress in Polymer Science. 2002 Nov;27(9):1721–801.
311. Zhang J-T, Bhat R, Jandt KD. Temperature-sensitive PVA/PNIPAAm semi-IPN hydrogels with enhanced responsive properties. Acta Biomaterialia. 2009 Jan;5(1):488–97.
312. Lohani A, Singh G, Bhattacharya SS, Verma A. Interpenetrating Polymer Networks as Innovative Drug Delivery Systems. Journal of Drug Delivery. 2014;2014(Figure 1):1–11.
313. Gu D, O'Connor AJ, G.H. Qiao G, Ladewig K. Hydrogels with smart systems for delivery of hydrophobic drugs. Expert Opinion on Drug Delivery. 2017;14(7):879–95.
314. Bennett SL, Melanson DA, Torchiana DF, Wiseman DM, Sawhney AS. Next-Generation HydroGel Films as Tissue Sealants and Adhesion Barriers. In: Journal of Cardiac Surgery. 2003. p. 494–9.
315. Stile RA, Healy KE. Thermo-responsive peptide-modified hydrogels for tissue regeneration. Biomacromolecules. 2001;2(1):185–94.
316. Jen AC, Wake MC, Mikos AG. Review: Hydrogels for cell immobilization. Vol. 50, Biotechnology and Bioengineering. 1996. p. 357–64.
317. Hoffman AS. Hydrogels for biomedical applications. Advanced Drug Delivery Reviews. 2012 Dec;64(SUPPL.):18–23.
318. Redaelli F, Sorbona M, Rossi F. Synthesis and processing of hydrogels for medical applications. In: Bioresorbable Polymers for Biomedical Applications. Elsevier; 2017. p. 205–28.
319. Ahmed EM. Hydrogel: Preparation, characterization, and applications. Journal of Advanced Research. 2013 Jul;6(2):105–21.
320. Bach JS, Detrez F, Cherkaoui M, Cantournet S, Ku DN, Corté L. Hydrogel fibers for ACL prosthesis: Design and mechanical evaluation of PVA and PVA/UHMWPE fiber constructs. Journal of Biomechanics. 2013;46(8):1463–70.
321. Kamoun EA, Kenawy ERS, Chen X. A review on polymeric hydrogel membranes for wound dressing applications: PVA-based hydrogel dressings. Journal of Advanced Research. 2017;8(3):217–33.

322. Joint Formulary Committee. Hydrogel sheet dressings. British Naional Formulary. London: BMJ Group & Pharmaceutical Press; 2018.
323. Mailra NMS a. U. Supramolecular gels: Function and uses. Chem Soc Rev. 2005;34:821–836.
324. Sami DA, Young SR. Orbital enucleation implants and ocular prostheses. In: Biomaterials and Regenerative Medicine in Ophthalmology. Elsevier; 2016. p. 311–48.
325. Kirchhof S, Goepferich AM, Brandl FP. Hydrogels in ophthalmic applications. European Journal of Pharmaceutics and Biopharmaceutics. 2015 Sep;95:227–38.
326. Green AE, Adkins JE, Rivlin RS. Large Elastic Deformations. Physics Today. 1971;24(12):57.
327. Davies GC, Hiller S, Bruce DM. A MEMBRANE MODEL FOR ELASTIC DEFLECTION OF INDIVIDUAL PLANT CELL WALLS. Journal of Texture Studies. 1998 Dec;29(6):645–67.
328. Ganapathy S, Amendola A, Lichfield R, Fowler PJ, Ling E. Elastomeric pumps for ambulatory patient controlled regional analgesia. Canadian journal of anaesthesia = Journal canadien d'anesthésie. 2000;47(9):897–902.
329. Carro G, Harper A, Lawton J. Evaluation of elastomeric and electronic medication pumps at an outpatient cancer center. Journal of Oncology Pharmacy Practice. 2010;16(1):14.
330. Selby JC, Shannon M a. Inflation of a circular elastomeric membrane into a horizontally semi-infinite liquid reservoir of finite vertical depth: Estimation of material parameters from volume-pressure data. International Journal of Engineering Science. 2009;47(5–6):718–34.
331. Jenkins CH, Leonard JW. Nonlinear Dynamic Response of Membranes: State of the Art. Applied Mechanics Reviews. 1991;44(7):319.
332. Karimi A, Navidbakhsh M, Shojaei A, Hassani K, Faghihi S. Study of Plaque Vulnerability in Coronary Artery Using Mooney–Rivlin Model: a Combination of Finite Element and Experimental Method. Biomedical Engineering: Applications, Basis and Communications. 2014;26(01):1450013.
333. Liang DK, Yang DZ, Qi M, Wang WQ. Finite element analysis of the implantation of a balloon-expandable stent in a stenosed artery. International Journal of Cardiology. 2005;104(3):314–8.
334. Prendergast PJ, Lally C, Daly S, Reid a J, Lee TC, Quinn D, et al. Analysis of prolapse in cardiovascular stents: a constitutive equation for vascular tissue and finite-element modelling. Journal of biomechanical engineering. 2003;125(5):692–9.
335. Martin D, Boyle F. Finite element analysis of balloon-expandable coronary stent deployment: Influence of angioplasty balloon configuration. International Journal for Numerical Methods in Biomedical Engineering. 2013;29(11):1161–75.
336. Goulbourne NC, Frecker MI, Mockensturm E. Electro-elastic modeling of a dielectric elastomer diaphragm for a prosthetic blood pump. In: Bar-Cohen Y, editor. 2004. p. 122.
337. Glozman D, Hassidov N, Senesh M, Shoham M. A self-propelled inflatable earthworm-like endoscope actuated by single supply line. IEEE Transactions on Biomedical Engineering. 2010;57(6):1264–72.
338. Hached S, Loutochin O, Corcos J. Novel , Remotely Controlled , Artificial Urinary Sphincter : A Retro-Compatible Device. 2014;19(4):1352–62.
339. Watkins E. Chronometric Infusor — An Apparatus for Protracted Ambulatory

Infusion Therapy. New England Journal of Medicine. 1963 Oct 17;269(16):850–1.
340. Steffens E, Quintens C, Derdelinckx I, Peetermans WE, Van Eldere J, Spriet I, et al. Outpatient parenteral antimicrobial therapy and antibiotic stewardship: opponents or teammates? Infection. 2019 Apr 15;47(2):169–81.
341. Valente M, Aldrete J a. Comparison of accuracy and cost of disposable, nonmechanical pumps used for epidural infusions. Regional anesthesia. 1997;22(3):260–2666.
342. LeBlanc KA, Bellanger D, Rhynes VK, Hausmann M. Evaluation of continuous infusion of 0.5% bupivacaine by elastomeric pump for postoperative pain management after open inguinal hernia repair. Journal of the American College of Surgeons. 2005;200(2):198–202.
343. Dadure C, Pirat P, Raux O, Troncin R, Rochette A, Ricard C, et al. Perioperative continuous peripheral nerve blocks with disposable infusion pumps in children: a prospective descriptive study. Anesthesia and analgesia. 2003;97(3):687–90.
344. Hardy EM, Williamson C, Sewell GJ. An evaluation of six infusion devices for the continuous infusion of cytotoxic drugs in ambulatory patients. Journal of Oncology Pharmacy Practice. 1995;1(1):15–22.
345. Klein SM, Greengrass RA, Gleason DH, Nunley JA, Steele SM. Major Ambulatory Surgery with Continuous Regional Anesthesia and a Disposable Infusion Pump. The Journal of the American Society of Anesthesiologists. 1999;91(2):563–5.
346. Boada S, Recasens J, Papaceit J, Solsona B, Saludes J, Escuder J, et al. Use of elastomeric pumps for continuous intravenous analgesia administration in ambulatory surgery pain management. Journal of Ambulatory Surgery. 2002;10:3–7.
347. Capdevila X, Macaire P, Aknin P, Dadure C, Bernard N, Lopez S. Patient-controlled perineural analgesia after ambulatory orthopedic surgery: a comparison of electronic versus elastomeric pumps. Anesthesia and analgesia. 2003;96(2):414–7, table of contents.
348. Ilfeld B. Delivery rate accuracy of portable, bolus-capable infusion pumps used for patient-controlled continuous regional analgesia. Regional Anesthesia and Pain Medicine. 2003;28(1):17–23.
349. Roberts S, Sewell GJ. Stability and compatibility of 5-fluorouracil infusions in the Braun Easypump®. Journal of Oncology Pharmacy Practice. 2003;9(2):109–12.
350. Skryabina EA, Dunn TS. Disposable infusion pumps. American Journal of Health-System Pharmacy. 2006;63(13):1260–8.
351. Robinson SL, Rowbotham DJ, Mushambi M. Electronic and disposable patient-controlled analgesia systems A comparison of the Graseby and Baxter systems after major gynaecological surgery. Anaesthesia. 1992;47(August 1991):161–3.
352. Negro S, Azuara M, Sánchez Y, Reyes R, Barcia E. Physical compatibility and in vivo evaluation of drug mixtures for subcutaneous infusion to cancer patients in palliative care. Supportive Care in Cancer. 2002 Jan 23;10(1):65–70.
353. Lockwood A, Brocchini S, Khaw PT. New developments in the pharmacological modulation of wound healing after glaucoma filtration surgery. Current Opinion in Pharmacology. 2013;13(1):65–71.
354. Alvarado JA, Hollander DA, Juster RP, Lee LC. Ahmed Valve Implantation with Adjunctive Mitomycin C and 5-Fluorouracil: Long-term Outcomes. American Journal of Ophthalmology. 2008 Aug;146(2):276-284.e2.

355. Schoenberg ED, Blake DA, Swann FB, Parlin AW, Zurakowski D, Margo CE, et al. Effect of Two Novel Sustained-Release Drug Delivery Systems on Bleb Fibrosis: An In Vivo Glaucoma Drainage Device Study in a Rabbit Model. Translational Vision Science & Technology. 2015 May 22;4(3):4.
356. Lockwood A. The Modulation of Wound Healing for Glaucoma Filtration Surgery. UCL Institute of Ophthalmology and UCL School of Pharmacy; 2014.
357. Hafez M. Trabeculectomy with collagen matrix implantation versus trabeculectomy with mitomycin C application for the treatment of primary congenital glaucoma. Journal of the Egyptian Ophthalmological Society. 2015;108(2):26.
358. Wong TTL, Mead AL, Khaw PT. Prolonged antiscarring effects of ilomastat and MMC after experimental glaucoma filtration surgery. Investigative ophthalmology & visual science. 2005 Jun 1;46(6):2018–22.
359. Daniels JT, Cambrey AD, Occleston NL, Garrett Q, Tarnuzzer RW, Schultz GS, et al. Matrix metalloproteinase inhibition modulates fibroblast-mediated matrix contraction and collagen production in vitro. Investigative Ophthalmology and Visual Science. 2003;44(3):1104–10.
360. Li L, Wang J-H, Xin Z. Synthesis and biocompatibility of a novel silicone hydrogel containing phosphorylcholine. European Polymer Journal. 2011 Sep;47(9):1795–803.
361. Parker AP, Reynolds P a, Lewis AL, Kirkwood L, Hughes LG. Investigation into potential mechanisms promoting biocompatibility of polymeric biomaterials containing the phosphorylcholine moiety. A physicochemical and biological study. Colloids and surfaces B, Biointerfaces. 2005 Dec 30;46(4):204–17.
362. Pal K, Banthia a K, Majumdar DK. Development of carboxymethyl cellulose acrylate for various biomedical applications. Biomedical materials (Bristol, England). 2006 Jun;1(2):85–91.
363. Lewis AL. PC Technology as a platform for drug delivery: from combination to conjugation. Expert opinion on drug delivery. 2006;3(November):289–98.
364. Paula JS, Ribeiro VRC, Chahud F, Cannellini R, Monteiro TC, de Lima Gomes EC, et al. Bevacizumab-Loaded Polyurethane Subconjunctival Implants: Effects on Experimental Glaucoma Filtration Surgery. Journal of Ocular Pharmacology and Therapeutics. 2013 Jul;29(6):566–73.
365. Ng XW, Liu KL, Veluchamy AB, Lwin NC, Wong TT, Venkatraman SS. A biodegradable ocular implant for long-term suppression of intraocular pressure. Drug Delivery and Translational Research. 2015;5(5):469–79.
366. Moura Filho ER, Sit AJ. Advances in glaucoma surgery. Expert Review of Ophthalmology. 2009;4(6):595–605.
367. Yuan F, Li L, Chen X, Yan X, Wang L. Biodegradable 3D-Porous Collagen Matrix (Ologen) Compared with Mitomycin C for Treatment of Primary Open-Angle Glaucoma: Results at 5 Years. J Ophthalmol. 2015;2015:637537.
368. Hait SK, Moulik SP. Determination of critical micelle concentration (CMC) of nonionic surfactants by donor-acceptor interaction with Iodine and correlation of CMC with hydrophile-lipophile balance and other parameters of the surfactants. Journal of Surfactants and Detergents. 2001 Jul;4(3):303–9.
369. Karlgard CCS, Wong NS, Jones LW, Moresoli C. In vitro uptake and release studies of ocular pharmaceutical agents by silicon-containing and p-HEMA hydrogel contact lens materials. International Journal of Pharmaceutics. 2003;257(1–

2):141–51.
370. Glisoni RJ, García-Fernández MJ, Pino M, Gutkind G, Moglioni AG, Alvarez-Lorenzo C, et al. β-Cyclodextrin hydrogels for the ocular release of antibacterial thiosemicarbazones. Carbohydrate polymers. 2013 Apr 2;93(2):449–57.
371. Kaczmarek JC, Tieppo A, White CJ, Byrne ME. Adjusting biomaterial composition to achieve controlled multiple-day release of dexamethasone from an extended-wear silicone hydrogel contact lens. Journal of Biomaterials Science, Polymer Edition. 2014 Jan 2;25(1):88–100.
372. Kim J, Peng CC, Chauhan A. Extended release of dexamethasone from silicone-hydrogel contact lenses containing vitamin E. Journal of Controlled Release. 2010;148(1):110–6.
373. García-Millán E, Koprivnik S, Otero-Espinar FJ. Drug loading optimization and extended drug delivery of corticoids from pHEMA based soft contact lenses hydrogels via chemical and microstructural modifications. International Journal of Pharmaceutics. 2015;487(1–2):260–9.
374. White CJ, Tieppo A, Byrne ME. Controlled drug release from contact lenses: A comprehensive review from 1965-present. Journal of Drug Delivery Science and Technology. 2011;21(5):369–84.
375. Schultz CL, Nunez IM, Silor DL, Neil ML. Contact lens containing a leachable absorbed material. USA; US5723131A, 1995.
376. Schultz CL, Mint JM. Drug delivery system for antiglaucomatous medication. USA; US6410045B1, 1999.
377. Hehl E-M, Beck R, Luthard K, Guthoff R, Drewelow B. Improved penetration of aminoglycosides and fluoroquinolones into the aqueous humour of patients by means of Acuvue contact lenses. European Journal of Clinical Pharmacology. 1999 Jun 10;55(4):317–23.
378. Colombo P, Bettini R, Ascentiis A De, Peppas NA. Analysis of the swelling and release mechanisms from drug delivery systems with emphasis on drug solubility and water transport. Journal of Controlled Release. 1996;39:231–7.
379. Ward JH, Peppas NA. Preparation of controlled release systems by free-radical UV polymerizations in the presence of a drug. Journal of Controlled Release. 2001 Apr;71(2):183–92.
380. Gulsen D, Chauhan A. Dispersion of microemulsion drops in HEMA hydrogel: A potential ophthalmic drug delivery vehicle. International Journal of Pharmaceutics. 2005;292(1–2):95–117.
381. Kim SW, Bae YH, Okano T. Hydrogels: Swelling, Drug Loading, and Release. Vol. 9, Pharmaceutical Research: An Official Journal of the American Association of Pharmaceutical Scientists. 1992. p. 283–90.
382. Sahiner N, Kravitz DJ, Qadir R, Blake DA, Haque S, John VT, et al. Creation of a Drug-Coated Glaucoma Drainage Device Using Polymer Technology. Archives of Ophthalmology. 2009 Apr 13;127(4):448.
383. Nagarwal RC, Kant S, Singh PN, Maiti P, Pandit JK. Polymeric nanoparticulate system: A potential approach for ocular drug delivery. Journal of Controlled Release. 2009;136(1):2–13.
384. Edelhauser HF, Rowe-Rendleman CL, Robinson MR, Dawson DG, Chader GJ, Grossniklaus HE, et al. Ophthalmic drug delivery systems for the treatment of retinal diseases: basic research to clinical applications. Investigative ophthalmology & visual science. 2010;51(11):5403–20.

385. Hudson I, Calvo Rojas G. CHMP Assessment report, Ozurdex. Vol. 457364, EMA. London; 2010.
386. Rodriguez-Aller M, Guinchard S, Guillarme D, Pupier M, Jeannerat D, Rivara-Minten E, et al. New prostaglandin analog formulation for glaucoma treatment containing cyclodextrins for improved stability, solubility and ocular tolerance. European journal of pharmaceutics and biopharmaceutics : official journal of Arbeitsgemeinschaft fur Pharmazeutische Verfahrenstechnik eV. 2015 May 8;
387. Abadia B, Calvo P, Ferreras A, Bartol F, Verdes G, Pablo L. Clinical Applications of Dexamethasone for Aged Eyes. Drugs and Aging. 2016;33(9):639–46.
388. Lee SS, Hughes PM, Robinson MR. Recent advances in drug delivery systems for treating ocular complications of systemic diseases. Current opinion in ophthalmology. 2009;20(6):511–9.
389. Rhen T, Cidlowski JA. Antiinflammatory Action of Glucocorticoids — New Mechanisms for Old Drugs. New England Journal of Medicine. 2005 Oct 20;353(16):1711–23.
390. National Center for Biotechnology Information. Dexamethasone [Internet]. PubChem Compound Database, CID=5743. 2005. Available from: https://pubchem.ncbi.nlm.nih.gov/compound/5743
391. ClinicalTrials.gov. NCT03751059 NSAID vs Steroid in Trabeculectomy Wound Management. 2020.
392. ClinicalTrials.gov. NCT00825864 Diclofenac vs Dexamethasone in Combined Surgery [Internet]. NIH U.S. National Library of Medicine. 2009. Available from: https://clinicaltrials.gov/ct2/show/NCT00825864?term=ozurdex&cond=Glaucoma&draw=2&rank=8
393. Rodrigues LB, Leite HF, Yoshida MI, Saliba JB, Junior ASC, Faraco AAG. In vitro release and characterization of chitosan films as dexamethasone carrier. International Journal of Pharmaceutics. 2009;368(1–2):1–6.
394. Wilson CG. Topical drug delivery in the eye. Experimental Eye Research. 2004 Mar;78(3):737–43.
395. ClinicalTrials.gov. NCT04075227 Topical 0.2% Loteprednol Etabonate vs. Topical 0.1% Dexamethasone in Impending Recurrent Pterygium [Internet]. NIH U.S. National Library of Medicine. 2019. Available from: https://clinicaltrials.gov/ct2/show/NCT04075227?term=ozurdex&cond=Glaucoma&draw=2&rank=6
396. ClinicalTrials.gov. NCT02006888 The Efficacy and Safety of IBI-10090 for the Treatment of Inflammation Associated With Cataract Surgery [Internet]. NIH U.S. National Library of Medicine. 2014. Available from: https://clinicaltrials.gov/ct2/show/NCT02006888
397. ClinicalTrials.gov. NCT02875158 Cyclophotocoagulation in Glaucoma [Internet]. NIH U.S. National Library of Medicine. 2018. Available from: https://clinicaltrials.gov/ct2/show/NCT02875158?term=ozurdex&cond=Glaucoma&draw=3&rank=13
398. Lobo A-M. Dexamethasone intravitreal implant for the treatment of noninfectious uveitis. Clinical Ophthalmology. 2011 Nov;1613.
399. Nakada MT, Stadel JM, Poksay KS, Crooke ST. Glucocorticoid regulation of beta-adrenergic receptors in 3T3-L1 preadipocytes. Molecular Pharmacology. 1987 Apr 1;31(4):377 LP – 384.
400. Lai E, Rosen OM, Rubin CS. Dexamethasone regulates the beta-adrenergic

receptor subtype expressed by 3T3 L1 preadipocytes and adipocytes. The Journal of Biological Chemistry. 1982;257(12):6691–6.
401. Ramalingam A, Hirai A, Thompson EA. Glucocorticoid Inhibition of Fibroblast Proliferation and Regulation of the Cyclin Kinase Inhibitor p21 Cip1. Molecular Endocrinology. 1997 May;11(5):577–86.
402. Harkness K a., Adamson P, Sussman J, Davies-Jones G, Greenwood J, Woodroofe M. Dexamethasone regulation of matrix metalloproteinase expression in CNS vascular endothelium. Brain. 2000;123(4):698–709.
403. Clark AF, Brotchie D, Read AT, Hellberg P, English-Wright S, Pang IH, et al. Dexamethasone alters F-actin architecture and promotes cross-linked actin network formation in human trabecular meshwork tissue. Cell Motility and the Cytoskeleton. 2005;60(2):83–95.
404. Thrimawithana TR, Young S, Bunt CR, Green C, Alany RG. Drug delivery to the posterior segment of the eye. Drug Discovery Today. 2011 Mar;16(5–6):270–7.
405. Bernard S. The response of ocular pressure to corticosteroids. International Ophthalmology Clinics. 1966;6(4):929–89.
406. Urban RC, Cotlier E. Corticosteroid-induced cataracts. Survey of Ophthalmology. 1986 Sep;31(2):102–10.
407. Jones R, Rhee DJ. Corticosteroid-induced ocular hypertension and glaucoma: A brief review and update of the literature. Current Opinion in Ophthalmology. 2006;17(2):163–7.
408. Roberti G, Oddone F, Agnifili L, Katsanos A, Michelessi M, Mastropasqua L, et al. Steroid-induced glaucoma: Epidemiology, pathophysiology, and clinical management. Survey of Ophthalmology. 2020;65(4):458–72.
409. ClinicalTrials.gov. NCT04403516 Dextenza in Pterygium Surgery [Internet]. NIH U.S. National Library of Medicine. 2020. Available from: https://clinicaltrials.gov/ct2/show/NCT04403516?term=Dextenza&draw=2&rank=4
410. Sapadin AN, Fleischmajer R. Tetracyclines: Nonantibiotic properties and their clinical implications. Journal of the American Academy of Dermatology. 2006 Feb;54(2):258–65.
411. Li H, Ezra DG, Burton MJ, Bailly M. Doxycycline prevents matrix remodeling and contraction by trichiasis-derived conjunctival fibroblasts. Investigative Ophthalmology and Visual Science. 2013;54(7):4675–82.
412. Smith V a, Cook SD. Doxycycline-a role in ocular surface repair. The British journal of ophthalmology. 2004;88(5):619–25.
413. Valentín S, Morales A, Sánchez JL, Rivera A. Safety and efficacy of doxycycline in the treatment of rosacea. Clinical, Cosmetic and Investigational Dermatology. 2009;2:129–40.
414. Do MP, Neut C, Delcourt E, Seixas Certo T, Siepmann J, Siepmann F. In situ forming implants for periodontitis treatment with improved adhesive properties. European Journal of Pharmaceutics and Biopharmaceutics. 2014 Oct;88(2):342–50.
415. Piacentini M, Borghetti RL, Zancanaro de Figueiredo MA, Cherubini K, Gonçalves Salum F. Doxycycline: An option in the treatment of ulcerated oral lesions? Journal of Clinical Pharmacy and Therapeutics. 2019 Dec 10;44(6):838–43.
416. Hanemaaijer R, Vlsser H, Koolwijk P, Sorsa T, Salo T, Golub LM, et al. Inhibition of MMP synthesis by doxycycline and chemically modified tetracyclines (cmts) in

human endothelial cells. Advances in Dental Research. 1998;12:114–8.
417. Liu J, Xiong W, Baca-Regen L, Nagase H, Baxter BT. Mechanism of inhibition of matrix metalloproteinase-2 expression by doxycycline in human aortic smooth muscle cells. Journal of Vascular Surgery. 2003;38(6):1376–83.
418. Stechmiller J, Cowan L, Schultz G. The role of doxycycline as a matrix metalloproteinase inhibitor for the treatment of chronic wounds. Biological research for nursing. 2010;11(4):336–44.
419. Georgoulas S, Dahlmann-Noor A, Brocchini S, Khaw PT. Modulation of wound healing during and after glaucoma surgery. In: Progress in brain research. 2008. p. 237–54.
420. ClinicalTrials.gov. NCT00064766 Norplant and Irregular Bleeding/Spotting [Internet]. NIH U.S. National Library of Medicine. 2003. Available from: https://clinicaltrials.gov/ct2/show/NCT00064766?term=doxycycline+implant&draw=2&rank=2
421. Kronberg B. Surfactant mixtures. Current Opinion in Colloid and Interface Science. 1997;2(5):456–63.
422. Nagarajan R, Ruckenstein E. Theory of Surfactant Self-Assembly: A Predictive Molecular Thermodynamic Approach. Langmuir. 1991;7(12):2934–69.
423. Thomas A. Micelle formation. In: Max Planck Institute of Colloids and Interfaces. 1992. p. 82–129.
424. Eriksson JC, Ljunggren S. A molecular theory of the surface tension of surfactant solutions. Colloids and Surfaces. 1989 Jan;38(1):179–203.
425. Tadros TF. Applied Surfactants: Principles and Applications. Weinheim: WILEY-VCH Verlag GmbH & Co. KGaA, Weinheim; 2006. 1–654 p.
426. Tanford C. Micelle shape and size. Journal of Physical Chemistry. 1972;76(21):3020–4.
427. Trivedi R, Kompella UB. Nanomicellar formulations for sustained drug delivery: strategies and underlying principles. Nanomedicine (London, England). 2010;5(3):485–505.
428. Mandal A, Bisht R, Rupenthal ID, Mitra AK. Polymeric micelles for ocular drug delivery : From structural frameworks to recent preclinical studies. Journal of Controlled Release. 2017;248:96–116.
429. Kapoor Y, Chauhan A. Drug and surfactant transport in Cyclosporine A and Brij 98 laden p-HEMA hydrogels. Journal of Colloid and Interface Science. 2008;322(2):624–33.
430. Kapoor Y, Thomas JC, Tan G, John VT, Chauhan A. Surfactant-laden soft contact lenses for extended delivery of ophthalmic drugs. Biomaterials. 2009;30(5):867–78.
431. Jiao J. Polyoxyethylated nonionic surfactants and their applications in topical ocular drug delivery. Advanced Drug Delivery Reviews. 2008;60(15):1663–73.
432. Amidon GL, Lennernäs H, Shah VP, Crison JR. A Theoretical Basis for a Biopharmaceutic Drug Classification: The Correlation of in Vitro Drug Product Dissolution and in Vivo Bioavailability. Vol. 12, Pharmaceutical Research: An Official Journal of the American Association of Pharmaceutical Scientists. 1995. p. 413–20.
433. Brewster ME, Loftsson T. Cyclodextrins as pharmaceutical solubilizers. Advanced Drug Delivery Reviews. 2007;59(7):645–66.
434. Sowmiya M, Tiwari AK, Saha SK. Journal of Colloid and Interface Science

Fluorescent probe studies of micropolarity , premicellar and micellar aggregation of non-ionic Brij surfactants. Journal of Colloid And Interface Science. 2010;344(1):97–104.
435. Shah V, Bharatiya B, Shukla AD, Mukherjee T, Shah DO. Adsorption of nonionic Brij and Tween surfactants at PTFE-water and air-water interfaces: Investigations on wetting, dispersion stability, foaming and drug solubilization. Colloids and Surfaces A: Physicochemical and Engineering Aspects. 2016 Nov;508:159–66.
436. Kapoor Y, Chauhan A. Ophthalmic delivery of Cyclosporine A from Brij-97 microemulsion and surfactant-laden p-HEMA hydrogels. International journal of pharmaceutics. 2008 Sep 1;361(1–2):222–9.
437. Sahoo RK, Biswas N, Guha A, Sahoo N, Kuotsu K. Nonionic surfactant vesicles in ocular delivery: Innovative approaches and perspectives. BioMed Research International. 2014;2014.
438. Saettone MF, Chetoni P, Cerbai R, Mazzanti G, Braghiroli L. Evaluation of ocular permeation enhancers: In vitro effects on corneal transport of four ??-blockers, and in vitro/in vivo toxic activity. International Journal of Pharmaceutics. 1996;142(1):103–13.
439. Ribeiro MENP, Moura CL De, Vieira MGS, Gramosa N V, Chaibundit C, Mattos MC De, et al. Solubilisation capacity of Brij surfactants. International Journal of Pharmaceutics. 2012;436(1–2):631–5.
440. Kapoor Y, Howell BA, Chauhan A. Liposome assay for evaluating ocular toxicity of surfactants. Investigative Ophthalmology and Visual Science. 2009;50(6):2727–35.
441. Kim J, Conway A, Chauhan A. Extended delivery of ophthalmic drugs by silicone hydrogel contact lenses. Biomaterials. 2008;29(14):2259–69.
442. NICEATM. Test Method Protocol for Solubility Determination. 2003.
443. University of Puget Sound. Solubility Tests for Unknowns [Internet]. Organic Chemisty Lab handout (Week 2). 2016. Available from: http://www2.ups.edu/courses/organicchemlab/c250lab.10/aqsolubility.htm
444. Finger W, Dreyer Jorgensen K. Inhibition of polymerization by oxygen in composite filling materials and enamel sealers. Schweizerische Monatsschrift fur Zahnheilkunde = Revue mensuelle suisse d'odonto-stomatologie. 1976 Aug;86(8):812–24.
445. Georgoulas S. Novel methods for the moduation of wound healing after glaucoma filtration surgrey. School of Pharmacy, University of London and UCL Institute of Ophthlamology and Moorfields Eye Hospital; 2010.
446. Almeida H, Amaral MH, Lobão P, Sousa Lobo JM. Applications of poloxamers in ophthalmic pharmaceutical formulations: an overview. Expert Opinion on Drug Delivery. 2013;10(9):1223–37.
447. Croisier F, Jérôme C. Chitosan-based biomaterials for tissue engineering. European Polymer Journal. 2013;49(4):780–92.
448. Keong LC, Halim AS. In Vitro models in biocompatibility assessment for biomedical-grade chitosan derivatives in wound management. International Journal of Molecular Sciences. 2009;10(3):1300–13.
449. Xue J, Xie J, Liu W, Xia Y. Electrospun Nanofibers: New Concepts, Materials, and Applications. Accounts of Chemical Research. 2017;50(8):1976–87.
450. Taylor GI. Disintegration of water drops in an electric field. Proceedings of the Royal Society of London Series A Mathematical and Physical Sciences. 1964 Jul

28;280(1382):383–97.
451. Taylor GI, Dyke MD Van. The force exerted by an electric field on a long cylindrical conductor. Proceedings of the Royal Society of London Series A Mathematical and Physical Sciences. 1966 Apr 5;291(1425):145–58.
452. Taylor GI, Dyke MD Van. Electrically driven jets. Proceedings of the Royal Society of London A Mathematical and Physical Sciences. 1969 Dec 2;313(1515):453–75.
453. Sundera Murthe S, Mohamed Saheed MS, Perumal V, Mohamed Saheed MS, Mohamed NM. Electrospun Nanofibers for Biosensing Applications. In: Nanobiosensors for Biomolecular Targeting. Elsevier; 2019. p. 253–67.
454. Ray SS, Chen SS, Li CW, Nguyen NC, Nguyen HT. A comprehensive review: Electrospinning technique for fabrication and surface modification of membranes for water treatment application. RSC Advances. 2016;6(88):85495–514.
455. Asmatulu R, Khan WS. Historical background of the electrospinning process. In: Synthesis and Applications of Electrospun Nanofibers. Elsevier; 2019. p. 17–39.
456. Schneider CA, Rasband WS, Eliceiri KW. NIH Image to ImageJ: 25 years of image analysis. Nature Methods. 2012;9(7):671–5.
457. Vo CLN, Park C, Lee BJ. Current trends and future perspectives of solid dispersions containing poorly water-soluble drugs. European Journal of Pharmaceutics and Biopharmaceutics. 2013;85(3 PART B):799–813.
458. Rohindra DR, Nand A V, Khurma JR. Swelling properties of chitosan hydrogels. The South Pacific Journal of Natural and Applied Sciences. 2004;22(1):32.
459. Corkhill PH, Jolly AM, Ng CO, Tighe BJ. Synthetic hydrogels : 1 . Hydroxyalkyl acrylate and methacrylate copolymers- water binding studies. 1987;28:1758–66.
460. Tranoudis I, Efron N. Water properties of soft contact lens materials. Contact lens & anterior eye : the journal of the British Contact Lens Association. 2004 Dec;27(4):193–208.
461. Tagalakis AD, Madaan S, Larsen SD, Neubig RR, Khaw PT, Rodrigues I, et al. In vitro and in vivo delivery of a sustained release nanocarrier-based formulation of an MRTF/SRF inhibitor in conjunctival fibrosis. Journal of Nanobiotechnology. 2018;16(1):1–11.
462. Iwasaki K, Kanamoto M, Takihara Y, Arimura S, Takamura Y, Kimura H, et al. Evaluation of Bleb Fluid after Baerveldt Glaucoma Implantation Using Magnetic Resonance Imaging. Scientific Reports. 2017;7(1):1–8.
463. Kawasaki S, Mizoue S, Yamaguchi M, Shiraishi A, Zheng X, Hayashi Y, et al. Evaluation of filtering bleb function by thermography. 2009;0:1331–6.
464. Aulton ME, Taylor K, editors. Aulton's Pharmaceutics: The Design and Manufacture of Medicines. Fourth. Churchill Livingstone/Elsevier; 2013. 115–125 p.
465. Bruschi ML, editor. Mathematical models of drug release. In: Strategies to Modify the Drug Release from Pharmaceutical Systems. Elsevier; 2015. p. 63–86.
466. Hixson AW, Crowell JH. Dependence of Reaction Velocity upon Surface and Agitation: III—Experimental Procedure in Study of Agitation. Industrial and Engineering Chemistry. 1931;23(10):1160–8.
467. Singhvi G, Singh M. Review : in-Vitro Drug Release Characterization Models. International Journal of Pharmaceutical Studies and Research. 2011;II(I):77–84.
468. Shaikh HK, Kshirsagar R V, Patil SG. MATHEMATICAL MODELS FOR DRUG RELEASE CHARACTERIZATION: A REVIEW. WORLD JOURNAL OF PHARMACY AND PHARMACEUTICAL SCIENCES. 2015;4(04):325–38.

469. Siepmann J, Peppas NA. Modeling of drug release from delivery systems based on hydroxypropyl methylcellulose (HPMC). 2001;48:139–57.
470. Chen Y, Wang J, Flanagan DR. Fundamental of diffusion and dissolution. Developing Solid Oral Dosage Forms: Pharmaceutical Theory and Practice: Second Edition. Elsevier Inc.; 2016. 253–270 p.
471. Bamba M, Puisieux F, Marty J-P, Carstensen JT. Release mechanisms in gelforming sustained release preparations. International Journal of Pharmaceutics. 1979 Jun;2(5–6):307–15.
472. Thakkar VT, Shah PA, Soni TG, Parmar MY, Gohel MC, Gandhi TR. Goodness-of-fit model-dependent approach for release kinetics of levofloxacin hemihydrates floating tablet. Dissolution Technologies. 2009;16(1):35–9.
473. Gohel MC, Panchal MK, Jogani V V. Novel mathematical method for quantitative expression of deviation from the Higuchi model. AAPS PharmSciTech. 2000;1(4):43–8.
474. Korsmeyer RW, Gurny R, Doelker E, Buri P, Peppas NA. Mechanisms of solute release from porous hydrophilic polymers. International Journal of Pharmaceutics. 1983;15(1):25–35.
475. Peppas NA. Analysis of Fickian and non-Fickian drug release from polymers. Pharmaceutica acta Helvetiae. 1985;60(4):110–1.
476. Kastellorizios M, Tipnis N, Burgess DJ. Foreign Body Reaction to Subcutaneous Implants. In 2015. p. 93–108.
477. Acarregui A, Herrán E, Igartua M, Blanco FJ, Pedraz JL, Orive G, et al. Multifunctional hydrogel-based scaffold for improving the functionality of encapsulated therapeutic cells and reducing inflammatory response. Acta Biomaterialia. 2014 Oct;10(10):4206–16.
478. Wu J, Xiao Z, He C, Zhu J, Ma G, Wang G, et al. Protein diffusion characteristics in the hydrogels of poly(ethylene glycol) and zwitterionic poly(sulfobetaine methacrylate) (pSBMA). Acta Biomaterialia. 2016;40:172–81.
479. Malvern. QAS3002 QUALITY AUDIT STANDARD MEASUREMENT PROTOCOL. 2016.
480. Yoon S Do, Park MH, Byun HS. Mechanical and water barrier properties of starch/PVA composite films by adding nano-sized poly(methyl methacrylate-co-acrylamide) particles. Carbohydrate Polymers. 2012;87(1):676–86.
481. ClinicalTrials.gov. NCT01538628 SpaceOAR System Pivotal Study [Internet]. NIH U.S. National Library of Medicine. 2014. Available from: https://clinicaltrials.gov/ct2/show/NCT01538628
482. ClinicalTrials.gov. NCT02353832 Stereotactic Ablative Radiotherapy (SABR) for Low Risk Prostate Cancer With Injectable Rectal Spacer [Internet]. NIH U.S. National Library of Medicine. 2019. Available from: https://clinicaltrials.gov/ct2/show/results/NCT02353832?term=spaceoar&draw=2&rank=4
483. ClinicalTrials.gov. NCT04004312 Single Fractions SBRT for Prostate Cancer [Internet]. NIH U.S. National Library of Medicine. 2019. Available from: https://clinicaltrials.gov/ct2/show/NCT04004312?term=spaceoar&draw=2&rank=5
484. Leiker AJ, Desai NB, Folkert MR. Rectal radiation dose-reduction techniques in prostate cancer: a focus on the rectal spacer. Future Oncology. 2018 Jun 25;fon-2018-0286.
485. SooHoo JR, Seibold LK, Laing AE, Kahook MY. Bleb morphology and histology in a

rabbit model of glaucoma filtration surgery using Ozurdex® or mitomycin-C. Molecular vision. 2012;18(February):714–9.
486. Ocular Therapeutix Inc. DEXTENZA [package insert] [Internet]. Bedford, MA; 2020. Available from: https://www.dextenza.com/wp-content/uploads/DEXTENZA-Full-Prescribing-Information.pdf
487. Sawhney AS, Jarrett P, Bassett M, Blizzard C. Drug Delivery through hydrogel Plugs US8409606B2. United States; US8409606B2, 2013.
488. Kim J, Chauhan A. Dexamethasone transport and ocular delivery from poly(hydroxyethyl methacrylate) gels. International Journal of Pharmaceutics. 2008;353(1–2):205–22.
489. Momose T, Ito N, Kanai A, Watanabe Y, Shibata M. Adsorption of levocabastine eye drops by soft contact lenses and its effects in rabbit eyes. CLAO J. 1997;23:96–9.
490. Lumbroso P, Nhamias M, Nhamias S, Tranche P. A preliminary study of the adsorption and release of preservatives by contact lenses and collagen shields. The CLAO journal : official publication of the Contact Lens Association of Ophthalmologists, Inc. 1996 Jan;22(1):61–3.
491. Israelachvili JN, Mitchell JD, Ninham BW. Theory of Self-Assembly of Hydrocarbon Amphiphiles into Micelles and Bilayers. Journal of the Chemical Society, Faraday Transactions 2. 1976;72:1525–68.
492. Yadav S, Sharma AK, Kumar P. Nanoscale Self-Assembly for Therapeutic Delivery. Frontiers in Bioengineering and Biotechnology. 2020;8(February):1–24.
493. Jusufi A, Lebard DN, Levine BG, Klein ML. Surfactant concentration effects on micellar properties. Journal of Physical Chemistry B. 2012;116(3):987–91.
494. Israelachvili JN, Mitchell JD, Ninham BW. Theory of Self-Assembly of Hydrocarbon Amphiphiles into Micelles and Bilayers. 1975;1525–68.
495. Saito N, Ohita Y, Kubo A. Synthesis of saframycins. IV. Selenium oxide oxidation of 4-oxo-hexahydro-1,5-imino-3-benzazocin-7,10-dione; promising method to construct saframycins C and D from saframycin B. Chemical and Pharmaceutical Bulletin. 1990;38(3):821–3.
496. Anghel DF, Winnik FM, Galatanu N. Effect of the surfactant head group length on the interactions between polyethylene glycol monononylphenyl ethers and poly(acrylic acid). Colloids and Surfaces A: Physicochemical and Engineering Aspects. 1999 Apr;149(1–3):339–45.
497. Krimm S. The hydrophobic effect: Formation of micelles and biological membranes, Charles Tanford,. Krimm S, editor. Journal of Polymer Science: Polymer Letters Edition. 2nd ed. 1980 Oct;18(10):687–687.
498. Allergan. OZURDEX® (dexamethasone intravitreal implant) For Intravitreal Injection - Prescribing Information. 2020.
499. EyePoint Pharmaceuticals Inc. DEXYCU® (dexamethasone intraocular suspension) 9% full U.S. Prescribing Information. [Internet]. 2020. Available from: https://dexycu.com/downloads/DEXYCU Prescribing Information_6-11-20.pdf
500. Parmar DN, Sharr MM. Cotton gauze foreign body granuloma following microvascular decompression. British Journal of Neurosurgery. 1999 Jan 6;13(1):87–9.
501. Al-Shahwan S, Edward DP. Foreign body granulomas secondary to retained sponge fragment following mitomycin C trabeculectomy. Graefe's Archive for Clinical and Experimental Ophthalmology. 2005;243(2):178–81.

502. Seidel JM, Malmonge SM. Synthesis of polyHEMA hydrogels for using as biomaterials. Bulk and solution radical-initiated polymerization techniques. Materials Research. 2000;3(3):79–83.
503. Chirila T V, Constable IJ, Crawford GJ, Vijayasekaran S, Thompson DE, Chen Y, et al. Poly(2-hydroxyethyl methacrylate) sponges as implant materials: in vivo and in vitro evaluation of cellular invasion. Biomaterials. 1993;14(1):26–38.
504. Matas B, Spencer W, Hayes T. Scanning electron microscopy of hydrophilic contact lenses. Archives of Ophthalmology. 1972;88(3):287–95.
505. Chirila T V, Chen Y, Griffin BJ, Constable IJ. Hydrophilic Sponges based on of Monomer Mixture Composition on the Pore Size. Polymer International. 1993;32:221–32.
506. Jeyanthi R, Rae KP. CONTROLLED RELEASE OF ANTICANCER POLY (HEMA) HYDROGEL MATRICES DRUGS FROM COLLAGEN- carrier into the cancerous lesion . For this pur- pose , copolymeric hydrogels of collagen and poly (HEMA) were prepared and character- ized ; the results of these stu. 1990;13:91–8.
507. Bonacucina G, Cespi M, Mencarelli G, Giorgioni G, Palmieri GF. Thermosensitive self-assembling block copolymers as drug delivery systems. Polymers. 2011;3(2):779–811.
508. Maulvi FA, Desai AR, Choksi HH, Patil RJ, Ranch KM, Vyas BA, et al. Effect of surfactant chain length on drug release kinetics from microemulsion-laden contact lenses. International Journal of Pharmaceutics. 2017;524(1–2):193–204.
509. Collins SP, Pope RK, Scheetz RW, Ray RI, Wagner PA, Little BJ. Advantages of environmental scanning electron microscopy in studies of microorganisms. Microscopy Research and Technique. 1993 Aug;25(5–6):398–405.
510. Baumgarten N. Environmental SEM premières. Nature. 1989 Sep;341(6237):81–2.
511. Xinming L, Yingde C, Lloyd AW, Mikhalovsky S V., Sandeman SR, Howel CA, et al. Polymeric hydrogels for novel contact lens-based ophthalmic drug delivery systems: A review. Contact Lens and Anterior Eye. 2008;31(2):57–64.
512. He Y, Hower J, Chen S, Bernards MT, Chang Y, Jiang S. Molecular Simulation Studies of Protein Interactions with Zwitterionic Phosphorylcholine Self-Assembled Monolayers in the Presence of Water. Langmuir. 2008 Sep 16;24(18):10358–64.
513. Ishihara K, Nomura H, Mihara T, Kurita K, Iwasaki Y, Nakabayashi N. Why do phospholipid polymers reduce protein adsorption? Journal of biomedical materials research. 1998 Feb;39(2):323–30.
514. Morais JM, Papadimitrakopoulos F, Burgess DJ. Biomaterials / Tissue Interactions : Possible Solutions to Overcome Foreign Body Response. 2010;12(2):188–96.
515. Shi D, Zhang X, Dong W, Chen M. Synthesis and biocompatibility of phosphoryl polymer and relationship between biocompatibility and water structure. Polymer Science Series B. 2012 May;54(5):335–41.
516. Adachi M, Navessin T, Xie Z, Li FH, Tanaka S, Holdcroft S. Thickness dependence of water permeation through proton exchange membranes. Journal of Membrane Science. 2010 Nov;364(1–2):183–93.
517. Tanaka M, Mochizuki A. Clarification of the Blood Compatibility Mechanism by Controlling the Water Structure at the Blood – Poly (meth) acrylate Interface Clarification of the Blood Compatibility Mechanism by. 2012;5063.

518. Goda T, Watanabe J, Takai M, Ishihara K. Water structure and improved mechanical properties of phospholipid polymer hydrogel with phosphorylcholine centered intermolecular cross-linker. Polymer. 2006 Feb;47(4):1390–6.
519. Hoare TR, Kohane DS. Hydrogels in drug delivery: Progress and challenges. Polymer. 2008;49(8):1993–2007.
520. Lewis AL, Driver M. Blending in with the Body. Journal of Chemical Education. 2002 Mar;79(3):321.
521. Numata K. Silk hydrogels for tissue engineering and dual-drug delivery. In: Silk Biomaterials for Tissue Engineering and Regenerative Medicine. Elsevier; 2014. p. 503–18.
522. Abasi S, Davis R, Podstawczyk DA, Guiseppi-Elie A. Distribution of water states within Poly(HEMA-co-HPMA)-based hydrogels. Polymer. 2019 Dec;185(November):121978.
523. Ping ZH, Nguyen QT, Chen SM, Zhou JQ, Ding YD. States of water in different hydrophilic polymers - DSC and FTIR studies. Polymer. 2001;42(20):8461–7.
524. Gun'ko V, Savina I, Mikhalovsky S. Properties of Water Bound in Hydrogels. Gels. 2017;3(4):37.
525. Mirejovsky D, Pate AS, Young G. Water properties of hydrogel contact lens materials: a possible predictive model for corneal desiccation staining. 1993;1080–8.
526. Thuresson K, Lindman B, Nyström B. Effect of Hydrophobic Modification of a Nonionic Cellulose Derivative on the Interaction with Surfactants. Rheology. The Journal of Physical Chemistry B. 1997 Aug;101(33):6450–9.
527. Winnik FM, Regismond STA. Fluorescence methods in the study of the interactions of surfactants with polymers. Colloids and Surfaces A: Physicochemical and Engineering Aspects. 1996 Nov;118(1–2):1–39.
528. Stodghill SP. Thermal Analysis – A Review of Techniques and Applications in the Pharmaceutical Sciences. American Pharmaceutical Review. 2010;13(2).
529. El-Arnaouty MB. Effect of ono and di – protic Acid on the Characterization of 2-hydroxyethyl-methacrylate based hydrogels Prepared by γ – radiation and its Application for Delivery. Journal of Radiation Research and Applied Sciences. 2010;3(3):763–90.
530. González-Henríquez CM, Pizarro G del C, Sarabia-Vallejos MA, Terraza CA, López-Cabaña ZE. In situ-preparation and characterization of silver-HEMA/PEGDA hydrogel matrix nanocomposites: Silver inclusion studies into hydrogel matrix. Arabian Journal of Chemistry. 2019 Nov;12(7):1413–23.
531. Narayanaswamy R, Torchilin VP. Hydrogels and their applications in targeted drug delivery. Molecules. 2019;24(3).
532. Sato S, Kim S. Macromolecular diffusion through polymer membranes. International Journal of Pharmaceutics. 1984 Dec;22(2–3):229–55.
533. Yigit EA, Ercal N. Release of N-acetylcysteine and N-acetylcysteine Amide From Contact Lenses. Eye & Contact Lens-Science and Clinical Practice. 2013;39(5):335–40.
534. Langer RS, Peppas NA. Present and future applications of biomaterials in controlled drug delivery systems. Biomaterials. 1981;2(4):201–14.
535. Kost J, Leong K, Langer R. Ultrasound-enhanced polymer degradation and release of incorporated substances. Proceedings of the National Academy of Sciences of the United States of America. 1989;86(20):7663–6.

536. Gao P, Nixon PR, Skoug JW. Diffusion in HPMC Gels. II. Prediction of Drug Release Rates from Hydrophilic Matrix Extended-Release Dosage Forms. Pharmaceutical Research. 1995 Jul;12(7):965–71.
537. Chastain JE. General Considerations in Ocular Drug Delivery. 2003;
538. Costa P, Lobo JMS. Modeling and comparison of dissolution profiles ´. European Journal of Pharmaceutical Sciences. 2001;13:123–33.
539. Soni T, Chotai N. Assessment of Dissolution Profile of Marketed Aceclofenac Formulations. Journal of Young Pharmacists. 2010 Jan;2(1):21–6.
540. Singh J, Gupta S, Kaur H. Prediction of in vitro Drug Release Mechanisms from Extended Release Matrix Tablets using SSR/R2 Technique. Trends in Applied Sciences Research. 2011 Apr 1;6(4):400–9.
541. ClinicalTrials.gov. NCT02873806 Two Trabecular Micro-bypass Stents & Postoperative Travoprost to Treat Glaucoma Subjects on Two Hypotensive Agents [Internet]. NIH U.S. National Library of Medicine. 2017. Available from: https://clinicaltrials.gov/ct2/show/NCT02873806?term=ozurdex&cond=Glaucoma&draw=2&rank=9
542. Li S, Quan D. Preparation and in vitro evaluation of an ilomastat microemulsion gel by a self-microemulsifying system. Pharmazie. 2012;67(2):156–60.
543. Galardy R, Cassabonne M, Giese C, Gilbert J, Lapierre F, Lopez H, et al. Low Molecular Weight Inhibitors in Corneal Ulceration. New York Academy of Science. 1994;6(732):315–23.
544. Kawana K, Kiuchi T, Yasuno Y, Oshika T. Evaluation of Trabeculectomy Blebs Using 3-Dimensional Cornea and Anterior Segment Optical Coherence Tomography. Ophthalmology. 2009 May;116(5):848–55.
545. Goldmann H. Das Minutenvolumen der menschlichen Vorderkammer bei Normalen und bei Fallen von primärem Glaukom [Minute Volume of the Human Anterior Chamber in Normal State and in Primary Glaucoma]. Ophthalmologica. 1950;120(3):150–6.
546. Georgoulas S, Ru Q, Brocchini S, Khaw PT. A novel single application prolonged release MMP inhibitor is superior to mitomycin in preventing scarring after experimental glaucoma surgery. Investigative Ophthalmology and Visual Science. 2008;49(5):4538.
547. Georgoulas SD. Novel methods for the modulation of wound healing after glaucoma filtration surgery. School of Pharmacy, University of London and UCL Institute of Ophthlamology and Moorfields Eye Hospital; 2010.
548. Kendall K. Agglomerate Strength. Powder metallurgy. 1988;31(1):28–31.
549. Fichtner F, Rasmuson Å, Alderborn G. Particle size distribution and evolution in tablet structure during and after compaction. International Journal of Pharmaceutics. 2005;292(1–2):211–25.
550. Wadke DA, Serajuddin ATM, Jacobson H. Preformulation testing. In: Lieberman HA, Lachman L, Schwartz J., editors. Pharmaceutical Dosage Forms: Tablets, Vol 1. New York, NY: Marcel Dekker; 1989. p. 1–73.
551. Shekunov BY, York P. Crystallization processes in pharmaceutical technology and drug delivery design. Journal of Crystal Growth. 2000 Apr;211(1–4):122–36.
552. Cannon GJ, Swanson JA. The macrophage capacity for phagocytosis. Journal of cell science. 1992 Apr;101 (Pt 4:907–13.
553. Skulason S, Holbrook WP, Kristmundsdottir T. Clinical assessment of the effect of a matrix metalloproteinase inhibitor on aphthous ulcers. Acta Odontologica

Scandinavica. 2009 Jan 2;67(1):25–9.
554. Chadha V, Bhat K. The evaluation of doxycycline controlled release gel versus doxycycline controlled release implant in the management of periodontitis. Journal of Indian Society of Periodontology. 2012;16(2):200.
555. Bolobajev J, Trapido M, Goi A. Effect of iron ion on doxycycline photocatalytic and Fenton-based autocatatalytic decomposition. Chemosphere. 2016;153:220–6.
556. Dalgakiran D, İnan T, Güner FS. Investigation of photoinduced polymerization of doxycycline-imprinted hydrogels: effect of template on initiator reactivity, conversion, and reaction rate. Turkish Journal of Chemistry. 2017;41:862–73.
557. Ramírez Barragán CA, Macías Balleza ER, García-Uriostegui L, Andrade Ortega JA, Toríz G, Delgado E. Rheological characterization of new thermosensitive hydrogels formed by chitosan, glycerophosphate, and phosphorylated β-cyclodextrin. Carbohydrate Polymers. 2018;201(April):471–81.
558. Tsai ML, Chang HW, Yu HC, Lin YS, Tsai YD. Effect of chitosan characteristics and solution conditions on gelation temperatures of chitosan/2-glycerophosphate/nanosilver hydrogels. Carbohydrate Polymers. 2011;84(4):1337–43.
559. Wang Q, Chen D. Synthesis and characterization of a chitosan based nanocomposite injectable hydrogel. Carbohydrate Polymers. 2016;136:1228–37.
560. Zhou HY, Jiang LJ, Cao PP, Li JB, Chen XG. Glycerophosphate-based chitosan thermosensitive hydrogels and their biomedical applications. Carbohydrate Polymers. 2015;117:524–36.
561. Deng A, Kang X, Zhang J, Yang Y, Yang S. Enhanced gelation of chitosan/β-sodium glycerophosphate thermosensitive hydrogel with sodium bicarbonate and biocompatibility evaluated. Materials Science and Engineering C. 2017;78:1147–54.
562. Sarwan T, Kumar P, Choonara YE, Pillay V. Hybrid Thermo-Responsive Polymer Systems and Their Biomedical Applications. Frontiers in Materials. 2020;7(March).
563. Lynch CR, Kondiah PPD, Choonara YE, du Toit LC, Ally N, Pillay V. Hydrogel Biomaterials for Application in Ocular Drug Delivery. Frontiers in Bioengineering and Biotechnology. 2020;8(March):1–18.
564. Ravishankar K, Dhamodharan R. Advances in chitosan-based hydrogels: Evolution from covalently crosslinked systems to ionotropically crosslinked superabsorbents. Reactive and Functional Polymers. 2020;149(February):104517.
565. Chenite A, Chaput C, Wang D, Combes C, Buschmann M., Hoemann C., et al. Novel injectable neutral solutions of chitosan form biodegradable gels in situ. Biomaterials. 2000;21(21):2155–61.
566. Chenite A. Rheological characterisation of thermogelling chitosan/glycerol-phosphate solutions. Carbohydrate Polymers. 2001 Sep;46(1):39–47.
567. Yu D-G, Shen X-X, Branford-White C, White K, Zhu L-M, Annie Bligh SW. Oral fast-dissolving drug delivery membranes prepared from electrospun polyvinylpyrrolidone ultrafine fibers. Nanotechnology. 2009 Feb 4;20(5):055104.
568. Boys CV. On the Production, Properties, and some suggested Uses of the Finest Threads. Proceedings of the Physical Society of London. 1887;9(1):8–19.
569. Garg K, Bowlin GL. Electrospinning jets and nanofibrous structures. Biomicrofluidics. 2011;5(1):1–19.

570. Formhals A. Process and apparatus for preparing artificial threads. United States; US1975504A, 1934.
571. Verreck G, Chun I, Rosenblatt J, Peeters J, Dijck A Van, Mensch J, et al. Incorporation of drugs in an amorphous state into electrospun nanofibers composed of a water-insoluble, nonbiodegradable polymer. Journal of Controlled Release. 2003 Oct;92(3):349–60.
572. Angkawinitwong U, Awwad S, Khaw PT, Brocchini S, Williams GR. Electrospun formulations of bevacizumab for sustained release in the eye. Acta Biomaterialia. 2017;64:126–36.
573. Xu Y, Zhou F, Zhou D, Mo J, Hu H, Lin L, et al. Degradation Behaviors of Biodegradable Aliphatic Polyesters and Polycarbonates. Journal of Biobased Materials and Bioenergy. 2020 Apr 1;14(2):155–68.
574. Youssef A, Hollister SJ, Dalton PD. Additive manufacturing of polymer melts for implantable medical devices and scaffolds. Biofabrication. 2017 Feb 28;9(1):012002.
575. Woodruff MA, Hutmacher DW. The return of a forgotten polymer - Polycaprolactone in the 21st century. Progress in Polymer Science (Oxford). 2010;35(10):1217–56.
576. Bartnikowski M, Dargaville TR, Ivanovski S, Hutmacher DW. Degradation mechanisms of polycaprolactone in the context of chemistry, geometry and environment. Progress in Polymer Science. 2019;96:1–20.
577. Díaz E, Sandonis I, Valle MB. In Vitro Degradation of Poly(caprolactone)/nHA Composites. Journal of Nanomaterials. 2014;2014:1–8.
578. Hayashi T. Biodegradable polymers for biomedical uses. Progress in Polymer Science. 1994 Jan;19(4):663–702.
579. Dwivedi R, Kumar S, Pandey R, Mahajan A, Nandana D, Katti DS, et al. Polycaprolactone as biomaterial for bone scaffolds: Review of literature. Journal of Oral Biology and Craniofacial Research. 2020 Jan;10(1):381–8.
580. Alexandridis P. Poly(ethylene oxide)/poly(propylene oxide) block copolymer surfactants. Current Opinion in Colloid & Interface Science. 1997 Oct;2(5):478–89.
581. Zhang Y, Song W, Geng J, Chitgupi U, Unsal H, Federizon J, et al. Therapeutic surfactant-stripped frozen micelles. Nature Communications. 2016;7(May):1–9.
582. Bodratti A, Alexandridis P. Formulation of Poloxamers for Drug Delivery. Journal of Functional Biomaterials. 2018 Jan 18;9(1):11.
583. Nivaggioli T, Alexandridis P, Hatton TA, Yekta A, Winnik MA. Fluorescence Probe Studies of Pluronic Copolymer Solutions as a Function of Temperature. Langmuir. 1995 Mar;11(3):730–7.
584. Perecin CJ, Yoshioka S, Chitta V, Gratens X, Léo P, De Oliveira A, et al. Magnetite Nanoparticles Encapsulated with PCL and Poloxamer by Nano Spray Drying technique. XIV Brazil MRS (Materials Research Society) Meeting, Rio, September 27 to October 01, 2015, Awarded Abstract: ASEE, Symposium B. 2015;6(4):68–73.
585. Zhang Y, Tang L, Sun L, Bao J, Song C, Huang L, et al. A novel paclitaxel-loaded poly(ε-caprolactone)/Poloxamer 188 blend nanoparticle overcoming multidrug resistance for cancer treatment. Acta Biomaterialia. 2010 Jun;6(6):2045–52.
586. Mei L, Zhang Y, Zheng Y, Tian G, Song C, Yang D, et al. A Novel Docetaxel-Loaded Poly (ε-Caprolactone)/Pluronic F68 Nanoparticle Overcoming Multidrug Resistance for Breast Cancer Treatment. Nanoscale Research Letters. 2009 Dec

16;4(12):1530–9.
587. Ma G, Song C, Sun H, Yang J, Leng X. A biodegradable levonorgestrel-releasing implant made of PCL/F68 compound as tested in rats and dogs. Contraception. 2006 Aug;74(2):141–7.
588. Kawakami K. Miscibility analysis of particulate solid dispersions prepared by electrospray deposition. International Journal of Pharmaceutics. 2012 Aug;433(1–2):71–8.
589. Desai J, Alexander K, Riga A. Characterization of polymeric dispersions of dimenhydrinate in ethyl cellulose for controlled release. International Journal of Pharmaceutics. 2006 Feb;308(1–2):115–23.
590. Wang X, Michoel A, Van den Mooter G. Solid state characteristics of ternary solid dispersions composed of PVP VA64, Myrj 52 and itraconazole. International Journal of Pharmaceutics. 2005 Oct;303(1–2):54–61.
591. Ceballos A, Cirri M, Maestrelli F, Corti G, Mura P. Influence of formulation and process variables on in vitro release of theophylline from directly-compressed Eudragit matrix tablets. Il Farmaco. 2005 Nov;60(11–12):913–8.
592. Li C, Li C, Le Y, Chen J-F. Formation of bicalutamide nanodispersion for dissolution rate enhancement. International Journal of Pharmaceutics. 2011 Feb;404(1–2):257–63.
593. García-Rodriguez JJ, de la Torre-Iglesias PM, Vegas-Sánchez MC, Torrado-Durán S, Bolás-Fernández F, Torrado-Santiago S. Changed crystallinity of mebendazole solid dispersion: Improved anthelmintic activity. International Journal of Pharmaceutics. 2011 Jan;403(1–2):23–8.
594. Lim H-T, Balakrishnan P, Oh DH, Joe KH, Kim YR, Hwang DH, et al. Development of novel sibutramine base-loaded solid dispersion with gelatin and HPMC: Physicochemical characterization and pharmacokinetics in beagle dogs. International Journal of Pharmaceutics. 2010 Sep;397(1–2):225–30.
595. Overhoff KA, Engstrom JD, Chen B, Scherzer BD, Milner TE, Johnston KP, et al. Novel ultra-rapid freezing particle engineering process for enhancement of dissolution rates of poorly water-soluble drugs. European Journal of Pharmaceutics and Biopharmaceutics. 2007 Jan;65(1):57–67.
596. Siegel RA, Langer R. Mechanistic studies of macromolecular drug release from macroporous polymers. II. Models for the slow kinetics of drug release. Journal of Controlled Release. 1990;14(2):153–67.
597. Simon L., Stella V., Charman W., Charman S. Mechanisms controlling diffusion and release of model proteins through and from partially esterified hyaluronic acid membranes. Journal of Controlled Release. 1999 Sep;61(3):267–79.
598. Siegel RA, Kost J, Langer R. Mechanistic studies of macromolecular drug release from macroporous polymers. I. Experiments and preliminary theory concerning completeness of drug release. Journal of Controlled Release. 1989;8(3):223–36.
599. Leuenberger H, Bonny JD, Kolb M. Percolation effects in matrix-type controlled drug release systems. International Journal of Pharmaceutics. 1995 Mar;115(2):217–24.
600. Nguyen-Kim V, Prévost S, Seidel K, Maier W, Marguerre A-K, Oetter G, et al. Solubilization of active ingredients of different polarity in Pluronic® micellar solutions – Correlations between solubilizate polarity and solubilization site. Journal of Colloid and Interface Science. 2016 Sep;477:94–102.
601. Miyata T, Uragami T, Nakamae K. Biomolecule-sensitive hydrogels. Advanced

Drug Delivery Reviews. 2002;54(1):79–98.
602. Misra GP, Singh RSJ, Aleman TS, Jacobson SG, Gardner TW, Lowe TL. Subconjunctivally implantable hydrogels with degradable and thermoresponsive properties for sustained release of insulin to the retina. Biomaterials. 2009 Nov;30(33):6541–7.
603. Kamath KR, Park K. Biodegradable hydrogels in drug delivery. Advanced Drug Delivery Reviews. 1993 Jul;11(1–2):59–84.
604. Wolle MA, West SK. Ocular Chlamydia trachomatis infection: elimination with mass drug administration. Expert Review of Anti-Infective Therapy. 2019;17(3):189–200.
605. West SK. Milestones in the fight to eliminate trachoma. Ophthalmic and Physiological Optics. 2020;40(2):66–74.
606. Mann I. INVESTIGATION OF THE SOURCES OF TRACHOMA IN THE WHITE SCHOOL POPULATION OF WESTERN AUSTRALIA. British Journal of Ophthalmology. 1960 Jun 1;44(6):321–3.
607. Mann I. Correlation of Race and Way of Life in Australia and the Territory of Papua and New Guinea with Incidence and Severity of Clinical Trachoma. American Journal of Ophthalmology. 1967 May;63(5):1302–9.
608. Hotez PJ. The rise or fall of neglected tropical diseases in East Asia Pacific. Acta Tropica. 2020 Feb;202:105182.
609. WHO. Trachoma [Internet]. Newsroom. 2020. Available from: https://www.who.int/news-room/facts-in-pictures/detail/trachoma
610. Cheng C-Y, Wang N, Wong TY, Congdon N, He M, Wang YX, et al. Prevalence and causes of vision loss in East Asia in 2015: magnitude, temporal trends and projections. British Journal of Ophthalmology. 2020 May;104(5):616–22.
611. Evans JR, Solomon AW, Kumar R, Perez Á, Singh BP, Srivastava RM, et al. Antibiotics for trachoma. Cochrane Database of Systematic Reviews. 2019 Sep 26;
612. Darougar S, Jones BR, Viswalingam N, Poirier RH, Allami J, Houshmand A, et al. Family-based suppressive intermittent therapy of hyperendemic trachoma with topical oxytetracycline or oral doxycycline. British Journal of Ophthalmology. 1980 Apr 1;64(4):291–5.
613. Al-shohani ADH. Hydrogel Formulations For Ophthalmic Delivery. University College London; 2016.
614. Alonso MJ, Sánchez A. The potential of chitosan in ocular drug delivery. Journal of Pharmacy and Pharmacology. 2003;55(11):1451–63.
615. Sogias IA, Williams AC, Khutoryanskiy V V. Why is Chitosan Mucoadhesive ? 2008;1837–42.
616. Quiñones JP, Peniche H, Peniche C. Chitosan based self-assembled nanoparticles in drug delivery. Polymers. 2018;10(3):1–32.
617. Parhi R. Drug delivery applications of chitin and chitosan: a review. Environmental Chemistry Letters. 2020;18(3):577–94.
618. Kim J, Kudisch M, Mudumba S, Asada H, Aya-Shibuya E, Bhisitkul RB, et al. Biocompatibility and pharmacokinetic analysis of an intracameral polycaprolactone drug delivery implant for glaucoma. Investigative Ophthalmology and Visual Science. 2016;57(10):4341–6.
619. Silva-Cunha A, Fialho SL, Naud MC, Behar-Cohen F. Poly-ε-caprolactone intravitreous devices: An in vivo study. Investigative Ophthalmology and Visual Science. 2009;50(5):2312–8.

620. Nasr FH, Khoee S, Dehghan MM, Chaleshtori SS, Shafiee A. Preparation and Evaluation of Contact Lenses Embedded with Polycaprolactone-Based Nanoparticles for Ocular Drug Delivery. Biomacromolecules. 2016;17(2):485–95.
621. Alami-Milani M, Zakeri-Milani P, Valizadeh H, Salehi R, Jelvehgari M. Preparation and evaluation of PCL-PEG-PCL micelles as potential nanocarriers for ocular delivery of dexamethasone. Iranian Journal of Basic Medical Sciences. 2018;21(2):153–64.
622. Jindal N, Mehta SK. Nevirapine loaded Poloxamer 407/Pluronic P123 mixed micelles: Optimization of formulation and in vitro evaluation. Colloids and Surfaces B: Biointerfaces. 2015 May;129:100–6.
623. Pellosi DS, Tessaro AL, Moret F, Gaio E, Reddi E, Caetano W, et al. Pluronic® mixed micelles as efficient nanocarriers for benzoporphyrin derivatives applied to photodynamic therapy in cancer cells. Journal of Photochemistry and Photobiology A: Chemistry. 2016 Jan;314:143–54.
624. Wei Z, Hao J, Yuan S, Li Y, Juan W, Sha X, et al. Paclitaxel-loaded Pluronic P123/F127 mixed polymeric micelles: Formulation, optimization and in vitro characterization. International Journal of Pharmaceutics. 2009 Jul;376(1–2):176–85.
625. Zhao L, Du J, Duan Y, Zang Y, Zhang H, Yang C, et al. Curcumin loaded mixed micelles composed of Pluronic P123 and F68: Preparation, optimization and in vitro characterization. Colloids and Surfaces B: Biointerfaces. 2012 Sep;97:101–8.
626. Giuliano E, Paolino D, Fresta M, Cosco D. Mucosal applications of poloxamer 407-based hydrogels: An overview. Pharmaceutics. 2018;10(3):1–26.
627. Goebbels M. Tear secretion and tear film function in insulin dependent diabetics. British Journal of Ophthalmology. 2000 Jan 1;84(1):19–21.
628. Mathers WD, Daley TE. Tear Flow and Evaporation in Patients with and without Dry Eye. Ophthalmology. 1996 Apr;103(4):664–9.
629. Gobbels M, Goebels G, Breitbach R, Spitznas M. Tear secretion in dry eyes as assessed by objective fluorophotometry. German journal of ophthalmology. 1992;1(5):350–3.
630. van Best JA, del Castillo Benitez JM, Coulangeon L-M. Measurement of basal tear turnover using a standardized protocol. Graefe's Archive for Clinical and Experimental Ophthalmology. 1995 Jan;233(1):1–7.
631. ClinicalTrials.gov. NCT02510794 Study of the Efficacy and Safety of the Ranibizumab Port Delivery System (RPDS) for Sustained Delivery of Ranibizumab in Participants With Subfoveal Neovascular Age-Related Macular Degeneration (AMD) (LADDER) [Internet]. NIH U.S. National Library of Medicine. 2015. Available from: https://clinicaltrials.gov/ct2/show/NCT02510794
632. Busbee BG, Ho AC, Brown DM, Heier JS, Suñer IJ, Li Z, et al. Twelve-Month Efficacy and Safety of 0.5 mg or 2.0 mg Ranibizumab in Patients with Subfoveal Neovascular Age-related Macular Degeneration. Ophthalmology. 2013 May;120(5):1046–56.
633. Henein C, Awwad S, Ibeanu N, Vlatakis S, Brocchini S, Tee Khaw P, et al. Hydrodynamics of Intravitreal Injections into Liquid Vitreous Substitutes. Pharmaceutics. 2019 Aug 1;11(8):371.
634. Shrestha R, Kharel Sitaula R, Karki P, Joshi SN, Rawal S. Combined Intravitreal Bevacizumab And Dexamethasone In Bilateral Lupus Retinopathy. International Medical Case Reports Journal. 2019 Oct;Volume 12:329–33.

635. Campochiaro PA, Marcus DM, Awh CC, Regillo C, Adamis AP, Bantseev V, et al. The Port Delivery System with Ranibizumab for Neovascular Age-Related Macular Degeneration Results from the Randomized Phase 2 Ladder Clinical Trial. Ophthalmology. 2019;126(8):1141–54.
636. Lemos V, Cabugueira A, Noronha M, Pinto LA, Reina M, Branco J, et al. Intraocular pressure in eyes receiving intravitreal antivascular endothelial growth factor injections. Ophthalmologica. 2015 Mar 13;233(3–4):162–8.
637. Lemos-Reis R, Moreira-Goncalves N, Melo A, Carneiro A, Falcão-Reis F. Immediate effect of intravitreal injection of bevacizumab on intraocular pressure. Clinical Ophthalmology. 2014 Jul;1383.
638. Farhood Q, Twfeeq S. Short-term intraocular pressure changes after intravitreal injection of bevacizumab in diabetic retinopathy patients. Clinical Ophthalmology. 2014 Mar;599.
639. Li E, Donati S, Lindsley KB, Krzystolik MG, Virgili G. Treatment regimens for administration of anti-vascular endothelial growth factor agents for neovascular age-related macular degeneration. Cochrane Database of Systematic Reviews. 2020 May 5;
640. Bock F, Matthaei M, Reinhard T, Böhringer D, Christoph J, Ganslandt T, et al. High-Dose Subconjunctival Cyclosporine A Implants Do Not Affect Corneal Neovascularization after High-Risk Keratoplasty. Ophthalmology. 2014 Sep;121(9):1677–82.
641. Cunha-Vaz J, Ashton P, Iezzi R, Campochiaro P, Dugel PU, Holz FG, et al. Sustained Delivery Fluocinolone Acetonide Vitreous Implants. Ophthalmology. 2014 Oct;121(10):1892-1903.e3.
642. Cabrera M, Yeh S, Albini TA. Sustained-Release Corticosteroid Options. Journal of Ophthalmology. 2014;2014:1–5.
643. Monsellato R, Trovato E, Turchetti P, Forestiere M, Pistone A, De Sio S, et al. Ocular hypertension management in long-term treatments with intravitreal dexamethasone implants: a 3-year experience. La Clinica Terapeutica. 2020;171(1):e11-14.
644. Cobo A, Sheybani R, Meng E. MEMS: Enabled Drug Delivery Systems. Advanced Healthcare Materials. 2015 May;4(7):969–82.
645. Saati S, Lo R, Li PY, Meng E, Varma R, Humayun MS. Mini drug pump for ophthalmic use. Transactions of the American Ophthalmological Society. 2009;107:60–71.
646. Humayun M, Santos A, Altamirano JC, Ribeiro R, Gonzalez R, de la Rosa A, et al. Implantable MicroPump for Drug Delivery in Patients with Diabetic Macular Edema. Translational Vision Science & Technology. 2014;3(6):5.
647. Lo R, Li PY, Saati S, Agrawal RN, Humayun MS, Meng E. A passive MEMS drug delivery pump for treatment of ocular diseases. Biomedical Microdevices. 2009;11(5):959–70.
648. Gutierrez-Hernandez J-C, Caffey S, Abdallah W, Calvillo P, Gonzalez R, Shih J, et al. One-Year Feasibility Study of Replenish MicroPump for Intravitreal Drug Delivery: A Pilot Study. Translational vision science & technology. 2014;3(4):1–8.
649. Pons-faudoa FP, Ballerini A, Sakamoto J, Sciences H, Monterrey T De, Garza AE, et al. the clinical landscape of therapeutics for chronic diseases. Vol. 21. 2020.
650. Pope JE, Deer TR. Intrathecal drug delivery for pain: a clinical guide and future directions. Pain management. 2015;5(3):175–83.

651. Farshchi Yazdi SAF, Corigliano A, Ardito R. 3-D Design and Simulation of a Piezoelectric Micropump. Micromachines. 2019 Apr 18;10(4):259.
652. Medtronic. Medtronic SYNCHROMED® II Programmable Pumps Implant Manual. 2011.
653. Mioduszewski J, Zarbo AG. Ambulatory infusion pumps: A practical view at an alternative approach. Seminars in Oncology Nursing. 1987;3(2):106–11.
654. Mohseni M, Ebneshahidi A. The flow Rate Accuracy of Elastomeric Infusion Pumps After Repeated Filling. Anesthesiology and Pain Medicine. 2014;14(2):2–5.
655. Kaye T. Prolonged infusion times with disposable elastomeric infusion devices. American journal of hospital pharmacy. 1994 Feb 15;51(4):533–4.
656. Rich DS. Evaluation of a disposable, elastomeric infusion device in the home environment. American journal of hospital pharmacy. 1992 Jul;49(7):1712–6.
657. Coley SC, Shaw PK, Leff RD. The performance of three portable infusion-pump devices set to deliver 2 mL/hr. American journal of health-system pharmacy : AJHP : official journal of the American Society of Health-System Pharmacists. 1997 Jun 1;54(11):1277–80.
658. Wermeling DP, Foster TS, Rapp RP, Kenady DE. Evaluation of a disposable, nonelectronic, patient-controlled-analgesia device for postoperative pain. Clinical pharmacy. 1987 Apr;6(4):307–14.
659. Veal DF, Altman CE, McKinnon BT, Fillingim O. Evaluation of flow rates for six disposable infusion devices. American journal of health-system pharmacy : AJHP : official journal of the American Society of Health-System Pharmacists. 1995 Mar 1;52(5):500–4.
660. Ackermann M, Maier S, Ing H, Bonnabry P. Evaluation of the design and reliability of three elastomeric and one mechanical infusers. Journal of oncology pharmacy practice : official publication of the International Society of Oncology Pharmacy Practitioners. 2007;13(2):77–84.
661. Salman D, Biliune J, Kayyali R, Ashton J, Brown P, McCarthy T, et al. Evaluation of the performance of elastomeric pumps in practice: are we under-delivering on chemotherapy treatments? Current Medical Research and Opinion. 2017;33(12):2153–9.
662. LeRiger M. Comparison of flow rate accuracy and consistency between the on-Q, baxter, and ambu pain infusion devices. World Journal of Anesthesiology. 2014;3(1):119.
663. Ilfeld BM, Morey TE, Enneking FK. Delivery Rate Accuracy of Portable Infusion Pumps Used for Continuous Regional Analgesia. Anesthesia and Analgesia. 2002;95:1331–6.
664. Felici A, Sorelli M, Bocchi L. Design and Implementation of a Monitoring System for Elastomeric Infusion Pumps. In: Badnjevic A, Skrbic R, Pokvic L, editors. International Conference on Medical and Biological Engineering in Bosnia and Herzegovina (CMBEBIH). Banja Luka; 2020. p. 201–4.
665. Charmillon A, Novy E, Agrinier N, Leone M, Kimmoun A, Levy B, et al. The ANTIBIOPERF study: a nationwide cross-sectional survey about practices for β-lactam administration and therapeutic drug monitoring among critically ill patients in France. Clinical Microbiology and Infection. 2016 Jul;22(7):625–31.
666. Chung IS, Cho HS, Kim JA, Lee KH. The flow rate of the elastomeric balloon infusor is influenced by the internal pressure of the infusor. Journal of Korean medical science. 2001 Dec;16(6):702–6.

667. Bouremel Y, Madaan S, Lee RMH, Eames I, Wojcik A, Khaw PT. Pursing of planar elastic pockets. Journal of Fluids and Structures. 2017;70(January):261–75.
668. Meleshko V V. Bending of an Elastic Rectangular Clamped Plate : Exact Versus 'Engineering' Solutions. Journal of Elasticity. 1997;48:1–50.
669. Yang WH, Feng WW. On Axisymmetrical Deformations of Nonlinear Membranes. Journal of Applied Mechanics. 1970;37(4):1002.
670. Imrak CE, Gerdemeli I. A numerical method for clamped thin rectangular plates carrying a uniformly distributed load. International Applied Mechanics. 2007 Jun;43(6):701–5.
671. Erdem İmrak C, Gerdemeli I. The problem of isotropic rectangular plate with four clamped edges. Sadhana. 2007 Jun 17;32(3):181–6.
672. Chaudhuri A, DasGupta A. On the static and dynamic analysis of inflated hyperelastic circular membranes. Journal of the Mechanics and Physics of Solids. 2014 Mar;64(1):302–15.
673. Hewitt IJ, Balmforth NJ, De Bruyn JR. Elastic-plated gravity currents. European Journal of Applied Mathematics. 2015 Feb 10;26(1):1–31.
674. Asejczyk-Widlicka M, Śródka W, Schachar R a, Pierścionek BK. Material properties of the cornea and sclera: a modelling approach to test experimental analysis. Journal of biomechanics. 2011 Feb 3;44(3):543–6.
675. Asejczyk-Widlicka M, Śródka DW, Kasprzak H, Pierscionek BK. Modelling the elastic properties of the anterior eye and their contribution to maintenance of image quality: the role of the limbus. Eye. 2007 Aug 23;21(8):1087–94.
676. Naficy S, Brown HR, Razal JM, Spinks GM, Whitten PG. Progress toward robust polymer hydrogels. Australian Journal of Chemistry. 2011;64(8):1007–25.
677. Lin WC, Fan W, Marcellan A, Hourdet D, Creton C. Large strain and fracture properties of poly(dimethylacrylamide)/silica hybrid hydrogels. Macromolecules. 2010;43(5):2554–63.
678. Cenedese C, Dalziel SB. Concentration and depth fields determined by the light transmitted through a dyed solution. Submitted to Experiments in Fluids. 1998;1–5.
679. Elsheikh A, Geraghty B, Alhasso D, Knappett J, Campanelli M, Rama P. Regional variation in the biomechanical properties of the human sclera. Experimental eye research. 2010 May;90(5):624–33.
680. Friberg TR, Lace JW. A comparison of the elastic properties of human choroid and sclera. Experimental eye research. 1988 Sep;47(3):429–36.
681. Pfitzner J. Poiseuille and his law. Anaesthesia. 1976 Mar;31(2):273–5.
682. Weisstein E. Spherical Cap [Internet]. MathWorld--A Wolfram Web Resource. 2008. Available from: http://mathworld.wolfram.com/SphericalCap.html
683. Polyanin, Andrei D; Manzhirov A V. Elementary Geometry. In: Handbook of Mathematics for Engineers and Scientists. Boca Raton: Chapman & Hall/CRC Press; 2006. p. 43–76.
684. Landau LD, Lifshitz EM. Theory of Elasticity 3rd edition. Pergamon Press; 1975.
685. Chandrashekhara K. Theory of Plates. Hyderabad: Universities Press (India) Limited; 2001.
686. Belyadi H, Fathi E, Belyadi F. Rock mechanical properties and in situ stresses. In: Hydraulic Fracturing in Unconventional Reservoirs. Elsevier; 2019. p. 215–31.
687. Landau LD, Lifshitz EM, Kosevich AM, Pitaevskii LP. Fundamental Equations. In: Theory of Elasticity. Elsevier; 1986. p. 1–37.

688. Boobnoff IG. Stresses in ship plates under water pressure. Morsk Sb. 1902;312(10):119–38.
689. Bouremel Y, Eames I, Madaan S, Brocchini S, Khaw PT. (Article in Press) Compression of pressurized elastic pockets. International Journal of Non-Linear Mechanics. 2018;
690. IUPAC. modulus of elasticity, E. In: IUPAC Compendium of Chemical Terminology. Research Triagle Park, NC: IUPAC; 1997. p. 12.
691. Askeland D, Phulé P. The science and engineering of materials. 5th editio. Veitch E, editor. Cengage Learning; 2006. 198 p.
692. Hooke R. De Potentia Restitutiva, or of Spring. Explaining the Power of Springing Bodies. Martyn J, editor. Collections. London; 1678.
693. Treloar LRG. The Physics of Rubber Elasticity. Oxford: Clarendon Press; 1975. 2 p.
694. Bigoni D. Nonlinear Solid Mechanics: Bifurcation Theory and Material Instability. Cambridge: Cambridge University Press; 2012.
695. Chen Q-Z, Bismarck A, Hansen U, Junaid S, Tran MQ, Harding SE, et al. Characterisation of a soft elastomer poly(glycerol sebacate) designed to match the mechanical properties of myocardial tissue. Biomaterials. 2008 Jan;29(1):47–57.
696. Bažant ZP, Kazemi MT. Size dependence of concrete fracture energy determined by RILEM work-of-fracture method. International Journal of Fracture. 1991;51(2):121–38.
697. Bazant ZP, Kazemi MT. Determination of fracture energy, process zone longth and brittleness number from size effect, with application to rock and conerete. International Journal of Fracture. 1990;44(2):111–31.
698. Blakney AK, Swartzlander MD, Bryant SJ. The effects of substrate stiffness on the in vitro activation of macrophages and in vivo host response to poly(ethylene glycol)-based hydrogels. Journal of Biomedical Materials Research Part A. 2012 Jun;100A(6):1375–86.
699. Moshayedi P, Ng G, Kwok JCF, Yeo GSH, Bryant CE, Fawcett JW, et al. The relationship between glial cell mechanosensitivity and foreign body reactions in the central nervous system. Biomaterials. 2014 Apr;35(13):3919–25.
700. Hencky H. Uber den spannungszustand in kreisrunden platten. Zeitschrift für angewandte Mathematik und Physik. 1915;63:311–317.
701. Chien WZ. Asymptotic behavior of a thin clamped circular plate under uniform normal pressure at very large deflection. Sci Rep Natn Tsing Hua Univ. 1948;5(1):71–94.
702. Dickey RW. The plane circular elastic surface under normal pressure. Archive for Rational Mechanics and Analysis. 1967;26(3):219–36.
703. Kao R, Perrone N. Large deflections of axisymmetric circular membranes. International Journal of Solids and Structures. 1971;7(12):1601–12.
704. Kelkar A, Elber W, Raju IS. Large deflections of circular isotropic membranes subjected to arbitrary axisymmetric loading. Computers and Structures. 1985;21(3):413–21.
705. Gent AN, Lewandowski LH. Blow-off pressures for adhering layers. Journal of Applied Polymer Science. 1987;33(5):1567–77.
706. Christensen RM, Feng WW. Nonlinear analysis of the inflation of an initially flat, circular, elastic disk. Journal of Rheology. 1986 Feb;30(1):157–65.
707. Jones R. A simplified approach to the large deflection of membranes.

International Journal of Non-Linear Mechanics. 1974 Apr;9(2):141–5.
708. Tian J, Liu J, Liu X, Xiao Y, Tang L. Intravitreal infusion: A novel approach for intraocular drug delivery. Scientific Reports. 2016;6(November):1–6.
709. Gaudreault J, Fei D, Rusit J, Suboc P, Shiu V. Preclinical pharmacokinetics of ranibizumab (rhuFabV2) after a single intravitreal administration. Investigative Ophthalmology and Visual Science. 2005;46(2):726–33.
710. Granger DN, Senchenkova E. Angiogenesis. In: Inflammation and the Microcirculation. San Rafael (CA): Morgan & Claypool Life Sciences; 2010.
711. Ribatti D. Inflammation and Angiogenesis. In: Inflammation and Angiogenesis. Cham: Springer International Publishing; 2017. p. 25–6.
712. Imhof BA, Aurrand-Lions M. Angiogenesis and inflammation face off. Nature Medicine. 2006;12(2):171–2.
713. Bekerman I, Gottlieb P, Vaiman M. Variations in Eyeball Diameters of the Healthy Adults. Journal of Ophthalmology. 2014;2014.
714. Ayyala RS, Parma SE, Karcioglu ZA. Optic Nerve Changes Following Posterior Insertion of Glaucoma Drainage Device in Rabbit Model. Journal of Glaucoma. 2004;13(2):145–8.
715. Kahook MY, Noecker RJ, Pantcheva MB, Schuman JS. Location of glaucoma drainage devices relative to the optic nerve. British Journal of Ophthalmology. 2006 Apr 13;90(8):1010–3.
716. ClinicalTrials.gov. NCT00473330 A Study of Ranibizumab Injection in Subjects With Clinically Significant Macular Edema (ME) With Center Involvement Secondary to Diabetes Mellitus (RISE) (RISE) [Internet]. NIH U.S. National Library of Medicine. 2017. Available from: https://clinicaltrials.gov/ct2/show/NCT00473330
717. ClinicalTrials.gov. NCT00473382 A Study of Ranibizumab Injection in Subjects With Clinically Significant Macular Edema (ME) With Center Involvement Secondary to Diabetes Mellitus (RIDE)(RIDE) [Internet]. NIH U.S. National Library of Medicine. 2017. Available from: https://clinicaltrials.gov/ct2/show/NCT00473382
718. Nguyen QD, Brown DM, Marcus DM, Boyer DS, Patel S, Feiner L, et al. Ranibizumab for Diabetic Macular Edema. Ophthalmology. 2012 Apr;119(4):789–801.
719. Martin DF, Maguire MG, Fine SL, Ying G, Jaffe GJ, Grunwald JE, et al. Ranibizumab and Bevacizumab for Treatment of Neovascular Age-related Macular Degeneration. Ophthalmology. 2012 Jul;119(7):1388–98.
720. ClinicalTrials.gov. NCT00593450 Comparison of Age-related Macular Degeneration Treatments Trials: Lucentis-Avastin Trial [Internet]. NIH U.S. National Library of Medicine. 2017. Available from: https://clinicaltrials.gov/ct2/show/NCT00593450
721. ClinicalTrials.gov. A Phase III Study to Evaluate the Port Delivery System With Ranibizumab Compared With Monthly Ranibizumab Injections in Participants With Wet Age-Related Macular Degeneration (Archway) (NCT03677934) [Internet]. NIH U.S. National Library of Medicine. 2020. Available from: https://clinicaltrials.gov/ct2/show/NCT03677934
722. ClinicalTrials.gov. NCT04108156 This Study Will Evaluate the Efficacy, Safety, and Pharmacokinetics of the Port Delivery System With Ranibizumab in Participants With Diabetic Macular Edema Compared With Intravitreal Ranibizumab (Pagoda)

[Internet]. NIH U.S. National Library of Medicine. 2020. Available from: https://clinicaltrials.gov/ct2/show/NCT04108156?term=port+delivery+system&draw=2&rank=1
723. ClinicalTrials.gov. NCT03683251 Extension Study for the Port Delivery System With Ranibizumab (Portal) (Portal) [Internet]. NIH U.S. National Library of Medicine. 2020. Available from: https://clinicaltrials.gov/ct2/show/NCT03683251?term=port+delivery+system&draw=2&rank=2
724. Ilfeld BM, Morey TE, Enneking FK. Delivery Rate Accuracy of Portable, Bolus-Capable Infusion Pumps Used for Patient- Controlled Continuous Regional Analgesia. Regional Anesthesia and Pain Medicine. 2003 Nov;28(1):17–23.
725. Mackey NA, Ilsley AH, Owen H, Plummer JL. Laboratory evaluation of the Baxter Patient-Controlled Analgesia Infusor System: a disposable patient-controlled analgesia device. Anesthesia and analgesia. 1993 Jul;77(1):117–20.
726. Ghoseiri K, Allami M, Soroush MR, Rastkhadiv MY. Assistive technologies for pain management in people with amputation: a literature review. Military Medical Research. 2018 Dec 23;5(1):1.
727. Kumar Saloi D, Kanti Taye M, Paul S. Disposable Non-Mechanical Elastomeric Balloon Pump for Continuous Epidural Infusion: an Effective and Reliable Means for Postoperative Analgesia. Journal of Evolution of Medical and Dental Sciences. 2016;5(02):154–60.
728. Veurink M, Stella C, Tabatabay C, Pournaras CJ, Gurny R. Association of ranibizumab (Lucentis®) or bevacizumab (Avastin®) with dexamethasone and triamcinolone acetonide: An in vitro stability assessment. European Journal of Pharmaceutics and Biopharmaceutics. 2011 Jun;78(2):271–7.
729. Lim KS. Control and optimisation of fluid flow in glaucoma drainage device surgery. Eye. 2018 Feb 19;32(2):230–4.
730. Stirbu O, J VA, M S, E MG, O B, Tuesta D. A New Implant for Deep Sclerectomy: Esnoper®. Vijaya L, Dada T, Singh K, Spaeth GL, editors. Current Journal of Glaucoma Practice with DVD. 2011 Sep;5:40–3.
731. Sun DD, Ju TR, Lee PI. European Journal of Pharmaceutics and Biopharmaceutics Enhanced kinetic solubility profiles of indomethacin amorphous solid dispersions in poly (2-hydroxyethyl methacrylate) hydrogels. European Journal of Pharmaceutics and Biopharmaceutics. 2012;81(1):149–58.
732. Tomić SL, Mićić MM, Dobić SN, Filipović JM, Suljovrujić EH. Smart poly(2-hydroxyethyl methacrylate/itaconic acid) hydrogels for biomedical application. Radiation Physics and Chemistry. 2010 May;79(5):643–9.
733. Norde W. ENERGY AND ENTROPY OF PROTEIN ADSORPTION. Journal of Dispersion Science and Technology. 1992 Aug 27;13(4):363–77.
734. Luensmann D, Jones L. Protein deposition on contact lenses: the past, the present, and the future. Contact lens & anterior eye : the journal of the British Contact Lens Association. 2012 Apr;35(2):53–64.
735. Roach P, Farrar D, Perry CC. Interpretation of Protein Adsorption: Surface-Induced Conformational Changes. Journal of the American Chemical Society. 2005 Jun;127(22):8168–73.
736. Ishihara K. Revolutionary advances in 2-methacryloyloxyethyl phosphorylcholine polymers as biomaterials. Journal of Biomedical Materials Research - Part A. 2019;107(5):933–43.

737. Goreish HH, Lewis AL, Rose S, Lloyd AW. The effect of phosphorylcholine-coated materials on the inflammatory response and fibrous capsule formation: in vitro and in vivo observations. Journal of biomedical materials research Part A. 2004 Jan 1;68(1):1–9.
738. Iwasaki Y, Ishihara K. Phosphorylcholine-containing polymers for biomedical applications. Analytical and bioanalytical chemistry. 2005 Feb;381(3):534–46.
739. Iwasaki Y, Ishihara K. Cell membrane-inspired phospholipid polymers for developing medical devices with excellent biointerfaces. Science and Technology of Advanced Materials. 2012 Dec 1;13(6):064101.
740. Selan L, Palma S, Scoarughi GL, Papa R, Veeh R, Di Clemente D, et al. Phosphorylcholine impairs susceptibility to biofilm formation of hydrogel contact lenses. American journal of ophthalmology. 2009 Jan;147(1):134–9.
741. Goda T, Ishihara K, Miyahara Y. Critical update on 2-methacryloyloxyethyl phosphorylcholine (MPC) polymer science. Journal of Applied Polymer Science. 2015;132(16):n/a-n/a.
742. Lewis AL, Stratford PW. Phosphorylcholine-coated stents. Journal of long-term effects of medical implants. 2002;12(4):231–50.
743. Lewis AL. Phosphorylcholine-based polymers and their use in the prevention of biofouling. Colloids and Surfaces B: Biointerfaces. 2000 Oct;18(3–4):261–75.
744. Moro T, Takatori Y, Ishihara K, Konno T, Takigawa Y, Matsushita T, et al. Surface grafting of artificial joints with a biocompatible polymer for preventing periprosthetic osteolysis. Nature materials. 2004 Nov;3(11):829–36.
745. Vertellus Biomaterials. PC Technology - Products [Internet]. 2019. Available from: http://www.pcbiomaterials.com/Products.html
746. Azom. Phosphorylcholine Biomaterial Coatings Improve Biocompatibility of Medical Devices [Internet]. 2013 [cited 2015 Sep 10]. Available from: http://www.azom.com/article.aspx?ArticleID=5692
747. Lee SJ, Bourne GR, Chen X, Sawyer WG, Sarntinoranont M. Mechanical characterization of contact lenses by microindentation: Constant velocity and relaxation testing. Acta biomaterialia. 2008 Sep;4(5):1560–8.
748. Pal L, Joyce MK, Fleming PD, Law DS. A Simple Method for Calculation of the Permeability Coefficient of Porous Media. 2006;(September):10–6.
749. Haldon RA, Lee BE. Structure and permeability of porous films of poly(hydroxy ethyl methacrylate). British Polymer Journal. 1972 Nov;4(6):491–501.
750. Busby G a., Grant MH, MacKay SP, Riches PE. Confined compression of collagen hydrogels. Journal of Biomechanics. 2013;46(4):837–40.
751. Webber RE, Creton C, Brown HR, Gong JP. Large strain hysteresis and mullins effect of tough double-network hydrogels. Macromolecules. 2007 Apr;40(8):2919–27.
752. Migliaresi C, Nicodemo L, Nicolais L, Passerini P. Physical characterization of microporous poly(2-hydroxyethyl methacrylate) gels. Journal of biomedical materials research. 1981 May;15(3):307–17.
753. Sugioka K, Cheng Y. Ultrafast lasers—reliable tools for advanced materials processing. Light: Science & Applications. 2014;3(4):e149.
754. Holmes AS. Laser fabrication and assembly processes for MEMS. Proceedings of SPIE. 2001;4274:297–306.
755. Bonse J, Hohm S, Kirner S V., Rosenfeld A, Kruger J. Laser-Induced Periodic Surface Structures— A Scientific Evergreen. IEEE Journal of Selected Topics in Quantum

Electronics. 2017 May;23(3).
756. Jalil SA, Lai B, ElKabbash M, Zhang J, Garcell EM, Singh S, et al. Spectral absorption control of femtosecond laser-treated metals and application in solar-thermal devices. Light: Science & Applications. 2020 Dec 4;9(1):14.
757. Darcy H. Les Fontaines publiques de la Ville de Dijon. Victor Dalmont. 1856;647.
758. Darcy H, Darcy A. Darcy's law. 1856;(published).
759. Liu L, Chakma A, Feng X. Gas permeation through water-swollen hydrogel membranes. Journal of Membrane Science. 2008 Mar 5;310(1–2):66–75.
760. Popa I. Skin Biology Bases to dermal delivery of cosmetics and transdermal used in skin research lab : An overview Tape stripping. In: ULLA Summer School, Belgium. Leuven; 2017. p. 1–11.
761. Senyiğit T, Padula C, Ozer O, Santi P. Different approaches for improving skin accumulation of topical corticosteroids. International journal of pharmaceutics. 2009;380(1–2):155–60.
762. Saija A, Tomaino A, Trombetta D, Giacchi M, Pasquale A De, Bonina F. Influence of different penetration enhancers on in vitro skin permeation and in vivo photoprotective effect of flavonoids. 1998;175:85–94.
763. Imhof RE. In-vivo and in-vitro applications of closed-chamber TEWL measurements. In: Intensive Course in Dermato-cosmetic Science. London; 2007. p. 1–29.
764. Yanik MF, Cinar H, Cinar HN, Chisholm AD, Jin Y, Ben-Yakar A. Functional regeneration after laser axotomy. Nature. 2004;432(7019):822.
765. Ng S-F, Rouse J, Sanderson D, Eccleston G. A Comparative Study of Transmembrane Diffusion and Permeation of Ibuprofen across Synthetic Membranes Using Franz Diffusion Cells. Pharmaceutics. 2010 May 18;2(2):209–23.
766. Eisenberg DL, Koo EY, Hafner G, Schuman JS. In vitro flow properties of glaucoma implant devices. Ophthalmic surgery and lasers. 1999;30(8):662–7.
767. Grierson I, Saheb H, Kahook MY, Johnstone MA, Ahmed IIK, Schieber AT, et al. A Novel Schlemm's Canal Scaffold. Journal of Glaucoma. 2015 Aug;24(6):460–8.
768. Sheybani A, Reitsamer H, Ahmed IIK. Fluid Dynamics of a Novel Micro-Fistula Implant for the Surgical Treatment of Glaucoma. Investigative Opthalmology & Visual Science. 2015 Jul 25;56(8):4789.
769. Moore DJ, Hussain AA, Marshall J. Age-related variation in the hydraulic conductivity of Bruch's membrane. Investigative ophthalmology & visual science. 1995 Jun;36(7):1290–7.
770. Yasuda H, Lamaze CE, Peterlin A. Diffusive and hydraulic permeabilities of water in water-swollen polymer membranes. Journal of Polymer Science Part A-2: Polymer Physics. 1971 Jun;9(6):1117–31.
771. Elliott JE, Bowman CN. Effects of solvent quality during polymerization on network structure of cross-linked methacrylate copolymers. Journal of Physical Chemistry B. 2002;106(11):2843–7.
772. Gong JP. Why are double network hydrogels so tough? Soft Matter. 2010;6(12):2583.
773. Furukawa H, Horie K, Nozaki R, Okada M. Swelling-induced modulation of static and dynamic fluctuations in polyacrylamide gels observed by scanning microscopic light scattering. Physical review E, Statistical, nonlinear, and soft matter physics. 2003 Sep 22;68(3 Pt 1):031406.

774. Hoch G, Chauhan A, Radke CJ. Permeability and diffusivity for water transport through hydrogel membranes. Journal of Membrane Science. 2003 Apr;214(2):199–209.
775. Tuncaboylu DC, Sari M, Oppermann W, Okay O. Tough and self-healing hydrogels formed via hydrophobic interactions. Macromolecules. 2011;44(12):4997–5005.
776. Dragan ES. Design and applications of interpenetrating polymer network hydrogels. A review. Chemical Engineering Journal. 2014 May;243:572–90.
777. Haraguchi K. Synthesis and properties of soft nanocomposite materials with novel organic/inorganic network structures. Polymer Journal. 2011 Mar;43(3):223–41.
778. Abdurrahmanoglu S, Can V, Okay O. Design of high-toughness polyacrylamide hydrogels by hydrophobic modification. Polymer. 2009;50(23):5449–55.
779. Liu D, Wang T, Liu X, Tong Z. Accelerated cell sheet detachment by copolymerizing hydrophilic PEG side chains into PNIPAm nanocomposite hydrogels. Biomedical materials (Bristol, England). 2012 Oct;7(5):055008.
780. Chen Q, Chen H, Zhu L, Zheng J. Fundamentals of double network hydrogels. J Mater Chem B. 2015;3(18):3654–76.
781. Sun J-Y, Zhao X, Illeperuma WRK, Chaudhuri O, Oh KH, Mooney DJ, et al. Highly stretchable and tough hydrogels. Nature. 2012;489(7414):133–6.
782. Salahshoor H, Rahbar N. Multi-scale mechanical and transport properties of a hydrogel. Journal of the mechanical behavior of biomedical materials. 2014 Sep;37:299–306.
783. Sakai T, Matsunaga T, Yamamoto Y, Ito C, Yoshida R, Suzuki S, et al. Design and fabrication of a high-strength hydrogel with ideally homogeneous network structure from tetrahedron-like macromonomers. Macromolecules. 2008 Jul;41(14):5379–84.
784. Okumura Y, Ito K. The polyrotaxane gel: A topological gel by figure-of-eight cross-links. Advanced Materials. 2001;13(7):485–7.
785. Koga T, Tanaka F. Elastic properties of polymer networks with sliding junctions. The European physical journal E, Soft matter. 2005 Jun;17(2):225–9.
786. Gong JP, Katsuyama Y, Kurokawa T, Osada Y. Double-Network Hydrogels with Extremely High Mechanical Strength. Advanced Materials. 2003 Jul 17;15(14):1155–8.
787. Haque MA, Kurokawa T, Gong JP. Super tough double network hydrogels and their application as biomaterials. Polymer. 2012;53(9):1805–22.
788. Okumura K. Toughness of double elastic networks. Europhysics Letters (EPL). 2004 Aug;67(3):470–6.
789. Tanaka Y. A local damage model for anomalous high toughness of double-network gels. Europhysics Letters (EPL). 2007 Jun;78(5):56005.
790. Lee KY, Bouhadir KH, Mooney DJ. Degradation Behavior of Covalently Cross-Linked Poly(aldehyde guluronate) Hydrogels. Macromolecules. 2000 Jan;33(1):97–101.
791. Xie J, Liu X, Liang J, Luo Y. Swelling properties of superabsorbent poly(acrylic acid-co -acrylamide) with different crosslinkers. Journal of Applied Polymer Science. 2009 Apr 15;112(2):602–8.
792. Meakin JR, Hukins DWL, Imrie CT, Aspden RM. Thermal analysis of poly(2-hydroxyethyl methacrylate) (pHEMA) hydrogels. Journal of Materials Science: Materials in Medicine. 2003;14(1):9–15.
793. Šprincl L, Kopeček J, Lím D. Effect of the structure of poly(glycol

monomethacrylate) gel on the calcification of implants. Calcified Tissue Research. 1973 Dec;13(1):63–72.
794. Gulsen D, Chauhan A. Effect of water content on transparency, swelling, lidocaine diffusion in p-HEMA gels. Journal of Membrane Science. 2006 Feb;269(1–2):35–48.
795. Nie J, Du B, Oppermann W. Influence of Formation Conditions on Spatial Inhomogeneities in Poly(N -isopropylacrylamide) Hydrogels. Macromolecules. 2004 Aug;37(17):6558–64.
796. Sayil C, Okay O. Macroporous poly(N -isopropyl)acrylamide networks: formation conditions. Polymer. 2001 Aug;42(18):7639–52.
797. Hirokawa Y, Okamoto T, Kimishima K, Jinnai H, Koizumi S, Aizawa K, et al. Sponge-like Heterogeneous Gels: Hierarchical Structures in Poly(N -isopropylacrylamide) Chemical Gels As Observed by Combined Scattering and Confocal Microscopy Method. Macromolecules. 2008 Nov 11;41(21):8210–9.
798. Lou X, Munro S, Wang S. Drug release characteristics of phase separation pHEMA sponge materials. Biomaterials. 2004;25(20):5071–80.
799. Kulicke W-M, Kniewske R, Klein J. Preparation, characterization, solution properties and rheological behaviour of polyacrylamide. Progress in Polymer Science. 1982;8(4):373–468.
800. Bastide J, Leibler L. Large-scale heterogeneities in randomly cross-linked networks. Macromolecules. 1988 Aug;21(8):2647–9.
801. Seo JH, Matsuno R, Takai M, Ishihara K. Cell adhesion on phase-separated surface of block copolymer composed of poly(2-methacryloyloxyethyl phosphorylcholine) and poly(dimethylsiloxane). Biomaterials. 2009;30(29):5330–40.
802. Haaf F, Sanner A, Straub F. Polymers of N-Vinylpyrrolidone: Synthesis, Characterization and Uses. Polymer Journal. 1985 Jan 15;17:143.
803. Domingues JAL, Bonelli N, Giorgi R, Fratini E, Gorel F, Baglioni P. Innovative Hydrogels Based on Semi-Interpenetrating p(HEMA)/PVP Networks for the Cleaning of Water-Sensitive Cultural Heritage Artifacts. Langmuir. 2013 Feb 26;29(8):2746–55.
804. Laftah WA, Hashim S, Ibrahim AN. Polymer hydrogels: A review. Polymer - Plastics Technology and Engineering. 2011;50(14):1475–86.
805. Levine H, Slade L. Water as a plasticizer: physico-chemical aspects of low-moisture polymeric systems. In: Franks F, editor. Water Science Reviews 3. Cambridge: Cambridge University Press; 2010. p. 79–185.
806. Athawale VD, Lele V. Factors influencing absorbent properties of saponified starch-g-(acrylic acid-co-acrylamide). Journal of Applied Polymer Science. 2000 Sep 12;77(11):2480–5.
807. Lin J, Tang Q, Wu J. The synthesis and electrical conductivity of a polyacrylamide/Cu conducting hydrogel. Reactive and Functional Polymers. 2007 Jun;67(6):489–94.
808. Jiang Z, Cao X, Guo L. Synthesis and swelling behavior of poly (acrylic acid-acryl amide-2-acrylamido-2-methyl-propansulfonic acid) superabsorbent copolymer. Journal of Petroleum Exploration and Production Technology. 2017 Mar 27;7(1):69–75.
809. Cheng W-M, Hu X-M, Zhao Y-Y, Wu M-Y, Hu Z-X, Yu X-T. Preparation and swelling properties of poly(acrylic acid-co-acrylamide) composite hydrogels. e-Polymers.

2017 Jan 1;17(1):95–106.
810. La Y-H, Sooriyakumaran R, McCloskey BD, Allen RD, Freeman BD, Al-Rasheed R. Enhancing water permeability of fouling-resistant POSS–PEGM hydrogels using 'addition–extraction' of sacrificial additives. Journal of Membrane Science. 2012 May;401–402:306–12.
811. Karadağ E, Saraydin D. Swelling of superabsorbent acrylamide/sodium acrylate hydrogels prepared using multifunctional crosslinkers. Turkish Journal of Chemistry. 2002;26(6):863–75.
812. Baselga J, Hernandez-Fuentes I, Pierola IF, Llorente M a. Elastic properties of highly crosslinked polyacrylamide gels. Macromolecules. 1987;20(12):3060–5.
813. Nossal R. Network formation in polyacrylamide gels. Macromolecules. 1985;18(1):49–54.
814. Zhu J, Marchant RE. Design properties of hydrogel tissue-engineering scaffolds. Expert Review of Medical Devices. 2011 Sep 9;8(5):607–26.
815. Zhang F-A, Yu C-L, Zhu X-H, Wei C. The effect of initiator system on acrylate emulsion copolymerization with higher hydroxyl monomer content. Polymers for Advanced Technologies. 2006 Jul;17(7–8):608–11.
816. CDC. The National Institute for Occupational Safety and Health (NIOSH) [Internet]. Table of IDLH values. 1994. Available from: https://www.cdc.gov/niosh/idlh/109999.html
817. Nagy ZZ, McAlinden C. Femtosecond laser cataract surgery. Eye and Vision. 2015 Dec 30;2(1):11.
818. Trikha S, Turnbull AMJ, Morris RJ, Anderson DF, Hossain P. The journey to femtosecond laser-assisted cataract surgery: new beginnings or a false dawn? Eye. 2013 Apr 1;27(4):461–73.
819. Chen X, Dunn AC, Sawyer WG, Sarntinoranont M. A biphasic model for micro-indentation of a hydrogel-based contact lens. Journal of biomechanical engineering. 2007 Apr;129(2):156–63.
820. Dare E V., Griffith M, Poitras P, Kaupp JA, Waldman SD, Carlsson DJ, et al. Genipin cross-linked fibrin hydrogels for in vitro human articular cartilage tissue-engineered regeneration. Cells Tissues Organs. 2009;190(6):313–25.
821. Wisniewski S, Kim SW. Permeation of water through poly(2-hydroxyethyl methacrylate) and related polymers: Temperature effects. Journal of Membrane Science. 1980 Jan;6:309–18.
822. Monticelli M V, Chauhan A, Radke CJ. The effect of water hydraulic permeability on the settling of a soft contact lens on the eye. Current eye research. 2005 May;30(5):329–36.
823. Pishko GL, Lee S, Wanakule P, Sarntinoranont M. Hydraulic Permeability of a Hydrogel-Based Contact Lens Membrane for Low Flow Rates. 2006;
824. Refojo MF. Permeation of water through some hydrogels. Journal of Applied Polymer Science. 1965 Oct;9(10):3417–26.
825. White L. The permeability of an Acrylamide polymer gel. 1960;64(5):1563–5.
826. Höhne P, Tauer K. How much weighs the swelling pressure. Colloid and Polymer Science. 2014;292(11):2983–92.
827. Wack H, Ulbricht M. Method and model for the analysis of gel-blocking effects during the swelling of polymeric hydrogels. Industrial and Engineering Chemistry Research. 2007;46(1):359–64.
828. Ganji F, Vasheghani-Farahani S, Vasheghani-Farahani E. Theoretical Description

of Hydrogel Swelling: A Review. Iranian Polymer Journal. 2010;19(5):375–98.
829. Berg JC, Lahrman HF, Roe CD. Particulate, absorbant, polymeric composition containing interparticle crosslinked aggregates. United States, US Patent 5,300,565. 1994.
830. Flory PJ, Rehner J. Statistical mechanics of cross-linked polymer networks II. Swelling. The Journal of Chemical Physics. 1943;11(11):521–6.
831. Flory PJ, Rehner J. Statistical mechanics of cross-linked polymer networks I. Rubberlike elasticity. The Journal of Chemical Physics. 1943;11(11):512–20.
832. Neervannan S, Dias LS, Southard MZ, Stella VJ. convective dissolution model.pdf. Pharmaceutical Research. 1994;11(9):1288–95.
833. eye wiki. Glaucoma_Drainage_Devices [Internet]. 2015. Available from: http://eyewiki.org/Glaucoma_Drainage_Devices
834. Friedman NJ. MIGS [Internet]. 2014. Available from: http://www.ophthalmologyweb.com/Featured-Articles/167574-Update-on-Minimally-Invasive-Glaucoma-Surgery/
835. Burt K, Freeman S, Jeanbart L, Tee L, Santos M. GDDs [Internet]. 2006. Available from: http://biomed.brown.edu/Courses/BI108/2006-108websites/group02glaucoma/devices.html

Chapter 7 Appendices

7.1. Appendix 1

7.1.1 Dynamic column method

For hydraulic conductivity calculation, Darcy's law is used. It states that flow is proportional to the applied pressure. Thus for a membrane disc of radius a (m), flow per unit area is designated by:

$$\frac{\mathbf{F}}{\pi\, \mathbf{a^2}} = \mathbf{L\ P}, \qquad (1)$$

Where L is the hydraulic conductivity of the membrane (m/s/Pa) and P is the applied pressure (Pa). Since

$$\boldsymbol{F} = \frac{\boldsymbol{dV}}{\boldsymbol{dt}}, \qquad (2)$$

$$\frac{\mathbf{dV}}{\mathbf{dt}} = \pi\, \mathbf{a^2\ L\ P} (3)$$

Pressure due to the column of fluid is given by P = p $\boldsymbol{g}$ h

Where p is the density of water (1000 Kg/m^3), g is the gravitational constant 9.81 m/s^2 and h is the height of the column in meters. Hence:

$$\frac{\mathbf{dV}}{\mathbf{dT}} = \pi\, \mathbf{a^2\ L\ p\ g\ h} \qquad (4)$$

After a time dt, change in volume is dV = - π r^2 dh, where r is the radius of the capillary column, i.e., column height falls. Therefore:

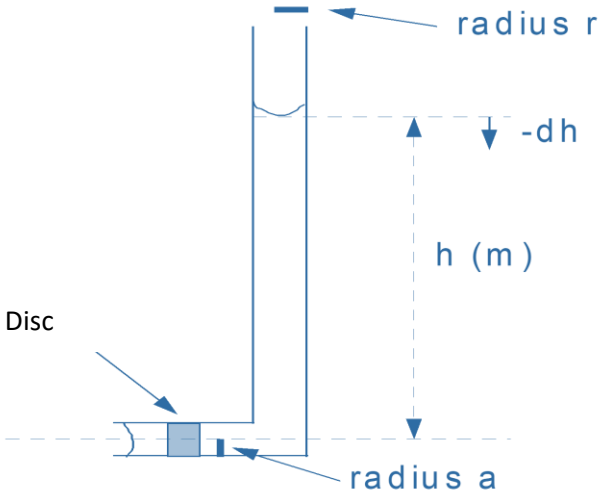

Figure 7-1. A schematic representation of the apparatus used in dynamic approach for aqueous permeability assessment.

$$-\frac{\pi r^2 dh}{dt} = \pi a^2 L \rho g h, \qquad (5)$$

Rearranging:

$$\frac{dh}{h} = -\frac{a^2 L \rho g}{r^2} dt, \quad (6)$$

Integrating:

$$\int \frac{dh}{h} = -\frac{a^2 L \rho g}{r^2} \int dt, \qquad (7)$$

Thus,

$$\ln h = -\frac{a^2 L \rho g}{r^2} t + c, \qquad (8)$$

Where c is the constant of integration. Boundary conditions are: t= 0, h = h_o and hence c = ln h_o

Hence:

$$\ln h = -\frac{a^2 L \rho g t}{r^2} + \ln h_0 , \quad (9)$$

$$\ln h - \ln h_0 = \frac{a^2 L \rho g t}{r^2} , \qquad (10)$$

$$\ln\left(\frac{h}{h_0}\right) = -\frac{a^2 L \rho g t}{r^2}, \qquad (11)$$

From $\log_b a = c$, $b^c = a$

$$\frac{h}{h_0} = e^{-\frac{a^2 L \rho g t}{r^2}}, \qquad (12)$$

$$h = h_0 e^{-\frac{a^2 L \rho g t}{r^2}}, \qquad (13)$$

From equation (11) a plot of ln h/h_0 against t should yield a straight line of gradient G. So,

$$\frac{\left[\ln\left(\frac{h}{h_0}\right)=\right]}{t} = G \quad (14)$$

Where, h and h_{0_i} are the final and initial heights of the water column (metres) and t is the time (seconds) between the final and initial measurement of the water column height.

And,

$$G = -\frac{a^2 L \rho g}{r^2} \qquad (15)$$

This gradient, G can be obtained by linear regression.

7.2. Appendix 2

Table 7-1. Compositions of all hydrogel formulations tested for aqueous permeability

Hydrogel	HEMA (mL)	MPC (g)	EMA (g)	HPMA (g)	VP (g)	PVP (g)	PC1059 (g)	EGDMA (µL)	PEGDMA 700 (g)	PEGDMA 2000 (g)	MBAM (g)	AIBN (g)	APS (g)	H_2O (mL)	Dilution (formulation: diluent)
1015	8.46	1.41	0.00	0.00	0.00	0.00	0.00	70.0	0.00	0.00	0.00	0.05	0.00	0.00	-
M1	15.80	1.41	0.00	0.00	0.00	0.00	0.00	70.0	0.00	0.00	0.00	0.05	0.00	0.00	-
M2	3.95	0.00	0.00	0.00	0.00	0.00	0.00	50.0	0.00	0.00	0.00	0.05	0.00	0.00	-
M3	7.46	0.00	0.00	0.00	0.00	0.00	0.00	50.0	0.00	0.00	0.00	0.05	0.00	1.95	-
M4	5.59	0.00	0.00	0.00	0.00	0.00	0.00	50.0	0.00	0.00	0.00	0.00	0.05	1.95	-
M5	1.86	0.00	0.00	0.00	0.00	0.00	0.00	50.0	0.00	0.00	0.00	0.00	0.05	3.95	-
M7	2.80	0.25	0.00	0.00	0.00	0.00	0.00	50.0	0.00	0.00	0.00	0.00	0.05	6.54	
M9	1.89	0.08	0.00	0.00	0.00	0.00	0.00	50.0	0.00	0.00	0.00	0.00	0.05	8.06	-
M19	5.84	0.00	0.00	0.00	0.00	0.00	0.00	50.0	0.00	0.00	0.00	0.00	0.05	4.11	-
M20	4.83	0.00	0.00	0.00	0.00	0.00	0.00	50.0	0.00	0.00	0.00	0.00	0.05	5.12	-
M21	3.84	0.00	0.00	0.00	0.00	0.00	0.00	50.0	0.00	0.00	0.00	0.00	0.05	6.12	-
M22	2.80	0.00	0.00	0.00	0.00	0.00	0.00	50.0	0.00	0.00	0.00	0.00	0.05	7.09	-
M23	5.84	0.00	0.00	0.00	0.00	0.00	0.00	50.0	0.00	0.00	0.00	0.00	0.05	4.11	-
M24	4.83	0.00	0.00	0.00	0.00	0.00	0.00	50.0	0.00	0.00	0.00	0.00	0.05	5.12	-
M25	3.84	0.00	0.00	0.00	0.00	0.00	0.00	50.0	0.00	0.00	0.00	0.00	0.05	6.12	-
M26	2.80	0.00	0.00	0.00	0.00	0.00	0.00	50.0	0.00	0.00	0.00	0.00	0.05	7.09	-
M27	5.84	0.00	0.00	0.00	0.00	0.00	0.00	50.0	0.00	0.00	0.00	0.00	0.05	4.11	-
M28	4.83	0.00	0.00	0.00	0.00	0.00	0.00	50.0	0.00	0.00	0.00	0.00	0.05	5.12	-
M29	3.84	0.00	0.00	0.00	0.00	0.00	0.00	50.0	0.00	0.00	0.00	0.00	0.05	6.12	-
M30	2.80	0.00	0.00	0.00	0.00	0.00	0.00	50.0	0.00	0.00	0.00	0.00	0.05	7.09	-
M31	5.84	0.00	0.00	0.00	0.00	0.00	0.00	50.0	0.00	0.00	0.00	0.00	0.05	4.11	-
M32	4.83	0.00	0.00	0.00	0.00	0.00	0.00	50.0	0.00	0.00	0.00	0.00	0.05	5.12	-
M33	3.84	0.00	0.00	0.00	0.00	0.00	0.00	55.0	0.00	0.00	0.00	0.00	0.05	6.12	-
M34	2.80	0.00	0.00	0.00	0.00	0.00	0.00	50.0	0.00	0.00	0.00	0.00	0.05	7.09	-
M35	5.84	0.00	0.00	0.00	0.00	0.00	0.00	50.0	0.00	0.00	0.00	0.00	0.05	4.11	-

Hydrogel	HEMA (mL)	MPC (g)	EMA (g)	HPMA (g)	VP (g)	PVP (g)	PC1059 (g)	EGDMA (µL)	PEGDMA 700 (g)	PEGDMA 2000 (g)	MBAM (g)	AIBN (g)	APS (g)	H_2O (mL)	Dilution (formulation: diluent)
M36	4.83	0.00	0.00	0.00	0.00	0.00	0.00	50.0	0.00	0.00	0.00	0.00	0.05	5.12	-
M37	3.84	0.00	0.00	0.00	0.00	0.00	0.00	55.0	0.00	0.00	0.00	0.00	0.05	6.12	-
M38	2.80	0.00	0.00	0.00	0.00	0.00	0.00	50.0	0.00	0.00	0.00	0.00	0.05	7.09	-
M39	23.70	4.24	0.00	0.00	0.00	0.00	0.00	74.0	0.00	0.00	0.00	0.05	0.00	0.00	-
M40	23.70	4.24	0.00	0.00	0.00	0.00	0.00	74.0	0.00	0.00	0.00	0.05	0.00	0.00	-
M41	23.70	4.24	0.00	0.00	0.00	0.00	0.00	74.0	0.00	0.00	0.00	0.05	0.00	0.00	-
CM1	8.82	0.41	0.00	0.00	0.00	0.00	0.00	70.0	0.00	0.00	0.00	0.05	0.00	0.00	-
CM2	8.35	0.91	0.00	0.00	0.00	0.00	0.00	70.0	0.00	0.00	0.00	0.05	0.00	0.00	-
CM4	7.90	1.92	0.00	0.00	0.00	0.00	0.00	70.0	0.00	0.00	0.00	0.05	0.00	0.00	-
CM5	6.96	2.41	0.00	0.00	0.00	0.00	0.00	70.0	0.00	0.00	0.00	0.05	0.00	0.00	-
CM6	1.98	0.35	0.00	0.00	0.00	0.02	0.00	20.0	0.00	0.00	0.00	0.05	0.00	0.00	-
CM7	0.99	0.18	0.00	0.00	0.00	0.00	0.00	10.0	0.00	0.00	0.00	0.05	0.00	1.00	-
CM10	7.90	0.71	0.00	0.00	0.00	0.00	0.09	40.0	0.00	0.00	0.00	0.05	0.00	0.00	-
CM11	9.20	0.00	0.00	0.00	0.00	0.00	0.08	70.0	0.00	0.00	0.00	0.05	0.00	0.00	-
CM12	3.95	1.41	0.00	4.23	0.00	0.00	0.00	70.0	0.00	0.00	0.00	0.05	0.00	0.00	-
CM13	3.95	1.41	4.23	0.00	0.00	0.00	0.00	70.0	0.00	0.00	0.00	0.05	0.00	0.00	-
CM17	6.42	1.50	0.00	0.00	15.00	0.00	0.00	74.0	0.00	0.00	0.00	0.05	0.00	0.00	-
CM18	5.49	1.50	0.00	0.00	25.01	0.00	0.00	74.0	0.00	0.00	0.00	0.05	0.00	0.00	-
CM19	4.55	1.50	0.00	0.00	35.01	0.00	0.00	74.0	0.00	0.00	0.00	0.05	0.00	0.00	-
CM20	2.69	1.50	0.00	0.00	45.01	0.00	0.00	74.0	0.00	0.00	0.00	0.05	0.00	0.00	-
CM21	3.95	1.41	0.00	0.00	55.01	0.00	0.00	74.0	0.00	0.00	0.00	0.05	0.00	0.00	-
CX1	7.90	1.41	0.00	0.00	0.00	0.00	0.00	35.0	0.00	0.00	0.00	0.05	0.00	0.00	-
CX2	7.90	1.41	0.00	0.00	0.00	0.00	0.00	140	0.00	0.00	0.00	0.05	0.00	0.00	-
CX3	7.90	1.42	0.00	0.00	0.00	0.00	0.00	700	0.00	0.00	0.00	0.05	0.00	0.00	-
CX4	7.90	1.41	0.00	0.00	0.00	0.00	0.00	0.00	0.07	0.00	0.00	0.05	0.00	0.00	-
CX5	7.90	1.41	0.00	0.00	0.00	0.00	0.00	0.00	0.00	0.08	0.00	0.05	0.00	0.00	-
CX6	7.89	1.41	0.00	0.00	0.00	0.00	0.00	0.00	0.00	0.00	0.04	0.05	0.00	0.00	-
CX7	7.90	1.41	0.00	0.00	0.00	0.00	0.00	0.00	0.00	0.00	0.15	0.05	0.00	0.00	-
CX10	7.90	1.41	0.00	0.00	0.00	0.00	0.00	210	0.00	0.00	0.00	0.05	0.00	0.00	-

Hydrogel	HEMA (mL)	MPC (g)	EMA (g)	HPMA (g)	VP (g)	PVP (g)	PC1059 (g)	EGDMA (µL)	PEGDMA 700 (g)	PEGDMA 2000 (g)	MBAM (g)	AIBN (g)	APS (g)	H_2O (mL)	Dilution (formulation: diluent)
CX11	7.90	1.41	0.00	0.00	0.00	0.00	0.00	20.0	0.00	0.00	0.00	0.02	0.00	6.45	-
CX15	2.80	0.25	0.00	0.00	0.00	0.00	0.00	48.0	0.00	0.00	0.05	0.00	0.05	6.70	-
CX16	2.80	0.50	0.00	0.00	0.00	0.00	0.00	0.00	0.00	0.00	0.25	0.00	0.05	6.25	-
I1	7.90	1.41	0.00	0.00	0.00	0.00	0.00	70.0	0.00	0.00	0.00	0.02	0.00	0.00	-
I2	7.90	1.41	0.00	0.00	0.00	0.00	0.00	70.0	0.00	0.00	0.00	1.00	0.00	0.00	-
I3	7.90	1.42	0.00	0.00	0.00	0.00	0.00	70.0	0.00	0.00	0.00	0.00	0.05	0.20	-
D1	7.90	1.41	0.00	0.00	0.00	0.00	0.00	70.0	0.00	0.00	0.00	0.05	0.00	0.00	3:1
D2	7.90	1.41	0.00	0.00	0.00	0.00	0.00	70.0	0.00	0.00	0.00	0.05	0.00	0.00	3:1:1
D3	7.90	1.41	0.00	0.00	0.00	0.00	0.00	70.0	0.00	0.00	0.00	0.05	0.00	0.00	1:1
D4	7.80	1.41	0.00	0.00	0.00	0.00	0.00	70.0	0.00	0.00	0.00	0.05	0.00	0.00	1:1
D12	7.90	1.41	0.00	0.00	0.00	0.00	0.00	0.00	0.00	0.00	0.07	0.00	0.01	0.00	4:1
D14	7.90	1.41	0.00	0.00	0.00	0.00	0.00	0.00	0.00	0.00	0.07	0.00	0.01	0.00	1:1
D15	6.40	1.50	0.00	0.00	1.50	0.00	0.00	70.0	0.00	0.00	0.00	0.05	0.00	0.00	1:1
D16	5.49	1.50	0.00	0.00	2.50	0.00	0.00	70.0	0.00	0.00	0.00	0.05	0.00	0.00	1:1
D17	4.60	1.50	0.00	0.00	3.50	0.00	0.00	70.0	0.00	0.00	0.00	0.05	0.00	0.00	1:1
D20	4.00	1.41	0.00	0.00	4.23	0.00	0.00	70.0	0.00	0.00	0.00	0.05	0.00	0.00	1:1
D21	7.90	1.41	0.00	0.00	0.00	0.00	0.00	70.0	0.00	0.00	0.00	0.05	0.00	0.00	0.8:1

D1–D3 were diluted with t-butanol; **D4** was diluted with glycerol; **D12, D14** and **D21** were diluted with THF; **D15–D20** were diluted with VP and THF (final amounts indicated in the table).